Dissertation zur Erlangung des Doktorgrades der Fakultät für Chemie
und Pharmazie der Ludwig-Maximilians-Universität München

From Lattice to Kinetics —

Molecular Engineering of Covalent Organic Frameworks for Rapid Energy Storage

Apeksha Singh

aus

Meerut, India

2025

Erklärung

Diese Dissertation wurde im Sinne von §7 der Promotionsordnung vom 28. November 2011 von Herrn Prof. Dr. Thomas Bein betreut.

Eidesstattliche Versicherung

Diese Dissertation wurde eigenhändig und ohne unerlaubte Hilfe erarbeitet.

München, den 21.11.2025

Apeksha Singh

Dissertation eingereicht am 21.11.2025

1. Gutachter: Prof. Dr. Thomas Bein

2. Gutachterin: Prof. Dr. Jennifer Lilia Marguerite Rupp

Mündliche Prüfung am 16.12.2025

Acknowledgements

This thesis represents the collective support, guidance, and encouragement of many individuals and institutions, to whom I am sincerely indebted.

First, I would like to express my profound gratitude to Prof. Dr. Thomas Bein for the opportunity to pursue my doctoral research in his group at LMU. His supervision, encouragement, and patience have been invaluable throughout this journey. I am especially thankful for the academic freedom he granted me to peruse a research direction in battery technology, distinct from the main scientific focus of the other group members. This trust allowed me to work independently, while his expertise and thoughtful advice provided essential guidance along the way. I am grateful to Thomas for securing the funding that not only made my projects possible but also provided access to cutting-edge facilities, valuable collaborations, and the opportunity to undertake ambitious research. I am also grateful for the many opportunities he created to participate in renowned scientific conferences, occasions that exposed me to inspiring speakers and enabled me to present my work before discerning audiences. Beyond science, I learned from his wisdom in our many conversations, and his support through difficult moments has left a lasting mark on me. Moving from Japan to Germany was a leap into the unknown, but thanks to him this journey has been not only intellectually and professionally rewarding but also personally transformative.

I extend my sincere thanks to my second supervisor Prof. Dr. Jennifer Rupp at TUM. Her openness, guidance, and encouragement have been deeply appreciated. Early in my doctoral journey, I was inspired by her work and presence in the scientific community; it has since been both an honor and a privilege to collaborate with her. Her leadership in science and her presence as a role model in STEM have been a continual source of motivation.

I am indebted to my collaborators at TU Dresden, Prof. Dr. Thomas Heine and Dr. Preeti Bahuriyal. Prof. Heine’s expertise has been crucial for our joint projects, while Preeti’s insights, reliability, and complementary knowledge have been invaluable. Her dedication and collegiality made our collaboration both productive and rewarding.

I would also like to thank Lucie for generously sharing her expertise in electrochemistry, to Roman, who from my very first day at AK Bein was a patient and generous unofficial mentor, and to Dominic (Domi), for his creative spirit in designing new materials. I also thank Dr. Steffen Schmitt and Dr. Markus Döblinger for their expertise in SEM and TEM, and for countless insightful exchanges.

To the entire AK Bein group, thank you for the stimulating working environment, for the readiness to help, and for the countless memories, whether in the lab or over casual conversations. Special thanks go to Tina, who kept our experiments running smoothly by taking care of so much behind the scenes, and to Corinna, whose kindness and support extended far beyond paperwork and visa matters, she has been a constant source of practical help and reassurance.

Of course, no account of my time here would be complete without mentioning the *"guys from downstairs"*, Marina, Domi, Ignacio (Nacho), Tianhao (Toni), Shizhe (Shorsch), and Klaudija. You all were my very first friends in Germany, welcoming me wholeheartedly into this new chapter of life. Together we created memories that I will always carry with me, so many that it's hard to single out just one. From this group, two friendships in particular have become truly precious, and I am excited to see how our paths continue to unfold in the years to come.

AK Bein has been not only a workplace but also a constant pillar, a source of stability and community since I moved to Germany, and it has been a privilege to be part of this scientific group.

On a more personal note, I want to thank my partner Jan, whom I was fortunate to meet during my Ph.D. journey at LMU. Despite the challenges and pressures of pursuing his own doctorate, he has been my anchor, and my companion through every high and low. His dedication and work ethic have been a constant source of motivation throughout this journey.

Finally, I wish to thank my family. My sister has always been my fiercest cheerleader, setting an example of integrity and hard work that continues to inspire me. My mother has given me the courage to dream ambitiously, the strength to stand independently, and the reassurance that no distance can diminish her support. I cannot close this chapter without remembering my father and grandfather, whose values and persona remain a guiding light in my life.

To all of you, thank you for shaping this chapter of my life. This thesis is as much a reflection of your support as it is of my own effort.

Abstract

Covalent organic frameworks (COFs) have garnered considerable interest as materials for energy storage systems (ESSs) owning to their robust porous architecture, flexibility in selecting redox-active building blocks, and their well-defined pores to facilitate directional and accelerated charge as well as ion transport. While conventional electrodes are frequently tied to scarce and environmentally damaging mining practices, traditional liquid electrolytes introduce inherent safety hazards, and together, these limitations highlight the promise of next-generation technologies derived from abundant, sustainable resources that ensure cleaner and safer energy storage. COFs unite ultralight architectures with exceptional tunability, porosity, and reliance on earth-abundant elements, placing them among one of the most promising candidates for next-generation sustainable energy storage. This thesis centers on the development of COF-based battery components, and investigation on the influence of their molecular architecture on the electrochemical dynamics and overall rate performance of the battery system:

In the first study, two Na-ion quasi-solid-state electrolytes (QSSEs) incorporating anionic COFs, $TpPaSO_3Na$ and $Tp(PaSO_3Na)_2$, were investigated as solid scaffolds, differing in pore width and sulfonate group density. The ionic liquid, *N*-methyl-*N*-propylpyrrolidinium bis(fluorosulfonyl)imide ($Pyr_{13}FSI$), was incorporated at varying mass fractions as the liquid component, yielding COF-based ionogel composites with impressive thermal stability (~375–431 °C), high ionic conductivities ($\sigma_i \sim 10^{-3}$ S cm^{-1}), and elevated sodium-ion transference numbers ($t_{Na^+} \sim 0.67$–0.79). Ab initio molecular dynamics (AIMD) simulations highlight how tailoring nanochannel dimensions and the concentration of anionic moieties along the pore walls governs sodium-ion transport, revealing a synergistic mechanism in which sodium-ions migrate via hopping along the anionic COF backbone while simultaneously undergoing "vehicle-type" transport through the solvated ionic liquid phase.

The second project shifts focus towards designing a bipolar 2D COF electrode, engineered for high-rate kinetics to enhance electrochemical performance, and evaluated across diverse Li-ion battery configurations. A novel highly crystalline bipolar-type WTTF-COF, was synthesized by integrating *p*-type electro-active *N*,*N*,*N′*,*N′*-tetrakis(4-aminophenyl)-1,4-phenylenediamine (W) and 4,4′,4″,4‴-([2,2'-bi(1,3-dithiolylidene)]-4,4′,5,5′-tetrayl)tetrabenzaldehyde (TTF) molecular building blocks via *n*-type imine linkages. The combination of electron-rich and electron-deficient redox functionalities,

along with π-π interactions between the COF layers, lead to a 12 e^- dual-ion redox chemistry per unit cell, corresponding to a high theoretical capacity of 315 mAh g^{-1}. In a Li-ion half-cell configuration, the WTTF electrode delivered an efficient pseudocapacitive dominated charge-storage mechanism, with reversible specific capacities of 271 mAh g^{-1} at 0.1 A g^{-1} (~0.3C rate) and 66 mAh g^{-1} at 5.0 A g^{-1} (~16C rate) within a stable wide potential window of 0.1–3.6 V versus Li/Li^+, storing both Li^+ and PF_6^- anions as charge carriers. Distinct diffusion pathways and diffusion coefficients for Li^+ and PF_6^- transport are resolved through electrochemical impedance spectroscopy (EIS) and theoretical modeling, revealing the intrinsic kinetic advantages of the framework. Furthermore, symmetric all-organic dual-ion full cells demonstrate the bipolar versatility of WTTF-COF, operating effectively as both cathode and anode, with enhanced pseudocapacitive/capacitive charge-storage dynamics, retaining reversibility and stability at scan rates as high as 200 mV s^{-1}.

Building upon the insights gained from the first two projects, we further probed the electrochemical kinetics of a novel bipolar PyTTF-COF electrode, focusing on the role of the COF scaffold as well as the influence of electrolyte environment, including ionic composition and concentration. To this end, we designed a 2D imine linked PyTTF-COF, synthesized by integrating a *p*-type 4,4',4'',4'''-([2,2'-bi(1,3-dithiolylidene)]-4,4',5,5'-tetrayl)tetraaniline ($TTF\text{-}NH_2$) building unit, and a novel *n*-type 7,7',7'',7'''-(pyrene-1,3,6,8-tetrayl)tetrakis(benzo[*c*][1,2,5]thiadiazole-4-carbaldehyde) (PyBT-CHO) monomer, forming a donor–acceptor (D–A) framework with a low optical band gap of ~1.84 eV, and a total 16 e^- dual-ion redox chemistry per unit cell. To investigate the dual-ion redox dynamics of PyTTF-COF, Li-ion half-cells were assembled by employing the PyTTF electrode to systematically probe the role of electrolyte composition. When paired with 1 ᴍ $LiPF_6$ or LiTFSI electrolytes, the electrode exhibited a broad operating window of 0.1–3.6 V vs. Li/Li^+. Strikingly, LiTFSI enabled far superior pseudocapacitive charge-storage kinetics and ion transport compared to $LiPF_6$, as reflected in specific capacities of 286 mAh g^{-1} and 184 mAh g^{-1} at 0.3 A g^{-1} (~1C rate), respectively. Beyond anion identity, concentration effects proved equally decisive; tuning LiTFSI from 1 to 3 ᴍ established clear correlations between salt content, ion-storage dynamics, and interfacial charge-transfer resistance, ultimately tailoring the overall redox-behavior of COF-based dual-ion batteries.

List of Abbreviations

2D	Two dimensional
3D	Three dimensional
AGGs	Ionic aggregates
AIBs	Aluminum-ion batteries
AIMD	Ab inito molecular dynamics
BNEF	Bloomberg new energy finance
CE	Counter electrode
CEI	Cathode-electrolyte interphase
CIPs	Contact ion pairs
CNTs	Carbon nanotubes
COFs	Covalent organic frameworks
CONs	Covalent organic nanosheets
CV	Cyclic voltammetry
D–A	Donor–acceptor
DFT	Density functional theory
EDG	Electron donating group
EDLCs	Electric double layer capacitors
EDX	Energy-dispersive X-ray spectroscopy
EEC	Equivalent electric circuit
EIS	Electrochemical impedance spectroscopy
EM	Electron microscopy
EVs	Electric vehicles
ESSs	Energy storage systems
EWG	Electron withdrawing group
FTIR	Fourier-transform infrared spectroscopy
GCD	Galvanostatic charge discharge cycling
HCEs	High concentration electrolytes
HOMO	Highest occupied molecular orbital
IEA	International energy agency

ILs	Ionic liquids
KIBs	Potassium-ion batteries
LHCEs	Localized high-concentration electrolytes
LIBs	Lithium-ion batteries
LSV	Linear sweep voltammetry
LUMO	Lowest unoccupied molecular orbital
MESP	Molecular electrostatic potential analysis
MNC	Magnesium nickel cobalt
MOFs	Metal organic frameworks
MSD	Mean square displacement
NEB	Nudged elastic band
NMR	Nuclear magnetic resonance
OEMs	Organic electrode materials
PXRD	Powder X-ray diffraction
QSSEs	Quasi-solid-state electrolytes
RE	Reference electrode
SEI	Solid-electrolyte interphase
SEM	Scanning electron microscopy
SHE	Standard hydrogen electrode
SIBs	Sodium-ion batteries
SSEs	Solid-state electrolytes
TEM	Transmission electron microscopy
TGA	Thermogravimetric analysis
TM	Transition metal
TRL	Technology readiness level
UV-vis	Ultraviolet-visible spectroscopy
VAC	Vapor-assisted conversion
WE	Working electrode
XPS	X-ray photoelectron spectroscopy
ZIBs	Zinc-ion batteries

Table of Contents

1

Introduction

This chapter provides an overview of the research subject presented in this thesis. It begins by establishing the broader context and significance of the field of secondary-ion batteries and covalent organic frameworks, highlighting the key challenges and gaps in the current state of knowledge. The motivation behind undertaking this research is discussed, along with its relevance to the field. This chapter also defines the specific objectives of the study, presenting the research questions that guide the investigation, aiming to orient the reader towards a clear understanding of the purpose and direction of the thesis, establishing a strong foundation for the research projects that follow.

NOTE: More specified introductions to the individual topics are presented at the beginning of each research chapter throughout the thesis.

1.1. Secondary-ion batteries

Secondary-ion batteries are a class of energy storage systems (ESSs) that have revolutionized modern energy storage by enabling efficient, portable, and reusable power sources for a wide range of applications, from consumer portable electronics to electric vehicles (EVs), and renewable energy systems. The term "*secondary*" refers to their rechargeability, distinguishing them from "*primary*" batteries, which are typically single-use.[1,2] Primary batteries rely on irreversible chemical reactions that lead to their eventual depletion on discharge, and once completely discharged, they must be discarded, contributing to environmental waste and necessitating resource-intensive production processes for replacements. The quest for sustainable energy solutions led to the origin of secondary (rechargeable) batteries, allowing for multiple cycles of use, which not only extends their lifespan but also reduces waste and resource consumption.

The first successful secondary battery was the lead-acid battery, invented by French scientist Gaston Planté in 1859.[3,4] It marked a significant leap in the energy storage, as it could be recharged by reversing the chemical reaction that occurred during the discharge process. This innovation laid the groundwork for a wide range of rechargeable battery technologies, including nickel-cadmium (NiCd) and nickel-metal hydride (NiMH) batteries, which gained popularity in the early 20th century.[3,5] However, these early systems had limitations in terms of energy density, weight, and environmental concerns. As the demand for lightweight, high-capacity, and portable energy sources grew, especially, with the rise of portable electronics and the vision for EVs, the researchers began to explore battery chemistries involving the movement of metal-ions into and out of electrodes. This led to the development of secondary-ion batteries, most notably lithium-ion batteries (LIBs), which emerged as a revolutionary advancement in the 1970s and 1980s, mainly incentivized by the ongoing oil crisis.[5] The British chemist M. Stanley Whittingham initiated early substantial research into lithium-based batteries, proposing the use of titanium disulphide (TiS_2) as a cathode material,[6,7] followed by significant contributions from John B. Goodenough by identifying lithium cobalt oxide ($LiCoO_2$ or LCO) as a superior cathode,[8] and Akira Yoshino for creating the first commercial prototype using a carbon-based anode.[9] These efforts culminated in the commercial launch of the first lithium-ion battery by Sony in 1991, marking the beginning of widespread use in portable electronics.[10] In recognition of their seminal contributions in the development of LIBs, Whittingham, Goodenough, and Yoshino were jointly awarded the Nobel Prize in Chemistry in 2019. As aptly stated by the Nobel Committee, "*these batteries have revolutionized wireless technology and paved the way for a fossil fuel-free society*".[11] In the years following the commercialization of LIBs, alternative secondary-ion batteries, such as sodium-ion (SIBs), potassium-ion (KIBs), and zinc-ion batteries (ZIBs) have emerged as promising candidates, particularly in response to the concerns regarding cost, safety, and availability of raw materials.[12]

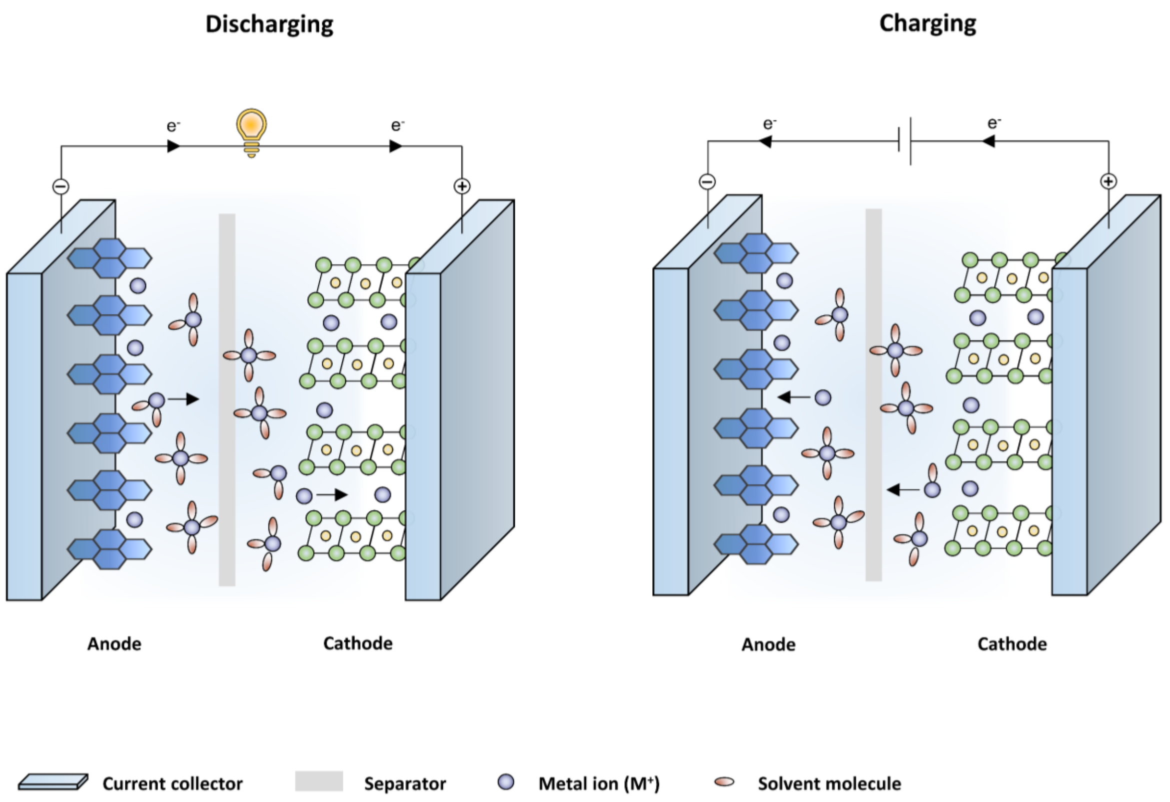

Figure 1.1 Working principle of secondary-ion batteries during discharging (left) and charging (right) processes.

The working principle of secondary-ion batteries is based on the reversible movement of metal ions, such as Li^+, Na^+, or K^+ between two electrodes through an electrolyte during charging and discharging cycles. These batteries consist primarily of three major components: (1) the anode (negative electrode), (2) the cathode (positive electrode), and (3) the electrolyte, which acts as a medium for ion transport (more detailed information on battery components is presented in Section 1.2).[2] When the battery is discharging to provide electrical energy to a device, positively charged metal ions move from the anode to the cathode through the electrolyte. Concurrently, electrons are released from the anode and flow through an external circuit to the cathode, generating an electric current that powers the device. These electrochemical reactions at both electrodes are carefully designed to be reversible, allowing the battery to be recharged. During charging, an external power source applies a voltage to force the ions to move back from the cathode to the anode, and simultaneously, the electrons flow in the opposite direction through the external circuit. Once the ions are stored again in the anode in their reduced form, the battery is ready for another discharge cycle. The ability to repeat this charge-discharge cycle hundreds or even thousands of times makes secondary-ion batteries highly suitable for long-term energy storage. Their efficient ion transport, high energy density, and cycle stability are the key features that distinguish them from other ESSs.

1.1.1. Lithium-ion batteries (LIBs)

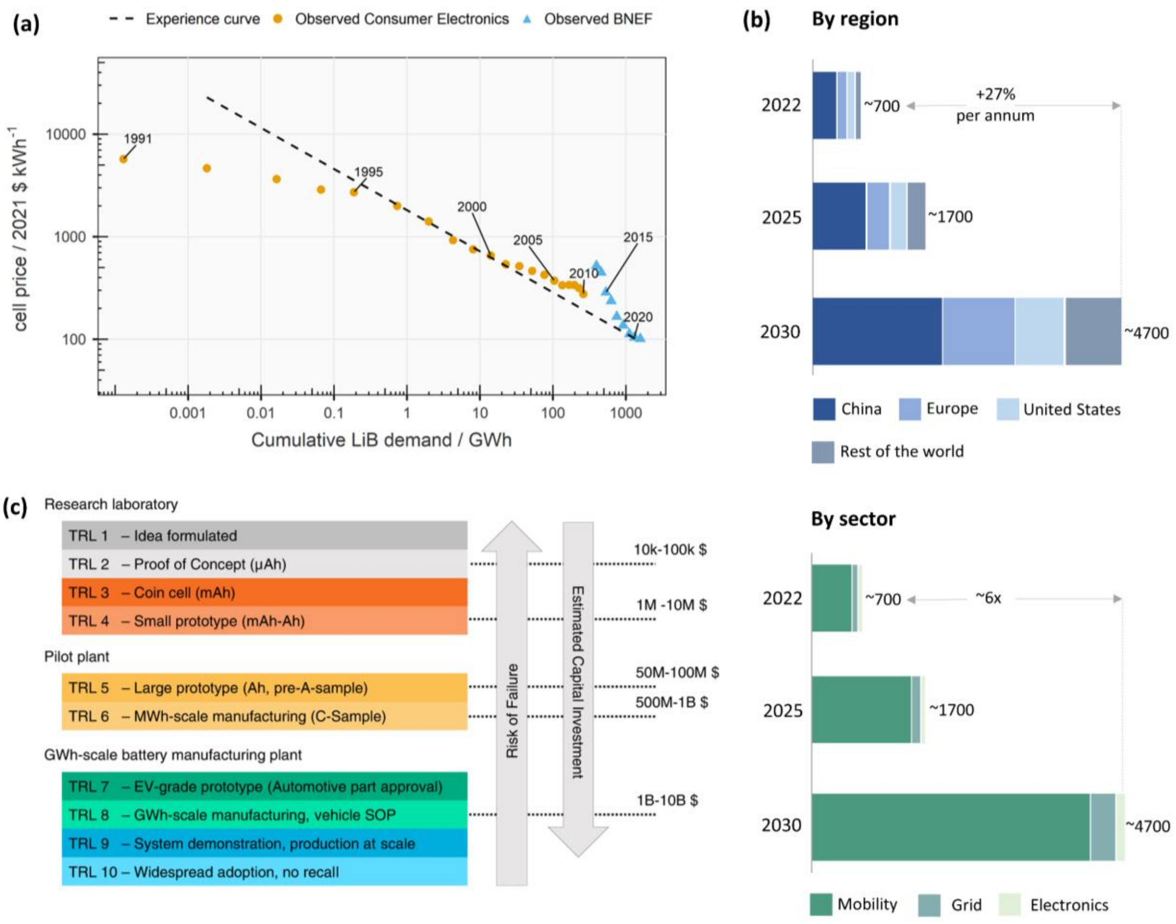

Figure 1.2 (a) Variation in lithium-ion battery cell prices relative to battery pack demand (GWh) from 1991 to 2021, including historical trends, observations from consumer electronics, and Bloomberg New Energy Finance (BNEF) data.[13] (b) Projected increase in demand for LIBs from 2022 to 2030, shown by region (top) and by sector (bottom). (c) The technology readiness level (TRL) scale for EV battery technology. As the TRL increases, the estimated capital investment also rises, while the risk of failure decreases, being highest at TRL 1 and lowest at TRL 10.[13]

The demand for LIBs has surged dramatically over the past two decades, owing to their exceptional combination of high energy density, long cycle life, low self-discharge rate, and scalability across a wide range of applications, attributes that remain unmatched by alternative chemistries such as SIBs, KIBs, and aluminum-ion batteries (AIBs).[13] This superior performance is fundamentally rooted in the electrochemical properties of lithium, the lightest metal (atomic mass 6.941 u), which exhibits a high negative standard reduction potential (−3.04 V vs. SHE) and a small ionic radius (0.76 Å).[14] These characteristics enable lithium ions to migrate efficiently between the anode and cathode with high diffusion coefficients during charge-discharge cycles, contributing to both fast kinetics and high energy storage capacity.[15] In the early 2000s, the rapid expansion of consumer electronics, including smartphones, laptops, and wearables served as the initial catalyst for LIB adoption. However, it was the automotive sector that truly propelled LIB demand to new heights.[16] The introduction of EVs, such as Tesla's Model S, demonstrated that LIBs could deliver energy densities of ~250–300 Wh kg^{-1}, a substantial leap from the ~120 Wh kg^{-1} offered by the first commercial LIBs developed by Sony in 1991, thereby making them viable alternatives to internal combustion engines.[13,15] Concurrently, intensive research and development (R&D) efforts led to significant advancements in both performance and cost. The cost of LIBs plummeted from over $10,000 kWh^{-1} in the early 2010s to approximately $100 kWh^{-1} by 2021, driven by innovations in materials and manufacturing (**Figure 1.2a**). Key breakthroughs included the transition from cobalt-heavy cathode materials, such as LCO, to more cost-effective and abundant alternatives like NMC$_{811}$ with reduced cobalt content, and lithium iron phosphate (LFP), known for its thermal stability and safety.[13,17–19] Other advancements, such as the stabilization of the solid-electrolyte interphase (SEI), the engineering of nanoscale electrode architectures to enhance ion transport, and the development of scalable manufacturing methods like dry electrode coating, have collectively contributed to lowering production costs while simultaneously improving power density, cycle life, and overall thermal performance.[13,20–22] As a result, LIBs have not only become more affordable but also more reliable and efficient across diverse applications.

According to the international energy agency (IEA), battery demand crossed 700 GWh in 2022, more than doubling since 2020, and is expected to exceed ~4700 GWh by 2030 (**Figure 1.2b**).[23] This exponential rise stems from global commitments to net-zero carbon targets, government subsidies, and improvements in EV affordability.[23] Simultaneously, stationary energy storage for grid applications, critical for balancing the intermittency of solar and wind power, has emerged as a key growth sector. However, this surge poses several challenges: (1) material scarcity, notably, Li, Ni, and Co, (2) supply chain vulnerabilities, (3) ecological concerns from mining, and (4) end-of-life battery disposal. These stress points underscore the need *not* just for next-generation LIB chemistries, but also for the development of entirely new battery systems (e.g., Na-ion, Ca-ion, solid-state or all-organic lithium systems). Addressing these issues necessitates both advanced energy storage research and a closer integration of academic and industrial interests.

As outlined by Frith *et al*.'s Technology Readiness Level (TRL) framework, academic research (TRL 1−4), requires significantly less funding ($10K−100K), but comes with a higher risk of failure and often overlooks scalability or user requirements (**Figure 1.2c**).[13,24] In contrast, moving technologies beyond TRL 5 requires increasingly large capital investments, often reaching $1−10 billion to scale battery production to 4−20 GWh annually or to bring a new EV platform to market. As the risks and costs rise with TRL progression, collaboration between academia and industry becomes critical.[24] A tight-net partnership can ensure that promising innovations can be de-risked, refined, and engineered for real-world applications, making scalable, high-performance, and cost-effective energy storage a reality.

Present geopolitical, humanitarian and ecological cost of electrification:

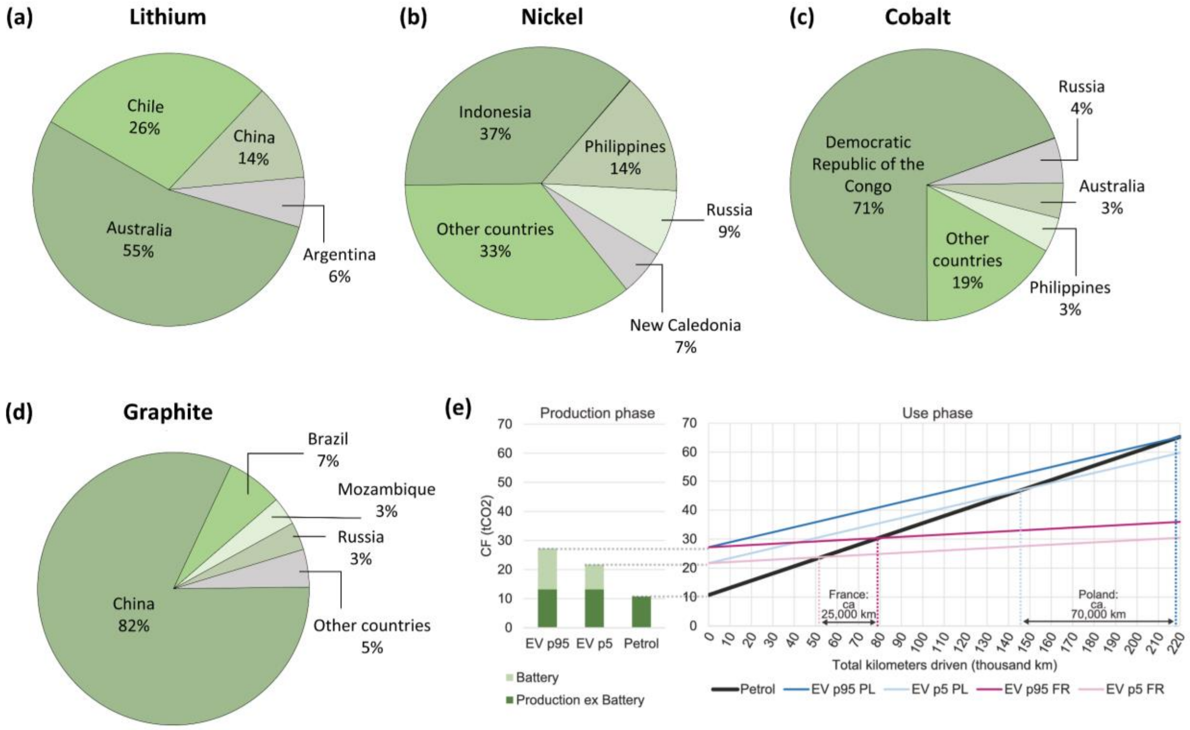

Figure 1.3 Global distribution of total reserves of (a) lithium, (b) nickel, (c) cobalt, and (d) graphite by country. (e) Comparison of the carbon footprint of a petrol vehicle and two electric vehicles (EVs) with built-in batteries corresponding to the 5th and 95th carbon footprint percentiles during production (left), and (right) total carbon footprint including the use phase is shown for operation in France (pink) and Poland (blue), with break-even mileages indicated by dashed vertical lines.[25]

The global transition towards renewable energy and electrified transportation has significantly increased the demand for LIBs, which depend on critical raw materials such as Li, Co, and Ni sources. The extraction of these minerals has led to substantial ecological degradation and humanitarian concerns. Primarily, lithium reserves are geographically concentrated, with approximately 58% of the global known resources located in so-called "Lithium Triangle" of Chile, Argentina, and Bolivia, while Australia accounts for ~55% of current global Li production.[26–28] According to the 2022 S&P Global report, extraction of one ton of lithium carbonate (Li_2CO_3) from brine consumes approximately 500,000 liters of water and emits around 15 kg CO_2–equivalent per kilogram of Li_2CO_3, with production volumes between 250,000 and 400,000 tons.[25] Cobalt production is even more geographically skewed, with approximately ~71% of global Co being mined in the Democratic Republic of the Congo (DRC), with ~50% of CF resulting from the mining processes, often under conditions that have been widely criticized for human rights violations.[28,29] The humanitarian consequences of mining critical battery raw materials, particularly Co, Ni, Li, and graphite have been extensively documented in both academic literature and investigative journalism.[29–31] A notable example is the 2016 *Washington Post* investigative series by Todd C. Frankel and Peter Whoriskey, which brought widespread public attention to the socio-environmental costs of battery material extraction, reaching audiences beyond the scientific community.[30,31] In DRC, an estimated 40,000 children are engaged in artisanal Co mining, often working in hazardous conditions without protective equipment. Further, prolonged exposure to Co dust can cause a severe form of pneumoconiosis, and chronic exposure has been associated with congenital birth defects in local populations.[29] On the other hand, Nickel reserves are more broadly distributed, with significant production in Indonesia (37% of global output), the Philippines, and Russia.[32] Life-cycle assessments (LCA) indicate that mining and refining one ton of battery-grade Ni from nickel sulphate ($NiSO_4.6H_2O$) can generate up to ~36 tons of CO_2-equivalent emissions.[25,28] Furthermore, China holds over 65% of global natural graphite production and dominates the anode material supply chain.[28,30,33] However, graphite mining and processing in China have raised concerns over air and water pollution, regulatory opacity, and labor practices. This uneven distribution of resources has profound humanitarian and geopolitical consequences, particularly as demand is projected to increase sixfold by 2030.

Consequently, although EVs offer lower operational emissions compared to internal combustion engines, the upstream emissions associated with battery production must be considered when evaluating their true environmental impact. For instance, in France, where electricity generation is largely decarbonized, the break-even mileage, the point at which an 5th percentile (lower environmental impact) EV compensates for its embedded emissions relative to a traditional vehicle is ~50,000 km.[25] In contrast, in a high-carbon grid scenario such as Poland, the break-even mileage can be achieved at ~140,000 km, potentially postponing the climate benefits of EV adoption by several years.[25]

While battery recycling reduces environmental impacts, mining rare earth metals will remain the primary source of materials due to rising EV demand and delayed returns from used batteries. Closed-loop recycling is essential but insufficient on its own, and therefore, an increase of research into organic electrode materials derived from abundant, renewable sources could provide truly sustainable solutions. Organic materials eliminate reliance on scarce, high-impact metals like Co and Ni. Therefore, at TRL 1−4 level, advancing organic battery chemistries is essential for a resilient and environmentally benign energy future.

1.1.2. Sodium-ion batteries (SIBs)

The development of sodium-ion batteries (SIBs) can be traced to the late 1960s, when researchers at the Ford Motor Company first demonstrated that Na^+ could migrate rapidly through ceramic electrolytes at elevated temperatures >300 °C.[3,34] Their work led to the first rechargeable sodium–sulfur (Na–S) system, which employed molten sodium metal as the anode, a solid ceramic electrolyte, and molten sulfur embedded in carbon felt as the cathode.[35] Although the elevated operating temperature (>300 °C) rendered this chemistry unsuitable for wide commercialization, the findings were foundational in advancing the study of solid electrolytes and stimulating interest in alkali metal-based electrochemical storage.[3]

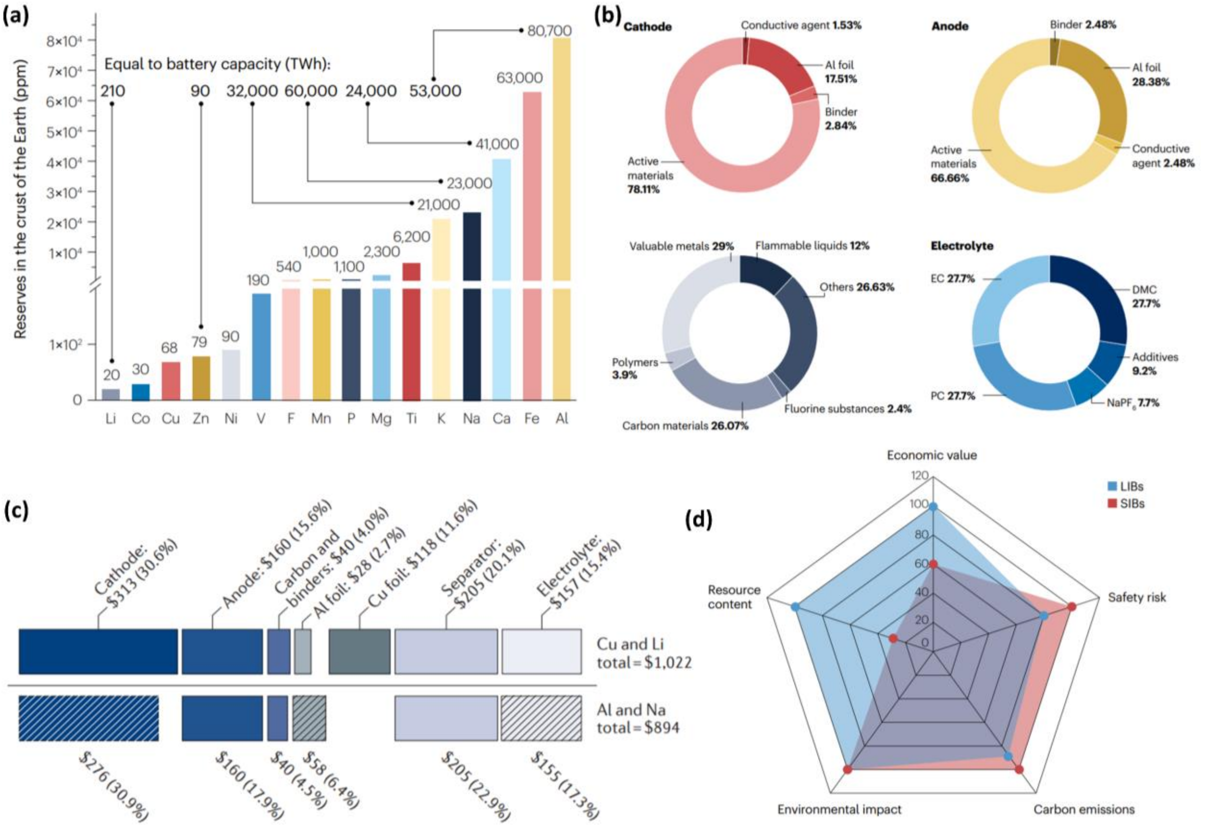

Figure 1.4 (a) Estimated global battery production potential (TWh) derived from the concentration of essential metal reserves in the Earth's crust (ppm).[36] (b) Compositional breakdown of constituents of anode, cathode, electrolyte and elemental cell for a SIB cell.[36] (c) Comparative cost analysis (USD) between two model cells: (top) utilizing $LiMn_2O_4$ (LMO) cathode, a synthetic graphite anode and Cu current collector with (bottom) the same cell model only replacing Li with Na and Cu with Al current collector.[37] Copyright 2018, Springer Nature. (d) Comparative plot of five critical parameters, resource availability, economic value per cell, safety risks, carbon emissions, and overall environmental impact, for 1 kg of end-of-life LIBs versus SIBs.[36] Copyright 2023, Springer Nature.

In parallel, progress in LIBs accelerated after the discovery of stable layered LCO cathodes and graphite anodes, which enabled high energy density and reversible cycling.[35,38] These breakthroughs pushed LIBs to the forefront of portable energy storage, and from the 1990s onward, the majority of industrial and academic efforts were directed toward lithium systems. As a result, sodium-ion research declined sharply for several decades, despite its early promise.[39] From a mechanistic perspective, SIBs function analogously to LIBs, operating through the intercalation and deintercalation of alkali metal ions within host structures. However, the larger size of the Na^+ (1.02 Å) compared with Li^+ (0.76 Å) has important implications on the overall battery performance.[14] This ~34% increase in size lowers cycle life and energy density delivered by sodium cells due to the affected diffusion pathways, and higher structural strain on electrode frameworks.[40] For instance, graphite has a layered structure with interlayer spacing of ~3.35 Å, which is ideal for lithium insertion. Li^+ intercalates between graphene sheets to form LiC_6 at a low potential (~0.1 V vs. Li/Li^+), which makes it an excellent anode. However, Na^+ ions are too large to fit stably into this spacing, preventing efficient intercalation, and thereby cannot form an equivalent NaC_6 phase.[41] Further, the compound NaC_6 is thermodynamically unstable, meaning sodium cannot stay intercalated in graphite under normal battery operating conditions.[41] These differences necessitated research on alternative electrode chemistries tailored to accommodate sodium's bulkier nature. For example, including hard carbon, with a larger interlayer spacing (>3.7 Å), offering practical capacity ~250–350 mAh g^{-1},[42] titanium-based oxides e.g., $Na_2Ti_3O_7$ or polymorphs of TiO_2[43] which provide structural stability but lower energy density, Prussian blue derivatives,[44] and alloying anodes such as Sn,[37] Sb,[45] and P[46] that deliver very high capacities but suffer from severe volume expansion during cycling.

Despite these limitations, sodium-based systems offer significant practical benefits. Sodium is the 6th most abundant element in the Earth's crust, with an average concentration of ~23,000 ppm (2.3%), whereas lithium is present at only ~20 ppm (0.002%), representing a more than 1,000-fold difference in natural availability (**Figure 1.4a**).[36] These geochemical realities directly influence material economics, such as in 2022, battery-grade Li_2CO_3 reached market prices of approximately US $78,000 per ton, while sodium carbonate remained near US $350 per ton, a cost difference exceeding two orders of magnitude.[36]

However, a cost analysis conducted by Vaalma *et al*. (2018) revealed that substituting lithium with sodium alone does not markedly improve the overall economic performance of a battery system.[47] The total cost of a cell arises from multiple components, including electrode active materials, electrolyte solvents and salts, functional additives, and external packaging, rather than from the alkali metal alone (**Figure 1.4b,c**).[36,47] An additional advantage of sodium-based systems is that Na^+ does not readily alloy with aluminum under standard operating conditions, enabling the use of aluminum current collectors for both electrodes.[47] In contrast, LIBs require copper on the anode side, which is considerably more expensive. Consequently, replacing both Li and Cu with Na and Al, respectively, in a cell model utilizing LMO cathode, and a synthetic graphite anode yields an estimated cost reduction of about \$128 per cell, with the majority of savings attributed to the substitution of Cu with Al rather than lithium with sodium (**Figure 1.4c**).[47] Another cost-saving advantage with fewer ecological ramifications is that SIBs do not require scarce Co- or Li-containing active materials for cathodes, instead cathode materials for SIBs mainly consist of abundant transition metals (**Figure 1.4b**).[36,47] Despite advances such as the adoption of Co-free cathodes and the use of Al current collectors, LIBs currently maintain greater economic value compared to SIBs. The latter still face limitations related to electrochemical performance, especially with respect to energy density and durability over prolonged cycling. Nevertheless, rising concerns about the scarcity and escalating costs of Li and Co have intensified research and development in alternative systems, making SIBs increasingly attractive as cost-effective and sustainable solutions for future large-scale energy storage.

Commercialization of SIBs: Over the past few years, several companies have begun commercializing SIB technology, primarily targeting stationary energy storage and limited electric mobility applications.[39] Leading Chinese manufacturers, such as *CATL* and *HiNa Battery Technology*, have launched pouch cells with energy densities ranging from ~140–160 Wh kg^{-1}, offering rapid charging capabilities and moderate cycle life. In Europe, companies like *Altris* have developed Prussian White sodium-ion cells that claim to combine sustainability and industrialization, while the French company *TIAMAT* focuses on ultra-fast charging cells for industrial and mobility applications. In the United States, *Natron Energy* pioneered commercial-scale Na-ion cells with Prussian blue analog electrodes, emphasizing long cycle life and high-rate performance for critical backup power and microgrid applications, although operations have recently ceased. Despite these advances, SIBs still face significant limitations, including lower energy density compared to LIBs, which restricts their suitability for high-energy applications such as long-range EVs.[39] Additionally, SIB adoption remains limited, representing <1% of the current global battery market, with projections rising only modestly to 3% by 2035 in a conservative scenario, or up to 15.5% in an optimistic one, depending on technological improvements in performance, cycling stability, and cost reduction.[36] Consequently, SIBs are positioned as a complementary technology to LIBs, particularly in applications where material abundance, safety, and cost are prioritized over maximum energy density, highlighting both their potential as well as the challenges that must be addressed for broader commercialization.

1.2. Battery components

As described in a previous section (Section 1.1), a battery cell is an integrated electrochemical system in which each component fulfills a distinct role to ensure efficient, safe, and durable operation. **Figure 1.5** illustrates the major components of a battery pack: electrodes, electrolyte, separator, and current collectors, which are deliberately engineered components, while the *solid-electrolyte interphase*

(SEI) and *cathode-electrolyte interphase* (CEI) are typically the self-formed interphases that emerge during early electrochemical cycling. The *anode* (negative electrode) functions as the host for Li^+ during charging, and its performance is closely tied to the formation of the SEI, which prevents continuous electrolyte decomposition at lower potential ~0.1 V vs. Li/Li^+ while allowing ion transport (see Section 1.2.1).[21] Opposite to this, the *cathode* (positive electrode) serves as the lithium source and sink during cycling, and its surface is often stabilized by the CEI to mitigate degradation at high potentials. While often overlooked, *binders* and *conductive additives* are essential to the integrity and performance of both electrodes. Polyvinylidene fluoride (PVDF) dissolved in *N*-methyl-2-pyrrolidone (NMP) solvent is the most common binder, providing chemical stability and adhesion of active materials to current collectors. Alternatives such as carboxymethyl cellulose (CMC) and styrene-butadiene rubber (SBR) have been increasingly adopted for water-based electrode processing, which is more environmentally benign and cost-effective. Conductive additives, typically carbon black (e.g. Ketjenblack, Acetyleneblack) or carbon nanotubes, improve the electrical conductivity of composite electrodes, especially important for cathode materials with inherently poor conductivity, such as $LiFePO_4$ (LFP). Although binders and additives represent only a small fraction of electrode mass (<20%), they play a decisive role in cycling stability and rate capability.

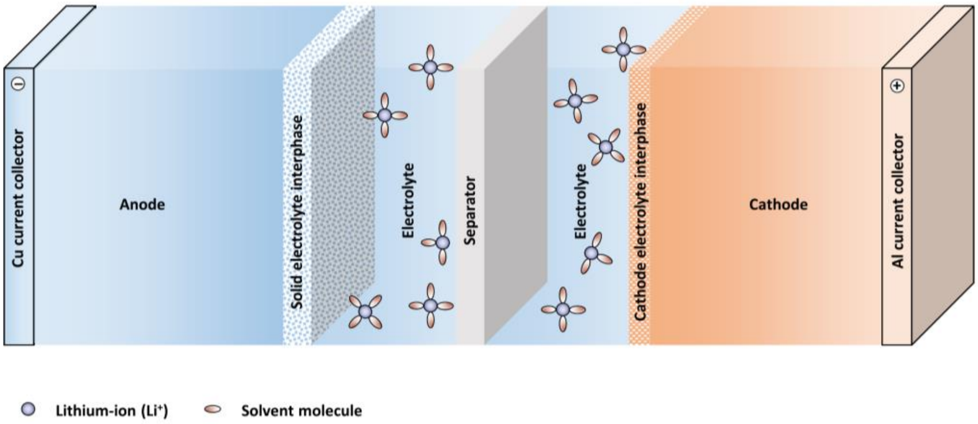

Figure 1.5 Schematic representation of major lithium-ion battery components.

The preparation of electrode slurry is a critical step in the battery production, as it dictates electrode homogeneity, adhesion, and thereby the electrochemical performance, and cycle life (**Figure 1.6**).[22] Typical active material loadings range from 60–75 wt.%, while binder and conductive additive together can range from ~20–15 wt.%, depending on the dispersion stability, and electronic conductivity of the active material, respectively.[22,48] Mixing sequence is critical: conductive carbon is dispersed first to avoid agglomeration, binder is dissolved in solvent, and active material is incorporated under controlled mixing speed ~1000–2000 rpm. Doctor blading uniformly spreads the slurry onto current collectors, followed by controlled drying to remove solvents and to yield a stable, adherent electrode film. Further, *vacuum degassing* evaporates the solvent and eliminates microbubbles, which is usually followed by compressing dried electrode films between heated rollers (*calendaring*) to adjust thickness, and improve electrode–collector contact, ensuring smooth electrode films, and consistent cycling stability.[22]

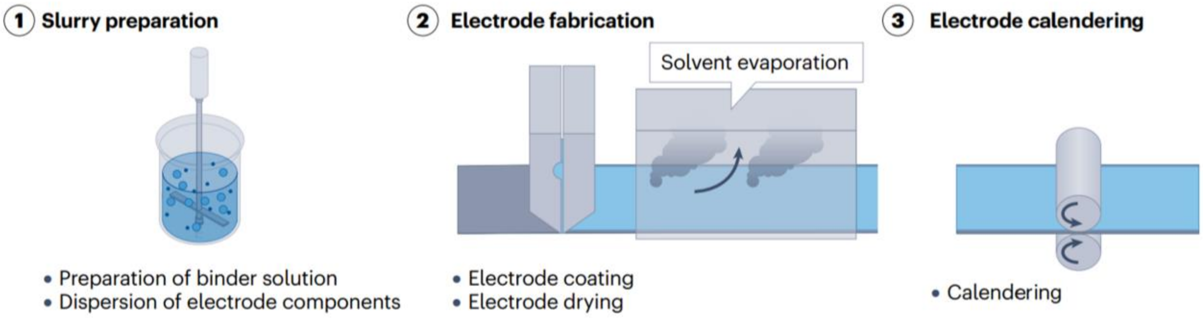

Figure 1.6 Schematic representation of the best practices for electrode slurry preparation.[22] Copyright 2025 Springer Nature.

The *electrolyte*, typically composed of a solvent and a lithium salt (in case of LIBs), provides the medium for ionic conduction, dictating conductivity and stability. Electrolyte additives are introduced to enhance interphase formation, suppress gas evolution, and extend cycle life (more detailed description is presented in Section 1.2.3). *Separators*, consisting of porous insulating membranes, prevent electronic contact between electrodes, simultaneously enabling ion flow. Common separator materials include polyethylene (PE) and polypropylene (PP), often arranged in multilayer configurations (PP/PE/PP) to improve mechanical and thermal stability.[49] A key safety feature is the "shutdown mechanism," where the separator pores collapse at elevated temperatures (~130 °C for PE), stopping ion transport and preventing thermal runaway.[49] Despite their importance, separators are electrochemically inactive, thereby adding to the battery mass without contributing to energy density. Therefore, researchers have focused on enhancing separator selectivity, safety, mechanical strength, and electrolyte wettability without significantly increasing thickness or weight. Coated separators with ceramic or polymer layers have also been developed to improve performance in high-power applications. *Current collectors* provide electronic pathways: In LIBs, Cu is used on the anode side due to its stability at low potentials, whereas Al is employed at the cathode side for its resistance to oxidation. As stated in Section 1.1.2., the choice of current collector significantly influences battery cost and weight.[47] Therefore, studies have been reported on investigating lighter and thinner foils, surface texturing, and conductive coatings to reduce interfacial resistance, and improve adhesion of active materials. Overall, desirable properties across components include high ionic and electronic conductivity, mechanical integrity, interfacial stability, and compatibility over long-term cycling.

1.2.1. Anode – The negative electrode

1.2.1.1. Inorganic anode materials

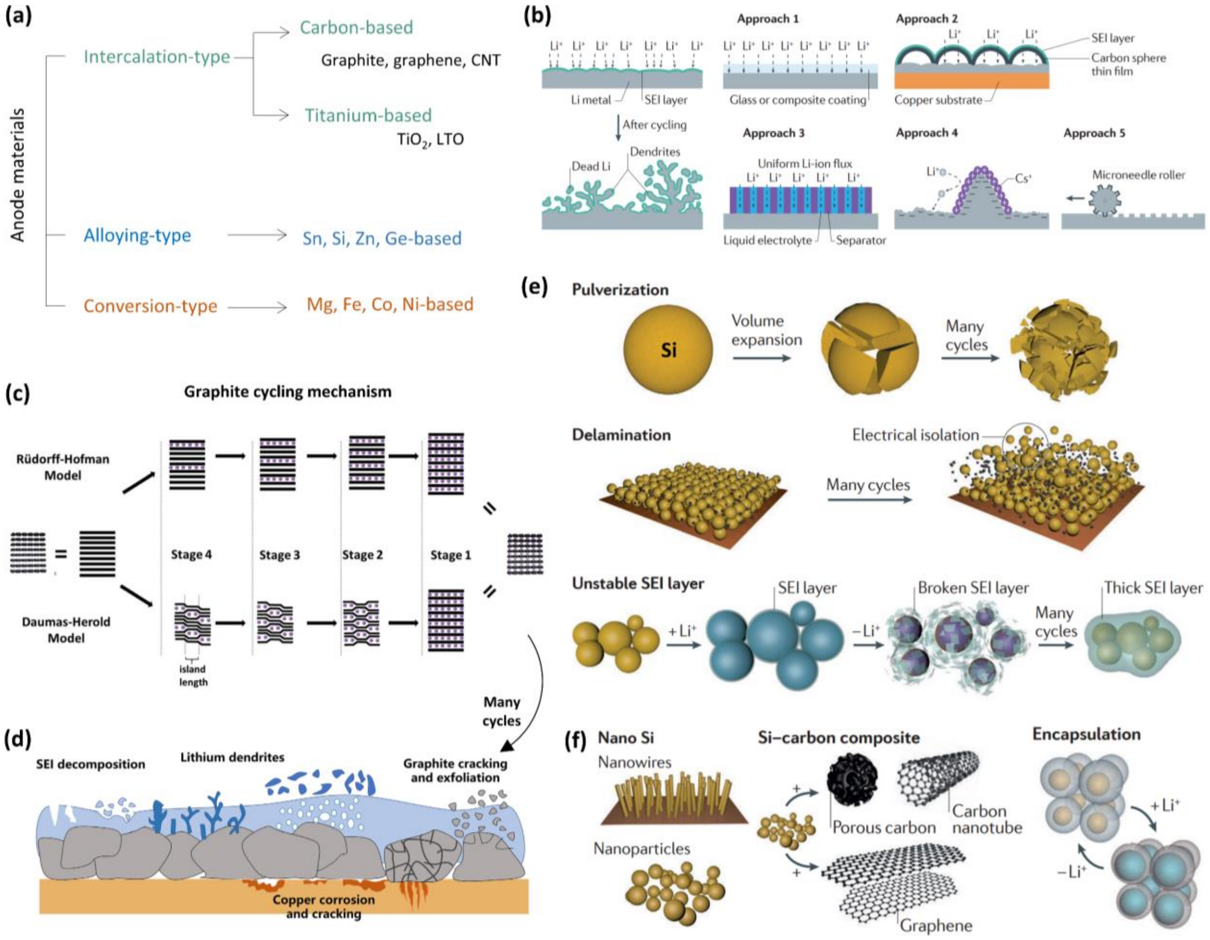

Figure 1.7 (a) Classification of inorganic anode materials into three primary categories: intercalation-type, alloying-type, and conversion-type, along with representative examples. (b) Schematic of Li-metal anode failure pathway and approaches to mitigate dendrite formation and enhance interfacial stability: (1) surface coatings with glassy or composite layers, (2) ultrathin carbon or graphene coatings, (3) promotion of uniform Li-ion flux, (4) electrolyte modification with Cs^+ additives, and (5) structural engineering via 3D architectures or Li-metal powder.[12] Copyright 2016 Springer Nature. (c) Illustration of the Rüfforff–Hofmann and Daumas–Herold insertion mechanisms of Li^+ ions in graphite hosts.[50] Principal degradation processes affecting (d) graphite anodes[51] and (e) Si anodes in LIBs,[12] respectively. (f) Morphological engineering and composite design strategies developed to alleviate the severe volume expansion of Si anodes.[12] Copyright 2016 Springer Nature.

Anode materials play a crucial role in the overall performance of LIBs by determining capacity, electrochemical, mechanical and thermal stability, and cycle life. They are generally categorized into three types: insertion materials, alloy-type materials, and conversion-type materials based on the Li^+ storage mechanism followed (**Figure 1.7a**).[52] Lithium metal was first introduced as an anode in 1976 and long considered the "*dream anode*" for its ultrahigh theoretical capacity ~3860 mAh g^{-1} and lowest electrochemical potential (−3.04 V vs. SHE), promising far greater energy density than graphite.[10]

However, by the 1980s researchers realized a major disadvantage, multiple cycles of (de-)plating lithium leading to dendrite growth and continuous electrolyte degradation forming thick and unstable SEI layers, forcing a shift toward safer graphite anodes **(Figure 1.7b)**.[10,12,53,54] Since the 2000s, due to low capacity output of graphite, a renewed interest had driven several outstanding strategies (see Figure 1.7b), such as, protective ceramic or composite coatings (Approach 1), ultrathin carbon/graphene interlayers (Approach 2), homogenized Li-ion flux engineering (Approach 3), electrolyte additives like Cs^+ (Approach 4), and 3D scaffolds or Li-metal powders (Approach 5).[12] However, despite decades of research, Li-metal anodes have remained far from being safe, stable or economic for commercial purposes. Among insertion materials, graphite has dominated commercial anodes for LIBs owing to its low operating potential (~0.01–0.5 V vs. Li/Li^+), good reversibility, and a theoretical capacity of 372 mAh g^{-1} corresponding to the formation of LiC_6 (Stage-1), see **Figure 1.7c**.[50] Lithium storage in graphite occurs through intercalation between graphene layers, a process historically described by two classical staging models. In 1938, the Rüdorff-Hofmann model introduced the concept of staging, where the intercalant (Li^+) ions occupy entire galleries in an ordered fashion, leading to a periodic expansion of the interlayer spacing with galleries either completely filled or empty.[50,55] However, this rigid and idealized description failed to capture experimental observations of partial occupancy and coexistence of stages. To address this, the Daumas-Herold model proposed a more flexible mechanism in which intercalant distributes locally within galleries, allowing regions of filled and empty layers to coexist and enabling sliding of adjacent graphene planes.[56] Whereas the Rüdorff-Hofmann framework implied constrained ion mobility, the Daumas-Herold model supported more continuous diffusion pathways.[50] Although graphite has been the dominant anode material for the past three decades due to its high stability and long cycle life, it exhibits significant limitations under high-rate cycling (**Figure 1.7d**).[51,54] Initial nucleation of lithium at the anode surface, followed by high-rate cycling can lead to dendrite growth posing safety concerns, and thereafter puncturing the SEI layer, resulting in a chemically and mechanically unstable electrode-electrolyte interface. Repeated intercalation/deintercalation further induces graphite exfoliation, where graphene layers partially separate, causing capacity fading and structural degradation. Additionally, accidental over-discharging can lead to Cu current collector corrosion.[51] These drawbacks have motivated the exploration of alternative titanium-based insertion materials. For instance, TiO_2 enables lithium insertion with a capacity of 170–200 mAh g^{-1} at ~1.5–1.8 V vs. Li/Li^+, offering enhanced safety and long cycle life, albeit with lower energy density.[57] Similarly, lithium titanate ($Li_4Ti_5O_{12}$ or LTO) operates at ~1.55 V vs. Li/Li^+ with ~175 mAh g^{-1} capacity; its "*zero-strain*" characteristic ensures exceptional cycle stability and fast charging, though the higher operating potential of this anode reduces overall cell voltage and energy density.[58]

Alloy-type anodes include silicon (Si), which forms $Li_{4.4}Si$, was envisioned as a transformative anode material capable of dramatically increasing energy density with an impressive theoretical capacity >4000 mAh g^{-1} and an operating voltage of ~0.3 V vs. Li/Li^+.[59] However, in practice, Si faces major challenges including ~300% volume expansion during charging cycle, causing particle pulverization, continuous electrolyte degradation leading to inefficient and thick SEI formation, and thereby rapid capacity fading (**Figure 1.7e**).[12,54] Although many studies have explored nanostructuring, compositing, and encapsulation to mitigate these effects, the material remains far from commercial utility (**Figure 1.7f**).[12] Consequently, Si is currently limited to minor fractions (5–15 wt%) in graphite/silicon (Si–C) composite anodes, where it provides only modest improvements in energy density and performance.[60]

Conversion-type anodes undergo reversible conversion reactions: $M_aX_b + yLi^+ + ye^- \rightleftharpoons aM + Li_yX_b$, where M = Mg, Fe, Co, Ni, etc., and X = N, O, P, and S, achieving high capacities ranging between 600–1000 mAh g^{-1}.[61] They operate typically between 0.5–1.5 V vs. Li/Li^+, with advantages of abundance and high storage capability, but disadvantages of large voltage hysteresis, structural instability, and low initial coulombic efficiency.[12,54,61]

1.2.1.2. Organic anode materials

As discussed in Section 1.1, 1.2.1.1, and later in 1.2.2.1, the accelerating global demand for sustainable and resource-efficient energy storage has intensified the search for alternatives to conventional inorganic electrode materials based on transition metals. Organic electrode materials (OEMs) have recently emerged as compelling candidates, owing to their structural versatility, environmental compatibility, and potential for cost-effective large-scale deployment.[62–64] Unlike transition metal (TM)-based electrodes, which depend on finite and geographically concentrated mineral resources, OEMs can be derived from earth-abundant, renewable feedstocks, circumventing the environmental and socio-economic issues associated with mining and refining processes. Additionally, their redox activity is usually governed by the electron distribution of functional groups rather than ion-radius constraints, enabling unique cross-compatibility across both aqueous and non-aqueous metal-ion batteries.[64]

Despite their many advantages, OEMs face several intrinsic limitations that hinder their practical implementation in commercial ESSs. One of the most critical challenges is their high solubility in common electrolyte solvents, which often leads to active material loss, rapid capacity fading, and short cycle life.[64,65] In addition, most OEMs exhibit inherently low electronic conductivity, requiring extensive use of conductive additives such as carbon blacks, graphene, or carbon nanotubes (CNTs) to ensure sufficient charge transport within the electrode composite.[64,66] While many OEMs demonstrate high gravimetric capacities due to multi-electron redox activity, they frequently suffer from low volumetric energy density and insufficient power density, stemming from their molecular nature, low packing density, and sluggish charge-transfer kinetics.[67,68] These drawbacks collectively limit the scalability and competitiveness of OEMs against inorganic electrode materials in high-performance battery applications.

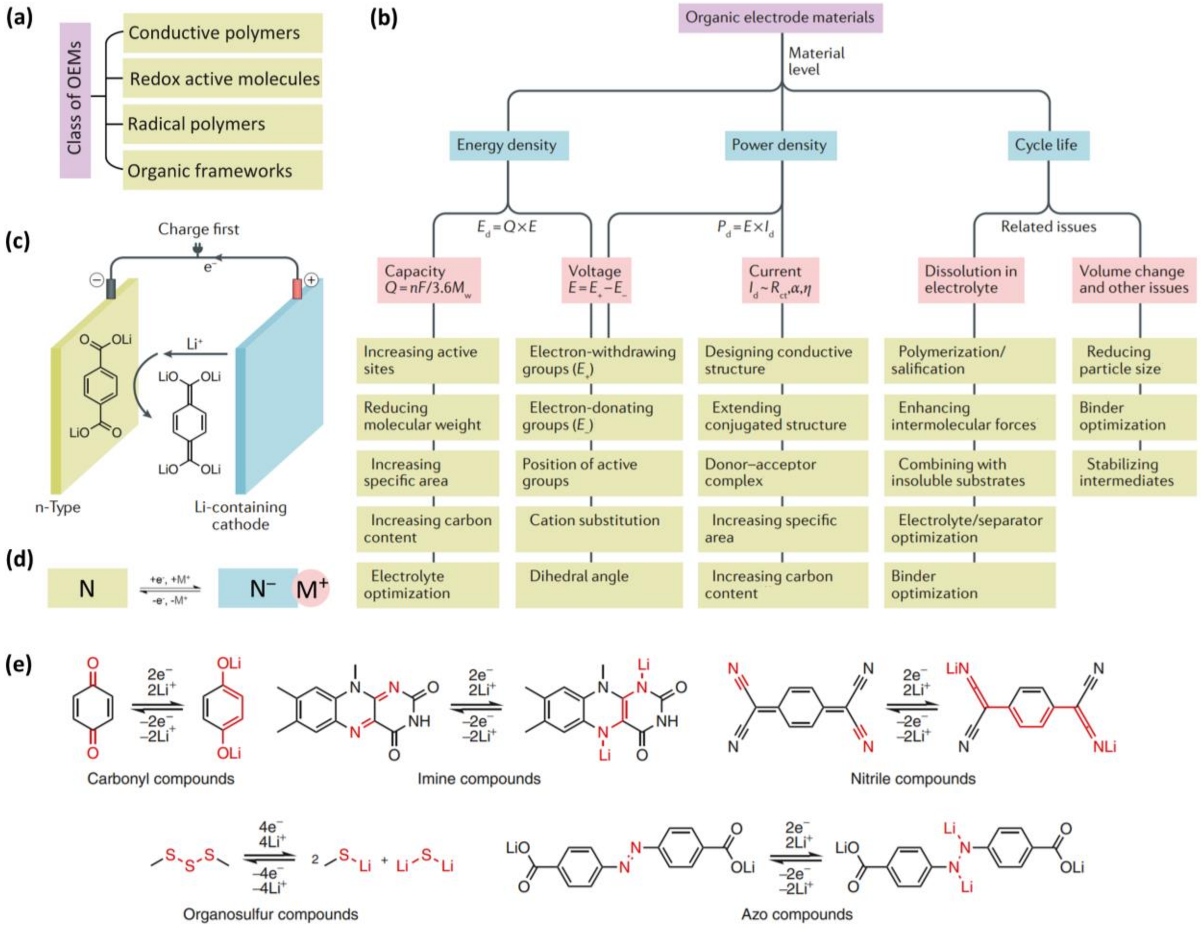

Figure 1.8 (a) Most prominent categories of organic electrode materials (OEMs) and (b) strategies to improve their overall performance by enhancing energy density, power density, and cycle life. Here, E_d is energy density, Q is the charge, E is the potential window, F is the Faraday's constant, M_w is the molecular weight of the OEM, $E\_$ and E_+ are the oxidation and reduction potentials, I_d is the current experienced, and R_{ct} is the charge transfer resistance.[64] (c) Schematic representation of the working principle of an *n*-type OEM acting as an anode,[64] with (d) illustrating the corresponding reaction mechanism. (e) Most established *n*-type compounds, carbonyl, imine, nitrile, organosulfur, and azo, and their corresponding reversible redox reactions, storing lithium as a charge carrier during reduction and releasing it during oxidation.[64] Copyright 2020 Springer Nature.

Nevertheless, the structural tunability of OEMs offers powerful opportunities to overcome these shortcomings (**Figure 1.8a,b**).[64] Solubility issues can be mitigated by designing redox-active units as extended conjugated polymers, or by embedding them within rigid, insoluble frameworks such as covalent organic frameworks (COFs) or metal organic frameworks (MOFs), where strong intermolecular forces suppress dissolution while maintaining electrochemical activity. Capacity output can be enhanced through molecular engineering strategies such as increasing the number of redox-active sites per repeat unit, reducing molecular weight to maximize active content, and expanding surface area via porous frameworks to improve ion accessibility. Further, power density can be significantly improved by rational structural design, such as, transitioning from amorphous polymers to ordered frameworks with directional ion transport pathways promoting fast-rate kinetics. Such design flexibility allows the same molecular backbone to be optimized for different battery chemistries, ultimately enabling the realization of high-capacity, stable, and high-power organic electrodes.

OEMs can be broadly classified into *p*-type, *n*-type, and bipolar systems**,** distinguished by the direction of their dominant redox processes.[62,64,66] *n*-Type materials undergo reversible reduction first at low potentials, i.e., accepting electron in the lowest unoccupied molecular orbital (LUMO) and thereby storing a wide range of metal-cations ($M^+ = Li^+$, Na^+, K^+).[64,68] *p*-Type and bipolar-type electrode will be discussed in detail in Section 1.2.2.2, and Section 1.4.2.2, respectively. *n*-Type electrodes can be utilized as both cathode and anode based on their redox ability, however, in this section we focus on the ability of *n*-type materials to serve as the negative electrode (**Figure 1.8 c,d**).[64] Their electron-accepting nature enables them to reversibly stabilize diverse cations beyond monovalent alkali metals, providing opportunities for applications in multivalent-ion batteries where transition-metal oxides often suffer from sluggish diffusion or structural instability. The redox activity of *n*-type organic materials arises from diverse functional groups with distinct electron-accepting capabilities (**Figure 1.8e**).[64] Carbonyl compounds C=O, such as, quinones, anhydrides, imides, have been extensively studied for their high theoretical capacities and tunable potentials.[69] Nitrile C≡N and imine C=N systems offer reversible storage at relatively low potentials, while azo N=N compounds contribute rich multi-electron chemistry.[70] Organosulfur-based materials provide high capacities through reversible S–S bond cleavage and reformation, although often challenged by dissolution and polysulfide shuttling.[71] By systematically engineering these functional motifs, researchers have demonstrated *n*-type anodes with operating potentials ranging from near 0 V up to ~2 V (vs. Li/Li^+ or Na/Na^+), enabling their integration into a wide spectrum of rechargeable battery chemistries.[68] In addition, several efforts have been made to develop *n*-type OEMs with increased operating potentials >3 V vs. the corresponding M/M^+ in reference. However, so far, such *n*-type materials have not been able to demonstrate optimal electrochemical stability.

1.2.2. Cathode – The positive electrode

1.2.2.1. Inorganic cathode materials

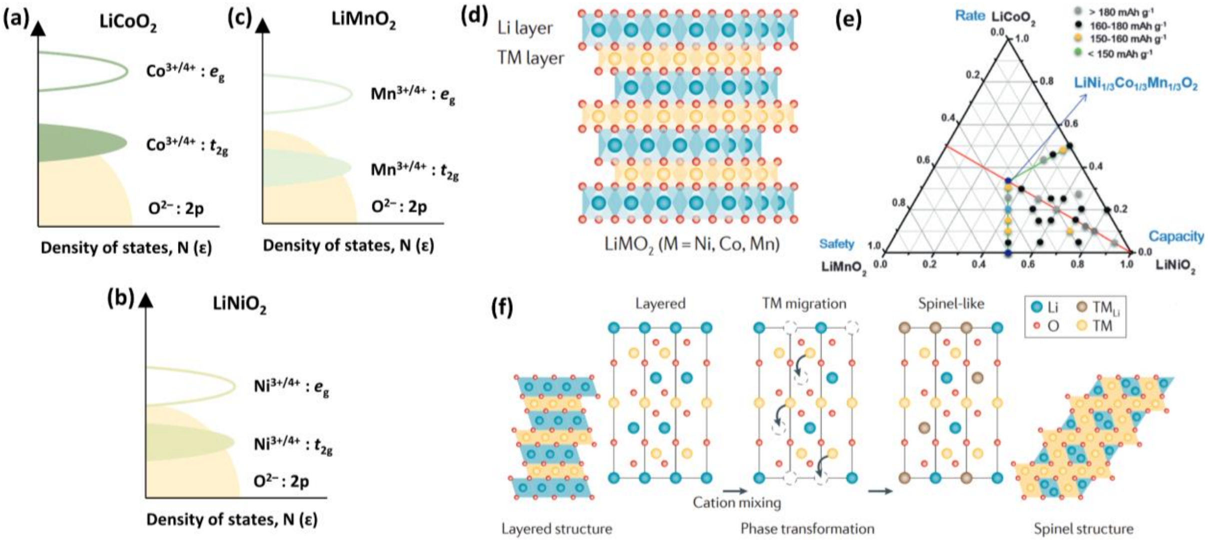

Figure 1.9 Comparison of the electronic density of states (DOS) profiles for three representative layered cathode compounds: **(**a) $LiCoO_2$, (b) $LiNiO_2$, and (c) $LiMnO_2$. (d) Crystal structures of the $LiMO_2$ family (M = Ni, Co, or Mn), illustrating the layered arrangement of lithium and transition-metal (TM) ions, which is critical for reversible Li^+ intercalation and deintercalation during battery cycling.[12] (e) Ternary compositional phase diagram of stoichiometric layered lithium TM oxides within the $LiCoO_2$–$LiNiO_2$–$LiMnO_2$ system. The diagram shows the relative positions of various compositions, with dots marking the $LiNi_{1-x-y}Co_xMn_yO_2$ (MNC) compounds that have been widely investigated as practical cathode materials due to their tunable electrochemical properties.[72] Copyright 2015 John Wiley & Sons. Inc. (f) Schematic representation of the layered-to-spinel phase transformation that can occur during repeated charging, a key degradation pathway that influences the long-term cycling stability and performance of layered oxide cathodes.[12] Copyright 2016 Springer Nature.

Inorganic cathodes, particularly Nickel (Ni), Manganese (Mn), and Cobalt (Co)- based layered oxides (MNC), are among the most widely studied and commercialized materials for rechargeable LIBs due to their high potential >3.4 V, high energy density and tunable redox properties (**Figure 1.9**).[12,73–75] The performance limits of layered cathode materials stem from the interaction between transition-metal (TM) orbitals and oxygen states.[73] In $LiCoO_2$, practical Li extraction stops at roughly half the theoretical capacity (full theoretical capacity ~274 mAh g^{-1}, achieved capacity ~140 mAh g^{-1}) since, removing more Li during the charging process pushes the $Co^{3+}/^{4+}$ t_{2g} electrons into strong overlap with oxygen's 2p orbitals, destabilizing the lattice and causing O_2 evolution **(Figure 1.9a**).[73] In contrast, $LiTMO_2$ (TM = Ni, Mn) do not share this limitation due to the placement of redox active e_g band of $LiNiO_2$ only slightly touching oxygen states (**Figure 1.9b**), and the $Mn^{3+/4+}$ redox active e_g band in

$LiMnO_2$ lies well above the 2p orbital of oxygen (**Figure 1.9c**), making them chemically more stable than $LiCoO_2$.[72,73,75] Therefore, the Fermi (or HOMO) level of a cathode determines the energy at which electrons are removed during Li^+ extraction, and the voltage window corresponds to the range over which Li^+ can be reversibly intercalated without causing structural or chemical instability.[72] Layered cathodes $LiNiO_2$ and $LiMnO_2$ can achieve capacities of ~220 mAh g^{-1} and ~180–200 mAh g^{-1}, respectively.[72,74] However, Ni and Mn-based $LiTMO_2$ face structural challenges, for instance, $LiNiO_2$ can undergo cation mixing and thermal issues, and $LiMnO_2$ tends to distort due to Jahn-Teller effects, eventually transforming from a layered to a spinel framework (**Figure 1.9d-f**).[12]

Each material, with different Mn, Ni, and Co content, balances capacity, chemical, and structural stability differently. The main advantages of MNC cathodes include high theoretical capacity, voltage tunability, and established manufacturing processes, while their disadvantages involve irreversible phase transitions, thermal instability, O_2 release, and resource concerns related to Co. Overall, MNC cathodes balance energy density and rate performance, but their long-term stability hinges on mitigating structural degradation during repeated cycling.

1.2.2.2. Organic cathode materials

Organic cathode materials, a class of OEMs, are composed primarily of earth-abundant, lightweight elements (C, H, N, O, S), granting them significant advantages in terms of sustainability, molecular tunability, and recyclability in comparison to the traditional inorganic cathode materials for metal-ion batteries.[62,64] Their redox behavior is governed by well-defined molecular orbitals rather than crystalline lattice constraints, enabling fine modulation of redox potential, electron affinity, and capacity through rational molecular design.[67] As already described in Section 1.2.1.2, both *n*-type and *p*-type materials can be utilized as active materials for cathodes based on their redox features. *p*-Type cathodes undergo reversible oxidation of donor moieties, accommodating charge via counter anion (A^-) insertion from the electrolyte during the charging process.[67] The electron-donating nature of *p*-type redox centers results from high-lying highest occupied molecular orbital (HOMO) levels, facilitating oxidation at elevated potentials, often in the range of 2.0–4.5 V vs. Li/Li^+ (**Figure 1.10a**).[67,76] In contrast, *n*-type cathodes require a prior discharge to load M^+, which they prefer to lose by undergoing reversible oxidation reaction, similar to inorganic cathodes, such as NMCs (**Figure 1.10b**).[64] *p*-Type organic cathodes offer distinct advantages over their *n*-type counterparts, for instance, their operation at high potentials arises from the intrinsic electron-donating nature of their π-rich backbones, which often undergo oxidation to generate stable radical cations. The rapid stabilization of these radical intermediates, by extended conjugation and favorable molecular orbital alignment, imparts intrinsically fast charge-transfer kinetics. Additionally, *p*-type cathodes store A^-, which have a much weaker solvation shell in comparison to the M^+, and therefore, the desolvation energy of A^- is much lower than for the counter cation. However, *p*-type cathodes typically exhibit modest capacities compared with *n*-

type materials, ranging between ~50–150 mAh g^{-1} due to the limited number of reversible electron transfers per donor unit (**Figure 1.10c**).[67]

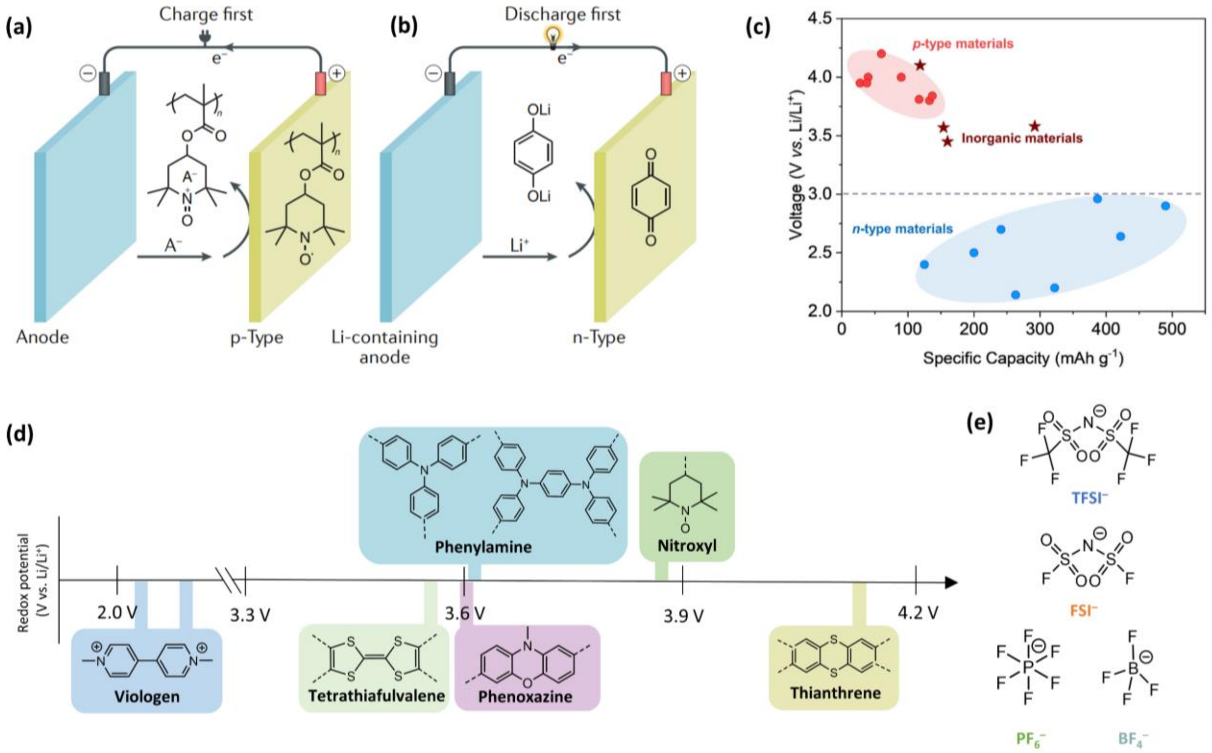

Figure 1.10 Schematic representation of the working principle of an (a) *p*-type and (b) *n*-type OEM acting as the positive electrode.[64] Copyright 2020 Springer Nature. (c) Voltage–capacity profiles of organic electrodes, highlighting *p*-type (red region) materials at higher voltages with lower capacities and *n*-type materials (blue region) at lower voltages with higher capacities. Inorganic references (stars) are shown for comparison.[67] (d) Most prominent *p*-type compounds, viologen, phenoxazine, phenylamine, tetrathiafulvalene, nitroxyl, and thianthrene along with their corresponding operating potentials versus lithium as reference. (e) Various anions, TFSI$^-$, FSI$^-$, PF$_6^-$, and BF$_4^-$, which can be reversibly stored in *p*-type organic cathodes.

A wide array of redox-active electron-rich groups has been investigated for *p*-type organic cathodes, including derivatives of viologen (~2.0–2.2 V),[77] phenoxazine (~3.6 V),[78] triphenylamine (~3.7 V),[79] tetrathiafulvalene (TTF, ~3.5 V),[65] nitroxyl (~3.6–3.8 V),[77] and thianthrene (~4.0 V vs. Li/Li$^+$)[80] (**Figure 1.10d**). Several studies have demonstrated that their operational potentials can be systematically tailored by intermolecular engineering, such as through π-conjugation extension or donor–acceptor (D–A) substituents.[76] Furthermore, by incorporating *n*-type redox moieties with *p*-type frameworks through intermolecular conjugation, bipolar-type organic cathodes can be engineered.[81] Such hybridization enables simultaneous anion and cation storage within a single molecular or polymeric backbone, thereby expanding the overall potential window and enhancing the practical capacity of the electrode. This dual redox behavior not only leverages the high working potential of *p*-

type units but also the multi-electron storage capability of *n*-type centers, offering a promising route toward high energy density organic cathode systems. Anion storage in *p*-type cathodes is commonly mediated by salts containing $A^- = PF_6^-$, $TFSI^-$, FSI^-, and BF_4^-.[67] These anions differ significantly in ionic radii: $BF_4^- < PF_6^- < FSI^- < TFSI^-$, influencing insertion kinetics, reversibility, and overall energy density (**Figure 1.10e**).[82,83] The tunability of anion intercalation chemistry opens pathways for optimizing the potential window and rate capabilities.

As discussed in detail in Section 1.2.1.2, (molecular) organic positive electrodes, similar to their anode counterparts, face intrinsic limitations such as dissolution in liquid electrolytes and poor electronic conductivity, both of which hinder long-term cycling stability and high-rate performance.[64] Similar strategies, such as polymerization of redox-active units into insoluble macromolecular backbones, and/or incorporation of *p*-type motifs in extended π-conjugated, robust, and porous architectures like COFs can be used to enhance electronic transport. These approaches not only suppress dissolution but also create continuous and interconnected ion/electron transport channels, thereby significantly improving both charge storage kinetics and electrochemical durability.

1.2.3. Electrolyte

Over the past three decades, battery research has been predominantly directed toward the development and performance optimization of electrode materials, while comparatively fewer studies have focused on the exploration and advancement of electrolytes.[84] This research disparity is particularly consequential, as the physiochemical properties of the electrolyte have a profound influence on the overall cell performance, with a dominant role in governing ionic conductivity, potential window, interfacial charge-transfer kinetics, and long-term stability.[85–88] Beyond supplying mobile ions, electrolytes fundamentally shape electrode–electrolyte interfacial chemistry, thereby dictating performance and degradation pathways.[20,21] Electrolytes in rechargeable batteries can be broadly classified into liquid, solid (organic and inorganic), and composite systems (**Figure 11a**).[89] Liquid electrolytes are dominated by carbonate-based solvents, such as ethylene carbonate (EC), dimethyl carbonate (DMC), ethyl methyl carbonate (EMC), diethyl carbonate (DEC), and propylene carbonate (PC), typically combined with a lithium salt, alongside ether-based solvents 1,3-dioxolane (DOL) and dimethoxyethane (DME) for Li–S systems, and ionic liquids imidazolium-, pyrrolidinium-, or phosphonium-based cations with bulky anions like bis(trifluoromethanesulfonyl)imide [$TFSI^-$], offering wide electrochemical stability windows and non-flammability.[87,88] Liquid carbonate-based electrolytes, while enabling superior ionic conductivity (10^{-2} S cm^{-1}) and low interfacial resistance, suffer from several intrinsic disadvantages that limit safety and performance.[90] EC, though solid at room temperature, becomes combustible when molten with a flash point ~160 °C, while PC has a flash point ~132 °C and DMC ignites easily ~17 °C.[91] These low ignition thresholds, combined with high volatility, make liquid electrolytes a major fire risk during a case of thermal runaway. Dahn and co-workers established ethylene carbonate (EC) as a stable co-solvent, and despite extensive efforts to identify superior alternatives, $LiPF_6$ in EC-based solvent systems remains the state-of-the-art electrolyte formulation for new electrode tests.[10] Therefore, understanding the chemistry behind electrolyte formulations and the associated SEI/CEI layers is unavoidable when testing new electrode materials. In this section, liquid electrolyte, formation of SEI layer, and the effect of anion and salt concentration will be discussed. Solid-state electrolytes (SSEs), mainly focusing on the COF-based electrolytes, and their importance will be elaborated in later Section 1.4.1.

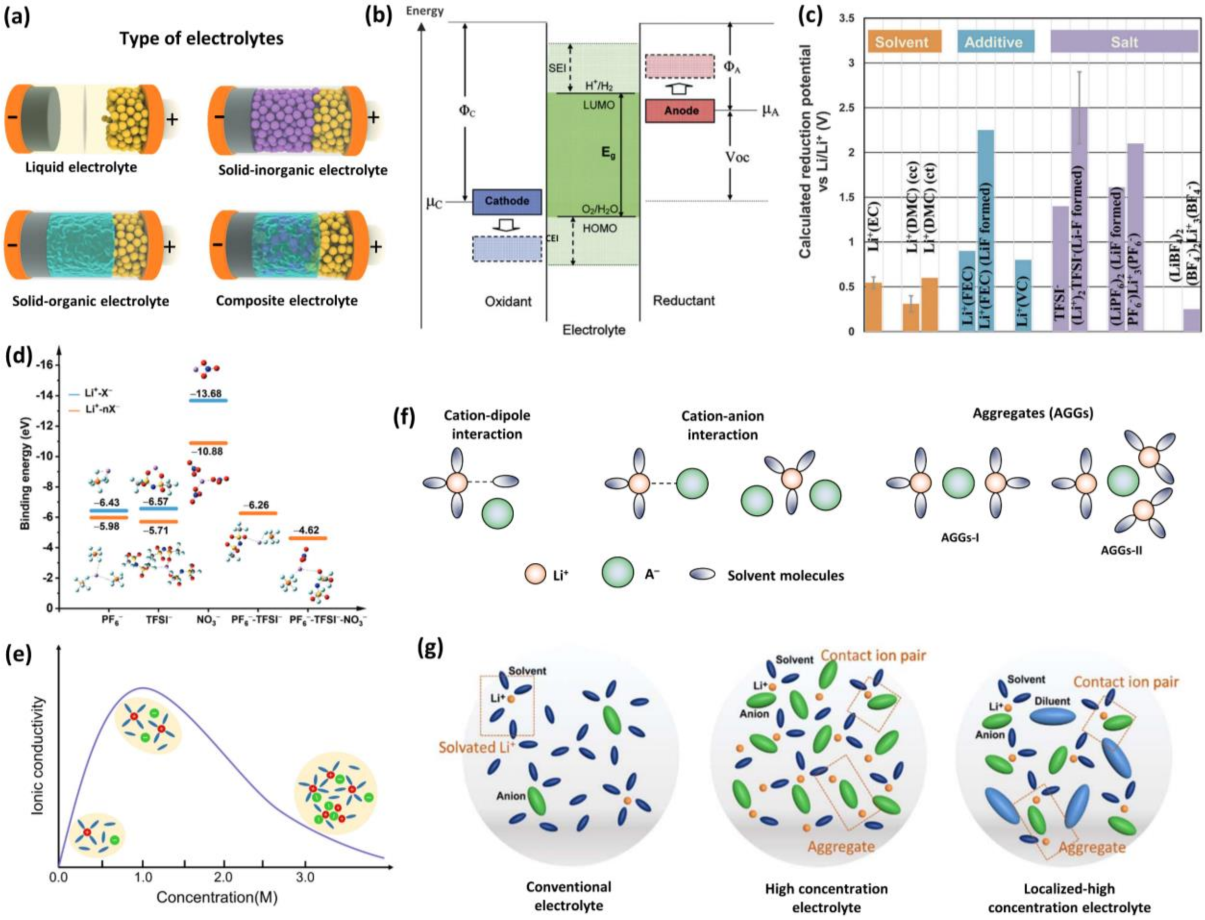

Figure 1.11 (a) Classification of electrolytes, liquid, solid-organic, solid-inorganic, and composite electrolytes.[89] (b) The energy levels of anode, cathode and electrolyte in a battery (schematic).[92] Copyright 2010 American Chemical Society. (c) The calculated reduction potentials of various electrolyte constituents, solvent, salt, and additives. (d) The binding energy levels for $Li^+{-}X^-$ and $Li^+{-}nX^-$, where n is the number of anions, and X^- being PF_6^-, $TFSI^-$ or NO_3^-.[93] Copyright 2024 John Wiley & Sons. Inc. (e) The relationship between the ionic conductivity and the salt concentration of the electrolyte system.[94] Copyright 2024 Angewandte Chemie. (f) Types of interactions between Li^+, anion (A^-) and solvent molecules. (g) Predicted interaction between Li^+, A^- and solvent molecules, in a conventional liquid electrolyte (1 M), high concentration electrolyte (>3 M) and localized-high concentration electrolyte.[95]

The electrolyte dictates the potential window of the battery window through its electrochemical stability (E_g), which is intrinsically linked to the HOMO and LUMO energies of the solvent–salt mixture (**Figure 1.11b,c**).[21,92] When the electrochemical potentials of anode (μ_A) and cathode (μ_C) lie within the electrochemical window of the electrolyte, passivating layers, SEI on the anode side and CEI on the cathode side, are formed due to reduction and oxidation of the electrolyte. Since the LUMO of the electrolyte typically lies higher than the potentials of a reduced (or charged) anode, the formation of the SEI layer is more usual than the formation of CEI.[21] Since a SEI layer is a product of electrolyte degradation, in addition to the solvent molecules, charge carriers are consumed during its formation. However, a uniform SEI layer, once formed, ceases the electron tunneling, and prevents further electrolyte decomposition, effectively extending the usable voltage range.[20,21,84,96] Additionally, an SEI layer is comprised of inorganic and organic sub-layers, consisting of Li_2CO_3, Li_2O, and LiF as inorganic constituents, and Li_2EDC and ROLi (where, R depends on the organic solvent) as the organic constituents.[21] Over the years, several studies have shown that an inorganic-rich SEI layer, especially if LiF-rich, is mechanically more stable and more ionically conductive, and thereby enhances the charge storage kinetics and the cycle life of the battery. Liquid electrolyte additives, such as fluoroethylene carbonate (FEC) have high reduction potential, and readily reduce at the anode to form a LiF-rich SEI layer.[97] Additionally, FEC can improve performance at low temperatures and stabilize high-voltage cathodes by reducing side reactions at the electrode–electrolyte interface.[97]

Liquid electrolytes deliver high ionic conductivity due to the low activation energy (ΔE) required for the ions to migrate through the liquid phase (ΔE_{mig}). However, liquid electrolytes face a high activation energy for ion migration through the SEI layer (ΔE_{SEI}), and high desolvation activation energy (ΔE_{des}) due to strong interactions between Li^+, counter anion, and especially solvent molecules with high dielectric constants.[20,85] Several electrolyte formulations have been proposed to weaken these interactions and to improve the kinetics of the electrochemical cell.[93–95] Recently, Liang *et al.* proposed combining three salts, $LiPF_6$, LiTFSI, and $LiNO_3$, with Li^+ binding energy in the order Li^+–$TFSI^-$ < Li^+–PF_6^- < Li^+–NO_3^- in one electrolyte system.[93] This strategy reduced the Li^+–anion interactions, by inducing electrostatic repulsion between the anions and therefore reducing the binding energies significantly for Li^+–$3A^-$ systems in comparison to Li^+–A^- systems (**Figure 1.11d**).[93] Further, high concentration electrolytes (>3 M) have been tested as electrolyte systems to improve electrochemical stability of the cell, despite their obvious limitations of high viscosity, low ionic conductivity, and high internal resistance (**Figure 1.11e**). In conventional electrolytes (~1.0–1.1 M), the salt concentration is low, and most cations are fully solvated by solvent molecules, leading to a predominance of cation–dipole (M^+–solvent) interactions or M^+–A^- interactions, providing high ionic conductivity but vulnerability to reduction or oxidation at electrode surfaces (**Figure 1.11f**).[98] Whereas, in high-concentration electrolytes (HCEs), the solvent-to-salt ratio is low, forcing most M^+ and A^- to form contact ion pairs (CIPs) or larger aggregates (AGGs), and significantly reduces the amount of free solvent molecules (**Figure 1.11f,g**).[95,98,99] HCEs alter the solvation environment, enhancing electrochemical stability, suppressing solvent decomposition, and favoring the formation of robust, inorganic-rich SEI layers. However, their high viscosity reduces ion mobility, limiting rate performance, and further makes cell fabrication expensive. To control the viscosity issue, HCEs can be diluted with an inert and non-coordinating co-solvent, forming localized high-concentration electrolytes (LHCEs) (**Figure 1.11g**).[95,99] LHCE systems preserve high stability and SEI quality, however so far only slightly improving viscosity and overall ionic conductivity. Overall, while HCEs and LHCEs systems are promising, they feature complicated mass transport mechanisms, which are yet to be fully understood.

1.2.4. References – I

[1] J. Ma, *Battery Technologies*, Wiley **2022**.

[2] R. Kumar, K. Aifantis, P. Hu, *Rechargeable Ion Batteries*, Wiley **2023**.

[3] J. B. Goodenough, *Nat Electron* **2018**, *1*, 204.

[4] Gaston Planté, *The Storage of Electrical Energy: And Researches in the Effects Created by Currents Combining Quantity with High Tension* **1887**.

[5] A. Yoshino, *Angewandte Chemie (International ed. in English)* **2012**, *51*, 5798.

[6] M. S. Whittingham, *Nano letters* **2020**, *20*, 8435.

[7] M. S. Whittingham, *Science (New York, N.Y.)* **1976**, *192*, 1126.

[8] K. Mizushima, P. C. Jones, P. J. Wiseman, J. B. Goodenough, *Solid State Ionics* **1981**, *3-4*, 171.

[9] Akira Yoshino, Kenichi Sanechika,Takayuki Nakajima, *Secondary battery: JP Patent* **1986**.

[10] J. Xie, Y.-C. Lu, *Nature communications* **2020**, *11*, 2499.

[11] Olof Ramström, *The Nobel Prize in Chemistry 2019*, Stockholm, Sweden **2019**.

[12] J. W. Choi, D. Aurbach, *Nat Rev Mater* **2016**, *1*, 16013.

[13] J. T. Frith, M. J. Lacey, U. Ulissi, *Nature communications* **2023**, *14*, 420.

[14] R. D. Shannon, *Acta Cryst A* **1976**, *32*, 751.

[15] M. Ue, K. Sakaushi, K. Uosaki, *Mater. Horiz.* **2020**, *7*, 1937.

[16] A. M. Ralls, K. Leong, J. Clayton, P. Fuelling, C. Mercer, V. Navarro, P. L. Menezes, *Materials (Basel, Switzerland)* **2023**, *16*, 17.

[17] M. S. Ziegler, J. Song, J. E. Trancik, *Energy Environ. Sci.* **2021**, *14*, 6074.

[18] S. Ahmed, P. A. Nelson, K. G. Gallagher, N. Susarla, D. W. Dees, *Journal of Power Sources* **2017**, *342*, 733.

[19] Oktavia Catsaros, *Lithium-Ion Battery Pack Prices See Largest Drop Since 2017, Falling to $115 per Kilowatt-Hour: BloombergNEF* **2024**.

[20] H. Adenusi, G. A. Chass, S. Passerini, K. V. Tian, G. Chen, *Advanced Energy Materials* **2023**, *13*, 2203307.

[21] A. Wang, S. Kadam, H. Li, S. Shi, Y. Qi, *npj Comput Mater* **2018**, *4*, 15.

[22] R. Tao, Y. Gu, Z. Du, X. Lyu, J. Li, *Nat. Rev. Clean Technol.* **2025**, *1*, 116.

[23] Jakob Fleischmann, Patrick Schaufuss, Mikael Hanicke, Evan Horetsky, Dina Ibrahim, Sören Jautelat, Lukas Torscht, Alexandre van de Rijt **2023**, https://www.mckinsey.com/industries/automotive-and-assembly/our-insights/battery-2030-resilient-sustainable-and-circular#/.

[24] M. Greenwood, J. M. Wrogemann, R. Schmuch, H. Jang, M. Winter, J. Leker, *Journal of Power Sources Advances* **2022**, *14*, 100089.

[25] L. Peiseler, V. Schenker, K. Schatzmann, S. Pfister, V. Wood, T. Schmidt, *Nature communications* **2024**, *15*, 10301.

[26] A. Alessia, B. Alessandro, V.-G. Maria, V.-A. Carlos, B. Francesca, *Journal of Cleaner Production* **2021**, *300*, 126954.

[27] E. Orquera, G. Xu, S. Northey, T. Werner, O. Tiku, D. Giurco, K. Matsubae, *Environ. Res.: Infrastruct. Sustain.* **2025**, *5*, 35008.

[28] A. L. Cheng, E. R. H. Fuchs, V. J. Karplus, J. J. Michalek, *Nature communications* **2024**, *15*, 2143.

[29] C. Banza Lubaba Nkulu, L. Casas, V. Haufroid, T. de Putter, N. D. Saenen, T. Kayembe-Kitenge, P. Musa Obadia, D. Kyanika Wa Mukoma, J.-M. Lunda Ilunga, T. S. Nawrot, O. Luboya Numbi, E. Smolders, B. Nemery, *Nature sustainability* **2018**, *1*, 495.

[30] Peter Whoriskey, *Washington Post* **2016**, https://www.washingtonpost.com/graphics/business/batteries/graphite-mining-pollution-in-china/?tid=batteriesbottom.

[31] Todd C. Frankel, *Washington Post* **2016**, https://www.washingtonpost.com/graphics/business/batteries/congo-cobalt-mining-for-lithium-ion-battery/?tid=batteriesbottom.

[32] E. M. Mervine, R. K. Valenta, J. S. Paterson, G. M. Mudd, T. T. Werner, I. Nursamsi, L. J. Sonter, *Nature communications* **2025**, *16*, 481.

[33] X. Rui, Y. Geng, X. Sun, H. Hao, S. Xiao, *Resources, Conservation and Recycling* **2021**, *173*, 105732.

[34] R. J. Bones, D. A. Teagle, S. D. Brooker, F. L. Cullen, *J. Electrochem. Soc.* **1989**, *136*, 1274.

[35] N. Yabuuchi, K. Kubota, M. Dahbi, S. Komaba, *Chemical reviews* **2014**, *114*, 11636.

[36] Y. Zhao, Y. Kang, J. Wozny, J. Lu, H. Du, C. Li, T. Li, F. Kang, N. Tavajohi, B. Li, *Nat Rev Mater* **2023**, *8*, 623.

[37] C. Hu, X. Hou, Z. Bai, L. Yun, X. Zhang, N. Wang, J. Yang, *Chin. J. Chem.* **2021**, *39*, 2931.

[38] H. Zhang, L. Wang, P. Zuo, *J. Mater. Chem. A* **2024**, *12*, 30971.

[39] A. Yao, S. M. Benson, W. C. Chueh, *Nat Energy* **2025**, *10*, 404.

[40] M. F. Pascal Ge, *Solid State Ionics* **1988**, *28-30*, 1172.

[41] H. Kim, J. Hong, G. Yoon, H. Kim, K.-Y. Park, M.-S. Park, W.-S. Yoon, K. Kang, *Energy Environ. Sci.* **2015**, *8*, 2963.

[42] K. Wang, Y. Jin, S. Sun, Y. Huang, J. Peng, J. Luo, Q. Zhang, Y. Qiu, C. Fang, J. Han, *ACS omega* **2017**, *2*, 1687.

[43] A. Rudola, K. Saravanan, C. W. Mason, P. Balaya, *J. Mater. Chem. A* **2013**, *1*, 2653.

[44] K. Ariyoshi, K. Matsumoto, *J. Phys. Chem. C* **2023**, *127*, 15114.

[45] H. Liao, H. Liu, Q. Gou, R. Zeng, D. Zhao, X. Yuan, F. Chen, G. Xie, Y. Hou, *Journal of Power Sources* **2025**, *625*, 235739.

[46] J. Ni, L. Li, J. Lu, *ACS Energy Lett.* **2018**, *3*, 1137.

[47] C. Vaalma, D. Buchholz, M. Weil, S. Passerini, *Nat Rev Mater* **2018**, *3*, 18013.

[48] F. Dai, M. Cai, *Commun Mater* **2022**, *3*, 64.

[49] K. Chen, Y. Li, H. Zhan, *IOP Conf. Ser.: Earth Environ. Sci.* **2022**, *1011*, 12009.

[50] J. Asenbauer, T. Eisenmann, M. Kuenzel, A. Kazzazi, Z. Chen, D. Bresser, *Sustainable Energy Fuels* **2020**, *4*, 5387.

[51] Y. Qiao, H. Zhao, Y. Shen, L. Li, Z. Rao, G. Shao, Y. Lei, *EcoMat* **2023**, *5*, e12321.

[52] J. Lu, T. Wu, K. Amine, *Nat Energy* **2017**, *2*, 17011.

[53] D. Lin, Y. Liu, Y. Cui, *Nature nanotechnology* **2017**, *12*, 194.

[54] I. T. Adebanjo, J. Eko, A. G. Agbeyegbe, S. F. Yuk, S. V. Cowart, E. A. Nagelli, F. J. Burpo, J. L. Allen, D. T. Tran, N. Bhattarai, K. Shah, J.-Y. Hwang, H. H. Sun, *Energy Adv.* **2025**, *4*, 820.

[55] U. Hofmann, W. Rüdorff, *Trans. Faraday Soc.* **1938**, *34*, 1017.

[56] D. Allart, M. Montaru, H. Gualous, *J. Electrochem. Soc.* **2018**, *165*, A380-A387.

[57] H. Shi, C. Shi, Z. Jia, L. Zhang, H. Wang, J. Chen, *RSC advances* **2022**, *12*, 33641.

[58] G. H. Jung, C. Jin, Y.-K. Sun, *Meet. Abstr.* **2009**, *MA2009-02*, 616.

[59] H. Huo, J. Janek, *ACS Energy Lett.* **2022**, *7*, 4005.

[60] H. F. Andersen, C. E. L. Foss, J. Voje, R. Tronstad, T. Mokkelbost, P. E. Vullum, A. Ulvestad, M. Kirkengen, J. P. Mæhlen, *Scientific reports* **2019**, *9*, 14814.

[61] D. Puthusseri, M. Wahid, S. Ogale, *ACS omega* **2018**, *3*, 4591.

[62] T. Banerjee, R. Kundu, *Energy Fuels* **2024**, *38*, 12487.

[63] P. M. Hari Prasad, G. Malavika, A. Pillai, S. Sadan, Z. S. Pillai, *NPG Asia Mater* **2024**, *16*, 37.

[64] Y. Lu, J. Chen, *Nature reviews. Chemistry* **2020**, *4*, 127.

[65] A. Jana, S. Bähring, M. Ishida, S. Goeb, D. Canevet, M. Sallé, J. O. Jeppesen, J. L. Sessler, *Chemical Society reviews* **2018**, *47*, 5614.

[66] J. Bitenc, K. Pirnat, O. Lužanin, R. Dominko, *Chemistry of materials a publication of the American Chemical Society* **2024**, *36*, 1025.

[67] H. Kye, Y. Kang, D. Jang, J. E. Kwon, B.-G. Kim, *Adv Energy and Sustain Res* **2022**, *3*, 2200030.

[68] A. Innocenti, H. Adenusi, S. Passerini, *InfoMat* **2023**, *5*, e12480.

[69] K. Zhao, X. Wang, W. Feng, A. Ponrouch, P. Poizot, M. Armand, Z. Zhou, H. Zhang, *Energy Environ. Sci.* **2025**, *18*, 7756.

[70] C. Luo, C. Wang, *Meet. Abstr.* **2019**, *MA2019-02*, 542.

[71] D.-Y. Wang, W. Guo, Y. Fu, *Accounts of chemical research* **2019**, *52*, 2290.

[72] W. Liu, P. Oh, X. Liu, M.-J. Lee, W. Cho, S. Chae, Y. Kim, J. Cho, *Angewandte Chemie (International ed. in English)* **2015**, *54*, 4440.

[73] A. Manthiram, A. Vadivel Murugan, A. Sarkar, T. Muraliganth, *Energy Environ. Sci.* **2008**, *1*, 621.

[74] A. Chakraborty, S. Kunnikuruvan, S. Kumar, B. Markovsky, D. Aurbach, M. Dixit, D. T. Major, *Chem. Mater.* **2020**, *32*, 915.

[75] T. Chen, H. Banda, J. Wang, J. J. Oppenheim, A. Franceschi, M. Dincă, *ACS central science* **2024**, *10*, 569.

[76] S. Haldar, A. Schneemann, S. Kaskel, *Journal of the American Chemical Society* **2023**, *145*, 13494.

[77] M. Yao, H. Sano, H. Ando, T. Kiyobayashi, *Scientific reports* **2015**, *5*, 10962.

[78] X. Zhang, Q. Xu, S. Wang, Y. Tang, X. Huang, *ACS Appl. Energy Mater.* **2021**, *4*, 11787.

[79] C. Su, F. Yang, L. Ji, L. Xu, C. Zhang, *J. Mater. Chem. A* **2014**, *2*, 20083.

[80] M. Fu, C. Zhang, Y. Chen, K. Fan, G. Zhang, J. Zou, Y. Gao, H. Dai, X. Wang, C. Wang, *Chemical communications (Cambridge, England)* **2022**, *58*, 11993.

[81] E. Youngsam Kim, K. Vi‐khanh Ta, F. Chen, Z. Yang, Y. Yu, C. Luo, *Batteries & Supercaps* **2024**, *7*, e202400325.

[82] Z. Huang, X. Li, Z. Chen, P. Li, X. Ji, C. Zhi, *Nature reviews. Chemistry* **2023**, *7*, 616.

[83] Z. Sun, K. Xi, J. Chen, A. Abdelkader, M.-Y. Li, Y. Qin, Y. Lin, Q. Jiang, Y.-Q. Su, R. Vasant Kumar, S. Ding, *Nature communications* **2022**, *13*, 3209.

[84] G. G. Eshetu, G. A. Elia, M. Armand, M. Forsyth, S. Komaba, T. Rojo, S. Passerini, *Advanced Energy Materials* **2020**, *10*, 2000093.

[85] B. Flamme, G. Rodriguez Garcia, M. Weil, M. Haddad, P. Phansavath, V. Ratovelomanana-Vidal, A. Chagnes, *Green Chem.* **2017**, *19*, 1828.

[86] C. Hei Chan, H. Ho Wong, S. Liang, M. Sun, T. Wu, Q. Lu, L. Lu, B. Chen, B. Huang, *Batteries & Supercaps* **2024**, *7*, e202400432.

[87] X. Yang, B. Zhang, Y. Tian, Y. Wang, Z. Fu, D. Zhou, H. Liu, F. Kang, B. Li, C. Wang, G. Wang, *Nature communications* **2023**, *14*, 925.

[88] J. Xu, J. Zhang, T. P. Pollard, Q. Li, S. Tan, S. Hou, H. Wan, F. Chen, H. He, E. Hu, K. Xu, X.-Q. Yang, O. Borodin, C. Wang, *Nature* **2023**, *614*, 694.

[89] S. Li, S.-Q. Zhang, L. Shen, Q. Liu, J.-B. Ma, W. Lv, Y.-B. He, Q.-H. Yang, *Advanced science (Weinheim, Baden-Wurttemberg, Germany)* **2020**, *7*, 1903088.

[90] Y. Liu, Y. Zhu, Y. Cui, *Nat Energy* **2019**, *4*, 540.

[91] Y. Chen, Y. Kang, Y. Zhao, L. Wang, J. Liu, Y. Li, Z. Liang, X. He, X. Li, N. Tavajohi, B. Li, *Journal of Energy Chemistry* **2021**, *59*, 83.

[92] J. B. Goodenough, Y. Kim, *Chem. Mater.* **2010**, *22*, 587.

[93] P. Liang, H. Hu, Y. Dong, Z. Wang, K. Liu, G. Ding, F. Cheng, *Adv Funct Materials* **2024**, *34*.

[94] Z. Liu, W. Hou, H. Tian, Q. Qiu, I. Ullah, S. Qiu, W. Sun, Q. Yu, J. Yuan, L. Xia, X. Wu, *Angewandte Chemie (International ed. in English)* **2024**, *63*, e202400110.

[95] X. Cao, H. Jia, W. Xu and J.G. Zhang, *J. Electrochem. Soc.* **2021**, *168*, 10522.

[96] Y. Peng, R. Tamate, K. Nishikawa, *ChemElectroChem* **2024**, *11*.

[97] M. Matsumoto, T. Sanada, N. Takao, M. Mogi, T. Matsuda, K. Ando, D. Imamura, H. Imai, *ECS Trans.* **2015**, *69*, 13.

[98] X. Li, F. Luo, N. Zhou, H. Adenusi, S. Fang, F. Wu, S. Passerini, *Advanced Energy Materials* **2025**, *15*, 2501272.

[99] J. Shi, C. Xu, J. Lai, Z. Li, Y. Zhang, Y. Liu, K. Ding, Y.-P. Cai, R. Shang, Q. Zheng, *Angewandte Chemie (International ed. in English)* **2023**, *62*, e202218151.

1.3. Covalent organic frameworks (COFs)

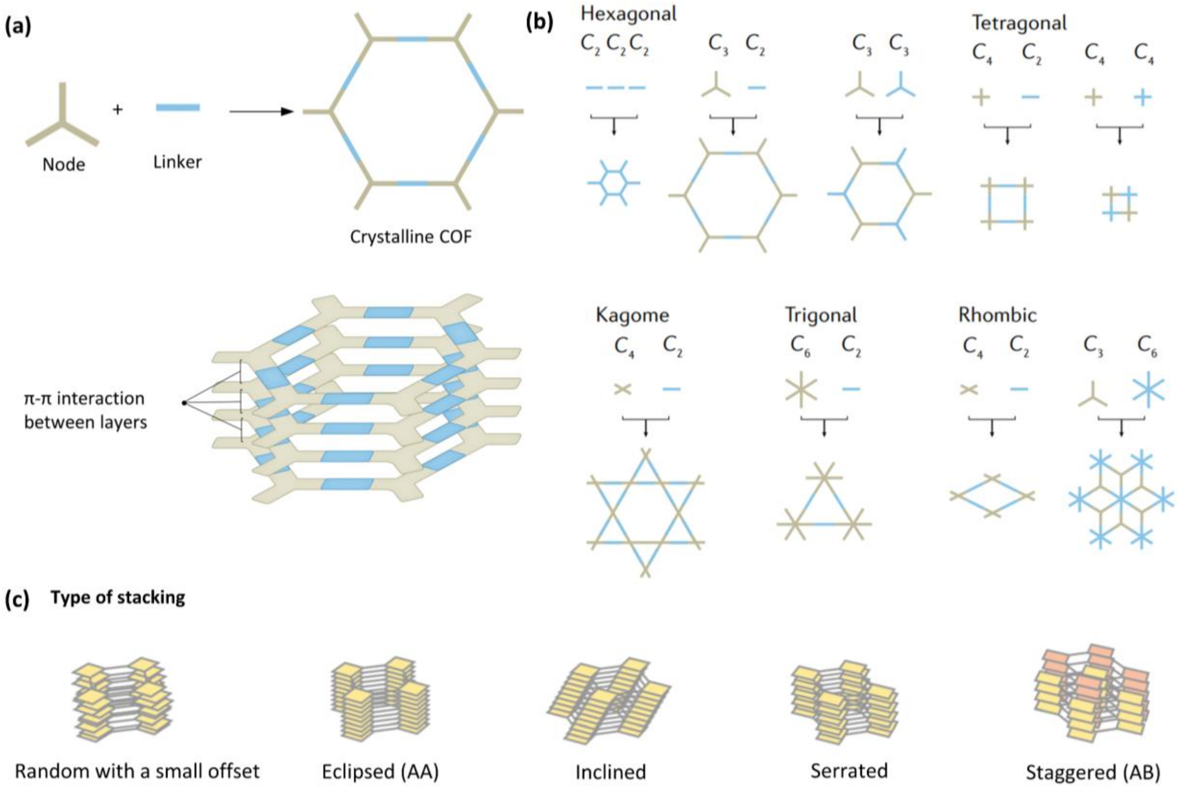

Figure 1.12 (a) Schematic representation of the formation of covalent organic frameworks (COFs).[1] (b) Topological diagrams depicting the guiding principles for designing 2D COFs with various lattice geometries, including hexagonal, tetragonal, kagome, trigonal, and rhombic pore structures.[1] Copyright 2023 Springer Nature. (c) Illustration of different possible stacking arrangements of 2D COF layers, highlighting variations such as random with small offset, eclipsed, inclined, serrated, and staggered.

Covalent organic frameworks (COFs) are an emerging class of organic crystalline porous materials that have garnered immense attention owing to their structural precision, tunable porosity, and exceptional stability.[1] COFs were first conceptualized and developed by Yaghi and co-workers in 2005, representing a milestone in reticular chemistry, wherein organic building blocks can be linked by strong covalent bonds into predetermined architectures with long-range order.[2] The pioneering example, COF-1, was synthesized through the condensation of 1,4-benzenediboronic acid (DBA) into a two-dimensional (2D) framework, followed by COF-5, which showcased the versatility of the design principle.[2] COFs are the first class of purely organic crystalline porous materials constructed via covalent bonds, paralleling the significance of another class of crystalline porous materials, i.e., metal–organic frameworks (MOFs), which are formed by coordination between metal-centers and organic building blocks.[3] Additionally, COFs share similarities with conventional organic polymers as well, for example, both are composed of light elements (C, H, O, N, and B) and rely on covalent connectivity of repeating units. However, while traditional polymers are generally amorphous or semicrystalline, COFs possess a well-defined, long-range ordered lattice. This crystallinity arises from the judicious selection of rigid linkers and nodes that direct the framework into periodic arrays, yielding highly predictable pore sizes, shapes, and functionalities.[1,4–7]

The design of COFs follows a modular strategy, involving three primary components: nodes (main building block), and auxiliary building blocks, and the linkages (**Figure 1.12a**).[1] The connectivity and symmetry of these building units dictate the resulting topology.[6] As depicted in **Figure 1.12b**, a hexagonal framework typically arises from either the combination of 3 linear linkers (C_2) or a trigonal planar linker (C_3) with linear linkers, yielding honeycomb-like architectures. On the other hand, tetragonal pore COFs can be yielded via connecting 2 square-planar linkers (C_4) together, or with linear building blocks, while Kagome topology emerges when tetrafunctional linkers (C_4) alternate with linear linkers to generate a lattice with dual pore sizes.[1,6] Rhombic and trigonal arrangements can be engineered through rational linker geometry selection, offering a broad structural landscape. Beyond 2D lattices, COFs can extend into three-dimensional (3D) architectures through tetrahedral or octahedral nodes, producing frameworks such as *dia* (diamond), *bor* (boracite), *ctn* (C_3N_4), etc.[1] More recently, cage-type 2D and 3D COFs with discrete polyhedral geometries have expanded the structural diversity further.[8,9] In this thesis we mainly focus on 2D COFs, and will discuss their structure, functionalities, and applications. Similar to graphene sheets in graphite, 2D layers (along the x-y plane) are stacked in z-direction by π–π interactions, yielding crystalline porous networks.[1,2,6] Furthermore, stacking modes in layered 2D COFs play a critical role in determining their porosity, stability, and electronic properties. While an ideal eclipsed (AA) stacking maximizes pore alignment, it is often destabilized by interlayer repulsions, leading to alternative stacking modes such as staggered (AB), inclined, serrated, or random arrangements with small offsets (**Figure 1.12c**).[5] These stacking variations not only influence the crystallinity and surface area but also profoundly affect charge transport and guest diffusion within the pores.[10,11]

Despite remarkable advances, COF synthesis and application face intrinsic challenges, often described as the "*trilemma*" articulated by the Lotsch group.[5] This trilemma arises from the competing requirements of c*rystallinity*, *stability*, and *functionality*, where enhancing one property often compromises the others. For example, frameworks constructed with highly reversible linkages exhibit superior crystallinity but may suffer from reduced chemical robustness, whereas stable irreversible linkages can lead to poorly ordered or amorphous products.[5] Balancing these three aspects remains at the forefront of COF research, driving innovation in synthetic methodologies, linker design, and post-synthetic modification, which will be discussed in detail in the next section.

1.3.1. Synthetic methodologies

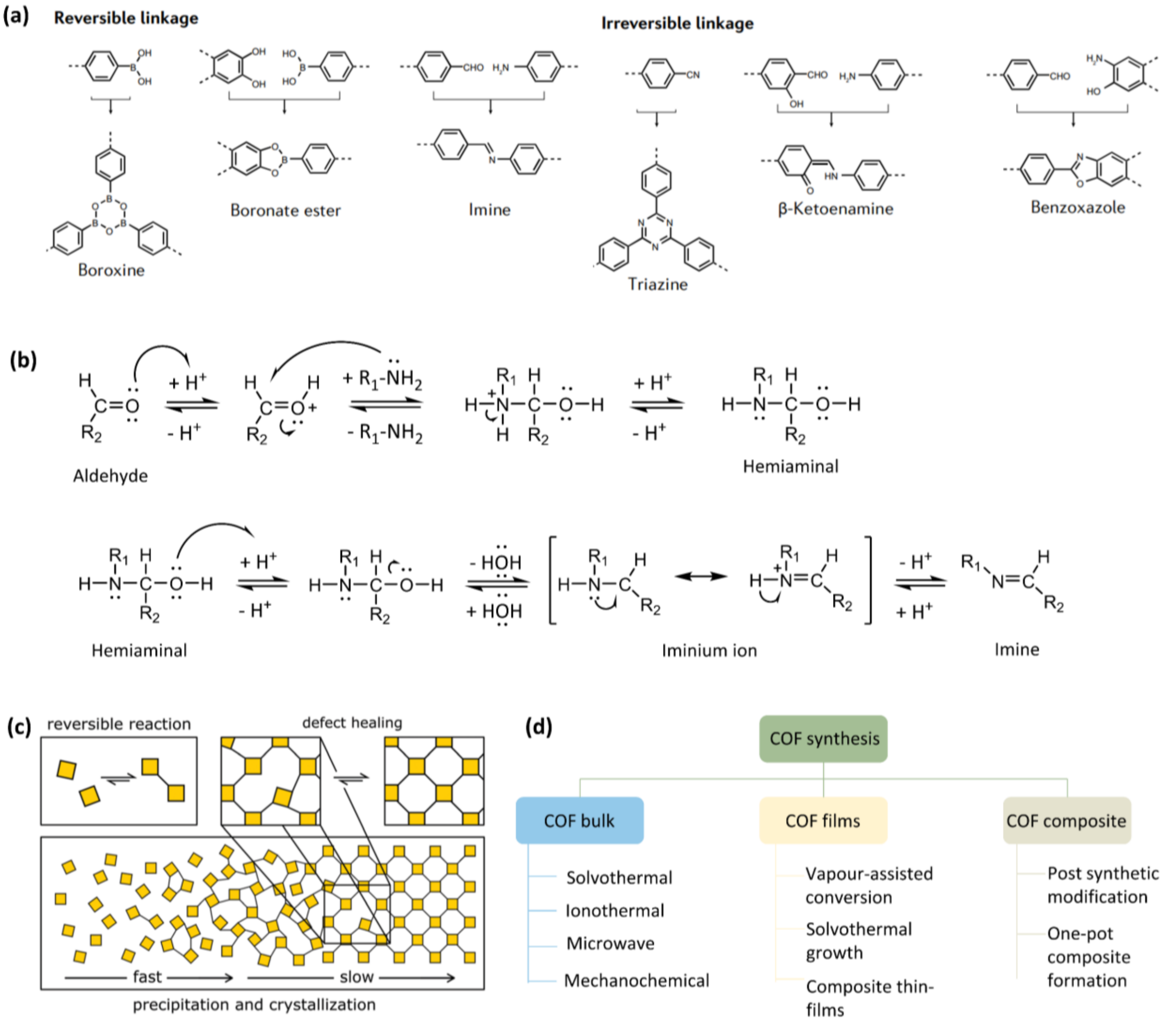

Figure 1.13 (a) Key reversible linkages (boroxine, boronate ester, imine) and (ultimately) irreversible linkages (triazine, β-ketoenamine, benzoxazole) employed in COF construction.[1] Copyright 2023 Springer Nature. (b) Reaction mechanism illustrating the formation of imine linkage. (c) Schematic depiction of imine-linked COF growth through slow crystallization, highlighting reversible bond dynamics and defect-healing processes.[5] (d) Overview of synthetic strategies for producing COFs in the form of bulk powders, thin films, and composite materials.

As briefly described in the previous section, the development of COFs is fundamentally governed by the challenge of simultaneously achieving high crystallinity, stability, and functionality within a single framework.[5] Reversibility during COF formation plays a significant role in this, for instance, reversible bond formation enables dynamic error correction, allowing the framework to “self-heal” defects and approach a thermodynamically stable and highly ordered crystalline structure.[5,12] Therefore, utilizing dynamic covalent chemistry in COF synthesis is of key importance, where reversible linkages such as boroxine, boronate ester, and imine bonds have enabled the formation of highly crystalline and long-range order frameworks (**Figure 1.13a,c**).[5,6,12] However, reversibility, leading to defect correction and crystallinity, often compromises chemical, thermal, and electrochemical stability. In many applications (described in detail in Section 1.3.2), COFs must operate under conditions harsher than those of their original synthesis, such as exposure to moisture, acidic or basic media, and elevated temperatures.[5] Under such conditions, reversible bonds are prone to cleavage, leading to loss of crystallinity as well as structural integrity. Imine COFs are considerably more robust than boronate esters, while still preserving a degree of reversibility during formation. Since the first demonstration of imine-linked 3D COF-300 in 2009, imine chemistry has inspired the design of numerous COFs with improved balance between order and stability.[13] The formation of imine bonds follows an acid-catalyzed condensation mechanism (**Figure 1.13b**). Protonation of the carbonyl oxygen increases electrophilicity at the carbonyl carbon, which undergoes nucleophilic attack by a primary amine. The resulting hemiaminal intermediate, stabilized through deprotonation, undergoes dehydration upon protonation of the hydroxyl group, leading to the formation of a resonance-stabilized iminium ion. Final deprotonation yields the imine linkage, also known as a Schiff base.[14] Crucially, the acidity of the reaction medium must be finely tuned such that it is sufficient to catalyze the dehydration step, but not excessive, as high acidity protonates the amine, suppressing nucleophilic addition.[5]

While irreversible linkages such as triazine,[15] benzoxazole,[16] and β-ketoenamine (via keto-enol tautomerism)[17] provide exceptional stability against hydrolysis, when utilized for electrochemical applications, their inability to undergo defect healing often results in poor crystallinity. To mitigate this limitation, modulation strategies have emerged, whereby reaction kinetics are deliberately slowed using modulators or solvent engineering.[18] The modulation approach, first seen in MOFs synthesis, can operate when small monofunctional molecules are introduced to the reaction mixture to compete with the main linkers during bond formation, thereby slowing down nucleation and framework growth.[19] By transiently capping reactive sites or engaging in reversible competitive interactions, modulators reduce the rate of irreversible aggregation and extend the time window for dynamic error correction, and thereby enabling the framework to reorganize toward a thermodynamically stable, highly ordered structure.[18]

COFs can be synthesized in diverse morphologies ranging from bulk powders to thin films and composites, with the choice of method dictating crystallinity, scalability, and functional integration (**Figure 1.13d**).[4,7,20] Bulk COF powders are most commonly obtained by solvothermal condensation, where organic monomers undergo condensation reactions in organic solvents under sealed, elevated-temperature conditions, typically 80−200 °C for ~3−7 days.[7,12,20] Alternative bulk strategies include ionothermal synthesis, utilizing solvent as a reaction catalyst, such as the formation crystalline imide-COF with anhydrous $ZnCl_2$ at elevated temperatures of ~200−300 °C under vacuum, completing the reaction within 10 hours.[21] On the other hand, microwave-assisted synthesis can be even more rapid

(~60 min) and provides energy-efficient crystallization.[22] Mechanochemical routes, first proposed by Banerjee *et al.*, exploit simple pestle grinding to achieve solvent-minimized and scalable production.[23] In parallel, thin-film fabrication has become critical for device-oriented applications, with methods such as vapor-assisted conversion (VAC),[24] direct solvothermal growth on substrates,[25] and composite film approaches including spin coating or drop casting.[26] COF films can be deposited/grown on substrates such as glass, fluorine tin oxide-coated glass (FTO), metallic mesh, etc. Beyond powders and films, COF composites extend functionality through either in situ one-pot syntheses, where COF domains nucleate and grow alongside other components, such as COF@CNT,[27] COF@graphene,[28] or post-synthetic modification, in which pre-formed COFs are chemically or physically integrated with secondary phases.[29,30] These synthetic methodologies provide tunable control over COF crystallinity, functionality as well as interfacial properties, thereby expanding their applicability across various application, like catalysis, energy storage, sensing, and membrane technologies, to be discussed in the next section.

1.3.2. Applications

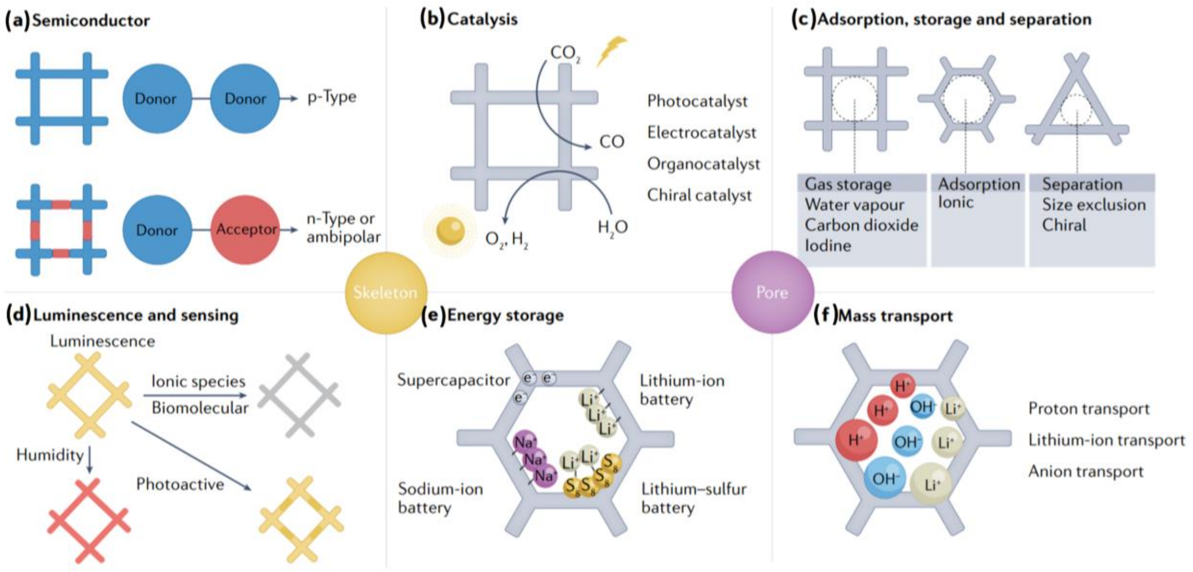

Figure 1.14 Schematic illustration of design principles for COFs for various applications, including (a) semiconductors, (b) catalysis, (c) adsorption, storage, and separation, (d) luminescence and sensing, (e) energy storage, and (f) mass transport.[1] Copyright 2023 Springer Nature.

Owing to their tunable ordered structure and electronic properties, COFs have emerged as a versatile class of organic materials with extensive (potential) applications across several advanced fields, making them a futuristic and revolutionary technology.[1,4,6,7] COFs as *semiconductors* represent one of the most promising directions in organic materials research because, unlike amorphous polymers, they uniquely combine repeating units, 1D channels, π-conjugated skeletons, and tunable electronic structures.[11,31–33] COFs can be engineered to exhibit *p*-type, *n*-type, or ambipolar/bipolar semiconduction, depending on the electronic characteristics of their building blocks and chemical linkages. For instance, strong electron donating (EDG) subunits, such as tetrathiafulvalene (TTF) based TTF-Ph-COF, demonstrate *p*-type behavior with hole mobilities as high as 0.2 $cm^2\ V^{-1}\ s^{-1}$, owing to periodically repeating TTF units in π-channels.[11] On the other hand, a phthalocyanine and benzothiadiazole-based COF, NiPc-BTBA-COF exhibited *n*-type conduction with electron mobility of ~0.6 $cm^2\ V^{-1}\ s^{-1}$.[33] Ambipolar transport has been achieved in donor–acceptor (D–A) frameworks such as the DA-COF, with HHTP as electron rich and BTDADA as electron deficient subunits, exhibiting 0.04 $cm^2\ V^{-1}\ s^{-1}$ electron and 0.01 $cm^2\ V^{-1}\ s^{-1}$ hole mobility.[32]

Photocatalysis in COFs can arise from both their 2D conjugated π-systems, 1D channels in *z*-direction, and tunable band structure via D–A–D heterojunctions, such as in Tz-BTPA-W COF, which allow for light harvesting and charge separation, and thereby showing potential as photocathodes.[34] *Electrocatalysis* is enabled by the incorporation of redox-active linkers and conductive backbones that facilitate electron transfer; for example, Co- or Mn-based metal-coordinated COFs are frequently employed for electrocatalysis.[35,36] Mn-PhenPy COF demonstrated exceptional turnover frequency of 617 h^{-1} and a CO evolution of ~222 $\mu mol\ cm^{-2}$ when utilized in a MEA cell for CO_2 electroreduction.[36]

The long-range ordered pores, tunable pore sizes and pore-topology of COFs enable ionic *adsorption, gas storage,* and *molecular separation*.[37] Furthermore, COFs have shown promise in *luminescence* and *sensing applications*, owing to their rigid π-conjugated structures and ordered channels allowing for efficient exciton migration, fluorescence emission, and photoluminescence.[38] Additionally, by tailoring functional groups of the building units and linkages, COFs can act as sensors for volatile organic compounds, toxic gases, metal-ions and biomolecules.[39]

Finally, COFs are being actively explored in *energy storage* and *mass transport* applications.[40–45] By the incorporation of redox-active linkers, and conductive backbones with their intrinsic high porosity and chemical stability, COFs can serve as promising candidates for supercapacitors,[46] LIBs,[47] and SIBs,[48] where they function as electrodes or active host materials. The 1D pore network allows rapid and directional ion transport, leading to high mass transport rates.[40] The applicability of COFs as battery components will be discussed in detail in the upcoming section. Overall, the modularity of COFs enables precise structural engineering to meet diverse functional requirements, placing them at the forefront of advanced materials research.

1.4. Covalent organic frameworks for battery applications

1.4.1. COF-based electrolyte material

Organic polymer electrolytes (OPEs) have been extensively investigated as solid or gel electrolytes for next-generation electrochemical energy storage devices due to their structural versatility and safer operation. Several classes of organic polymers, such as polyethylene oxide (PEO),[49] polyvinylidene fluoride (PVDF),[50] poly(methyl methacrylate) (PMMA),[51] polyethylene glycol (PEG)[52] and poly(ionic liquid)-based systems,[53] have been employed either in solid-state or gel configurations. Solid-state systems typically exhibit ionic conductivities in the range of $\sim10^{-6}$–10^{-4} S cm^{-1} at room temperature, while after incorporating plasticizers, like organic solvents and ionic liquids (ILs), or by following the copolymer design strategies, ionic conductivities $\geq10^{-3}$ S cm^{-1}, similar to liquid electrolytes, could be achieved.[54,55] Fundamentally, the ion transport mechanism in OPEs involves segmental motion of the polymer chains, where coordination sites provided by electronegative atoms, such as ether oxygen in PEO or functional moieties ($-COO^-$, $-SO_3^-$) facilitate cation solvation and hopping from one energetically favorable site to another.[49,55] While, OPEs have an advantage of flexible molecular design, tailoring the polymer backbone to control crystallinity and mechanical flexibility, they suffer from several challenges. For instance, the presence of inevitable crystalline domains and entanglement of long polymer chains in OPEs reduces segmental mobility of the chains, and thereby lowering ionic conductivity.[55]

Taking inspiration from the OPEs, researchers have looked towards other organic, highly tunable electrolyte alternatives, such as COFs.[56] COFs not only have the advantage of tunability, which allows easy incorporation of moieties, such as $-COO^-$, $-SO_3^-$, –OH, –C=O and imidazolium, through building blocks, but also provide 1D channels (and others in 3D COFs) with periodically occurring coordinating motifs as continuous ion-conduction pathways, unlike the amorphous domains in many OPEs.[45,56–62] Furthermore, the covalent bonding within COFs can impart high thermal stability and robust chemical resistance, ensuring safer operation compared to flammable organic solvents and less stable polymer electrolytes. By rational design, discussed in Section 1.4.1.1 and 1.4.1.2, COFs can achieve an electrochemical stability window of >4.5–5 V, high ionic conductivity of $\sim10^{-3}$ S cm^{-1}, and high cation transference number (t_+) of ~0.9, allowing compatibility with high-voltage cathodes as well as high-rate electrodes.

1.4.1.1. All-solid-state electrolyte

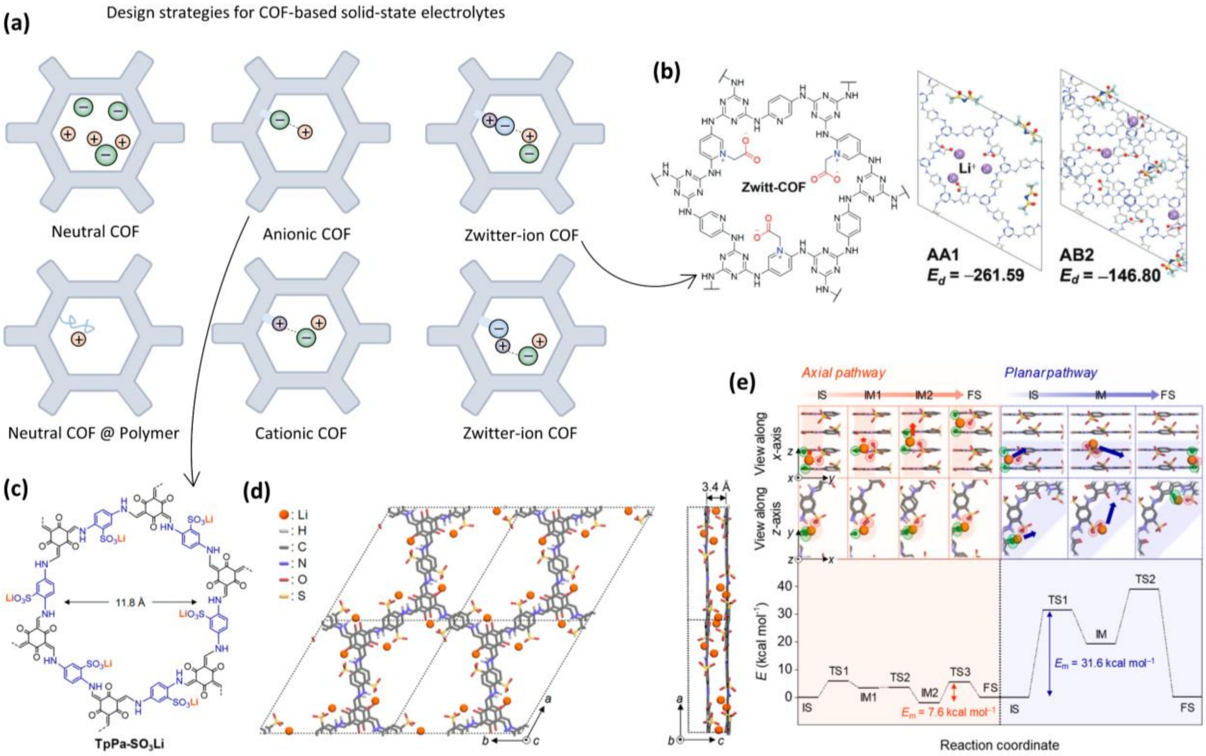

Figure 1.15 (a) Design strategies for COF-based solid-state electrolytes (SSEs) as neutral COF, neutral COF with polymer side chains (neutral COF @ polymer), anionic COF, cation COF, and Zwitter-ion COFs. The orange ball represents metal cations (M$^+$), the green ball represents the counter anion (A$^–$), purple and blue balls represent auxiliary cation and anion. (b) Example of zwitterionic COF (Zwitt-COF), together with its AA- and AB-stacking configurations upon LiTFSI incorporation, along with the corresponding dissociative adsorption energies of LiTFSI, reported in kcal mol^{-1}.[58] Copyright 2023 Wiley-VCH. (c) Example of COF–TpPaSO$_3$Li, and (d) its crystal structure and the interlayer stacking distance between adjacent COF sheets.[62] (e) Theoretical analysis of Li-ion migration with axially and planar pathways in the COF (top), accompanied by the corresponding energy profiles (bottom). The migration process is illustrated through initial (IS), intermediate (IM), transition (TS), and final (FS) states.[62] Copyright 2019 American Chemical Society.

The ionic conductivity of an electrolyte depends on several interconnected factors, including (1) concentration of mobile ions, (2) their mobility, and (3) the energy barrier that governs their migration (E_a).[55] High ionic conductivity requires not only a large number of charge carriers but also efficient transport pathways that minimize ion trapping and reduce E_a. In practice, both cations and anions contribute to total ionic conduction, however, for classical rechargeable metal-ion batteries, only M$^+$ transport is desirable, since energy storage relies on the reversible insertion and extraction of the metal cation, M$^+$= Li$^+$, Na$^+$, Mg$^+$ etc. In contrast, A$^–$ movement is undesirable as it lowers the effective t_+ and further leads to the formation of a concentration gradient due to anion accumulation near the electrode surface, and henceforth acting as an extra energy barrier.[63] Therefore, an ideal electrolyte maximizes the number of mobile M^+ while simultaneously suppressing A^- migration, through immobilization strategies. For instance, covalent tethering or electrostatic trapping of A^- can effectively enhances the t_+.[62,64] Moreover, designing structural environments that promote cation coordination flexibility, and fast hopping dynamics can reduce E_a.[58,61] These design principles also form the foundation for COF-based electrolyte materials, where tailored porosity, functionality, and framework polarity have been exploited. As illustrated in **Figure 1.15a**, four main categories of COF-based solid-state electrolytes have emerged:

Neutral COF electrolytes are designed so that the framework itself does not carry a permanent charge but instead incorporates polar functional groups, such as −C=O, −OH, or −O−, as coordination sites for solvated cations such as Li^+ or Na^+.[45,65–67] The conduction mechanism in neutral COFs is typically analogous to that of polymer electrolytes, i.e., ion migration occurs through repeated coordination–dissociation processes between M^+ and electron-rich donor groups, arranged in an ordered manner along the framework walls, creating directional and interconnected transport channels. However, a larger stacking distance can lead to higher values of E_a and restricted migration, which limits the functionality aspect of the COF design.[40] To enhance conduction, polymer chains such as polyethylene oxide (PEO) have been integrated into COF building blocks. Li^+@TPB-BMTP-COF demonstrates periodically aligned oligo(ethylene oxide) flexible chains along the pore walls of the COF, facilitating superior ion pair (M^+– A^-) dissociation, and M^+ hopping via segmental motion of polymer chains in well-defined oriented pores, resulting in an ionic conductivity of 6.04×10^{-6} S cm^{-1} at 40 °C.[67] Furthermore, Zhang *et al.* tested the impact of length of the polymer chain on the ionic conductivity for COF-PEO-x-Li, with x= 3, 6, and 9, and reported a proportional relationship between ionic conductivity and the length of the PEO side-chain.[66] Therefore, this combination of ordered nanochannels and flexible polymer segments promotes efficient, directional ion migration, reducing E_a for ion transport while retaining the mechanical stability and porosity of the COF.

Anionic COF electrolytes are designed such that the COF framework itself bears a negative charge, typically introduced through incorporation of anionic functional groups, either through linkers or the linkage, into the COF backbone.[45,61,62,68] Since, the framework itself carries negatively charged moieties, it can undergo straightforward cation exchange with alkali metal ions such as Li^+ or Na^+, thereby eliminating the requirement to add lithium or sodium salts, reducing the risk of salt precipitation, and simplifying the electrolyte composition.[62] The negatively charged groups, such as $–SO_3^-$,[62] $–COO^-$,[61] and $–BO_3^-$,[68] are covalently tethered to the pore walls, creating a negatively charged scaffold that immobilizes the anion, while providing hopping sites for the cation. Consequently, only the metal cations remain mobile within the pores, leading to a substantial increase in the t_+, often approaching unity.[61,62] The primary advantage of anionic COFs lies in this anion immobilization mechanism, which eliminates concentration polarization and ensures that current flow is dominated by cations. This combination of anion immobilization and directional cation hopping was demonstrated by Jeong and co-workers, where all-solid COF-TpPaSO$_3$Li exhibited single cation transport with t_{Li^+}= 0.9, and ionic conductivity of 2.7 × 10^{-5} S cm^{-1} (**Figure 1.15c,d**).[62] Notably, DFT calculations revealed that the Li$^+$ migration barrier was much higher for ion migration in the *xy*-plane compared to the *z*-plane, i.e. through the COF pores, and thereby proving the concept of COF-pores acting as directional pathway for ion transport (**Figure 1.15e**).[62]

Cationic COF electrolytes consist of periodically reccurring positively charged functional groups, such as quaternary ammonium (–NR$_4^+$) or imidazolium, judicially positioned in the framework backbone.[60,64] Subsequent addition of lithium or sodium salt into the framework leads to the coordination of positive units with the anion of the salt, weakening the cation–anion interactions. Therefore, the positively charged pore wall reduces the ion pair dissociation energy and provides hopping sites for the cation. COF Li-CON-TFSI, consisting of –NR$_3^+$ linker and TFSI$^-$ counter anion, delivered a Li-ion ionic conductivity of 2.09 × 10^{-4} S cm^{-1} at 70 °C.[64]

Finally, *Zwitter-ion COFs* are often a combination of anionic and cationic COF electrolytes, consisting of both positively and negatively charged groups integrated into the framework backbone, leading to an overall charge-neutral structure that nevertheless carries localized ionic functionalities.[45,58] A recent investigation by Kang *et al.* demonstrated the synthesis of Zwitt-COF from its precursor N-COF through a reaction with sodium iodoacetate (**Figure 1.15b**).[58] This structural transformation induced a preference for AA-stacking in the Zwitt-COF, contrasting with the AB-stacking favored by the parent framework, thereby enabling highly directional transport of mobile ions. Notably, the all-solid Zwitt-COF–LiTFSI complex exhibited outstanding Li$^+$ conductivity of ~1.65 × 10^{-4} S cm^{-1} at room temperature, accompanied by a t_{Li^+} of 0.3.[58]

1.4.1.2. Quasi-solid-state electrolyte (QSSE)

As outlined in Section 1.2.3, conventional liquid electrolytes based on organic carbonates exhibit intrinsic safety and stability concerns, including high flammability, volatility, and susceptibility to leakage upon mechanical failure, as well as the inherently low structural compactness of the resulting cells.[55,69] Moreover, their fluidic nature facilitates uncontrolled lithium dendrite growth, which can lead to short-circuiting and thermal runaway. On the other hand, solid-state electrolytes (SSEs) offer nonflammability, mechanical robustness that can inhibit dendrite penetration, and compact cell architecture. However, SSEs continue to face critical limitations, most notably high interfacial resistance caused by poor electrode-electrolyte contact and relatively low ionic conductivity at ambient temperature.[55] Quasi-solid-state electrolytes (QSSEs) offer a promising compromise between these two extremes, seeking to harness the merits of both liquid and solid electrolytes while mitigating their respective limitations.[53,61,70] QSSEs are typically constructed by incorporating a small fraction of liquid or plasticizing agents within a solid matrix.[70] This hybrid architecture provides ion solvation, and low interfacial resistance, similar to liquid electrolytes, while the solid framework offers mechanical stability, avoid spillage, and possibly suppresses dendrite formation. In QSSEs, ion transport typically proceeds via two complementary pathways, bulk diffusion of solvated ions through confined liquid domains, and directional migration along ordered channels or functional groups provided by the solid matrix.[53,55,57,70] The structural design of QSSEs can be highly tunable by integrating a polymeric or crystalline scaffold with plasticizers such as organic solvents or ILs, to achieve the desired balance between thermal stability and conductivity.

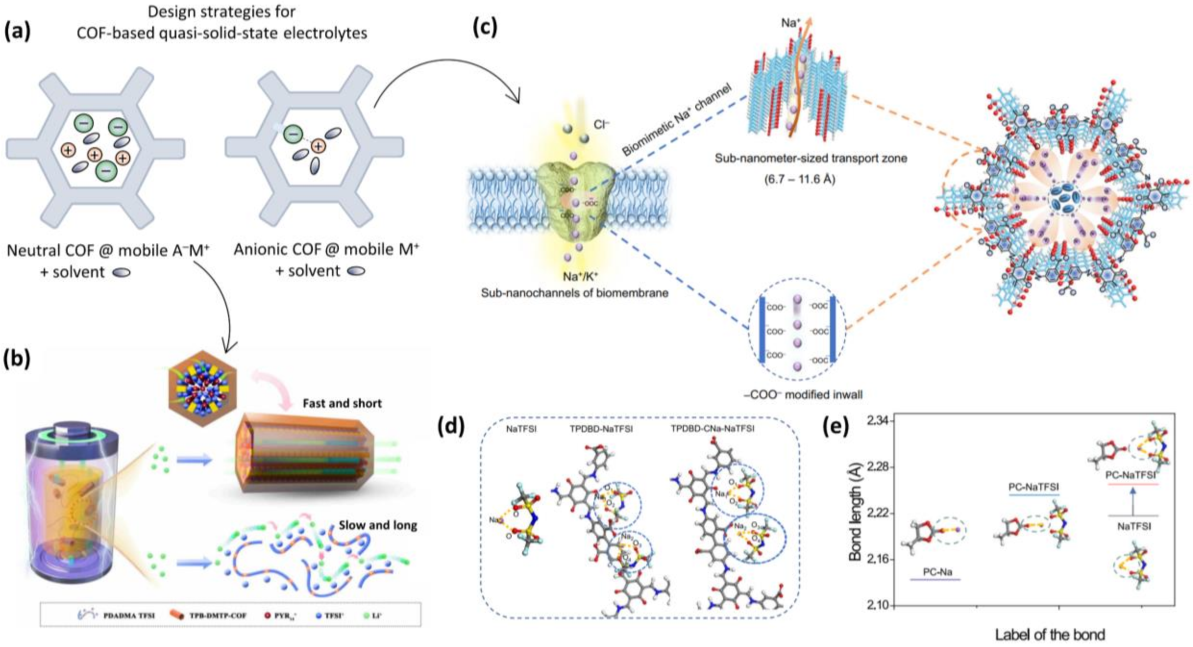

Figure 1.16 (a) Design strategies for COF-based quasi-solid-state electrolytes (QSSEs) as neutral COFs with mobile ions and solvent molecules, and anionic-COFs with mobile M^+ along with solvent molecules, confined in the COF sub-nanochannels. (b) Schematic illustration of Li^+ migration in COF-TPB-DMTP-based polymeric ionic liquid/ $Pyr_{14}TFSI$ (PIL/IL) gel electrolyte, demonstrating the preferential Li^+ conduction pathway through the COF pore than the PIL/IL phase.[57] Copyright 2021 American Chemical Society. (c) The rational design of the bio-inspired COF-based QSSEs. The ion conduction mechanism through the COF pores replicates the migration of Na^+/ K^+ in biological membranes exhibiting negatively charged (–COO^-) inwalls.[61] (d) Optimized binding coordinates of COF-TPDBD and COF-TPDBD-COO^- with NaTFSI salt, with the white, gray, red, blue, and purple balls denoting H, C, O, N, and Na atoms, respectively.[61] (e) Impact of PC solvent incorporation on the Na–O coordination distance of NaTFSI within the COF-TPDBD-CNa-NaTFSI system.[61]

Ionic liquids (ILs), such as 1-ethyl-3-methylimidazolium bis(trifluoromethylsulfonyl)imide ([EMIM][TFSI]),[71] 1-butyl-3-methylimidazolium bis(trifluoromethanesulfonyl)imide ([BMIM][TFSI]),[53] 1-methyl-1-propylpyrrolidinium bis(fluorosulfonyl)imide ($[Pyr_{13}][FSI]$)[72] etc., have been utilized as plasticizers due to their negligible volatility, wide electrochemical stability window (~4.5 V vs. Li/Li^+), intrinsic ionic conductivity (~10^{-3} S cm^{-1}) , and strong solvation ability. When integrated to OPEs, ionic liquids have shown to soften the solid-host framework by lowering its glass transition temperature (T_g), which increases chain dynamics and enables faster ion migration.[53,70] In principle, ILs are molten salts, composed of bulky, asymmetric organic cations and inorganic or organic anions, with their low melting points arising from poor lattice packing between the large, charge-delocalized ions.[72] In ILs, cations and anions are held together by Coulombic interactions, resulting in high cohesive energy within the liquid phase, consequently, a substantial energy input is required to separate them into the gas phase, which makes ionic liquids effectively non-volatile.[72]

Recently, COFs have been explored as highly promising solid matrices for QSSEs following two primary strategies (**Figure 1.16a**): (1) incorporating lithium salts and solvents into neutral COF frameworks, thereby exploiting the functional groups of COFs to weaken the M^+–A^- interactions, while utilizing the ordered channels to direct ion migration facilitated with respect to solvent phase,[57] and (2) designing anionic COFs that immobilize counter A^-, leaving mobile M^+ to migrate freely, with plasticizers further promoting solvation and accelerating ion transport.[61] COF-TPB-DMTP, when added to the polymeric ionic liquid/ Pyr_{14}TFSI (PIL/IL)-based gel electrolyte, exhibited approximately twofold higher ionic conductivity (2.8×10^{-4} S cm^{-1} at 30 °C) than PIL/IL-based gel electrolyte without COF.[57] The COF framework disrupted the ionic interactions between Pyr_{14}^+ and $TFSI^-$, thereby generating a mobile anionic solvation shell that enhanced Li^+ hopping within the COF pores. Additionally, density functional theory (DFT) calculations revealed that ion transport preferentially occurred through the COF channels rather than the bulk PIL/IL phase (**Figure 1.16b**).[57]

Furthermore, in a recent study, the addition of a methoxy-functionalized COF, COF-OMe to a glyme-based IL/LiTFSI electrolyte reduced the dissociation energy of the Li^+–$TFSI^-$ ion pair, effectively suppressed dendrite growth, and prolonged cycling stability in lithium-metal batteries.[60] Yan and colleagues proposed a bio-inspired strategy for constructing COF-based QSSEs, in which ion transport within the COF channels mimics the migration of Na^+ and K^+ ions across biological membranes lined with negatively charged carboxylate ($-COO^-$) groups (**Figure 1.16c**).[61] Two types of composite electrolytes were developed: (i) COF-TPDBD-NaTFSI, consisting of a neutral COF-TPDBD framework with NaTFSI salt, and (ii) COF-TPDBD-CNa-NaTFSI, in which the pore walls of COF-TPDBD are functionalized with $-COO^-$ groups coordinated to Na^+, in combination with NaTFSI salt. In the latter system, the $-COO^-$ functionalities not only facilitate the dissociation of Na^+ and $TFSI^-$ ions but also provide localized binding and hopping sites along the COF scaffold for Na^+ transport (**Figure 1.16d**).[61] Incorporation of a small fraction of PC solvent to the COF-TPDBD-CNa-NaTFSI system was further shown to elongate the Na−O coordination distance in NaTFSI, thereby weakening Na^+−$TFSI^-$ association. At the same time, confinement of PC molecules within the COF pores, driven by strong interaction energies with the TPDBD-CNa framework, suppresses PC volatilization and enhances Na^+ conductivity, reaching ~1.30×10^{-4} S cm^{-1} at 30 °C.[61] Both approaches exemplify how COF-based QSSEs can bridge the gap between solid rigidity and liquid-like ionic conductivity, advancing the development of safe, high-performance electrolytes for next-generation energy storage.

1.4.2. COF-based electrode material

1.4.2.1. Design strategies

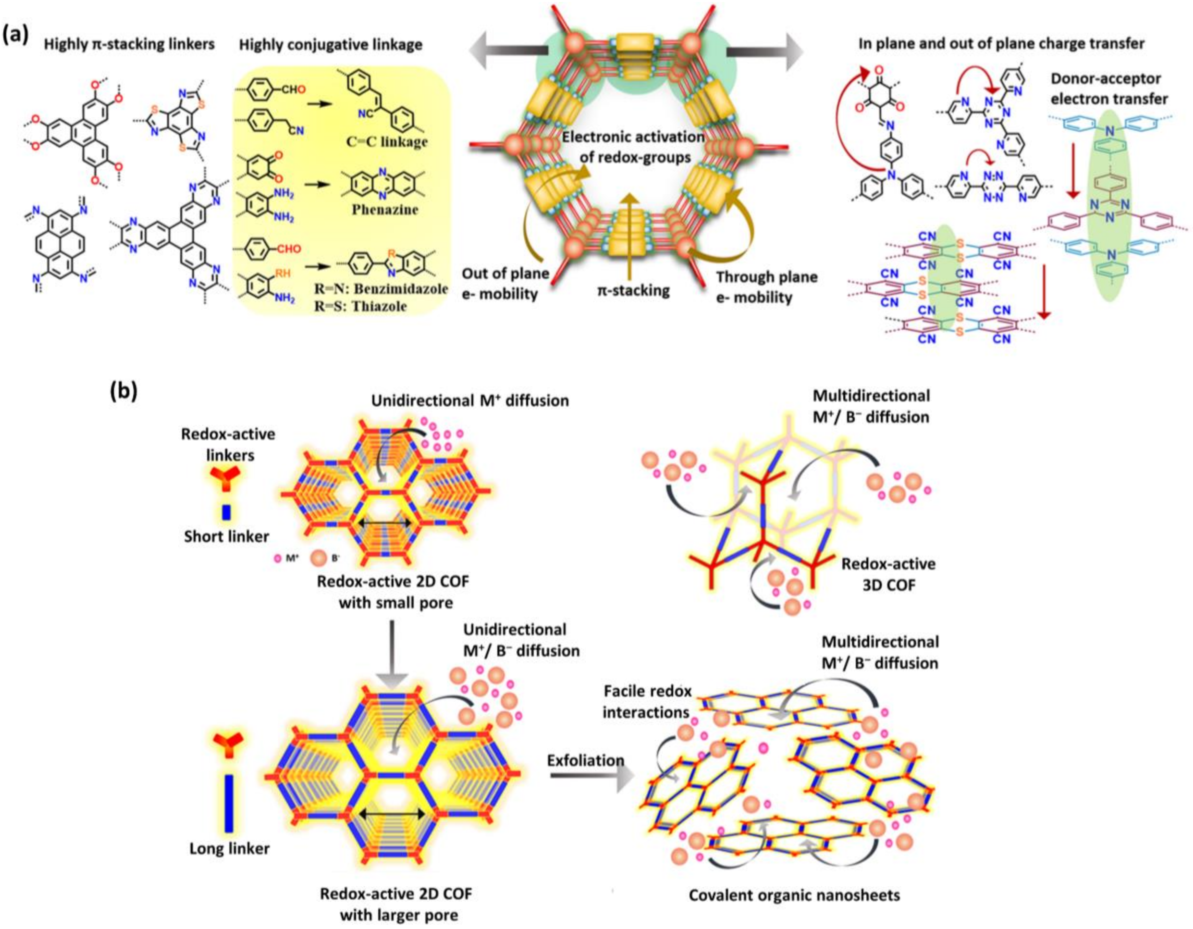

Figure 1.17 (a) Design strategies to elevate in-plane and out-of-plane e^- mobility in 2D-COF via rational incorporation of strongly π-stacked and highly conjugated building units, as well as donor–acceptor (D–A) heterojunctions.[40] (b) Influence of pore architecture and exfoliation of 2D COFs layers on enhancing ion transport (cation: M^+; bulky anion: B^-) and facilitating redox interactions between functional moieties and guest ions in COF-based electrodes.[40]

COFs have emerged as exceptionally promising electrode materials in secondary-ion and multivalent-ion batteries (Li-ion, Na-ion, Zn-ion, Al-ion, dual-ion, etc.) owing to a confluence of structural, chemical, and electronic features that can be precisely tuned.[10,48,73,74] Foremost among these are the presence of redox-active groups, high specific surface area with modifiable pore topology, and highly conjugated, π-stacked "graphite-like" layers that form ordered 1D nanochannels conducive to both ion and electron transport. Redox-active moieties such as quinones,[48] imines,[47] triphenylamines,[75] phenazines,[76] thiadiazoles,[77] etc. can be embedded in either the framework nodes or the covalent linkages, providing the resulting COF architecture with intrinsic electrochemical activity. For instance, triphenylamine-based 2D TA-TP COF can undergo reversible 2 e^- redox reactions at triphenylamine sites, while imine linkages provide additional four reversible redox centers per unit cell.[47] The density and accessibility of such redox sites are amplified by the ordered and open pore channels in COFs, allowing full utilization of the framework.[40] Unlike amorphous polymers where redox sites may be sterically inaccessible, COFs facilitate periodic exposure of these functional groups, exhibiting higher rate capabilities and specific capacities.

Similar to OEMs, COFs can be categorized as *n*-type, *p*-type, or bipolar/ambipolar materials depending on whether their dominant electrochemical process involves cation insertion (electron uptake), anion insertion (electron loss), or both, a classification that stems from the redox nature of their organic building blocks and linkages, as will be discussed in detail in Section 1.4.2.2. The rational choice of linkers and linkages not only governs the intrinsic redox chemistry of the framework but also dictates the degree of π-π stacking and conjugation, which in turn regulate the electronic conductivity in a COF-based electrode (**Figure 1.17a**).[40] Planar linkers with rigid aromatic polycycles and highly conjugative linkages favor π-overlap, reducing interlayer slip or twist, increasing interlayer orbital overlap, thereby enhancing out-of-plane (*z*-axis) electron mobility. By contrast, twisted or non-planar linkers/linkages, such as the imine linkage, may disrupt these interactions, raising band gaps and impeding both in-plane and out-of-plane conduction. Alternating electron-rich (EDG or donors) and electron-deficient (EWG or acceptor) units within the COF backbone, establish D−A heterojunctions, promoting internal charge-transfer pathways that enhance both in-plane (*xy*) and out-of-plane (*z*) conductivity.[40,78] Charge transfer between donor and acceptor domains facilitates a hopping mechanism in which electrons migrate from electron-rich to electron-poor centers, lowering charge-transfer resistance and sustaining continuous electron flow.[40] This mitigates one of the central limitations of COFs, i.e. their inherently moderate conductivity, and allows the ionic conduction to be synergistically coupled with efficient electron transport, thereby improving power density and rate capability in electrochemical devices.

The redox activity of COFs can be fundamentally altered by the electronic configuration of their building blocks, particularly through the relative positions of molecular orbitals, HOMO and LUMO. *n*-Type COFs, constructed from electron-deficient moieties, possess stabilized LUMO levels that facilitate electron uptake and cation insertion. Conversely, *p*-type COFs, based on electron-rich donors feature elevated HOMO levels that readily donate electrons, supporting anion or counterion insertion. The incorporation of EDG raises the HOMO energy, lowering oxidation potentials, while strong EWG lowers the LUMO energy and enables easy reduction.[40] However, the actual redox potentials of COFs often deviate from those of their isolated building units. This arises because the extended conjugation and polymeric band structure of COFs generate delocalized valence (VB) and conduction bands (CB).[40] Electron push–pull interactions, interlayer π–π stacking, intralayer hydrogen bonding, and charge-transfer pathways redistribute electron density, altering the effective redox behavior relative to the molecular building blocks.

Equally significant in the context of batteries are the structural characteristics of COFs, namely their high surface area and modular porosity. With BET surface areas typically in the 700−4000 m^2 g^{-1} range and pore sizes spanning from micropores to mesopores, COFs provide abundant accessible channels for electrolyte infiltration and ion diffusion (**Figure 1.17b**).[40] Ordered 1D channels in 2D frameworks or 3D pore networks in 3D COFs minimize tortuosity, reducing ionic resistance and facilitating the transport of bulky species (with solvent shell) such as Na^+, K^+, Zn^{2+}, Al^{3+}, or bulky anions (B^-) in *p*-type and bipolar electrodes.[47,79] Structural engineering can further enhance ion kinetics through the exfoliation (chemical or mechanical) of layered COFs into covalent organic nanosheets (CONs), which maximize exposure of electroactive sites and shorten diffusion pathways.[80] Collectively, these electronic and structural design features render COFs highly adaptable electrode materials for diverse secondary-ion batteries.

1.4.2.2. Redox functionalities

The operation of LIBs relies on a reversible charge–discharge process in which Li-ions shuttle between the positive and negative electrodes through an electrolyte, while electrons flow through an external circuit.[81] COFs have emerged as a promising class of OEMs because of their modular architectures, porosity, and chemical tunability. By incorporating polar functional groups such as carbonyls, imines, and heteroatoms, COFs can strongly interact with M^+ or A^-, facilitating reversible redox processes. As discussed above, *n*-type COFs operate at lower potentials vs. M/M^+, undergoing reduction first and storing metal cations such as Li^+, Na^+, K^+, or Zn^{2+}. Their electron-accepting functionalities (e.g., quinones, imides) allow multiple redox events per repeat unit, giving rise to high gravimetric capacities (mAh g^{-1}). In contrast, *p*-type COFs oxidize first at higher potentials and predominantly store anions such as PF_6^-, FSI^-, or $TFSI^-$. *p*-Type COFs usually benefit from enhanced radical cation stability, which improves redox kinetics and supports rapid charge–discharge performance. Therefore, while *n*-type COFs excel in capacity output, *p*-type materials often offer faster kinetics, highlighting the complementary nature of the two classes.[82]

Bipolar-type or ambipolar COFs combine both redox features, enabling the storage of metal cations at low potentials and counter anions at high potentials, respectively.[10,73,75,83–86] This dual functionality could yield both high capacity and rapid kinetics, placing them in the category of *pseudocapacitive* *materials*, systems that store charge with “battery-like” energy density but at “capacitor-like” rates. Such redox versatility permits their application in symmetric and dual-ion batteries.

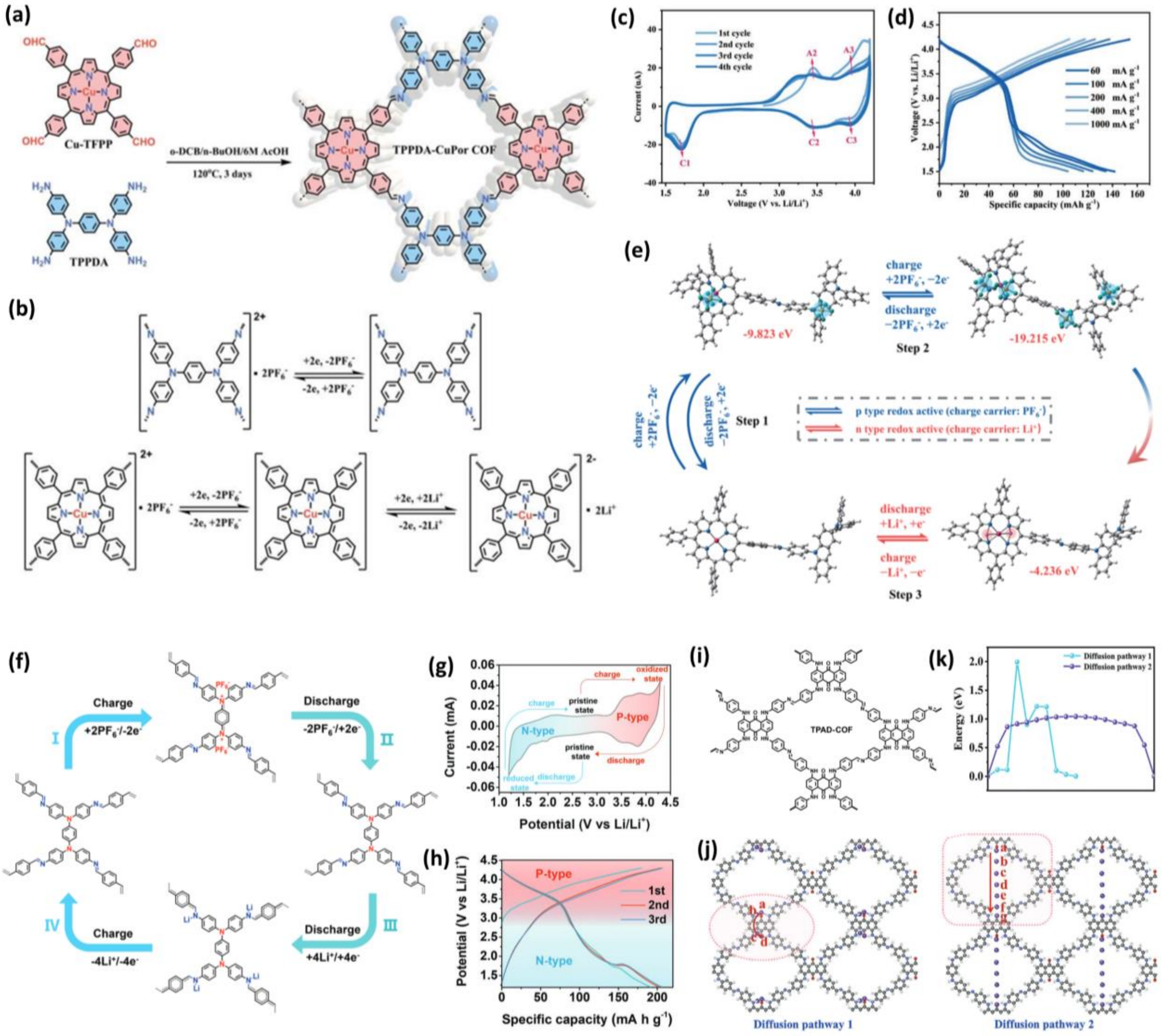

Figure 1.18 (a) Synthetic scheme of TPPDA-CuPor COF, and (b) the redox features of the individual building units, TPPDA and CuPor.[75] (c) Cyclic voltammograms and (d) galvanostatic charge discharge profiles of Li-ion half-cell utilizing TPPDA-CuPor COF electrode as WE, Li-foil as CE and RE.[75] (e) Proposed charge-discharge mechanism of TPPDA-CuPor COF electrode.[75] Copyright 2022 Royal Society of Chemistry. (f) Redox mechanism of bipolar TA-TP COF electrode, along with corresponding (g) cyclic voltammograms depicting the *n*-type and *p*-type redox features and (h) charge-discharge profiles of Li-ion half-cell at current density of 0.2 A g^{-1}.[47] Copyright 2021 Wiley -VCH. (i) Schematic structure of bipolar TPAD-COF, (j) along with preferential Na^+ diffusion pathways, in-plane (left) and out-of-plane (right), and (k) the calculated energies corresponding to the pathways.[10] Copyright 2024 Wiley -VCH.

In dual-ion batteries (DIBs), both cations and anions from the electrolyte participate in charge storage, typically with cations intercalating into the anode and anions intercalating into the cathode, enabling wide operating voltages, and fast kinetics. [10,73,75,83–86] When the working principle of dual-ion batteries combines with the same bipolar-type material used for both anode and cathode, it can deliver dual-ion symmetric batteries, with a single bipolar electrode, possessing redox-active sites accessible across a wide potential window, allowing reversible charge storage on both ends of the spectrum, and thereby serving as both anode and cathode.[87,88]

Since the exact redox potentials and mechanisms of COFs often deviate from those of their molecular building blocks due to framework effects such as extended conjugation and pore confinement, combination of theoretical modeling and experimental measurements helps decipher the probable redox and ion diffusion mechanism of COF-based electrodes. For instance, density functional theory (DFT) calculations, molecular electrostatic potential (MESP) and experimental techniques, including X-ray photoelectron spectroscopy (XPS), Fourier-transform infrared spectroscopy (FTIR), Raman spectroscopy, nuclear magnetic resonance (NMR), energy-dispersive X-ray spectroscopy (EDX), and electrochemical impedance spectroscopy (EIS), can be utilized for unravelling the electrochemical pathways of the COF electrodes. Such insights are crucial for guiding the rational design of next-generation COF-based electrodes for advanced energy storage.

Recently, a bipolar-type COF, TPPDA-CuPor COF was synthesized by combining *N*,*N*,*N*,*N*-tetra(p-aminophenyl)-p-phenylenediamine (TPPDA) and copper-5,10,15,20-tetrakis(4-formylphenyl)-porphyrin (Cu-TFPP) via imine linkages, and utilized as a cathode in a Li-ion half-cell (**Figure 1.18a-e**).[75] Both TPPDA and Cu-TFPP units exhibited 2 e^- reversible oxidation each at the higher potentials ~3.2–3.7 V vs. Li/Li^+, while the Cu-TFPP subunit could also store 2 Li-ions at the lower potential ~1.75 vs. Li/Li^+ (**Figure 1.18b,d**). With a total of 6 e^- redox chemistry, TPPDA-CuPor COF delivered a specific capacity of ~145 mA g^{-1} at 60 mA g^{-1} (**Figure 1.18c**). DFT calculations revealed the most probable redox sequence: initially, two PF_6^- anions are stored at one TPPDA site and one Cu–TFPP site, followed by the storage of an additional two PF_6^- anions at the same TPPDA and Cu–TFPP sites. During discharge (negative potential sweep), the PF_6^- anions are released, while two Li^+ ions are subsequently accommodated at the Cu−TFPP subunit (**Figure 1.18e**). Furthermore, Wu *et al.* demonstrated the bipolar-type COF TA-TP, synthesized by coupling the *p*-type *N*,*N*,*N*,*N*-tetra(p-aminophenyl)-p-phenylenediamine (TP) and terephthalaldehyde (TA) linker via *n*-type imine (C=N) linkage (**Figure 1.18f-h**).[47] TA-TP COF exhibited a wide stable potential window of ~1.2–4.2 V vs. Li/Li^+, with a specific capacity of 200 mAh g^{-1} at 0.2 A g^{-1} current flux. The electrochemical performance was attributed to the reversible storage of two PF_6^- anions at the TP unit and four Li^+ ions at the imine linkages per unit cell. Furthermore, preferential diffusion pathways in the bipolar TPAD-COF were investigated by Cheng and co-workers, initially demonstrating that the electrode can accommodate two PF_6^- anions during charging and two Na^+ cations during discharging (**Figure 1.18i-**

k).[10] To simplify the analysis, they focused on two possible diffusion pathways for Na^+: (i) in-plane migration along the COF sheets (pathway 1) and (ii) out-of-plane migration across the interlayer galleries (pathway 2) (**Figure 1.18j**). Owing to the strong π–π stacking interactions between the COF sheets, enabled by the planar geometry of the building units, the in-plane pathway was found to be energetically more favorable (**Figure 1.18k**). This facilitated directional ion transport within the COF framework, thereby enhancing reversibility of the redox process, and delivering a specific capacity of 186 mAh g^{-1} at 0.05 A g^{-1}.[10] To conclude, engineering COFs through functionality, pore topology, and 1D nanochannels offers a powerful lever to control ion and electron transport, transforming them from structural curiosities into possible game-changers for energy storage, an endeavor that has been the central focus of this thesis.

1.4.3. References – II

[1] K. T. Tan, S. Ghosh, Z. Wang, F. Wen, D. Rodríguez-San-Miguel, J. Feng, N. Huang, W. Wang, F. Zamora, X. Feng, A. Thomas, D. Jiang, *Nat Rev Methods Primers* **2023**, *3*, 1.

[2] A. P. Côté, A. I. Benin, N. W. Ockwig, M. O'Keeffe, A. J. Matzger, O. M. Yaghi, *Science (New York, N.Y.)* **2005**, *310*, 1166.

[3] O. M. Yaghi, G. Li, H. Li, *Nature* **1995**, *378*, 703.

[4] X. Chen, K. Geng, R. Liu, K. T. Tan, Y. Gong, Z. Li, S. Tao, Q. Jiang, D. Jiang, *Angewandte Chemie (International ed. in English)* **2020**, *59*, 5050.

[5] F. Haase, B. V. Lotsch, *Chemical Society reviews* **2020**, *49*, 8469.

[6] M. S. Lohse, T. Bein, *Adv Funct Materials* **2018**, *28*, 1705553.

[7] K. Geng, T. He, R. Liu, S. Dalapati, K. T. Tan, Z. Li, S. Tao, Y. Gong, Q. Jiang, D. Jiang, *Chemical reviews* **2020**, *120*, 8814.

[8] Y. Cheng, H. Du, Y. Wang, J. Xin, Y. Dong, X. Wang, X. Zhou, B. Gui, J. Sun, C. Wang, *Journal of the American Chemical Society* **2025**, *147*, 6355.

[9] Q. Zhu, X. Wang, R. Clowes, P. Cui, L. Chen, M. A. Little, A. I. Cooper, *Journal of the American Chemical Society* **2020**, *142*, 16842.

[10] L. Cheng, X. Yan, J. Yu, X. Zhang, H.-G. Wang, F. Cui, Y. Wang, *Advanced materials (Deerfield Beach, Fla.)* **2025**, *37*, e2411625.

[11] S. Jin, T. Sakurai, T. Kowalczyk, S. Dalapati, F. Xu, H. Wei, X. Chen, J. Gao, S. Seki, S. Irle, D. Jiang, *Chemistry (Weinheim an der Bergstrasse, Germany)* **2014**, *20*, 14608.

[12] C. G. Gruber, L. Frey, R. Guntermann, D. D. Medina, E. Cortés, *Nature* **2024**, *630*, 872.

[13] F. J. Uribe-Romo, J. R. Hunt, H. Furukawa, C. Klöck, M. O'Keeffe, O. M. Yaghi, *Journal of the American Chemical Society* **2009**, *131*, 4570.

[14] N. S. P. Vollhardt, *Organic Chemistry: Structure and Function, Eighth edition*, W. H. Freeman and Company, New York, New York **2018**.

[15] X. Liu, R. Qi, S. Li, W. Liu, Y. Yu, J. Wang, S. Wu, K. Ding, Y. Yu, *J. Am. Chem. Soc.* **2022**, *144*, 23396.

[16] P.-F. Wei, M.-Z. Qi, Z.-P. Wang, S.-Y. Ding, W. Yu, Q. Liu, L.-K. Wang, H.-Z. Wang, W.-K. An, W. Wang, *J. Am. Chem. Soc.* **2018**, *140*, 4623.

[17] S. Kandambeth, A. Mallick, B. Lukose, M. V. Mane, T. Heine, R. Banerjee, *J. Am. Chem. Soc.* **2012**, *134*, 19524.

[18] M. Calik, T. Sick, M. Dogru, M. Döblinger, S. Datz, H. Budde, A. Hartschuh, F. Auras, T. Bein, *Journal of the American Chemical Society* **2016**, *138*, 1234.

[19] A. Schaate, P. Roy, A. Godt, J. Lippke, F. Waltz, M. Wiebcke, P. Behrens, *Chemistry (Weinheim an der Bergstrasse, Germany)* **2011**, *17*, 6643.

[20] J. Hu, Z. Huang, Y. Liu, *Angewandte Chemie (International ed. in English)* **2023**, *62*, e202306999.

[21] J. Maschita, T. Banerjee, G. Savasci, F. Haase, C. Ochsenfeld, B. V. Lotsch, *Angewandte Chemie* **2020**, *132*, 15880.

[22] Z. Alsudairy, N. Brown, C. Yang, S. Cai, F. Akram, A. Ambus, C. Ingram, X. Li, *Precision chemistry* **2023**, *1*, 233.

[23] S. Karak, S. Kandambeth, B. P. Biswal, H. S. Sasmal, S. Kumar, P. Pachfule, R. Banerjee, *J. Am. Chem. Soc.* **2017**, *139*, 1856.

[24] D. D. Medina, J. M. Rotter, Y. Hu, M. Dogru, V. Werner, F. Auras, J. T. Markiewicz, P. Knochel, T. Bein, *J. Am. Chem. Soc.* **2015**, *137*, 1016.

[25] T. Sick, A. G. Hufnagel, J. Kampmann, I. Kondofersky, M. Calik, J. M. Rotter, A. Evans, M. Döblinger, S. Herbert, K. Peters, D. Böhm, P. Knochel, D. D. Medina, D. Fattakhova-Rohlfing, T. Bein, *J. Am. Chem. Soc.* **2018**, *140*, 2085.

[26] L. Yao, A. Rodríguez-Camargo, M. Xia, D. Mücke, R. Guntermann, Y. Liu, L. Grunenberg, A. Jiménez-Solano, S. T. Emmerling, V. Duppel, K. Sivula, T. Bein, H. Qi, U. Kaiser, M. Grätzel, B. V. Lotsch, *J. Am. Chem. Soc.* **2022**, *144*, 10291.

[27] H. Gao, Q. Zhu, A. R. Neale, M. Bahri, X. Wang, H. Yang, L. Liu, R. Clowes, N. D. Browning, R. S. Sprick, M. A. Little, L. J. Hardwick, A. I. Cooper, *Advanced Energy Materials* **2021**, *11*.

[28] X. Liu, Y. Jin, H. Wang, X. Yang, P. Zhang, K. Wang, J. Jiang, *Advanced materials (Deerfield Beach, Fla.)* **2022**, *34*, e2203605.

[29] S. P. Fernandes, L. Frey, K. M. Cid-Seara, O. Oliveira, N. Guldris, E. Carbó-Argibay, C. Rodríguez-Abreu, Y. V. Kolen'ko, A. M. Silva, D. D. Medina, L. M. Salonen, *Microporous and Mesoporous Materials* **2022**, *343*, 112162.

[30] T. Xue, R. Guntermann, A. Biewald, D. Blätte, D. D. Medina, A. Hartschuh, T. Bein, *ACS applied materials & interfaces* **2024**, *16*, 48085.

[31] D. Jiang, V. G. W. Tan, Y. Gong, H. Shao, X. Mu, Z. Luo, S. He, *Chemical reviews* **2025**, *125*, 6203.

[32] X. Feng, L. Chen, Y. Honsho, O. Saengsawang, L. Liu, L. Wang, A. Saeki, S. Irle, S. Seki, Y. Dong, D. Jiang, *Advanced materials (Deerfield Beach, Fla.)* **2012**, *24*, 3026.

[33] X. Ding, J. Guo, X. Feng, Y. Honsho, J. Guo, S. Seki, P. Maitarad, A. Saeki, S. Nagase, D. Jiang, *Angewandte Chemie (International ed. in English)* **2011**, *50*, 1289.

[34] R. Guntermann, D. Helminger, L. Frey, P. M. Zehetmaier, C. Wangnick, A. Singh, T. Xue, D. D. Medina, T. Bein, *Angewandte Chemie (International ed. in English)* **2024**, *63*, e202407166.

[35] J.-D. Feng, W.-D. Zhang, Z.-G. Gu, *ChemPlusChem* **2024**, *89*, e202400069.

[36] L. Spies, M. E. G. Carmo, G. J. Marrenjo, S. Reuther, P. Ganswindt, A. O. T. Patrocinio, T. Bein, O. F. Lopes, J. Schneider, *Adv Funct Materials* **2025**.

[37] G. O. Aksu, S. Keskin, *ACS materials letters* **2025**, *7*, 954.

[38] D. Bessinger, K. Muggli, M. Beetz, F. Auras, T. Bein, *J. Am. Chem. Soc.* **2021**, *143*, 7351.

[39] X. Liu, D. Huang, C. Lai, G. Zeng, L. Qin, H. Wang, H. Yi, B. Li, S. Liu, M. Zhang, R. Deng, Y. Fu, L. Li, W. Xue, S. Chen, *Chemical Society reviews* **2019**, *48*, 5266.

[40] S. Haldar, A. Schneemann, S. Kaskel, *Journal of the American Chemical Society* **2023**, *145*, 13494.

[41] Y. Xu, J. Gong, Q. Li, X. Guo, X. Wan, L. Xu, H. Pang, *Nanoscale* **2024**, *16*, 11429.

[42] S. Suleman, X. Cheng, M. Gu, Y. Kim, *Commun Mater* **2025**, *6*, 1.

[43] V. A. Sonar, A. A. Kulkarni, P. Sonar, D. P. Dubal, *Batteries & Supercaps* **2025**, *8*, e202400537.

[44] T. Yang, X. Xu, Y. Yang, W. Fan, Y. Wu, S. Ji, J. Zhao, J. Liu, Y. Huo, *Energy Mater Adv* **2024**, *5*, 78.

[45] Y. Wang, Q. Hao, Q. Lv, X. Shang, M. Wu, Z. Li, *Chemical communications (Cambridge, England)* **2024**, *60*, 10046.

[46] R. Guntermann, J. M. Rotter, A. Singh, D. D. Medina, T. Bein, *Small science* **2025**, *5*, 2400585.

[47] M. Wu, Y. Zhao, R. Zhao, J. Zhu, J. Liu, Y. Zhang, C. Li, Y. Ma, H. Zhang, Y. Chen, *Adv Funct Materials* **2022**, *32*, 2107703.

[48] R. Shi, L. Liu, Y. Lu, C. Wang, Y. Li, L. Li, Z. Yan, J. Chen, *Nature communications* **2020**, *11*, 178.

[49] Z. Xue, D. He, X. Xie, *J. Mater. Chem. A* **2015**, *3*, 19218.

[50] Q. Wu, M. Fang, S. Jiao, S. Li, S. Zhang, Z. Shen, S. Mao, J. Mao, J. Zhang, Y. Tan, K. Shen, J. Lv, W. Hu, Y. He, Y. Lu, *Nature communications* **2023**, *14*, 6296.

[51] A. Hosseinioun, P. Nürnberg, M. Schönhoff, D. Diddens, E. Paillard, *RSC advances* **2019**, *9*, 27574.

[52] H. Tian, X. Huang, C. Yang, Y. Wu, C. Zhang, Y. Yang, *ACS applied materials & interfaces* **2024**, *16*, 34069.

[53] A. Nag, M. A. Ali, A. Singh, R. Vedarajan, N. Matsumi, T. Kaneko, *J. Mater. Chem. A* **2019**, *7*, 4459.

[54] H. Adenusi, G. A. Chass, S. Passerini, K. V. Tian, G. Chen, *Advanced Energy Materials* **2023**, *13*, 2203307.

[55] Q. Zhao, S. Stalin, C.-Z. Zhao, L. A. Archer, *Nat Rev Mater* **2020**, *5*, 229.

[56] Y. Zhu, Q. Bai, S. Ouyang, Y. Jin, W. Zhang, *ChemSusChem* **2024**, *17*, e202301118.

[57] Z. Wang, W. Zheng, W. Sun, L. Zhao, W. Yuan, *ACS Appl. Energy Mater.* **2021**, *4*, 2808.

[58] T. W. Kang, J.-H. Lee, J. Lee, J. H. Park, J.-H. Shin, J.-M. Ju, H. Lee, S. U. Lee, J.-H. Kim, *Advanced materials (Deerfield Beach, Fla.)* **2023**, *35*, e2301308.

[59] Z. Shan, M. Wu, Y. Du, B. Xu, B. He, X. Wu, G. Zhang, *Chem. Mater.* **2021**, *33*, 5058.

[60] X. Tan, J. Zhong, Y. Tong, L. Guo, Y. Xie, J. Zhao, *Polymer* **2025**, *317*, 127911.

[61] Y. Yan, Z. Liu, T. Wan, W. Li, Z. Qiu, C. Chi, C. Huangfu, G. Wang, B. Qi, Y. Yan, T. Wei, Z. Fan, *Nature communications* **2023**, *14*, 3066.

[62] K. Jeong, S. Park, G. Y. Jung, S. H. Kim, Y.-H. Lee, S. K. Kwak, S.-Y. Lee, *Journal of the American Chemical Society* **2019**, *141*, 5880.

[63] Y. Liu, Y. Zhu, Y. Cui, *Nat Energy* **2019**, *4*, 540.

[64] H. Chen, H. Tu, C. Hu, Y. Liu, D. Dong, Y. Sun, Y. Dai, S. Wang, H. Qian, Z. Lin, L. Chen, *Journal of the American Chemical Society* **2018**, *140*, 896.

[65] Z. Cheng, L. Lu, S. Zhang, H. Liu, T. Xing, Y. Lin, H. Ren, Z. Li, L. Zhi, M. Wu, *Nano Res.* **2023**, *16*, 528.

[66] G. Zhang, Y.-L. Hong, Y. Nishiyama, S. Bai, S. Kitagawa, S. Horike, *Journal of the American Chemical Society* **2019**, *141*, 1227.

[67] Q. Xu, S. Tao, Q. Jiang, D. Jiang, *Journal of the American Chemical Society* **2018**, *140*, 7429.

[68] X.-X. Wang, X.-W. Chi, M.-L. Li, D.-H. Guan, C.-L. Miao, J.-J. Xu, *Chem* **2023**, *9*, 394.

[69] Y. Chen, Y. Kang, Y. Zhao, L. Wang, J. Liu, Y. Li, Z. Liang, X. He, X. Li, N. Tavajohi, B. Li, *Journal of Energy Chemistry* **2021**, *59*, 83.

[70] X. Yang, B. Zhang, Y. Tian, Y. Wang, Z. Fu, D. Zhou, H. Liu, F. Kang, B. Li, C. Wang, G. Wang, *Nature communications* **2023**, *14*, 925.

[71] G. Ma, F. Pan, X. Zhou, Z. Yong, X. Wang, C. Li, W. Bai, S. Wang, *ACS Appl. Electron. Mater.* **2024**, *6*, 1434.

[72] J. B. Haskins, W. R. Bennett, J. J. Wu, D. M. Hernández, O. Borodin, J. D. Monk, C. W. Bauschlicher, J. W. Lawson, *The journal of physical chemistry. B* **2014**, *118*, 11295.

[73] W. Li, Q. Huang, H. Shi, W. Gong, L. Zeng, H. Wang, Y. Kuai, Z. Chen, H. Fu, Y. Dong, C. Zhang, *Adv Funct Materials* **2024**, *34*, 2310668.

[74] R. Kushwaha, C. Jain, P. Shekhar, D. Rase, R. Illathvalappil, D. Mekan, A. Camellus, C. P. Vinod, R. Vaidhyanathan, *Advanced Energy Materials* **2023**, *13*, 2301049.

[75] L. Gong, X. Yang, Y. Gao, G. Yang, Z. Yu, X. Fu, Y. Wang, D. Qi, Y. Bian, K. Wang, J. Jiang, *J. Mater. Chem. A* **2022**, *10*, 16595.

[76] E. Vitaku, C. N. Gannett, K. L. Carpenter, L. Shen, H. D. Abruña, W. R. Dichtel, *J. Am. Chem. Soc.* **2020**, *142*, 16.

[77] G. Fu, D. Yang, S. Xu, S. Li, Y. Zhao, H. Yang, D. Wu, P. S. Petkov, Z.-A. Lan, X. Wang, T. Zhang, *J. Am. Chem. Soc.* **2024**, *146*, 1318.

[78] V. Singh, J. Kim, B. Kang, J. Moon, S. Kim, W. Y. Kim, H. R. Byon, *Advanced Energy Materials* **2021**, *11*, 2003735.

[79] T. Zhu, Y. Kong, B. Lyu, L. Cao, B. Shi, X. Wang, X. Pang, C. Fan, C. Yang, H. Wu, Z. Jiang, *Nature communications* **2023**, *14*, 5926.

[80] S. Wang, Q. Wang, P. Shao, Y. Han, X. Gao, L. Ma, S. Yuan, X. Ma, J. Zhou, X. Feng, B. Wang, *Journal of the American Chemical Society* **2017**, *139*, 4258.

[81] A. Yoshino, *Angewandte Chemie (International ed. in English)* **2012**, *51*, 5798.

[82] H. Kye, Y. Kang, D. Jang, J. E. Kwon, B.-G. Kim, *Adv Energy and Sustain Res* **2022**, *3*, 2200030.

[83] Q. Xu, Z. Liu, Y. Jin, X. Yang, T. Sun, T. Zheng, N. Li, Y. Wang, T. Li, K. Wang, J. Jiang, *Energy Environ. Sci.* **2024**, *17*, 5451.

[84] Q. Xu, K. Fu, Z. Liu, T. Sun, L. Xu, X. Ding, L. Gong, Q. Yu, J. Jiang, *Adv Funct Materials* **2025**, *1*, 2506111.

[85] E. Youngsam Kim, K. Vi‐khanh Ta, F. Chen, Z. Yang, Y. Yu, C. Luo, *Batteries & Supercaps* **2024**, *7*, e202400325.

[86] Y. Liu, Y. Lu, A. Hossain Khan, G. Wang, Y. Wang, A. Morag, Z. Wang, G. Chen, S. Huang, N. Chandrasekhar, D. Sabaghi, D. Li, P. Zhang, D. Ma, E. Brunner, M. Yu, X. Feng, *Angewandte Chemie (International ed. in English)* **2023**, *62*, e202306091.

[87] W. Li, H. Ma, W. Tang, K. Fan, S. Jia, J. Gao, M. Wang, Y. Wang, B. Cao, C. Fan, *Nature communications* **2024**, *15*, 9533.

[88] G. Dai, Y. He, Z. Niu, P. He, C. Zhang, Y. Zhao, X. Zhang, H. Zhou, *Angewandte Chemie (International ed. in English)* **2019**, *58*, 9902.

1.5. Motivation and outline of the thesis

The possible exhaustion of fossil fuel reserves, limited availability of critical elements, and even more so the dangerous consequences of global warming underscore the urgent need for green energy strategies, while without advanced storage technologies, the intermittency of renewable sources remains a fundamental bottleneck. Therefore, to build a modern, sustainable society, with efficient storage solutions capable of bridging the gap between supply and demand, high-performing energy systems must be derived from abundant, non-toxic resources, without environmental and ethical compromise. COFs, designed within the context of reticular chemistry, have emerged as excellent organic alternatives to conventional battery components, serving as host materials for electrodes, as base electrolytes, and as passivating layers. The modularity of COFs enables precise structural engineering to meet diverse functional requirements, placing them at the forefront of advanced materials research for energy storage applications.

This thesis focuses on engineering versatile COF-based components, demonstrating how their structural precision and functional adaptability can be harnessed to advance the frontier of sustainable energy storage, as outlined below:

In the first project, presented in *Chapter 3*, two quasi-solid-state COF electrolytes were designed, with an anionic COF scaffold featuring uniformly distributed sulfonate anions as hopping sites for sodium ions, and ionic liquid at varying mass fractions as the liquid component. Ionic conductivity measurements of these hybrid systems identified the optimal compositions for each COF architecture, while preserving their intrinsic thermal stability and mitigating leakage risks owing to the gel-like nature of the composites. Furthermore, the study underscored the critical influence of tuning COF nanochannel dimensions and the density of sulfonate functionalities along the pore walls. These structural modifications unveiled distinct sodium-ion transport pathways, arising from a synergistic interplay between sodium-ions hopping through the anionic COF backbone and a vehicle-type mechanism mediated by solvated sodium-ions within the ionic liquid phase.

In the second project, detailed in *Chapter 4*, the focus was shifted towards COF-based electrodes, with an emphasis on probing their redox behavior and ion-diffusion properties as host materials. Here, a highly crystalline electroactive bipolar-type COF was synthesized by connecting two *p*-type building blocks via *n*-type linkage, enabling simultaneous storage of metal cations and counter anions, and thereby serving as Li-ion battery electrodes. A comprehensive investigation of the structural, chemical, and electrochemical properties of the COF was conducted through a combination of experimental characterization and computational modeling. Charge-carrier diffusion was examined experimentally, and the underlying different transport mechanisms of cations and anions within the framework were further elucidated through computational analysis. To demonstrate the practical implementation of the

COF in all-organic lithium-ion batteries, symmetric full cells were fabricated, employing the COF dually as both the negative and positive electrode.

In the third project, presented in *Chapter 5*, the concept of COF-based electrodes was further advanced by fine-tuning both the electrolyte constituents and the intrinsic COF architecture. A novel, highly crystalline COF was constructed by integrating an *n*-type building block with a *p*-type linker, forming a donor–acceptor (D–A) framework with a low optical band gap. The bipolar COF was employed as an electrode, enabling reversible dual cation–anion storage, and examined by means of comprehensive electrochemical analyses. This work highlights how the interplay between charge-carrier characteristics, electrolyte composition, and framework architecture can control the electrochemical performance of bipolar COF electrodes in dual-ion configurations.

2

Characterization

This chapter provides a brief overview of the key techniques employed in the characterization of the COF materials and the corresponding electrochemical behavior. Firstly, the various methods used to analyze and identify the chemical composition, structural features, physical and photophysical properties are described, highlighting their significance in understanding the material's characteristics at both the molecular and macroscopic levels. Following this, the theoretical foundations and practical implementation of electrochemical methodologies are presented, emphasizing their importance in assessing the electrochemical behavior, stability and potential for practical applications.

NOTE: Information on the instruments used in this work is presented at the end of the individual descriptions, any exceptions from the standard measurement practice are mentioned specifically in the experimental sections throughout the document.

2.1. Materials characterization

2.1.1. Fourier transform infrared spectroscopy (FTIR)

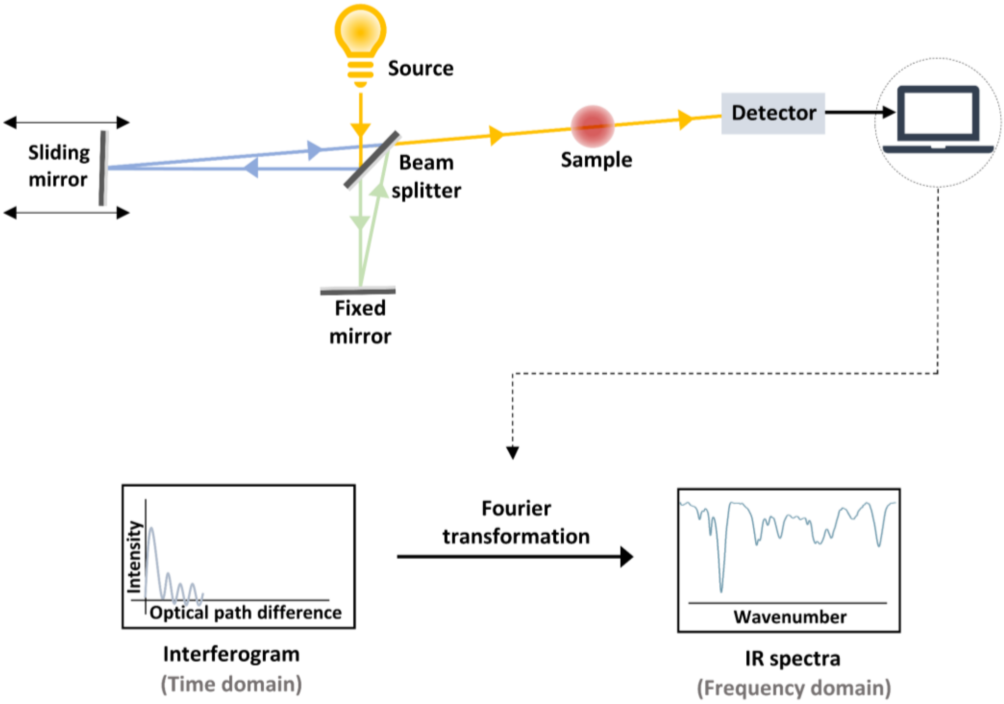

Figure 2.1 Schematic illustration of the working principle of an FTIR spectrometer.

Fourier transform infrared (FTIR) spectroscopy is a powerful and non-destructive technique to identify the molecular structure and composition of organic materials by analyzing the vibrational modes of its molecules. FTIR spectroscopy works on the basic principle that molecules absorb specific frequencies of infrared radiation that can assist in their physical characterization. FTIR typically utilizes the mid-infrared region (4000−400 cm^{-1}) of the IR spectrum, and each molecule has a unique IR absorption spectrum, like a fingerprint, corresponding to the different bond and molecular vibrations, which can be used to identify and characterize the substance.[1,2] The absorption occurs if the energy of the IR radiation matches the energy required to excite the vibration of the particular molecule. Therefore, IR radiation is absorbed when the energy of the incoming IR photon matches the energy difference between the current vibrational state and an excited vibrational state of the molecule. The vibrations can be characterized as stretching vibrational modes (symmetric and asymmetric) and bending vibrational modes (scissoring, rocking, wagging and twisting) based on relative movements of the atoms in the molecule. Further, for absorption of IR radiation to occur, the change of vibrational state should result in a change of the dipole moment of the molecule, and therefore, if the corresponding vibrational mode does not change the dipole moment (for example with symmetric stretch vibrations in symmetric molecules), this particular vibration is typically IR-inactive. Instead of measuring the absorption at each individual wavelength, FTIR utilizes Fourier transformation which allows the simultaneous measurement of all wavelengths resulting in faster data acquisition.

An FTIR spectrometer is equipped with an IR *source* emitting infrared radiation (**Figure 2.1**). This IR beam is then split into two parts by the *beam splitter*, reflecting on two mirrors, one is the *fixed mirror* and another is the *sliding mirror*. The fixed mirror remains stationary and reflects the first portion of the IR beam back to the beam splitter, ensuring that the path length of this portion of the IR beam remains constant.[1,2] The sliding mirror oscillates back and forth, and this movement of the mirror changes the path length of the second portion of the IR beam which is then reflected back to the beam splitter to recombine with the first portion of the IR beam. This creates interference in the IR beam and therefore this setup is called interferometer (or Michelson interferometer). The beam illuminates the sample and certain frequencies of the IR beam are absorbed depending on the molecular structure of the sample. The intensity of the transmitted or reflected light is determined by a *detector*. Finally, the absorption at a particular wavelength is contained in the obtained interferogram (time/pathway domain), which is then Fourier transformed into an IR spectrum (frequency domain) with high signal-to-noise ratio.

Instrument: The IR spectra were captured using a Bruker Vertex 70 FTIR instrument, featuring a globar (silicon carbide) as mid-infrared beam source along with a KBr beam splitter, and two gold mirrors. The MCT detector was cooled by liquid nitrogen (LN_2), and FTIR spectra were measured with a resolution of 4 cm^{-1} and averaged over 1000 scans.

2.1.2. X-ray diffraction (XRD)

X-ray diffraction (XRD) is a powerful analytical technique for materials research to determine the crystalline structure and lattice parameters of crystalline materials. During the XRD measurement, the X-rays interact with the atoms of the crystal and the subsequently scattered X-rays can interfere with each other constructively (intensifying the signal) and destructively (diminishing the signal). The constructive interference results in a diffraction pattern corresponding to the crystal symmetry of the material, and therefore by analyzing the intensities and angles of the diffracted beams, the crystal structure can ultimately be determined. In 1913, William Henry Bragg and his son William Lawrence Bragg derived a relation between the wavelength of incident X-rays (λ), the angle of incidence (θ) at which a constructive interference occurs and the distance between the crystal planes (d), mathematically expressed as:[3]

$$n\lambda = 2d\ sin\theta \qquad \text{(Equation 2.1)}$$

where n is the order of diffraction, which can only be an integral. As depicted in **Figure 2.2a**, when monochromatic X-rays hit a crystal, one ray may be scattered from one plane and the other from the plane below the first plane; the extra distance travelled by the lower ray is the sum of the distances travelled into and out of the crystal planes, and equals $2d\ sin\theta$. Bragg's law (**Eq. 2.1**) predicts that for constructive interference to take place, the path difference between X-rays scattered from two successive planes should be an integral multiple of the wavelength of the incident X-rays. When Bragg's condition is satisfied, a diffracted beam is detected.

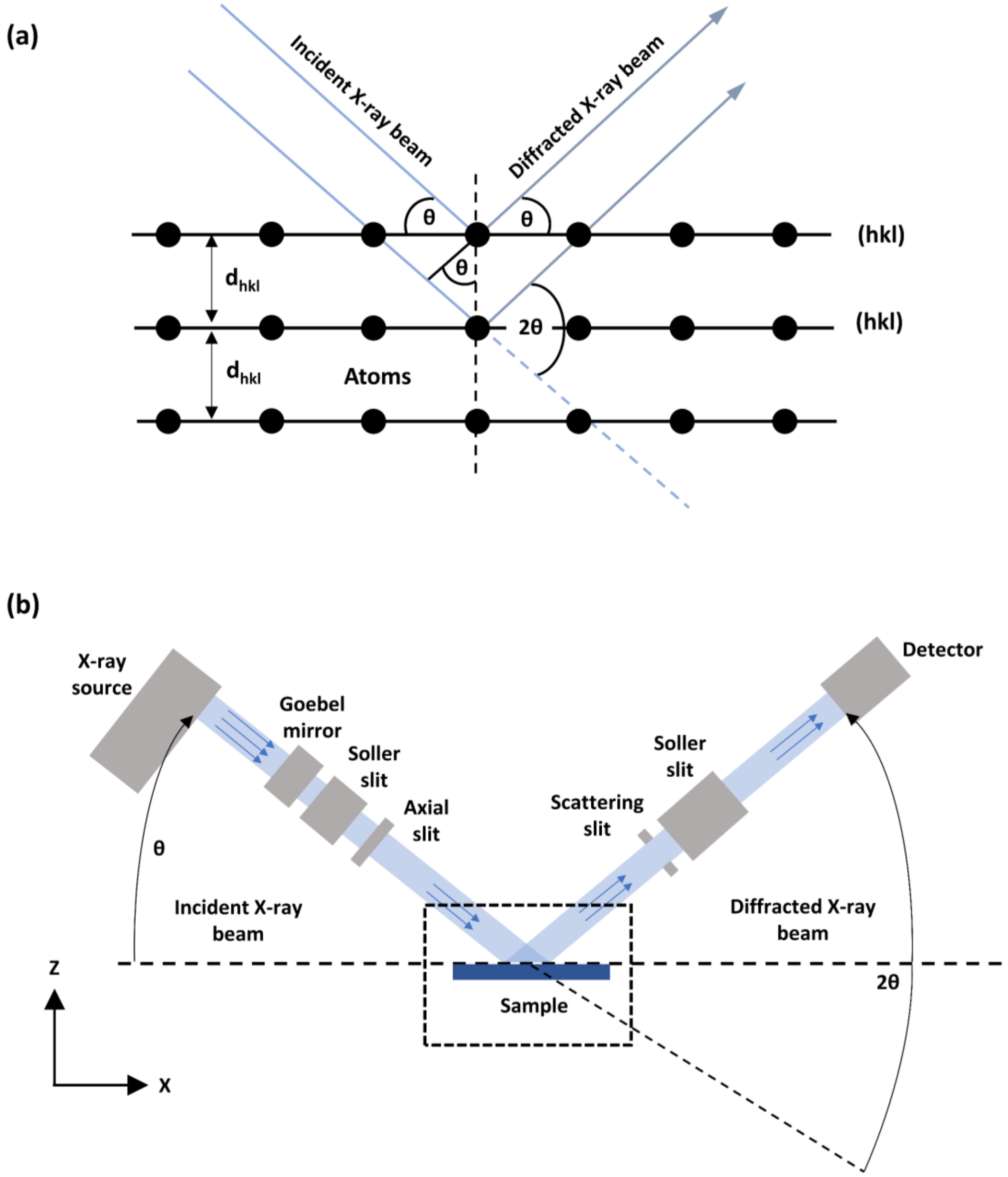

Figure 2.2 Schematic illustration of (a) Bragg's law and (b) the working principle of an X-ray diffractometer.

As presented in **Figure 2.2b**, the *X-ray source* consists of a cathode ray tube where electrons are accelerated and collide with a metal target, producing X-rays of specific wavelengths followed by a filter or monochromator to filter out unwanted wavelengths. The generated *incident X-ray beam* is directed towards the *sample* which can be powdered, thin films or single crystals. The intensities of the *diffracted X-ray beams* are measured by the *detector* at different angles, creating (often) sharp peaks in diffraction pattern. However, broadening of the diffraction peaks may occur due to extremely small crystallites, leading to fewer planes of atoms to contribute towards constructive interference of X-rays. Scherrer's formula directly links the broadening of the diffraction peaks to the crystallite size:[4]

$$D = \frac{K\lambda}{\beta \cos\theta} \qquad \text{(Equation 2.2)}$$

where, D is the crystallite size, K is Scherrer's constant, λ is the wavelength of the X-rays, β is the full width at half maximum (FWHM) of the diffraction peak, and θ is the angle (Bragg's angle) of the incident X-ray. This law assumes that the peak broadening is mainly caused by the small crystallite size while, in fact, broadening can be caused by other factors such as instrument imperfections, temperature, microstrain or disorder in the crystal lattice.

Instrument: Diffractograms were obtained using a Bruker D8 Discover, featuring a LynxEye position-sensitive detector, configured in Bragg-Brentano geometry.

2.1.3. Gas sorption

Nitrogen gas sorption is a widely used technique for characterizing the surface area, pore size, and pore volume of solid materials, in this case, COFs. N_2 sorption relies on the physical interaction between nitrogen molecules and the surface of porous materials called physisorption. Physisorption is a reversible process since weak van der Waals forces are involved and no chemical bonds are formed between the adsorbate (N_2 gas) molecules and the surface (COF). At a temperature of 77 K (boiling temperature of liquid nitrogen), the gas molecules adhere to the surface of the material through van der Waals forces, and the amount of gas molecules adsorbed with increasing partial pressure can be measured. Subsequently, as the relative pressure (p/p_0) approaches 1, the pressure is again reduced allowing the nitrogen molecules to leave the surface. For the complete process, the relationship between the *amount of gas adsorbed* and the *relative pressure* (p/p_0) yields an *isotherm*, which can be categorized into eight types according to the International Union of Pure and Applied Chemistry (IUPAC) classification (**Figure 2.3**). Since the adsorption behavior is influenced by the pore size and surface characteristics of the material, different types of isotherm correspond to different material properties:[5]

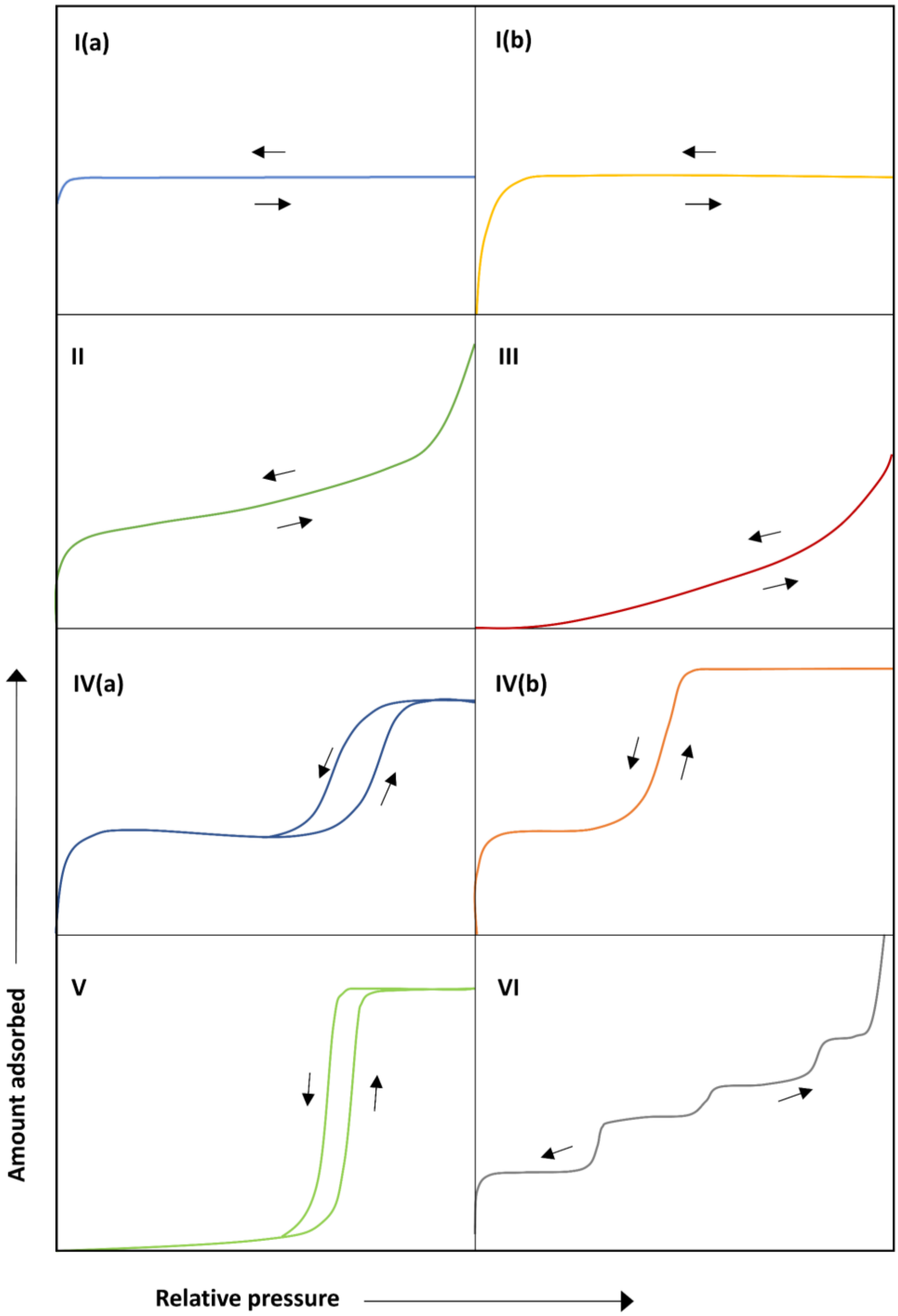

Figure 2.3 Depiction of various types of physisorption isotherms as recognised by IUPAC.

Type I: Also known as the Langmuir-isotherm, represents microporous materials (pore size < 2 nm), showing a steep uptake at low pressures due to the completely filled micropores. Type I is further classified into Type I(a), describing materials with narrow micropores, and Type I(b), which refers to materials possessing wider micropores and narrow mesopores.

Type II: Represents non-porous or macroporous materials with a continuous adsorption curve.

Type III: Represents non-porous or microporous materials that show weak interactions with the adsorbate.

Type IVa: Represents mesoporous materials (2-50 nm), exhibiting a hysteresis loop due to capillary condensation in the pores.

Type IVb: Represents mesoporous materials (2-50 nm), exhibiting reversible isotherm with smaller pore width.

Type V: Represents weak interactions between adsorbate and adsorbent, similar to Type III, however, with a hysteresis loop.

Type VI: Represents uniform non-porous surfaces, exhibiting multilayer adsorption.

The Brunauer-Emmett-Teller (BET) theory, named after Stephen Brunauer, Paul Emmett, and Edward Teller, is utilized to describe the physical adsorption of gas molecules on a solid surface and to calculate the surface area of porous materials.[6] The BET theory is an extension of the Langmuir adsorption model, which assumes that adsorption occurs only as a monolayer on a surface.[7] In contrast, BET theory recognizes that multiple layers of gas molecules can adsorb on the surface, making it more versatile for characterizing real-world surfaces. According to BET, the first layer of adsorbed molecules attaches directly to the surface, while subsequent layers are adsorbed onto the previously adsorbed gas molecules. BET assumes that (i) the gas molecules can adsorb in multiple layers, and the rate of adsorption and desorption is balanced for each layer, (ii) the first layer of adsorption is governed by the heat of adsorption, which is different from the heat of liquefaction that governs the subsequent layers, (iii) there is no lateral interaction between molecules within the same layer, and (iv) the surface is homogeneous in terms of adsorption sites.[8] Further, the BET theory is applicable over a limited range of the adsorption isotherm, typically in the range of 0.05 < p/p_0 < 0.30 (where p is the equilibrium pressure and p_0 is the saturation pressure). The BET equation is derived to express the relationship between the amount of gas adsorbed and the relative pressure p/p_0:

$$\frac{\frac{p_o}{p}}{n(1-\frac{p_o}{p})} = \frac{(C-1)}{n_m C}\frac{p}{p_o} + \frac{1}{n_m C} \qquad \text{(Equation 2.3)}$$

where C is the BET constant, n_m is the amount of the adsorbate adsorbed for a monolayer, and n is the amount of adsorbate adsorbed at a relative pressure p/p_0.

Instrument: The isotherms were recorded using Quantachrome Autosorb 1 and Autosorb iQ instruments at a temperature of 77 K. BET surface areas for the respective COFs were calculated based on the pressure range $0.05 \leq p/p_0 \leq 0.30$.

2.1.4. Thermogravimetric analysis (TGA)

Thermogravimetric analysis (TGA) is an analytical technique used to measure the change in the mass of a material as a function of temperature or time under controlled atmospheric conditions. TGA provides valuable insights into the thermal stability, composition, and decomposition behavior of materials. During the experiment, the sample is heated at a controlled rate, typically between 1-20 ℃ per minute, while a thermocouple ensures precise temperature control. As the sample undergoes physical or chemical changes, such as decomposition, oxidation, reduction, or the loss of moisture and volatile compounds, the instrument continuously records the mass change. These data can be plotted as a “thermogram”, showing mass change (in percentage or absolute terms) against temperature or time (**Figure 2.4**). The temperature at which significant mass loss begins is often referred to as the material’s thermal stability (this is sometimes misleading because these processes occur under dynamic conditions). The *decomposition temperature* (onset and endpoint) provides crucial information about the suitability of materials for high-temperature applications.

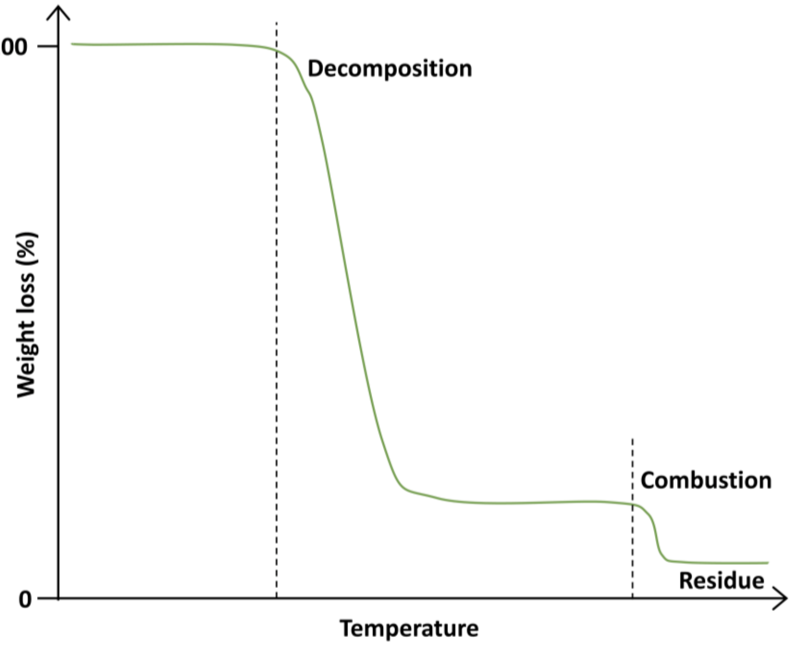

Figure 2.4 Schematic of a typical thermogravimetric analysis (TGA) curve or thermogram.

The first derivative of the TGA curve (mass change rate) provides sharper peaks, making it easier to identify the temperature at which decomposition events occur. TGA-DTA (Differential Thermal Analysis) or TGA-DSC (Differential Scanning Calorimetry) curves show a more accurate temperature of maximum mass loss rate and quantify heatflow (with the latter), providing a complete picture of thermal events like melting, crystallization, and decomposition.[9]

Instrument: The thermal stability measurements were performed on a Netzsch Jupiter ST 499 C instrument equipped with a Netzsch TASC 414/4 controller. Samples were heated from room temperature to 900 °C under a synthetic air flow at a heating rate of 10 °C min^{-1}.

2.1.5. Electron microscopy (EM)

Electron Microscopy (EM) operates by using a beam of electrons to produce high-resolution images, offering a significant advantage over traditional light microscopy, which relies on visible light.[10] The fundamental reason for this enhanced performance lies in the drastically shorter wavelength of electrons compared to visible light, allowing EM to achieve far greater magnification and resolution. The technique consists of several critical steps, which may vary slightly depending on the specific type of EM in use, such as scanning electron microscopy (SEM), and transmission electron microscopy (TEM), discussed in detail in Section 2.1.5.1 and 2.1.5.2, respectively.

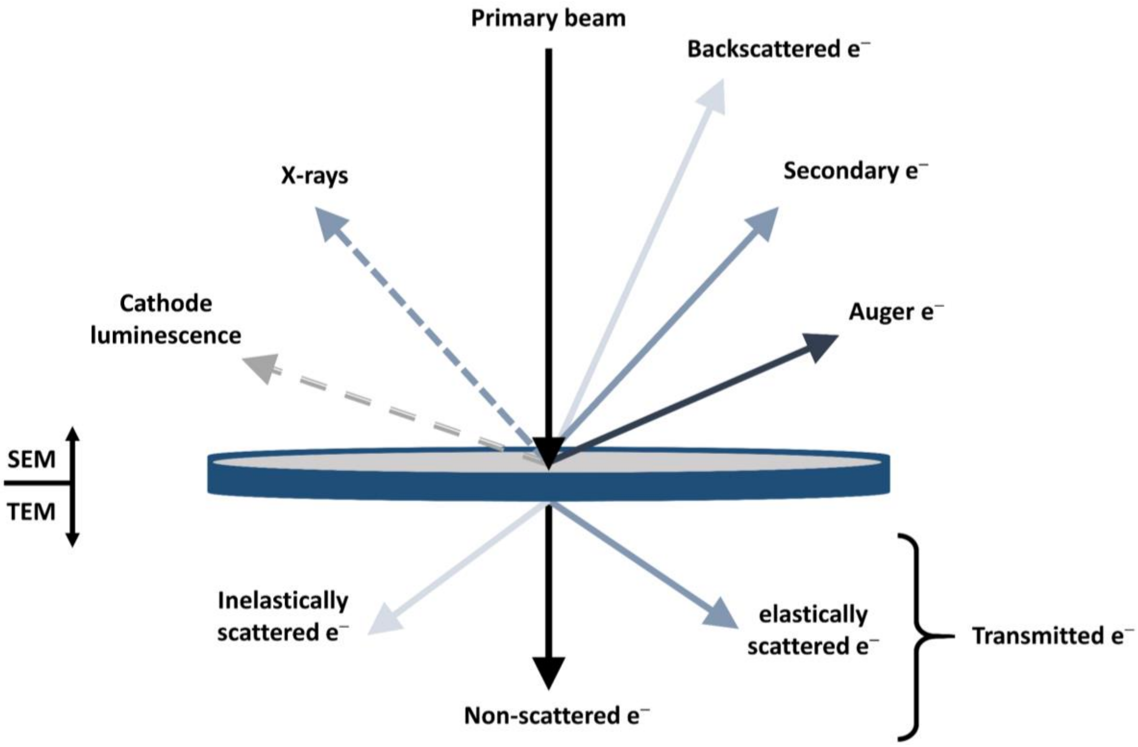

Figure 2.5 Schematic illustration of particles involved in electron microscopy (EM).

At the core of the process is the electron gun, which serves as the source of the *primary electron beam*. Electrons are typically generated by heating a tungsten filament or via a field emission gun (FEG) which provides a more coherent and precise electron beam. Once emitted, the electron beam is meticulously focused using electromagnetic lenses. Upon interaction with the sample, the electron beam induces a range of signals that arise from the specific interactions between the incident electrons and (mainly) with the electron shells of atoms within the material (**Figure 2.5**). The transmitted e$^-$ are detected in

TEM, providing information on the inner structure of the sample. Electrons can also be reflected back to the surface through elastic interactions, without the loss of kinetic energy, leaving the sample again as *backscattered e*$^-$. Th electron beam can also scatter inelastically with the atoms within the sample, originating *secondary e*$^-$, *Auger e*$^-$ or *X-rays*. For SEM analysis, secondary e$^-$ and backscattered e$^-$ are mainly detected providing information on the surface morphology and contrast in the image based on atomic number, respectively.[11,12]

2.1.5.1. Scanning electron microscopy (SEM)

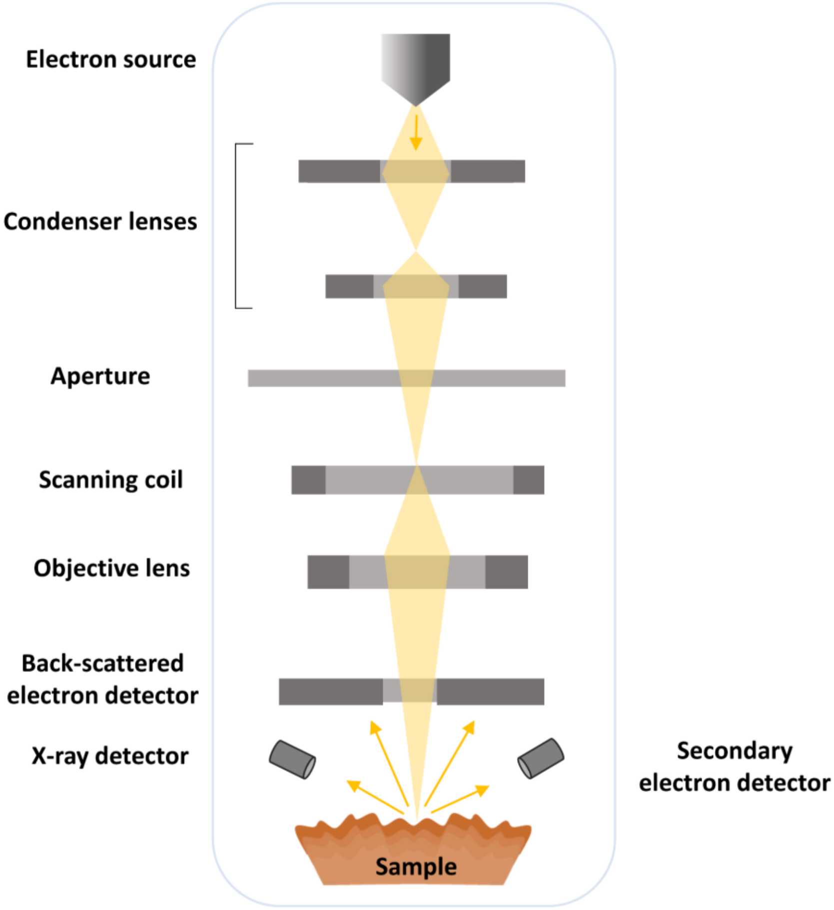

Figure 2.6 Schematic illustration of working principle of scanning electron microscopy (SEM) with beam path illustrated.

Scanning electron microscopy (SEM) is a powerful imaging technique used to observe the surface morphology and structure of materials at the nanometer scale. SEM provides detailed, three-dimensional-like images of a sample's surface by scanning it with a focused high-energy electron beam. The beam interacts with the atoms in the sample, producing signals that provide information about the surface's topography, composition, and other properties. The *electron source* or the *electron gun* produces an electron beam, typically generated by a tungsten filament, as depicted in **Figure 2.6**.[13,14] As the electron beam strikes the *sample*, secondary electrons (low-energy electrons) are ejected from the surface of the sample. These low-energy electrons are primarily used to form the SEM image, providing high-resolution detail of the surface morphology. Back-scattered electrons (or higher-energy electrons), reflected back from the sample, provide contrast in the image based on atomic number, with heavier elements appearing brighter. The secondary and backscattered electrons are collected by detectors and converted into a signal that forms an image on a screen. The image resolution depends on the electron beam's interaction with the surface and the interaction volume beneath the surface, and the detector’s sensitivity. Specialized detectors can also capture generated characteristic X-rays, which can be used for Energy-Dispersive X-ray spectroscopy (EDX) to determine the elemental composition of the sample (presented in detail in section 2.1.5.3).

The SEM samples are prepared by coating a thin layer of the material over a conductive material such as carbon or gold to avoid charging and ensure clear imaging. The SEM chamber is typically kept under high vacuum to prevent electrons from scattering in the air, which further allows for clear imaging.

Instrument: SEM images were obtained using an FEI Helios NanoLab G3 UC scanning electron microscope equipped with a Schottky field-emission electron source operated at 3-5 kV.

2.1.5.2. Transmission electron microscopy (TEM)

Transmission Electron Microscopy (TEM) operates on the principle of transmitting a beam of high-energy electrons through an ultra-thin sample, where electron-sample interactions produce various signals. These signals are then used to form high-resolution images, with the capability of resolving features as small as 0.1 nm and therefore gather detailed information about the internal structure, composition, and properties of the sample material. This high resolution is achievable due to the highly energetic electron beam, typically accelerated at voltages between 60−400 kV, focused by a series of electromagnetic condenser lenses and directed toward a thin sample, usually less than 200 nm thick.[15] Such thin samples are essential because electrons strongly interact with matter, and only very thin sections allow electrons to transmit through the sample for image formation.

A schematic illustration of the working principle of a TEM is presented in **Figure 2.7**. A typical TEM setup includes an *electron source*, *condenser lenses* to focus the beam, a specimen stage to hold the *sample*, an *objective lens* for initial image formation, and *projector lenses* for further magnification. The *selected area aperture* and *objective aperture* are used to enhance contrast by limiting scattered electrons that would otherwise reduce image clarity. As the electron beam passes through the sample, the transmitted electrons are influenced by the internal structure of the sample, which is then imaged by objective and projector lenses to produce an image. The final image can be detected by a fluorescent screen or an area detector, converting the high-energy electron signal into a visible or digital image.[15] The contrast in TEM images arises from a complex interaction between electrons and mass-thickness differences, where denser areas scatter more electrons and appear darker, and phase difference, which results from the interference of diffracted electrons when interacting with crystalline regions.

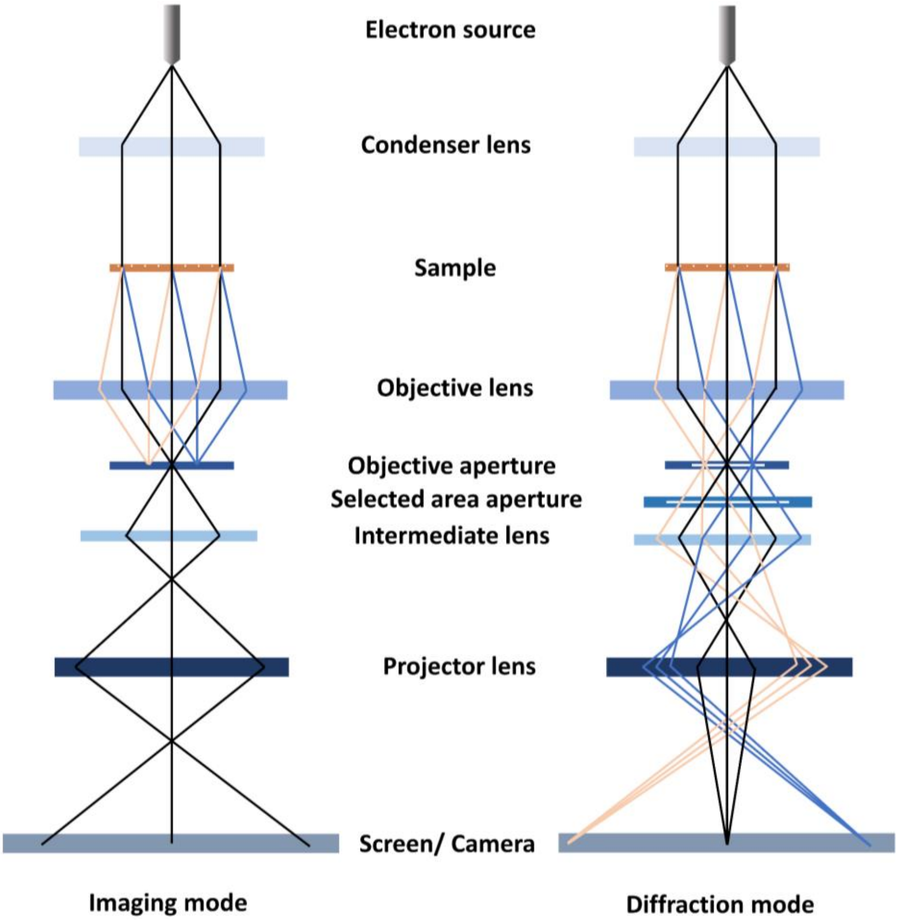

Figure 2.7 Schematic illustration of imaging and diffraction mode of transmission electron microscopy (TEM).

The arrangement of electromagnetic lenses allows the user to switch between different modes, including bright-field, dark-field, and diffraction modes. In diffraction mode, electron diffraction patterns are produced via Bragg scattering, which is particularly useful for analyzing crystalline materials, such as COFs. These patterns can provide detailed information about the crystal structure, lattice spacing, and orientation of the sample.

Similar to SEM, the entire TEM system operates under high vacuum conditions to maintain the high energy of the electron beam and minimize interactions with air molecules that could degrade the beam and reduce resolution.

Instrument: TEM images were obtained on an FEI Titan Themis instrument equipped with a field emission gun operated at 300 kV.

2.1.5.3. Energy-dispersive X-ray spectroscopy (EDX)

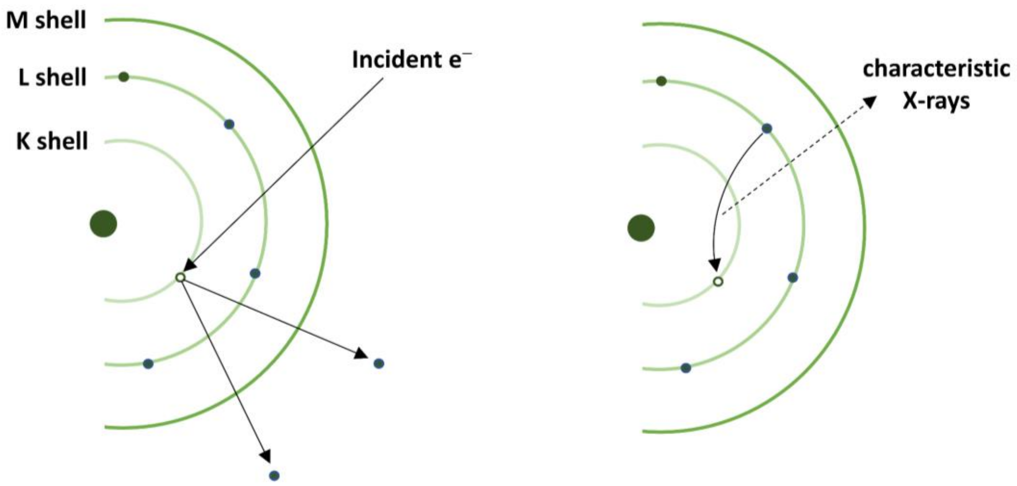

Figure 2.8 Schematic illustration of the working principle of energy-dispersive X-ray spectroscopy (EDX).

Energy-Dispersive X-ray Spectroscopy (EDX) is an essential technique for elemental analysis in electron microscopy, providing both qualitative and quantitative data on the composition of a wide range of materials.[16] When a high-energy electron beam (from SEM in this case) strikes the atoms in the sample, it displaces the inner-shell electrons from the electron orbitals of the individual atoms, and subsequently creating vacancies in the inner electron shells, making the atom unstable. To restore stability, electrons from higher energy levels transition downward to fill these vacancies (as depicted in **Figure 2.8**). This process releases energy in the form of characteristic X-rays, and each element emits X-rays at distinct energies, unique to its atomic structure. These emitted X-rays are captured by an EDX detector, which converts the X-ray photons into electrical signals. These signals are then processed and displayed as an energy spectrum, where each peak corresponds to the characteristic X-ray energies of specific elements within the sample. The intensity of these peaks is directly proportional to the concentration of the respective elements, facilitating both qualitative identification and quantitative compositional analysis.

Instrument: EDX measurements were performed in conjunction with SEM on a Dual beam FEI Helios G3 UC instrument equipped with an X-Max 80 EDS detector from Oxford Instruments plc. The EDX spectra were recorded at 5 kV.

2.1.6. Ultraviolet-visible spectroscopy (UV-vis)

UV-Vis spectroscopy (Ultraviolet-Visible Spectroscopy) is a widely used analytical technique based on the absorbance of light in the ultraviolet (UV; 200−400 nm) and visible light (400−700 nm) regions of the electromagnetic spectrum. It is primarily used to study the electronic transitions of molecules and materials, particularly those involving conjugated systems, aromatic rings, or metal complexes. In molecules, electrons are confined to discrete energy levels, which are described by molecular orbitals. Upon absorption of electromagnetic radiation, these electrons undergo excitation from a lower-energy orbital, known as the ground state, to a higher-energy orbital, referred to as the excited state. The difference in energy between these two states corresponds to the wavelength of the absorbed light. This relationship is quantitatively expressed by the equation:

$$E = h\nu = \frac{hc}{\lambda} \qquad \text{(Equation 2.4)}$$

where E is the energy difference between the ground and excited states, ν is the frequency of the light, h is Planck's constant, c is the speed of the light, and λ is the wavelength of the absorbed light. The nature of the electronic transition is dictated by the type of orbitals involved, and the energy required for these transitions determines whether absorption occurs within the ultraviolet (UV) or visible regions of the electromagnetic spectrum. The most common types of electronic transitions that occur in UV-Vis spectroscopy are related to molecular orbitals**,** particularly bonding (σ, π) and non-bonding (n) orbitals, and their corresponding antibonding orbitals (σ*, π*). For instance, high energy transitions (e.g., $\sigma \rightarrow \sigma^*$) absorb light in the vacuum UV region (short wavelengths, below 200 nm), moderate energy transitions (e.g., $\pi \rightarrow \pi^*$ and $n \rightarrow \sigma^*$) absorb light in the UV region (200−400 nm), and lower energy transitions (e.g., $n \rightarrow \pi^*$) absorb light in the visible region (400−700 nm) or near-IR region. In general, the more conjugated a system is, the less energy is required for $\pi \rightarrow \pi^*$ transitions, meaning the absorption will shift toward longer wavelengths (lower energy) in the UV-Vis spectrum. This shift is known as a bathochromic shift or redshift.

The amount and wavelength of the absorbed light provides valuable information about the structure, concentration, and properties of compounds. The absorption spectrum is a plot of absorbance (or transmittance) as a function of wavelength, and is characteristic of the specific chemical bonds and electronic transitions within the molecules, thus it can be used for qualitative and quantitative analysis. Lambert-Beer's law can be utilized to determine the concentration of the solution by measuring absorbance of the sample, such as:

$$A = -log_{10}\frac{I}{I_0} = \varepsilon cl \qquad \text{(Equation 2.5)}$$

where A is the absorbance, ε is the molar absorptivity (molar extinction coefficient), c is the concentration of the absorbing species in the solution, and l is the path length through the sample. I_0 is the intensity of light before passing through the sample, and I is the intensity of light after passing through the sample.

The Tauc plot is a widely employed graphical method used to determine the optical band gap of semiconducting materials. Originally introduced by J. Tauc for amorphous semiconductors, it establishes a relationship between the photon energy (hv) and the absorption coefficient of the material (α) through the equation:[17]

$$(\alpha hv)^n = A(hv - E_g) \qquad \text{(Equation 2.6)}$$

where E_g represents the optical band gap, A is a proportionality constant, and n defines the type of electronic transition, typically n = 0.5 stands for indirect allowed transitions and n = 2 for direct allowed transitions. By plotting $(\alpha hv)^n$ vs. hv, a linear region can be obtained near the absorption edge, and extrapolating this line to the energy axis yields the E_g.

However, COFs are typically synthesized as fine powders or films that might exhibit a significant level of light scattering, making direct measurement of the absorption coefficient difficult. To overcome this limitation, the Kubelka–Munk (KM) theory can be applied, where the KM model converts diffuse reflectance data obtained from UV–Vis spectroscopy into a quantity proportional to absorption using the transformation:[18]

$$F(R) = \frac{(1-R)^2}{2R} \qquad \text{(Equation 2.7)}$$

where R is the measured reflectance and the function $F(R)$ acts as an equivalent to α in the Tauc equation, allowing estimation of the optical band gap even for opaque materials. This approach provides insights into how variations in linker conjugation, substituents, and topology tune the optical properties, guiding the rational design of COFs with desired electronic properties.[19]

Instrument: UV-vis spectra were recorded using a Perkin-Elmer Lambda 1050 spectrometer equipped with a 150 mm integrating sphere, photomultiplier tube (PMT) and InGaAs detector.

2.2. Electrochemical characterization

2.2.1. Cyclic voltammetry (CV)

Cyclic voltammetry (CV) is essential in battery research for studying the redox behavior of materials, understanding their electrochemical properties, and diagnosing performance issues. It provides key insights into the reversibility, kinetics, stability, and degradation of battery materials. CV allows the identification of the redox potentials at which the battery's active materials undergo oxidation and reduction reactions. These potentials provide important information about the voltage window in which the battery operates.

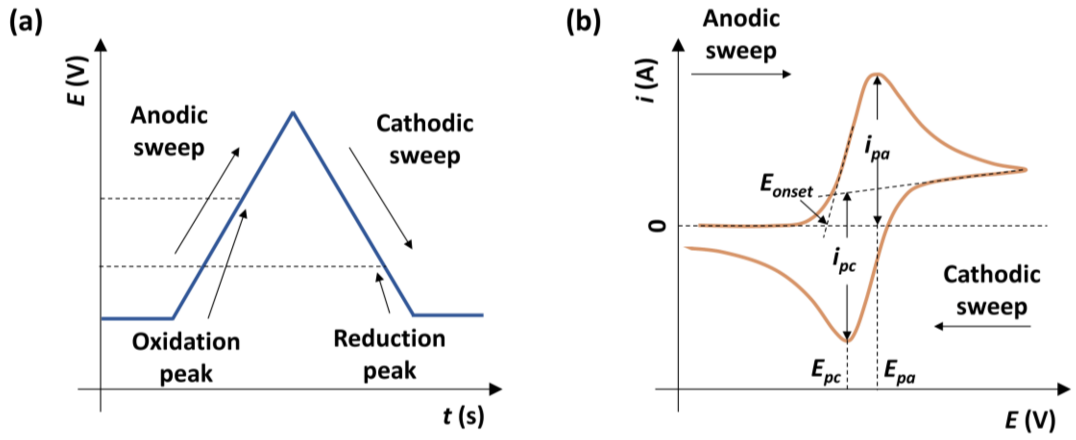

Figure 2.9 Schematic illustration of the working principle of cyclic voltammetry (CV). (a) Applied potential (E, in V) as a function of time (t, in s) for a generic cyclic voltammetry producing a (b) "duck-shaped" cyclic voltammogram, representing both anodic and cathodic sweeps. E_{onset} is the potential where the oxidation (or reduction) begins, E_{pc} and E_{pa} are the potentials at which reduction peak current (i_{pc}) and oxidation peak current (i_{pa}) appears, respectively.

The principle of CV revolves around measuring the current response of an electrochemical system as the potential applied to the working electrode is swept linearly over time, forming a cyclic pattern (**Figure 2.9a**).[20] The sweep consists of two main phases, forward sweep, during which the potential is increased (or decreased) linearly, causing the oxidation (or reduction) of the electroactive species at the working electrode, and after reaching a defined voltage limit, the sweep direction is reversed, and the opposite redox reaction occurs during reverse sweep. If during the forward sweep, the applied voltage forces the electroactive species to undergo oxidation (lose electrons), then it is called "*anodic sweep*". And consequently, if during the reverse sweep, the applied voltage forces the electroactive species to undergo reduction (accept electrons), then it is called "*cathodic sweep*".[20,21]

As depicted in **Figure 2.9b**, during anodic sweep, as the potential reaches a certain value, the species starts to oxidize at E_{onset}, indicating that the species are forming its oxidized state by losing electrons and an *oxidation peak* appears. On the reverse sweep, the oxidized species starts to reduce back to its original state by gaining electrons, and a *reduction peak* appears. The potential at which the oxidation (E_{pa}) or reduction (E_{pc}) peak occurs corresponds to the formal redox potential of the species and provides information about the redox properties of the system. The peak current (i_{pa} or i_{pc}) is proportional to the concentration of the electroactive species and the rate of electron transfer. The height of the peak not only depends on the number of electrons involved, concentration and diffusion of ionic species but also on the scan rate (ν) of the measurement, as described by the Randles–Ševčík equation:

$$i_p = (2.69\ \times 10^5) n^{3/2} A D^{1/2} C \nu^{1/2} \qquad \text{(Equation 2.8)}$$

where i_p denotes the peak current, n is the number of electrons involved in the redox process, A represents the electrode surface area, D is the diffusion coefficient of the redox-active species, C is its bulk concentration in the electrolyte, and ν is the scan rate of the measurement performed at 25 °C.

In batteries, a power law can be applied to rate-dependent CV to analyze the electrochemical processes at the electrode surface and to distinguish between different types of charge storage mechanisms, such as faradaic diffusion-controlled (battery-like) processes and non-faradaic surface-controlled (capacitive) processes. The relationship between the peak current (i_p) and the scan rate (ν) can often be expressed using a power law:[22,23]

$$i_p = a\nu^b \qquad \text{(Equation 2.9)}$$

where both a and b are constants. The value of b can provide insights into the charge storage mechanism in a cell, for instance, a b-value of 0.5 implies slower diffusion dependence, while a b-value of 1 indicates faster capacitive behavior. Furthermore, Dunn’s method is utilized to quantitatively separate the current responses into diffusive- and capacitive-dependent:[23]

$$i(V) = \ k_1\nu + k_2\nu^{1/2} \qquad \text{(Equation 2.10)}$$

where $i(V)$ is the current response at a specific potential, $k_1\nu$ is the fraction of total current dominated by capacitive behavior, and $k_2\nu^{1/2}$ signifies the diffusive contribution. This equation can be used to deconvolute the CV data to determine how much of the current is due to capacitive storage and how much is due to diffusion-limited processes.

Instrument: Cyclic voltammetry measurements were carried out on a Metrohm Autolab potentiostat/galvanostat PGSTAT302N equipped with a FRA32M module.

2.2.2. Linear sweep voltammetry (LSV)

Linear Sweep Voltammetry (LSV) is a valuable technique in battery research, used for investigating the electrochemical behavior of battery materials, assessing the stability of electrolytes and electrodes, and characterizing key processes like degradation and corrosion. LSV is commonly used to measure the voltage range in which an electrolyte remains stable. By sweeping the potential, the onset of decomposition reactions of the electrolyte can be identified, which determines the electrochemical stability and the safe operating voltage range of the battery. The potential is swept from a lower voltage to a higher one (or vice versa) to explore oxidation (or reduction) behavior of the electrolyte or electrode materials. Similar to CV, the onset of current indicates the voltage (E_{onset}) where a reaction starts, such as electrolyte decomposition, and the peak current (I_p) corresponds to the oxidation or reduction of active materials.

During voltammetry, the current increases with scan rate due to enhanced reaction kinetics and diffusion effects. As the scan rate increases, the applied potential changes more rapidly, accelerating the electron transfer reactions at the electrode surface, which leads to higher faradaic currents (**Figure 2.10**). Additionally, faster scan rates create a steeper concentration gradient near the electrode, causing larger number of electroactive species to diffuse rapidly to the surface, further increasing the current.

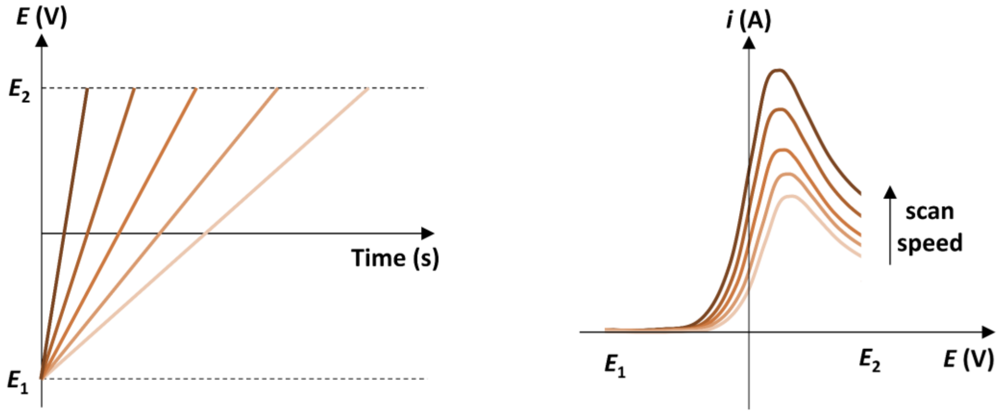

Figure 2.10 Schematic illustration of relation between scan-speed and observed current in a linear sweep voltammetry (LSV).

Instrument: Linear-sweep voltammetry (LSV) measurements were carried out on a Metrohm Autolab potentiostat/galvanostat PGSTAT302N equipped with a FRA32M module.

2.2.3. Galvanostatic charge-discharge cycling (GCD)

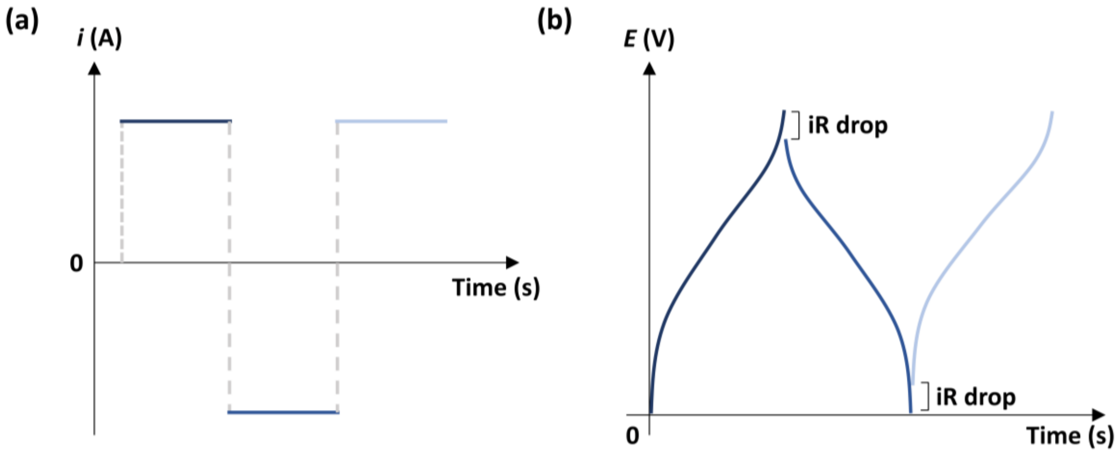

Figure 2.11 Schematic illustration of the working principle of galvanostatic charge-discharge (GCD).

GCD cycling provides detailed information about the charge-discharge behavior, efficiency, and stability of energy storage devices, making it an essential technique in battery and capacitor research. In GCD, the electrochemical cell is charged and discharged at galvanostatic mode (constant current), while the voltage is monitored as a function of time (**Figure 2.11a**).[24] During the charge cycle, a constant positive current is applied to the cell, resulting in a gradual increase in the voltage until it reaches a pre-set upper cut-off voltage. Whilst, during a discharge cycle, a constant negative current is applied, leading to decrease in the voltage until it reaches a lower cut-off voltage. The duration of a (dis-)charge cycle of the device under constant current provides information about the energy capacity of the cell. Typically, longer charge/discharge times indicate higher energy storage capacity. The specific capacity (Unit: mAh g^{-1} for batteries) is calculated from the charge or discharge time and the applied current using the following formula:

$$Specific\ capacity\ (SC) = \frac{I \times t}{m} \qquad \text{(Equation 2.11)}$$

where I (A) is the current applied, t (h) is the duration of charge (or discharge) cycle, and m (g) is the mass of the active material of the electrode. Further, coulombic efficiency (CE) represents the ratio of the charge extracted during discharge to the charge supplied during charging. The formula employed to determine the coulombic efficiency (CE) is:

$$Coulombic\ efficiency\ (CE) = \frac{Specific\ discharge\ capacity}{Specifc\ charge\ capacity} \times 100 \qquad \text{(Equation 2.12)}$$

A coulombic efficiency of ~99% indicates that most of the charge input during charging is recovered during discharging and therefore, no significant charge is lost due to side reactions, such as electrolyte decomposition or parasitic processes.

Moreover, the voltage profile of GCD measurements provides key insights into the charge storage mechanism of energy devices. For instance, batteries rely on faradaic redox reactions, and typically show distinct voltage plateaus during charge and discharge, reflecting the electrochemical processes occurring within the electrodes. In contrast, supercapacitors store charge through non-faradaic, electrostatic processes, resulting in a linear voltage profile without plateaus. Pseudocapacitor electrode materials, which combine both mechanisms, exhibit slight curvature or small plateaus in their GCD curves.[22] These features help to differentiate between the energy storage behaviors and to assess the performance of the device in terms of energy and power density. During (dis-)charging cycles, the voltage profile usually shows an abrupt voltage drop at the moment the current is switched from charge to discharge (or vice versa). This immediate voltage drop is called the "*iR drop*", which is a direct consequence of the internal resistance of the cell, and serves as a useful indicator of self-discharge and overall efficiency of an electrochemical cell (**Figure 2.11b**). A lower internal resistance exhibits smaller iR drops, leading to better energy and power performance of the battery.

Instrument: Galvanostatic charge-discharge (GCD) measurements were conducted using an Autolab Multipotentiostat M101 by applying different current densities corresponding to the respective projects.

2.2.4. Electrochemical impedance spectroscopy (EIS)

Electrochemical impedance spectroscopy (EIS) is a highly versatile and non-destructive analytical technique that provides detailed information about electrochemical systems by probing their impedance in response to a small alternating current or voltage signal across a range of frequencies. It can provide a detailed understanding of electrochemical phenomena, such as charge transfer, mass transport, and double-layer capacitance at the electrode-electrolyte interface.

In potentiostatic EIS, a small sinusoidal AC voltage ($E(t) = E_0 \sin(\omega t)$) *perturbation* is applied as the *input signal* to an electrochemical system and the frequency (f) of the AC signal is swept over a broad range, from a few millihertz (mHz) to several megahertz (MHz) (**Figure 2.12a**).[25] The small perturbation, ranging between 10−20 mV, ensures that the system operates within its linear regime, where the relationship between voltage and current is approximately proportional. The response or the *output signal* of the system is measured in terms of current ($I(t) = I_0 \sin(\omega t + \phi)$), where the resulting current is phase-shifted (ϕ) relative to the input signal, and this shift contains information about the system's capacitive or inductive properties (**Figure 2.12b**).[25]

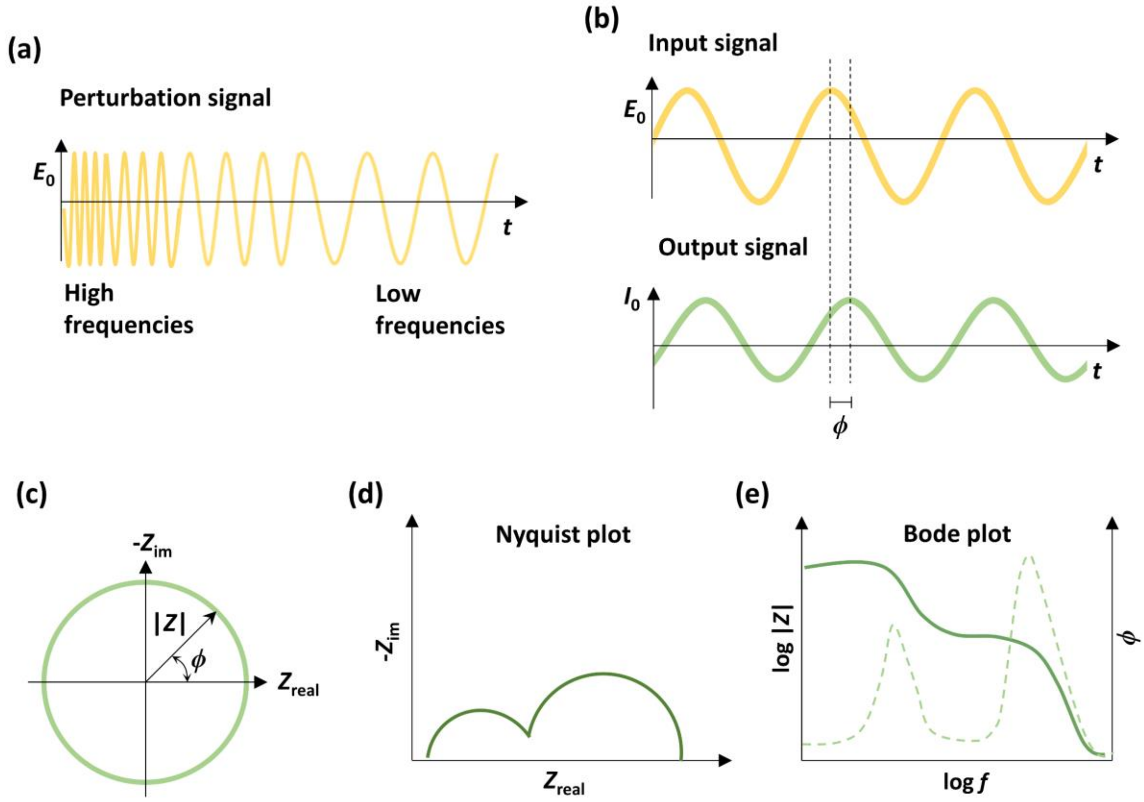

Figure 2.12 Schematic illustration of the working principle of potentiostatic electrochemical impedance spectroscopy (EIS). (a) The applied excitation sinusoidal perturbation signal and (b) sinusoidal current response along with the phase shift. (c) Complex impedance $|Z|$ in vector representation with Z_{real} at the abscissa and Z_{im} on the ordinate with phase angle (ϕ). The electrochemical impedance spectrum represented as typical Nuquist and Bode plots.

The core principle of EIS involves calculating the impedance (Z), which is a complex quantity describing the resistance imposed by the AC system, utilizing the voltage and current in the frequency domain:[25]

$$Z(\omega) = \frac{E(\omega)}{I(\omega)} = Z_{real} + jZ_{im} \qquad \text{(Equation 2.13)}$$

where, Z_{real} is the real component of impedance, Z_{im} is the imaginary component of impedance, and j is the imaginary unit, representing the phase shift. Z_{real} corresponds to pure resistance, while the Z_{im} reflects capacitive or inductive effects. The magnitude of impedance $|Z|$ can be calculated using the following equation:[25]

$$|Z| = \sqrt{Z_{real}^2 + Z_{im}^2} \qquad \text{(Equation 2.14)}$$

EIS data is commonly represented using Nyquist and Bode plots (**Figure 2.12d,e)**. In a Nyquist plot, the real part of impedance is plotted on the x-axis, while the imaginary part is on the y-axis, with each point representing the impedance at a particular frequency. This representation often produces semicircles, corresponding to processes like charge transfer, and straight lines, indicating diffusion control. The diameter of these semicircles is related to the charge transfer resistance, which is a key parameter in determining the reaction kinetics of the system. A Bode plot, on the other hand, shows the impedance magnitude and phase angle as a function of frequency, making it easier to visualize how different processes dominate at different frequencies.

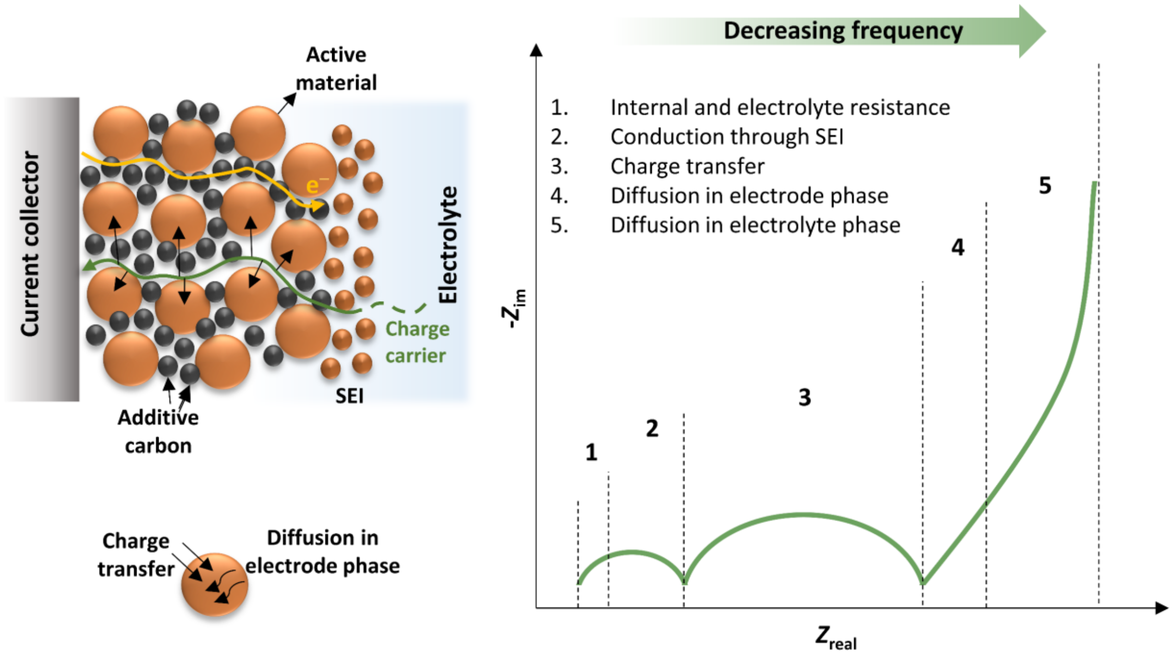

Figure 2.13 Schematic illustration of the interpretation of a Nyquist plot.

The key to EIS is that different electrochemical processes dominate the impedance response at different frequencies, for instance, at very high frequencies, the impedance is dominated by elements with a fast response, such as the (ohmic) solution resistance (electrolyte resistance) or any high-frequency processes (e.g., electronic conduction). While, at mid frequency range, processes such as charge transfer (related to the electron transfer reactions at the electrode) and double-layer capacitance (the accumulation of charge at the electrode/electrolyte interface) are dominant. Finally, at low frequencies, mass transport processes like diffusion begin to dominate. This is often modeled by the Warburg impedance, which arises due to ion diffusion to and from the electrode surface, and appears as a straight line with a slope of 45° in a Nyquist plot (**Figure 2.13**).[26]

To interpret EIS data, they are often modelled using equivalent electrical circuits (EECs) consisting of elements like resistors (R), capacitors (C), inductors (L), constant phase elements (Q), and Warburg element (W). These components represent real physical processes in the system. For example, a resistor can model solution resistance, a capacitor may represent the double-layer capacitance, and a Warburg element may describe ion diffusion. By fitting the measured data to these models, quantitative insights into various parameters such as charge transfer resistance, double-layer capacitance, and diffusion coefficients can be extracted.

Instrument: EIS measurements were performed with an Autolab potentiostat workstation equipped with a FRA32M module over the frequency range of 10^6–0.1 Hz with an applied perturbation voltage of 10 mV. The obtained Nyquist plots were modeled using either *Z*sim or *Z*fit software.

2.2.5. Warburg element

In 1899, Emil Warburg first described a diffusion-dependent contribution to the impedance in an electrochemical cell. In a Nyquist plot, the *Warburg element* is represented by a linear segment inclined at approximately 45° to the real axis in the low-frequency region, typically below 10 Hz, corresponding to the regime of semi-infinite linear diffusion.[27] Accordingly, the Warburg impedance serves as a diagnostic indicator of diffusion-controlled charge or mass transport phenomena, arising from the finite rate of ionic diffusion within the medium. The magnitude and profile of this diffusion impedance are intrinsically linked to the diffusion coefficient of the involved species. To quantify this, the Warburg plot (Z_{re} vs $\omega^{-1/2}$), is constructed at specific potential steps during cycling, utilizing the following equation:[28]

$$Z_{real} = R_T + \sigma\omega^{-1/2} \qquad \text{(Equation 2.15)}$$

where Z_{real} is the real component of impedance, R_T is the total resistance, ω is the angular frequency, and σ is the Warburg coefficient (Ω s$^{-1/2}$) obtained as the slope of the graph. The fingerprint region of the Warburg impedance is low-frequency domain, and therefore Z_{real} associated with low frequency was considered while building the Warburg plots. Further, the diffusion coefficient can be calculated from the Warburg coefficient using the following relationship:[28]

$$D = \frac{R^2T^2}{2n^4F^4C^2A^2\sigma^2} \qquad \text{(Equation 2.16)}$$

where R is the gas constant (8.314 J K^{-1} mol^{-1}), T is the operational temperature of the electrochemical cell (298.15 K), n is the number of electrons transferred from electrolyte to the electrode, F is Faraday's constant (96458 C mol^{-1}), C is the concentration of the charge carriers in the electrolyte solution (1.0 M), and A is the surface area of the electrode, respectively. Potential dependent EIS provides the ability to monitor how the diffusion coefficient changes with different applied potentials.

Instrument: The measurements were performed on a BioLogic VMP-3e Multichannel Potentiostat workstation at a frequency range of 10^6-0.1 Hz with an applied perturbation voltage of 10 mV. The obtained Nyquist plots were modeled using the *Z*fit software.

2.2.6. Cell assembly

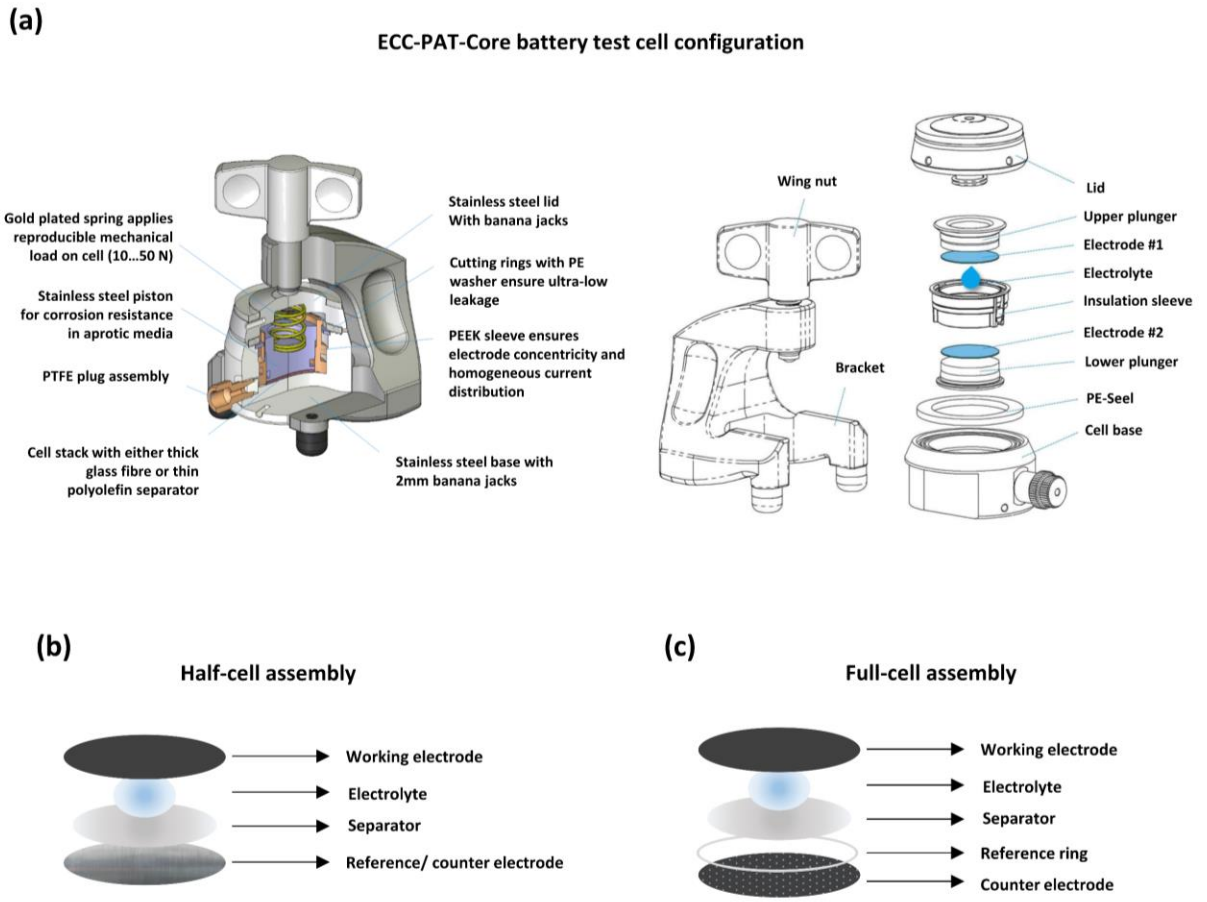

Figure 2.14 (a) Schematic representation of PAT-Core electrochemical test cell configuration from EL-Cell GmbH[29,30] in (b) half-cell and (c) full-cell assembly.

To perform electrochemical measurements, half- and full-cells were assembled using an ECC-PAT-Core battery test cell from EL-CELL GmbH (see **Figure 2.14a**). The body of ECC-PAT cells is composed primarily of *stainless steel* and *PEEK* (polyether ether ketone), rendering them compatible with standard aprotic organic electrolytes utilized in Li-ion batteries, Na-ion batteries, and supercapacitors. A *gold-plated spring* is employed to apply uniform mechanical pressure on the precise ϕ =18 mm electrodes, ensuring consistent performance. The cells feature a low-leakage sealing system using *PE washers* and allow for easy and accurate electrolyte filling during assembly. A notable advantage of the ECC-PAT cells is their sustainability, which surpasses that of traditional one-time-use coin cells. The ECC-PAT cells allow rapid and straightforward assembly, facile cleaning, and convenient access to the electrodes for post-mortem analysis.[29,30]

Half-cell and full-cell testing assemblies are critical components in the evaluation of the performance of lithium-ion and sodium-ion batteries. In a half-cell configuration, the anode or cathode is tested against a reference (and counter) electrode, typically lithium metal for lithium-ion batteries and sodium metal for sodium-ion batteries (**Figure 2.14b**). This configuration enables to investigate the electrochemical behavior of individual electrodes, encompassing their capacity, voltage profile, and stability. This configuration is particularly useful for the assessment of novel electrode materials prior to their integration into a complete battery system. Additionally, EIS is easier to deconvolute in a half-cell because it isolates the contribution of a single electrode, allowing for more precise analysis of charge transfer and resistance.

Conversely, a full-cell testing assembly comprises both an anode and a cathode, along with a reference electrode, thereby emulating the configuration of a commercial battery. In the context of lithium and sodium batteries, this configuration is employed to assess the overall performance, encompassing parameters such as energy density, cycle life, and efficiency. Full-cell testing is critical for understanding how the anode and cathode interact and perform together under realistic conditions. It is imperative to calibrate the mass loading of the electrodes in order to accurately determine the capacity of the full cell. The mass loading of the electrodes can be calibrated according to the following equation:[28]

$$SC_A \times M_A \geq SC_C \times M_C \qquad \text{(Equation 2.17)}$$

where SC_A is the anode-specific capacity (in mAh g^{-1}), SC_C is the cathode-specific capacity (in mAh g^{-1}), M_A (in g) is mass loading at the anode and M_C (in g) is the mass loading of the cathode. The anode mass loading is usually made slightly higher than the cathode to maintain lithium balance and prevent plating.

Instrument: All electrochemical measurements were performed with half- or full-cell configurations assembled using an ECC-PAT-Core battery test cell from EL-CELL GmbH if not stated otherwise throughout the thesis.

2.3. References

[1] B. C. Smith, *Fundamentals of Fourier Transform Infrared Spectroscopy*, CRC Press, Boca Raton **2011**.

[2] P. R. Griffiths, J. A. de Haseth, *Fourier Transform Infrared Spectrometry*, Wiley **2007**.

[3] W. H. Bragg, W. L. Bragg, *Proceedings of the Royal Society of London. Series A* **1913**, *88*, 428.

[4] P. Scherrer, *Nachrichten von der Gesellschaft der Wissenschaften zu Göttingen* **1918**, *2*, 98.

[5] M. Thommes, K. Kaneko, A. V. Neimark, J. P. Olivier, F. Rodriguez-Reinoso, J. Rouquerol, K. S. W. Sing, *Pure and Applied Chemistry* **2015**, *87*, 1051.

[6] S. Brunauer, P. H. Emmett, E. Teller, *J. Am. Chem. Soc.* **1938**, *60*, 309.

[7] I. Langmuir, *J. Am. Chem. Soc.* **1916**, *38*, 2221.

[8] W. G. McMILLAN, E. TELLER, *The Journal of physical and colloid chemistry* **1951**, *55*, 17.

[9] R. B. Prime, H. E. Bair, S. Vyazovkin, P. K. Gallagher, A. Riga, in *Thermal Analysis of Polymers* (Eds.: J. D. Menczel, R. B. Prime), Wiley **2009**, p. 241.

[10] M. W. Davidson, M. Abramowitz, in *Encyclopedia of Imaging Science and Technology* (Ed.: J. P. Hornak), Wiley **2002**.

[11] E. Ruska, *Rev. Mod. Phys.* **1987**, *59*, 627.

[12] G. van Tendeloo, S. Bals, S. van Aert, J. Verbeeck, D. van Dyck, *Advanced materials (Deerfield Beach, Fla.)* **2012**, *24*, 5655.

[13] A. A. Azad Mohammed, *Proc. 2018 Int. Conf. on Hydraulics and Pneumatics, Baile Govora, Romania* **2018**.

[14] T. E. Davies, H. Li, S. Bessette, R. Gauvin, G. S. Patience, N. F. Dummer, *Can J Chem Eng* **2022**, *100*, 3145.

[15] D. B. Williams, C. B. Carter, *Transmission Electron Microscopy*, Springer US, Boston, MA **1996**.

[16] A. G.-R. DC Bell, *Energy Dispersive X-ray Analysis in the Electron Microscope*, Garland Science, London **2003**.

[17] J. Tauc, *Amorphous and Liquid Semiconductors*, Springer US, Boston, MA **1974**.

[18] P. Kubelka, Munk, *F. Z. Tech. Phys.* **1931**, *12*, 593.

[19] R. Guntermann, L. Frey, A. Biewald, A. Hartschuh, T. Clark, T. Bein, D. D. Medina, *J. Am. Chem. Soc.* **2024**, *146*, 15869.

[20] N. Elgrishi, K. J. Rountree, B. D. McCarthy, E. S. Rountree, T. T. Eisenhart, J. L. Dempsey, *J. Chem. Educ.* **2018**, *95*, 197.

[21] R. Stephanie, *Nat. Rev. Clean Technol.* **2025**, *1*, 112.

[22] C. Choi, D. S. Ashby, D. M. Butts, R. H. DeBlock, Q. Wei, J. Lau, B. Dunn, *Nat Rev Mater* **2020**, *5*, 5.

[23] J. Wang, J. Polleux, J. Lim, B. Dunn, *J. Phys. Chem. C* **2007**, *111*, 14925.

[24] A. J. Bard, L. R. Faulkner, H. S. White, *Electrochemical Methods: Fundamentals and Applications.*, Wiley **2022**.

[25] A. C. Lazanas, M. I. Prodromidis, *ACS measurement science au* **2023**, *3*, 162.

[26] S. Wang, J. Zhang, O. Gharbi, V. Vivier, M. Gao, M. E. Orazem, *Nat Rev Methods Primers* **2021**, *1*, 1.

[27] E. Warburg, *Annalen der Physik* **1899**, *303*, 493.

[28] R. Nandan, N. Takamori, K. Higashimine, R. Badam, N. Matsumi, *J. Mater. Chem. A* **2022**, *10*, 5230.

[29] *ECC-Combi. Electrochemical test cell applicable both as 2- and 3-electrode test cell* **Extracted on 2025**, https://www.el-cell.com/products/test-cells/legacy-test-cells/ecc-ref/.

[30] *Electrochemical Test Cell ECC-PAT-Core.* **Extracted on 2025**, https://el-cell.com/wp-content/uploads/downloads/manuals/Manual_ECC-PAT-Core_Release_2.02.pdf.

3

This chapter is based on the following article-

Unveiling the Sodium-Ion Diffusion Mechanism in Covalent Organic Framework−Based Quasi-Solid-State Electrolytes

Apeksha Singh,‡1 Preeti Bhauriyal,‡2 Roman Guntermann,[1] Thomas Heine,[2-5] Thomas Bein[1],*

[1]Department of Chemistry and Center for NanoScience (CeNS), Ludwig-Maximilians- Universität München (LMU Munich), Butenandtstrasse 5-13 (E), 81377 Munich, Germany

[2]Faculty of Chemistry and Food Chemistry, Technische Universität Dresden, Bergstrasse 66, 01069 Dresden, Germany

[3]Helmholtz-Zentrum Dresden-Rossendorf (HZDR), Bautzner Landstr. 400, 01328 Dresden, Germany

[4]Center for Advanced Systems Understanding (CASUS), Untermarkt 20, 02826 Görlitz, Germany

[5]Department of Chemistry and ibs for nanomedicine, Yonsei University, Seodaemun-gu, Seoul 120-749, South Korea

KEYWORDS: sodium-ion conductivity, ab inito molecular dynamics (AIMD) simulations

‡These authors contributed equally.

Manuscript in preparation

3.1. Abstract

Covalent organic frameworks (COFs) have emerged as promising base materials for electrolytes, leveraging their pores to facilitate directional and accelerated ion conduction. This study introduces two quasi-solid-state COF electrolytes, featuring uniformly distributed sulfonate anions as hopping sites for sodium ions, and investigates the effect of their varied functionalities on the Na^+ diffusion mechanism. The sulfonate COFs are coupled with 1-methyl-1-propylpyrrolidinium bis(fluorosulfonyl)imide ($Pyr_{13}FSI$), without additional sodium salt, to generate electrolyte composites with high ionic conductivities in the range of 10^{-3} S cm^{-1}. These composites not only inherit thermal stability from the combination of COFs and ionic liquid, but also eliminate the risk of leakage due to their gel composition. We demonstrate the importance of altering the dimensions of COF channels and the density of sulfonate groups along the walls by elucidating the unique sodium-ion diffusion mechanisms.

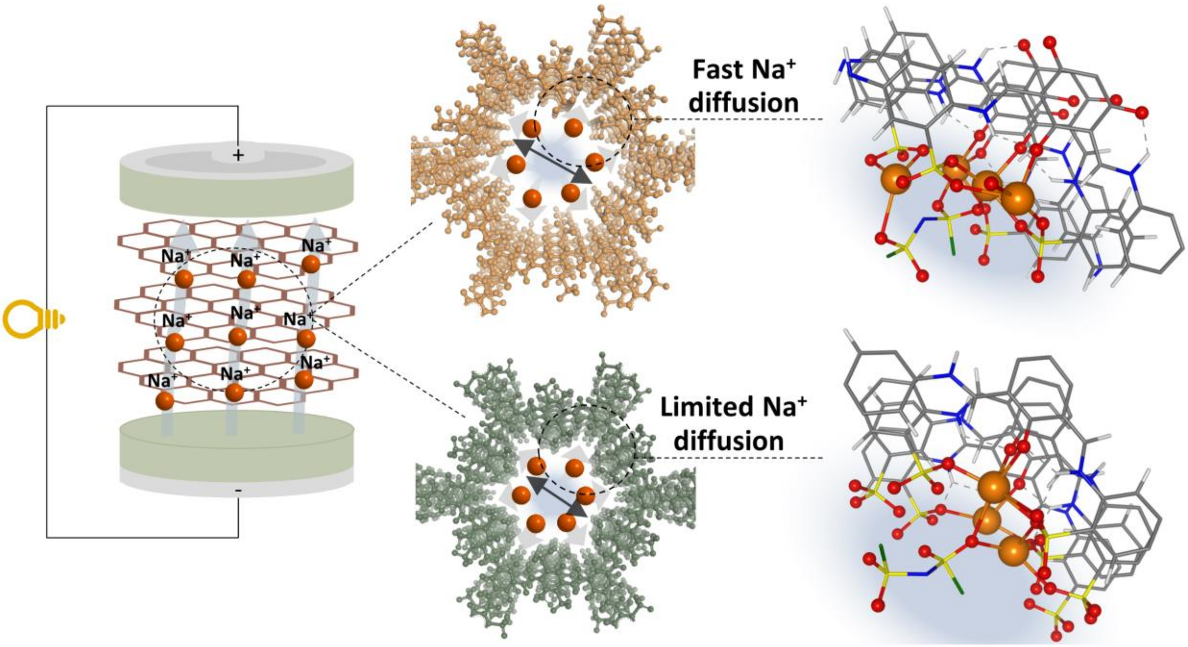

3.2. Introduction

Sodium-ion batteries (SIBs) are considered to be among the most appealing candidates to replace their state-of-the-art lithium counterparts.[1–3] Since their introduction to the market in 1991, lithium-ion batteries (LIBs) have been the predominant choice in the energy storage sector, primarily attributed to their exceptional energy density.[4,5] However, LIBs face certain limitations such as risk of thermal runaway, expensive and limited lithium (Li) and cobalt (Co) reserves, and the environmental and socioeconomic repercussions of mining these metals.[3,6] Sodium-ion batteries, on the other hand, have advantages of using abundant sodium (Na) as charge carrier and environmentally benign raw materials for electrodes, which make SIBs a cost-competitive and more sustainable alternative.[3,7–11] In the past decade, the electric vehicle industries have focused on developing energy storage systems (ESSs) with high energy density, longer cyclability and faster charging rates.[12,13] However, the current technology trades off high power density (PD) for high energy density (ED) due to several reasons: (1) slow diffusion of alkali metal cations into the electrode material,[13] (2) slow diffusion of metal cations in the electrolyte,[14,15] and (3) high energy barrier and high desolvation energy at the electrode-electrolyte interface.[16,17] The electrolyte plays an important role in defining and improving the rate capabilities of the electrode and the overall battery performance.[18,19] For instance, the Newman model illustrates how the efficiency of a battery can be constrained when the diffusion of anions surpasses that of cations.[18] The traditional liquid electrolytes are characterized by low cation transference number (t_+) < 0.5 and high desolvation energy.[20,21] Further, the potential safety risks associated with these organic-liquid electrolytes can potentially override their advantage of possessing low resistance towards the migration of ionic species.[22]

Inorganic crystalline solid-state electrolytes, such as sodium superionic conductors (NASICON) and sodium sulfides, demonstrate single cation transport with an ionic conductivity at the order of 10^{-3} S cm^{-1}.[23–25] However, due to their rigid structures, these electrolyte materials exhibit high electrode-electrolyte interfacial resistance, which acts as a rate-limiting factor.[24,26] On the other hand, organic-polymer electrolytes (PEs) can exhibit superior electrode contact and structural tunabilty.[27,28] The ion conduction within a bulk polymer, such as polyethylene oxide (PEO), is governed by the combination of cation complexation with oxygen atoms and segmental motion of the polymer chains.[29] Therefore, the potential of amorphous polymer electrolytes is controlled by the glass transition temperature (T_g) of the polymer, which imposes a temperature restriction on the cation migration.[26] Therefore, it is crucial to design safer electrolyte materials with an effective cation transport mechanism, especially for fast-charging batteries.

Covalent organic frameworks (COFs), porous crystalline polymer structures, have garnered significant attention in the energy storage community, serving as materials for both electrodes and electrolytes.[30,31] The physical and chemical properties of COFs can be widely modulated by tailoring the symmetry, structure and functionalities of their building blocks.[32,33] Further, their channels can act as highways for directional transport of the alkali metal ions.[31,34] In the past, several designs have been explored for COFs as electrolyte materials, mainly by incorporating either Lewis acidic moieties to trap the anion of a salt or by integrating anionic sites into the COF structure to achieve single cation transport.[35,36] In contrast to amorphous polymers, these well-defined crystalline frameworks can eliminate the dependence of cation migration on electrolyte reorganization and enable cation hopping from one energetically favorable site to another.[26] Moreover, the addition of plasticizers, such as ionic liquids (ILs), has been demonstrated to accelerate the migration of ionic species and to establish efficient electrode contact without compromising safety standards.[37]

In the present work, we investigate the correlation of structural, chemical and transport properties in two COF@IL composites as quasi-solid-state electrolytes (QSSEs) for SIBs. Firstly, two porous COFs containing sulfonate groups ($-SO_3^-$) as the coordinating anion species with Na-ions were synthesized, and characterized using various spectroscopic techniques. Further, to reduce interfacial and migration impedance, ionogels were prepared using the respective COFs and *N*-propyl-*N*-methylpyrrolidinium bis(fluorosulfonyl)imide ($Pyr_{13}FSI$) ionic liquid at different mass fractions. Ionic conductivity measurements of these ionogels revealed the most suitable composition for the respective COF systems. Finally, we explore the structural impact of these systems on ion migration through computational studies, and propose a Na^+ transport mechanism in these COF-based QSSEs.

3.3. Results and discussion

3.3.1. Materials synthesis and characterization

COF- $TpPaSO_3H$ and COF- $TpPa(SO_3H)_2$ were synthesized by utilizing 2,4,6-trihydroxybenzene-1,3,5-tricarbaldehyde (Tp) as the node and, 1,4-phenylenediamine-2-sulfonic acid ($PaSO_3H$) and 2,5-diaminobenzene-1,4-disulfonic acid ($Pa(SO_3H)_2$) as the linear building blocks, respectively (Scheme 3.1 and 3.2, Section 3.6.2, Appendix). The COFs were synthesized using dioxane and mesitylene as solvents under solvothermal conditions at 120°C. COFs consisting of the trigonal monomer Tp exhibit high chemical and electrochemical stability, deriving from the combination of reversible and irreversible reactions during solvothermal synthesis.[38,39] However, this class of COFs often suffers from low crystallinity due to the keto-enol tautomerism occurring in addition to the Schiff base reaction under solvothermal conditions. Therefore, a modulation strategy reported by our group was applied to improve crystallinity and obtain well-ordered nanoscale pore structures.[32] In this case, benzaldehyde, acting as a modulator, competes with the building blocks, enhancing self-healing mechanisms and decelerating COF crystallization. This results in the generation of highly crystalline and porous frameworks.

Powder X-ray diffraction (PXRD) patterns revealed improved crystallinity compared to COFs of these combinations reported in the literature.[31,34] By correlating experimental PXRD data with simulated PXRD patterns obtained from first-principles structure optimizations at the PBE level, we successfully identified the crystal structure of both COFs.[40–43] By means of screening different possible stacking modes, we identified two structural models (inclined and serrated) that closely corresponded to the experimental PXRD signals (Figure 3.5 and 3.6, Section 3.6.2, Appendix). Among these, the serrated stacking arrangement emerged as the energetically stable system (Table 3.1 and 3.2, Section 3.6.2, Appendix). Pawley refinement was performed using the Reflex module of Materials Studio to fit the obtained experimental data with the theoretically obtained stable structures of the respective COFs (**Figure 3.1a,d**). The resulting lattice parameters are a = 22.54 Å, b = 22.55 Å, c = 7.02 Å, α = 90.39°, β = 89.11°, and γ = 120.14° for $TpPaSO_3H$, and a = 22.55 Å, b = 22.50 Å, c = 7.01 Å, α = 87.45°, β = 83.11°, and γ = 120.03° for $TpPa(SO_3H)_2$. Additionally, the indexed *hkl* (100) plane was attributed to the diffraction at 4.7° 2θ for $TpPaSO_3H$ and at 5.0° 2θ for $TpPa(SO_3H)_2$. While the peak for the *hkl* (001) plane, corresponding to the z-stacking, appears at 26.6° 2θ for $TpPaSO_3H$ with an interplanar distance of 3.5 Å and at 26.1° 2θ for $TpPa(SO_3H)_2$ with an interplanar distance of 3.7 Å. Both COFs feature a honeycomb structure with hexagonal pores of 17.1 Å and 13.0 Å (atom-to-atom diameter) for $TpPaSO_3H$ and $TpPa(SO_3H)_2$, respectively (Figure 3.1b,e). Moreover, in the serrated stacking configuration of these COFs, sulfonate groups in alternate layers are arranged in opposite directions rather than directly on top of each other.[44] This results in interlayer displacement while maintaining planarity, representing the most stable structural arrangement for these sulfonic acid COFs (Table 3.1, and 3.2, Section 3.6.2, Appendix). Scanning electron microscopy (SEM) images (Figure 3.7, Section 3.6.2, Appendix) revealed a sponge-coral fibrillar morphology of both COF- $TpPaSO_3H$ and COF- $TpPa(SO_3H)_2$.[44] $TpPaSO_3H$ possesses about 500 nm long intergrown fibrils, while $TpPa(SO_3H)_2$ features thinner fibrils agglomerated to larger nanoparticles. Transmission electron microscopy (TEM) analysis (Figure 3.1c,f) was conducted to further confirmed the crystallinity of the COFs. Characteristic COF domains can be seen in the TEM images of COF-$TpPaSO_3H$ and $TpPa(SO_3H)_2$. To produce sodiated COFs, cation exchange reactions were carried out to replace the acidic proton of the sulfonic acid ($-SO_3H$) group with Na^+ (Figure 3.1g). To achieve this, COF- $TpPaSO_3H$ and $TpPa(SO_3H)_2$ were stirred in 6M NaOAc solution for 72 h at room temperature to obtain COF- $TpPaSO_3Na$ and COF- $TpPa(SO_3Na)_2$, respectively (Scheme 3.3 and 3.4, Section 3.6.3, Appendix). The retained crystallinity of the COFs after the cation exchange reaction was revealed through PXRD patterns, which exhibited an intense peak at lower 2θ angles (Figure 3.8, Section 3.6.3, Appendix).

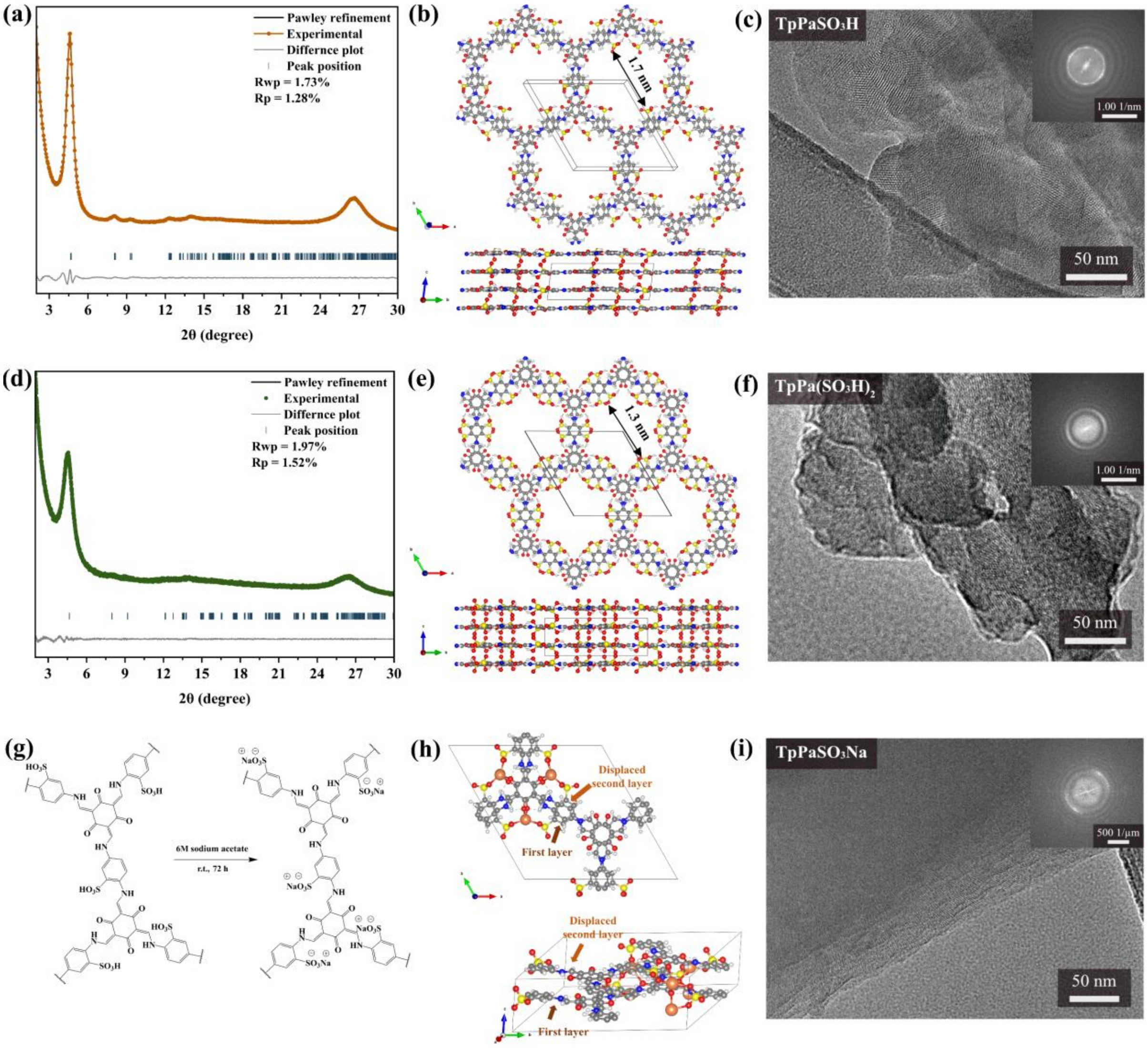

Figure 3.1 Structural characterization. PXRD profiles and Pawley refinement of (a) COF TpPaSO$_3$H and (d) COF TpPa(SO$_3$H)$_2$, and corresponding simulated structure of (c) COF TpPaSO$_3$H and (d) COF TpPa(SO$_3$H)$_2$. Transmission electron microscopy (TEM) images of the bulk (c) COF TpPaSO$_3$H and (f) COF TpPa(SO$_3$H)$_2$. (g) Schematic presentation of cation exchange reaction of COF TpPaSO$_3$H to synthesize COF TpPaSO$_3$Na, along with (i) TEM image. (h) A closer look at the simulated stacking behavior of COF TpPaSO$_3$Na featuring layer displacement. Gray, white, red, blue and yellow- colored balls represent C, H, O, N and S atoms, respectively.

Theoretical calculations indicated that, similar to their unsodiated counterparts, COF-TpPaSO$_3$Na and COF-TpPa(SO$_3$Na)$_2$ retain the serrated structural/ stacking arrangement (Figure 3.9, 3.10, Table 3.3 and 3.4, Section 3.6.3, Appendix). The anticipated serrated stacking of the COFs aligns closely with the experimental PXRD results (Figure 3.11a,b, Section 3.6.3, Appendix). Upon closer examination, the incorporation of sodium (Na) fosters a more organized arrangement characterized by a subtle displacement among the sheets in the serrated stacking pattern and a consistent planarity between two neighboring layers. This structured arrangement emerges due to the interaction of Na ions with the oxygen (O) atoms of the sulfonate and keto groups, as shown in Figure 3.1h. Scanning electron microscopy (SEM) images reveal the sponge-coral fibrillar morphology of $TpPaSO_3Na$ and $TpPa(SO_3Na)_2$, similar to the pristine sulfonic acid COFs (Figure 3.12, Section 3.6.3, Appendix). $TpPa(SO_3Na)_2$ exhibits smaller particle sizes than $TpPaSO_3Na$. SEM-EDX analysis confirmed the substantial concentration of Na per S atom in the samples, providing evidence for the effectiveness of the cation-exchange reaction (refer to Figure 3.13, 3.14, Table 3.5 in the Section 3.6.3, Appendix). Additionally, the crystallinity of the sodiated COFs were confirmed by TEM analysis (Figure 3.1i, Figure 3.1, Section 3.6.3, Appendix).

To evaluate the porosity of sodiated COFs, N_2 gas physisorption experiments were performed at a temperature of 77 K. The nitrogen sorption for the COFs $TpPaSO_3Na$ and $TpPa(SO_3Na)_2$ revealed Type I sorption isotherm profiles (Figure 3.16a,b, Section 3.6.3, Appendix). For both COFs, the adsorption isotherms show a fully reversible behavior and the uptake of nitrogen saturated at about 50 $cm^3\,g^{-1}$ at low partial pressure ($pp_o^{-1} < 0.05$), which is typical for such microporous keto-enol COFs.[45] Additionally, the Brunauer–Emmett–Teller (BET) surface areas of these porous COFs were estimated to be 179 $m^2\,g^{-1}$ for $TpPaSO_3Na$ and 172 $m^2\,g^{-1}$ for $TpPa(SO_3Na)_2$. Further, the quenched solid density functional theory (QSDFT) model was employed to extract the pore size distribution of these COFs from the isotherms. The calculations revealed pores of ~1.5 nm for COF- $TpPaSO_3Na$, while the pore size in $TpPa(SO_3Na)_2$ reduced to ~1.1 nm (refer to Figure 3.17a,b, Section 3.6.3, Appendix).

To prepare COF@IL composite ionogels, we added 1-methyl-1-propylpyrrolidinium bis(fluorosulfonyl)imide ($Pyr_{13}FSI$) ionic-liquid to the COFs $TpPaSO_3Na$ and $TpPa(SO_3Na)_2$ at various COF:IL wt/wt% ratios (60:40, 50:50, 40:60, 20:80, and 15:85) inside an argon-filled glovebox. The composites were stirred overnight inside the glovebox to ensure that the electrolyte samples were homogeneous and free from ambient atmosphere (Figure 3.18, Section 3.6.3, Appendix). Fourier transform infrared (FTIR) spectroscopy was employed to study the interactions between the pristine COFs and $Pyr_{13}FSI$ ionic-liquid (Figure 3.19a,b, Section 3.6.3, Appendix). To differentiate between the IR bands associated with COFs and IL, FTIR analysis was conducted with $TpPaSO_3Na$, $TpPa(SO_3Na)_2$, $Pyr_{13}FSI$, and their corresponding ionogels across different weight ratios. The vibrations corresponding to the $[FSI]^-$ anion, including the symmetric and asymmetric stretching of S–N–S at 741 cm^{-1} and 824 cm^{-1} increase with an increase in ionic-liquid content. Conversely, the vibrations corresponding to the COFs, C=O, C−C aromatic, C−N, and S=O at approximately 1573 cm^{-1}, 1430 cm^{-1}, 1220-1186 cm^{-1}, and 1024 cm^{-1}, respectively, diminish with an increase in the amount of $Pyr_{13}FSI$. To understand the interactions of the organic ions present in the ionic-liquid with Na^+ and the COF structures, density functional theory (DFT) calculations were employed using a simulation model of a 1 × 1 × 1 set of COF unit cells that includes a single $Pyr_{13}FSI$ molecule.[41,42,46,47] Two different orientations of $Pyr_{13}FSI$ IL in the COF pores were compared on the basis of their binding energies with the COF $TpPaSO_3Na$ (Figure 3.2a). The energetically more stable orientation of IL shown in Figure 3.2a (TOP) furnishes the binding energy (BE) of (−1.56 eV). The distribution models of Na^+, $[FSI]^-$, and $[Pyr_{13}]^+$ in COF $TpPaSO_3Na$ suggest a preferable placement of $[FSI]^-$ near the edge zone, close to Na^+ ions and sulfonate groups. Additionally, $[FSI]^-$ forms bonds with Na ions, specifically Na-F and Na-O bonds. The $[Pyr_{13}]^+$ are predicted to be confined towards the center of the COF pore due to electrostatic repulsion. Additionally, a comparable orientation of the ionic liquid (IL) is noted in the $TpPa(SO_3Na)_2$ COF. However, this orientation exhibits a higher binding energy (-2.84 eV), indicating a stronger interaction of the IL in close proximity to Na ions within the $TpPa(SO_3Na)_2$ COF.

3.3.2. Transport properties

During the design of the COFs, we selected the linear building blocks $PaSO_3H$ and $Pa(SO_3H)_2$, based on the presence of sulfonate groups (SO_3^-). Several prior publications on solid-organic electrolyte materials have noted the enhancement of carrier ion conduction due to the high Lewis basicity and stability of the sulfonate anion (SO_3^-).[31,48] The presence of periodically recurring hopping sites in the form of sulfonate anions decorating the COF walls motivates the examination of their transport properties. The transport properties of an electrolyte are crucial in determining the rate-capabilities of a battery since an electrolyte with higher ionic conductivity can promptly offer charge carriers at elevated current rates without developing overpotential in an electrochemical cell. For an electrolyte to possess high ionic conductivity, it should facilitate the dissociation of ion pairs, exhibit minimal resistance for ion motion, and allow for high ion concentrations.[26] Here, we utilize the AC impedance technique to determine the ionic conductivity of all samples in the temperature range between 30 to 65 °C. The resulting impedance data were individually fitted for an equivalent electrical circuit (EEC) to determine the corresponding resistances to ion conduction (Figure 3.20, Section 3.6.4, Appendix). Ionic conductivities were calculated using Equation 3.1 (Section 3.6.1, Appendix) utilizing the bulk resistance (R_b) determined from impedance of the individual measurement. At a given temperature, the resistance value is the resultant of the activation energy required to produce free ion pairs and their mobility.[26] Both the COFs, $TpPaSO_3Na$ and $TpPa(SO_3Na)_2$, demonstrated linear behavior in the corresponding Arrhenius plot based on the data at different temperatures (Equation 3.2, Section 3.6.1; Figure 3.21, Section 3.6.4, Appendix). Further, COF $TpPa(SO_3Na)_2$ exhibited a higher ionic conductivity than COF $TpPaSO_3Na$ at all recorded temperatures, with ionic conductivities of 2.5×10^{-4} S cm^{-1} and 2.0×10^{-4} S cm^{-1} at 50 °C for $TpPa(SO_3Na)_2$ and $TpPaSO_3Na$, respectively (Table 3.6, Section 3.6.4, Appendix). The higher conductivity values for $TpPa(SO_3Na)_2$ could be attributed to the higher concentration of charged species available in the electrolyte sample. To further improve the performance of the sulfonate COF electrolyte systems, ionogel composites were prepared and the transport properties of the resulting COF@IL systems were investigated. The results revealed linear patterns in the Arrhenius plots (Figure 3.2b,d) for all COF: IL systems, regardless of the amount of ionic liquid or the sulfonate group (SO_3^-). This confirms a monophasic behavior throughout the temperature range. Adding ionic liquid in various mass concentrations to the respective COFs showed a specific trend in ionic conductivity, i.e, COF: $Pyr_{13}FSI$ 20:80> 15:85> 40:60> 50:50> 60:40 (Figure 3.2c). As the fraction of the ionic liquid increases, there is a corresponding increase of the ionic species in the system, which in turn results in a higher conductivity and in a decrease of the resulting charge transfer resistance (Table 3.6, Section 3.6.4, Appendix). However, an excess amount of ionic liquid creates clusters of ionic species, giving less free volume for ionic liquid within the pores, which elevates the overall activation energy and thus restricts the mobility of ions (Figure 3.22a,b, Section 3.6.4, Appendix).[49] At 50 °C, ionogels containing COF $TpPaSO_3Na$ demonstrated higher ionic conductivity ranging between $2.1 - 5.6 \times 10^{-3}$ S cm^{-1} in comparison to the ionogels with COF $TpPa(SO_3Na)_2$, which displayed conductivity values ranging from $1.7- 4.1 \times 10^{-3}$ S cm^{-1} at the equivalent ratios. Among all the prepared samples, the ratios COF: $Pyr_{13}FSI$ 20:80 (naming: $TpPaSO_3Na$: $Pyr_{13}FSI$ 20:80 = $TpPaSO_3Na@Pyr_{13}FSI$ and $TpPa(SO_3Na)_2$: $Pyr_{13}FSI$ 20:80 = $TpPa(SO_3Na)_2@Pyr_{13}FSI$) showed the best performance for both sulfonated COF-ionogels, and therefore were further analyzed in detail.

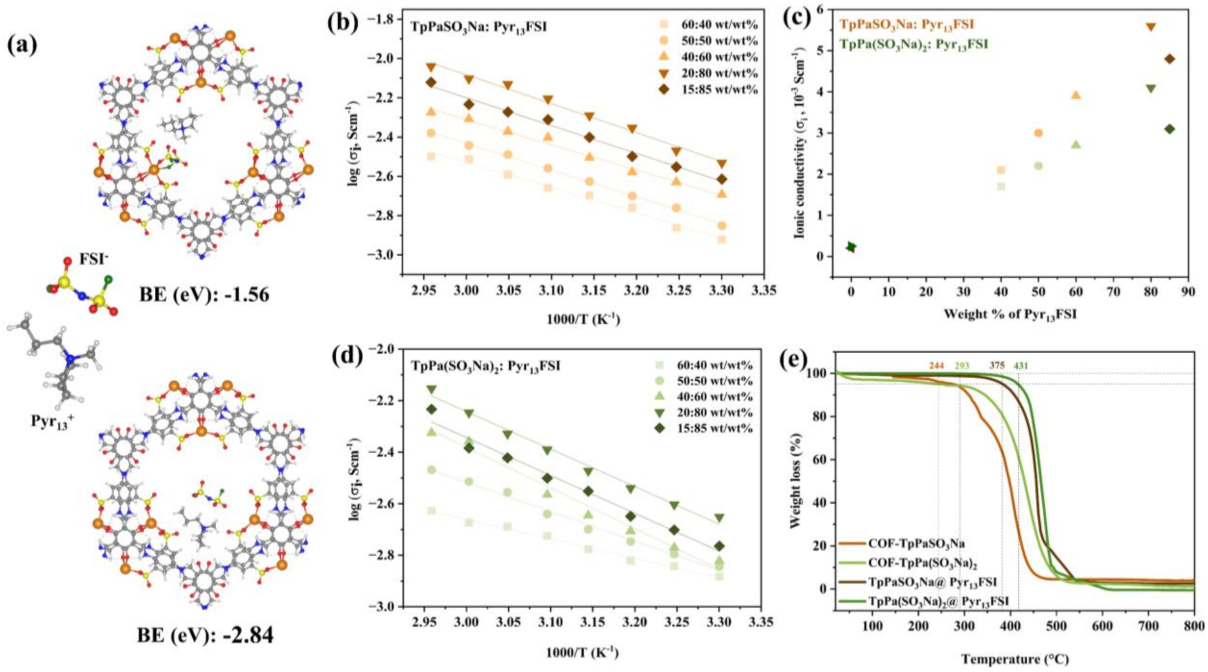

Figure 3.2 (a) The binding energies (BE) between COF $TpPaSO_3Na$ and $Pyr_{13}FSI$ ionic liquid in two different binding orientations (at specific ratio). Arrhenius curves of COF: $Pyr_{13}FSI$ composites at various wt/wt% fractions for (b) $TpPaSO_3Na$ and (d) $TpPa(SO_3Na)_2$, respectively. (c) Comparative ionic conductivity values for COF: $Pyr_{13}FSI$ composites as a function of weight-percent of ionic-liquid. (e) Thermogravimetric analysis (TGA) of electrolyte materials, identified in the figure.

The fraction of ionic current carried by cations is responsible for beneficial redox reactions, hence, an essential factor for augmenting the operational rate-efficiency of a battery. A larger cation transport number limits unwanted energy consumption by restricting anionic motion and inhibits the development of a concentration overpotential.[50] We utilized the combination of AC impedance and DC polarization techniques and applied the Bruce-Vincent equation (Equation 3.3, Section 3.6.1, Appendix) to calculate the Na-ion transference number (t_{Na^+}) (Table 3.7, Section 3.6.4, Appendix). TpPaSO$_3$Na@Pyr$_{13}$FSI demonstrate a t_{Na^+} of 0.79, whereas TpPa(SO$_3$Na)$_2$@Pyr$_{13}$FSI displays a lower t_{Na^+} of 0.67. Both the systems exhibit higher cation transport numbers compared to the traditional carrier salts in organic solvents or ionic-liquid electrolyte systems.[24] The higher Na-ion transference number can be attributed to the plausible interactions formed between Lewis acidic groups present in sulfonate COFs and [FSI]$^-$ anions. The thermal stability of these quasi-solid-state electrolyte materials was assessed through thermogravimetric analysis (TGA). As shown in Figure 3.2e, pristine COFs experienced improved thermal stability after addition of ionic-liquid, i.e. ~375 °C for TpPaSO$_3$Na@Pyr$_{13}$FSI and ~431 °C for TpPa(SO$_3$Na)$_2$@Pyr$_{13}$FSI. QSSEs TpPaSO$_3$Na@Pyr$_{13}$FSI and TpPa(SO$_3$Na)$_2$@Pyr$_{13}$FSI demonstrate one of the highest ionic conductivities and thermal stability amongst previously reported COF-based electrolytes (Table 3.8, Section 3.6.4, Appendix).

3.3.3. Ion diffusion mechanism

To reveal the structure and transport properties of Na$^+$ in Pyr$_{13}$FSI ionic-liquid confined in sulfonate COFs, ab inito molecular dynamics (AIMD) simulations were performed. We primarily focus on the transport of Na$^+$ through the pores (in the z-direction), with comprehensive computational setup and conceptual details provided in the Section 3.6.1, Appendix. In the channel perpendicular to the 2D-COF layers, Pyr$_{13}$FSI molecules were initially distributed in a random manner at a density of ~1.35 g mL^{-1}. Subsequently, they were allowed to equilibrate for 2 ps at 300 K through AIMD simulation, with the simulated structures illustrated in Figure 3.23, Section 3.6.5, Appendix. Following the equilibration, geometric data were gathered over a 50 ps period at 324 K. Figure 3.3a,c and Figure 3.24 (Section 3.6.5, Appendix) show the snapshots from AIMD trajectories for TpPaSO$_3$Na@ Pyr$_{13}$FSI and TpPa(SO$_3$Na)$_2$@ Pyr$_{13}$FSI. The images reveal that throughout the simulation, ILs undergo rearrangement, actively solvating Na ions and reducing their proximity to the COF pore walls. This effect is particularly pronounced in TpPaSO$_3$Na@Pyr$_{13}$FSI, suggesting a potential enhancement in the diffusion of Na$^+$.

The mean square displacement (MSD) of Na$^+$ was calculated from the AIMD trajectories to understand the effect of the presence of ketone/sulfonate groups and Pyr$_{13}$FSI on the ion transport properties in COF systems (refer to Figure 3.3d). The slope of the MSD curve for a specie corresponds directly to the diffusion coefficient of that specie, making MSD analysis a potent tool for examining the mobility of ions. TpPaSO$_3$Na@Pyr$_{13}$FSI exhibits a larger MSD slope compared to TpPa(SO$_3$Na)$_2$@Pyr$_{13}$FSI, which indicates increased ionic motion. Accordingly, the diffusion coefficients, obtained by fitting the slope of the MSD profiles, are 13.00×10^{-7} cm^2 s^{-1} and 7.06×10^{-7} cm^2 s^{-1} for TpPaSO$_3$Na@Pyr$_{13}$FSI and TpPa(SO$_3$Na)$_2$@Pyr$_{13}$FSI, respectively. Notably, TpPaSO$_3$Na@Pyr$_{13}$FSI exhibits diffusive behavior at room temperature with a linear time dependence of the MSD.

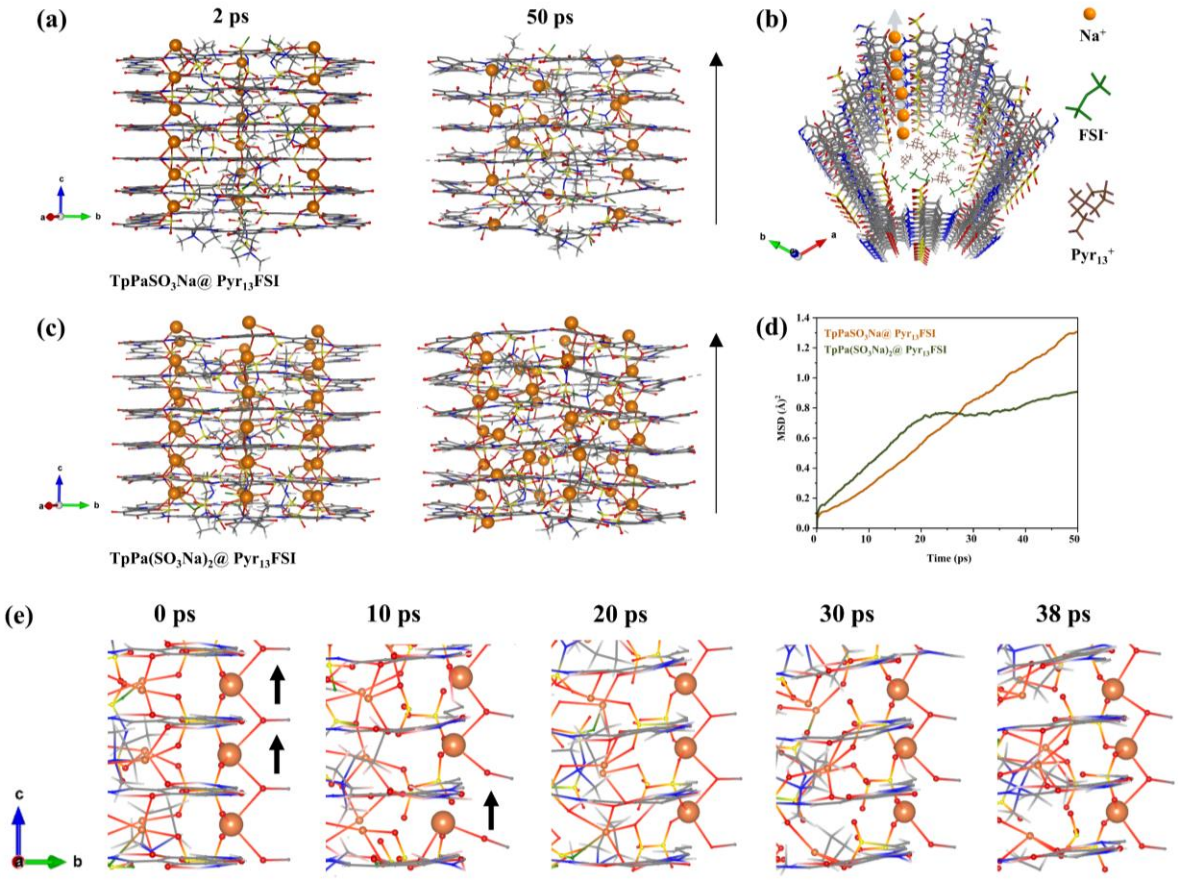

Figure 3.3 Side view of the simulation structures of (a) TpPaSO$_3$Na@Pyr$_{13}$FSI and (c) TpPa(SO$_3$Na)$_2$@Pyr$_{13}$FSI equilibrated by AIMD at 300 K for 2 ps and at 324 K for 50 ps. (b) Ion transport mechanism in TpPaSO$_3$Na@Pyr$_{13}$FSI. (d) Comparative MSD plots of Na$^+$ obtained from AIMD trajectories. (e) Visualization of Na ion diffusion event in TpPaSO$_3$Na@Pyr$_{13}$FSI during the AIMD simulation within the timescale of 0 to 38 ps.

In the case of TpPa(SO$_3$Na)$_2$@Pyr$_{13}$FSI, the diffusion of Na$^+$ within the pore initially follows a linear behavior similar to that observed in TpPaSO$_3$Na@Pyr$_{13}$FSI. However, after 20 ps, the diffusion curve levels off and becomes flat. This plateau can be attributed to the confinement of the sodium ion motion. During the time scale of 20 ps to approximately 40 ps, the sodium ions explore neighboring SO$_3^-$ groups that surround them. Figure 3.3e illustrates the mechanistic progression of sodium ion diffusion, displaying sequential configurations over a 50 ps timeframe. Notably, from 0 to 10 ps and up to 20 ps, there is observable diffusion of sodium ions through the pore. However, after 20 ps, the diffusion becomes restricted in the vicinity of the SO_3^- groups. These interactions with the SO_3- groups limit the movement of the sodium ions in $TpPa(SO_3Na)_2@Pyr_{13}FSI$, resulting in the observed flat region in the MSD plot. After 40 ps, the diffusion curve starts showing a linear variation again, but with a smaller slope. This suggests that the confinement effect imposed by the SO_3^- groups slows down the diffusion of Na^+ in $TpPa(SO_3Na)_2@Pyr_{13}FSI$, leading to a reduced overall displacement compared to the displacement in $TpPaSO_3Na@Pyr_{13}FSI$. Importantly, the confinement is prominent in $TpPa(SO_3Na)_2@Pyr_{13}FSI$ due to the higher concentration of anionic SO_3^- groups and the smaller free volume for $Pyr_{13}FSI$ that restrict the motion of the sodium ions. This observation quantitatively explains the importance of incorporating ionic liquid as a '*plasticizer*' to enhance the sodium ion conductivity in COF-based electrolytes.

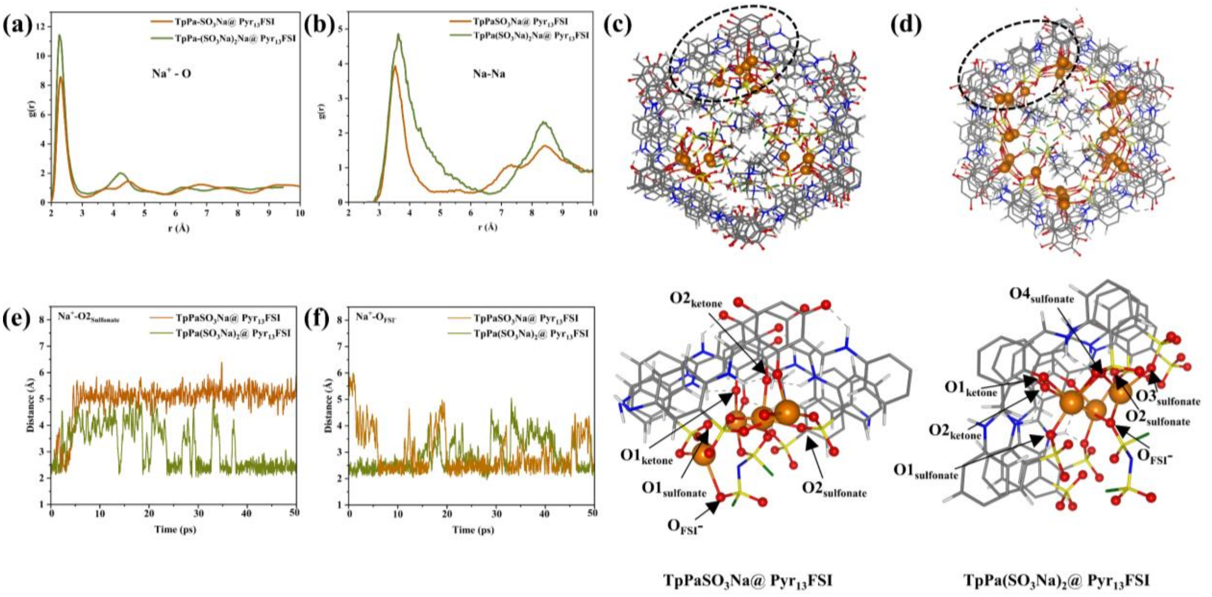

Figure 3.4 The pair correlation function (g(r)) of $TpPaSO_3Na@Pyr_{13}FSI$ and $TpPa(SO_3Na)_2@Pyr_{13}FSI$ demonstrating the interactions of Na ions with (a) O atoms and (b) other neighboring Na ions. Snapshots of AIMD trajectories of (c) $TpPaSO_3Na@Pyr_{13}FSI$ and (d) $TpPa(SO_3Na)_2@Pyr_{13}FSI$ (t = 50 ps). The figure below displays an enlarged view of the dynamics in the black ellipse, representing the Na-ions under consideration for analyzing time-evolved distance plots. Distance plots of (e) $Na{-}O_{sulfonate}$ and (f) $Na{-}O_{FSI}$- for $TpPaSO_3Na@Pyr_{13}FSI$ and $TpPa(SO_3Na)_2@Pyr_{13}FSI$.

To fundamentally understand the increased Na^+ diffusivity in $TpPaSO_3Na@Pyr_{13}FSI$, the pair correlation function (g(r)) of Na-ions and oxygen atoms was calculated for both COF systems (Figure 3.4a,b). In both COF systems, we observed a sharp peak at ~2.3 Å for Na−O (Figure 3.4a), which validates the presence of Na−O bonds in the first coordination sphere and indicating substantial interactions. This aligns with the findings observed in the AIMD structural snapshots. Furthermore, for

TpPaSO$_3$Na@Pyr$_{13}$FSI, the pair correlation function of a sodium ion, surrounded by oxygen atoms and other neighboring sodium ions, reveals weaker peaks in short ranges, as depicted in Figure 6a,b. This observation implies larger bond lengths for Na−O and Na−Na bonds compared to TpPa(SO$_3$Na)$_2$@Pyr$_{13}$FSI. Consequently, it can be inferred that the Na$^+$ ions in TpPaSO$_3$Na@Pyr$_{13}$FSI are more dispersed in the Pyr$_{13}$FSI ionic liquid space, unlike in TpPa(SO$_3$Na)$_2$@Pyr$_{13}$FSI, where Na ions are localized near the inner wall of the COF.

For a closer observation, the time-evolved distance plots of sodium ions and first coordination sphere oxygen atoms of interest (highlighted by dotted circle in Figure 3.4c,d) in TpPaSO$_3$Na@Pyr$_{13}$FSI and TpPa(SO$_3$Na)$_2$@Pyr$_{13}$FSI were analyzed (Figure 3.4e,f, Figure 3.25, 3.26, Section 3.6.5, Appendix). In both COF systems, time-evolved distance plots demonstrate increased distances of Na−O$_{\text{ketone}}$ bonds and decreased distances of Na−O$_{\text{FSI}}$- bonds. Meanwhile, the more dynamic Na−O$_{\text{sulfonate}}$ bonds either persist or undergo dissociation. This suggests that the proximity of Na$^+$ to O$_{\text{sulfonate}}$ and O$_{\text{FSI}}$- supports the formation of continuous ion transport pathways, fostering more seamless ionic conduction within COFs. Consequently, ion transport occurs through a synergistic interplay of hopping, arising from Na-O$_{\text{sulfonate}}$ interactions, and a vehicle-type mechanism involving solvated Na ions in Pyr$_{13}$FSI ionic liquid. However, in TpPa(SO$_3$Na)$_2$@ Pyr$_{13}$FSI, the surfeit neighboring sulfonate groups as appeared in Figure 3.24 (Section 3.6.5, Appendix) foster new Na-O interactions, potentially relying on a hopping mechanism, restricting Na-ion diffusion and flattening of MSD plot. Therefore, the distinct Na$^+$ conduction characteristics observed in pristine COF- and ionogel-electrolytes can be attributed to variations in the pore size of the COFs and the density of SO$_3^-$ groups within the pore walls.

In future work with these materials it will be of interest to focus on device fabrication, using these electrolyte systems to evaluate the overall performance of batteries, and to elucidate interfacial phenomena, ion transport dynamics, and long-term stability, thereby providing insights for further optimization of the COF-based electrolyte designs.

3.4. Conclusion

To summarize, here we present two crystalline COFs, containing sulfonate groups, as base materials for quasi solid-state electrolytes (QSSEs) for sodium-ion batteries. The ordered structure of the frameworks enabled the anionic backbone of SO_3^- groups in the hexagonal channel systems to serve as hopping sites for Na^+, facilitating a directional migration through the COF channels. Further, the serrated structure of these COFs allowed for a favorable adsorption of Na in the cavity of sulfonate and keto groups of the COFs, while maintaining the planarity between two neighboring layers. The newly designed composite ionogels containing the COFs $TpPaSO_3Na$ and $TpPa(SO_3Na)_2$, with ionic liquid $Pyr_{13}FSI$ serving as plasticizer, possessed ionic conductivities ranging at the order of 10^{-3} S cm^{-1}. The composite electrolytes with the COF $TpPaSO_3Na$ exhibited overall higher ionic conductivity and transport number t_{Na^+} than electrolytes with COF $TpPa(SO_3Na)_2$, pointing to distinct diffusion mechanisms governed by the concentration of SO_3^- groups present in the COF skeletons. Ab inito molecular dynamics (AIMD) simulations demonstrated that ion transport in $Pyr_{13}FSI$ ionic liquid involves a synergistic interplay between hopping, driven by Na-$O_{sulfonate}$ interactions, and a vehicle-type mechanism featuring solvated Na ions. Moreover, solvated Na^+ ions exhibit faster diffusion in $TpPaSO_3Na@Pyr_{13}FSI$ compared to more de-solvated ions in $TpPa(SO_3Na)_2@Pyr_{13}FSI$, which predominantly rely on a hopping mechanism. Hence, in this study we demonstrated that by altering the COF scaffold, we can strongly impact the diffusion of the charge carriers through a composite electrolyte. Given the enormous accessible architectural and functional space of COFs, we expect that these results and concepts will open new vistas towards the design of efficient and sustainable sodium-based quasi solid-state electrolytes.

3.5. References

[1] K. M. Abraham, *ACS Energy Lett.* **2020**, *5*, 3544.

[2] Christoph Vaalma, Daniel Buchholz, Marcel Weil and Stefano Passerini, *Nat Rev Mater* **2018**, *3*.

[3] Christoph Vaalma, Daniel Buchholz, Marcel Weil and Stefano Passerini, *Nat Rev Mater*, *3*.

[4] A. Yoshino, *Angewandte Chemie (International ed. in English)* **2012**, *51*, 5798.

[5] J. Xie, Y.-C. Lu, *Nature communications* **2020**, *11*, 2499.

[6] J. B. Goodenough, Y. Kim, *Chem. Mater.* **2010**, *22*, 587.

[7] H. Kim, *ACS materials Au* **2023**, *3*, 571.

[8] W. Shao, H. Shi, X. Jian, Z.-S. Wu, F. Hu, *Adv Energy and Sustain Res* **2022**, *3*.

[9] M. Sawicki, L. L. Shaw, *RSC Adv.* **2015**, *5*, 53129.

[10] Q. Wei, X. Chang, D. Butts, R. DeBlock, K. Lan, J. Li, D. Chao, D.-L. Peng, B. Dunn, *Nature communications* **2023**, *14*, 7.

[11] C. Delmas, *Advanced Energy Materials* **2018**, *8*.

[12] Y. Liu, Y. Zhu, Y. Cui, *Nat Energy* **2019**, *4*, 540.

[13] K. G. Gallagher, S. E. Trask, C. Bauer, T. Woehrle, S. F. Lux, M. Tschech, P. Lamp, B. J. Polzin, S. Ha, B. Long, Q. Wu, W. Lu, D. W. Dees, A. N. Jansen, *J. Electrochem. Soc.* **2016**, *163*, A138-A149.

[14] K. Xu, A. von Cresce, U. Lee, *Langmuir the ACS journal of surfaces and colloids* **2010**, *26*, 11538.

[15] T. R. Jow, S. A. Delp, J. L. Allen, J.-P. Jones, M. C. Smart, *J. Electrochem. Soc.* **2018**, *165*, A361-A367.

[16] K. Li, J. Zhang, D. Lin, D.-W. Wang, B. Li, W. Lv, S. Sun, Y.-B. He, F. Kang, Q.-H. Yang, L. Zhou, T.-Y. Zhang, *Nature communications* **2019**, *10*, 725.

[17] Takeshi Abe, Fumihiro Sagane, Masahiro Ohtsuka, Yasutoshi Iriyama and Zempachi Ogumi, *J. Electrochem. Soc* **2005**, *152*, A2151.

[18] Marc Doyle, Thomas F. Fuller and John Newman, *Electrochimica Acta.* **1994**, *39*, 2073.

[19] C. Wang, B. B. Xu, X. Zhang, W. Sun, J. Chen, H. Pan, M. Yan, Y. Jiang, *Small (Weinheim an der Bergstrasse, Germany)* **2022**, *18*, e2107064.

[20] K. Westman, R. Dugas, P. Jankowski, W. Wieczorek, G. Gachot, M. Morcrette, E. Irisarri, A. Ponrouch, M. R. Palacín, J.-M. Tarascon, P. Johansson, *ACS Appl. Energy Mater.* **2018**, *1*, 2671.

[21] A. V. Cresce, S. M. Russell, O. Borodin, J. A. Allen, M. A. Schroeder, M. Dai, J. Peng, M. P. Gobet, S. G. Greenbaum, R. E. Rogers, K. Xu, *Physical chemistry chemical physics PCCP* **2016**, *19*, 574.

[22] G. Jeong, H. Kim, H. S. Lee, Y.-K. Han, J. H. Park, J. H. Jeon, J. Song, K. Lee, T. Yim, K. J. Kim, H. Lee, Y.-J. Kim, H.-J. Sohn, *Scientific reports* **2015**, *5*, 12827.

[23] Z. Deng, T. P. Mishra, E. Mahayoni, Q. Ma, A. J. K. Tieu, O. Guillon, J.-N. Chotard, V. Seznec, A. K. Cheetham, C. Masquelier, G. S. Gautam, P. Canepa, *Nature communications* **2022**, *13*, 4470.

[24] G. G. Eshetu, G. A. Elia, M. Armand, M. Forsyth, S. Komaba, T. Rojo, S. Passerini, *Advanced Energy Materials* **2020**, *10*, 2000093.

[25] K. J. Kim, M. Balaish, M. Wadaguchi, L. Kong, J. L. M. Rupp, *Advanced Energy Materials* **2021**, *11*, 2002689.

[26] Q. Zhao, S. Stalin, C.-Z. Zhao, L. A. Archer, *Nat Rev Mater* **2020**, *5*, 229.

[27] X. Wang, C. Zhang, M. Sawczyk, J. Sun, Q. Yuan, F. Chen, T. C. Mendes, P. C. Howlett, C. Fu, Y. Wang, X. Tan, D. J. Searles, P. Král, C. J. Hawker, A. K. Whittaker, M. Forsyth, *Nature materials* **2022**, *21*, 1057.

[28] Z. Sun, K. Xi, J. Chen, A. Abdelkader, M.-Y. Li, Y. Qin, Y. Lin, Q. Jiang, Y.-Q. Su, R. Vasant Kumar, S. Ding, *Nature communications* **2022**, *13*, 3209.

[29] Z. Xue, D. He, X. Xie, *J. Mater. Chem. A* **2015**, *3*, 19218.

[30] R. Shi, L. Liu, Y. Lu, C. Wang, Y. Li, L. Li, Z. Yan, J. Chen, *Nature communications* **2020**, *11*, 178.

[31] K. Jeong, S. Park, G. Y. Jung, S. H. Kim, Y.-H. Lee, S. K. Kwak, S.-Y. Lee, *Journal of the American Chemical Society* **2019**, *141*, 5880.

[32] M. Calik, T. Sick, M. Dogru, M. Döblinger, S. Datz, H. Budde, A. Hartschuh, F. Auras, T. Bein, *Journal of the American Chemical Society* **2016**, *138*, 1234.

[33] J. M. Rotter, R. Guntermann, M. Auth, A. Mähringer, A. Sperlich, V. Dyakonov, D. D. Medina, T. Bein, *Chemical science* **2020**, *11*, 12843.

[34] Y. Yan, Z. Liu, T. Wan, W. Li, Z. Qiu, C. Chi, C. Huangfu, G. Wang, B. Qi, Y. Yan, T. Wei, Z. Fan, *Nature communications* **2023**, *14*, 3066.

[35] Y. Fu, Y. Wu, S. Chen, W. Zhang, Y. Zhang, T. Yan, B. Yang, H. Ma, *ACS nano* **2021**, *15*, 19743.

[36] T. W. Kang, J.-H. Lee, J. Lee, J. H. Park, J.-H. Shin, J.-M. Ju, H. Lee, S. U. Lee, J.-H. Kim, *Advanced materials (Deerfield Beach, Fla.)* **2023**, *35*, e2301308.

[37] Z. Wang, W. Zheng, W. Sun, L. Zhao, W. Yuan, *ACS Appl. Energy Mater.* **2021**, *4*, 2808.

[38] C. R. DeBlase, K. E. Silberstein, T.-T. Truong, H. D. Abruña, W. R. Dichtel, *Journal of the American Chemical Society* **2013**, *135*, 16821.

[39] S. Kandambeth, A. Mallick, B. Lukose, M. V. Mane, T. Heine, R. Banerjee, *J. Am. Chem. Soc.* **2012**, *134*, 19524.

[40] G. Kresse, J. Furthmüller, *Physical review. B, Condensed matter* **1996**, *54*, 11169.

[41] P. E. Blöchl, *Physical review. B, Condensed matter* **1994**, *50*, 17953.

[42] G. Kresse, D. Joubert, *Physical review. B, Condensed matter* **1999**, *59*, 1758.

[43] J. P. Perdew, J. A. Chevary, S. H. Vosko, K. A. Jackson, Pederson, D. J. Singh, C. Fiolhais, *Physical review. B, Condensed matter* **1992**, *46*, 6671.

[44] Z. Gao, L. Le Gong, X. Q. He, X. M. Su, L. H. Xiao, F. Luo, *Inorganic chemistry* **2020**, *59*, 4995.

[45] S. Chandra, T. Kundu, K. Dey, M. Addicoat, T. Heine, R. Banerjee, *Chem. Mater.* **2016**, *28*, 1489.

[46] G. Kresse, J. Hafner, *Physical review. B, Condensed matter* **1993**, *47*, 558.

[47] J. P. Perdew, K. Burke, M. Ernzerhof, *Physical review letters* **1996**, *77*, 3865.

[48] F. Yu, J.-H. Ciou, S. Chen, W. C. Poh, J. Chen, J. Chen, K. Haruethai, J. Lv, D. Gao, P. S. Lee, *Nature communications* **2022**, *13*, 390.

[49] A. Nag, M. A. Ali, A. Singh, R. Vedarajan, N. Matsumi, T. Kaneko, *J. Mater. Chem. A* **2019**, *7*, 4459.

[50] J. Evans, C. A. Vincent, P. G. Bruce, *Polymer* **1987**, *28*, 2324.

3.6. Appendix

3.6.1. Methods

3.6.1.1. Structural characterization

Powder X-ray diffraction (PXRD): Diffractograms were recorded on a Bruker D8 Discover instrument equipped with a LynxEye position-sensitive detector in Bragg-Brentano geometry, using Cu-Kα radiation.

Structure modelling: The proposed structures of respective COFs were simulated using the Accelrys Materials Studio software package. Pawley refinement for the modeled structures was carried out using the Reflex module.

Scanning electron microscopy (SEM): SEM images were obtained using a FEI Helios NanoLab G3 UC scanning electron microscope equipped with a Schottky field-emission electron source operated at 3-5 kV.

Energy Dispersive X-ray (EDX) microanalysis: Analysis was performed on a Dual beam FEI Helios G3 UC instrument equipped with an X-Max 80 EDS detector from Oxford Instruments plc. The EDX spectra were recorded at 5 kV.

Fourier-transform infrared spectroscopy (FTIR): The spectra were captured using a Bruker Vertex 70 FTIR instrument, featuring a liquid nitrogen (LN_2) cooled MCT detector.

Thermogravimetric analysis (TGA): The thermal stability measurements were performed on a Netzsch Jupiter ST 499 C instrument equipped with a Netzsch TASC 414/4 controller. All the samples were heated from room temperature to 900 °C under a synthetic air flow (25 mL min^{-1}) at a heating rate of 10 K min^{-1}.

Nitrogen sorption: The isotherms were recorded using Quantachrome Autosorb 1 and Autosorb iQ instruments at a temperature of 77 K. BET surface areas for the respective COFs were calculated based on the pressure range of $0.05 \leq p/p_0 \leq 0.2$.

3.6.1.2. Transport properties

Ionic conductivity: Ionic conductivities for COF-based electrolytes were measured using the AC impedance technique with a Metrohm Autolab PGSTAT potentiostat/galvanostat. Individual samples were sandwiched between two stainless-steel electrodes to carry out electrochemical impedance spectroscopy (EIS) measurements over a frequency range of 10^6 to 0.1 Hz with an AC perturbation voltage of 10 mV over a temperature range of 30-65 °C. EIS data for all the samples were recorded with incremental temperature steps of 5 °C, stabilized for 10 min, respectively.

Ionic conductivity was measured using the AC impedance technique. To carry out the measurements, the samples were sandwiched between two stainless steel electrodes. The dimensions of the powder pellet were measured using a Digital Vernier Caliper instrument, and for the gel samples, the thickness was standardized by adding a stainless-steel ring between the electrodes and placing the individual gel samples into the inner circle of the ring-shaped disk. The thickness and the inner diameter of this disk were taken as the dimensions of the measured samples.

The following equations were used to calculate ionic conductivity:[1]

$$\sigma_i = \frac{l}{R_b \times A} \qquad \text{(Equation 3.1)}$$

where σ_i is the ionic conductivity (S cm^{-1}), l is the thickness (cm), A is the contact area (cm^2), and R_b is the bulk resistance (Ω) of the electrolyte.

To understand the ion-transport mechanism of the electrolyte systems, Arrhenius plots were constructed using the following equation:[2]

$$\sigma_i = \frac{\sigma_0}{T} exp^{\frac{-E_a}{RT}} \qquad \text{(Equation 3.2)}$$

where σ_i is ionic conductivity (S cm^{-1}), σ_0 is the pre-exponential factor, T is the temperature (K), E_a is the total activation energy, and R is the gas constant.

Transference number: The sodium-ion transference number was calculated using the Vincent–Bruce–Evans method, which utilizes a combination of electrochemical impedance spectroscopy (EIS) and DC polarization techniques. The cells for this measurement were assembled with a Na/Electrolyte/Na configuration inside an argon-filled glove box. AC impedance was measured before and after DC polarization via a potentiostat/ galvanostat working station Metrohm Autolab PGSTAT302N.

The transference number of sodium ions was determined employing the Vincent–Bruce–Evans method, a technique that combines electrochemical impedance spectroscopy (EIS) and direct current (DC) polarization methods. Cells for this measurement were constructed with a Na/Electrolyte/Na configuration in a glove box filled with argon. Impedance was measured over a frequency range of 10^6 to 0.1 Hz with an AC perturbation voltage of 10 mV.

The following equation was used to calculate the sodium-ion transference number:[3]

$$t_{Na^+} = \frac{I_{ss}(\Delta V - I_0 R_0)}{I_0(\Delta V - I_{ss} R_{ss})} \qquad \text{(Equation 3.3)}$$

where I_0 is the initial current, I_{ss} is the steady-state current, R_0 is the resistance before polarization experiment, R_{ss} is the resistance after attaining steady-state, and ΔV is the applied perturbation voltage.

3.6.1.3. Theoretical calculations

The DFT calculations were performed using the Vienna ab initio simulation package, with the projector augmented wave pseudopotentials used to describe the interaction between the core and the valence electrons.[4–7] The Perdew−Burke−Ernzerhof (PBE) exchange correlation functional was employed with the plane wave basis set and kinetic energy cutoff of 470 eV.[8,9] Calculations used Gimme's D-3 dispersion correction which typically provides excellent geometries and properly describes the short-range van der Waals interactions, which are crucial for the target systems.[10] Structural optimization was done with k-point sampling of a 2 × 2 × 6 mesh within the Monkhorst-Pack scheme. A convergence threshold of 0.01 eV/Å in force was reached for structural optimization.

Importantly, the unit cells of individual COFs were enlarged to become 1 × 1 × 3 supercells in x, y, and z directions, respectively. The supercells of COFs were then filled with $Pyr_{13}FSI$ ionic liquid (IL) at a density (~1.35 g/mL) close to the bulk one using the Amorphous module in Packmol software.[11] The total amount of $Pyr_{13}FSI$ in each pore can be estimated by the following formula,

$$N = (\rho V N_A)/W \qquad \text{(Equation 3.4)}$$

where ρ is the density of IL, V is the accessible volume of each pore in a unit cell, N_A Avogadro's number, and W is mass per mole of IL.

After equilibration in the NVT ensemble at 300 K for 2 ps, a production simulation was run in the NVT ensemble at 324 K for 50 ps at a time step of 1 fs. A Nosé Hoover chain thermostat was applied for temperature control.[12,13] The temperature of 700 K was below the critical limit for the decomposition of all the chemical entities involved in our work. Considering the large size of COF@ILs, only the Γ-point was used in the k-point sampling for AIMD simulations. Crystal structures and diffusion paths are visualized using the programs VESTA and VMD.

The mean square displacement (MSD) of sodium ions is expressed as,[14]

$$MSD\ (t) = \frac{1}{N}\sum_{i=1}^{N} |r_i(t) - r_i(0)|^2 \qquad \text{(Equation 3.5)}$$

where N is the total number of sodium ions, and $r_i(t)$ is the coordinate of sodium ion i at time t.

The self-diffusion coefficient is then calculated as:[15]

$$D = \frac{1}{2}\lim_{t\to\infty}\frac{MSD(t)}{t} \qquad \text{(Equation S3)}$$

Herein, our focus primarily lies on the diffusion of charge carriers along the z-direction. This is due to (1) the elongated one-dimensional pore structure with a larger cross-section in the xy-plane and a smaller cross-section along the z-axis, and (2) the presence of charged functional groups along the pore walls. Thus, a higher activation energy for ion transport parallel to the pore walls (xy-plane) is experienced compared to moving along the z-axis. Hence, the ion diffusion is primarily controlled by ion movement along the z-axis.[16]

3.6.2. COF synthesis and characterization

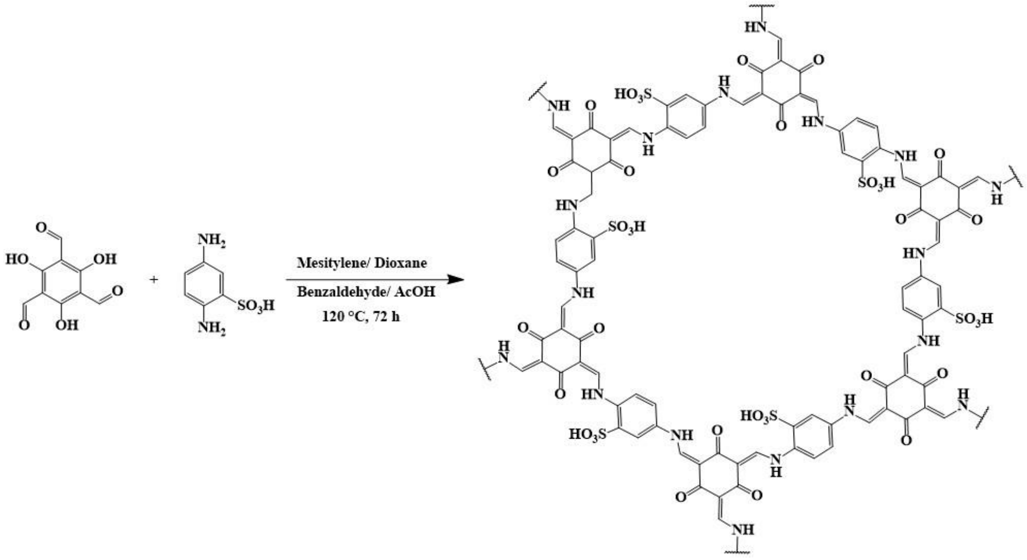

Scheme 3.1 Synthesis of COF-TpPaSO_3H.

2,4,6-Trihydroxybenzene-1,3,5-tricarbaldehyde (Tp, 21 mg, 0.1 mmol, Tokyo Chemical Industry Co., Ltd.), 1,4-phenylenediamine-2-sulfonic acid (PaSO_3H, 28 mg 0.15 mmol, Tokyo Chemical Industry Co., Ltd.), benzaldehyde (2 µL) and 0.2 mL of 6 M aqueous acetic acid were added into a Pyrex tube containing a mixture of dioxane (0.2 mL) and mesitylene (0.8 mL) inside an argon-filled glovebox. The reaction tube was then sonicated for 10 min and heated at 120 ℃ for 3 days. The resulting COF powder was thoroughly washed with dimethylacetamide followed by deionized water and acetone. The obtained red-brown COF powder was then dried at room temperature under vacuum for 6 h.

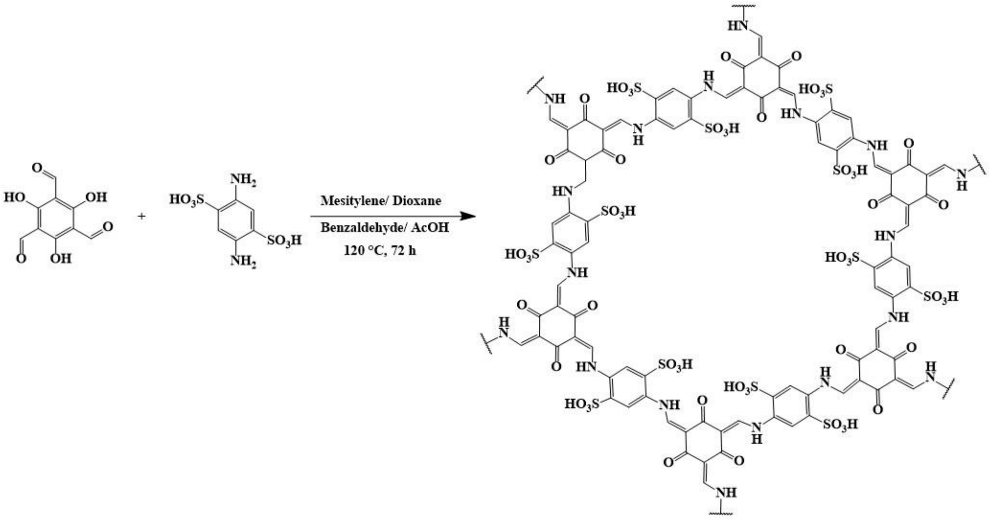

Scheme 3.2 Synthesis of COF-TpPa(SO_3H)$_2$.

2,4,6-Trihydroxybenzene-1,3,5-tricarbaldehyde (Tp, 10.5 mg, 0.05 mmol, Tokyo Chemical Industry Co., Ltd.), 2,5-diaminobenzene-1,4-disulfonic acid (Pa(SO_3H)$_2$, 20 mg, 0.07 mmol, BLDpharm), benzaldehyde (2 µL) and 0.1 mL of 6 M aqueous acetic acid were added into a Pyrex tube containing a mixture of dioxane (0.4 mL) and mesitylene (0.1 mL) inside an argon-filled glovebox. The reaction tube was then sonicated for 10 min and heated at 120 ℃ for 3 days. The resulting COF powder was thoroughly washed with dimethylacetamide followed by deionized water and acetone. The obtained red-brown COF powder was then dried at room temperature under vacuum for 6 h.

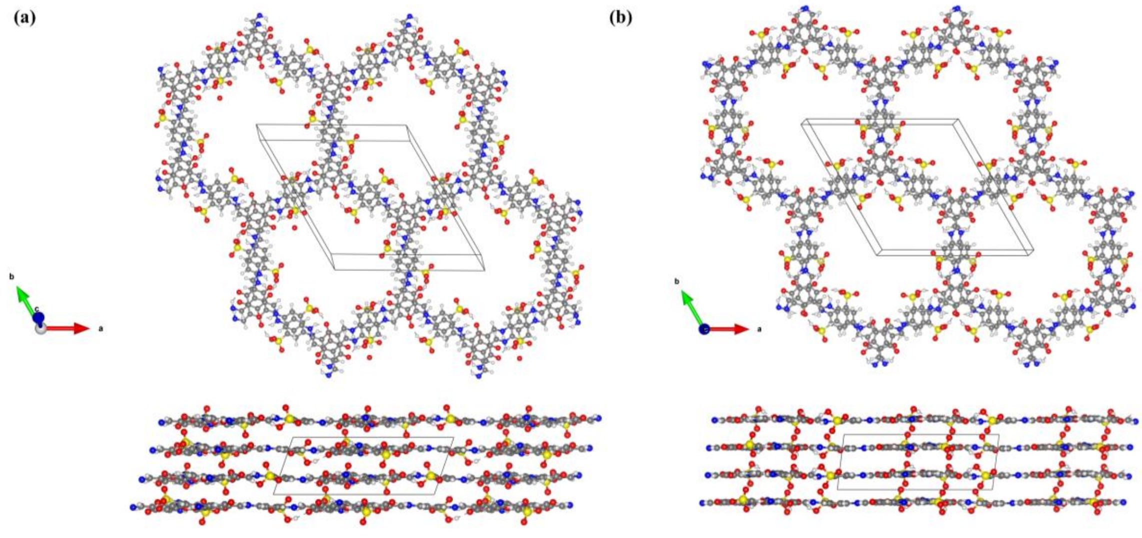

Figure 3.5 Simulated structures of COF- TpPaSO_3H; (a) inclined, and (b) serrated, respectively.

Table 3.1 Stable stacking arrangements (calculated), relative energy difference, and lattice parameters of COF $TpPaSO_3H$.

Structural arrangement	Relative energy difference (eV)	Lattice parameters
inclined	0.67	a=22.59, b=22.38, c=7.29 Å; α=91.04, β=76.81, γ=120.03°
serrated	0.00	a=22.54, b=22.55, c=7.02Å; α=90.39, β=89.11, γ=120.14°

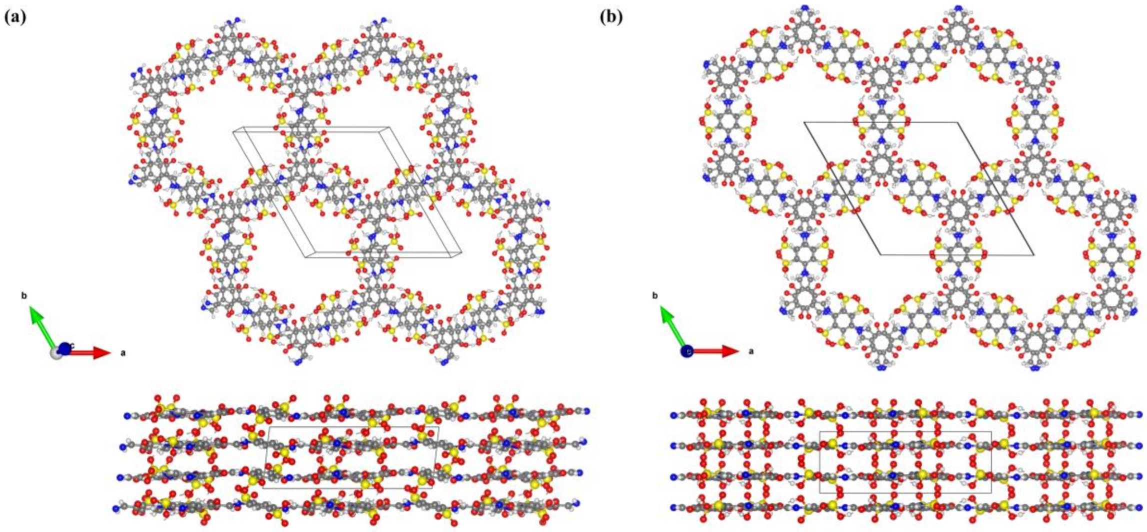

Figure 3.6 Simulated structures of COF- $TpPa(SO_3H)_2$; (a) inclined, and (b) serrated, respectively.

Table 3.2 Stable stacking arrangements (calculated), relative energy difference, and lattice parameters of COF $TpPa(SO_3H)_2$.

Structural arrangement	Relative energy difference (eV)	Lattice parameters
inclined	0.012	a=22.55, b=22.49, c=7.29 Å; α=71.28, β=94.65, γ=120.33°
serrated	0.00	a=22.55, b=22.50, c=7.01 Å; α=87.45, β=83.11, γ=120.03°

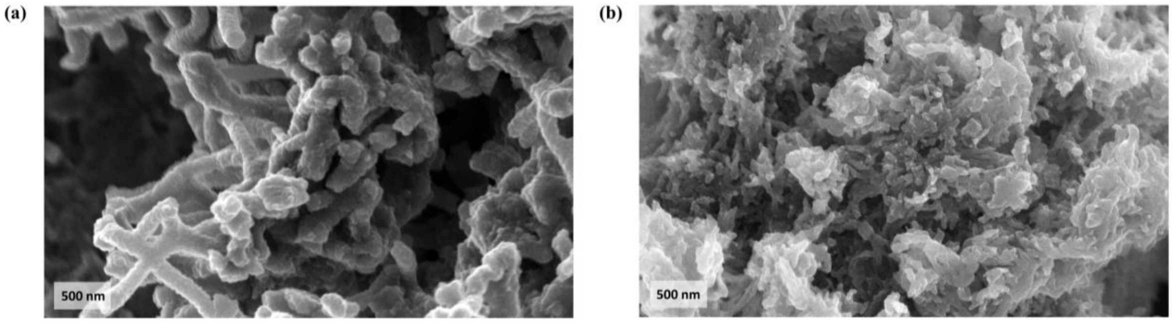

Figure 3.7 Simulated structures of COF- TpPa$(SO_3H)_2$; (a) inclined, and (b) serrated, respectively.

3.6.3. Electrolyte preparation and characterization

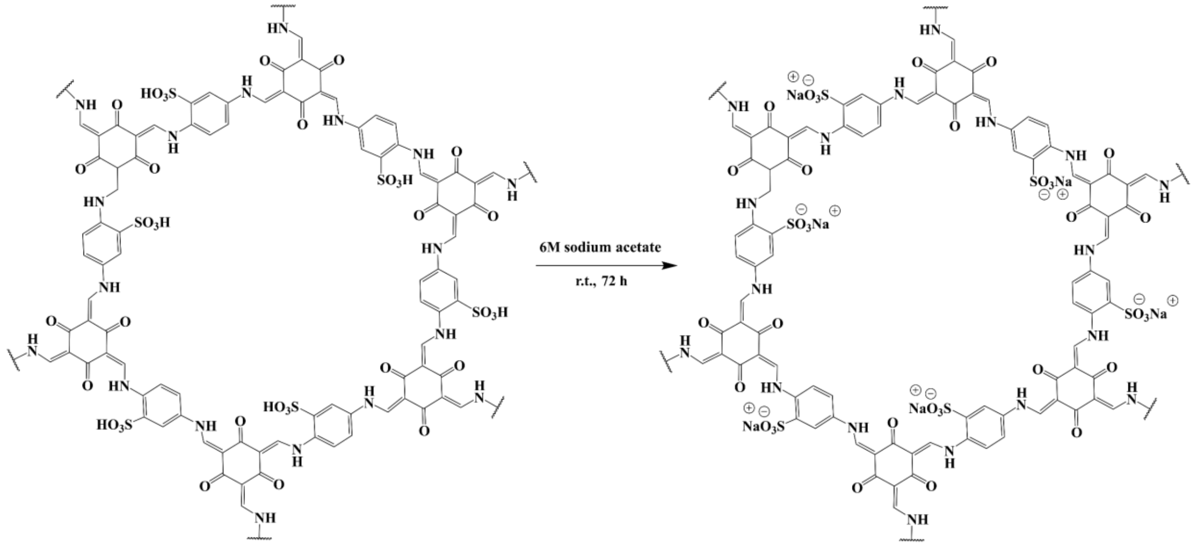

Scheme 3.3 Synthesis of COF-TpPaSO_3Na.

COF-TpPaSO3H was stirred in 20 mL 6 M sodium acetate solution at room temperature for 72 h to obtain COF-TpPaSO_3Na. The sodiated COF was then washed thoroughly with distilled water to remove excess salt and then vacuum dried for 6 hr. COF-TpPaSO_3Na changed color from red-brown to bright red due to the formation of O-Na bonds.

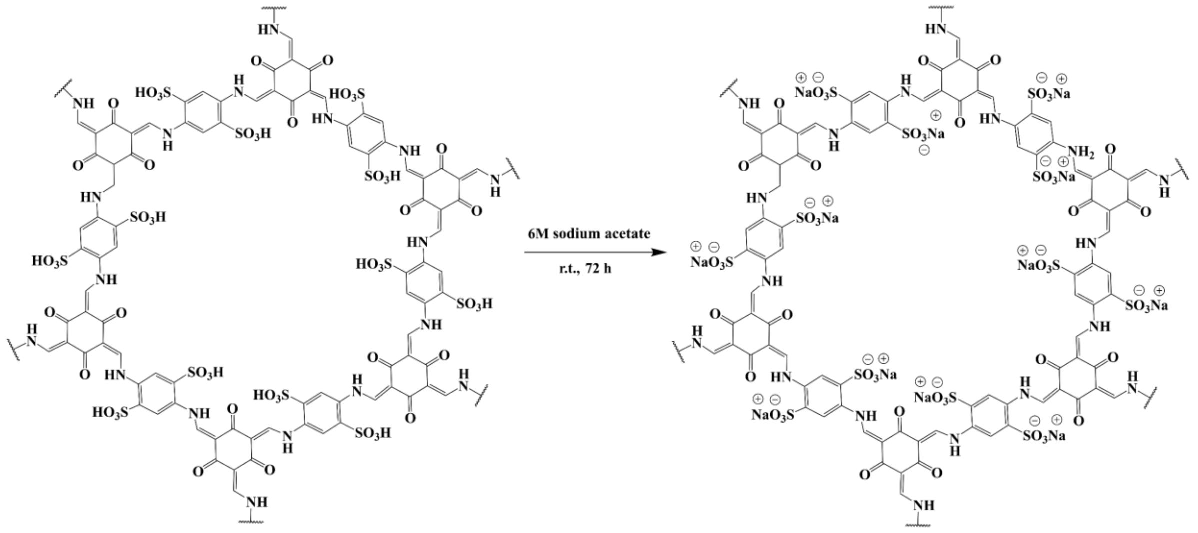

Scheme 3.4 Synthesis of COF- Synthesis of TpPa(SO_3Na)$_2$

COF-TpPa(SO_3H)$_2$ was stirred in 20 mL 6 M sodium acetate solution at room temperature for 72 h to obtain COF-TpPa(SO_3Na)$_2$. The sodiated COF was then washed thoroughly with distilled water to remove excess salt and then vacuum dried for 6 hr. Both the COFs changed color from red-brown to bright red due to the formation of O-Na bonds.

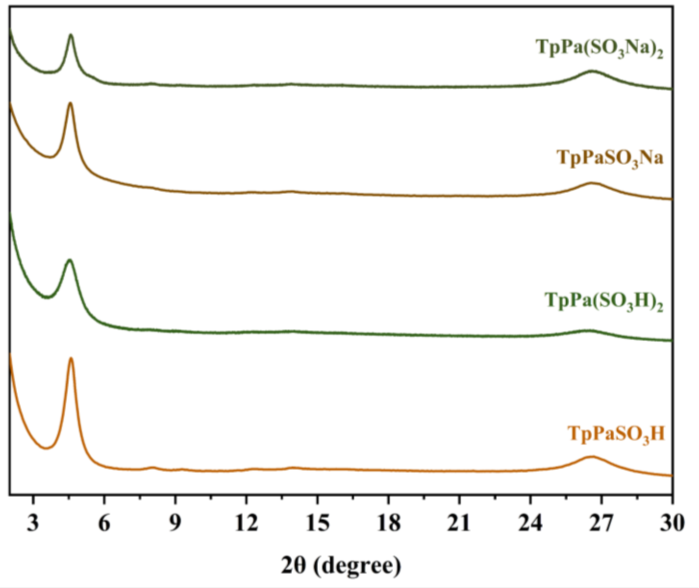

Figure 3.8 Comparative experimental powder X-ray diffractograms of COF- TpPaSO$_3$H, TpPaSO$_3$Na, TpPa(SO_3H)$_2$, and TpPa(SO_3Na)$_2$.

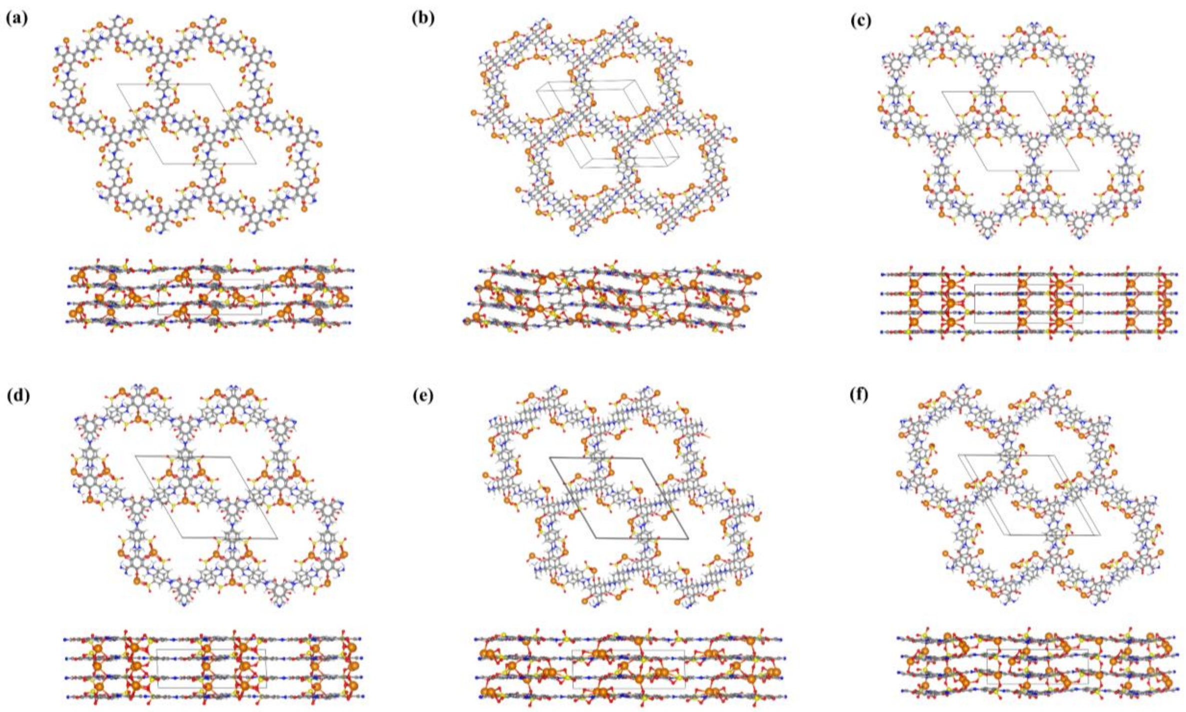

Figure 3.9 Simulated structures of COF- TpPaSO$_3$Na (a) eclipsed, (b) inclined-1, (c) serrated-1, (d) d-serrated-2, (e) serrated-3, and (f) inclined-2. Grey, while, blue, red, yellow and orange colors represent the elements C, H, N, O, S and Na, respectively.

Table 3.3 Stable stacking arrangements, relative energy difference, and lattice parameters of COF- TpPaSO$_3$Na.

Structural arrangement	Relative energy difference (eV)	Lattice parameters
a-eclipsed	2.69	a=22.70, b=22.47, c=6.92 Å; α=86.80, β=91.08, γ=120.58°
b-inclined	0.93	a=22.09, b=22.59, c=7.35 Å; α=86.17, β=65.55, γ=118.78°
c-serrated-1	0.00	a=22.55, b=22.42, c=6.86 Å; α=89.83, β=89.84, γ=119.94°
d-serrated-2	3.11	a=22.68, b=22.40, c=6.79 Å; α=92.55, β=88.73, γ=120.68°
e-serrated-3	2.43	a=22.60, b=22.76, c=6.70 Å; α=90.64, β=91.08, γ=120.58°
f-inclined-2	2.80	a=22.22, b=22.79, c=6.88 Å; α=97.37, β=76.19, γ=120.26°

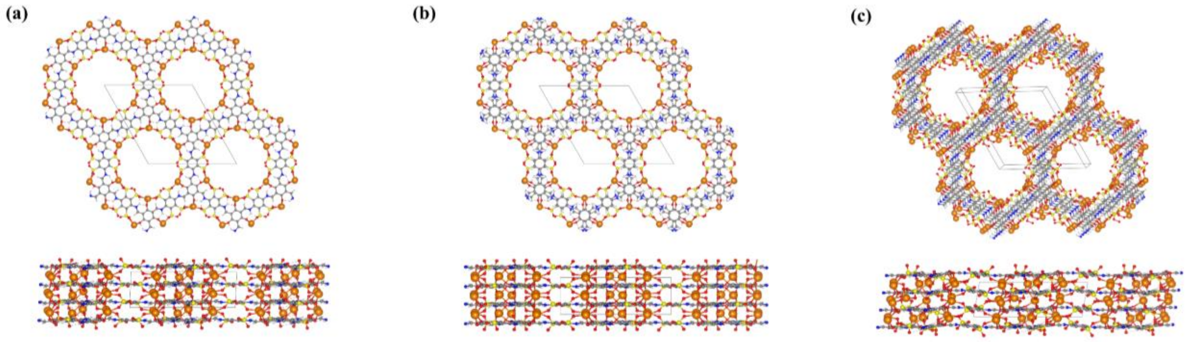

Figure 3.10 Simulated structures of COF- TpPa$(SO_3Na)_2$ (a) eclipsed, (b) serrated, and (c) inclined. Grey, while, blue, red, yellow and orange colors represent the elements C, H, N, O, S and Na, respectively.

Table 3.4 Stable stacking arrangements, relative energy difference, and lattice parameters of COF- TpPa$(SO_3Na)_2$.

Structural arrangement	Relative energy difference (eV)	Lattice parameters
a-eclipsed	0.91	a=22.48, b=22.50, c=7.02 Å; α=87.99, β=89.98, γ=119.97°
b-serrated	0.00	a=22.40, b=22.43, c=6.96 Å; α=90.51, β=89.19, γ=120.05°
c-inclined	2.65	a=22.26, b=22.55, c=6.98 Å; α=87.54, β=79.35, γ=119.08°

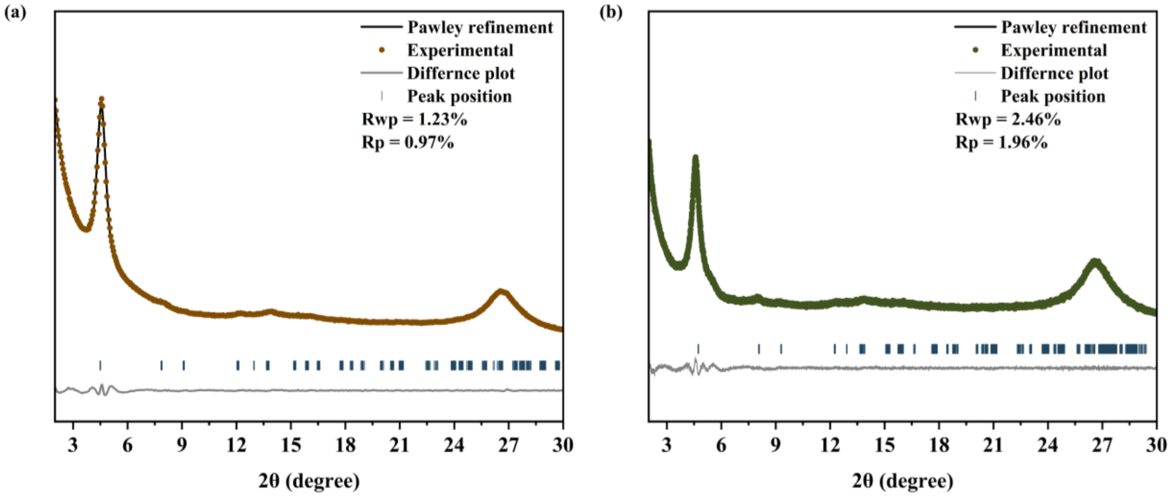

Figure 3.11 Experimental PXRD, Pawley refinement of the simulated structure, difference plot between experimental data and Pawley-refined data, and Bragg reflections of (a) $TpPaSO_3Na$ and (b) TpPa$(SO_3Na)_2$, respectively.

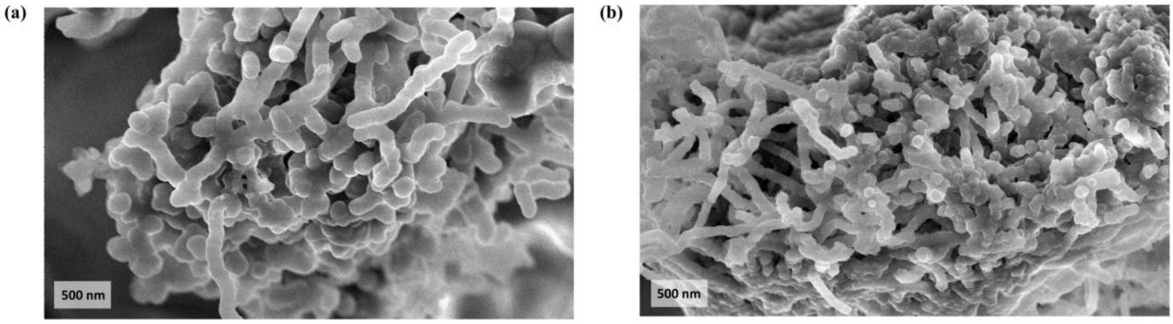

Figure 3.12 Scanning electron microscopy (SEM) images of pristine COFs (a) $TpPaSO_3Na$ and (b) $TpPa(SO_3Na)_2$, respectively.

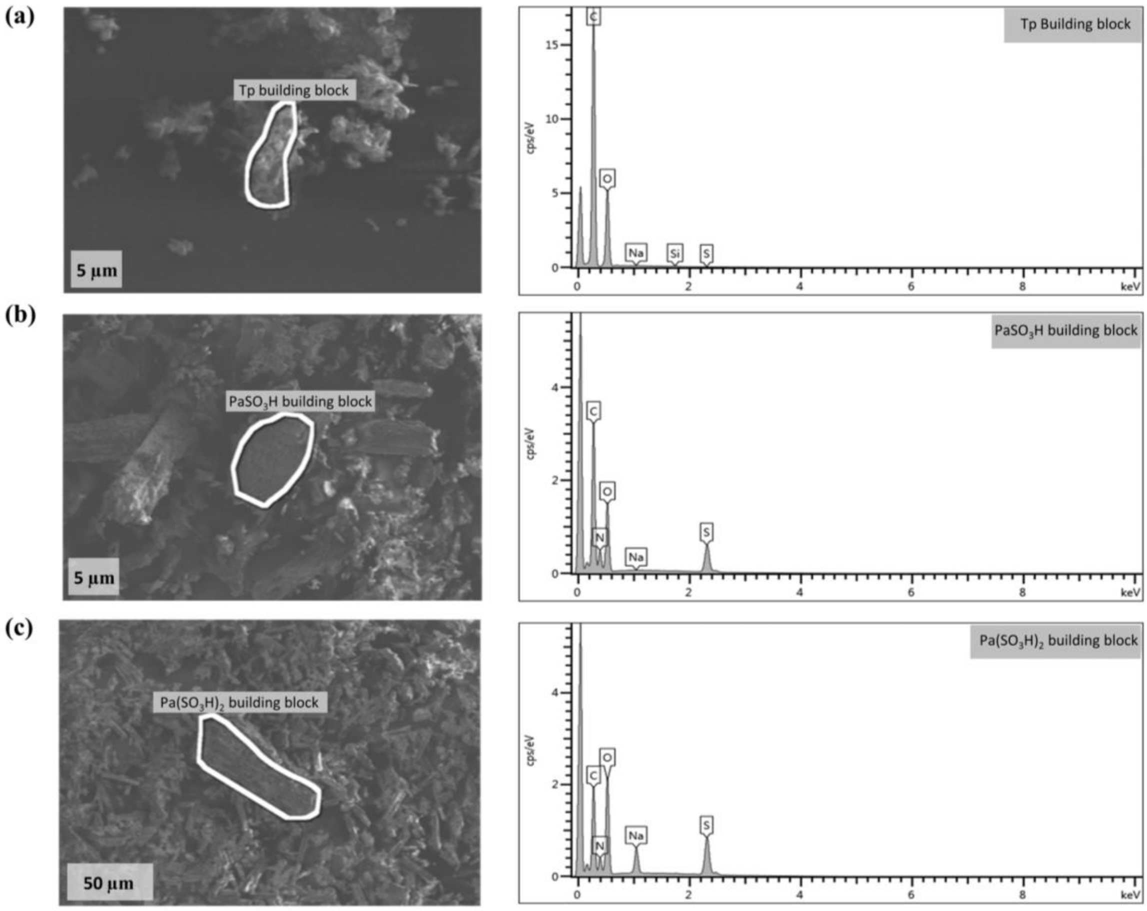

Figure 3.13 SEM-EDX analysis for (a) Tp, (b) $Pa(SO_3H)$, and (c) $Pa(SO_3H)_2$ building blocks.

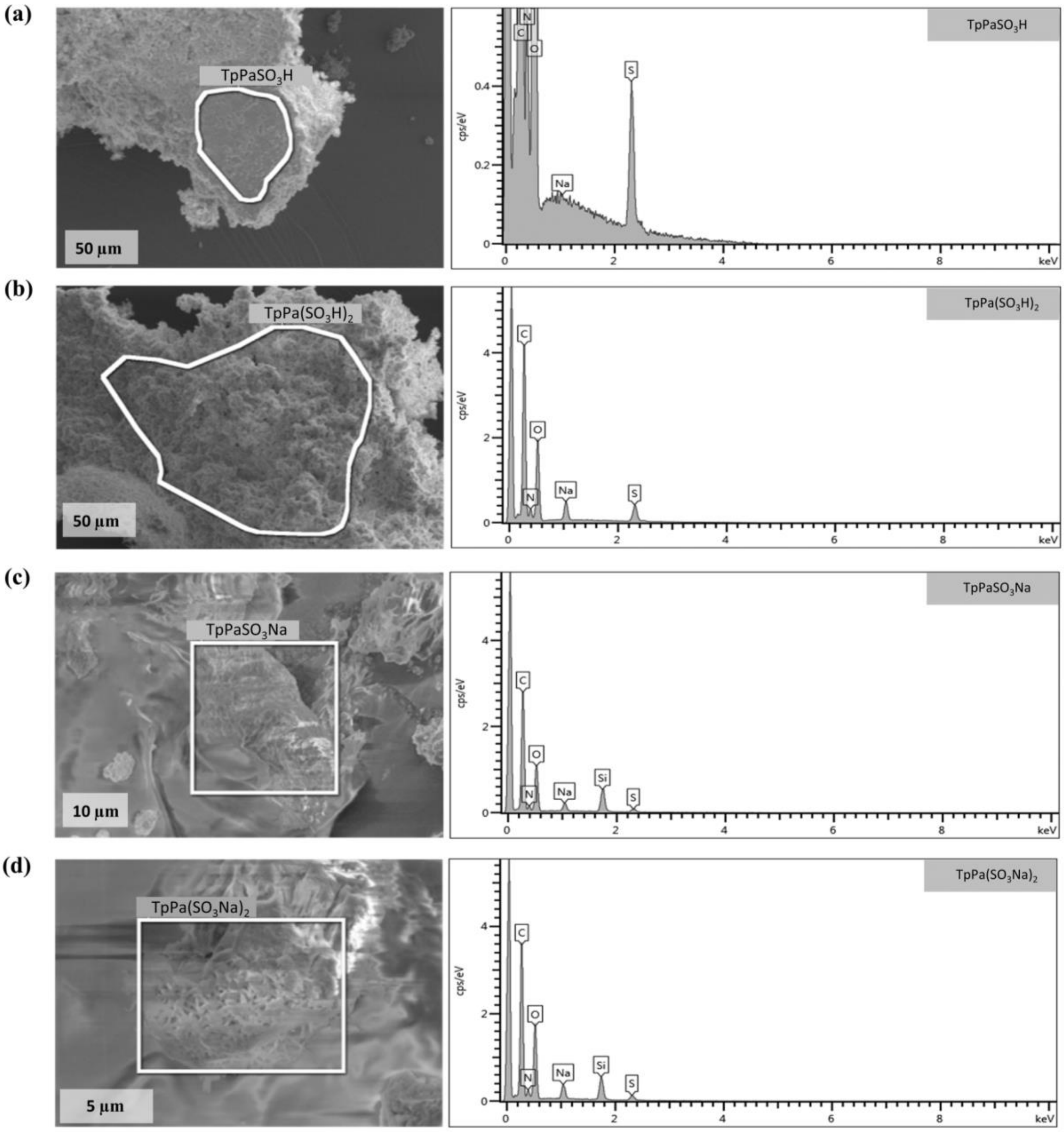

Figure 3.14 SEM-EDX analysis for COF- (a) $TpPaSO_3H$, (b) $TpPa(SO_3H)_2$, (c) $TpPaSO_3Na$, and $TpPa(SO_3Na)_2$.

Table 3.5 Atom percentage of samples from EDX measurements, focusing on S and Na content.

S.No.	Sample	Atom%	
		S	Na
1.	Tp	0.00	0.00
2.	$PaSO_3H$	100.00	0.00
3.	$Pa(SO_3H)_2$	84.40	15.60
4.	$TpPaSO_3H$	100.00	0.00
5.	$TpPa(SO_3H)_2$	75.46	24.54
6.	$TpPaSO_3Na$	58.84	41.52
7.	$TpPa(SO_3Na)_2$	50.76	49.23

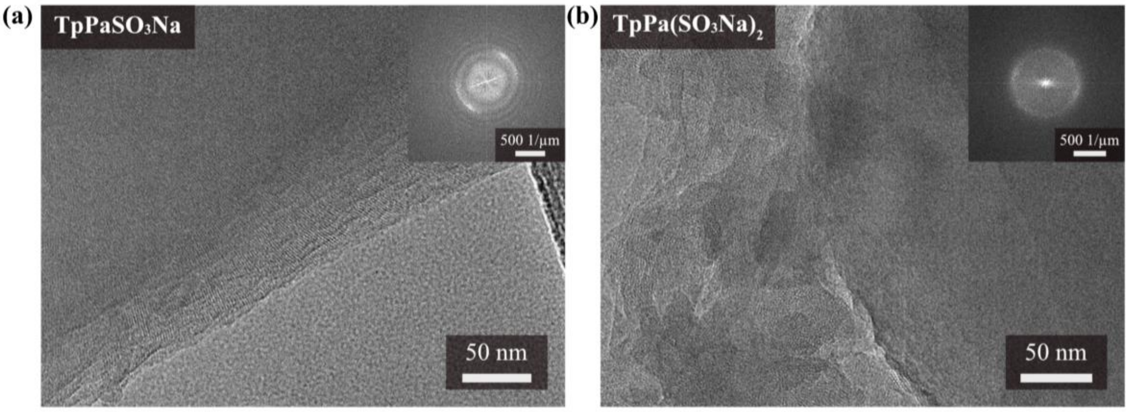

Figure 3.15 Transmission electron microscopy (TEM) images of pristine COFs (a) $TpPaSO_3Na$ and (b) $TpPa(SO_3Na)_2$, respectively.

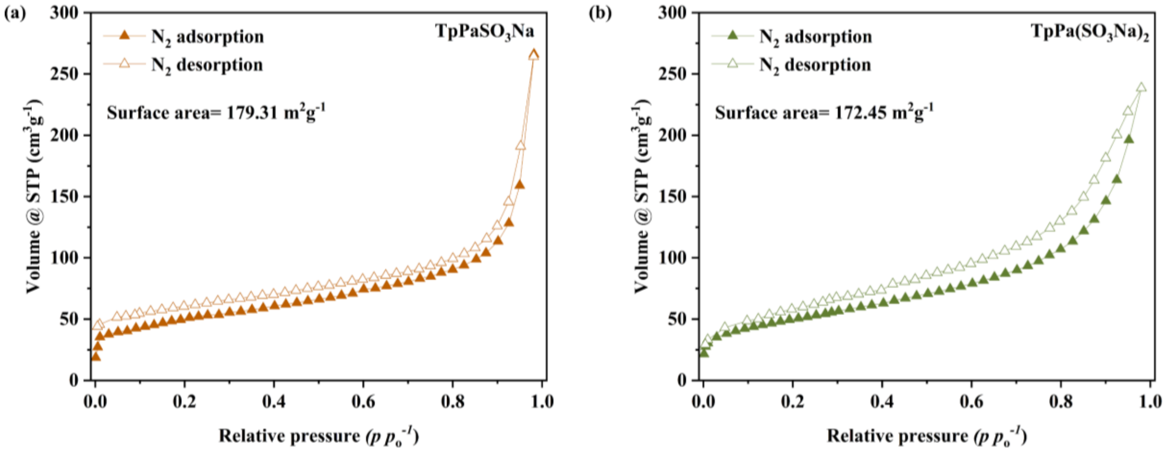

Figure 3.16 Nitrogen (N_2) gas sorption isotherms of pristine COFs (a) $TpPaSO_3Na$ and (b) $TpPa(SO_3Na)_2$, respectively.

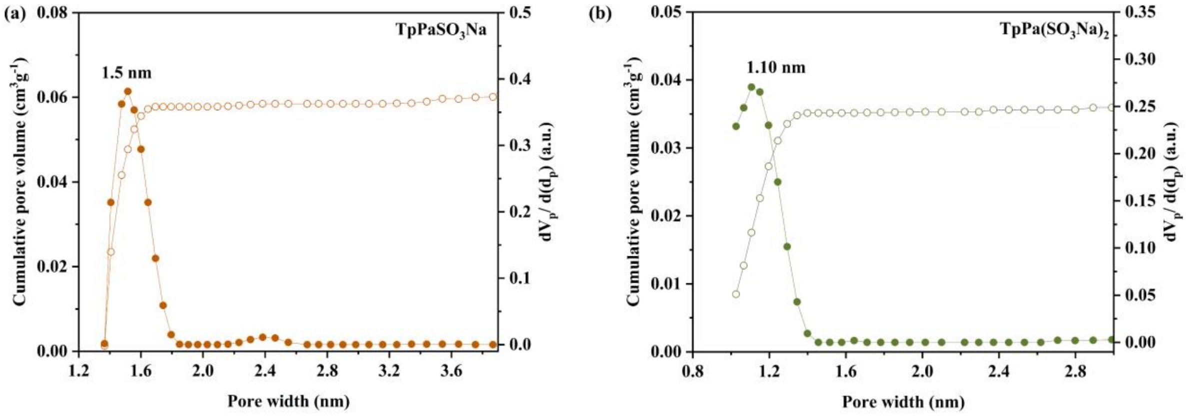

Figure 3.17 Pore size distribution and cumulative pore volume profiles of pristine COFs (a) $TpPaSO_3Na$, and (b) $TpPa(SO_3Na)_2$, respectively.

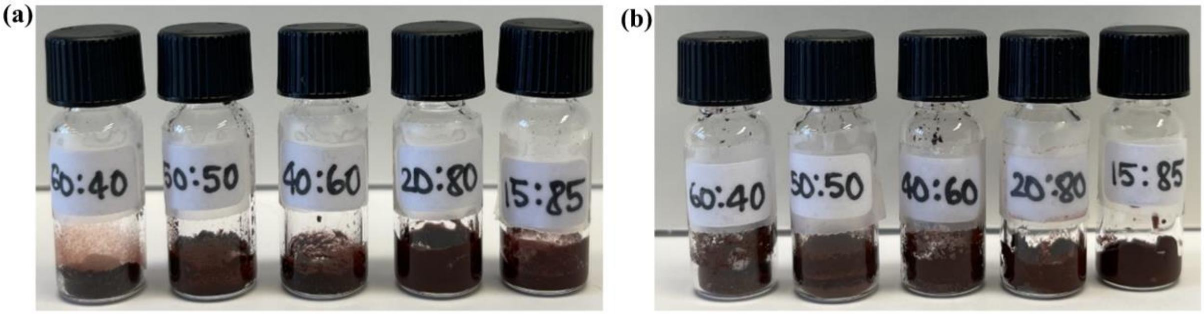

Figure 3.18 TpPaSO$_3$Na: Pyr$_{13}$FSI (left), and TpPa(SO$_3$Na)$_2$: Pyr$_{13}$FSI (right) composites at various COF:IL wt/wt% ratios.

The Pyr$_{13}$FSI ionic liquid was added to COF TpPaSO$_3$Na and COF TpPa(SO$_3$Na)$_2$ at different weight percentages, i.e., COF:IL 60:40, 50:50, 40:60, 20:80, and 15:85 inside an argon filled glovebox, respectively. The composites were stirred inside the glovebox overnight to ensure homogenous and atmosphere-free electrolyte samples. The freshly prepared samples were used to carry out further electrochemical characterization.

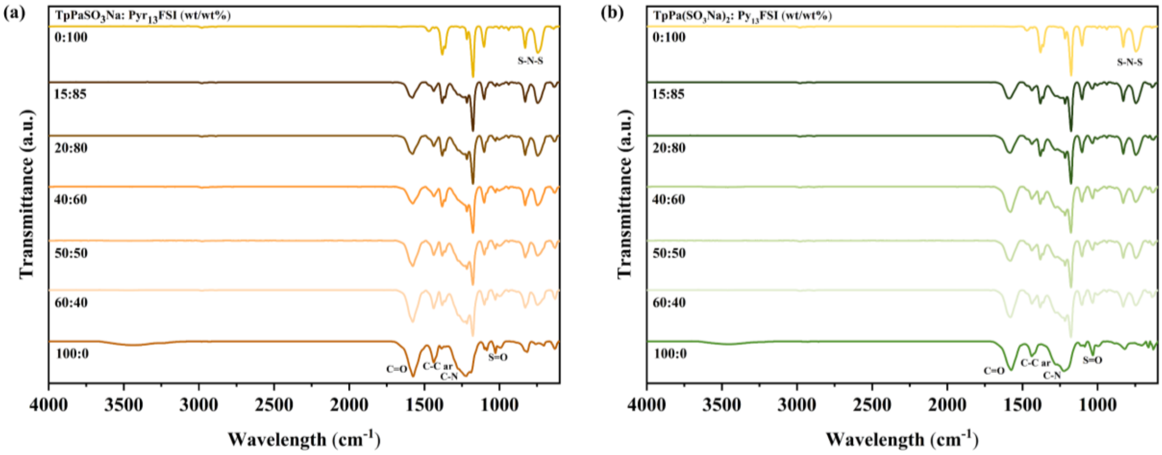

Figure 3.19 FTIR spectra of pristine COF and COF:Pyr$_{13}$FSI composites at various wt/wt% ratios for (a) TpPaSO$_3$Na and (b) TpPa(SO$_3$Na)$_2$, respectively.

3.6.4. Transport properties

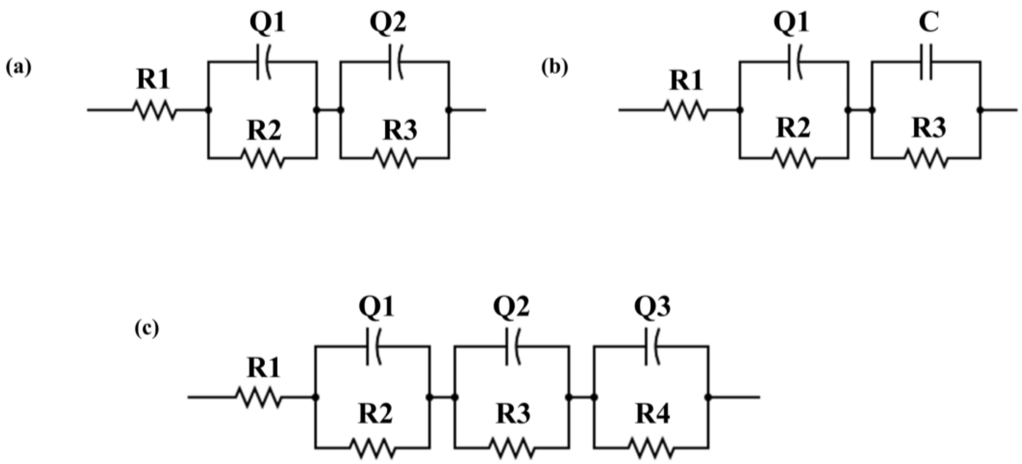

Figure 3.20 Equivalent electric circuits (EEC) utilized to fit the impedance data obtained for electrolyte materials with a fit error < 2.0.

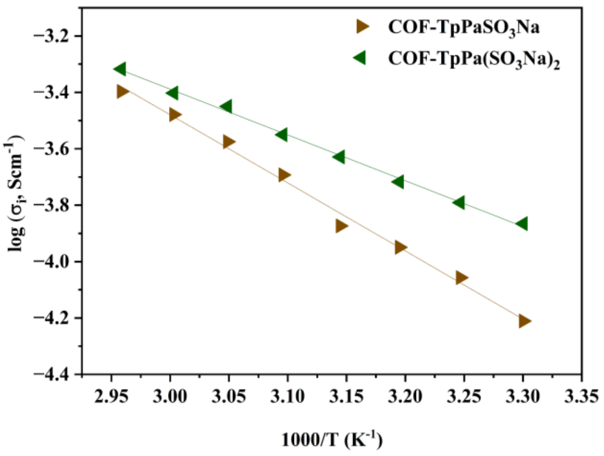

Figure 3.21 Comparative Arrhenius plots of pristine COF TpPaSO$_3$Na and COF TpPa(SO$_3$Na)$_2$.

Table 3.6 Ionic conductivity parameters: equivalent electric circuit, bulk resistance, and ionic conductivity at 50 °C for COF:$Pyr_{13}FSI$ composites at various wt/wt% ratios.

S.No.	**Sample**	**Equivalent electric circuit**	**Resistance (R_b, Ω)**	**Ionic conductivity (σ_i, 10^{-3} S cm^{-1}) at 50 °C**	**Activation Energy (E_a, kJ mol^{-1})**
1.	$TpPaSO_3Na$	R(QR)(QR)	464	0.20	20.06
2.	$TpPa(SO_3Na)_2$	R(QR)(CR)	377	0.25	13.50
3.	$TpPaSO_3Na$: $Pyr_{13}FSI$ (60:40)	R(QR)(QR)(QR)	45	2.11	12.24
4.	$TpPaSO_3Na$: $Pyr_{13}FSI$ (50:50)	R(QR)(QR)(QR)	31	3.02	12.45
5.	$TpPaSO_3Na$: $Pyr_{13}FSI$ (40:60)	R(QR)(QR)(QR)	24	3.96	10.45
6.	$TpPaSO_3Na$: $Pyr_{13}FSI$ (20:80)	R(QR)(QR)(QR)	17	5.63	11.36
7.	$TpPaSO_3Na$: $Pyr_{13}FSI$ (15:85)	R(QR)(QR)(QR)	20	4.84	11.79
8.	$TpPa(SO_3Na)_2$: $Pyr_{13}FSI$ (60:40)	R(QR)(QR)(QR)	53	1.72	10.11
9.	$TpPa(SO_3Na)_2$: $Pyr_{13}FSI$ (50:50)	R(QR)(QR)(QR)	42	2.24	12.46
10.	$TpPa(SO_3Na)_2$: $Pyr_{13}FSI$ (40:60)	R(QR)(QR)(QR)	35	2.73	13.26
11.	$TpPa(SO_3Na)_2$: $Pyr_{13}FSI$ (20:80)	R(QR)(QR)(QR)	23	4.12	12.10
12.	$TpPa(SO_3Na)_2$: $Pyr_{13}FSI$ (15:85)	R(QR)(QR)(QR)	30	3.19	12.70

R_b (R_2) is the resistance of the bulk electrolyte obtained from the optimised equivalent electric circuit (ECC). E_a is the activation energy for the system, calculated from the Arrhenius equation 3.2.

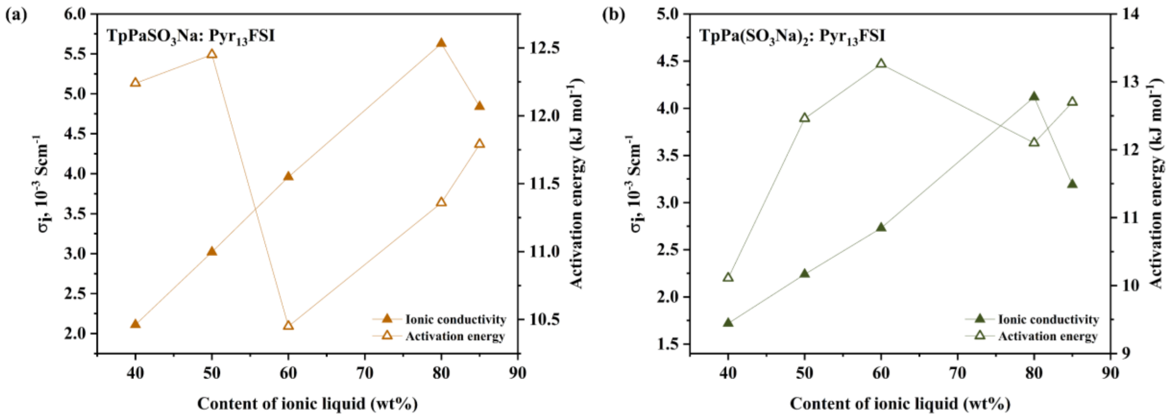

Figure 3.22 Activation energy and ionic conductivity values of COF:$Pyr_{13}FSI$ composites at various wt/wt% ratios for (a) $TpPaSO_3Na$ and (b) $TpPa(SO_3Na)_2$, respectively.

Table 3.7 Transference number parameters: applied perturbation voltage, impedance before and after DC polarization experiment, initial current, and steady-state current obtained for $TpPaSO_3Na@Pyr_{13}FSI$ and $TpPa(SO_3Na)_2@Pyr_{13}FSI$.

Sample	ΔV**(mV)**	R_0**(Ω)**	I_0**(μA)**	I_{ss}**(μA)**	R_{ss}**(Ω)**	t_{Na^+}
$TpPaSO_3Na@Pyr_{13}FSI$	10	801	0.20	0.14	1420	0.79
$TpPa(SO_3Na)_2@Pyr_{13}FSI$	10	850	0.23	0.11	2590	0.67

Table 3.8 Comparison of transport properties, electrochemical and thermal stability of relevant electrolyte materials for this study.

Electrolyte material	**Li^+/Na^+**	**Organic-liquid additive**	**Ionic conductivity (σ_i, Scm^{-1}/°C)**	**Transference number**	**Thermal stability (°C)**	**Ref.**
Zwitt-COF	Li^+	NA	$1.65 \times 10^{-4}/25$	0.31	176	[17]
TpPa-SO3Li	Li^+	NA	$2.7 \times 10^{-5}/25$	0.90	200	[16]
IL-1.0 @NUST-7	Li^+	BMP-BTI	$2.60 \times 10^{-3}/120$	-	400	[18]
PDADMA TFSI/ $Pyr_{14}TFSI$	Li^+	$Pyr_{14}TFSI$	$1.26 \times 10^{-3}/60$	-	342	[19]
TPDBD-CNa-QSSE	Na^+	PC	$1.30 \times 10^{-4}/25$	0.90	264	[20]
NaOOC-COF	Na^+	NA	$4.63 \times 10^{-4}/80$	0.90	250	[21]
Ge-COFs	Na^+	PC	$3.4 \times 10^{-5}/100$	-	150	[22]
PMP-FSI	Na^+	$Py_{13}FSI$	$7.0 \times 10^{-3}/60$	-	400	[23]
$TpPaSO_3Na$@ $Pyr_{13}FSI$	Na^+	$Pyr_{13}FSI$	$5.63 \times 10^{-3}/50$	0.79	375	This work
TpPa $(SO_3Na)_2$@ $Pyr_{13}FSI$	Na^+	$Pyr_{13}FSI$	$4.12 \times 10^{-3}/50$	0.67	431	This work

3.6.5. Computational

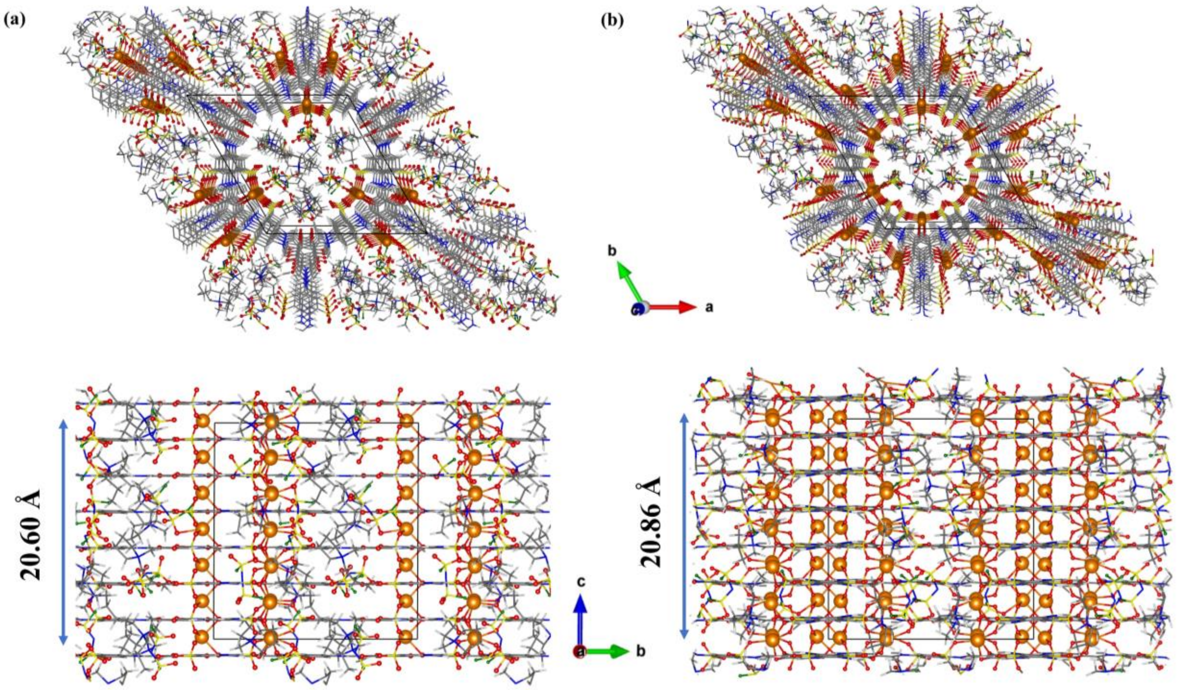

Figure 3.23 Top and side view of the simulation structures of (a) TpPaSO$_3$Na@Pyr$_{13}$FSI and (b) TpPa(SO$_3$Na)$_2$@Pyr$_{13}$FSI equilibrated by AIMD simulations at 300 K for 2 ps.

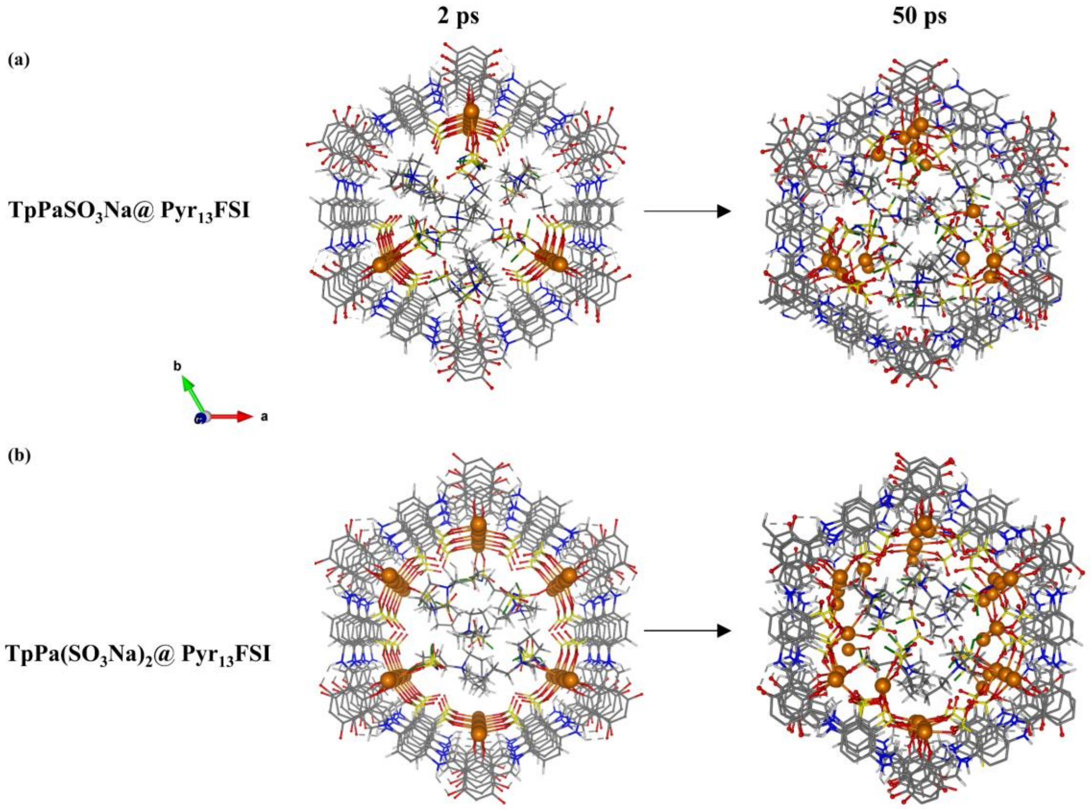

Figure 3.24 Top view of the simulation structures of (a) TpPaSO$_3$Na@Pyr$_{13}$FSI and (b) TpPa(SO$_3$Na)$_2$@Pyr$_{13}$FSI equilibrated by AIMD simulations at 324 K for 2 ps and 50 ps.

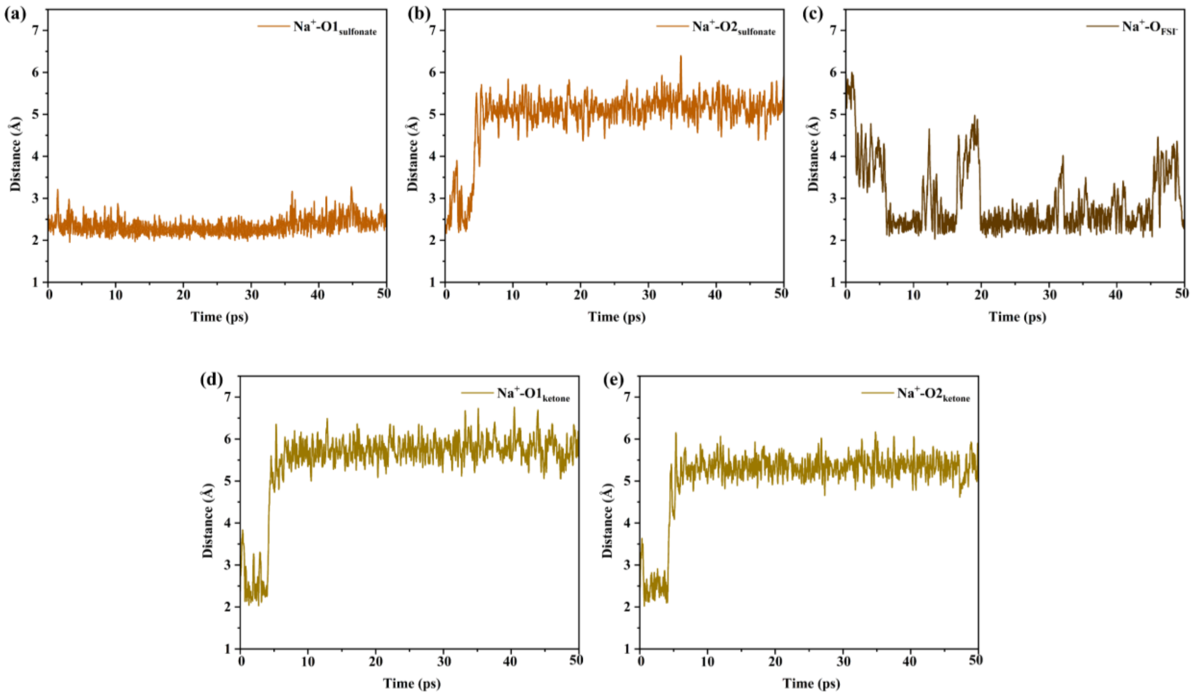

Figure 3.25 Time evolved distance plot of Na$^+$ with (a) O1$_{sulfonate}$, (b) O2$_{sulfonate}$, (c) O$_{FSI}$-, (d) O1$_{ketone}$, and (e) O2$_{ketone}$ for TpPaSO$_3$Na@Pyr$_{13}$FSI obtained by AIMD simulations at 324 K for 50 ps.

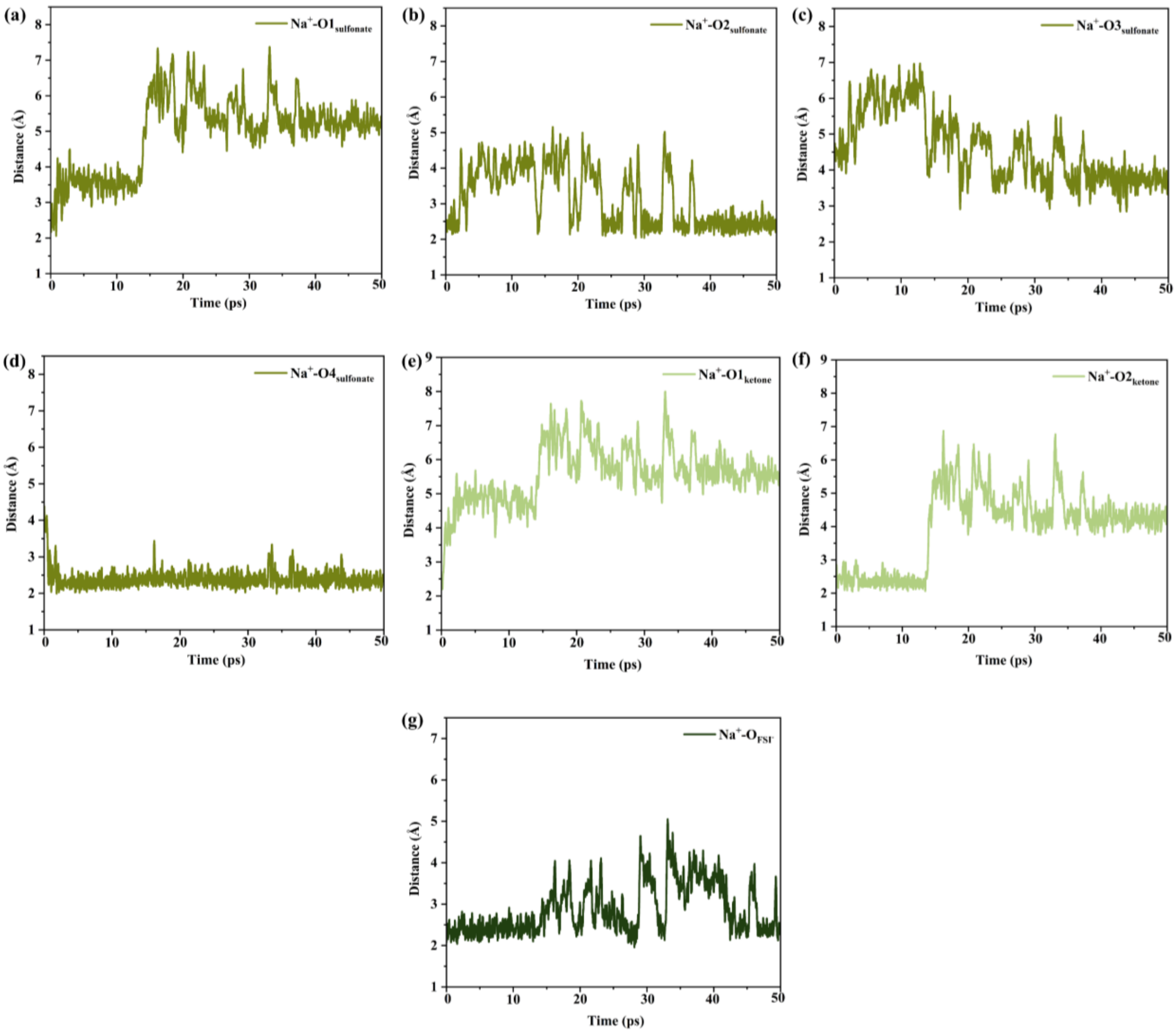

Figure 3.26 Time evolved distance plot of Na+ with (a) O1sulfonate, (b) O2sulfonate, (c) O3sulfonate, (d) O4sulfonate, (e) O1ketone, (f) O2ketone, and (g) OFSI- for TpPa(SO3Na)2@Pyr13FSI obtained by AIMD simulations at 324 K for 50 ps.

3.6.6. References

[1] M. S. Grewal, K. Kisu, S.-I. Orimo, H. Yabu, *iScience* **2022**, *25*, 104910.

[2] Q. Zhao, S. Stalin, C.-Z. Zhao, L. A. Archer, *Nat Rev Mater* **2020**, *5*, 229.

[3] A. Nag, M. A. Ali, A. Singh, R. Vedarajan, N. Matsumi, T. Kaneko, *J. Mater. Chem. A* **2019**, *7*, 4459.

[4] G. Kresse, D. Joubert, *Physical review. B, Condensed matter* **1999**, *59*, 1758.

[5] G. Kresse, J. Furthmüller, *Physical review. B, Condensed matter* **1996**, *54*, 11169.

[6] G. Kresse, J. Hafner, *Physical review. B, Condensed matter* **1993**, *47*, 558.

[7] P. E. Blöchl, *Physical review. B* **1994**, *50*, 15.

[8] J. P. Perdew, K. Burke, M. Ernzerhof, *Physical review letters* **1996**, *77*, 3865.

[9] S. Grimme, *Journal of computational chemistry* **2006**, *27*, 1787.

[10] S. Grimme, J. Antony, S. Ehrlich, H. Krieg, *The Journal of chemical physics* **2010**, *132*, 154104.

[11] L. Martínez, R. Andrade, E. G. Birgin, J. M. Martínez, *Journal of computational chemistry* **2009**, *30*, 2157.

[12] S. Nosé, *Molecular Physics* **1984**, *52*, 255.

[13] S. Nosé, *The Journal of chemical physics* **1984**, *81*, 511.

[14] M. Brehm, M. Thomas, S. Gehrke, B. Kirchner, *The Journal of chemical physics* **2020**, *152*, 164105.

[15] H. Mehrer, *Diffusion in solids: fundamentals, methods, materials, diffusion-controlled processes*, Springer, Berlin, New York **2007**.

[16] K. Jeong, S. Park, G. Y. Jung, S. H. Kim, Y.-H. Lee, S. K. Kwak, S.-Y. Lee, *Journal of the American Chemical Society* **2019**, *141*, 5880.

[17] T. W. Kang, J.-H. Lee, J. Lee, J. H. Park, J.-H. Shin, J.-M. Ju, H. Lee, S. U. Lee, J.-H. Kim, *Advanced materials (Deerfield Beach, Fla.)* **2023**, *35*, e2301308.

[18] Z. Shan, M. Wu, Y. Du, B. Xu, B. He, X. Wu, G. Zhang, *Chem. Mater.* **2021**, *33*, 5058.

[19] Z. Wang, W. Zheng, W. Sun, L. Zhao, W. Yuan, *ACS Appl. Energy Mater.* **2021**, *4*, 2808.

[20] Y. Yan, Z. Liu, T. Wan, W. Li, Z. Qiu, C. Chi, C. Huangfu, G. Wang, B. Qi, Y. Yan, T. Wei, Z. Fan, *Nature communications* **2023**, *14*, 3066.

[21] G. Zhao, L. Xu, J. Jiang, Z. Mei, Q. An, P. Lv, X. Yang, H. Guo, X. Sun, *Nano Energy* **2022**, *92*, 106756.

[22] S. Ashraf, C. Liu, S. Li, I.-U. Haq, M. Mehmood, P. Li, B. Wang, *ACS applied materials & interfaces* **2020**, *12*, 40372.

[23] C.-Y. Li, J. Patra, C.-H. Yang, C.-M. Tseng, S. B. Majumder, Q.-F. Dong, J.-K. Chang, *ACS Sustainable Chem. Eng.* **2017**, *5*, 8269.

4

This chapter is based on the following article-

Covalent Organic Framework Bipolar Pseudocapacitive Electrodes in an All-Organic Symmetric Lithium-Ion Battery

Apeksha Singh,[1] Preeti Bhauriyal,[2] Lucie Quincke,[3] Dominic Blätte,[1] Roman Guntermann,[1] Jennifer LM Rupp,[3] Thomas Heine,[2, 4-6] and Thomas Bein*[1]

[1]Department of Chemistry and Center for NanoScience (CeNS), Ludwig-Maximilians- Universität München (LMU Munich), Butenandtstrasse 5-13 (E), 81377 Munich, Germany

[2]Faculty of Chemistry and Food Chemistry, Technische Universität Dresden, Bergstrasse 66, 01069 Dresden, Germany

[3]Department of Chemistry, TUM School of Natural Sciences, Technical University of Munich (TUM), Lichtenbergstrasse 4, 85748 Garching, Germany

[4]Helmholtz-Zentrum Dresden-Rossendorf (HZDR), Bautzner Landstr. 400, 01328 Dresden, Germany

[5]Center for Advanced Systems Understanding (CASUS), Untermarkt 20, 02826 Görlitz, Germany

[6]Department of Chemistry and ibs for nanomedicine, Yonsei University, Seodaemun-gu, Seoul 120-749, South Korea

KEYWORDS: all-organic electrode, pseudocapacitance, ion-storage dynamics, diffusion coefficient, density functional theory (DFT), symmetric lithium-ion battery

Published as: *Adv. Energy Mater.* **2025**,*15*, e01494

4.1. Abstract

Covalent organic frameworks (COFs) have emerged as promising active materials for secondary-ion battery electrodes, owing to their robust porous structure and the flexibility in selecting redox-active building blocks. Here, a novel highly crystalline, electro-active, bipolar-type **WTTF**-COF, obtained by integrating p-type *N*,*N*,*N′*,*N′*-tetrakis(4-aminophenyl)-1,4-phenylenediamine (**W**) and 4,4′,4″,4‴-([2,2'-bi(1,3-dithiolylidene)]-4,4′,5,5′-tetrayl)tetrabenzaldehyde (**TTF**) molecular building blocks via n-type imine linkages, is reported, serving as a Li-ion battery electrode. In Li-ion half cells, **WTTF**-COF as a cathode features 12-electron dual-ion redox chemistry per unit cell within a stable, unusually wide potential window of 0.1–3.6 V versus Li/Li^+, corresponding to a high theoretical capacity of 315 mAh g^{-1}, with an experimental reversible specific capacity of 271 mAh g^{-1} at 0.1 A g^{-1}. The hybrid redox features coupled with the long-range ordered nanostructure of **WTTF**-COF enable an efficient pseudo-capacitive charge-storage mechanism. Different diffusion pathways and diffusion coefficients for Li^+ and PF_6^- transport are established through detailed diffusion measurements and theoretical modeling. Among hybrid storage electrodes, **WTTF**-COF is reported to offer the option to serve as both anode and cathode up to a high rate of 200 mV s^{-1}, as demonstrated in fully organic symmetric cell tests. Summarizing, judiciously designed COFs are suitably established for efficient bipolar electrode applications.

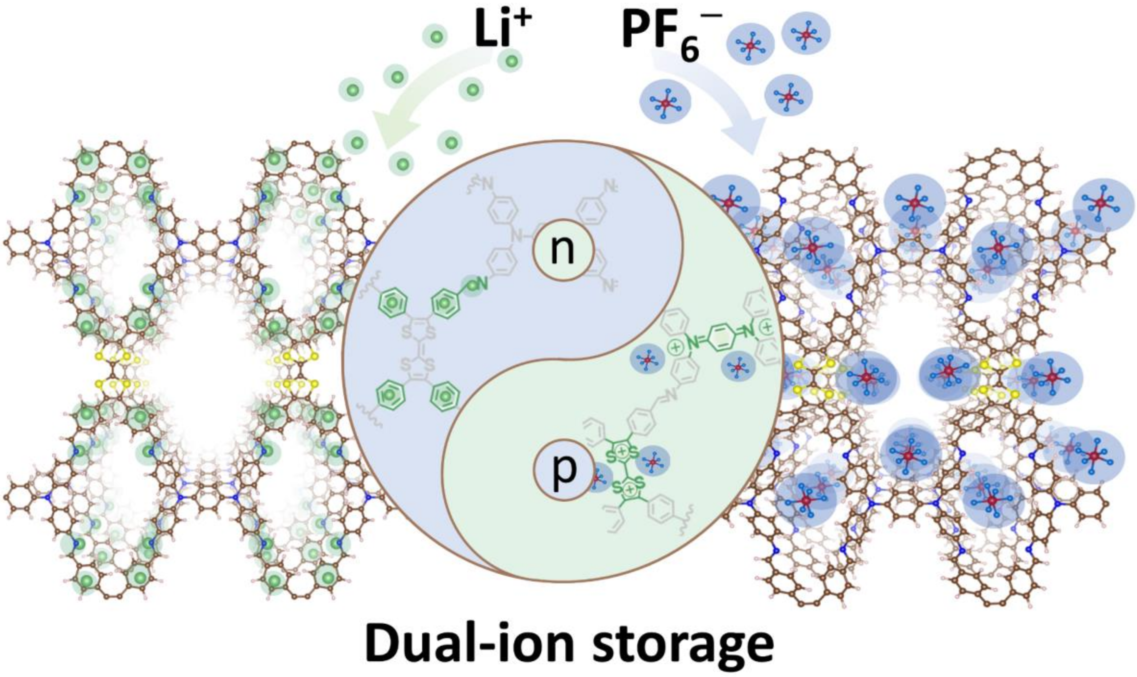

4.2. Introduction

Over the past decade, the scientific community has concentrated its efforts on enhancing the power densities of lithium-ion batteries (LIBs) with the objective of facilitating the adaptation of electric vehicles (EVs) into the automotive market.[1–3] The sustainable integration of EVs relies on several critical factors, such as conscious choice of non-critical and socio-economically acceptable chemistries while assuring cost effectiveness at wide cruising range and rapid charging.[4] Conventional battery electrode materials inhibit fast ionic charge storage due to the involvement of diffusion-dependent Faradaic reactions.[5–7] In contrast, electric double layer capacitors (EDLCs) provide immediate energy and fast charging since the charge-transfer is governed by surface-dependent non-Faradaic reactions.[8–10] Pseudocapacitive materials can store charge at a similar rate as non-Faradaic EDLCs either through surface-redox Faradaic processes, called redox-pseudo-capacitance and/or rapid migration of charge-carriers for physical trapping into the defined channels of the active material, called intercalation-pseudocapacitance.[6,11] However, the trade-off between electrode materials with high capacity yet sluggish kinetics and those with rapid kinetics yet limited capacity poses a challenge to combined energy and power storage concepts. The answer to this conundrum lies in exploring electrode materials capable of potential hybrid high-power and high-energy operation. Hence, electrode materials are targeted that provide: (1) accelerated charge transfer dynamics aided by (inter)penetrating molecular structures or surface-redox processes, (2) superior heterogeneous redox moieties, and (3) high electronic conductance.[12–15]

More recently, this has led to the establishment of inorganic electrodes that have potential to function as both, a battery-type and a pseudocapacitive electrode, such as by adjusting the voltage range. These include hybrid electrodes like 2D-TiS_2, or some phase polymorphs of Nb_2O_5,TiO_2 and MoO_3 , and recent reports on lithium titanate anodes.[16–18] Despite their promise, increasing awareness about the ecological consequences associated with mining rare elements present in inorganic Li^+ classic intercalation electrodes and their limited operation window for hybrid battery type/psydocapacitive binary oxide have spurred a renewed interest in the development of organic electrodes.[19–21] Furthermore, the tunable nature of organic electrodes positions them as a compelling alternative to inorganic hybrids, paving the way for efficient K^+ and Na^+ storage in post-lithium-ion.[22–24] Organic electrodes can be categorized as n-type (for cation doping such as Li^+, K^+, Na^+ etc.), p-type (for anion doping such as PF_6^-, $TFSI^-$, BF_4^- etc.), and bipolar-type (for cation and anion doping) depending on their redox chemistry.[19,23,25–27] In general, n-type materials function as anodes, undergoing reduction by readily accepting electrons, whereas p-type materials serve as cathodes, undergoing oxidation by donating electrons.

A bipolar-type electrode can be utilized in a symmetric battery configuration, which relies on the same material for both electrodes, offering several advantages, such as the ability to create stacked battery designs, manufacturing the active material more efficiently by optimizing one material rather than two, and a deeper comprehension of the cycling process.[22,28–33] Typically, redox-active moieties such as carbonyls, imines, quinones, polysulfides and organic radicals are utilized in all-organic batteries.[19] In particular, radical centers provide accelerated charge transfer due to high reactivity of the unpaired electron(s) that readily participate in redox reactions, lower the activation energy for electron flow, establish rapid dynamic equilibria with their parent molecules and other intermediates, or involve negligible bond rearrangement.[10,24,34] *N,N,N',N'*-tetramethyl-p-phenylenediamine, commonly known as Wurster's blue and tetrathiafulvalene are notable strong electron donors due to their ability to delocalize charge over their respective conjugated structures.[22,35–37] Delocalization of electrons facilitates rapid charge transport in Wurster's blue and tetrathiafulvalene moieties, resulting in their respective analogs been utilized to design conductive molecules or polymers.[10,38,39] However, their high solubility in organic solvents, which may include the liquid electrolytes, can result in capacity-decay and limited cyclability.[38–42] Additionally, mesoporous polymers have been utilized for organic electrodes due to their tunable physical and electrochemical properties; however, the irregular and amorphous network structure of these polymers can confer limited diffusion characteristics.[10,43]

Covalent organic frameworks (COFs) are a class of porous polymers composed of organic building blocks linked together by strong covalent bonds, forming an extended, rigid, and robust (2D) or three-dimensional (3D) crystalline network.[44,45] In contrast to organic molecules or polymers, the presence of strong covalent bonds, along with high molecular weight and a long-range ordered porous network, leads to negligible solubility of COFs in aprotic solvents. In recent years, COFs have become widely popular as electrode materials for secondary-ion batteries due to the versatile choice of redox-active monomers and their arrangement to precisely control and tailor the properties for energy applications.[12,15,46] The collaboration of p-type, n-type and bipolar-type monomers in COFs has led to interesting storage mechanisms and elevation in redox-potentials.[47–50] However, many previous studies included the incorporation of conductive moieties such as carbon nanotubes (CNTs) or metal centers, which could lead to misleading results.[47,48,50,51] Moreover, while numerous studies have combined p-type (or n-type) monomers to form bipolar-type electrodes, the application of COF-based electrodes in symmetric all-organic lithium batteries has yet to be established.

In this study, we present a novel highly crystalline **WTTF**-COF, synthesized by combining electroactive *N,N,N',N'*-tetrakis(4-aminophenyl)-1,4-phenylenediamine (**W**) and 4,4',4'',4'''-([2,2'-bi(1,3-dithiolylidene)]-4,4',5,5'-tetrayl)tetrabenzaldehyde (**TTF**) building blocks, as bipolar-type electrodes for lithium-ion batteries. We examine the structural, chemical and electrochemical properties of **WTTF**-COF through a combined experimental and computational approach. The diffusion of the charge carriers Li^+ and PF_6^- is also investigated through potential-dependent electrochemical impedance spectroscopy (EIS) over the potential range of 0.1-3.6 V vs. Li/Li^+, and later confirmed through computational studies. Finally, a symmetric full cell utilizing **WTTF** dually, as a negative and as a positive electrode, was fabricated to establish the implementation of **WTTF**-COF as a bipolar-type electrode for lithium-ion organic batteries.

4.3. Results and discussions

4.3.1. Materials synthesis and characterization

WTTF-COF was synthesized by utilizing the tetragonal monomers **W** and **TTF** in a Schiff base solvothermal condensation reaction (Scheme 4.1, Section 4.6.2, Appendix). Building blocks accommodating the p-type subunits **W** and **TTF** were selected to bond through imine-linkages (n-type) to produce a bipolar-type **WTTF**-COF to be later investigated as an electrode material (**Figure 4.1a**). To synthesize a long-range ordered nanostructured COF, a modulation approach was applied by adding traces of benzaldehyde as a modulating additive to control the rate of nucleation and improve the crystallinity of the resulting **WTTF**-COF.[44,52] The experimental and simulated elemental analysis of the synthesized COF is presented in the Section 4.6.2, Appendix (Table 4.1). The formation of **WTTF**-COF was determined by employing Fourier transform infrared (FTIR) spectroscopy (Figure 4.8, Section 4.6.2, Appendix). FTIR analysis was carried out for the individual building blocks (**W** and **TTF**) and the resulting COF. For **WTTF**-COF, the characteristic absorption band at 1620 cm^{-1} has been assigned to the C=N bond vibration. Additionally, both the N−H stretching vibration at 3100-3500 cm^{-1}, belonging to the amine group in **W** monomer, and the C=O stretching vibration at 1606 cm^{-1} associated with the aldehyde functional group present in **TTF** monomer, disappeared from the COF sample, indicating completion of the reaction without residual monomer units. Furthermore, the absence of a resonance peak at ~190 ppm, corresponding to the aldehyde functional group, in the solid-state ^{13}C cross-polarization magic angle spinning (CP-MAS) NMR spectra of the bulk COF establishes the formation of the imine linkage (Figure 4.9, Section 4.6.2, Appendix).

Powder X-ray diffraction (PXRD) revealed the formation of highly crystalline **WTTF**-COF (Figure 4.10, Section 4.6.2, Appendix). The intense diffraction pattern was observed at angles of 3.30°, 4.41°, 5.52°, 7.97°, and 9.5° 2θ. Density-functional based tight-binding (DFTB) calculations were performed to generate the model structure of **WTTF**-COF in the AMSprogram suite.[53,54] The building blocks (**W** and **TTF)** can be assembled into a 2D COF via two potential linkages, (1) orthogonal linkage: orthogonal long axes of monomers**,** and (2) co-linear linkage: parallel but offset long axes of monomers (Figure 4.11, Section 4.6.2, Appendix). For these two possible linkages, various stacking arrangements of the **WTTF**-COF were investigated and compared with the experimental PXRD patterns (Figure 4.12-4.14, Table 4.2, Section 4.6.2, Appendix).

As a result, the orthogonal linkage of the **W** vs. **TTF** node in the **WTTF**-COF model furnished a PXRD pattern that matched the experimental diffractogram, especially for the AA-eclipsed and AA-inclined stackings. The AA-inclined stacking was found to be more stable than AA-eclipsed (Table 4.3, Section 4.6.2, Appendix), however, the COF could attain a mixture of these two stackings. To simulate a random stacking, statistical models developed in previous work with 10 COF layers (with AA-eclipsed and AA-inclined stackings) were used, as shown in **Figure 4.1c**, and S15a, Section 4.6.2, Appendix.[55] The model generated simulated PXRD patterns that are in close agreement with their experimental counterpart (Figure 4.15b, Section 4.6.2, Appendix). Pawley refinement was conducted by utilizing the Reflex module of Material Studio to confirm the alignment of the simulated structure with the experimental diffractogram with Rwp = 2.65% and Rp = 1.89%. (**Figure 4.1d**, 4.15, Section 4.6.2, Appendix). The optimized cell parameters of the random stacking model are a = 19.73 Å, b = 26.88 Å, c = 37.82 Å, α = 98.04°, β = 89.62°, and γ = 89.19°. The COF exhibit a rhombic pore framework with an atom-to-atom pore width of 1.5 nm (**Figure 4.1b**). The interlayer distance due to the π-π stacking between the two sheets was calculated to be 0.37 nm.

Scanning electron microscopy (SEM) analysis was performed to elucidate the morphology of the synthesized **WTTF**-COF (**Figure 4.1e** and 4.16, Section 4.6.2, Appendix). The SEM images unveiled a striking coral-like morphology interspersed with intergrown flakes being on average 500nm. This distinctive morphology, previously documented for some 2D-COFs employing the **W** building block, substantiates the 2D structural framework of the **WTTF**-COF.[10,37] Furthermore, transmission electron microscopy (TEM) was employed to validate the crystallinity and structure of **WTTF**-COF (**Figure 4.1f**). The TEM images revealed the presence of characteristic long-range ordered COF domains ~100 nm within the analyzed sample. The interlayer spacing between two COF sheets was determined to be 0.32 nm, aligning closely with the theoretical values derived from the simulated structure.

Porosity and surface area are key for controlling the efficacy of an electrode material. A high surface area electrode facilitates enhanced accessibility to reaction sites, resulting in superior charge transfer and elevated capacitance. To assess the porosity of the **WTTF**-COF, nitrogen gas (N_2) physisorption was performed on the COF sample at 77 K (Figure 4.17a, Section 4.6.2, Appendix). The resulting isotherm profile exhibited Type I sorption behavior with a fully reversible adsorption isotherm.[50] This reversible isotherm reached saturation at approximately 175 cm^3 g^{-1} within a partial pressure (pp_o^{-1}) range of less than 0.05. The overall Brunauer–Emmett–Teller (BET) surface area of the COF was determined to be 657 m^2 g^{-1}. The quenched solid density functional theory (QSDFT) model was applied to ascertain the pore size in **WTTF**-COF (Figure 4.17b, Section 4.6.2, Appendix), revealing the presence of 1.5 nm pores, aligning well with the simulated structure. To ensure the thermal stability of **WTTF**-COF for battery applications, thermogravimetric analysis (TGA) was conducted (Figure 4.18, Section 4.6.2, Appendix). The COF sample was heated from room temperature to 900 °C under a

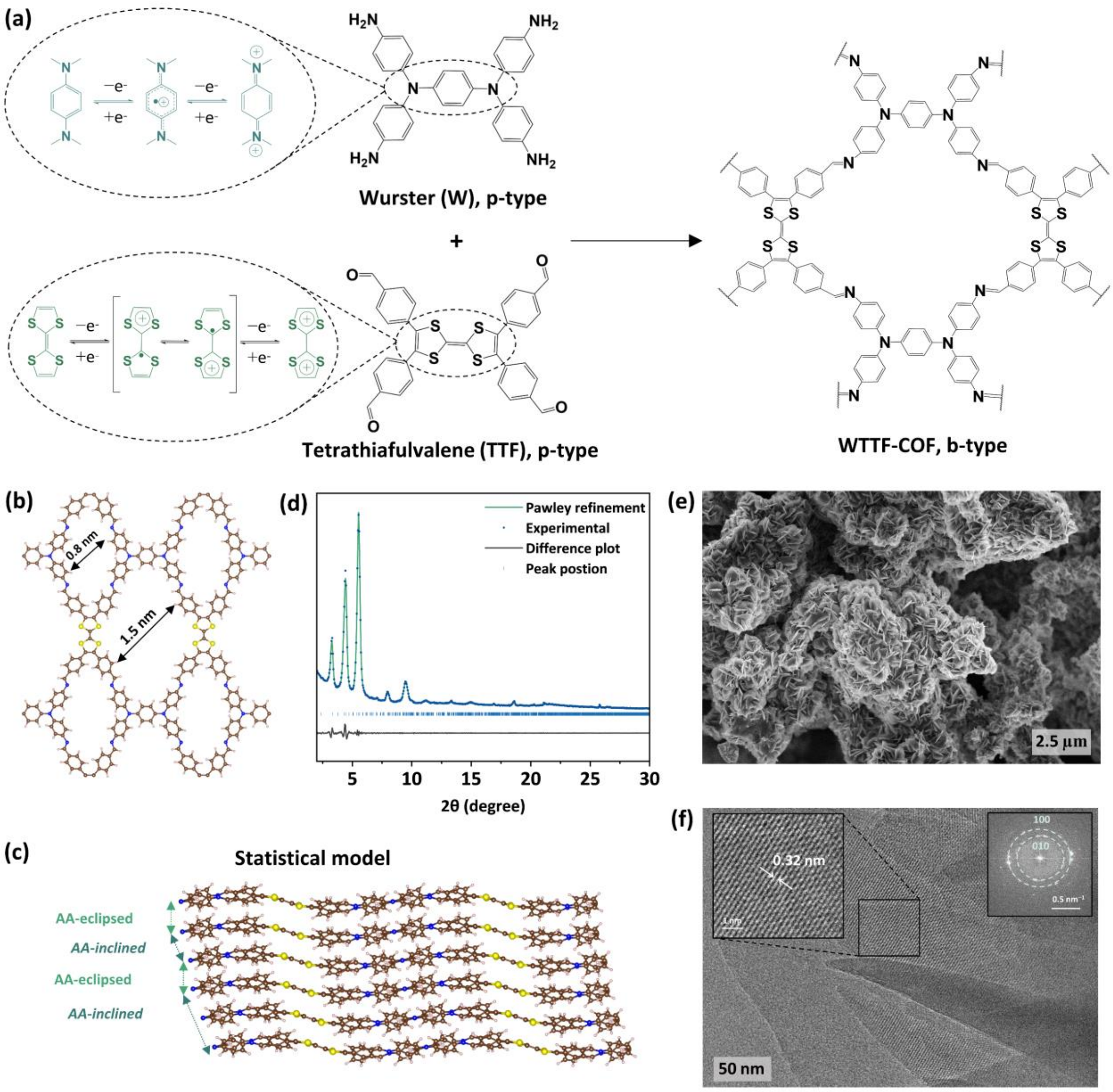

Figure 4.1 Synthetic scheme and structural characterization. (a) Schematic representation of the synthesis of **WTTF**-COF utilizing monomers **W** and **TTF** along with their redox features. (b) Simulated structure of **WTTF**-COF with a view displayed along the z-direction (first layer) displaying the pore topology, (c) view along the x-direction showing the random pi-pi stacking and (d) corresponding experimental and Pawley refined PXRD pattern. (e) SEM and (f) TEM images of the bulk **WTTF**-COF.

synthetic air flow at a heating rate of 10°C per min, indicating stability of the COF under these dynamic conditions of up to 350 °C.

To determine the band gap of the COF, the optical properties were investigated through UV-vis spectroscopy (**Figure 4.2a**).[56] A strong absorption onset corresponding to the S_1 excitation starting from 720 nm was observed for **WTTF**-COF. Further, Tauc plot analysis revealed a direct band gap of ~1.85 eV for the pristine COF. Cyclic voltammetry was performed to examine the oxidation onset to identify the highest occupied molecular orbital (HOMO) and the lowest unoccupied molecular orbital (LUMO) energy level of the conjugated COF system (Figure 4.19, Section 4.6.3, Appendix). As a result, a HOMO of -5.28 eV and a LUMO of -3.43 eV relative to the vacuum level was calculated for the COF by calibrating against Fc/Fc^+ (**Figure 4.2b**). To gain further insight into the electronic properties of **WTTF**-COF, the band structure was obtained (**Figure 4.2c**) for 1-layer AA-inclined stacking model using density functional theory (DFT) calculations.[57] The conduction band minimum (CBM) and the valence band maximum (VBM) are located at the X and Z points, respectively. The band structure revealed that the VB and CB exhibit relatively flat dispersion in the xy-plane, as evidenced by the band structure traversing the Γ to X to S to Y paths. This suggests that the charge carrier mobility in the xy-plane of the COF is relatively low. In contrast, the situation differs in the z-direction (Γ-Z), where, due to interlayer orbital interactions, a notable band dispersion is observed in the vertical direction of the layers. This results in enhanced predicted electronic mobility between the layers due to π-π interactions between the layers. Additionally, the charge density distribution indicates that the CB is attributed to the imine linkage, exhibiting a pronounced charge delocalization around it, and the VB contains **TTF** and **W** contributions, thereby producing p-type redox active centers, as evidenced by the charge localization observed in **Figure 4.2d**. Similar observations can be derived from the frontier orbitals of **WTTF**-COF fragment (Figure S20, Section 4.6.3, Appendix).

4.3.2. Electrochemical Characterization

To validate the functionality of the **WTTF**-COF as a bipolar-type electrode for Li-ion batteries, **WTTF**-based electrodes were prepared. Here, **WTTF**-COF served as the active material (60 wt.%), complemented by ketjen black (20 wt.%) as the carbon additive and polyvinylidene fluoride (PVDF) (20 wt.%) as the binder. These constituents were thoroughly mixed to form a homogeneous slurry using *N*-methyl-2-pyrrolidone (NMP) as the solvent. Copper (Cu) foil was selected as the current collector due to its stability across abroad potential range versus lithium metal.[58] SEM analysis revealed the presence of small particles of ketjen black conductive carbon (~50 nm) dispersed throughout, as well as the coral-like morphology with intergrown flakes of **WTTF**-COF that remained intact after slurry preparation (Figure 4.21, Section 4.6.3, Appendix) and prior to electrochemical testing. To determine the electrochemical performance of the bipolar-type electrode in Li-ion batteries, half-cells were fabricated inside an argon filled glovebox. Lithium foil was utilized as counter (CE) and reference electrode (RE), **WTTF** (coated on Cu-foil) was used a working electrode (WE) and 1 м $LiPF_6$ in ethylene carbonate (EC): diethyl carbonate (DEC) (1:1 v/v%) was used as the liquid electrolyte (Figure 4.22, Section 4.6.3, Appendix). The resulting electrochemical cells exhibited an open circuit voltage (OCV) of about 2.7 V vs. Li/Li^+.

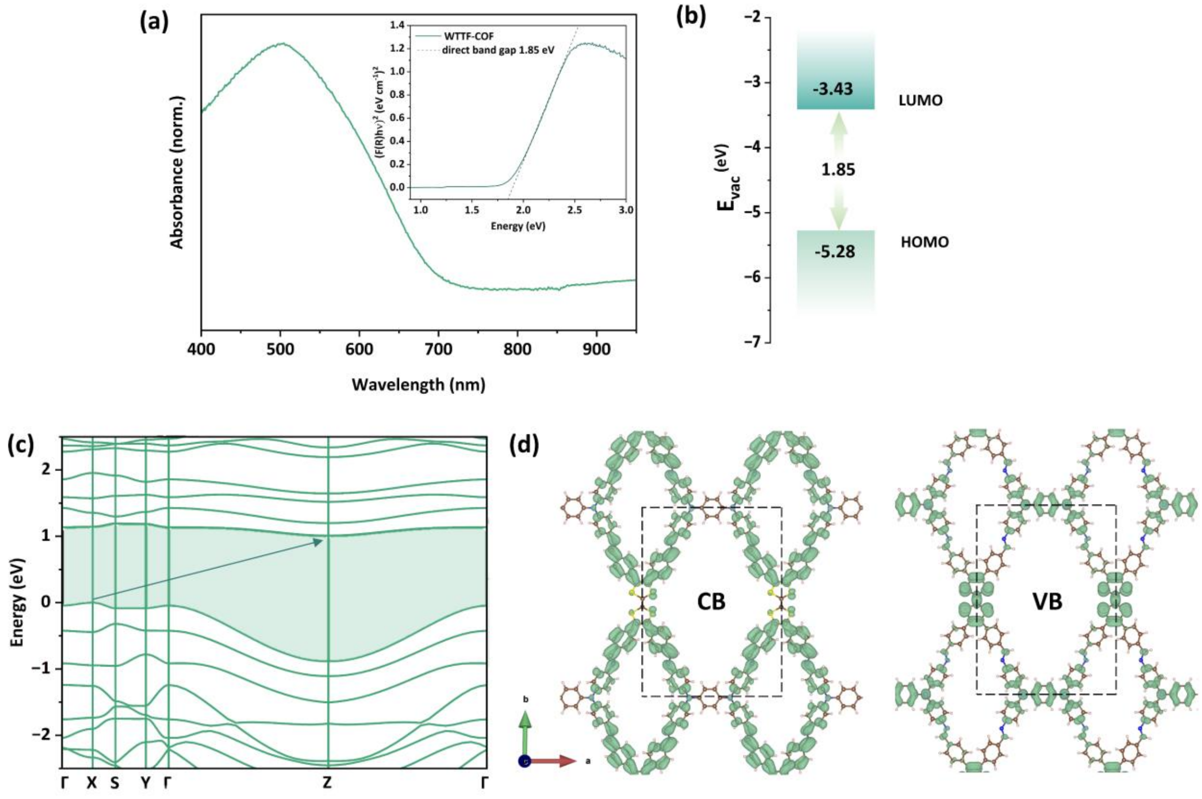

Figure 4.2 Optoelectronic features and electrochemical parameters. (a) Normalized UV-vis absorbance spectra and the associated Tauc plot for direct band gap calculation of WTTF-COF. (b) Calculated energy positions of highest occupied molecular orbital (HOMO) and lowest unoccupied molecular orbital (LUMO) of **WTTF**-COF. (c) HSE06 band structure of inclined-AA stacked **WTTF**-COF and (d) corresponding charge density distribution at the conduction band (CB) and the valence band (VB) (isosurface value = 0.0025 e.$Å^{-3}$).

Initially, cyclic voltammetry measurements were conducted at a slow scan rate of 0.1 mV s^{-1} to ascertain the stable working potential range of **WTTF** as an electrode against Li/Li^+ (Figure 4.23a,b, Section 4.6.3, Appendix). The cyclic voltammetry analysis of the half-cells delineated a stable an wide potential range of 0.1-3.6 V vs. Li/Li^+, and showed multiple reversible redox processes: During the *first cathodic cycle*, a reduction of the electrolyte was observed at approximately 1.02 V vs. Li/Li^+, accompanied by irreversible Li^+ intercalation into the carbon additive starting for voltages below 0.6 V vs. Li/Li^+ (Figure 4.23, Section 4.6.3, Appendix).[59] Additionally, the anodic scan revealed the onset of oxidation around 2.6 V vs. Li/Li^+, and during the reverse scan, a prominent reversible reduction peak at 3.3 V vs. Li/Li^+ can be observed. In the *2nd and subsequent cycles*, the reduction peak for the electrolyte degradation disappeared and a stable cycling is established over the range of 0.2 to 3.3 V for the **WTTF**. This may be indicative for the formation of a uniform solid electrolyte interphase (SEI) layer. Furthermore, electrochemical impedance spectroscopy (EIS) was conducted on a three-electrode system, where **WTTF** was used as WE, lithium foil as CE, and lithium ring as RE (as presented in Figure 4.24a, Section 4.6.3, Appendix), before and after initial 3 cycles at 0.1 mV s^{-1}. EIS analysis was performed over the frequency range of 0.1 - 10^6 Hz with an applied perturbation voltage of 10 mV at OCV as: WE vs. CE, WE vs. RE, and CE vs. RE, to deconvolute the total impedance (WE vs. CE) into impedances due to WE and CE, respectively (Figure 4.24b,c,d, Section 4.6.3, Appendix).[60] In the low frequency region, the Nyquist plots feature semi-finite diffusion characteristics for WE vs. RE and WE vs. CE, while for CE vs. RE show an inductive behavior. Further, the observed decrease in overall (WE vs. CE) charge transfer resistance (R_{ct}) after cycling can be attributed to reduced R_{ct} values in both WE vs. RE and CE vs. RE measurements (Figure 4.24, Section 4.6.3, Appendix). This decrease in R_{ct} could be due to efficient SEI layer formation on both WE and CE,[61,62] surface exfoliation of the lithium foil (for decrease at CE),[61] and/or enhancement of ion transport through improved electrolyte penetration into the porous COF electrode with cycling (for decrease at WE).[63]

Galvanostatic charge-discharge measurements were executed with cells comprising WTTF | 1 м $LiPF_6$ EC:DEC (1:1, v/v%) | Li at various current densities ranging from 0.1 to 5 A g^{-1} to evaluate the performance of the COF-based electrodes (**Figure 4.3a**). In addition to showing the overall performance of the battery, galvanostatic curves provide significant information regarding the charge transfer processes. For instance, in a battery-like electrode material, charge storage is primarily governed by ion intercalation or phase change reactions, typically demonstrating relatively flat plateaus or regions where the voltage remains constant for significant portions of the charge or discharge process. On the other hand, capacitor-like electrodes show a linear dependence of capacity with respect to potential due to the fast surface ion-adsorption reactions.[11] Pseudocapacitive materials feature more gradual, often sloping curves without distinct plateaus caused by the dominance of fast and reversible faradaic surface-redox/intercalation reactions.[6,11] The galvanostatic charge-discharge measurements of the **WTTF** electrode revealed pseudolinear or hysteresis relations between the obtained specific capacity and the scanned voltage range of 0.1-3.6 V vs. Li/Li^+ at all measured current densities. The first discharge cycle (OCV to 0.1 V vs. Li/Li^+) at 0.1 A g^{-1}) resulted in a specific capacity of 380 mAh g^{-1}, while the following charging cycle (0.1 to 3.6 V vs. Li/Li^+) showed a lower specific capacity of 275 mAh g^{-1}, indicating the capacity for the material and cell geometry after stabilization (Figure 4.25, Section 4.6.3, Appendix). The galvanostatic (dis-)charge profiles exhibit a slight hysteresis at various current densities. While this behavior is undesired, it is not uncommon for pseudocapacitive materials, and becomes more pronounced as the material transitions toward battery-like characteristics.[6,64] Further, the galvanostatic (dis-)charge measurements established reversible charge-storage behavior of **WTTF**, providing impressive reversible specific capacities of 275, 242, 200, 157, 132, 86, and 66 mAh g^{-1} at the applied current densities of 0.1, 0.3, 0.5, 0.7, 1.0, 3.0, and 5.0 A g^{-1}, respectively. Thereafter, decreasing the current density to 0.1 A g^{-1}, the electrochemical cell exhibited a specific capacity of 271 mAh g^{-1} (**Figure 4.3b**). Moreover, after the first 5 cycles, stable and high Coulombic efficiencies of ~99 ± 1 % could be measured. The PXRD pattern of the cycled **WTTF**-electrode revealed a slight decrease in peak intensities as compared to the pre-cycled electrode, which may reflect some loss of material. However, the characteristic peaks remain discernible and maintain their peak width, indicating retention of the crystalline framework and the crystalline domain size. (Figure 4.26, Section 4.6.3, Appendix). Further, the SEM images of the cycled electrode exhibit the similar coral morphology with intergrown flakes of **WTTF**-COF with blunter edges, probably resulting from surface electrochemical reactions (Figure 4.27, Section 4.6.3, Appendix).

A typical pseudocapacitive electrode material is able to store charge at elevated rates, therefore, to evaluate the cycling time with respect to current densities, the galvanostatic cycling measurements were further analyzed (**Figure 4.3c**). The half-cell utilizing the **WTTF** bipolar-type electrode was able to complete one full cycle within 48, 15.8, 3.4, and 1.5 mins at employed current flux of 0.5, 1.0, 3.0, and 5.0 A g^{-1}, respectively. To confirm the cycling stability of the bipolar-type electrode, galvanostatic long-term cycling was conducted at a high current density of 1.0 A g^{-1} (**Figure 4.3d**). During cycling at such a high current density, the electrochemical cell utilizing **WTTF** as working electrode experienced a dip in specific capacity, and thereafter an increase with stable cycling retaining a coulombic efficiency of ~99 ± 1 % until 350 cycles. This temporal behavior has been previously reported for porous electrodes during initial cycles as the electrode may undergo surface and structural modifications, such as electrolyte degradation.[65] Moreover, at higher current densities, rapid kinetics can initially limit ion access to the COF pores, however, with continued cycling, improved electrolyte penetration along with structural relaxation may contribute to the observed capacity recovery.[66] To the best of our knowledge, our electrochemical cells employing **WTTF** as the electrode exhibit the highest stable potential window and one of the highest specific capacities recorded for a COF-based bipolar-type system without the inclusion of CNT as additive (**Figure 4.3e**, Table 4.4, Section 4.6.3, Appendix).[37,47–51]

Charge storage in organic electrodes adorned with redox moieties unfolds through several mechanisms, predominantly driven by Faradaic processes and pseudocapacitive behavior.[10,27] Organic electrodes rely on redox reactions, wherein charge carriers traverse between the electrode and the electrolyte, effectuating the oxidation (p-type) and reduction (n-type) of the redox-active sites within the organic matrix.[19] Organic electrodes, such as redox-active polymers or COFs, can exhibit remarkable pseudocapacitive behavior due to the rapid and reversible redox reactions occurring at the electrode surface, thereby contributing to an exceptional power density and notable cycling stability.[67] In Wurster's blue and tetrathiafulvalene molecular fragments, the stabilization of radical species formed during the redox processes facilitates the rapid and efficient charge transfer. Therefore, the design of the molecular architecture of **WTTF**-COF through the combination of **W-** and **TTF-**derived building blocks offers an opportunity to investigate the charge-storage dynamics.

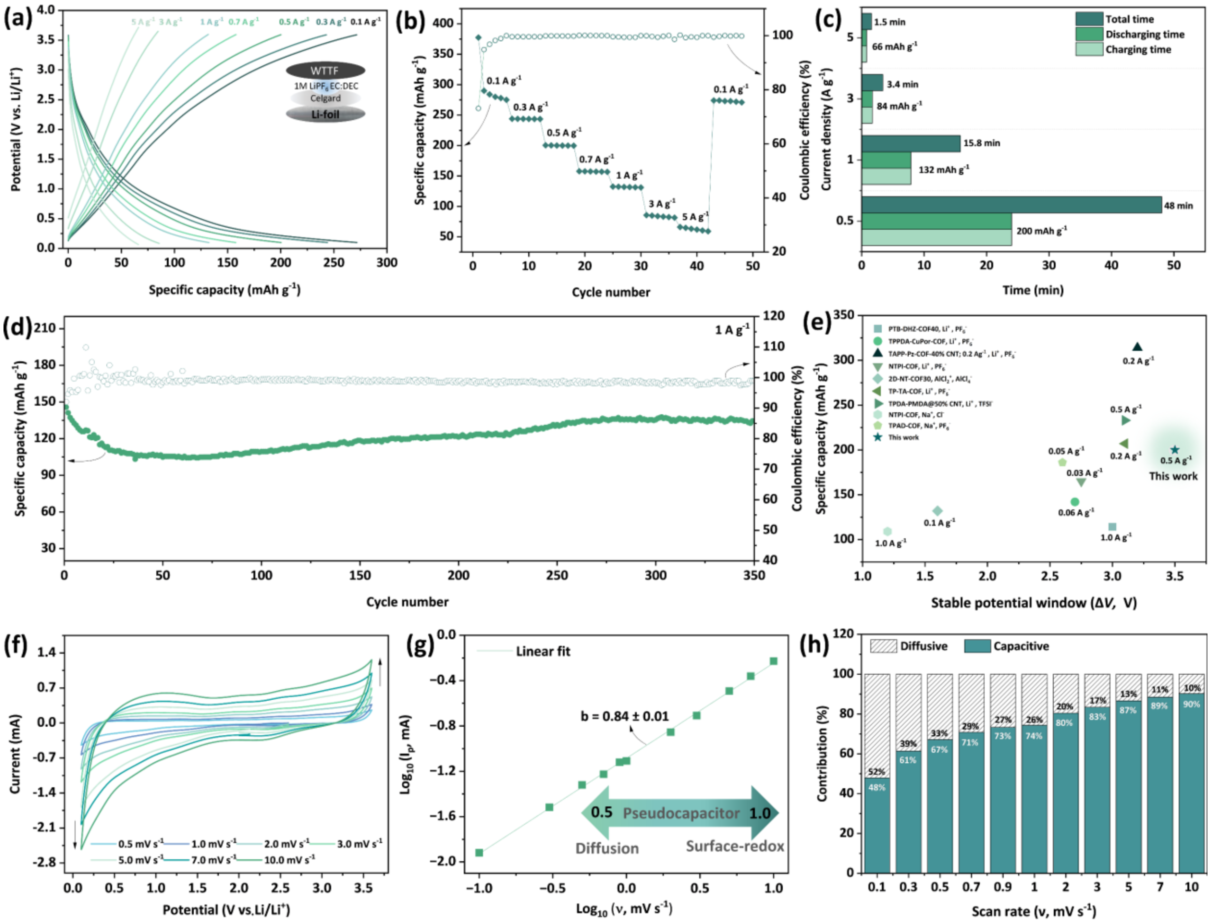

Figure 4.3 (a) Galvanostatic charge-discharge profiles of WTTF as cathode in a Li-ion half-cell using 1 M $LiPF_6$ EC:DEC (1:1, v/v%) as electrolyte at various current densities, scanned between 0.1-3.6 V vs. Li/Li^+, with half-cell configuration in inset. The 5th cycle is presented at every applied current density. (b) The obtained specific capacities (mAh g^{-1}) and corresponding coulombic efficiencies (%) at applied current densities ranging between 0.1-5.0 A g^{-1}. (c) The comparative total times required for a full cycle at different applied current densities. (d) Long-term cycling at a current density of 1 A g^{-1} for 350 cycles. (e) Comparison of battery performance of previously reported bipolar-type COF-based electrodes (more information is presented in Table 4.4, Section 4.6.3, Appendix). (f) Cyclic voltammograms at various scanning speeds ranging between 0.5-10.0 mV s^{-1} and scanned over a potential window of 0.1-3.6 V vs. Li/Li^+. (g) A plot between $\log_{10}$ of i_p vs. $\log_{10}$ of ν to derive the b-value for the **WTTF** electrode. (h) The deconvolution of total charge-storage into diffusive and capacitive contributions with respect to the applied scan rate.

To understand the charge-storage mechanism of the bipolar-type **WTTF** electrode, cyclic voltammetry measurements were conducted over the potential window of 0.1-3.6 V vs. Li/Li^{+} at different scan speeds ranging from 0.5-10 mV s^{-1} (**Figure 4.3f**, Figure 4.28a, Section 4.6.3, Appendix). Across all applied rates, the obtained cyclic voltammograms featured a combination of quasi-rectangular (box-like) shape with superimposed reversible redox peaks that appears over the full potential window. The quasi-rectangular CV shape reflects redox processes with a pseudo-capacitive response. To evaluate the kinetics of the Li-ion intercalation processes, we analyze the peak current in scan-rate tests via half-cell tests.

To quantify the capacitive behavior, particularly pseudocapacitive in this instance, the following power law was employed:[6,48]

$$i_p = a\nu^b \qquad \text{(Equation 4.1)}$$

where i_p denotes the measured redox peak current, ν represents the applied scan-rate, and both a and b are adjustable constants. The value of b offers crucial insights into the charge storage mechanism within the cell, for instance, a b-value of 0.5 implies a solid state and generally slow diffusion dependence, while a b-value close to 1 indicates a surface-capacitive controlled and faster kinetic.[6,11] The b-value, derived from the slope of logarithm of i_p vs. logarithm of ν, was determined to be b= 0.84 ± 0.01 for the electrochemical cell WTTF | 1 ᴍ LiPF$_6$ EC:DEC (1:1, v/v%) | Li (**Figure 4.3g**). The high b-value for the **WTTF** electrode is clearly attributed to a high-rate pseudocapacitive charge storage mechanism. Furthermore, Dunn's method was employed to segregate diffusion-dependent processes from redox pseudocapacitive and non-faradaic reactions. The analysis is based on the following equation:[6,68]

$$i(V) = k_1\nu + k_2\nu^{1/2} \qquad \text{(Equation 4.2)}$$

where $i(V)$ is the current response at a specific potential. In this equation, $k_1\nu$ indicates a significant capacitive contribution, and $k_2\nu^{1/2}$ signifies the diffusive contribution.[68] The values of k_1 and k_2 were determined by analyzing the slope and intercept of the plot of $i(V)/\nu^{1/2}$ and $\nu^{1/2}$, respectively (Figure 4.28b, Section 4.6.3, Appendix). For the half-cells employing **WTTF** as working electrode, a predicted increase in capacitive contribution was observed with an increase in scan-rate (ν): At a slow scanning speed of 0.1 mV s^{-1}, the electrode exhibited a higher diffusion-controlled charge-storage contribution of almost 52%, while at a higher rate of 10 mV s^{-1}, the cells demonstrated 90% capacitive/pseudocapacitive contribution to the total charge-storage dynamics (**Figure 4.3h**). These findings show that significant specific capacities can be achieved at high current densities, confirming the capability of the **WTTF**-based electrode in maintaining swift charge storage, driven by the high-rate redox kinetics of the incorporated building units.

4.3.3. Redox mechanism

To unveil the dual-ion storage mechanism in the **WTTF** electrode for Li-ion batteries, firstly, a molecular electrostatic potential (MESP) analysis was performed on the asymmetric molecular fragments of the COF (**Figure 4.4a,b**). In the reduced state [WTTF]$^{-4}$, the negative potential (red colored region) was localized on the imine nitrogens, establishing the imine linkage as a favorable site for Li-ion binding during discharge of the battery.

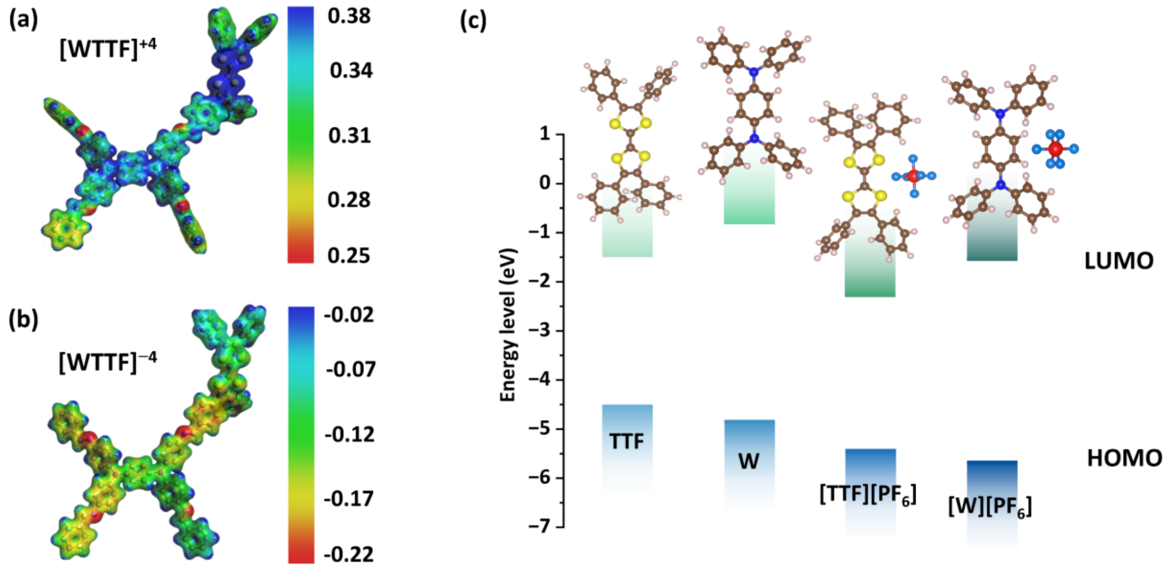

Figure 4.4 Electrostatic surface potential plots of (a) [WTTF]$^{+4}$ and (b) [WTTF]$^{-4}$ molecular fragments. The color bar corresponds to the minimum and maximum value of the Coulomb potential (a.u.). The positive and negative potentials are depicted by blue and red colors, respectively. All MESP plots are drawn with an isosurface value of 0.03. (c) Comparison of HOMO-LUMO gaps of TTF and W fragments for PF_6^- anion binding.

Whereas, in the oxidized state [WTTF]$^{+4}$, positive potential (blue colored region) accumulated on **TTF** and **W** centers, confirming the p-type nodes as PF_6^- anion binding sites during the charging process. Further, to identify the initial binding of PF_6^- anion to **WTTF** at the **TTF** and **W**-sites, the reducing abilities of individual **TTF-** and **W**-nodes were compared based on the HOMO-LUMO energy levels (**Figure 4.4c**). The higher HOMO energy of the **TTF**-node indicated easier oxidization than the **W**-node, suggesting binding of first PF_6^- anions to the **TTF**-sites. Following this rationale, the second PF_6^- anion was observed to bind to the **W**-site rather than to [TTF][PF_6]. This information was used in the unit cell of periodic **WTTF** to study the binding energy of the first PF_6^- anion, which was obtained to be -4.06 eV. For Li^+ ion, the most favorable binding site at the imine nitrogen exhibited a binding energy of -0.66 eV as shown in Figure 4.29, Section 4.6.4, Appendix. Additionally, Li^+ ions showed a preference for binding to the phenyl rings of the **TTF** unit, with a binding energy of -0.15 eV. In contrast, Li^+ binding to the phenyl rings of the **W** unit was found to be unstable.

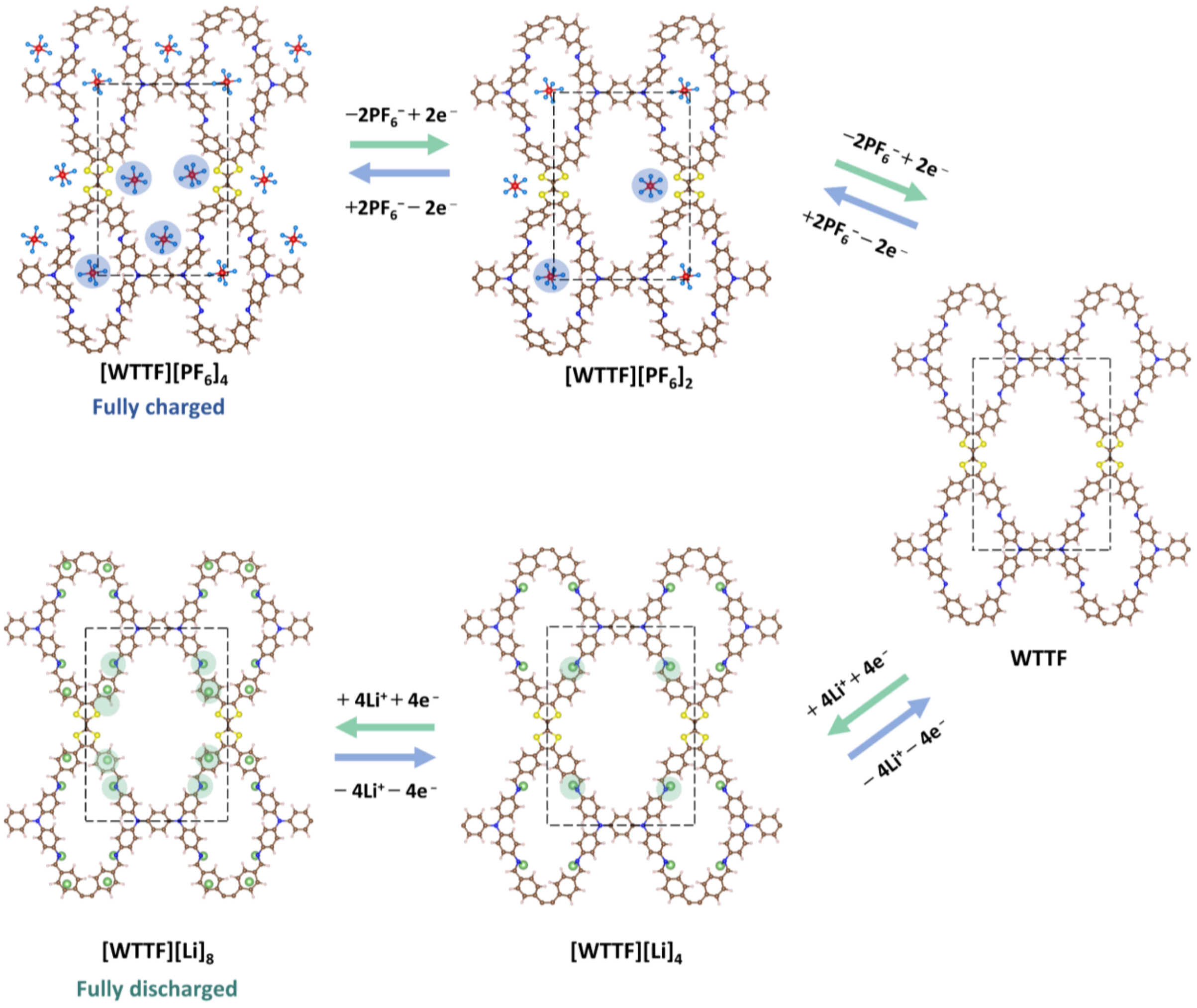

Figure 4.5 Schematic representation of proposed charge-discharge mechanism of bipolar-type WTTF-COF electrode.

The charge-discharge mechanism of **WTTF** was thoroughly examined, as depicted in **Figure 4.5**, 4.30, 4.31, Section 4.6.4, Appendix. Theoretically, the total electron storage number per unit cell during the complete charge-discharge process is 12 (considering charge transfer in both directions). In the fully charged (oxidized) state, **WTTF** binds four PF_6^- anions (two PF_6^- anions at both the **W** and **TTF** centers), forming $[WTTF][PF_6]_4$ with a net binding energy of -3.94 eV per PF_6^- per unit cell. Upon initiating the discharge process, $[WTTF][PF_6]_4$ reduces to $[WTTF][PF_6]_2$ by losing one PF_6^- anion from each site (**W** and **TTF**), with a binding energy of −3.99 eV per PF_6^- anion. Further reduction leads to the formation of [WTTF], followed by lithiation upon further reduction of the COF, forming the lithiated discharge state $[WTTF][Li]_4$, where Li^+ ions bind to four imine nitrogen atoms with a binding energy of −0.67 eV per Li. As discharging continues, Li^+ ions intercalate into the interlayer spaces of **WTTF**, as shown in

Figure 4.30, Section 4.6.4, Appendix. The final discharge state, [WTTF][Li]$_8$, occurs with a binding energy of -0.48 eV per Li$^+$, corresponding to the intercalation of four Li$^+$ ions between the phenyl groups of the **TTF** units. Further lithiation of **WTTF** leads to thermodynamic instability with a positive binding energy. The theoretical maximum capacity is calculated to be 315 mAh g^{-1}, closely aligning with the experimental capacity of 271 mAh g^{-1} at a current density of 0.1 A g^{-1}.

To further elucidate the cycling mechanism, ex-situ FTIR spectroscopy was performed on the WTTF bare electrode, after being fully discharged to 0.1 V and fully charged to 3.6 V vs. Li/Li$^+$ (Figure 4.32, Section 4.6.4, Appendix). At 0.1 V, the C=N stretching vibration broadens around 1625 cm^{-1}, which could attribute towards lithium interactions with the imine linkage. Upon charging to 3.6 V, the absorption peak at this wavenumber weakened, indicating a reversible redox reaction at the imine linkage. Additionally, a new absorbance signal emerged at 842 cm^{-1} at 3.6 V, corresponding to the (asymmetric) stretching vibration of the PF_6^- anion.

4.3.4. Charge-storage kinetics

To gain an understanding of the mechanisms governing electrochemical processes in **WTTF**-based cells, EIS measurements were conducted by applying an AC perturbation signal superimposed over DC bias between different potentials vs. Li/Li$^+$ to mimic the (dis-)charge process, and correlating the impedance changes to the specific stages of operation.[62] Initially, the electrochemical cell WTTF | 1 M LiPF$_6$ EC:DEC (1:1, v/v%) | Li underwent galvanostatic charge-discharge at a current density of 0.1 A g^{-1} for 3 cycles to establish a SEI layer. Thereafter, the **WTTF**-based half-cells were subjected to 300 cycles of charge-discharge at a constant current of 1.0 A g^{-1} to establish an aged/stable system. From a completely discharged state (potential at 0.1 V vs. Li/Li$^+$), EIS measurements were then subsequently conducted between the applied positive sweep-steps between a potential range of 0.1- 3.6 V vs. Li/Li$^+$ (and negative sweep-steps between 3.6- 0.1 V Li/Li$^+$), and the impedance was measured at n steps with n = 42 (**Figure 4.6a**,**b**, 4.33, Section 4.6.5, Appendix). The impedance spectrum at the different potential steps was analyzed by fitting the obtained Nyquist plots to an equivalent electric circuit (ECC) to determine the resistances experienced during individual processes occurring at specific frequency ranges (refer to Figure 4.34, Table 4.5, Section 4.6.5, Appendix).[69–72]

Furthermore, the resistance values due to the SEI layer (R_{SEI}) and charge transfer (R_{ct}) with respect to the potential during charging and discharging cycles were investigated. As expected, the R_{SEI}, ranging between ~ 16.0 - 54.0 Ω, was lower than the overall R_{ct}, ranging between ~70.0 - 180 Ω at all the measured potentials during positive (charge cycle) as well as negative sweep (discharge cycle) of the cell.[71] The half-cell utilizing **WTTF** as bipolar electrode experienced an increase in the R_{SEI} and the R_{ct} with an increase in potential during charging cycles. While, during the discharging cycle, a decrease in overall impedance was observed with decrease in potential. This behavior might be attributed to the faster diffusion of Li^+ in comparison to the larger PF_6^- anion.

To further analyze the obtained Nyquist plots, a semi-infinite straight line transitioning at 45° at low frequency denoting the Warburg component was characterized. The presence of Warburg impedance in an EIS spectrum indicates diffusion as a limiting factor in the electrochemical reaction. Therefore, by analyzing the low-frequency region of the spectrum, the kinetic limitations on the basis of diffusion coefficient can be understood for electrochemical cells using the **WTTF** electrode. To do so, the diffusion coefficient (D) of the charge-carriers with respect to potential vs. Li/Li^+ for the electrochemical cell WTTF | 1 M $LiPF_6$ EC:DEC (1:1, v/v%) | Li was calculated using the following equation:[73–75]

$$D = \frac{R^2T^2}{2n^4F^4C^2A^2\sigma^2} \qquad \text{(Equation 4.3)}$$

where R is the gas constant (8.314 J K^{-1} mol^{-1}), T is the operational temperature of the electrochemical cell (298 K), n is the number of electrons transferred from electrolyte to the electrode ($n = 1$), F is Faraday's constant (96458 C mol^{-1}), C is the concentration of the charge carriers in the electrolyte solution (1 M), A is the surface area of the electrode (2.54 cm^2), and σ is the Warburg coefficient ($\Omega\ s^{-1/2}$), respectively. The Warburg coefficient (σ) could be obtained from the slope of Warburg plots (Z_{re} vs. $\omega^{-1/2}$) at individual step potentials during cycling (Figure 4.35-4.38, Section 4.6.5, Appendix). The following equation was utilized to graph the Warburg plots:[73]

$$Z_{re} = R_T + \sigma\omega^{-1/2} \qquad \text{(Equation 4.4)}$$

where, Z_{re} is the real component of impedance, R_T is the total resistance, and ω is the angular frequency, respectively. The characteristic region of the Warburg impedance is the low- frequency domain, and therefore Z_{re} associated with low frequency was considered while creating the Warburg plots.[71,73] The relation between the calculated Warburg coefficient and potential vs. Li/Li^+ is presented in the Figure 4.38, Section 4.6.5, Appendix. The diffusion coefficient at every potential step was then calculated by employing eq (3) (Table 4.6, Section 4.6.5, Appendix). The effective diffusion coefficient (D) was determined to be in the range between 1.81×10^{-10} to 9.87×10^{-13} $cm^2\ s^{-1}$ within the potential window of 0.1- 3.6 V vs Li/Li^+ for the electrochemical cell WTTF | 1 M LiPF6 EC:DEC (1:1, v/v%) | Li during positive and negative sweep (**Figure 4.6e**).

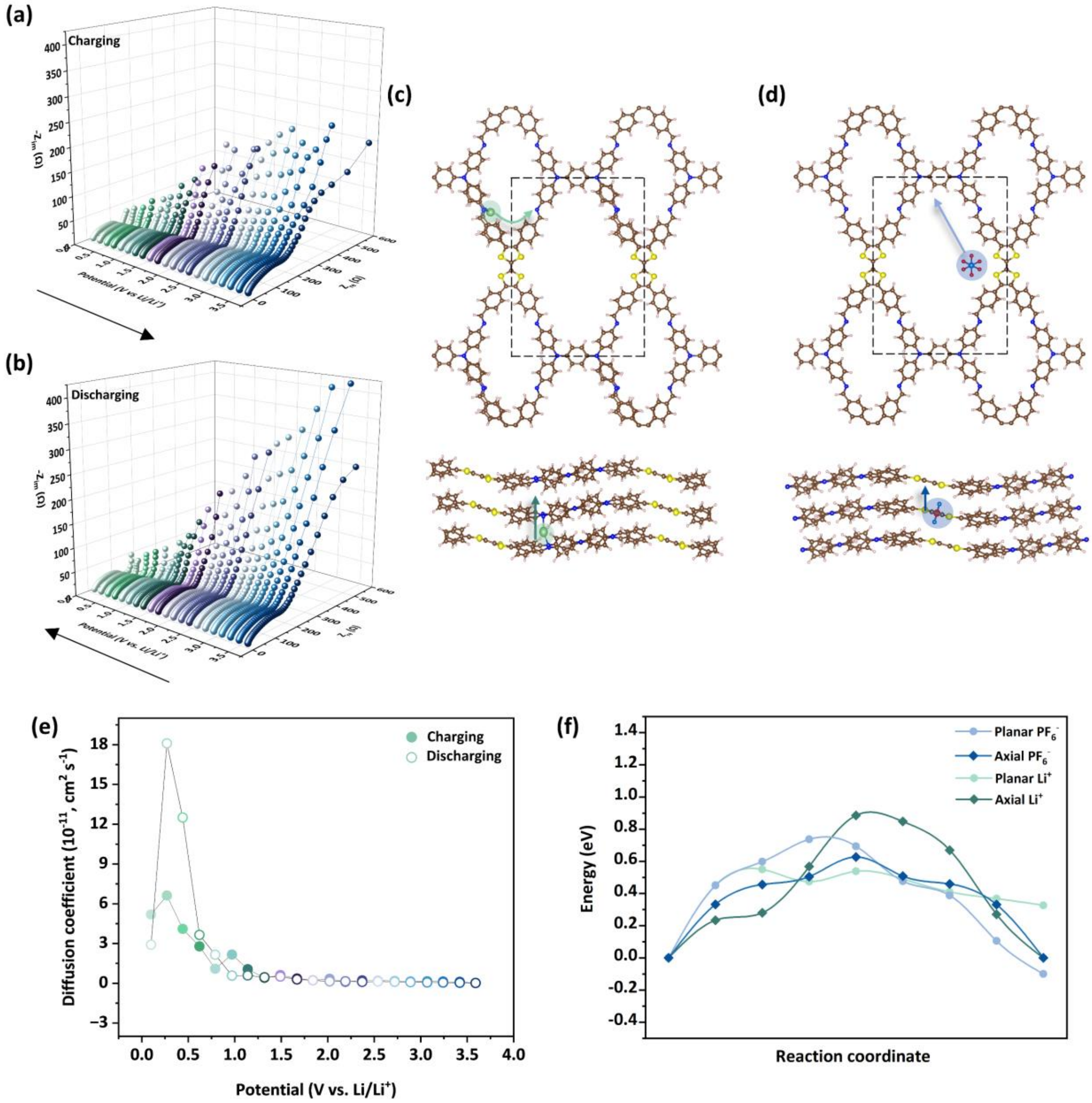

Figure 4.6 Determination of the diffusion coefficient. Potential-dependent electrochemical impedance spectrum for half-cells WTTF | 1 M $LiPF_6$ EC:DEC (1:1, v/v%) | Li during (a) charging and (b) discharging cycles over the potential window of 0.1-3.6 V vs. Li/Li^+ with impedance measured at n number of steps with n = 42, and (e) the corresponding calculated diffusion coefficient (D). Diffusion pathways along with the transition states for (c) Li^+ cations and (d) PF_6^- anions on **WTTF**-COF, and (f) the associated energy barrier plots.

An inverse relation between the Warburg coefficient and the diffusion coefficient can be identified since the Warburg component signifies slow diffusion processes. Further, the lower potential region between 1.0 - 0.1 V vs. Li/Li^+ experienced faster diffusion and a lower Warburg coefficient during charge as well as discharge cycles. During the discharging cycle (negative sweep from 3.6-0.1 V vs. Li/Li^+), at ~0.4 V (n-type region) a diffusion coefficient (D) as high as 1.81×10^{-10} cm^2 s^{-1} could be observed (Figure 4.40, Section 4.6.5, Appendix). In contrast, in the p-type region the diffusion coefficient is much smaller ~1.28 × 10^{-12} cm^2 s^{-1}. The surge in diffusion coefficient at lower potentials aligns with the pseudocapacitive behavior as stated in the Dunn analysis. Furthermore, these finding are in line with the elevated values of R_{ct} at the higher potential region vs. the reference electrode, which indicates more efficient diffusion of Li^+ as charge carriers than PF_6^-, probably due to its smaller size or better permeability through the SEI layer**.**

To analyze the diffusion of Li^+ ions and PF_6^- anions, minimum energy pathways were calculated for both ions on **WTTF**-COF using the nudged elastic band (NEB) method.[76] Two diffusion pathways, representing axial and in-plane diffusion for both Li^+ and PF_6^- ions were examined, as illustrated in **Figure 6c**,**d**. During axial diffusion, Li^+ and PF_6^- ions diffuse from one interlayer space/layer site to an adjacent interlayer space/layer site, moving perpendicular to the COF surface. During in-plane diffusion, Li^+ ions migrate from one imine nitrogen to a neighboring imine nitrogen by passing through the **TTF**-unit, whereas PF_6^- anions migrate from the **TTF**-site to the **W**-site. The Li^+ ions and PF_6^- anions exhibit opposite preferences for their most favorable diffusion pathways. The in-plane pathway on the interlayer surface of **WTTF**-COF was preferred for Li^+ diffusion with an energy barrier of 0.55 eV, compared to the axial diffusion barrier of 0.88 eV (**Figure 4.6f**). In contrast, the larger size of PF_6^- anions restricts diffusion through interlayer spaces, resulting in a relatively higher in-plane energy barrier of 0.74 eV compared to the smoother axial diffusion with an energy barrier of 0.63 eV. The relatively elevated barriers may be attributable to the execution of the calculation in the gas phase, excluding solvation or dynamic effects due to computational constraints. Nevertheless, the observed trend exhibits congruence with the outcomes of experimental studies. Overall, the highest theoretical diffusion coefficient for Li ions was obtained to be 2.8 × 10^{-11} cm^2 s^{-1}, which is higher than that for PF_6^- anions at 4.13 × 10^{-13} cm^2 s^{-1}, indicating faster diffusion of Li^+ ions compared to PF_6^- anions, which is consistent with the experimental findings. Moreover, the contrasting diffusion preferences of cations and anions underscore the critical role of both rapid redox kinetics of the structural units and the long-range ordered framework of the COF in attaining superior surface-redox and intercalation pseudocapacitive charge-storage.

4.3.5. Symmetric cell

Symmetric cells, wherein both electrodes are composed of identical materials, have long served as a pivotal instrument in battery research. This configuration offers a straightforward approach for examining the intrinsic properties and performance metrics of electrode and electrolyte materials.[29,33,77] Given the hybrid redox mechanism inherent to the **WTTF** bipolar-type electrode, it becomes particularly intriguing to investigate whether the **WTTF**-COF can be effectively employed as a dual-functioning electrode within a symmetric cell configuration. Firstly, the dQ/dV method was employed to identify the most electrochemically active region of the **WTTF** electrode, thereby establishing its stable operating potential window relative to Li/Li$^+$ (Figure 4.41, Section 4.6.6, Appendix).[77] A potential window spanning 0.2 - 3.4 V vs Li/Li$^+$ was selected to mitigate the risk of side reactions and electrode degradation in a symmetric cell. Further, to construct a symmetric cell employing the **WTTF** electrode as both anode and cathode, two distinct half-cells were initially fabricated with the configuration WTTF | 1 м $LiPF_6$ EC:DEC (1:1, v/v%) | Li. The individual half-cells were subjected to galvanostatic cycling to condition one cell to a completely charged state intercalating PF_6^- in **WTTF** (cycled up to 3.6 V vs. Li/Li$^+$; named WTTF@PF_6^-) and another cell to a completely discharged state intercalating Li$^+$ in **WTTF** (cycled down to 0.1 V vs Li/Li$^+$; named WTTF@Li$^+$). This approach minimizes the uptake of Li$^+$ during electrolyte reduction and ensures an OCV ~2.2 V between both the electrodes. Subsequently, the two respective electrodes were utilized to assemble a symmetric cell with an electrochemical cell configuration of WTTF@Li | 1 м 1$LiPF_6$ EC:DEC (1:1, v/v) | WTTF@PF_6, incorporating a Li-ring as the reference electrode (**Figure 4.7a**,**b**).

Cyclic voltammetry was performed at a scan speed of 1 mV s^{-1} for three cycles over the desired potential window of 0.2 - 3.4 V vs. Li/Li$^+$ (Figure 4.42, Section 4.6.6, Appendix). After ascertaining the stable potential range, CV was conducted at elevated scan speeds from 1.0- 200 mV s^{-1} (**Figure 4.7c**, 4.43, Section 4.6.6, Appendix). The obtained voltammograms resemble the cyclic voltammograms of half-cells using **WTTF** as working electrode, but also contain specific characteristics, such as a sharp anodic peak at high scanning rate between 0.2 - 0.3 V vs. Li/Li$^+$. With the elimination of lithium foil as counter electrode, the **WTTF**-electrode was able to sustain the exceptionally high scan speed of 200 mV s^{-1}, establishing the rapid charge-storage kinetics of the bipolar-type electrode.

Further, to investigate the charge-storage dynamics of the symmetric cell utilizing **WTTF-COF**, equation (1) was employed to determine the b-value as the slope of $\log_{10} i_p$ vs. $\log_{10} \nu$ (Figure 4.44, Section 4.6.6, Appendix).[6] The all-organic symmetric cells exhibited a higher b-value of 0.89 than a half-cell using **WTTF** as electrode, indicating faster charge-storage enabled by the exclusion of the lithium metal electrode. The voltammograms were further investigated to delineate the capacitive and diffusive contributions to the total charge storage by employing equation (2). A graph between $i(V)/\nu^{1/2}$ and $\nu^{1/2}$ was analyzed to identify the fractions k_1 and k_2 and to calculate the capacitive and diffusive responses (Figure 4.45, Section 4.6.6, Appendix).[6,68] Strikingly, the symmetric cell exhibited capacitive contributions of 93 - 99% over the scan speeds (ν) ranging between 1.0-40 mV s^{-1}, which are much higher than for the cells utilizing lithium-foil as counter electrode (**Figure 4.7d**).

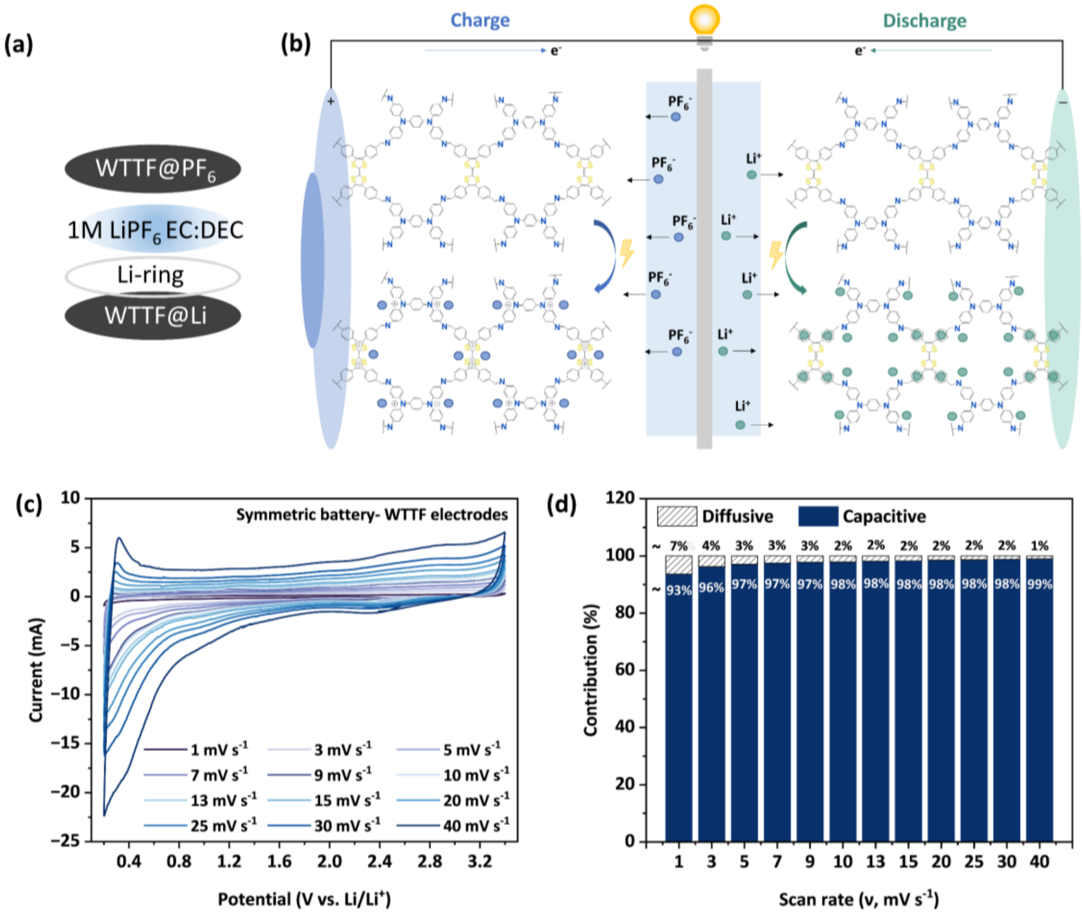

Figure 4.7 Symmetric full cell. (a) Schematic representation of symmetric cell configuration using WTTF@Li as negative electrode and WTTF@PF_6 as positive electrode, a Li-ring as reference electrode and 1 M $LiPF_6$ EC:DEC (1:1, v/v) as electrolyte. (b) Working principle of all-organic symmetric lithium ion battery utilising WTTF electrodes on both sides. (c) Cyclic voltammograms of the symmetric full-cell WTTF@Li | 1 M $LiPF_6$ EC:DEC (1:1, v/v) | WTTF@PF_6 obtained at various scanning speeds ranging between 1.0 - 40.0 mV s^{-1}, scanned over a potential window of 0.2 - 3.4 V vs. Li/Li^+. (d) Deconvolution of total charge-storage in the symmetric cell into diffusive and capacitive contributions with respect to the applied scan rate.

Galvanostatic charge-discharge experiments were conducted to evaluate the charge storage capacity and delivery efficiency of the symmetric cell, as well as to elucidate the kinetics of the all-organic **WTTF**-COF-based symmetric cell. Constant current fluxes of 0.3, 0.5, 0.7 and 1.0 A g^{-1} were applied within a potential range of 0.2 - 3.4 V vs. Li/Li^+ (Figure 4.46, Section 4.6.6, Appendix). The resulting galvanostatic profiles mirrored those of the half-cells, exhibiting a pseudolinear relationship between specific capacity and potential response with a smooth curve representing pseudocapacitive charge-storage behavior in the full cell. In this context, the specific capacities were calculated by employing. the weight of the electrode used as the working electrode (refer to Section 4.6.1, Appendix). The symmetric cell using **WTTF**-electrodes exhibited the specific discharging capacities of 30, 28, 25, and

22 mAh g^{-1} at applied current lower specific charging capacities 26, 24, 19, and 18 mAh g^{-1} were observed at applied current densities of 0.3, 0.5, 0.7 and 1.0 A g^{-1}, respectively. Therefore, the symmetric cell exhibited coulombic efficiencies of 86, 85, 76, and 81% at 0.3, 0.5, 0.7 and 1.0 A g^{-1} applied current fluxes. The low coulombic efficiencies observed can be attributed to electrode spillage, where Li^+ ions undergo parasitic reactions with the electrolyte at the electrode surface, such as electrolyte reduction or degradation. Burns et. al. have studied this phenomenon in symmetric cells utilizing graphite as electrodes.[77] In half-cells with lithium metal as the counter electrode, the abundant availability of Li^+ masks such type of capacity loss. The optimization of electrolyte concentration or the implementation of an artificial SEI coating over the electrode surface would represent a potential avenue for enhancing the efficiency of a symmetric cell. Nonetheless, this pioneering attempt at the construction of a COF-based symmetric Li-ion battery has yielded promising outcomes, as evidenced by the reversible cyclic voltammograms and galvanostatic profiles, which illustrate the viability of **WTTF**-based bipolar-type electrode in a symmetric cell.

4.4. Conclusion

To summarize, we synthesized a highly-crystalline novel 2D **WTTF**-COF by combining redox-active p-type moieties **W** and **TTF** through imine linkages, intended to serve as bipolar-type electrode for all-organic lithium batteries. **WTTF**-COF exhibited inclined stacking behavior and coral-like powder morphology interspersed with intergrown flakes, and features a direct bandgap of 1.85 eV. In Li-ion half-cells, **WTTF** as cathode demonstrated an exceptionally stable potential window of 0.1 - 3.6 V vs. Li/Li^+ and a high reversible specific capacity of 271 mAh g^{-1} at a current density of 0.1 A g^{-1}, along with stable cycling at elevated current density of 1.0 A g^{-1} with a coulombic efficiency of ~99 ± 1% to at least 350 cycles. The **WTTF**-electrode exhibited a surface-redox and intercalation pseudocapacitive charge storage mechanism enabled by the presence of redox-active moieties and tunnel-like nanostructure. Thorough computational studies unveiled the hybrid redox features of the **WTTF**-electrode with the charge storage facilitated by both Li^+ and PF_6^- ions, and resulting in an experimental combined diffusion coefficient (D) ranging between 1.81×10^{-10} to 9.87×10^{-13} cm^2 s^{-1} over the operational potential window. Ultimately, the successful implementation of **WTTF** as a bipolar-type electrode in a symmetric cell paves the way for the development of all-organic symmetric lithium batteries utilizing COFs as both positive and negative electrodes.

4.5. References

[1] H. Zhang, X. Hu, Z. Hu, S. J. Moura, *Nat Rev Electr Eng* **2024**, *1*, 35.

[2] Y. Liu, Y. Zhu, Y. Cui, *Nat Energy* **2019**, *4*, 540.

[3] K. Liu, Y. Liu, D. Lin, A. Pei, Y. Cui, *Science advances* **2018**, *4*, eaas9820.

[4] C. Bauer, S. Burkhardt, N. P. Dasgupta, L. A.-W. Ellingsen, L. L. Gaines, H. Hao, R. Hischier, L. Hu, Y. Huang, J. Janek, C. Liang, H. Li, J. Li, Y. Li, Y.-C. Lu, W. Luo, L. F. Nazar, E. A. Olivetti, J. F. Peters, J. L. M. Rupp, M. Weil, J. F. Whitacre, S. Xu, *Nat Sustain* **2022**, *5*, 176.

[5] A. Kumar, *Energy Storage* **2024**, *6*.

[6] S. Fleischmann, J. B. Mitchell, R. Wang, C. Zhan, D.-E. Jiang, V. Presser, V. Augustyn, *Chemical reviews* **2020**, *120*, 6738.

[7] L. Kong, Y. Zhu, P. J. Williams, M. Kabbani, F. R. Brushett, J. L. M. Rupp, *J. Mater. Chem. A* **2024**, *12*, 4299.

[8] S. S. Cheema, N. Shanker, S.-L. Hsu, J. Schaadt, N. M. Ellis, M. Cook, R. Rastogi, R. C. N. Pilawa-Podgurski, J. Ciston, M. Mohamed, S. Salahuddin, *Nature* **2024**, *629*, 803.

[9] J. Sun, B. Luo, H. Li, *Adv Energy and Sustain Res* **2022**, *3*.

[10] J. M. Rotter, R. Guntermann, M. Auth, A. Mähringer, A. Sperlich, V. Dyakonov, D. D. Medina, T. Bein, *Chemical science* **2020**, *11*, 12843.

[11] C. Choi, D. S. Ashby, D. M. Butts, R. H. DeBlock, Q. Wei, J. Lau, B. Dunn, *Nat Rev Mater* **2020**, *5*, 5.

[12] S. Haldar, A. Schneemann, S. Kaskel, *Journal of the American Chemical Society* **2023**, *145*, 13494.

[13] L. Zhao, T. Wang, F. Zuo, Z. Ju, Y. Li, Q. Li, Y. Zhu, H. Li, G. Yu, *Nature communications* **2024**, *15*, 3778.

[14] X. Wang, L. Qi, H. Wang, *ACS applied materials & interfaces* **2019**, *11*, 30453.

[15] S. Haldar, P. Bhauriyal, A. R. Ramuglia, A. H. Khan, S. de Kock, A. Hazra, V. Bon, D. L. Pastoetter, S. Kirchhoff, L. Shupletsov, A. De, M. A. Isaacs, X. Feng, M. Walter, E. Brunner, I. M. Weidinger, T. Heine, A. Schneemann, S. Kaskel, *Advanced materials (Deerfield Beach, Fla.)* **2023**, *35*, e2210151.

[16] L. Kong, C. Zhang, J. Wang, W. Qiao, L. Ling, D. Long, *ACS nano* **2015**, *9*, 11200.

[17] M. Zukalová, M. Kalbáč, L. Kavan, I. Exnar, M. Graetzel, *Chem. Mater.* **2005**, *17*, 1248.

[18] T. Brezesinski, J. Wang, S. H. Tolbert, B. Dunn, *Nature materials* **2010**, *9*, 146.

[19] Y. Lu, J. Chen, *Nature reviews. Chemistry* **2020**, *4*, 127.

[20] Y. Chen, C. Wang, *Accounts of chemical research* **2020**, *53*, 2636.

[21] A. Banerjee, N. Khossossi, W. Luo, R. Ahuja, *J. Mater. Chem. A* **2022**, *10*, 15215.

[22] M. Mohammadiroudbari, J. Huang, E. Y. Kim, Z. Yang, F. Chen, C. Luo, *J. Mater. Chem. A* **2023**, *11*, 16636.

[23] R. Shi, L. Liu, Y. Lu, C. Wang, Y. Li, L. Li, Z. Yan, J. Chen, *Nature communications* **2020**, *11*, 178.

[24] S. Wu, W. Wang, M. Li, L. Cao, F. Lyu, M. Yang, Z. Wang, Y. Shi, B. Nan, S. Yu, Z. Sun, Y. Liu, Z. Lu, *Nature communications* **2016**, *7*, 13318.

[25] T. Sun, H. Du, S. Zheng, J. Shi, X. Yuan, L. Li, Z. Tao, *Small methods* **2021**, *5*, e2100367.

[26] Y. Cho, D. Jang, J.-J. Park, H. Kye, J. E. Kwon, B.-G. Kim, *ACS Appl. Energy Mater.* **2023**.

[27] X. Feng, X. Wu, X. Chen, J. Yuan, S. Lv, B. Ren, X. Sun, E. Liu, S. Tan, P. Gao, *Energy Storage Materials* **2021**, *42*, 454.

[28] G. Dai, Y. He, Z. Niu, P. He, C. Zhang, Y. Zhao, X. Zhang, H. Zhou, *Angewandte Chemie (International ed. in English)* **2019**, *58*, 9902.

[29] J. Kim, H. Kim, S. Lee, G. Kwon, T. Kang, H. Park, O. Tamwattana, Y. Ko, D. Lee, K. Kang, *J. Mater. Chem. A* **2021**, *9*, 14485.

[30] S. I. Etkind, J. Lopez, Y. G. Zhu, J.-H. Fang, W. J. Ong, Y. Shao-Horn, T. M. Swager, *ACS Sustainable Chem. Eng.* **2022**, *10*, 11739.

[31] C. Peng, F. Wang, Q. Chen, X. Yan, C. Wu, J. Zhang, W. Tang, L. Chen, Y. Wang, J. Mao, S. Dou, Z. Guo, *Adv Funct Materials* **2024**.

[32] L. Zheng, J. Ren, H. Ma, M. Yang, X. Yan, R. Li, Q. Zhao, J. Zhang, H. Fu, X. Pu, M. Hu, J. Yang, *J. Mater. Chem. A* **2022**, *11*, 108.

[33] G. Son, V. Ri, D. Shin, Y. Jung, C. B. Park, C. Kim, *Advanced science (Weinheim, Baden-Wurttemberg, Germany)* **2023**, *10*, e2301993.

[34] H. Kye, Y. Kang, D. Jang, J. E. Kwon, B.-G. Kim, *Adv Energy and Sustain Res* **2022**, *3*, 2200030.

[35] Y.-G. Weng, W.-Y. Yin, M. Jiang, J.-L. Hou, J. Shao, Q.-Y. Zhu, J. Dai, *ACS applied materials & interfaces* **2020**, *12*, 52615.

[36] Y.-G. Weng, Z.-H. Ren, Z.-R. Zhang, J. Shao, Q.-Y. Zhu, J. Dai, *Inorganic chemistry* **2021**, *60*, 17074.

[37] M. Wu, Y. Zhao, R. Zhao, J. Zhu, J. Liu, Y. Zhang, C. Li, Y. Ma, H. Zhang, Y. Chen, *Adv Funct Materials* **2022**, *32*, 2107703.

[38] A. Jana, S. Bähring, M. Ishida, S. Goeb, D. Canevet, M. Sallé, J. O. Jeppesen, J. L. Sessler, *Chemical Society reviews* **2018**, *47*, 5614.

[39] H. Glatz, E. Lizundia, F. Pacifico, D. Kundu, *ACS Appl. Energy Mater.* **2019**, *2*, 1288.

[40] S. Iwamoto, Y. Inatomi, D. Ogi, S. Shibayama, Y. Murakami, M. Kato, K. Takahashi, K. Tanaka, N. Hojo, Y. Misaki, *Beilstein journal of organic chemistry* **2015**, *11*, 1136.

[41] Y. Inatomi, N. Hojo, T. Yamamoto, S. Watanabe, Y. Misaki, *ChemPlusChem* **2012**, *77*, 973.

[42] W. Hu, N. Chen, D. Chen, B. Tong, *ChemElectroChem* **2022**, *9*.

[43] C. Zeng, J. Chen, H. Yang, A. Yang, C. Cui, Y. Zhang, X. Li, S. Gui, Y. Wei, X. Feng, X. Xu, P. Xiao, J. Liang, T. Zhai, Y. Cui, H. Li, *Matter* **2022**, *5*, 4015.

[44] C. G. Gruber, L. Frey, R. Guntermann, D. D. Medina, E. Cortés, *Nature* **2024**, *630*, 872.

[45] M. S. Lohse, T. Bein, *Adv Funct Materials* **2018**, *28*, 1705553.

[46] R. Dantas, C. Ribeiro, M. Souto, *Chemical communications (Cambridge, England)* **2023**, *60*, 138.

[47] Q. Xu, Z. Liu, Y. Jin, X. Yang, T. Sun, T. Zheng, N. Li, Y. Wang, T. Li, K. Wang, J. Jiang, *Energy Environ. Sci.* **2024**, *17*, 5451.

[48] L. Yao, C. Ma, L. Sun, D. Zhang, Y. Chen, E. Jin, X. Song, Z. Liang, K.-X. Wang, *Journal of the American Chemical Society* **2022**, *144*, 23534.

[49] Y. Liu, Y. Lu, A. Hossain Khan, G. Wang, Y. Wang, A. Morag, Z. Wang, G. Chen, S. Huang, N. Chandrasekhar, D. Sabaghi, D. Li, P. Zhang, D. Ma, E. Brunner, M. Yu, X. Feng, *Angewandte Chemie (International ed. in English)* **2023**, *62*, e202306091.

[50] L. Gong, X. Yang, Y. Gao, G. Yang, Z. Yu, X. Fu, Y. Wang, D. Qi, Y. Bian, K. Wang, J. Jiang, *J. Mater. Chem. A* **2022**, *10*, 16595.

[51] W. Li, Q. Huang, H. Shi, W. Gong, L. Zeng, H. Wang, Y. Kuai, Z. Chen, H. Fu, Y. Dong, C. Zhang, *Adv Funct Materials* **2024**, *34*, 2310668.

[52] M. Calik, T. Sick, M. Dogru, M. Döblinger, S. Datz, H. Budde, A. Hartschuh, F. Auras, T. Bein, *Journal of the American Chemical Society* **2016**, *138*, 1234.

[53] M. Elstner, D. Porezag, G. Jungnickel, J. Elsner, M. Haugk, T. Frauenheim, S. Suhai, G. Seifert, *Phys. Rev. B* **1998**, *58*, 7260.

[54] S. Gu, J. Chen, R. Hao, X. Chen, Z. Wang, I. Hussain, G. Liu, K. Liu, Q. Gan, Z. Li, H. Guo, Y. Li, H. Huang, K. Liao, K. Zhang, Z. Lu, *Chemical Engineering Journal* **2023**, *454*, 139877.

[55] Y. Zhang, M. Položij, T. Heine, *Chem. Mater.* **2022**, *34*, 2376.

[56] R. Guntermann, D. Helminger, L. Frey, P. M. Zehetmaier, C. Wangnick, A. Singh, T. Xue, D. D. Medina, T. Bein, *Angewandte Chemie (International ed. in English)* **2024**, *63*, e202407166.

[57] G. Kresse, J. Hafner, *Physical review. B, Condensed matter* **1993**, *47*, 558.

[58] F. Dai, M. Cai, *Commun Mater* **2022**, *3*, 64.

[59] D. Hirshberg, O. Yariv, G. Gershinsky, E. Zinigrad, D. Aurbach, *J. Electrochem. Soc.* **2015**, *162*, A7001-A7007.

[60] D. Qu, W. Ji, H. Qu, *Commun Mater* **2022**, *3*.

[61] S. Oswald, F. Riewald, H. A. Gasteiger, *J. Electrochem. Soc.* **2022**, *169*, 40552.

[62] T. P. Jayakumar, R. Badam, N. Matsumi, *ACS Appl. Energy Mater.* **2020**, *3*, 3337.

[63] L. Xu, Y. Xiao, Z.-X. Yu, Y. Yang, C. Yan, J.-Q. Huang, *Angewandte Chemie (International ed. in English)* **2024**, *63*, e202406054.

[64] A. van der Ven, K. A. See, L. Pilon, *Battery Energy* **2022**, *1*.

[65] C. Peng, C. Yang, P. Chen, Y.-J. Cheng, J. Xia, K. Guo, *Applied Surface Science* **2023**, *623*, 156994.

[66] Y. Chen, L. Shi, A. Li, S. Zhang, M. Guo, X. Chen, J. Zhou, H. Song, *J. Electrochem. Soc.* **2017**, *164*, A2000-A2006.

[67] A. Yoshimura, K. Hemmi, H. Moriwaki, R. Sakakibara, H. Kimura, Y. Aso, N. Kinoshita, R. Suizu, T. Shirahata, M. Yao, H. Yorimitsu, K. Awaga, Y. Misaki, *ACS applied materials & interfaces* **2022**, *14*, 35978.

[68] J. Wang, J. Polleux, J. Lim, B. Dunn, *J. Phys. Chem. C* **2007**, *111*, 14925.

[69] A. C. Lazanas, M. I. Prodromidis, *ACS measurement science au* **2023**, *3*, 162.

[70] P. K. Jones, U. Stimming, A. A. Lee, *Nature communications* **2022**, *13*, 4806.

[71] S. Wang, J. Zhang, O. Gharbi, V. Vivier, M. Gao, M. E. Orazem, *Nat Rev Methods Primers* **2021**, *1*, 1.

[72] W. Choi, H.-C. Shin, J. M. Kim, J.-Y. Choi, W.-S. Yoon, *J. Electrochem. Sci. Technol* **2020**, *11*, 1.

[73] R. Nandan, N. Takamori, K. Higashimine, R. Badam, N. Matsumi, *ACS Appl. Energy Mater.* **2024**, *7*, 2088.

[74] L. Wang, J. Zhao, X. He, J. Gao, J. Li, C. Wan, C. Jiang, *International Journal of Electrochemical Science* **2012**, *7*, 345.

[75] Y.-S. Lee, K.-S. Ryu, *Scientific reports* **2017**, *7*, 16617.

[76] G. Henkelman, B. P. Uberuaga, H. Jónsson, *The Journal of chemical physics* **2000**, *113*, 9901.

[77] J. C. Burns, L. J. Krause, D.-B. Le, L. D. Jensen, A. J. Smith, D. Xiong, J. R. Dahn, *J. Electrochem. Soc.* **2011**, *158,* A1417.

4.6. Appendix

4.6.1. Methods

4.6.1.1. Structural characterization

Powder X-ray diffraction (PXRD): Diffractograms were obtained using a Bruker D8 Discover instrument, featuring Cu-Kα radiation and a LynxEye position-sensitive detector, configured in Bragg-Brentano geometry.

Structure modelling: The proposed structures of **WTTF**-COF were simulated utilising Density functional based tight binding (DFTB) calculations (detailed description presents in Section 1.3). Later, Pawley refinement of the modelled structure was carried out with the Reflex module using the Accelrys Materials Studio software package.

Scanning electron microscopy (SEM): SEM images were obtained using a FEI Helios NanoLab G3 UC scanning electron microscope equipped with a Schottky field-emission electron source operated at 3-5 kV.

Transmission electron microscopy (TEM): TEM images were obtained on a FEI Titan Themis instrument equipped with a field emission gun operated at 300 kV.

Fourier-transform infrared spectroscopy (FTIR): The spectra were captured using a Bruker Vertex 70 FTIR instrument, featuring a liquid nitrogen (LN_2) cooled MCT detector.

Thermogravimetric analysis (TGA): The thermal stability measurements were performed on a Netzsch Jupiter ST 499 C instrument equipped with a Netzsch TASC 414/4 controller. The sample was heated from room temperature to 900 °C under a synthetic air flow at a heating rate of 10 °C min^{-1}.

Nitrogen sorption: The isotherms were recorded using Quantachrome Autosorb 1 and Autosorb iQ instruments at temperature of 77 K. The BET surface area for the COF was calculated based on the pressure range $0.05 \leq p/p_0 \leq 0.2$.

4.6.1.2. Battery performance

Electrode preparation: To study the ability of **WTTF**-COF to serve as electrode for LIBs, firstly, lithium-ion half-cells were fabricated. A homogeneous slurry was prepared by thoroughly mixing (60 wt.%) COF-WTTF as host material, (20 wt.%) Ketjen black as conductive carbon additive, (20 wt.%) polyvinylidene fluoride (PVDF) as binder, and *N*-methyl-2-pyrrolidone (NMP) as solvent. The slurry was then coated over a copper foil using the doctor blade technique, dried overnight at 65 °C, and later vacuum-dried at 100 °C for 6 h. Finally, the electrodes were cut into disks with a diameter of 18 mm with an average mass loading of 1.0-1.5 mg cm^{-2}.

Half-cell assembly

Lithium-ion half-cells were fabricated using **WTTF** bipolar electrode as working electrode, Li-foil (Sigma-Aldrich) as counter and reference electrode, Celgard (2325 (PP/PE/PP), ⌀: 21.6 mm, thickness: 0.025 mm, CCC/HS:90279000) as separator, and 1 ᴍ $LiPF_6$ in ethylene carbonate (EC): diethyl carbonate (DEC) (1:1, v/v) as electrolyte. The cells were assembled inside an argon filled glove box (Labstar 1250/750, MBraun, Germany) in a coin cell configuration using the El-CELL ECC-Std electrochemical test cell. The resulting electrochemical cell exhibited an OCV ~2.7 V vs. Li/Li^+.

Cyclic voltammetry (CV): Cyclic voltammetry measurements were carried out on an Metrohm Autolab potentiostat/galvanostat PGSTAT302N equipped with an FRA32M module over the maximum potential range of 0.1 - 3.6 V vs. Li/Li^+ at scan rates varying between 0.1-10 mVs^{-1}.

Galvanostatic charge-discharge cycling: Galvanostatic (dis-)charge measurements were conducted using an Autolab Multipotentiostat M101 by applying different current densities ranging from 0.1-5 Ag^{-1} in a voltage window of 0.1 - 3.6 V vs. Li/Li^+.

Potential-dependent electrochemical impedance spectroscopy (EIS): The measurements were performed on a BioLogic VMP-3e Multichannel Potentiostat working station using sequential single-sine perturbation over a frequency range of 10^6-0.1 Hz with an applied perturbation voltage of 10 mV over the potential window of 0.1-3.6 V vs. Li/Li^+. The electrochemical cell WTTF | 1 ᴍ $LiPF_6$ EC:DEC (1:1, v/v%) | Li underwent galvanostatic charge-discharge at a current density of 0.1 A g^{-1} for 3 cycles to establish a stable SEI layer. Afterwards, the **WTTF**-COF based half-cells were subjected to 300 cycles of charge-discharge at a constant current density of 1.0 A g^{-1} to establish an aged/stable system. From a completely discharged state (potential at 0.1 V vs. Li/Li^+), EIS measurements were subsequently conducted by applying AC perturbation signal superimposed over DC bias with the positive sweep-step between a potential range of 0.1 - 3.6 V vs. Li/Li^+ (and a negative sweep-step between 3.6 - 0.1 V vs. Li/Li^+), and the impedance was measured at n number of steps with n = 42 (refer to Figure 4.33).

3-electrode assembly

3 electrode electrochemical cells were fabricated using **WTTF** bipolar electrode as working electrode, Li-foil (Sigma-Aldrich) as counter, and Li-ring as reference electrode, Celgard (2325 (PP/PE/PP),

⌀: 21.6 mm, thickness: 0.025 mm, CCC/HS:90279000) as separator, and 1 м $LiPF_6$ in EC:DEC (1:1, v/v) as electrolyte. The cells were assembled inside an argon filled glove box (Labstar 1250/750, MBraun, Germany) in a coin cell configuration using the El-CELL ECC-Std electrochemical test cell.

Electrochemical impedance spectroscopy (EIS): The measurements were performed on an Autolab potentiostat working station equipped with an FRA32M module using sequential single-sine perturbation over the frequency range of 10^6-0.1 Hz with an applied perturbation voltage of 10 mV.

Symmetric-cell assembly

To confirm the ability of the **WTTF**-COF to act a bipolar electrode, Li-ion symmetric cells were fabricated using **WTTF** as both negative and positive electrode. In order to minimise the loss of Li^+ and achieve >0 V open circuit voltage (OCV) in the symmetric battery, **WTTF** electrodes were charged (cycled up to 3.6 V vs. Li/Li^+; WTTF@PF_6) and discharged (cycled down to 0.1 V vs. Li/Li^+; WTTF@Li) individually in a half-cell configuration. To assemble a symmetric battery, a three-electrode cell was utilised, using "WTTF@PF_6" as cathode, "WTTF@Li" as anode, a lithium ring as reference electrode, 1 м $LiPF_6$ in EC:DEC (1:1, v/v) as electrolyte, and Celgard (2325 (PP/PE/PP), ⌀: 21.6 mm, thickness: 0.025 mm, CCC/HS:90279000) as separator. The cells were assembled inside an argon filled glove box (Labstar 1250/750, MBraun, Germany) in a coin cell configuration using an El-CELL ECC-Std electrochemical test cell. The resulting electrochemical cell exhibited an OCV ~2.2 V between both electrodes.

The mass loading of the electrodes in the full cell needs to be adjusted according to the following equation:

$$SC_A \times M_A \geq SC_C \times M_C \qquad \text{(Equation 4.4)}$$

where, SC_A is the anode-specific capacity (in mAh g^{-1}), SC_C is the cathode-specific capacity (in mAh g^{-1}), M_A (in g) is mass loading at the anode and M_C (in g) is the mass loading of the cathode.

To determine the active potential window vs. Li/Li^+ for the symmetric cell, the dQ/dV curve for the bipolar WTTF electrode was considered.

Cyclic voltammetry (CV): Cyclic voltammetry measurements were carried out on an Metrohm Autolab potentiostat/galvanostat PGSTAT302N equipped with an FRA32M module over the potential range of 0.2- 3.4 V vs Li/Li^+ at scan rates varying between 1.0-200 mV s^{-1}.

Galvanostatic charge-discharge cycling: Galvanostatic (dis-)charge measurements were conducted using an Autolab Multipotentiostat M101 by applying different current densities ranging from 0.3 - 1.0 A g^{-1} in a voltage window of 0.2 - 3.4 V vs. Li/Li^+.

4.6.1.3. Theoretical calculations

Structure simulation: The geometries were optimized using the self-consistent-charge density functional based tight binding (SCC-DFTB)[1] method as implemented in the Amsterdam Modelling Suite (AMS) ADF 2023.1042[2] with the 3ob-3-1 parameter set.[3]

Band structure and redox mechanism: The calculations regarding the band structure and charge-discharge mechanism were performed employing the Vienna ab initio Simulation Package (VASP) code based on density functional theory (DFT).[4] The generalized gradient approximation (GGA) involving the Perdew–Burke–Ernzerhof (PBE) functional with D3-BJ van der Waals correction was adopted to process the exchange-correlation term and accurately account for the long-range van der Waals forces.[5–7] The ions are modeled with the projector augmented-wave (PAW) method.[8,9] The plane wave cutoff energy was set to 520 eV, with the convergence threshold of force less than 0.001 eV/Å during geometry optimization with a 4 × 4 × 1 k-mesh grid. The nudged elastic band (NEB) method implemented in VASP was employed for the transition state searches.[10]

The average binding energy per Li-ion was calculated as:

$$E_{B.E.} = (E_{COF+xLi} - E_{COF} - xE_{Li})/x \qquad \text{(Equation 4.5)}$$

where, $E_{COF+xLi}$ and E_{COF} are the total energies of the COF with and without x number of Li atoms, respectively. E_{Li} is the energy of Li bulk metal.

The molecular calculations to determine the HOMO and LUMO of the model molecules of COF fragments, their charged complexes, and *TTF* and *W* model molecules are performed in Gaussian 09 program (version D.01).[11] The B3LYP method with the D3 BJ-damping function and def2-SVP basis set are utilized to optimize the molecular structures.

4.6.2. Synthesis and characterization

4.6.2.1. Synthesis

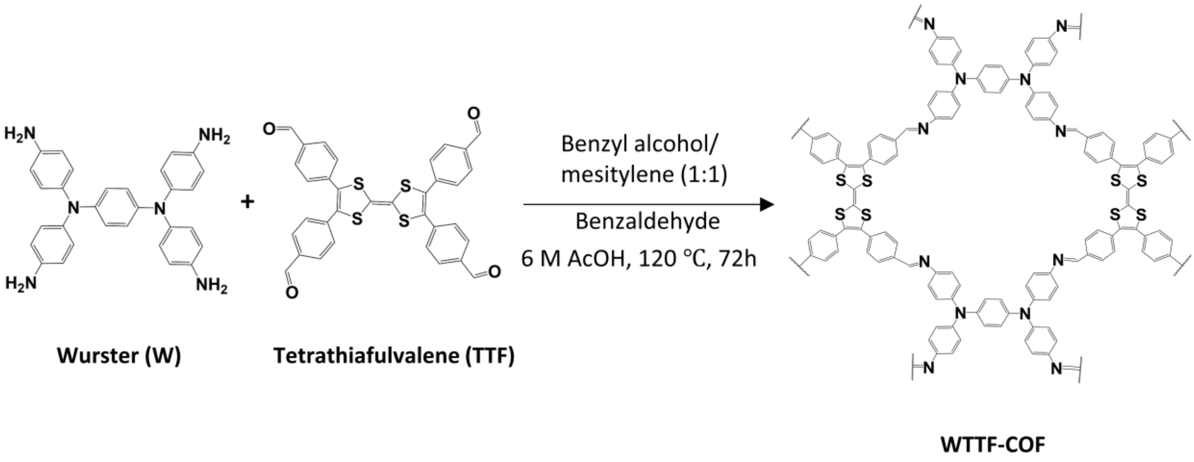

Scheme 4.1 Synthesis of **WTTF**-COF.

4,4',4'',4'''-([2,2'-Bi(1,3-dithiolylidene)]-4,4',5,5'-tetrayl)tetrabenzaldehyde (**TTF**, 9.31 mg, 0.015 mmol, BLD Pharmatech GmbH), *N*,*N*,*N'*,*N'*-tetrakis(4-aminophenyl)-1,4-phenylenediamine (**W**, 7.08 mg 0.015 mmol, Biosynth, Ltd.), benzaldehyde (2μL) and 0.1 mL of 6 M aqueous acetic acid were added to a Pyrex tube containing a mixture of benzyl alcohol (0.5 mL) and mesitylene (0.5 mL) inside an argon filled glove-box. The reaction tube was then heated at 120 ℃ for 3 days. The resulting COF powder was thoroughly washed with tetrahydrofuran (THF). The obtained red-brown COF powder was then dried under vacuum for 6 h.

Table 4.1 Elemental analysis of synthesized **WTTF**-COF.

WTTF- COF	N	C	H	S
Simulated	8.4	74.8	3.8	12.8
Experimental	6.3	72.4	4.6	10.0

4.6.2.2. Characterization

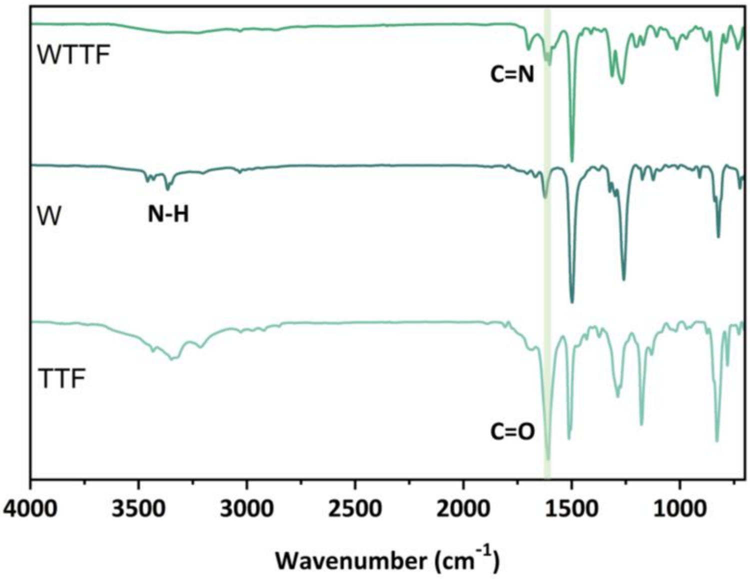

Figure 4.8 Fourier transform infrared (FTIR) spectroscopy analysis of building blocks **W** and **TTF**, and resulting **WTTF**-COF. N−H stretching vibration associated to amine group and C=O stretching vibration associated to aldehyde functional group present in **W** and **TTF** monomers, respectively. The green strip representing the emergence of characteristic peak for C=N bond vibration for **WTTF**-COF.

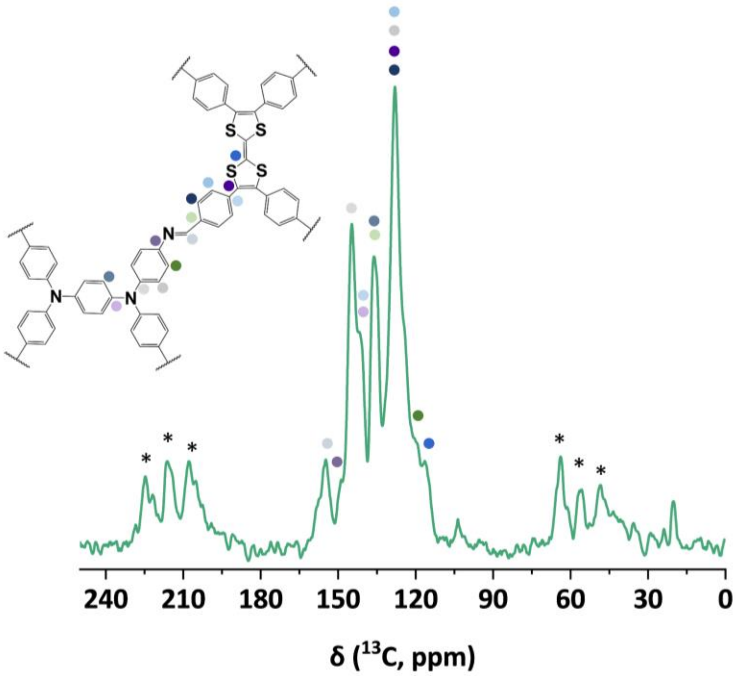

Figure 4.9 Solid-state ^{13}C cross-polarization magic angle spinning (CP-MAS) NMR spectra of bulk **WTTF**-COF. The peaks designated with asterisks correspond to the spinning sidebands. No resonance corresponding to aldehyde groups is observed near 190 ppm, confirming the establishment of an imine-linked structure.

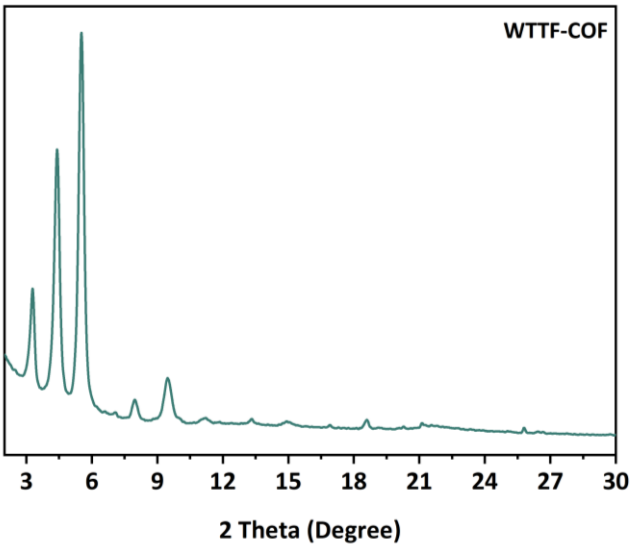

Figure 4.10 Experimental powder X-ray diffractogram of **WTTF**-COF.

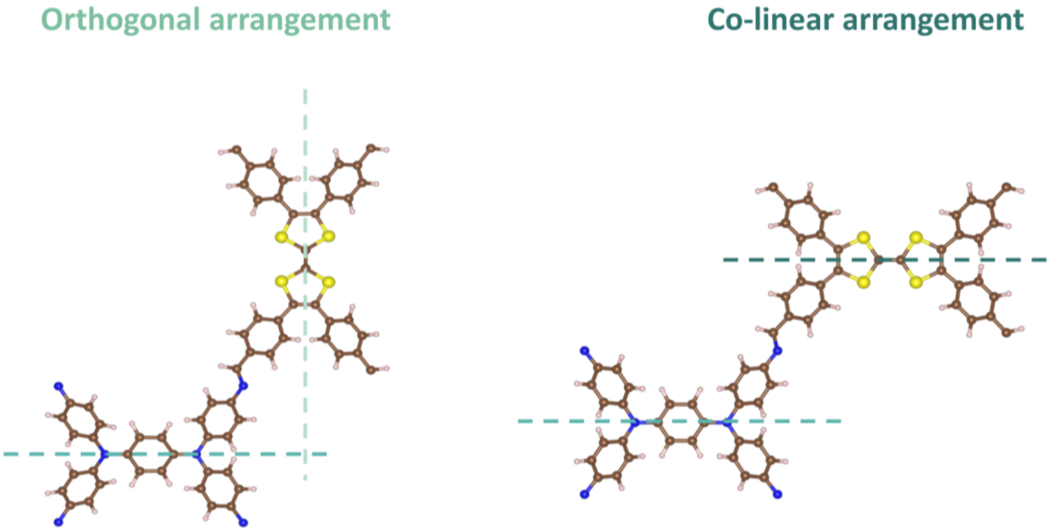

Figure 4.11 Pictorial representation of orthogonal and co-linear arrangements for assembling **W** and **TTF** building blocks in COF. *Orthogonal arrangement*: orthogonal long axes of monomers **W** and **TTF**. *Co-linear arrangement*: co-linear but offset long axes of monomers **W** and **TTF**.

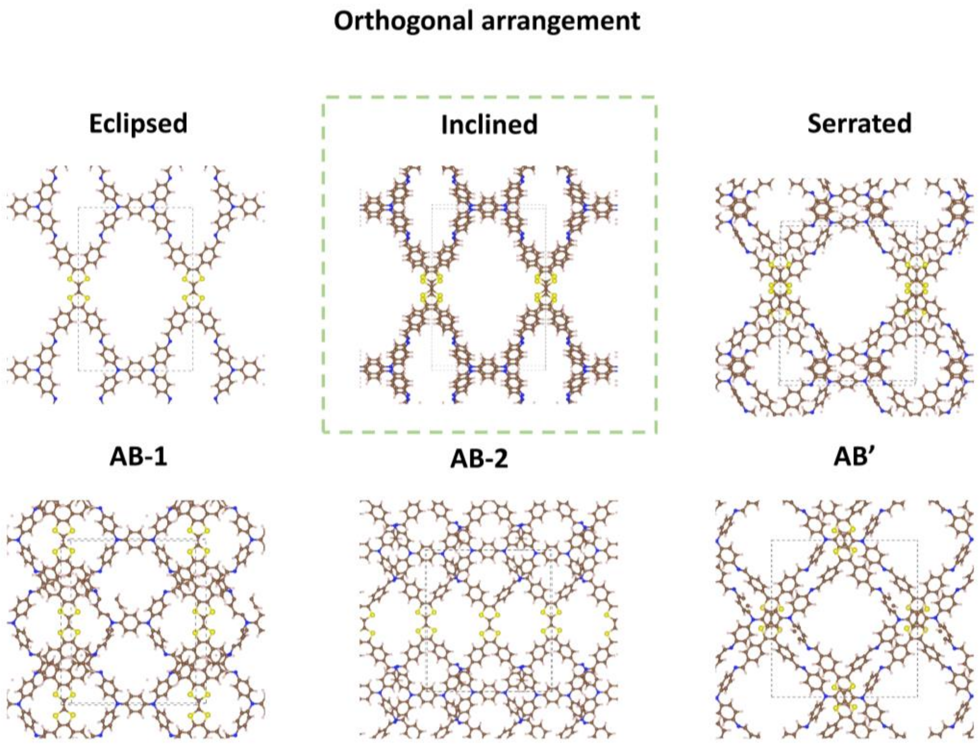

Figure 4.12 Simulated structural models of orthogonal arrangement for assembling **W** and **TTF** building blocks in **WTTF**-COF.

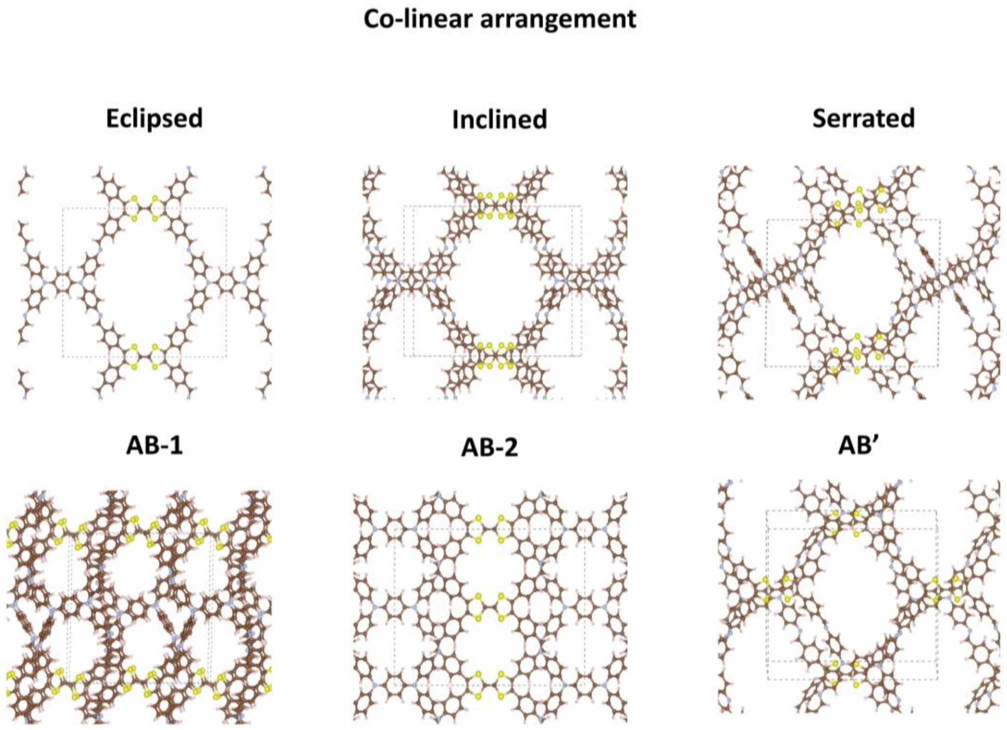

Figure 4.13 Simulated structural models of co-linear arrangement for assembling **W** and **TTF** building blocks in **WTTF**-COF.

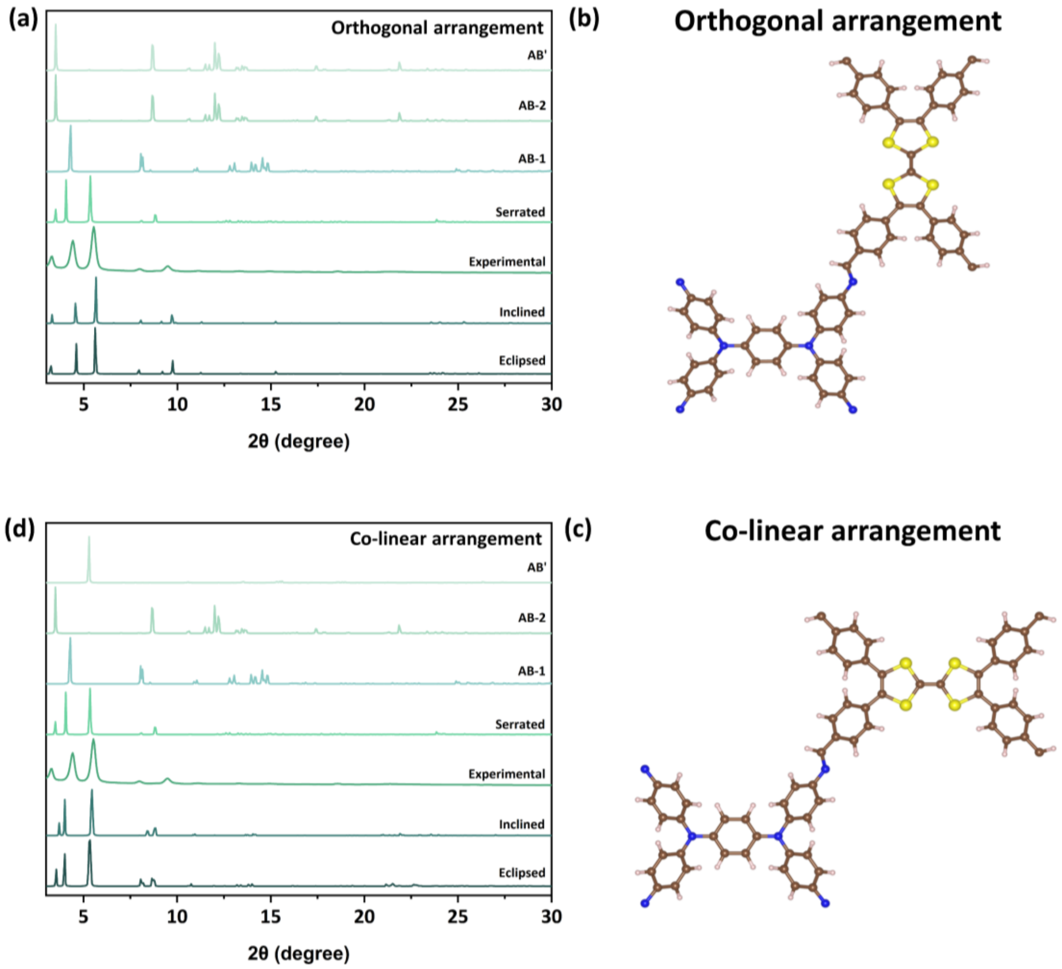

Figure 4.14 The simulated PXRD patterns of **WTTF**-COF employing orthogonal and co-linear arrangements of the building blocks.

Table 4.2 Lattice parameters of simulated structural models of bulk **WTTF**-COF featuring orthogonal and co-linear arrangements.

	Eclipsed	**Inclined**	**Serrated**	**AB-1**	**AB-2**	**AB’**
Orthogonal arrangement	a= 19.23 Å	a= 19.66 Å	a= 21.82 Å	a= 21.18 Å	a= 22.28 Å	a= 22.74 Å
	b=27.36 Å	b=26.97 Å	b= 25.47 Å	b= 25.76 Å	b= 25.20 Å	b= 24.66 Å
	c= 3.78 Å	c= 3.78 Å	c= 7.49 Å	c= 7.16 Å	c= 8.13 Å	c= 6.84 Å
	α= 90.00°	α= 101.57°	α= 95.74°	α= 92.31°	α= 89.77°	α= 90.10°
	β= 90.00°	β= 89.58°	β= 91.49°	β= 102.86°	β= 88.37°	β= 89.46°
	γ= 90°	γ= 89.37°	γ= 89.42°	γ= 90.19°	γ= 90.37°	γ= 90.00°
Co-linear arrangement	a= 25.97 Å	a= 26.10 Å	a=26.77 Å	a= 22.13 Å	a=27.35 Å	a=26.09 Å
	b= 21.26 Å	b= 21.01 Å	b=20.56 Å	b= 21.19 Å	b=20.26 Å	b=20.93 Å
	c= 4.13 Å	c= 4.11 Å	c= 7.35 Å	c= 7.65 Å	c= 7.22 Å	c= 8.15 Å
	α= 90.00°	α= 90.00°	α= 90.00°	α= 91.48°	α= 90.00°	α= 71.79°
	β= 90.00°	β= 69.48°	β= 89.26°	β= 94.44°	β= 89.98°	β= 91.87°
	γ= 90.00°	γ= 90.00°	γ= 89.09°	γ= 88.83°	γ= 89.94°	γ= 89.94°

Table 4.3 Relative energy (R.E.) difference between AA-eclipsed and AA-inclined stacking of **WTTF**-COF in the orthogonal arrangements.

Stacking	**Eclipsed**	**Inclined**
R.E. (eV)	0.24	0.00

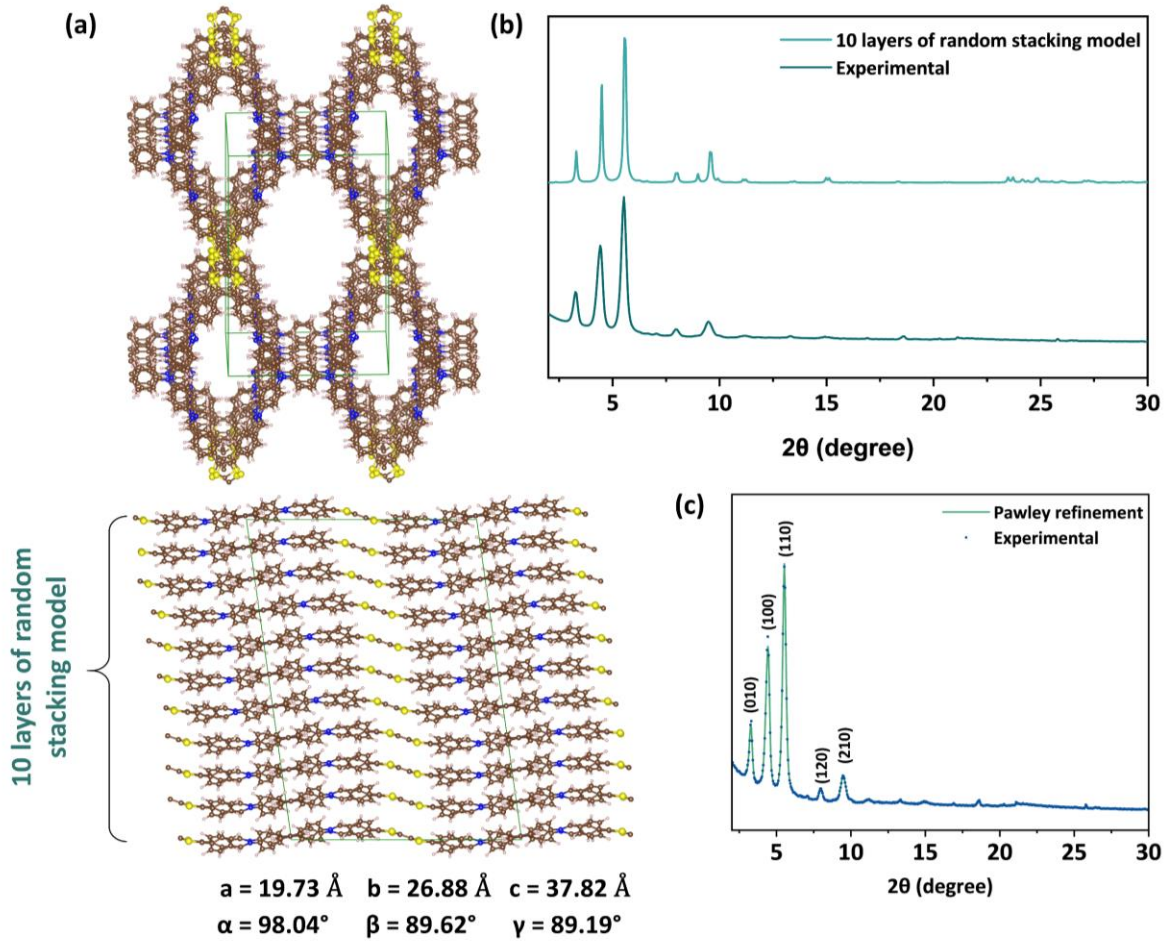

Figure 4.15 (a) Top and side view of WTTF-COF with 10 layers of random stacking model (mixture of AA-eclipsed and AA-inclined stacking), (b) corresponding simulated PRXD pattern, and (c) experimental and Pawley refined PXRD pattern of **WTTF**-COF with most prominent peaks indexed to the corresponding (*hkl*) planes.

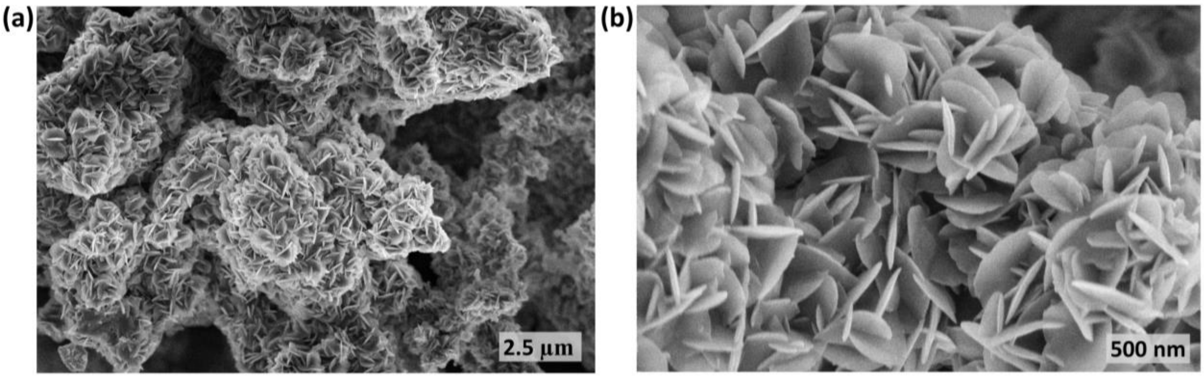

Figure 4.16 Scanning electron microscopy (SEM) images of **WTTF**-COF bulk powder.

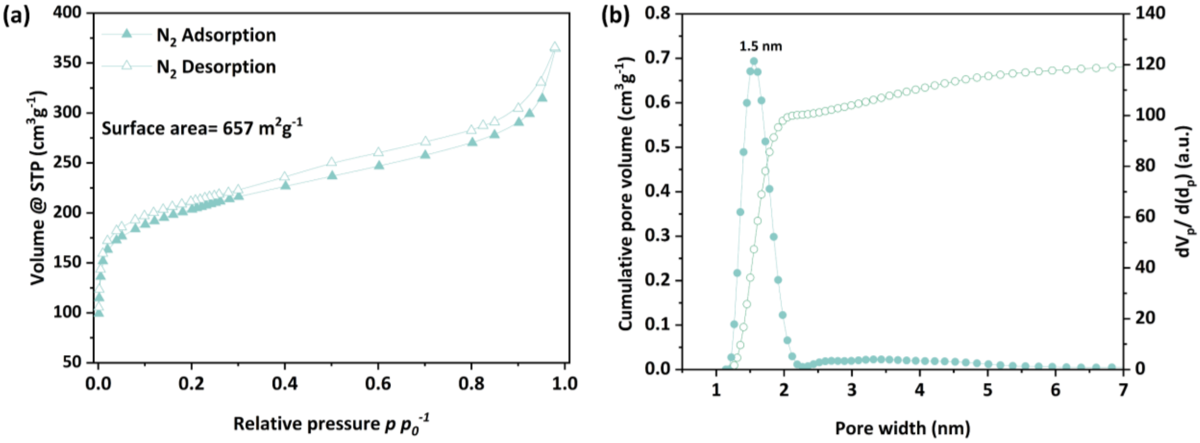

Figure 4.17 (a) Nitrogen (N_2) gas sorption isotherm and (b) pore size distribution and cumulative pore volume profile of **WTTF**-COF.

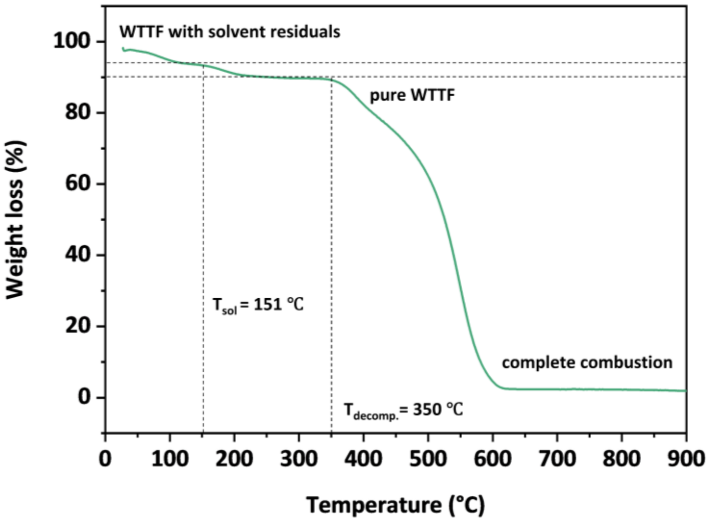

Figure 4.18 Thermogravimetric analysis (TGA) of **WTTF**-COF obtained by heating the sample from room temperature to 900 °C under a synthetic air flow at a heating rate of 10 °C min^{-1}.

4.6.3. Electrochemical characterization

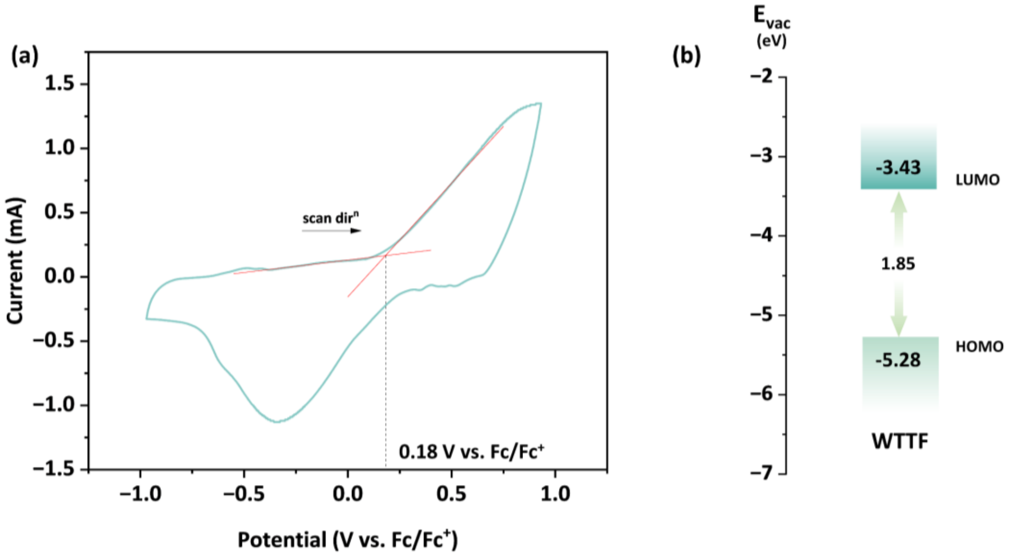

Figure 4.19 (a) Cyclic voltammogram of WTTF-COF calibrated against Fc/Fc$^+$ redox couple using 0.1 м tetrabutylammonium hexafluorophosphate (NBu_4PF_6) in an anhydrous acetonitrile solution as electrolyte. (b) Calculated energy positions of highest occupied molecular orbital (HOMO) and lowest unoccupied molecular orbital (LUMO) of WTTF-COF.

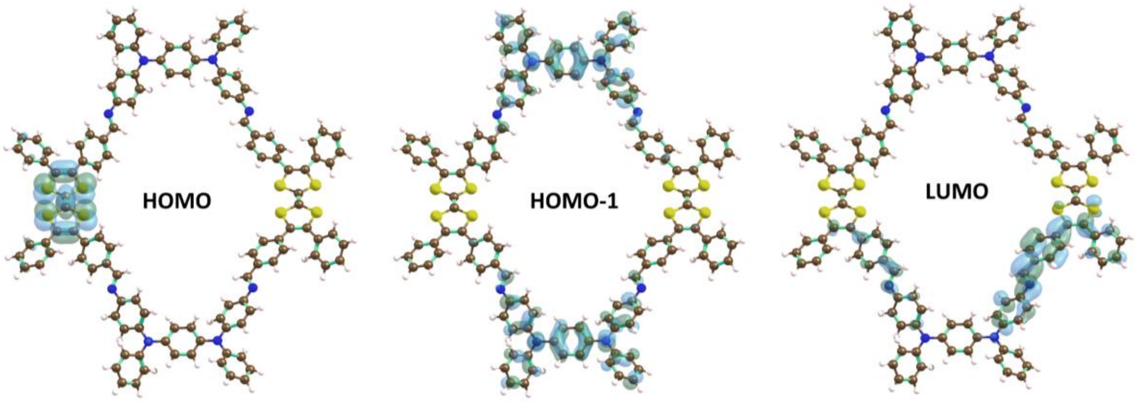

Figure 4.20 The frontier orbitals of **WTTF**-COF. HOMO and HOMO-1 are localized on the TTF and Wurster nodes (binding sites for PF_6^- anions), while the LUMO is localized on the imine linkage (binding sites for Li$^+$ cations).

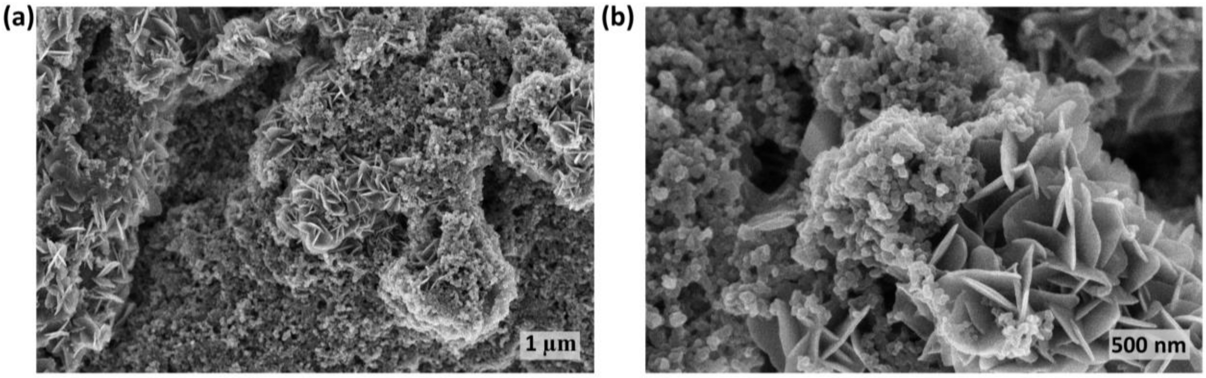

Figure 4.21 Scanning electron microscopy (SEM) images of **WTTF** electrode.

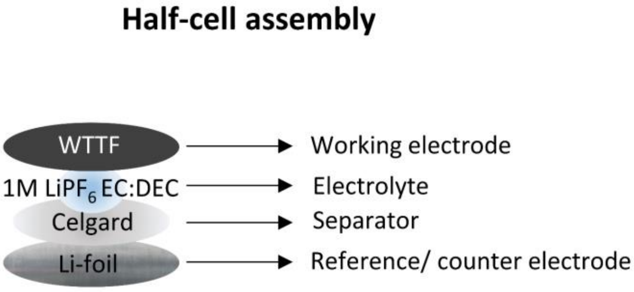

Figure 4.22 Schematic representation of half-cell assembly using **WTTF**-COF as working electrode; 1 м $LiPF_6$ in ethylene carbonate (EC): diethyl carbonate (DEC) (1:1 v/v%) was used as the liquid electrolyte, celgard as separator to avoid short-circuit, and Li-foil (thickness- 0.75 mm) as reference and counter electrode; yielding the electrochemical cell denoted as WTTF | 1 м $LiPF_6$ EC:DEC (1:1, v/v%) | Li.

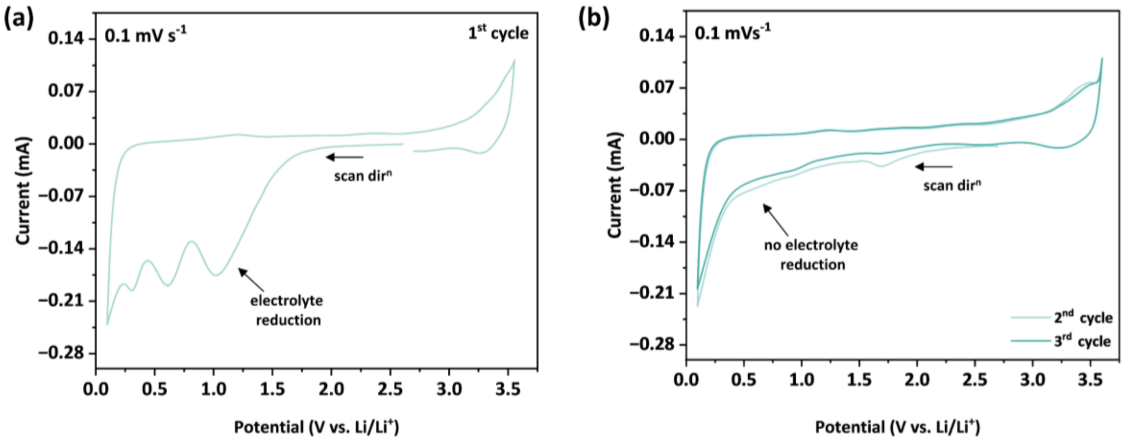

Figure 4.23 Cyclic voltammetry measurements of half-cell utilizing WTTF-COF electrode as working electrode, Li-foil as counter and reference electrode and 1 м $LiPF_6$ in EC:DEC (1:1 v/v%) as the liquid electrolyte at a scanning speed of 0.1 mV s^{-1} between potential range 0.1-3.6 V vs. Li/Li^+ for (a) first cycle with depiction of SEI formation and (b) 2nd and 3rd cycle without electrolyte degradation.

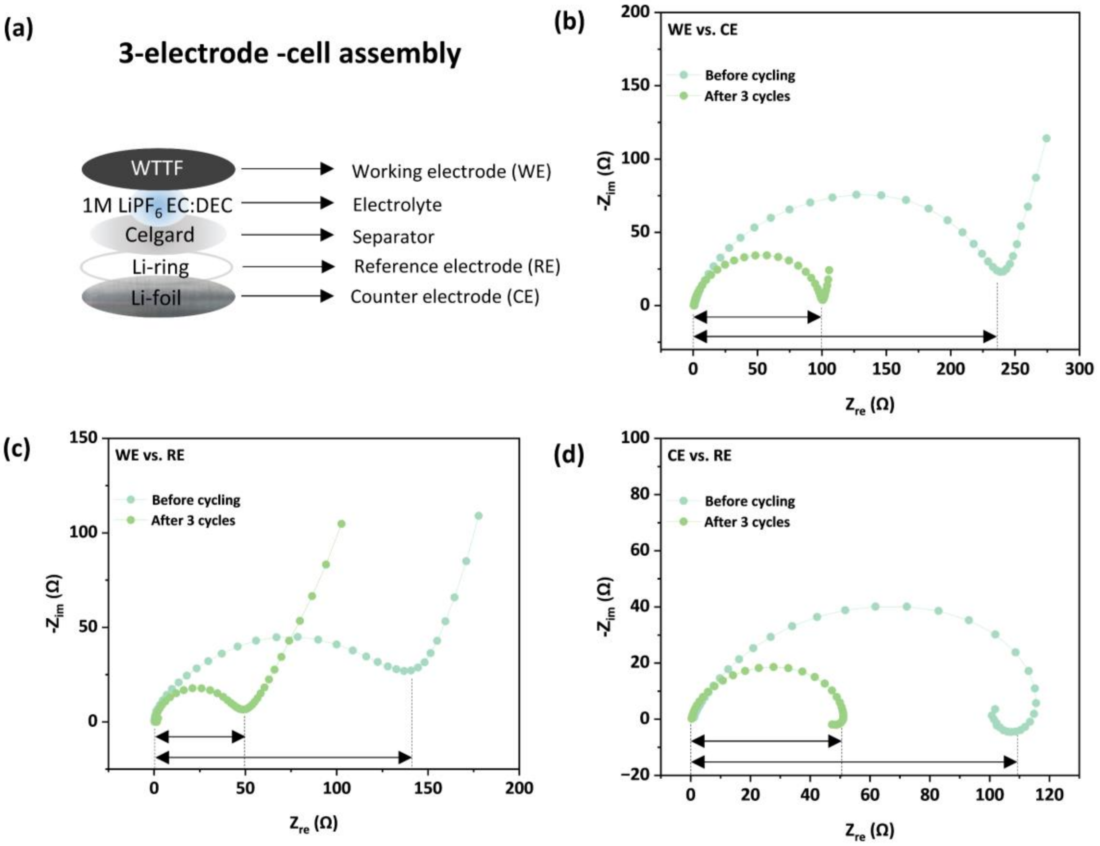

Figure 4.24 Electrochemical impedance spectroscopy (EIS). Nyquist plots for (a) the three-electrode electrochemical cell WTTF (WE) | 1 м $LiPF_6$ EC:DEC (1:1, v/v%) | Li/Li^+ (RE) || Li (CE), measured as (b) WE vs. CE, (c) WE vs. RE, and (c) CE vs. RE, before and after initial 3 cyclic voltammetry cycles at a scan rate of 0.1 mVs^{-1}.

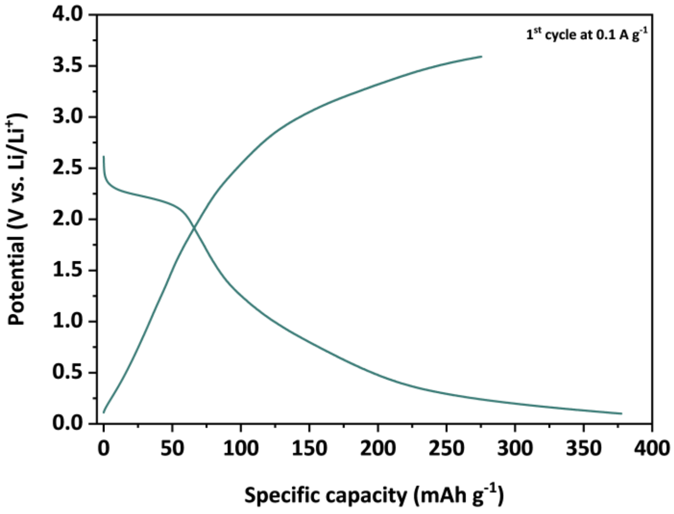

Figure 4.25 Initial galvanostatic charge-discharge profile of **WTTF** serving as cathode in a Li-ion half-cell using Li-foil as reference and counter electrode and 1 м $LiPF_6$ EC:DEC (1:1, v/v%) as electrolyte at current density of 1.0 A g^{-1}, scanned between 0.1-3.6 V vs. Li/Li^+.

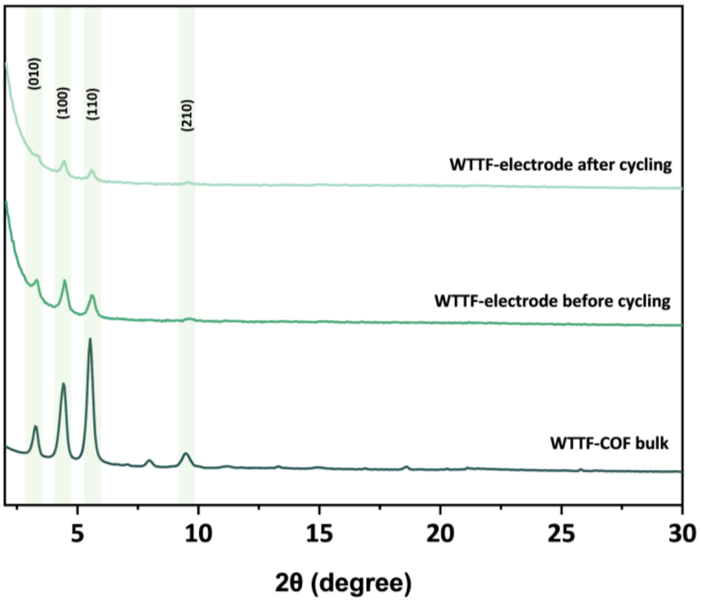

Figure 4.26 PXRD pattern of WTTF-COF, WTTF-electrode (WTTF-COF: Ketjenblack: PVDF = 60:20:20 wt.%) before and after 5 (dis-)charge cycles at a current density of 0.1 A g^{-1}, with most prominent peaks indexed to the corresponding (hkl) planes.

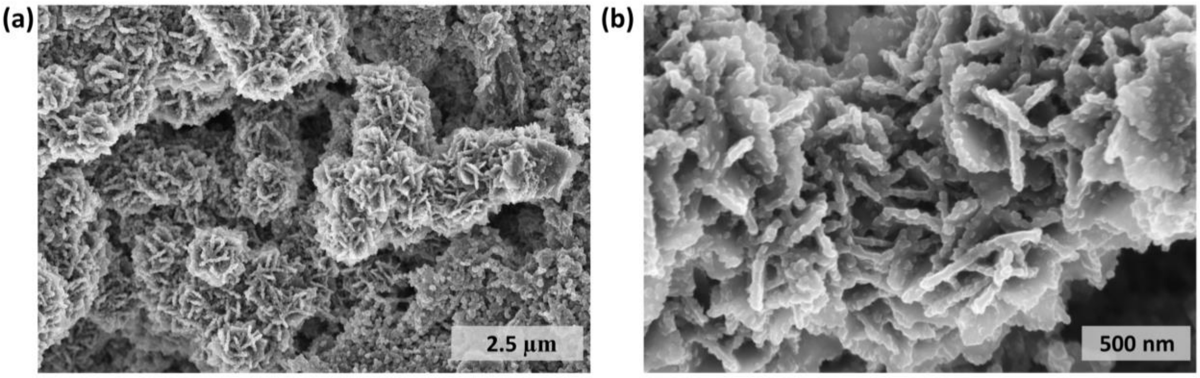

Figure 4.27 Scanning electron microscopy (SEM) images of an **WTTF** electrode after 5 (dis-)charge cycles at a current density of 0.1 A g^{-1}.

Table 4.4 Comparison of battery performance of previously reported bipolar-type COF-based electrodes. Abbreviations for conductive carbons are presented in the table notes.

Bipolar electrode	**Redox-active group in linker**	**Redox-active linkage**	**Charge carrier**	**Conductive additive**	**Potential window (V)**	**Specific capacity (mAh g^{-1})**	**Cell type demonstration**	**Ref.**
PTB-DHZ-COF40	Tertiary amine	Hydrazone	Li$^+$, PF$_6^-$	20% CNT	1.2–4.2	114.2 at 1 A g^{-1}	Half-cell	[12]
TPPDA-CuPor-COF	Porphyrin, Tertiary amine	Imine	Li$^+$, PF$_6^-$	40% Super P	1.5–4.2	142 at 0.06 A g^{-1}	Half-cell	[13]
TAPP-Pz-COF-40%CNT	Porphyrin, phenazine	Imine	Li$^+$, PF$_6^-$	40% CNT, 20% KB	1.2–4.4	314 at 0.2 A g^{-1}	Half-cell	[14]
NTPI-COF	Tertiary amine, naphthalenediimide	-	Li$^+$, PF$_6^-$	30% Super P	1.5–4.25	165 at 0.03 A g^{-1}	Half-cell	[15]
2D-NT-COF30	Triazine, imide	-	AlCl$_2^+$, AlCl$_4^-$	30% CNT	0.5–2.1	132 at 0.1 A g^{-1}	Half-cell	[16]
TP-TA-COF	Tertiary amine	Imine	Li$^+$, PF$_6^-$	30% KB	1.2–4.3	207 at 0.2 A g^{-1}	Half-cell	[17]
COF$_{TPDA-PMDA}$@50%CNT	Tertiary amine, polyimide	-	Li$^+$, TFSI$^-$	50 % CNT	1.2–4.3	233 at 0.5 A g^{-1}	Half-cell	[18]
NTPI-COF	Tertiary amine, polyimide	-	Na$^+$, Cl$^-$	20% AB	-0.9–0.3	109 at 1 A g^{-1}	Half-cell and Symmetric full cell (aqueous battery)	[19]
TPAD-COF	Quinone, secondary amine	Imine	Na$^+$, PF$_6^-$	30% AB	1.5–4.1	186 at 0.05 A g^{-1}	Half-cell and full-cell	[20]
WTTF-COF	Tertiary amine, dithiolylide-ne	Imine	Li$^+$, PF$_6^-$	20% KB	0.1–3.6	200 at 0.5 A g^{-1}	Half-cell and Symmetric full cell (Li-ion battery)	This work

KB= Ketjenblack, CNT= Carbon nanotube, AB= Acetylene black, and Super P= Super performing conductive carbon black.

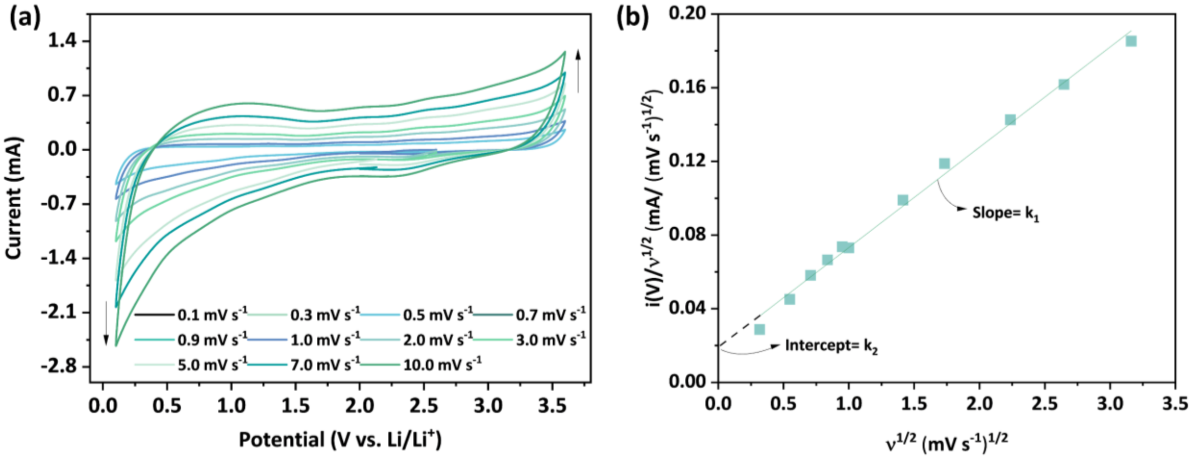

Figure 4.28 (a) Cyclic voltammograms at various scanning speeds of 0.1, 0.3, 0.5, 0.7, 0.9, 1.0, 2.0, 3.0, 5.0, 7.0, 9.0, and 10.0 mV s^{-1} and scanned over a potential window of 0.1-3.6 V vs. Li/Li^{+}. (b) Determination of the values of k_1 and k_2 as the slope and intercept between $i(V)/v^{1/2}$ vs. $v^{1/2}$ where V = 1 V vs. Li/Li^{+} during anodic sweep for half-cells utilizing **WTTF**-COF as working electrode. The deconvolution of total charge-storage into diffusive and capacitive contributions with respect to the applied scan rate.

4.6.4. Redox mechanism

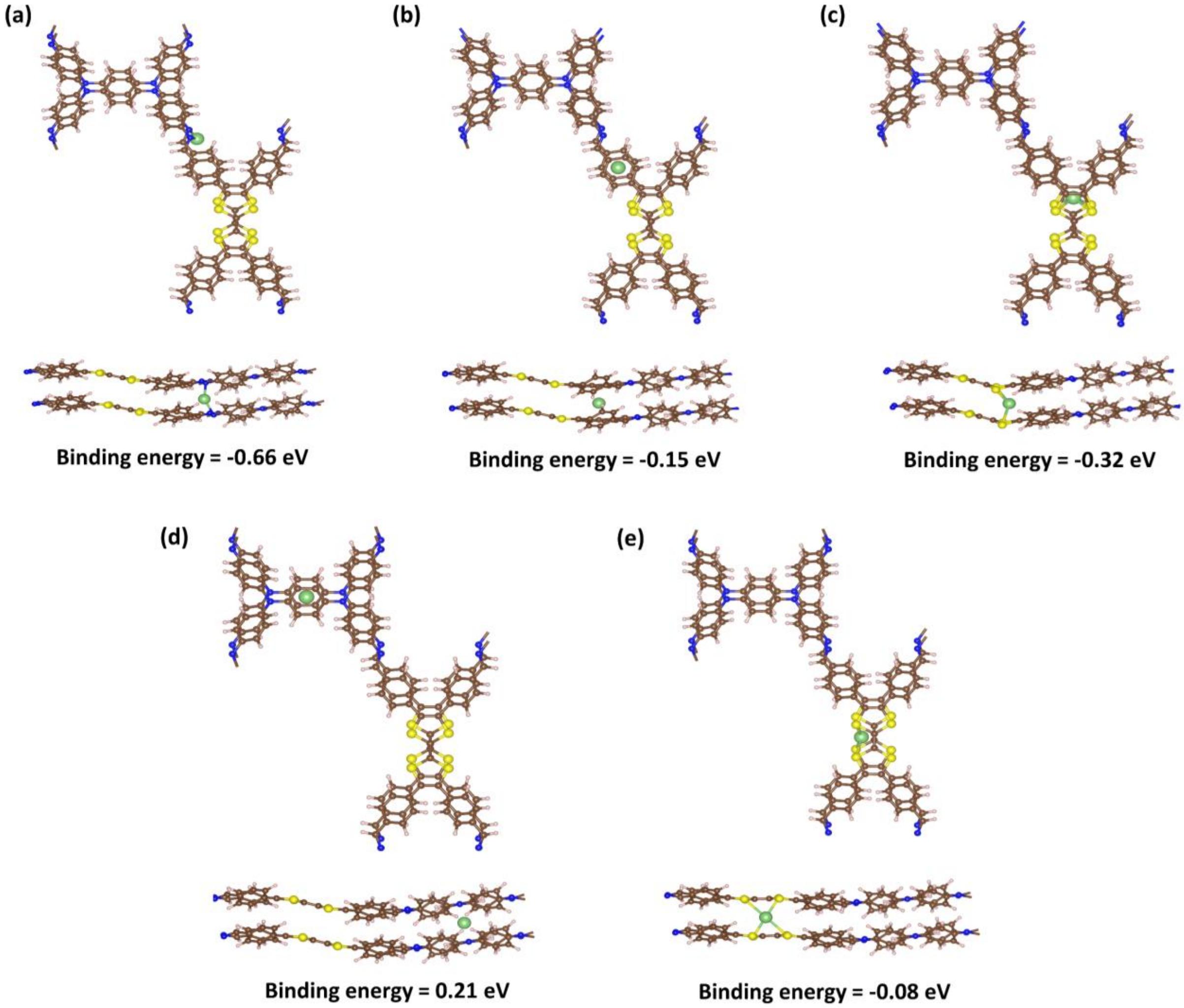

Figure 4.29 Possible binding configurations of Li-ion (green sphere) on **WTTF**-COF electrode.

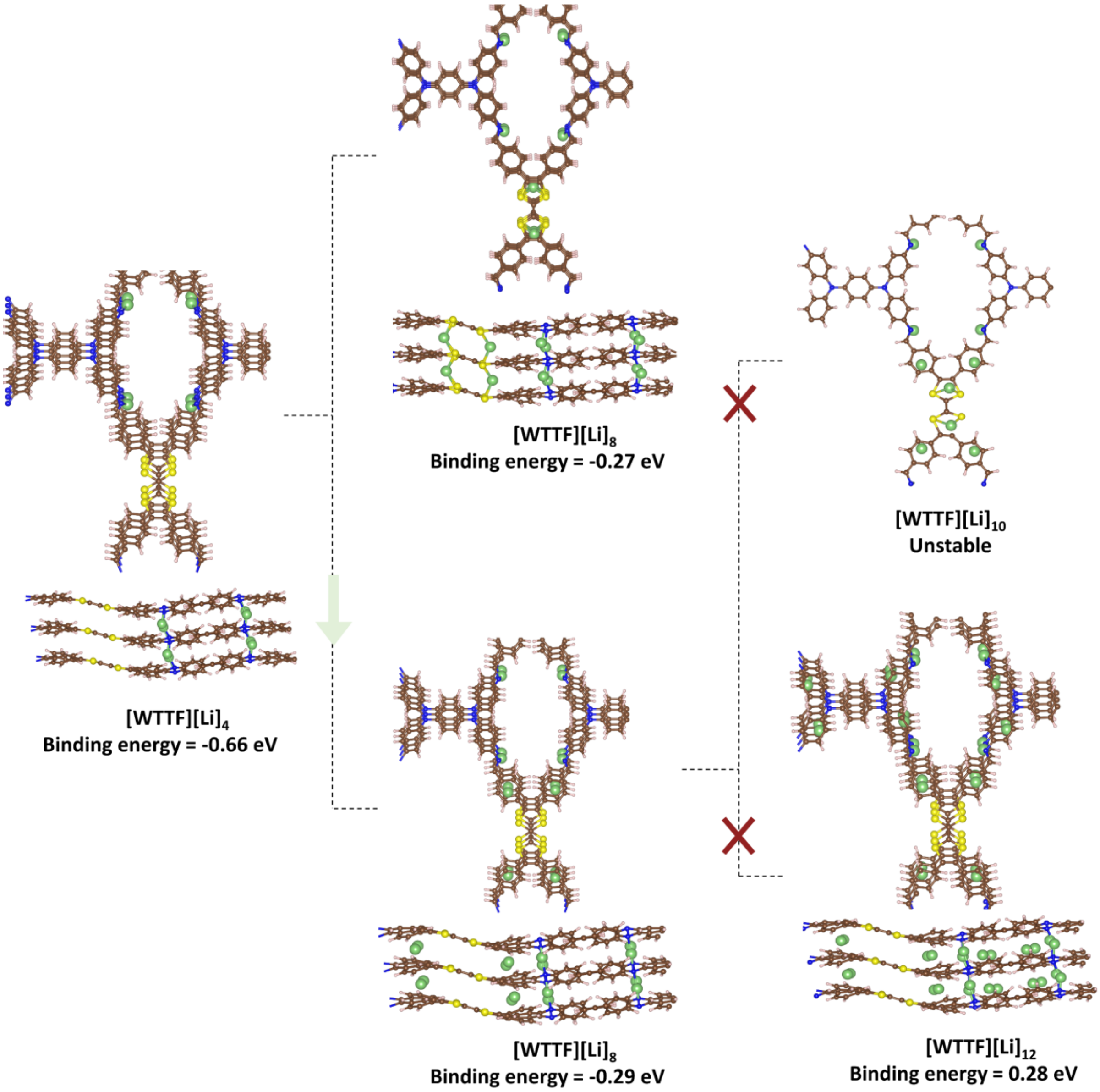

Figure 4.30 Possible mechanisms for charge storage in WTTF-COF electrode (Li-ions: green spheres).

Explanation for Li-ion binding mechanisms:

The binding energy per step is calculated as:

$$E_{B.E.} = (E_{COF+x_2Li} - E_{COF+x_1Li} - (x_2 - x_1)E_{Li})/(x_2 - x_1) \qquad \text{(Equation 4.7)}$$

where, E_{COF+x_2Li} and E_{COF+x_1Li} are the total energies of COF with x_2 and x_1 being number of Li atoms, respectively. E_{Li} is the energy of Li bulk metal.

After the Li-ions bind to all four imine nitrogens, additional lithiation can occur at the thiophene or phenyl rings of the TTF sites, as indicated by the binding site exploration in Figure 4.29 and 4.30. Figure 4.30 illustrates that binding at the phenyl ring through intercalation is energetically more favorable, with a binding energy of -0.29 eV. Further lithiation is not thermodynamically favorable, or it results in structural instability.

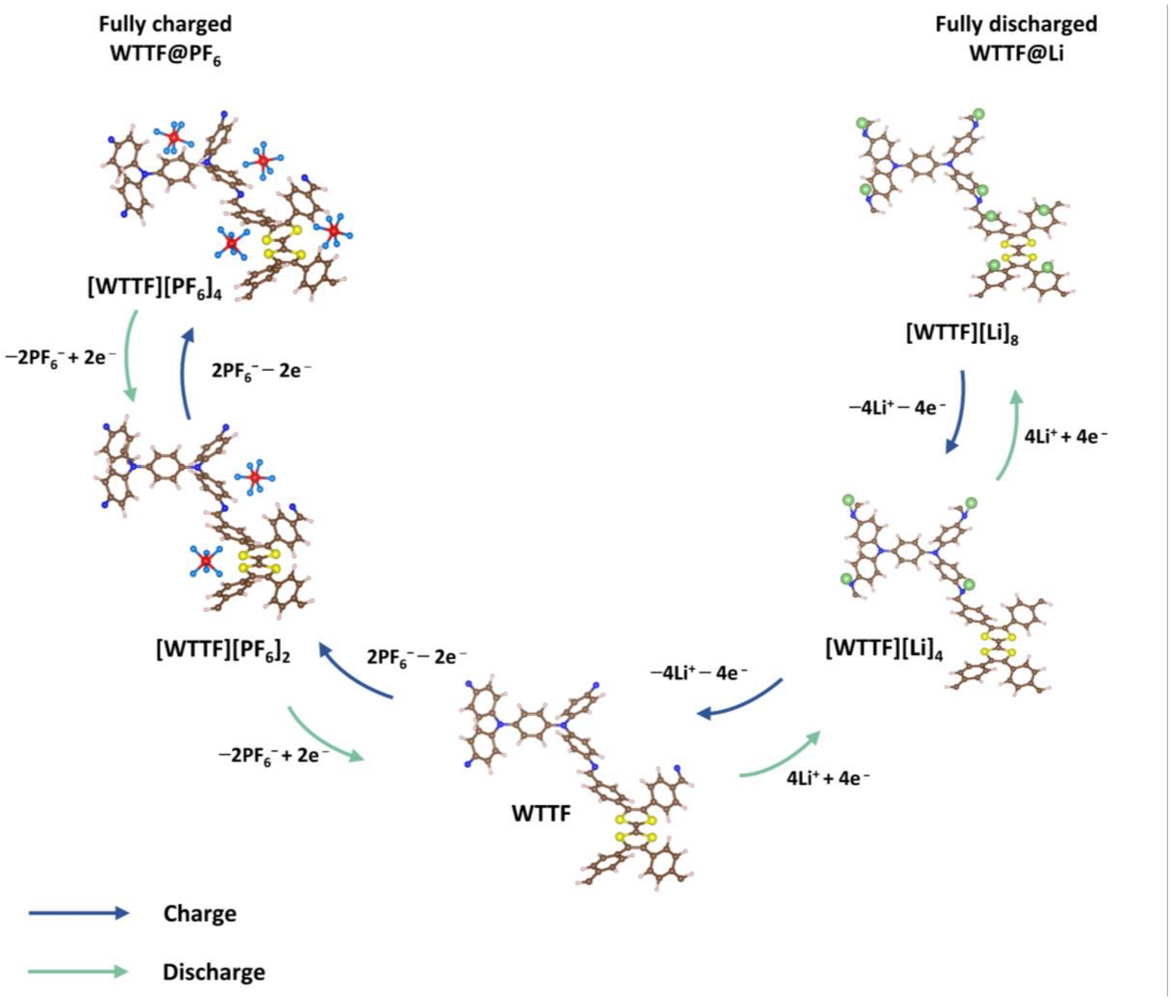

Figure 4.31 Proposed cycling redox mechanisms for charge storage in **WTTF**-COF electrode (Li^+ ions: green, PF_6^- ions: blue-red).

Theoretical capacity calculation:

$$\text{Theoretical capacity (mAh g}^{-1}\text{)} = n \times F \times 1000/3600 \times M \qquad \text{(Equation 4.8)}$$

where, n (= 12) is the number of electrons involved in the redox reaction per formula unit of the active material, F (= 96500) is Faraday's constant, M (= 1021) is the molar mass of the active material in grams per mole, and 1000/3600 is the factor to get the unit mAh g^{-1}.

For WTTF-COF electrode, the theoretical capacity = 315 mAh g^{-1}

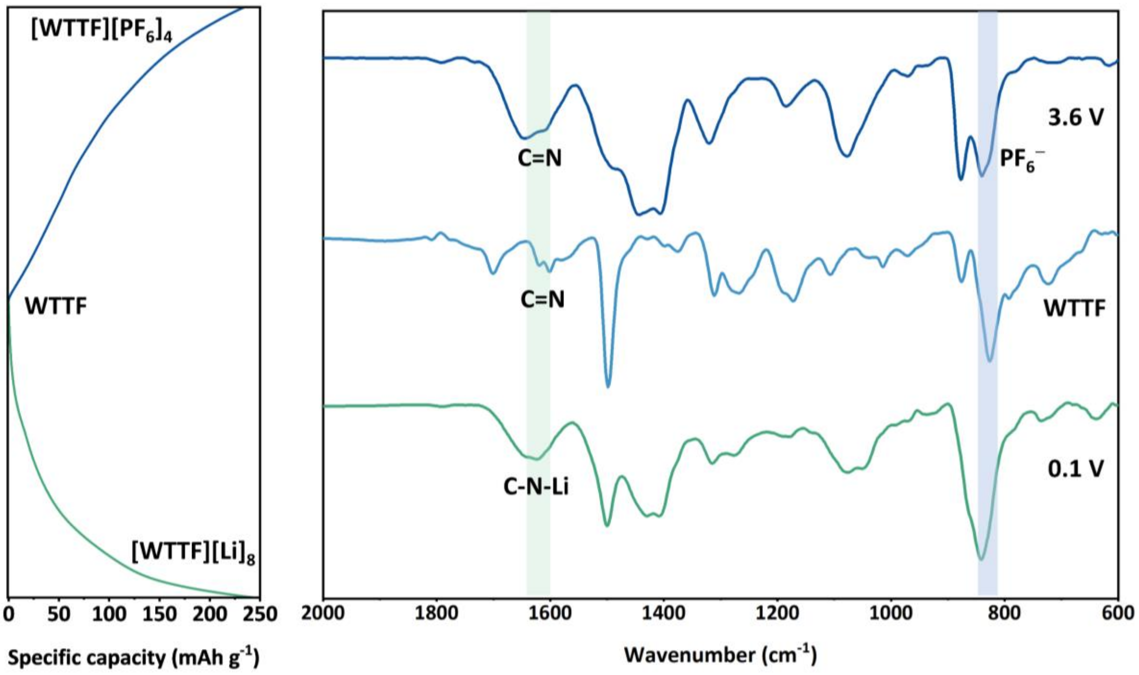

Figure 4.32 Ex-situ Fourier transform infrared (FTIR) spectroscopy analysis of **WTTF**-COF electrode before cycling, and after cycling to 0.1 V and to 3.6 V vs. Li/Li$^+$.

4.6.5. Charge-storage kinetics

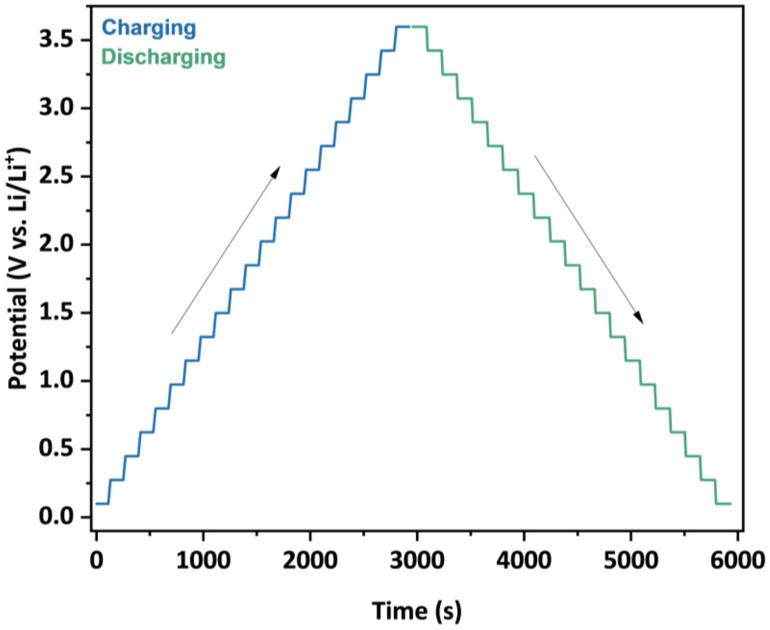

Figure 4.33 Potential-dependent electrochemical impedance spectroscopy (EIS) measurement at different potentials vs. Li/Li$^+$. Plot between applied potential with no. of steps (n= 42) and time (s).

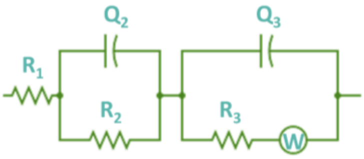

Figure 4.34 The equivalent electric circuit utilized to fit the data obtained by the EIS measurements during a full cycle for the electrochemical cell WTTF | 1 м $LiPF_6$ EC:DEC (1:1, v/v%) | Li.

Table 4.5 Electrochemical impedance spectroscopy (EIS) analysis at different potentials vs. Li/Li$^+$ for the electrochemical cell **WTTF** | 1 M $LiPF_6$ EC:DEC (1:1, v/v%) | Li between the operational window. Units are presented in the table notes.

	Potential	R_1	R_2	Q_2	n_2	f_2	R_3	Q_3	n_3	f_3	Chi^2
Charging cycling	0.1	5.203	48.68	3.81E-05	0.536	19827.57	72.69	0.000203	0.559	297.8852	3.69E-06
	0.27	5.268	42.55	3.53E-05	0.547	23062.57	85.63	0.00023	0.523	289.3573	1.74E-05
	0.44	5.239	43.23	3.58E-05	0.545	22443.5	88.44	0.000229	0.524	271.0579	2.04E-05
	0.62	5.328	37.06	3.02E-05	0.565	26566.39	100.6	0.000245	0.495	280.9382	3.06E-05
	0.79	5.272	42.63	3.27E-05	0.553	23099.78	95.46	0.000221	0.520	263.2805	2.86E-05
	0.97	5.271	30.73	2.48E-05	0.589	30843.54	114.9	0.000255	0.467	301.5655	3.64E-05
	1.14	5.434	36.15	2.81E-05	0.572	26807.57	109.6	0.000233	0.490	283.2404	4.24E-05
	1.32	5.456	43.48	3.09E-05	0.557	22677.39	101	0.000199	0.526	265.3577	2.25E-05
	1.49	5.447	32.71	2.53E-05	0.586	28491.63	121.7	0.000242	0.472	276.0666	3.63E-05
	1.67	5.566	37.32	2.64E-05	0.576	26233.88	116.3	0.000215	0.496	268.8331	2.66E-05
	1.84	5.473	37.11	2.79E-05	0.573	25419.19	122	0.000224	0.487	253.8014	0.000121
	2.02	5.439	30.97	2.36E-05	0.596	29012.74	134	0.000237	0.464	266.6174	4.82E-05
	2.19	5.475	51.15	3.28E-05	0.546	18926.79	103	0.000155	0.560	257.2021	0.000129
	2.37	5.442	35.54	2.69E-05	0.578	26354.18	132.3	0.000211	0.482	264.3769	5.00E-05
	2.54	5.429	32.46	2.52E-05	0.588	28170.83	140.2	0.000213	0.471	272.5637	6.22E-05
	2.72	5.382	30.99	2.45E-05	0.592	29232.72	144.2	0.000213	0.466	277.9947	8.99E-05
	2.89	5.424	33.95	2.59E-05	0.582	27891.01	140.5	0.000196	0.479	283.7172	0.000146
	3.07	5.625	41.02	2.94E-05	0.563	24120.42	129.4	0.000166	0.511	291.1541	9.89E-05
	3.24	5.489	52.7	3.36E-05	0.542	19028.59	110	0.000121	0.569	312.5818	0.000119
	3.42	5.562	51.42	3.14E-05	0.546	20281.78	113.8	0.000115	0.567	330.7184	0.000215
Discharging cycle	3.59	5.527	54.26	3.17E-05	0.543	19350.4	107.8	9.98E-05	0.582	383.5209	3.19E-05
	3.42	4.851	19.45	1.67E-05	0.657	34375.84	176.5	0.000214	0.428	330.6868	1.71E-05
	3.24	4.479	18.66	1.83E-05	0.656	30158.54	180.2	0.000243	0.414	298.3236	3.91E-05
	3.07	4.442	17.49	1.74E-05	0.666	30185.99	177	0.000241	0.413	328.4406	3.96E-05
	2.89	4.406	18.29	1.77E-05	0.660	30585.03	172.8	0.000236	0.416	343.5483	3.98E-05
	2.72	4.296	18.77	1.81E-05	0.660	28413.04	174	0.000253	0.411	317.518	6.84E-05
	2.54	4.216	18.95	1.84E-05	0.660	27388.95	174.3	0.000264	0.407	305.6766	6.75E-05
	2.37	4.392	18.3	1.61E-05	0.668	30559.51	168.7	0.000246	0.414	344.3547	4.73E-05
	2.19	4.804	19.09	1.57E-05	0.662	33534.98	160.2	0.00022	0.427	395.3946	1.77E-05
	2.02	4.594	18.2	1.45E-05	0.673	32970.57	162.7	0.000239	0.419	369.1238	3.58E-05
	1.84	4.515	17.3	1.38E-05	0.680	33518.16	162.8	0.000242	0.416	375.1963	2.40E-05
	1.67	5.146	22.4	1.75E-05	0.640	33288.59	148.1	0.000212	0.441	401.258	1.65E-05
	1.49	4.516	16.77	1.32E-05	0.686	33446.54	158.7	0.000244	0.415	395.5552	4.10E-05
	1.32	4.901	19.69	1.62E-05	0.656	33815.39	148.2	0.000224	0.431	425.9274	2.16E-05
	1.14	5.312	26.07	2.05E-05	0.618	30744.18	135.4	0.000206	0.454	417.1939	2.79E-05
	0.97	5.498	35.84	2.62E-05	0.581	25736.87	118.2	0.000185	0.489	391.5498	6.65E-05
	0.79	4.554	17.78	1.47E-05	0.671	34522.16	145.6	0.000228	0.425	475.937	6.97E-05
	0.62	4.515	16.96	1.48E-05	0.674	34810.61	144.2	0.000226	0.424	505.9157	6.60E-05
	0.44	4.624	17.54	1.65E-05	0.661	35505.16	138.9	0.000214	0.431	554.3993	6.87E-05
	0.27	5.026	22.33	2.13E-05	0.624	33070.26	126.6	0.000196	0.450	580.038	8.40E-05

R_1= internal resistance (Ω), R_2= resistance (Ω) due to SEI (R_{SEI}), and R_3= resistance (Ω) due to charge-transfer (R_{ct}). Q_2= constant phase element ($\Omega^{-1}s^n$) associated with R_2, n_2 is the exponent associated with Q_2, f_2 is the frequency (Hz) associated with R_2,Q_2, and n_2. Q_3= constant phase element ($\Omega^{-1}s^n$) associated with R_3 , n_3 is the exponent associated with Q_3, f_3 is the frequency (Hz) associated with R_3,Q_3, and n_3. Frequency was calculated using the following formula: $f= 1/2\pi(RQ)^{1/n}$ (Hz).

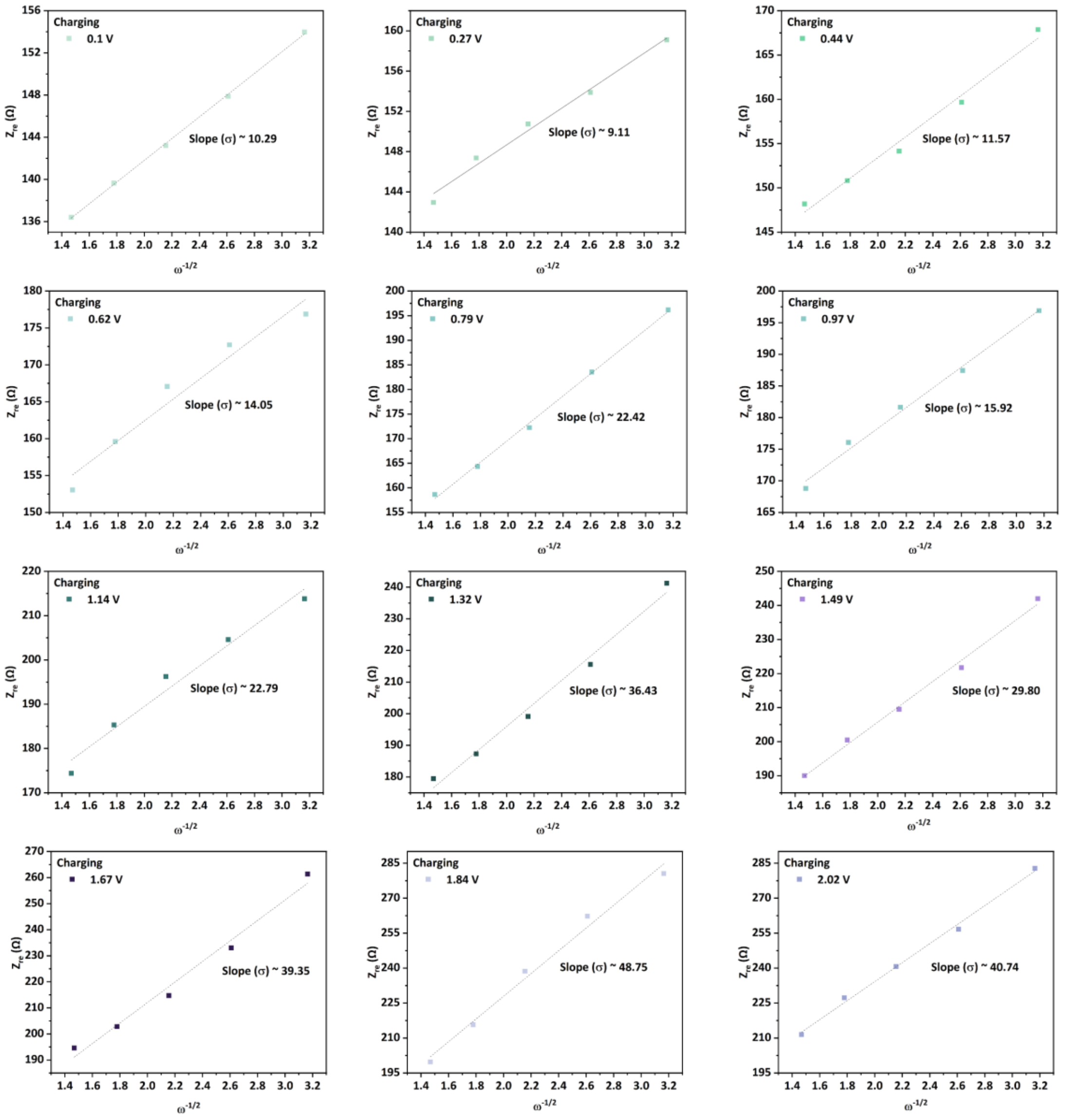

Figure 4.35 Warburg plots for the electrochemical cell WTTF | 1 M $LiPF_6$ EC:DEC (1:1, v/v%) | Li during positive sweep between potential range of 0.1 - 2.02 V vs. Li/Li^+.

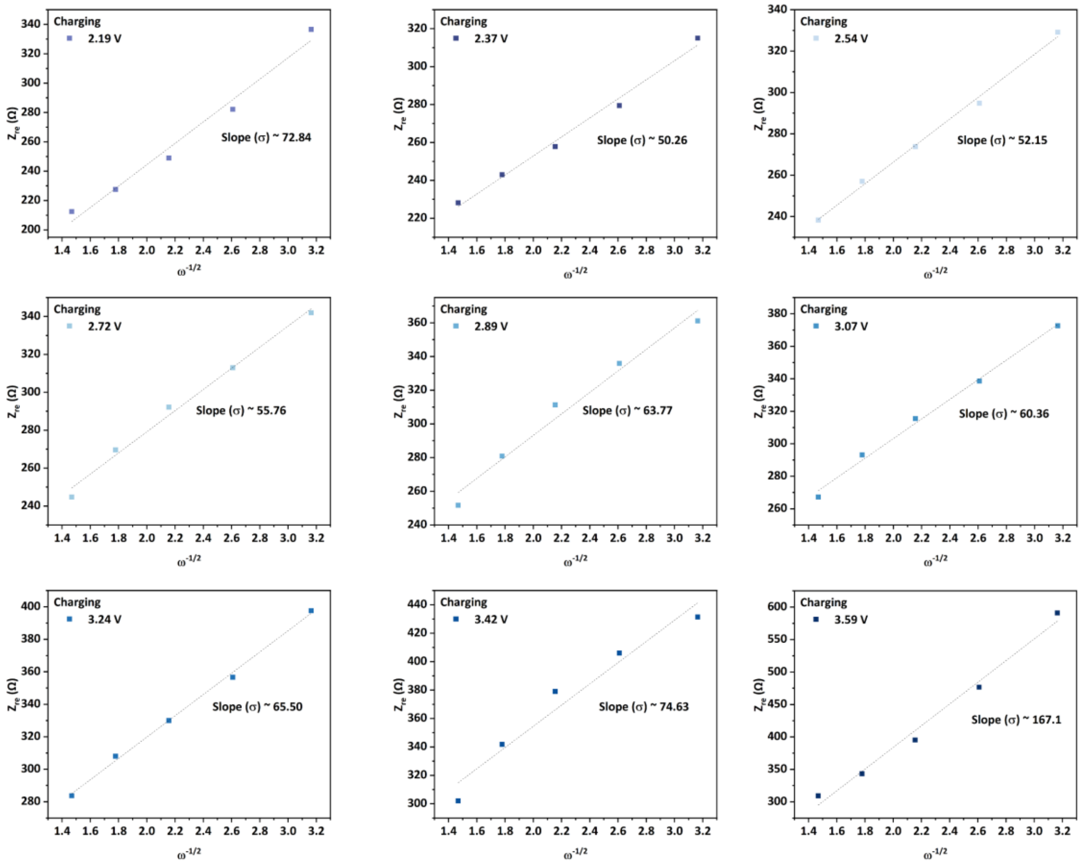

Figure 4.36 Warburg plots for the electrochemical cell **WTTF** | 1 ᴍ $LiPF_6$ EC:DEC (1:1, v/v%) | Li during positive sweep between potential range of 2.19 - 3.59 V vs. Li/Li^+.

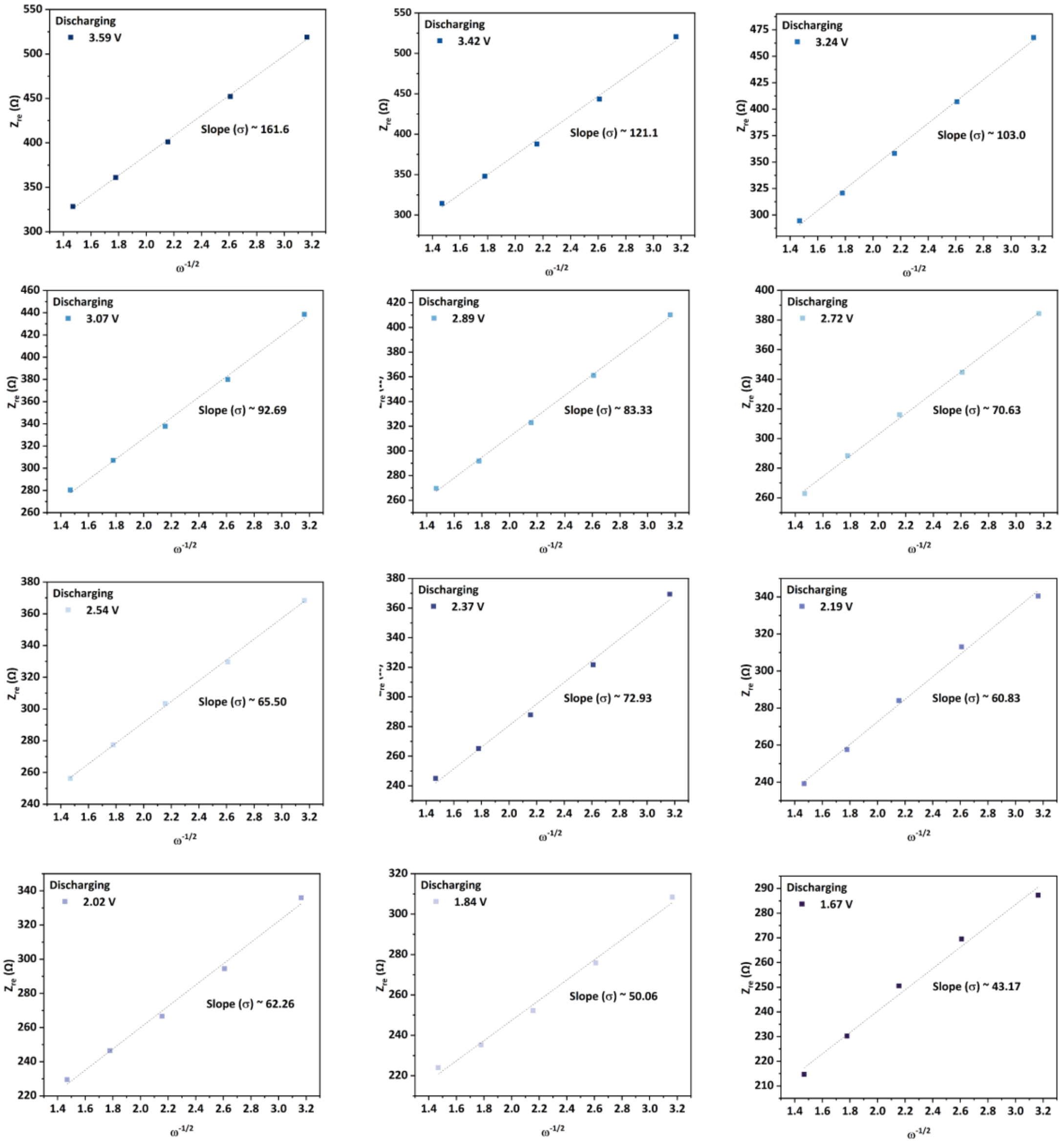

Figure 4.37 Warburg plots for the electrochemical cell **WTTF** | 1 м $LiPF_6$ EC:DEC (1:1, v/v%) | Li during negative sweep between potential range of 3.59 - 1.67 V vs. Li/Li^+.

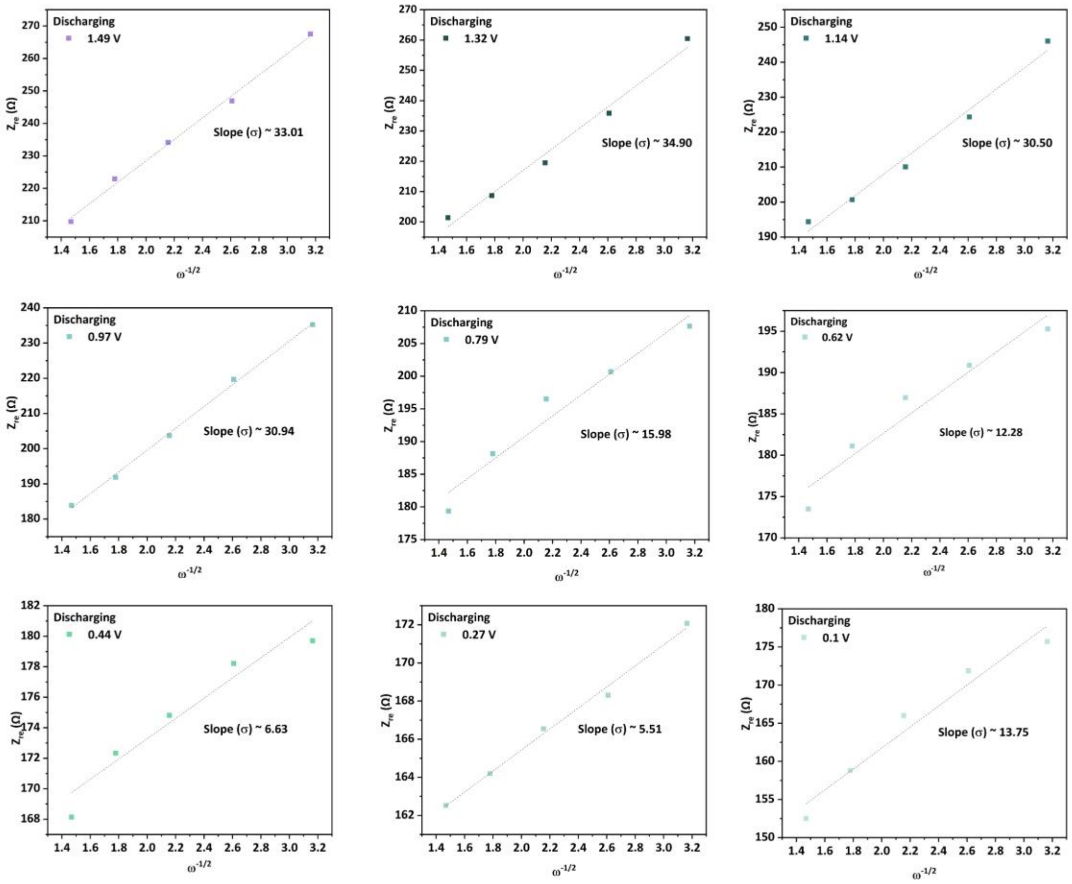

Figure 4.38 Warburg plots for the electrochemical cell **WTTF** | 1 м $LiPF_6$ EC:DEC (1:1, v/v%) | Li during negative sweep between potential range of 1.49 - 0.1 V vs. Li/Li^+.

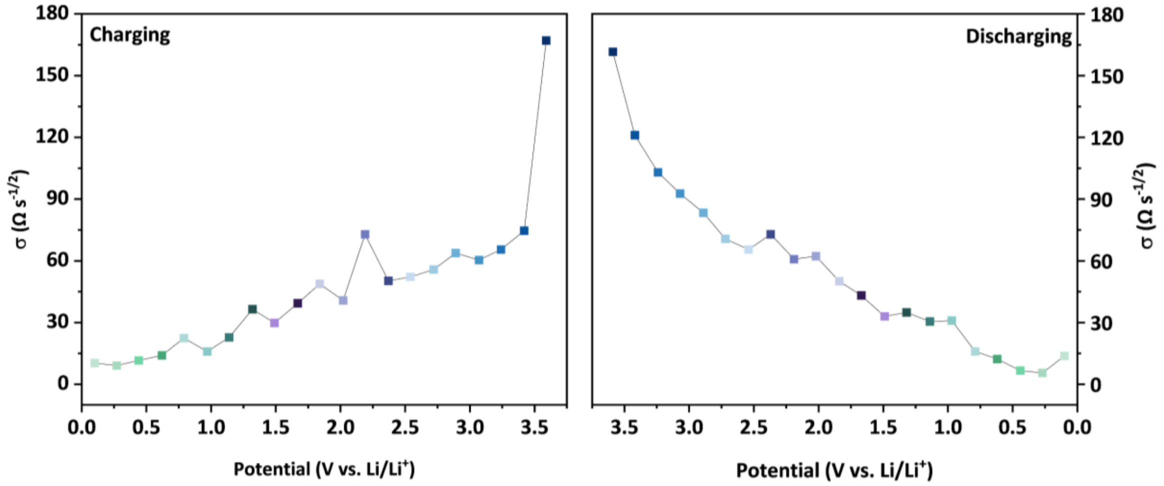

Figure 4.39 Warburg coefficient for the electrochemical cell WTTF | 1 м $LiPF_6$ EC:DEC (1:1, v/v%) | Li utilizing for **WTTF**-COF as working electrode during positive and negative sweeps between potential range of 0.1 - 3.6 V vs. Li/Li^+.

Table 4.6 Diffusion coefficient calculation for **WTTF**-COF electrode during positive and negative sweeps of the electrochemical cell WTTF | 1 м LiPF$_6$ EC:DEC (1:1, v/v%) | Li between potential range of 0.1 - 3.6 V vs. Li/Li$^+$.

Charging			**Discharging**		
Potential (V vs. Li/Li$^+$)	**Slope (σ, Ω s$^{-1/2}$)**	**Diffusion coefficient (cm^2 s^{-1})**	**Potential (V vs. Li/Li$^+$)**	**Slope (σ, Ω s$^{-1/2}$)**	**Diffusion coefficient (cm^2 s^{-1})**
0.1	10.29	5.19×10^{-11}	3.59	161.6	2.10×10^{-13}
0.27	9.11	6.62×10^{-11}	3.42	121.1	3.75×10^{-13}
0.44	11.57	4.10×10^{-11}	3.24	103	5.18×10^{-13}
0.62	14.05	2.78×10^{-11}	3.07	92.69	6.40×10^{-13}
0.79	22.42	1.09×10^{-11}	2.89	83.33	7.91×10^{-13}
0.97	15.92	2.17×10^{-11}	2.72	70.63	1.01×10^{-12}
1.14	22.79	1.06×10^{-11}	2.54	65.5	1.28×10^{-12}
1.32	36.43	4.14×10^{-12}	2.37	72.93	1.03×10^{-12}
1.49	29.8	6.19×10^{-12}	2.19	60.83	1.48×10^{-12}
1.67	39.35	3.55×10^{-12}	2.02	62.26	1.42×10^{-12}
1.84	48.75	2.31×10^{-12}	1.84	50.06	2.19×10^{-12}
2.02	40.74	3.31×10^{-12}	1.67	43.17	2.95×10^{-12}
2.19	72.84	1.04×10^{-12}	1.49	33.01	5.04×10^{-12}
2.37	50.26	2.18×10^{-12}	1.32	34.9	4.51×10^{-12}
2.54	52.15	2.02×10^{-12}	1.14	30.5	5.91×10^{-12}
2.72	55.76	1.77×10^{-12}	0.97	30.94	5.74×10^{-12}
2.89	63.77	1.35×10^{-12}	0.79	15.98	2.15×10^{-12}
3.07	60.36	1.51×10^{-12}	0.62	12.28	3.64×10^{-11}
3.24	65.5	1.28×10^{-12}	0.44	6.63	1.25×10^{-10}
3.42	74.63	9.87×10^{-13}	0.27	5.51	1.81×10^{-10}
3.59	167.1	1.97×10^{-13}	0.1	13.75	2.91×10^{-11}

$\boldsymbol{R} =$ 8.314 J K^{-1} mol^{-1}, $\boldsymbol{T}$ =298.15 K, $\boldsymbol{n} =$ 1, $\boldsymbol{F}$= 96458 C mol^{-1}, $\boldsymbol{C}$ =1.0 м, $\boldsymbol{A}$ = 0.000254 m^2

$R^2T^2/2n^4F^4C^2A^2$= 5.49474 × 10^{-13}

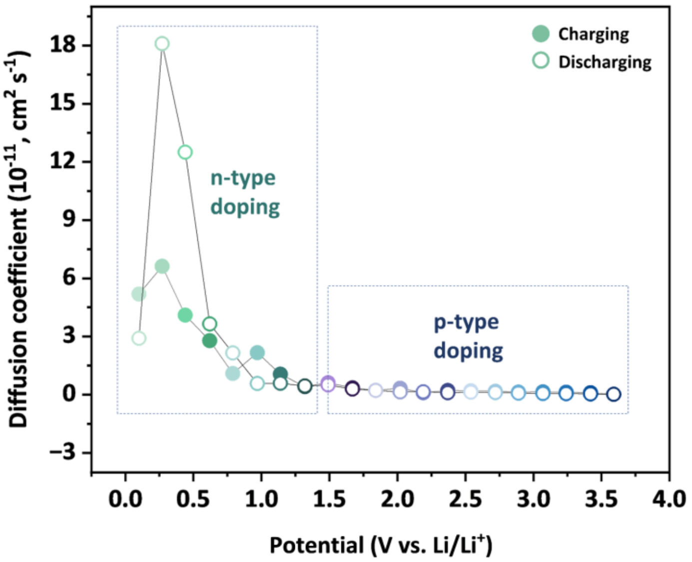

Figure 4.40 The schematic illustration to demonstrate the plausible n-type and p-type doping regions and corresponding calculated diffusion coefficient (D) over the range of 0.1 - 3.6 V vs. Li/Li$^+$ for half-cells WTTF | 1 M $LiPF_6$ EC:DEC (1:1, v/v%) | Li during a full cycle.

4.6.6. Symmetric cell

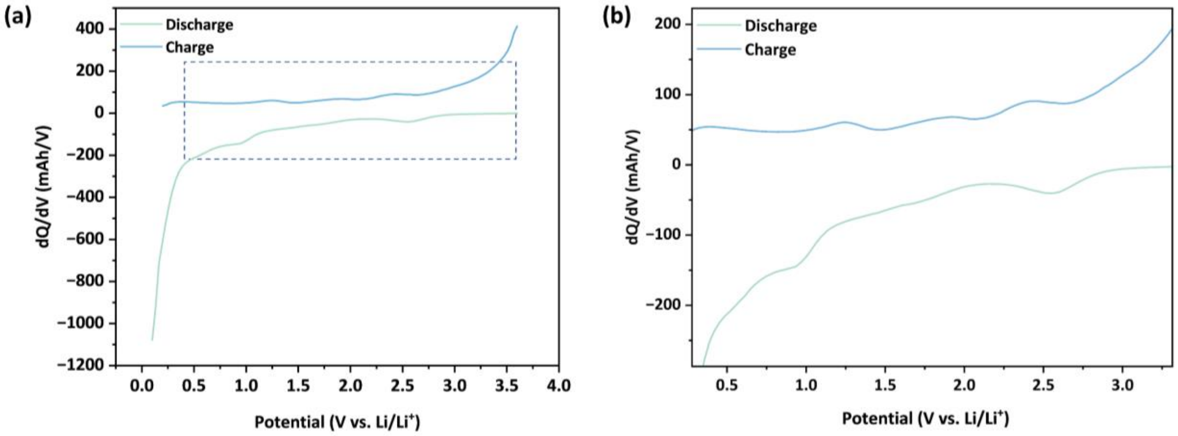

Figure 4.41 (a) dQ/dV curves for **WTTF**-COF electrode during charging and discharging cycle within the potential range of 0.1 - 3.6 V vs. Li/Li$^+$ and **(b)** of 0.2 - 3.4 V vs. Li/Li$^+$.

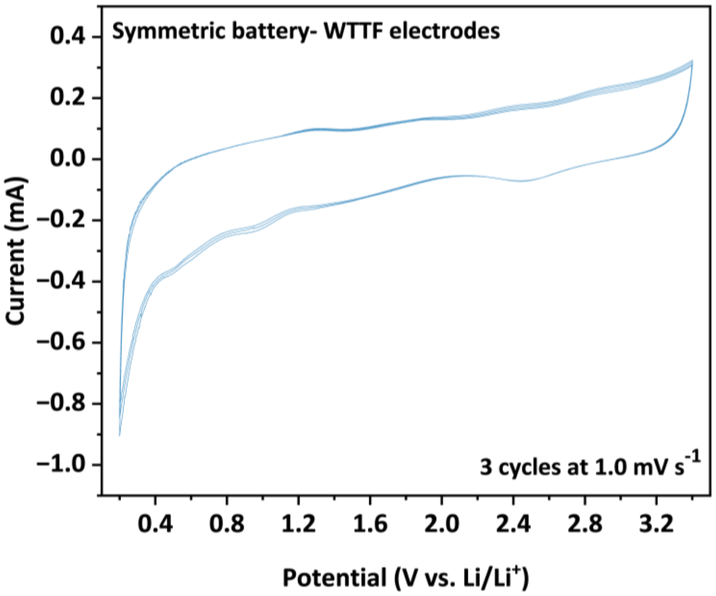

Figure 4.42 Cyclic voltammetry measurements of symmetric full cell utilizing **WTTF**-COF as positive as well as negative electrode at a scan speed of 1.0 mV s^{-1} for initial 3 cycles within the potential range of 0.2 - 3.4 V vs. Li/Li$^+$.

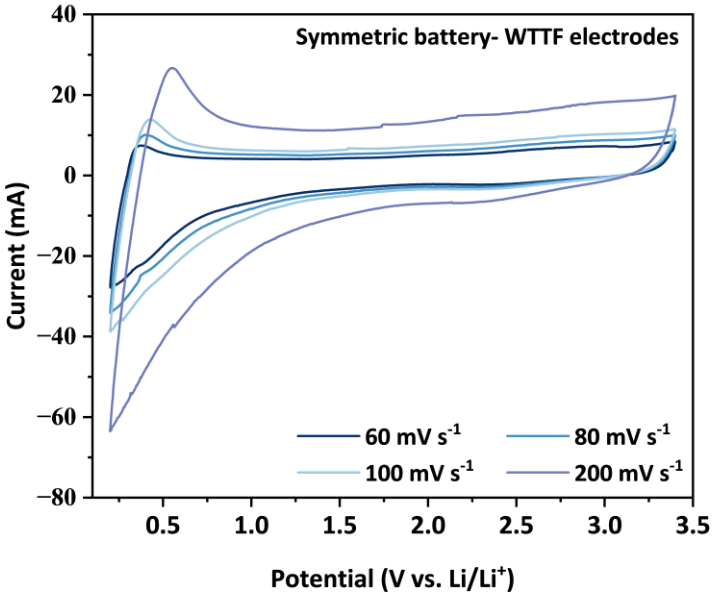

Figure 4.43 Cyclic voltammetry measurements of symmetric full cell utilizing **WTTF**-COF as positive as well as negative electrode at scan speeds of 60, 80, 100 and 200 mV s^{-1} within the potential range of 0.2 - 3.4 V vs. Li/Li$^+$.

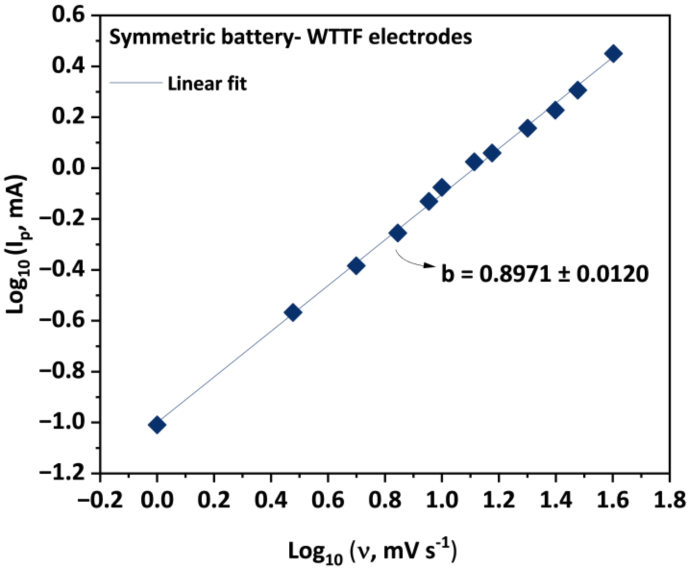

Figure 4.44 Charge-storage kinetics of symmetric full cell utilizing **WTTF**-COF as positive as well as negative electrode. Plot between $\log_{10}$ of i_p vs $\log_{10}$ of ν, where ν= 1.0, 3.0, 5.0, 7.0, 9.0, 10, 13, 15, 20, 25, 30, and 40 mV s^{-1} to obtain the b-value.

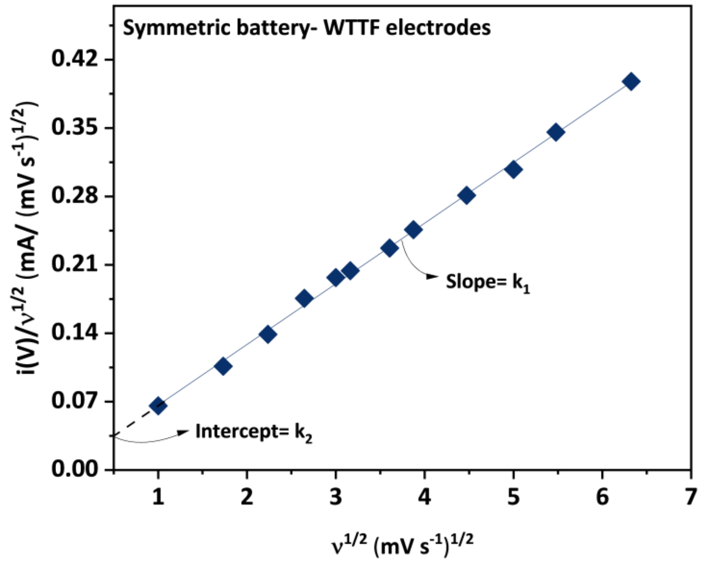

Figure 4.45 Charge-storage kinetics of symmetric full cell utilizing **WTTF**-COF as positive as well as negative electrode. Plot between $i(V)/\nu^{1/2}$ and $\nu^{1/2}$, where ν = 1.0, 3.0, 5.0, 7.0, 9.0, 10, 13, 15, 20, 25, 30, and 40 mV s^{-1} to obtain the values of k_1 and k_2.

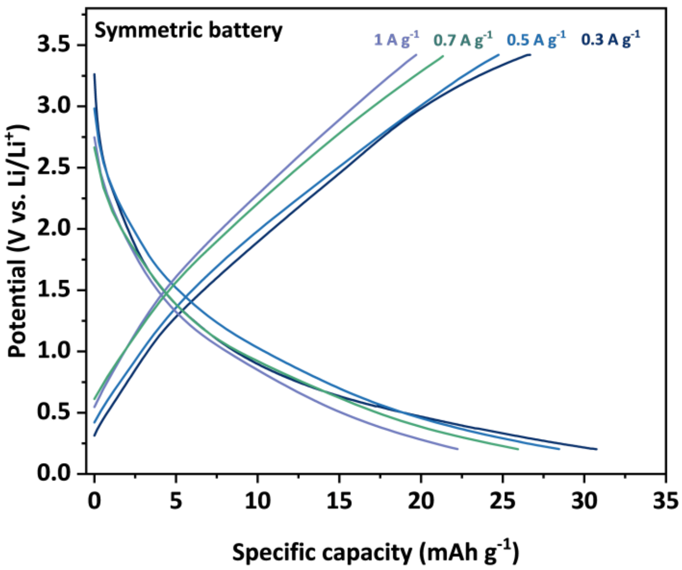

Figure 4.46 Galvanostatic charge-discharge profiles for symmetric full cell utilizing **WTTF**-COF as electrodes at applied current densities of 0.3, 0.5, 0.7 and 1.0 A g^{-1} within the potential range of 0.1 - 3.6 V vs. Li/Li^+.

4.6.7. References

[1] M. Elstner, D. Porezag, G. Jungnickel, J. Elsner, M. Haugk, T. Frauenheim, S. Suhai, G. Seifert, *Phys. Rev. B* **1998**, *58*, 7260.

[2] Vrije Universiteit, Amsterdam, The Netherlands, *ADF 2023.1, SCM, Theoretical Chemistry* **2023**.

[3] M. Gaus, X. Lu, M. Elstner, Q. Cui, *Journal of chemical theory and computation* **2014**, *10*, 1518.

[4] G. Kresse, J. Hafner, *Physical review. B, Condensed matter* **1993**, *47*, 558.

[5] J. P. Perdew, K. Burke, M. Ernzerhof, *Physical review letters* **1996**, *77*, 3865.

[6] S. Grimme, S. Ehrlich, L. Goerigk, *Journal of computational chemistry* **2011**, *32*, 1456.

[7] S. Grimme, J. Antony, S. Ehrlich, H. Krieg, *The Journal of chemical physics* **2010**, *132*, 154104.

[8] P. E. Blöchl, *Physical review. B, Condensed matter* **1994**, *50*, 17953.

[9] G. Kresse, D. Joubert, *Physical review. B, Condensed matter* **1999**, *59*, 1758.

[10] G. Henkelman, B. P. Uberuaga, H. Jónsson, *The Journal of chemical physics* **2000**, *113*, 9901.

[11] M. J. k. Frisch, G. W. Trucks, H. B. Schlegel, G. E. Scuseria, M. A. Robb, J. R. Cheeseman, G. Scalmani, V. Barone, B. Mennucci, G. Petersson **2015**.

[12] W. Li, Q. Huang, H. Shi, W. Gong, L. Zeng, H. Wang, Y. Kuai, Z. Chen, H. Fu, Y. Dong, C. Zhang, *Adv Funct Materials* **2024**, *34*, 2310668.

[13] L. Gong, X. Yang, Y. Gao, G. Yang, Z. Yu, X. Fu, Y. Wang, D. Qi, Y. Bian, K. Wang, J. Jiang, *J. Mater. Chem. A* **2022**, *10*, 16595.

[14] Q. Xu, Z. Liu, Y. Jin, X. Yang, T. Sun, T. Zheng, N. Li, Y. Wang, T. Li, K. Wang, J. Jiang, *Energy Environ. Sci.* **2024**, *17*, 5451.

[15] S. Gu, J. Chen, R. Hao, X. Chen, Z. Wang, I. Hussain, G. Liu, K. Liu, Q. Gan, Z. Li, H. Guo, Y. Li, H. Huang, K. Liao, K. Zhang, Z. Lu, *Chemical Engineering Journal* **2023**, *454*, 139877.

[16] Y. Liu, Y. Lu, A. Hossain Khan, G. Wang, Y. Wang, A. Morag, Z. Wang, G. Chen, S. Huang, N. Chandrasekhar, D. Sabaghi, D. Li, P. Zhang, D. Ma, E. Brunner, M. Yu, X. Feng, *Angewandte Chemie (International ed. in English)* **2023**, *62*, e202306091.

[17] M. Wu, Y. Zhao, R. Zhao, J. Zhu, J. Liu, Y. Zhang, C. Li, Y. Ma, H. Zhang, Y. Chen, *Adv Funct Materials* **2022**, *32*, 2107703.

[18] L. Yao, C. Ma, L. Sun, D. Zhang, Y. Chen, E. Jin, X. Song, Z. Liang, K.-X. Wang, *Journal of the American Chemical Society* **2022**, *144*, 23534.

[19] D. Geng, H. Zhang, Z. Fu, Z. Liu, Y. An, J. Yang, D. Sha, L. Pan, C. Yan, Z. Sun, *Advanced science (Weinheim, Baden-Wurttemberg, Germany)* **2024**, *11*, e2407073.

[20] L. Cheng, X. Yan, J. Yu, X. Zhang, H.-G. Wang, F. Cui, Y. Wang, *Advanced materials (Deerfield Beach, Fla.)* **2025**, *37*, e2411625.

5

This chapter is based on the following article-

Tuning Redox Behavior of Pyrene–benzothiadiazole/TTF–Based Covalent Organic Framework Electrodes in Dual-Ion Batteries.

Apeksha Singh,[1] Dominic Blätte,[1] Roman Guntermann,[1] Lucie Quincke,[2] Jennifer LM Rupp,[2] and Thomas Bein*[1]

[1]Department of Chemistry and Center for NanoScience (CeNS), Ludwig-Maximilians- Universität München (LMU Munich), Butenandtstrasse 5-13 (E), 81377 Munich, Germany

[2]Department of Chemistry, TUM School of Natural Sciences, Technical University of Munich (TUM), Lichtenbergstrasse 4, 85748 Garching, Germany

KEYWORDS: dual-ion redox chemistry, electrolyte composition, ion-storage dynamics

Manuscript accepted in Angewandte Chemie

5.1. Abstract

Covalent organic frameworks (COFs) have emerged as promising electrode materials for secondary-ion batteries, where redox-active building blocks and linkages enable tunable redox properties, while ordered pores serve as nanochannels for fast ion transport. We report a novel highly crystalline 2D PyTTF-COF, synthesized by integrating *n*-type pyrene–benzothiadiazole (PyBT) and *p*-type tetrathiafulvalene (TTF) subunits via an *n*-type imine linkage, yielding a bipolar electrode capable of reversible 16 e$^-$ dual cation–anion storage. Initially, the dual-ion redox synergy was tested in a Li-ion half-cell, where PyTTF served as cathode, and 1 M $LiPF_6$ or LiTFSI electrolytes were employed to probe anion-dependent electrochemical behavior. Electrochemical evaluation in Li-ion half cells revealed a wide electrochemical window of 0.1−3.6 V vs. Li/Li$^+$, with markedly enhanced charge-storage kinetics and ion diffusion with LiTFSI relative to $LiPF_6$ electrolytes. The PyTTF electrode delivered specific capacities of 286 mAh g^{-1} (LiTFSI) and 184 mAh g^{-1} ($LiPF_6$) at 0.3 A g^{-1}, highlighting the strong influence of anion identity. Systematic variation of LiTFSI salt concentration (1−3 M) revealed strong correlations between electrolyte composition, ion storage dynamics, and interfacial charge-transfer resistance. This study highlights, for the first time, the critical importance of tailoring both charge-carrier identity and concentration to unlock the full potential of bipolar COF electrodes for dual-ion batteries.

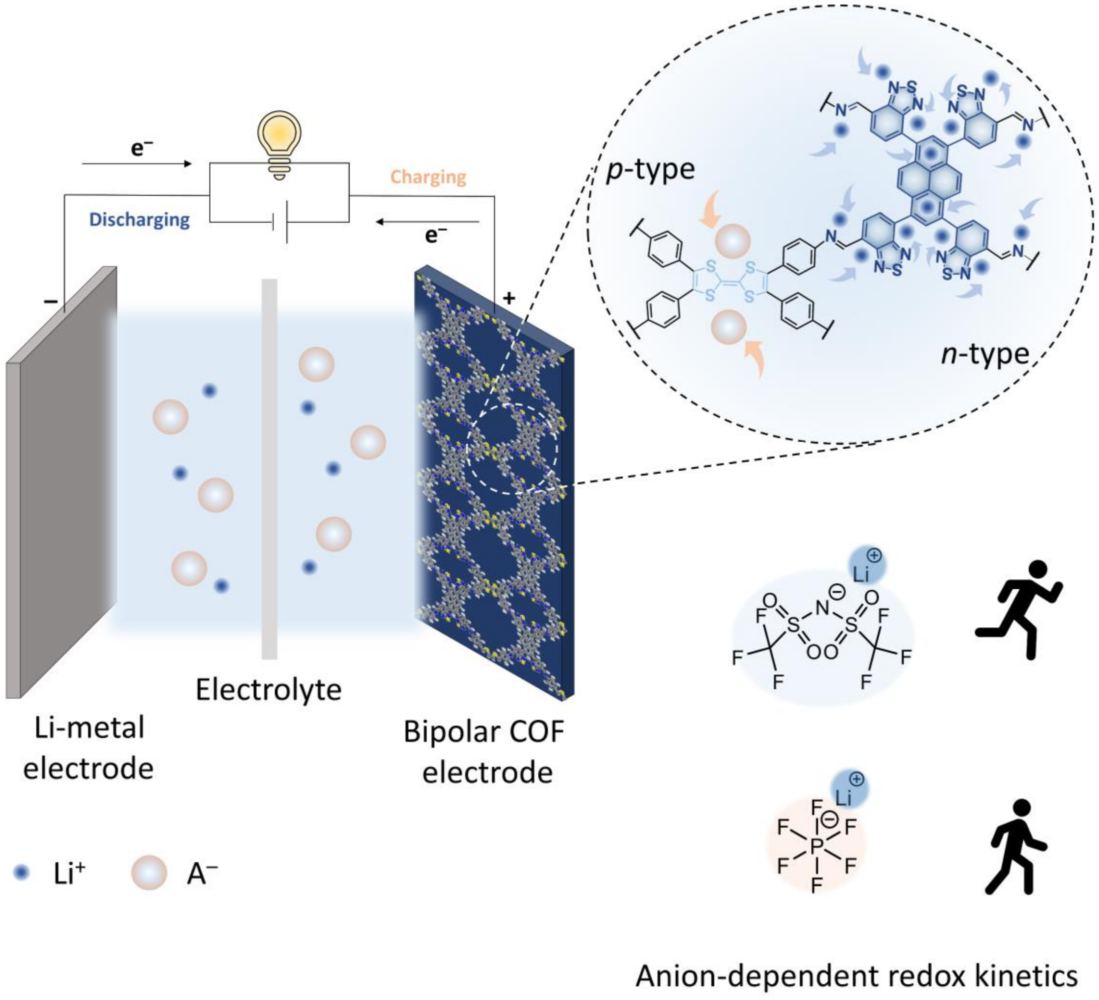

5.2. Introduction

Lithium-ion batteries (LIBs) represent the forefront of contemporary energy storage technologies, owing to their high energy density, prolonged cycle life, and operational efficiency.[1–3] LIBs have dominated the energy storage market since their commercialization in the 1990s, conventionally comprising a graphite-derived negative electrode operating at low potentials and a high-voltage oxide-based positive electrode, such as $LiCoO_2$, $LiMn_2O_4$, etc.[1] Over the past decades, significant efforts have been directed toward enhancing the overall energy density, rate performance and operating voltages, while simultaneously addressing the environmental and ethical concerns associated with mining toxic and scarce metals.[2,4] Consequently, there has been growing interest in innovative organic electrode materials (OEMs), particularly redox-active polymers and molecules, which offer both sustainability and electrochemical versatility.[5,6]

Covalent organic frameworks (COFs) have recently emerged as a highly promising class of OEMs, attracting considerable attention in the field of energy storage.[7,8] Through precise molecular engineering and strategic selection of building blocks, COFs can achieve highly reversible ion insertion/extraction processes, positioning them as promising candidates for lithium and beyond lithium batteries.[9] Unlike conventional OEMs, COFs exhibit both an extended conjugated structure, and intrinsically ordered conduction pathways, which collectively contribute to superior structural stability and enhanced charge transport properties.[10] These distinctive characteristics render COFs particularly advantageous for energy storage applications, offering moreover key benefits such as insolubility in liquid electrolytes, exceptional thermal stability, and remarkable design flexibility, thereby surpassing the limitations of traditional OEMs.[6,11]

Similar to conventional organic electrodes, COFs can be strategically designed to exhibit *n*-type, *p*-type, or bipolar-type (*b*-type) redox features, depending on the nature of redox functionalities of the monomers and the linkage.[9] The *n*-type redox-active motifs such as alkene (C=C), carbonyl (C=O), imine (C=N), azo (N=N), and cyclic diones like quinones offer elevated gravimetric capacities, while *p*-type moieties, including polysulfides, triphenylamine, and organic radicals facilitate rapid redox kinetics.[12–18] *n*-Type COFs, by accepting electrons into their lowest unoccupied molecular orbital (LUMO), enable the insertion of alkali metal cations ($M^+ = Li^+, Na^+, K^+$).[19] In contrast, *p*-type COFs host anionic species (A^-) such as PF_6^-, $TFSI^-$, FSI^-, BF_4^-, etc. by donating electrons from their highest occupied molecular orbital (HOMO).[20] Additionally, *b*-type COFs, consisting of both *n*-type and *p*-type centers, enable the reversible storage of both cations and anions over the stable operational potentials, significantly enhancing their electrochemical versatility within a single material.[12,14–16,19,21] The redox synergy associated with dual-ion storage is likely influenced by both the identity of the metal cation and the anion, as well as the composition of the electrolyte, yet these effects remain largely unexplored for *b*-type COF electrodes.[22,23]

Tetrathiafulvalene (TTF) and derivatives are potent organic electron donors, undergoing two reversible one-electron oxidations (TTF → $TTF^{+\bullet}$ → TTF^{2+}), with the intermediate radical cation ($TTF^{+\bullet}$) possessing an unpaired electron delocalized across the extended π-conjugated framework, facilitating rapid redox kinetics.[11,12,24] Pyrene–benzothiadiazole (PyBT)-based conductive polymers have demonstrated a high degree of charge delocalization, a narrow band gap of 1.95 eV, and a low-lying LUMO predominantly localized on the benzothiadiazole (BT) moiety.[25] This preferential LUMO localization on the BT unit, rather than on the rigid polycyclic aromatic pyrene subunit, contributes to the enhanced structural stability of the electrode by mitigating the risk of M^+ over-insertion, which would otherwise distort the aromatic ring system of pyrene.[5,25] Consequently, the incorporation of BT units serves as an effective design strategy to balance electronic delocalization for structural robustness. While TTF-units have been utilized in high-voltage COF electrodes based on anion storage at elevated potentials, the incorporation of PyBT as *n*-type subunit within a COF architecture has yet to be investigated.[24]

Herein, we report the design and synthesis of a highly crystalline COF, PyTTF-COF, via the Schiff-base condensation of an *n*-type pyrene–benzothiadiazole (PyBT) unit with a *p*-type tetrathiafulvalene (TTF) unit, and its subsequent application as an active electrode material for dual-ion batteries. The structural, physicochemical, and electronic properties of PyTTF-COF were comprehensively characterized to establish its crystallinity and intrinsic functionalities. A previous study from our group on COF-based bipolar electrodes established that the storage of cations and anions within a bipolar architecture can result in distinct ion transport/ storage chemistries.[12] Building upon this concept, we now explore the influence of different anion chemistries while maintaining a constant cation species on the ion-storage dynamics. To this end, we fabricated Li-ion half-cells using PyTTF electrode as working electrode (WE), employing two analogous electrolytes consisting of 1 м LiTFSI and 1 м $LiPF_6$ in a propylene carbonate (PC): diethylene carbonate (DEC) (1:1 v/v) solvent system, respectively. This comparative study elucidates the influence of anion identity on charge-storage kinetics and overall electrochemical performance, as probed by cyclic voltammetry (CV), galvanostatic charge–discharge (GCD), and potential-dependent electrochemical impedance spectroscopy (EIS). Finally, the superior performance displayed by the LiTFSI-based half-cell motivated a detailed investigation into the evolving behavior of ion-storage processes of the bipolar-type PyTTF electrode under varying charge-carrier concentrations.

5.3. Results and discussion

5.3.1. Synthesis and characterization

To enhance the cationic storage capability of the COF electrode, a novel *n*-type building block PyBT-CHO, 7,7',7'',7'''-(pyrene-1,3,6,8-tetrayl)tetrakis(benzo[*c*][1,2,5]thiadiazole-4-carbaldehyde) was synthesized following a modified reported procedure.[26,27] As described in Section 5.6.3.1, Appendix, the organic synthesis was carried out in a four-step synthetic sequence. Initially, two key intermediates were prepared: 1,3,6,8-tetrakis(4,4,5,5-tetramethyl-1,3,2-dioxaborolan-2-yl)pyrene via Suzuki–Miyaura borylation, and 7-bromo-4-(5,5-dimethyl-1,3-dioxan-2-yl)benzo[*c*][1,2,5]thiadiaz-ole through an acid-catalyzed protection reaction, respectively (Figure 5.4−5.7, Section 5.6.3.2, Appendix). These intermediates were subsequently subjected to Pd(0) catalyzed Suzuki–Miyaura cross-coupling using $Pd(PPh_3)_4$ as catalyst, affording the protected intermediate 1,3,6,8-tetrakis(7-(5,5-dimethyl-1,3-dioxan-2-yl)benzo[*c*][1,2,5]thiadiazol-4-yl)pyrene (Figure 5.8,5.9, Section 5.6.3.2, Appendix). Finally, acid-mediated deprotection afforded the targeted PyBT-CHO monomer in an isolated yield of 64% (Figure 5.10,5.11, Section 5.6.3.2, Appendix).

To rationally design a *b*-type COF, we strategically selected the *n*-type PyBT-CHO unit, previously demonstrated to accommodate up to 10 alkali metal cations (M^+), and an electron-rich *p*-type 4,4',4'',4'''-([2,2'-bi(1,3-dithiolylidene)]-4,4',5,5'-tetrayl)tetraaniline ($TTF-NH_2$) monomer.[12,27] The TTF-node readily undergoes two-step oxidation forming TTF^{2+}, effectively facilitating negative ion (A^-) storage by balancing charge (Figure 5.1a,b).[11,24] To synthesize the PyTTF-COF, Schiff base condensation was carried out under solvothermal conditions by dissolving the building blocks in a 1:1 v/v mixture of benzyl alcohol and 1,2-dichlorobenzene, along with 0.1 mL of 6 M acetic acid added as a catalyst, and heating at 120 °C for 72 hours (Scheme 5.1, Section 5.6.3.3, Appendix).[28] In addition, two modulating agents, benzaldehyde and aniline, were screened to improving the crystallinity of the resulting PyTTF-COF, with 1.5 equiv. aniline as modulator furnishing the most crystalline sample (Figure 5.12, Section 5.6.3.3, Appendix).[29] The successful formation of imine bonds was confirmed by Fourier transform infrared (FT-IR) spectroscopy, which revealed an absorbance band at ~1620 cm^{-1}, attributed to the C=N bond, along with a concurrent reduction of the vibrational feature of C=O at ~1740 cm^{-1} (Figure 5.13, Section 5.6.3.4, Appendix).

Powder X-ray diffraction (PXRD) analysis was carried out for the synthesized bulk material (Figure 5.14, Section 5.6.3.4, Appendix). The resulting diffraction pattern revealed that PyTTF-COF exhibits high crystallinity, characterized by distinct reflections at 2θ values up to about 11°. Further, the synthesized PyTTF-COF demonstrated good stability against acidic and basic conditions (Figure 5.15, Section 5.6.3.4, Appendix). To elucidate the structural framework of the synthesized two-dimensional (2D) PyTTF-COF, we initially employed a previously reported strategy involving tetragonal building blocks (considering their long axes) connected through orthogonal and co-linear linkages, respectively.[10,12] In an orthogonal configuration, the longer axes of adjacent building block motifs intersect at ~90°, while in a co-linear arrangement, the longer axes of the building

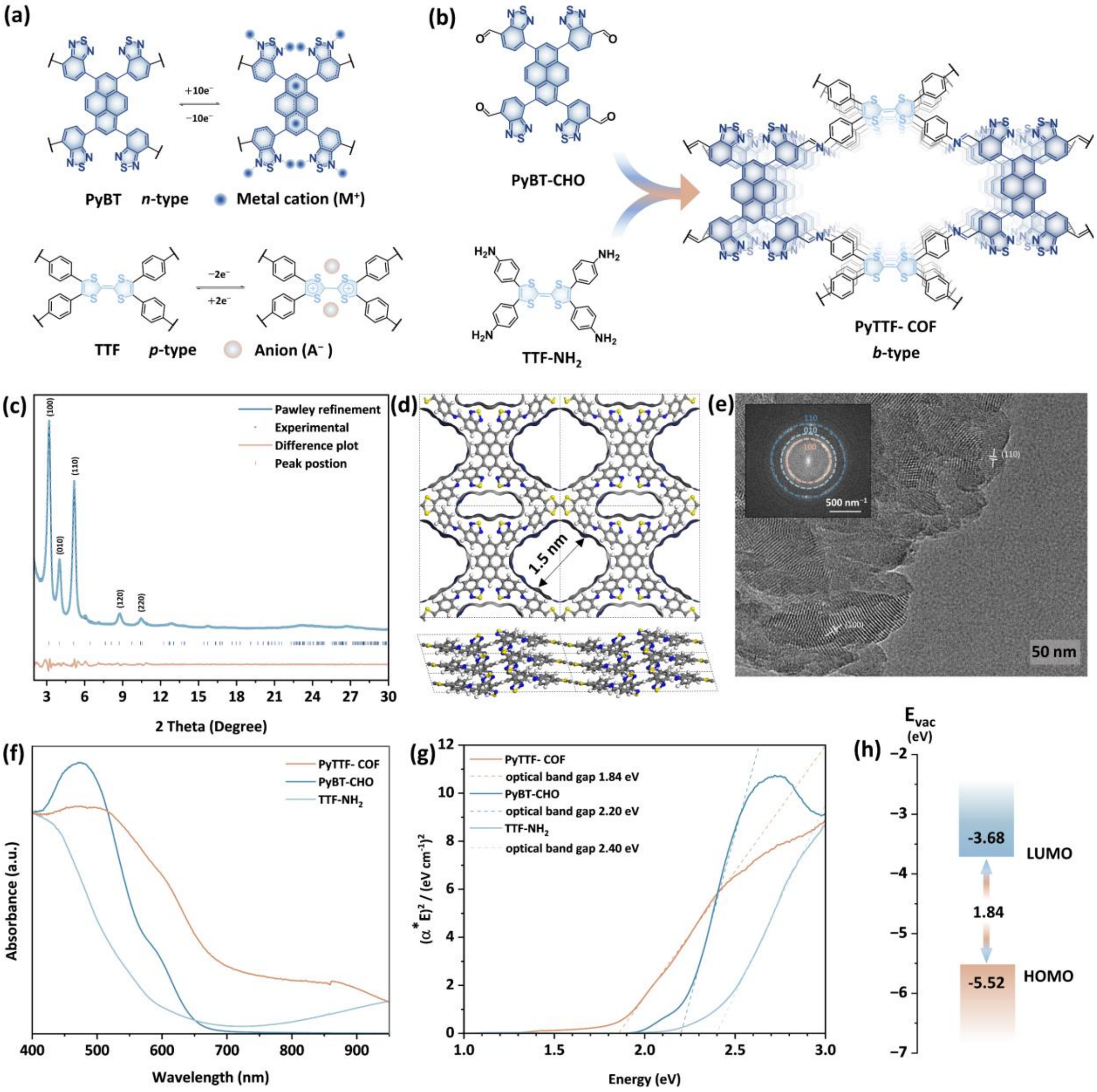

Figure 5.1 (a) Schematic illustration of redox features of *n*-type PyBT and *p*-type TTF subunits, and (b) synthetic scheme for PyTTF-COF. (c) Experimental PXRD pattern of the synthesized PyTTF-COF together with the Pawley-refined profile derived from the optimized structural model with (d) the respective simulated crystal structure displayed along *z*-direction and *x*-direction showing pore topology and π–π-stacking, respectively. (e) TEM image and the respective indexed Fourier-transformed image (inset) of the crystalline PyTTF-COF. (f) Normalized UV–vis absorbance spectra, and (g) the corresponding Tauc plot for direct band gap estimation of PyTTF-COF and its molecular building PyBT-CHO and TTF-NH2 (measured as solids). (h) Energy-level diagram of PyTTF-COF, displaying the calculated frontier orbital positions of HOMO and LUMO.

blocks align parallel to each other with a lateral offset (Figure 5.16, Table 5.1, Section 5.6.3.4, Appendix). Structural simulations of these dual-pore frameworks were carried out using the Forcite module in Materials Studio, exploring various configurations of the BT-unit, and employing an AA-eclipsed stacking model (Figures

5.17-20, Table 5.2, Section 5.6.3.4, Appendix). Among the four simulated assemblies, the orthogonal linkage generated the diffraction pattern with the closest match to the experimental one, and was thus further examined under different stacking and spatial arrangements (Figures 5.21-5.26, Table 5.3, Section 5.6.3.4, Appendix). Given the presence of the C=O stretching band in the FT-IR spectrum of the COF, a *linear*-PyBT model was also constructed in which the PyBT monomer only partially reacted, acting as a linear linker (Figure 5.21, Section 5.6.3.4, Appendix).[10] However, the simulated pattern resulting from this structural motif deviates drastically from the experimental PXRD pattern, suggesting that such incomplete linkage is unlikely to represent the dominant framework. Among the various predicted topologies, the AA-eclipsed orthogonal framework, featuring BT units preferentially oriented toward the smaller pore channels, was identified as the most favorable configuration (Figure 5.26, Section 5.6.3.4, Appendix). Pawley refinement applied to this optimized structure yielded excellent agreement with the experimental data, as indicated by the low residual factor (R_p = 2.71%, and R_{wp} = 3.70%). The structure refined in the *P2* space group exhibits a pseudotetragonal unit cell, with cell parameters a = 28.36 Å, b = 21.77 Å, c = 4.01 Å, α = 90.00°, β = 105.98°, and γ = 90.00° (Figure 5.1c; Table 5.3, Section 5.6.3.4, Appendix). Key diffraction peaks, observed in the experimental PXRD pattern of PyTTF-COF at 2θ values of 3.2°, 4.0°, 5.1°, 8.7°, and 10.4°, could be assigned to the *hkl* (100), (010), (110), (120), and (220) lattice planes, respectively. The PyTTF-COF exhibits an atom-to-atom larger pore width of 1.58 nm, and a smaller pore width of 0.80 nm, along with a *d*-spacing value of 0.4 nm (Figure 5.1d).

Transmission electron microscopy (TEM) images provide further insight into the structure and domain sizes of the PyTTF-COF particles, revealing long-range ordered domains of ~75 nm, and confirming the high crystallinity of the COF. Further, distinct diffraction spots/rings obtained via FFT of the image could be indexed to specific crystal planes, such as the (100), (010), and (110) planes of the COF lattice (Figure 5.1e). Scanning electron microscopy (SEM) revealed a spherical coral-like morphology of the synthesized PyTTF-COF (Figure 5.27a). Closer inspection revealed that these spherical structures, approximately 8–10 µm in diameter, are composed of densely interwoven, worm-like agglomerates with individual strands measuring around ~5 µm in length (Figure 5.27b). These tubular subunits themselves are constructed from smaller spherical ingrown primary particles roughly ~300 nm in size. This multi-level morphology results in a textured porous structure, which could be beneficial for facilitating liquid electrolyte penetration in an electrochemical system.[18,30]

Nitrogen (N_2) adsorption-desorption isotherms were measured at 77 K to evaluate the porosity of the COF (Figure 5.28a). The isotherms exhibited a Type-I reversible profile, reaching saturation at approximately 170 $cm^3\ g^{-1}$ within a partial pressure ($p\, p_o^{-1}$) range < 0.05, which is indicative of a microporous structure.[10,12] The specific surface area was calculated using the Brunauer–Emmett–Teller (BET) method over the relative pressure range of $0.05 \leq p\, p_o^{-1} \leq 0.2$, yielding 611 $m^2\ g^{-1}$. Finally, the pore size distribution was calculated using the nonlocal density functional theory (NLDFT) model, revealing a dominant pore size centered around ~1.49 nm, aligning well with the simulated structure of PyTTF-COF (Figure 5.28b). To evaluate the thermal robustness of the synthesized COF for potential battery-related applications, thermogravimetric analysis (TGA) was performed under oxidative conditions (Figure 5.29). The sample was subjected to a temperature ramp from room temperature to

900 °C at a constant heating rate of 10 °C min^{-1} under a flow of synthetic air. The resulting thermogram indicates that PyTTF-COF remained thermally stable up to ~363 °C.

To investigate the optical properties and electronic structure of the individual building blocks and the resulting COF, UV–Vis spectra of PyBT-CHO, TTF-NH_2, and PyTTF-COF were recorded (Figure 5.1f). PyBT-CHO exhibited a distinct absorption onset at ~720 nm, attributed to the $S_0 \rightarrow S_1$ transition, while TTF-NH_2 showed an absorption onset at ~700 nm with a slight extension into the near-infrared (NIR) region, corresponding to its intrinsic electronic transitions. Upon framework formation, PyTTF-COF displayed a red-shifted and broadened absorption edge tailing into the NIR, indicating a narrowed band gap arising from extended electronic delocalization in the π-conjugated donor–acceptor (D–A) framework.[31] Additionally, the extension into the NIR may stem from either the TTF subunit (as shown above) or the innate transitions within the conjugated COF backbone, or both. To further estimate the optical band gaps, Tauc plot analysis was conducted to reveal direct band gaps of 2.20 eV, 2.40 eV, and 1.84 eV for PyBT-CHO, TTF-NH_2, and PyTTF-COF, respectively (Figure 5.1g). To gain more insight into the frontier orbitals of the COF, a CV measurement was performed, as described in Section 5.6.1, Appendix and Figure 5.30, Section 5.6.3.4, Appendix). The oxidation onset potential (E_{ox}) was employed to estimate the HOMO energy level, yielding a value of −5.52 eV, and thereafter calculating a corresponding LUMO level of −3.68 eV using the optical band gap, both values referenced to the vacuum level and calibrated against Fc/Fc^+ (Figure 5.1h).

5.3.2. Electrochemical Characterization

To evaluate the electrochemical performance of the PyTTF electrode, Li-ion half-cells were fabricated utilizing PyTTF-COF as active cathode material (working electrode, WE) as described in section S1.2, Supporting Information. Firstly, an electrode slurry was prepared by dry-mixing the components; PyTFF (60 wt.%), Ketjenblack (KB, 20 wt.%), and polyvinylidene fluoride (PVDF, 20 wt.%), serving as active material, carbon additive, and binder, respectively. The mixture was then dispersed in *N*-methyl-2-pyrrolidone (NMP) and stirred using a mechanical vortex mixer for 3 h to obtain a homogeneous slurry.[32] Viscosity was adjusted by tuning the solvent content to ensure coatable rheology, and the slurry was subsequently cast onto copper foil using a doctor blade with a wet film thickness of 125 µm. The SEM images of the porous electrode revealed a well-preserved, distinctive PyTTF COF morphology, featuring tubular subunits composed of ~300 nm spherical particles, interspersed with carbon nanoparticles approximately 50 nm in diameter (Figure 5.31, Section 5.6.4, Appendix).

To comprehensively evaluate the electrochemical behavior of the PyTTF electrode and elucidate the underlying ion transport and storage mechanisms, we fabricated Li-ion half-cells using PyTTF as WE

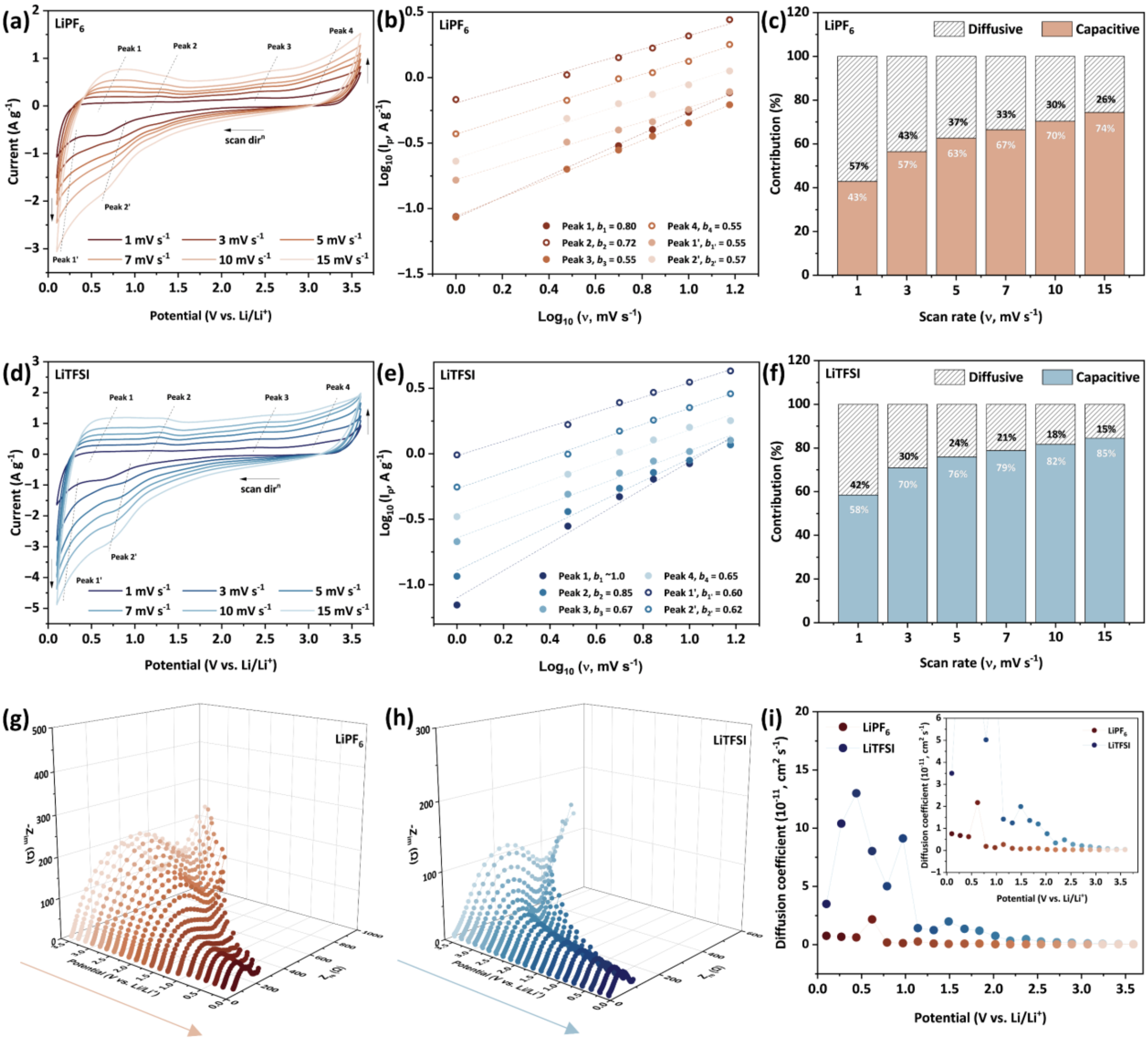

Figure 5.2 Cyclic voltammogram of electrochemical Li-ion half-cells employing PyTTF-COF as WE, Li-foil as CE and RE, and (a) 1 ᴍ LiPF$_6$ and (d) 1 ᴍ LiTFSI in PC:DEC (1:1 v/v) as the liquid electrolyte, respectively, recorded at ν ranging between 1.0−15.0 mV s^{-1} between the potential window of 0.1−3.6 V vs. Li/Li$^+$. The associated *b*-values obtained as the slope of log$_{10}$ (i_p) vs. log$_{10}$ (ν) with i_p corresponding to the most prominent redox peaks for (b) 1 ᴍ LiPF$_6$- and (e) 1 ᴍ LiTFSI-based cells. Deconvolution of total charge-storage into diffusion-controlled and capacitive components as a function of applied ν for (c) 1 ᴍ LiPF$_6$- and (f) 1 ᴍ LiTFSI- half-cells. Potential-dependent EIS profiles obtained during negative sweep direction for (g) 1 ᴍ LiPF$_6$- and (h) 1 ᴍ LiTFSI- half-cells, and (i) the corresponding diffusion coefficients extracted from the impedance analysis.

(⌀: 18 mm), and employed two liquid electrolytes: 1 ᴍ LiPF$_6$ in a 1:1 v/v mixture of propylene carbonate (PC) and diethylene carbonate (DEC), and 1 ᴍ LiTFSI in the same PC:DEC solvent system (Figure 5.32, Section 5.6.4, Appendix), respectively. Initially, CV analyses were carried out at a scan rate (*ν*) of 1.0 mV s^{-1} for both electrolyte-variant half-cells, establishing a stable electrochemical window spanning 0.1−3.6 V vs. Li/Li$^+$ for further testing (Figure 5.33a,c, Section 5.6.4, Appendix). Henceforth, all potentials will be reported vs. Li/Li$^+$, unless stated otherwise. At ~0.8 V, a strong reduction onset (E_{re}) was observed during the first negative potential scan, characteristic of the electrolyte reduction.[33,34] In both electrochemical cells, successive CV cycles at 1.0 mV s^{-1} rate produced nearly superimposable voltammograms, with LiTFSI cells delivering higher gravimetric current than their $LiPF_6$ counter-parts (Figure 5.33b,d, Section 5.6.4, Appendix). Further, CVs at elevated scan-speeds ranging from $v = 3.0−15.0$ mV s^{-1} were measured, as depicted in Figure 5.2a,d. The observed oxidation peaks ($E_{\mathrm{p,ox}}$) were labeled as peak 1 (~0.6 V), peak 2 (~1.25 V), peak 3 (~2.44 V) and peak 4 (~3.2 V), and the most prominent reduction peaks ($E_{\mathrm{p,re}}$) as peak 1' (~0.18 V) and peak 2' (~0.75 V). We attribute the peaks at lower potentials vs. Li/Li$^+$ to the *n*-type redox features, while the peaks at higher potential to the *p*-type redox features of PyTTF electrode. The absolute values of the specific peak currents (i_p) at different scan rates were employed to determine the exponent (*b*-value) of the power-law relationship: $i_p = av^b$ (Equation 5.2), as elaborated in Section 5.6.2.1, Appendix.[35,36] According to this model, the *b*-values serve as semi-quantitative indicators of the underlying charge-storage mechanism ranging from intercalation to capacitive for the material: specifically, $b \approx 1$ indicates faster surface-controlled (capacitive) behavior, while $b \approx 0.5$ suggests slower diffusion-controlled kinetics; values $0.5 < b < 1$ imply hybrid charge storage, commonly associated with pseudocapacitive contributions.[37] Unlike battery-like materials, pseudocapacitive materials store charge either by surface redox reactions and/or by directional intercalation, providing higher rate kinetics without compromising the overall energy output.[22,37,38] Gaining insights into the charge-storage mechanism over the operational potential window is crucial for the effective evaluation of bipolar electrode materials due to potential-dependent cation-anion co-storage, and therefore, *b*-values for peaks 1−4 and peaks 1',2' were determined as the slope of $\log_{10}(i_p)$ vs. $\log_{10}(v)$ (Figure 5.2b,e).[19,22] Across the examined potential range, 0.1−3.6 V, the LiTFSI-based system consistently exhibited higher *b*-values of ~1, 0.85, 0.67, 0.65, 0.60 and 0.62, compared to the $LiPF_6$-based system with $b = 0.80$, 0.72, 0.55, 0.55, 0.55 and 0.57 for peaks 1−4 and peaks 1',2', respectively, implying a significant influence of anion identity on the observed redox dynamics. Additionally, the experienced potential polarization (ΔE) with an increased scan rate is smaller in the case of LiTFSI cells, indicating more favorable charge-storage dynamics than $LiPF_6$ cells (Figure 5.34, Section 5.6.4, Appendix).

Dunn's analysis was employed to deconvolute the current response in the voltammograms, enabling a distinction between capacitive or pseudocapacitive and diffusion-controlled charge-storage mechanisms, as outlined in Section 5.6.2.1, Equation 5.4 and illustrated in Figure 5.35, Section 5.6.4, Appendix.[36] A dominant capacitive contribution is indicative of faster charge-transfer kinetics and enhanced rate performance, whereas a higher diffusion-controlled component reflects limitations arising from ion transport within the electrode bulk.[35,37] A comparative analysis revealed that LiTFSI-based electrochemical half-cells exhibit a more pronounced capacitive or pseudocapacitive behavior across various scan rates than their $LiPF_6$-based counterparts.

To elucidate the evolution of ion-diffusion kinetics across the potential window of 0.1−3.6 V for both systems, potential-dependent electrochemical impedance spectroscopy (EIS) was employed.[12,39–41] An AC perturbation of 10 mV was superimposed on a DC bias at various potentials to simulate the cycling process, enabling correlation of impedance variations with specific operational stages (full methodology provided in Sections 5.6.1.2 and 5.6.2.2, Appendix).[12] Sequential EIS measurements were performed during both the positive sweep (0.1 → 3.6 V) and the reverse sweep (3.6 → 0.1 V), recording impedance at $n = 42$ discrete potential steps (Figure 5.36-37, Figure 5.2g,h). In both systems, the charge-transfer resistance (R_{ct}), represented as the semicircle diameter in the high-to-mid frequency domain of the Nyquist plot, increased with rising potential, then diminished as the potential was lowered. Previously, this trend has been attributed to the faster diffusion of Li^+ ions relative to the counter anion.[12] Nyquist plots were further analyzed to extract the Warburg contribution, indicative of diffusion limitations. In the low-frequency regime, the Warburg element appears as a 45° linear tail, from which the Warburg coefficient (σ) was determined.[12,40,42] This was achieved by plotting the real part of the impedance (Z_{re}) against the inverse square root of the angular frequency ($\omega^{-1/2}$) at each potential step for both forward and reverse sweeps (see Section 5.6.2.2, Equation 5.6, Figures 5.38-5.45, Section 5.6.5, Appendix). Since the σ value (Unit: $\Omega\ s^{-1/2}$) quantifies resistance to ionic mass transport, a larger σ value corresponds to slower ion diffusion. For both electrolytes, σ increased with potential, and decreased upon reversing the sweep (Figure 5.46, Section 5.6.5, Appendix). Notably, LiTFSI-based cells exhibited lower Warburg coefficients than their $LiPF_6$ counterparts, particularly at lower potentials, indicating superior Li^+ diffusion kinetics.

For individual half-cells using PyTTF as electrode and LiTFSI and $LiPF_6$ electrolyte analogs, the Warburg coefficients were utilized to calculate the diffusion coefficient of the charge-carriers at different operating potentials between 0.1−3.6 V, using the following equation:[9,12,40]

$$D = \frac{R^2 T^2}{2n^4 F^4 C^2 A^2 \sigma^2} \qquad \text{(Equation 5.1)}$$

where R is the gas constant (R = 8.314 J K^{-1} mol^{-1}), T is the operational temperature (T = 298 K), n is the number of electrons transferred from electrolyte to the electrode (n = 1), F is Faraday's constant (F = 96 458 C mol^{-1}), C is the concentration of the charge carriers in the electrolyte solution (C = 1 M), A is the geometric surface area of the PyTTF electrode (A = 2.54 cm^2), and D ($cm^2\ s^{-1}$) is the effective diffusion coefficient of charge carriers, respectively (Table 5.4,5.5). For cells containing LiTFSI, the calculated diffusion coefficients spanned from 1.82×10^{-10} to 3.78×10^{-13} $cm^2\ s^{-1}$ across the investigated potential range. In contrast, cells with $LiPF_6$ exhibited generally lower diffusion coefficients, ranging from 1.01×10^{-11} to 2.71×10^{-13} $cm^2\ s^{-1}$ over the same voltage window

(Figure 5.2i, Figure 5.47, Section 5.6.5, Appendix). In both electrolyte systems, D varied inversely with σ, as expected from equation (5.1). At low potentials (< ~1.2 V), the diffusion coefficient increased significantly, reaching a maximum in the LiTFSI system before declining with increasing potential toward 3.6 V. Notably, in the higher potential region (~2.0–3.6 V), D values converged for both electrolyte types; however, the LiTFSI-based cells exhibited a sharper decline upon potential increase than the $LiPF_6$ system. The enhanced low-potential diffusion in LiTFSI-containing cells could be tentatively attributed to the structural and electronic characteristics of the $TFSI^-$ anion. With its delocalized negative charge and bulky structure, this could result in weaker $Li^+–A^-$ associations than those typically present with the more compact PF_6^- anion.[43–45] This weaker ion pairing may reduce the $Li^+–A^-$ association energy, facilitating faster Li^+ migration, especially at the electrode-electrolyte interphase in the low-potential regime, which is the dominant region for Li^+ storage and release. Furthermore, contact angle measurement of PyTTF electrode with analogous electrolyte solutions, along with complementary EIS measurements revealed similarly low contact angles and comparable R_{sol} values for both systems. Hence, no significant influence of surface wettability could be associated to the observed electrochemical performances (Figure 5.48-5.49, Section 5.6.5, Appendix).

5.3.3. Battery Performance

To experimentally establish the capacity output of the PyTTF COF electrode, galvanostatic charge−discharge measurements were conducted for electrochemical half-cells using the PyTTF electrode as WE, Li-foil as CE and RE, and both liquid electrolyte variations, respectively, at varying current densities between 0.3−1.0 A g^{-1} (Figure 5.50, Figure 5.3a-c). The initial discharge cycles, spanning from the open-circuit potential (OCP) to 0.1 V, exhibit a pronounced plateau around ~1.0 V for both systems, consistent with the electrolyte reduction processes observed in the corresponding voltammograms (Figure 5.35). In both electrochemical cells, the subsequent cycles exhibited a reduced specific capacity compared to the initial discharge (Figure 5.3c), largely attributable to irreversible phenomena occurring predominantly during the first cycle, such as electrolyte decomposition leading to the formation of a solid electrolyte interphase (SEI), and possible irreversible lithium insertion or conversion reactions.[33,34]

Additionally, dQ/dV curves were plotted for the charge-discharge cycles at a current density of 0.3 A g^{-1}, revealing the most distinct redox activities for both LiTFSI- and $LiPF_6$-based half-cells. As presented in Figure 5.51, Section 5.6.6, Appendix, the $LiPF_6$ system exhibited more nuanced responses in comparison to the LiTFSI analog, which may hint towards higher polarization experienced by the $LiPF_6$ system. Furthermore, galvanostatic charge-discharge measurements confirmed the reversible charge-storage behavior of PyTTF electrode even at higher rates for both systems (Figure 5.3c). LiTFSI half-cells achieved higher reversible specific capacities of 286, 186, 125, 93, and 80 mAh g^{-1}, while the

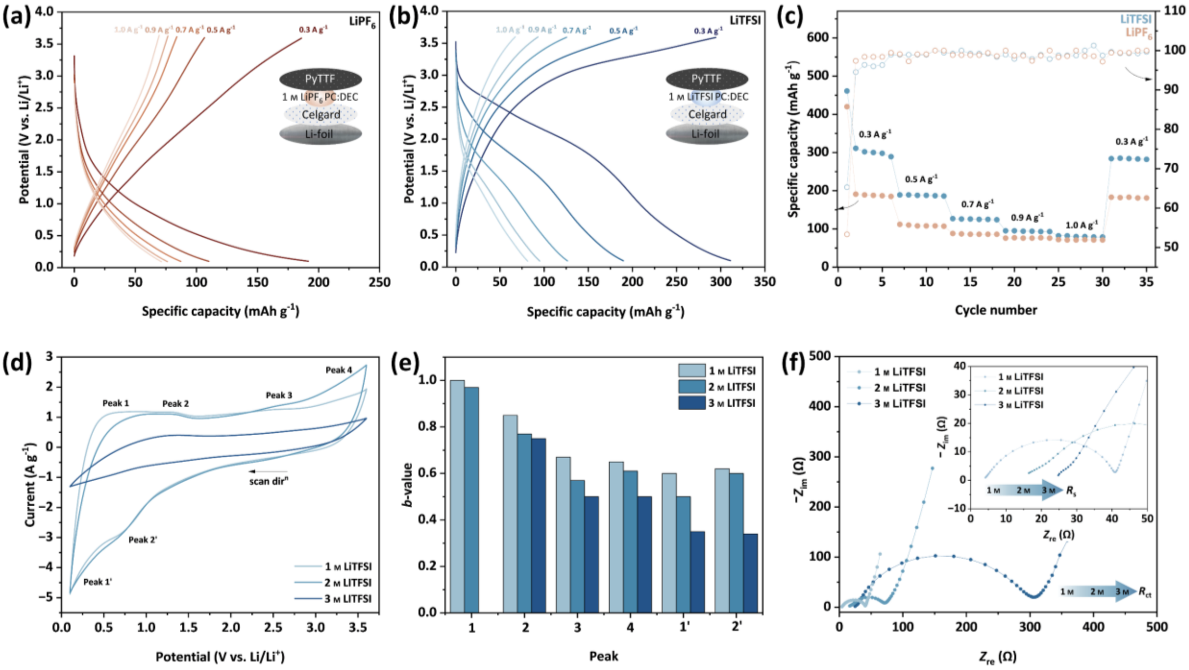

Figure 5.3 Galvanostatic charge/discharge measurements at current densities varying from 0.3−1.0 A g^{-1} within the potential range of 0.1−3.6 V for electrochemical half cells using PyTTF as cathode, Li-foil as CE and RE, and (a) 1 M LiPF$_6$ in PC:DEC 1:1 (v/v), and (b) 1 M LiTFSI in PC:DEC 1:1 (v/v) as liquid electrolytes, respectively. (c) Comparative specific capacities and corresponding coulombic efficiencies. (d) Comparative cyclic voltammograms at v = 15 mV s^{-1} for PyTTF-half cells using 1−3 M LiTFSI in PC:DEC 1:1 (v/v) as liquid electrolytes, and (e) the corresponding *b*-values for the most prominent redox-peaks. (f) Nyquist plots obtained by measuring electrochemical impedance spectra after CV measurements for half cells employing 1−3 M LiTFSI in PC:DEC 1:1 (v/v) as liquid electrolytes, respectively

corresponding LiPF$_6$ cells provided capacities of 184, 107, 85, 75, and 71 mAh g^{-1} at applied current densities of 0.3, 0.5, 0.7, 0.9, and 1.0 A g^{-1}, respectively, with 0.3 A g^{-1} ≈ 1C rate. Relative to each other, the two analogous systems exhibited more pronounced capacity differences at lower current densities, whereas these differences reduced markedly at elevated current densities of 0.9 and 1.0 A g^{-1}, likely because the bulkier TFSI$^-$ anion becomes the diffusion-limited under high-rate conditions, offsetting its advantage of weaker Li$^+$–A$^-$ coupling. SEM analysis showed that cycled electrodes retained ~300 nm spherical particles with slightly rounded edges, likely from interfacial reactions (Figure 5.52, Section 5.6.5, Appendix). Summarizing these observations, the PyTTF electrode demonstrates competitive rate capability, a broad and stable potential window of 3.5 V, and an unprecedented concentration of redox-active sites among previously reported bipolar electrodes (refer to Table 5.6, Section 5.6.5, Appendix).

The tunable and modular architecture of COFs enables the selection of electroactive building blocks and conjugated linkages, allowing for the design of frameworks capable of hosting multiple, reversible redox reactions at well-defined potentials.[12–18] Henceforth, based on prior studies, we propose a plausible redox mechanism for the PyTTF electrode (Figure 5.53).[12,24,25] Accordingly, by integrating the *n*-type PyBT-node, the *p*-type TTF-node, and the *n*-type imine linkage, the *b*-type PyTTF COF is theoretically capable of accommodating for up to 16 redox-active species per unit cell. Upon discharge at 0.1 V, in the reduced state, the PyTTF electrode can store up to 14 Li^+ ions, while upon successive charging to 3.6 V (or in the oxidized state) it can store 2 counter A^-, per unit cell. This multi-electron redox process corresponds to a calculated theoretical capacity of 318 mAh g^{-1} for the PyTTF electrode (Section 5.6.6, Appendix).

Ex-situ energy-dispersive X-ray (EDX) spectroscopy was employed to characterize PyTTF electrodes following discharge to 0.1 V and subsequent charge to 3.6 V in cells containing either LiTFSI or $LiPF_6$ electrolytes. The atomic percentages of fluorine (F) and phosphorus (P) were compared with those obtained from the pre-cycled electrode (Figure 5.54-5.58, Table 5.7, Section 5.6.5, Appendix). In the $LiPF_6$-based cells, a progressive increase in both P and F content upon charging to 3.6 V (PF_6^- anion storage) was observed, whereas in the LiTFSI-based cells, a similar increase was noted for the F content ($TFSI^-$ storage). These results appear to be compatible with the proposed reaction mechanism. Furthermore, ex-situ PXRD measurements of cycled electrodes revealed slightly diminished peak intensities, while preserved reflection profiles and peak widths, indicating an intact crystalline framework (Figure 5.59).

Given the superior electrochemical performance exhibited by the 1 M LiTFSI in PC:DEC electrolyte relative to its $LiPF_6$ analog, additional Li-ion half-cells were assembled using 2 M and 3 M LiTFSI in PC:DEC solvent mixtures to examine the influence of salt concentration (Figure 5.60). Rate-dependent CV measurements were conducted at scan rates ranging from 1.0−15.0 mV s^{-1} over a potential window of 0.1−3.6 V for both 2 M and 3 M systems (Figures 5.61-5.62). The electrochemical response of the 2 M LiTFSI cells was broadly comparable to that with the 1 M electrolyte, with slightly attenuated redox features in the lower-potential region and enhanced features at higher potentials, possibly attributable to the increased anion concentration (Figure 5.3d). In the half-cell configuration employing Li-foil as the counter electrode, Li^+ availability is effectively unrestricted; however, the A^- population may be partially depleted through irreversible side reactions occurring during the initial cycles.[46] By contrast, cells employing the 3 M LiTFSI electrolyte exhibited markedly lower current responses across all scan rates, diminished redox features, and increased polarization (Figure 5.62a, Figure 5.3d). The *b*-values extracted from $\log_{10}(i_p)$ vs. $\log_{10}(v)$ plot analysis for the most prominent redox $E_{p,ox}$ and $E_{p,re}$ peaks, followed the trend 1 M > 2 M > 3 M, respectively (Figure 5.3e). Notably, the 3 M system displayed *b*-values < 0.5 for $E_{p,re}$ peaks, indicative of a charge-transfer process slower than the ideal diffusion-controlled regime (Figure 5.62b, Figure 5.3e). These findings suggest that, in addition to diffusion limitations, the high-concentration electrolyte cell suffers from kinetic constraints, implying a multifactorial performance bottleneck.

To further investigate these effects, EIS was performed on cells containing 1−3 M LiTFSI before and after CV cycling, using a 10 mV AC perturbation over the frequency range 0.1−10^6 Hz (Figure 5.63, Section 5.6.6, Appendix). The obtained data were fitted to equivalent electrical circuits (EECs) to extract the solution resistance (R_{sol}), SEI layer resistance (R_{SEI}), and R_{ct} (Figure 5.64, Section 5.6.6, Appendix).[41,42] For the 1−2 M systems, R_{ct} decreased after cycling, while 3 M system experienced an increase in R_{ct} (Table 5.8, Section 5.6.6, Appendix). Across all concentrations, the R_{ct} followed the order 1 M < 2 M < 3 M, consistent with the CV observations. Electrochemical cells containing 2 M and 3 M LiTFSI electrolytes exhibited reduced R_{SEI} values following cycling compared to their initial states, whereas the cell with the lower concentration electrolyte, 1 M, experienced an increase in R_{SEI} after cycling. This behavior may be attributable to the tendency of highly concentrated electrolytes, as suggested in previous studies, to foster the development of a more stable, inorganic-rich SEI layer.[22,47] Furthermore, the elevated R_{sol} observed in the 2 M, and more markedly in the 3 M system likely reflect increased electrolyte viscosity, the formation of $\mathrm{Li^+}$–$\mathrm{TFSI^-}$ aggregates, or both, which impede overall charge-storage kinetics (Figure 5.3f).[48–50] These findings underscore the importance of systematically optimizing electrolyte composition, not only with respect to salt identity but also to concentration, particularly in bipolar COF-based electrode capable of storing both $\mathrm{M^+}$ and $\mathrm{A^-}$. Given the wide electrochemical window and especially high stability at low voltages against Li/$\mathrm{Li^+}$, there is potential to operate these COFs also with oxide-based solid state electrolytes like Li-garnets, to boost further energy density in the future.[51–53] This would combine the high storage capacity with wide operation window for these bipolar-COFs as electrodes.

5.4. Conclusion

In summary, we have developed a novel, highly crystalline bipolar-type PyTTF-COF to serve as electrode for dual-ion batteries by combining anion (A^-) storing *p*-type (TTF) and metal-cation (Li^+) storing *n*-type pyrene–benzothiadiazole (PyBT) subunits. The resulting bulk PyTTF-COF exhibits a lower optical band gap of ~1.84 eV in comparison to the HOMO-LUMO gaps of the individual building units, attributed to the extended π-conjugation in the donor–acceptor (D–A) architecture. The performance of the PyTTF electrode was individually screened with different lithium salts as charge carriers with A^- (= PF_6^-, $TFSI^-$) in a 1 м 1:1 v/v mixture of PC:DEC as electrolyte in a half-cell assembly. Over the wide stable operating window of 0.1−3.6 V vs. Li/Li^+, LiTFSI-based cells exhibited superior charge-storage kinetics, ion-diffusion, and specific capacity output (286 mAh g^{-1} at 0.3 A g^{-1}), than the analogous $LiPF_6$ cells (184 mAh g^{-1} at 0.3 A g^{-1}), probably owing to weaker Li^+–$TFSI^-$ associations relative to the more compact PF_6^- anion. Furthermore, systematic variation of salt concentration (1−3 м LiTFSI), established a clear correlation between electrolyte composition, ion storage dynamics, and interfacial charge-transfer resistance revealed through electrochemical analysis. Concluding, in addition to COF design, our study reveals the importance of charge-carrier identity and electrolyte concentration as key factors controlling the behavior of bipolar COF electrodes in dual-ion batteries.

5.5. References

[1] A. Yoshino, *Angewandte Chemie (International ed. in English)* **2012**, *51*, 5798.

[2] C.-Y. Wang, T. Liu, X.-G. Yang, S. Ge, N. V. Stanley, E. S. Rountree, Y. Leng, B. D. McCarthy, *Nature* **2022**, *611*, 485.

[3] T. Wulandari, D. Fawcett, S. B. Majumder, G. E. J. Poinern, *Battery Energy* **2023**, *2*, 20230030.

[4] C. Bauer, S. Burkhardt, N. P. Dasgupta, L. A.-W. Ellingsen, L. L. Gaines, H. Hao, R. Hischier, L. Hu, Y. Huang, J. Janek et al., *Nat Sustain* **2022**, *5*, 176.

[5] P. M. Hari Prasad, G. Malavika, A. Pillai, S. Sadan, Z. S. Pillai, *NPG Asia Mater* **2024**, *16*, 37.

[6] Y. Lu, J. Chen, *Nature reviews. Chemistry* **2020**, *4*, 127.

[7] S. Cui, W. Miao, H. Peng, G. Ma, Z. Lei, L. Zhu, Y. Xu, *Chemistry (Weinheim an der Bergstrasse, Germany)* **2024**, *30*, e202303320.

[8] S. Suleman, X. Cheng, M. Gu, Y. Kim, *Commun Mater* **2025**, *6*, 78.

[9] S. Haldar, A. Schneemann, S. Kaskel, *Journal of the American Chemical Society* **2023**, *145*, 13494.

[10] R. Guntermann, J. M. Rotter, A. Singh, D. D. Medina, T. Bein, *Small science* **2025**, *5*, 2400585.

[11] Y. Inatomi, N. Hojo, T. Yamamoto, S. Watanabe, Y. Misaki, *ChemPlusChem* **2012**, *77*, 973.

[12] A. Singh, P. Bhauriyal, L. Quincke, D. Blätte, R. Guntermann, J. L. M. Rupp, T. Heine, T. Bein, *Advanced Energy Materials* **2025**, e01494.

[13] W. Li, Q. Huang, H. Shi, W. Gong, L. Zeng, H. Wang, Y. Kuai, Z. Chen, H. Fu, Y. Dong et al., *Adv Funct Materials* **2024**, *34*, 2310668.

[14] Q. Xu, K. Fu, Z. Liu, T. Sun, L. Xu, X. Ding, L. Gong, Q. Yu, J. Jiang, *Adv Funct Materials* **2025**, 2506111.

[15] L. Gong, X. Yang, Y. Gao, G. Yang, Z. Yu, X. Fu, Y. Wang, D. Qi, Y. Bian, K. Wang et al., *J. Mater. Chem. A* **2022**, *10*, 16595.

[16] Q. Xu, Z. Liu, Y. Jin, X. Yang, T. Sun, T. Zheng, N. Li, Y. Wang, T. Li, K. Wang, J. Jiang, *Energy Environ. Sci.* **2024**, *17*, 5451.

[17] S. Gu, J. Chen, R. Hao, X. Chen, Z. Wang, I. Hussain, G. Liu, K. Liu, Q. Gan, Z. Li, H. Guo, Y. Li, H. Huang, K. Liao, K. Zhang, Z. Lu, *Chemical Engineering Journal* **2023**, *454*, 139877.

[18] M. Wu, Y. Zhao, R. Zhao, J. Zhu, J. Liu, Y. Zhang, C. Li, Y. Ma, H. Zhang, Y. Chen, *Adv Funct Materials* **2022**, *32*, 2107703.

[19] Wenjun Li, Huilin Ma, Wu Tang, Kexin Fan, Shan Jia, Jian Gao, Ming Wang, Yan Wang, Bei Cao, Cong Fan **2024**, *15*, 9533.

[20] Hyojin Kye, Yeongkwon Kang, Deogjin Jang, Ji Eon Kwon, Bong-Gi Kim **2022**, *3*, 2200030.

[21] J. Holoubek, Z. Chen, P. Liu, *ChemSusChem* **2023**, *16*, e202201245.

[22] Z. Guo, G. Cheng, Z. Xu, F. Xie, Y.-S. Hu, C. Mattevi, M.-M. Titirici, M. Crespo Ribadeneyra, *ChemSusChem* **2023**, *16*, e202201583.

[23] W. Li, H. Ma, W. Tang, K. Fan, S. Jia, J. Gao, M. Wang, Y. Wang, B. Cao, C. Fan, *Nature communications* **2024**, *15*, 9533.

[24] G. Valente, R. Dantas, P. Ferreira, R. Grieco, N. Patil, A. Guillem-Navajas, D. Rodríguez-San Miguel, F. Zamora, R. Guntermann, T. Bein et al., *J. Mater. Chem. A* **2024**, *12*, 24156.

[25] C. Zhang, Y. Qiao, P. Xiong, W. Ma, P. Bai, X. Wang, Q. Li, J. Zhao, Y. Xu, Y. Chen et al., *ACS nano* **2019**, *13*, 745.

[26] S. Bhunia, S. K. Das, R. Jana, S. C. Peter, S. Bhattacharya, M. Addicoat, A. Bhaumik, A. Pradhan, *ACS applied materials & interfaces* **2017**, *9*, 23843.

[27] D. Bessinger, L. Ascherl, F. Auras, T. Bein, *Journal of the American Chemical Society* **2017**, *139*, 12035.

[28] C. G. Gruber, L. Frey, R. Guntermann, D. D. Medina, E. Cortés, *Nature* **2024**, *630*, 872.

[29] M. Calik, T. Sick, M. Dogru, M. Döblinger, S. Datz, H. Budde, A. Hartschuh, F. Auras, T. Bein, *Journal of the American Chemical Society* **2016**, *138*, 1234.

[30] Y. Chen, L. Shi, A. Li, S. Zhang, M. Guo, X. Chen, J. Zhou, H. Song, *J. Electrochem. Soc.* **2017**, *164*, A2000-A2006.

[31] R. Guntermann, D. Helminger, L. Frey, P. M. Zehetmaier, C. Wangnick, A. Singh, T. Xue, D. D. Medina, T. Bein, *Angewandte Chemie (International ed. in English)* **2024**, *63*, e202407166.

[32] A. Kraytsberg, Y. Ein-Eli, *Advanced Energy Materials* **2016**, *6*, 1600655.

[33] A. Wang, S. Kadam, H. Li, S. Shi, Y. Qi, *npj Comput Mater* **2018**, *4*, 15.

[34] H. Adenusi, G. A. Chass, S. Passerini, K. V. Tian, G. Chen, *Advanced Energy Materials* **2023**, *13*, 2203307.

[35] S. Fleischmann, J. B. Mitchell, R. Wang, C. Zhan, D.-E. Jiang, V. Presser, V. Augustyn, *Chemical reviews* **2020**, *120*, 6738.

[36] J. Wang, J. Polleux, J. Lim, B. Dunn, *J. Phys. Chem. C* **2007**, *111*, 14925.

[37] C. Choi, D. S. Ashby, D. M. Butts, R. H. DeBlock, Q. Wei, J. Lau, B. Dunn, *Nat Rev Mater* **2020**, *5*, 5.

[38] L. Kong, P. J. Williams, F. Brushett, J. L. M. Rupp, *Advanced Energy Materials* **2025**, *15*, e03080.

[39] Jun Wang, Emmanuel Pamet, Shengli Yan, Wenhua Zhao, Jianhui Zhang, Xiaotong He, Zhazira Supiyeva, Qamar Abbas, Xuexue Pan **2023**, *150*, 107488.

[40] R. Nandan, N. Takamori, K. Higashimine, R. Badam, N. Matsumi, *ACS Appl. Energy Mater.* **2024**, *7*, 2088.

[41] W. Choi, H.-C. Shin, J. M. Kim, J.-Y. Choi, W.-S. Yoon, *J. Electrochem. Sci. Technol* **2020**, *11*, 1.

[42] Alexandros Ch. Lazanas, Mamas I. Prodromidis **2023**, *2*, 162.

[43] Z. Song, Z. Xing, J. Yang, J. Chen, W. Hu, P. Li, W. Feng, G. G. Eshetu, E. Figgemeier, S. Passerini et al., *Angewandte Chemie (International ed. in English)* **2025**, *64*, e202424543.

[44]Z. Song, X. Wang, W. Feng, M. Armand, Z. Zhou, H. Zhang, *Advanced materials (Deerfield Beach, Fla.)* **2024**, *36*, e2310245.

[45] D. M. Seo, O. Borodin, S.-D. Han, P. D. Boyle, W. A. Henderson, *J. Electrochem. Soc.* **2012**, *159*, A1489-A1500.

[46] J. C. Burns, L. J. Krause, D.-B. Le, L. D. Jensen, A. J. Smith, D. Xiong, J. R. Dahn, *J. Electrochem. Soc.* **2011**, *158*, A1417.

[47] L. Xiang, X. Ou, X. Wang, Z. Zhou, X. Li, Y. Tang, *Angewandte Chemie (International ed. in English)* **2020**, *59*, 17924.

[48] G. A. Giffin, *Nature communications* **2022**, *13*, 5250.

[49] O. Borodin, J. Self, K. A. Persson, C. Wang, K. Xu, *Joule* **2020**, *4*, 69.

[50] Q. Li, W. Xue, J. Peng, L. Yang, H. Pan, X. Yu, H. Li, *Adv Energy and Sustain Res* **2021**, *2*, 2100010.

[51] K. J. Kim, M. Balaish, M. Wadaguchi, L. Kong, J. L. M. Rupp, *Advanced Energy Materials* **2021**, *11*, 2002689.

[52] M. Balaish, J. C. Gonzalez-Rosillo, K. J. Kim, Y. Zhu, Z. D. Hood, J. L. M. Rupp, *Nat Energy* **2021**, *6*, 227.

[53] M. Balaish, K. J. Kim, H. Chu, Y. Zhu, J. C. Gonzalez-Rosillo, L. Kong, H. Paik, S. Weinmann, Z. D. Hood, J. Hinricher et al., *Chemical Society reviews* **2025**, *54*, 8925.

5.6. Appendix

5.6.1. Methods

5.6.1.1. Structural characterization

Nuclear magnetic resonance (NMR): NMR spectra were recorded on Bruker AV 400 and AV 400 TR spectrometers. Chemical shifts are expressed in parts per million (δ scale) and are calibrated using residual (undeuterated) solvent peaks as an internal reference (^{1}H-NMR: $CDCl_3$: 7.26; ^{13}C-NMR: $CDCl_3$: 77.16).

High resolution mass spectrometry with electron ionization (HRMS-EI): HRMS-EI was performed with a Thermo Finnigan MAT 95 instrument.

Powder X-ray diffraction (PXRD): Diffractograms were obtained using a Bruker D8 Discover instrument, featuring Cu-Kα radiation and a LynxEye position-sensitive detector, configured in Bragg-Brentano geometry.

Structure modelling: The structure models for PyTTF-COF were constructed using the Accelrys Materials Studio software package. For every COF model, the highest possible symmetry/space group was applied. The structure models were optimized using the Forcite module with the Universal Force Field. Profile fits using the Pawley method were carried out as implemented in the Reflex module of the Materials Studio software. Thompson-Cox-Hastings peak profiles were used, and peak asymmetry was corrected using the Berar-Baldinozzi method.

Fourier-transform infrared spectroscopy (FTIR): The spectra were captured using a Bruker Vertex 70 FTIR instrument, featuring a liquid nitrogen (LN_2) cooled MCT detector.

Scanning electron microscopy (SEM): SEM images were obtained using a FEI Helios NanoLab G3 UC scanning electron microscope equipped with a Schottky field-emission electron source operated at 3−5 kV.

Energy Dispersive X-ray (EDX) microanalysis: Analysis was performed on a Dual beam FEI Helios G3 UC instrument equipped with an X-Max 80 EDS detector from Oxford Instruments plc. The EDX spectra were recorded at 5 kV.

Transmission electron microscopy (TEM): TEM images were obtained on a FEI Titan Themis instrument equipped with a field emission gun operated at 300 kV.

Nitrogen sorption: The isotherms were recorded using Quantachrome Autosorb 1 and Autosorb iQ instruments at a temperature of 77 K. The BET surface area for the COF was calculated based on the pressure range $0.05 \leq p\, p_0^{-1} \leq 0.2$.

Thermogravimetric analysis (TGA): The thermal stability measurements were performed on a Netzsch Jupiter ST 499 C instrument equipped with a Netzsch TASC 414/4 controller. The sample was heated from room temperature to 900 °C under a synthetic air flow at a heating rate of 10 °C min^{-1}.

Ultraviolet-visible spectroscopy (UV-Vis): UV-VIS spectra were recorded using a Perkin-Elmer Lambda 1050 spectrometer equipped with a 150 mm integrating sphere, photomultiplier tube (PMT) and InGaAs detector. Diffuse reflectance spectra were collected with a Praying Mantis (Harrick) accessory and were referenced to barium sulfate powder as white standard. The specular reflection of the sample surface was removed from the signal using apertures that allow only light scattered at angles > 20° to pass.

Cyclic voltammetry (CV) for determining HOMO and LUMO energy levels: CV measurements were recorded in a three-electrode configuration with Ag/Ag^+ as reference electrode (RE), Pt wire as counter electrode (CE) and an ITO substrate with COF as working electrode (WE). A homogeneous slurry was prepared by thoroughly mixing (60 wt.%) PyTTF-COF as host material, (20 wt.%) Ketjenblack as conductive carbon additive, (20 wt.%) polyvinylidene fluoride (PVDF) as binder, and *N*-methyl-2-pyrrolidone (NMP) as solvent. The slurry was then drop-cast on an ITO substrate, followed by drying the electrodes at 60 °C for 24 h, and at 120 °C under vacuum for 6 h. Anhydrous acetonitrile, containing 0.1 м tetrabutylammonium hexafluorophosphate, was used as electrolyte. The measurement was performed at a scan rate of 10 mV s^{-1} under argon atmosphere.

5.6.1.2. Battery performance

PyTTF electrode (working electrode, WE) preparation: A homogeneous slurry was prepared by thoroughly mixing (60 wt.%) PyTTF-COF as host material, (20 wt.%) Ketjenblack as conductive carbon additive, (20 wt.%) polyvinylidene fluoride (PVDF) as binder, and *N*-methyl-2-pyrrolidone (NMP) as solvent. The slurry was then coated over a copper foil using the doctor blade technique, dried overnight at 65 °C, and later vacuum-dried at 100 °C for 6 h. Finally, the electrodes were cut into disks with a diameter (⌀) of 18 mm and an average mass loading of 1.0-1.2 mg per disk. The mass loading of active material is 60% of the total (solid) mass of the slurry, which was determined by subtracting the weight of bare copper foil from the coated copper foil. The mass loading of individual electrode disks was used for individual measurements.

Electrolyte preparation: Lithium salts, including lithium hexafluorophosphate ($LiPF_6$, battery grade, ≥99.99% trace metals basis, Aldrich) and lithium trifluoromethanesulfonimide (LiTFSI, 99.95%, Aldrich), were used to prepare 1−3 ᴍ electrolyte solutions. These salts were dissolved in a 1:1 (v/v) mixture of propylene carbonate (PC, anhydrous, ≥99.7%, Aldrich) and diethyl carbonate (DEC), anhydrous, ≥99%, Aldrich), respectively. For electrochemical measurements, 20 µL of the electrolyte solution was introduced per cell.

Lithium-ion half-cell assembly: Lithium-ion half-cells were fabricated using a PyTTF electrode as working electrode, Li-foil (Sigma-Aldrich) as counter and reference electrode, Celgard (2325 (PP/PE/PP), ⌀: 21.6 mm, thickness: 0.025 mm, CCC/HS:90279000) as separator, and electrolyte. The cells were assembled inside an argon-filled glove box (Labstar 1250/750, MBraun, Germany) in a coin cell configuration using the El-CELL ECC-Std electrochemical test cell.

Cyclic voltammetry (CV): CV measurements were carried out on an Metrohm Autolab potentiostat/galvanostat PGSTAT302N equipped with a FRA32M module over the maximum potential range of 0.1–3.6 V vs. Li/Li^+ at scan rates varying between 1.0−15 mV s^{-1}.

Galvanostatic charge-discharge (GCD) cycling: GCD measurements were conducted using an Autolab Multipotentiostat M101 by applying different current densities ranging from 0.3−1.0 A g^{-1} in a voltage window of 0.1−3.6 V vs. Li/Li^+. Throughout the main article and supporting information, all potentials are being reported vs. Li/Li^+, unless stated otherwise.

Electrochemical impedance spectroscopy (EIS): The measurements were performed on an Autolab potentiostat workstation equipped with a FRA32M module over the frequency range of 10^6−0.1 Hz with an applied perturbation voltage of 10 mV.

Potential-dependent electrochemical impedance spectroscopy (EIS): The measurements were performed on a BioLogic VMP-3e Multichannel Potentiostat workstation over a frequency range of 10^6−0.4 Hz with an applied perturbation voltage of 10 mV over the potential window of 0.1−3.6 V. The electrochemical cells underwent galvanostatic charge-discharge at a current density of 0.3 A g^{-1} for 5 cycles to establish an aged/stable system. From a completely discharged state (potential at 0.1 V), EIS measurements were subsequently conducted with positive sweep-steps over a potential range of 0.1−3.6 V (and a negative sweep-steps between 3.6−0.1 V), and the impedance was measured at n number of potential steps with n = 42.

5.6.2. Theory

5.6.2.1. Cyclic voltammetry (CV), power law and Randles–Ševčík equation

This section presents a detailed overview of the cyclic voltammetry (CV) technique employed to determine formal potentials and to thoroughly investigate the charge storage kinetics at the PyTTF electrode, thereby offering critical insights for identifying the most suitable electrochemical model to interpret the ionic diffusion coefficient.[1–3] Rate-dependent CV measurements are particularly useful for discerning the dominant charge storage behavior, whether governed by diffusion-controlled faradaic processes characteristic of battery-type systems, surface-limited non-faradaic ion adsorption typical of electrical double-layer capacitors (EDLCs), or faradaic reactions involving surface redox transformations or ion intercalation, indicative of pseudocapacitive mechanisms. The distinction between the two extreme regimes can be evaluated by examining how the current response scales with the sweep rate during a CV experiment. This relationship typically follows a power-law, expressed as:[3,4]

$$i_p = av^b \qquad \text{(Equation 5.2)}$$

where i is the current, v is the sweep rate, a is a constant, and b is the kinetic exponent that indicates the nature of the charge-storage mechanism. When $b \approx 0.5$, the system is predominantly diffusion-limited, reflecting the slower transport of ions through the bulk of the material. In contrast, a b-value of $0.5 < b \leq 1.0$ implies higher rate kinetics, where the charge-storage process is governed by high-rate surface-redox reactions, or directional intercalation. In contrast, $b < 0.5$ indicates *slower* than ideal diffusion control, suggesting kinetically limited charge transfer or/and transport hindrance.

Within the diffusion-limited regime, the current response observed during cyclic voltammetry can be quantitatively described by the Randles–Ševčík equation:[5,6]

$$i_p = (2.69\ \times 10^5)n^{3/2}AD^{1/2}Cv^{1/2} \qquad \text{(Equation 5.3)}$$

where i_p denotes the peak current, n is the number of electrons involved in the redox process, A represents the electrode surface area, D is the diffusion coefficient of the redox-active species, C is its bulk concentration in the electrolyte, and v is the scan rate. The Randles-Ševčík equation relates peak current to the square root of the sweep rate under the assumption of semi-infinite linear diffusion, a well-defined redox couple, and reversible electron transfer.[4–6] This equation has long been employed to extract diffusion coefficients from rate-dependent CV data, offering a straightforward means to quantify ion mobility in electrochemical systems. However, the validity of this model diminishes in systems exhibiting capacitive or pseudocapacitive behavior. In such cases, where the logarithmic slope deviates from $0.5 \approx b\ < 1.0$, the charge storage mechanism transitions away from faradaic bulk diffusion control to processes dominated by faradaic surface-confined redox reactions or directional intercalation, or non-faradaic electrostatic double-layer charging.[1,2] In such cases, the current becomes linearly dependent on the sweep rate, violating the conditions under which the Randles–Ševčík model holds. Applying this model in the pseudocapacitive regime would therefore lead to an inaccurate estimation of the diffusion coefficient, as the underlying mechanism is not diffusion-limited. Therefore, prior to employing the Randles–Ševčík equation for quantitative analysis of diffusion coefficient, it is imperative to evaluate the b-value to ensure the system adheres to diffusion-limited behavior and that the underlying assumptions remain valid.

The Dunn method is employed to gain deeper insight into charge-storage mechanisms, particularly in materials where both capacitive and diffusion-controlled processes may coexist.[3] This analytical framework builds on the observation that current measured during a CV experiment at any given potential can originate from two sources: a surface-controlled capacitive and/or pseudocapacitive process and a diffusion-limited faradaic process. By recognizing their distinct dependencies on scan rate, the total current $i(V)$ can be expressed as a sum of contributions: [3,4]

$$i(V) = k_1 v + k_2 v^{1/2} \qquad \text{(Equation 5.4)}$$

where, $k_1 v$ represents the capacitive and pseudocapacitive current, which scales linearly with v, while $k_2 v^{1/2}$ corresponds to the diffusion-controlled current, which scales with the square root of the scan rate. This decomposition enables a semi-quantitative separation of the two kinetic contributions at each potential across the CV profile. This results in a potential-resolved map showing which fraction of the current arises from fast surface processes versus slower diffusion processes. This is particularly useful for materials with complex or hybrid mechanisms, where neither a purely capacitive nor purely diffusive model alone is sufficient.

5.6.2.2. Electrochemical impedance spectroscopy (EIS) and Warburg element

This section focuses on the potentiostatic electrochemical impedance spectroscopy (PEIS) technique, emphasizing the principles of semi-infinite diffusion and the Warburg element, followed by a semi-quantitative estimation of the ionic diffusion coefficient.[7–9] Typically, PEIS is conducted by applying a small-amplitude single-sine wave perturbation superimposed on a direct current (DC) bias to the electrochemical system, with the resulting current response measured across a broad frequency spectrum. [10] To ensure the validity of the linear approximation, i.e., a proportional relationship between the applied voltage and the current response, it is imperative to employ a low perturbation amplitude, such as 10 mV.[7,11]

By applying a perturbation signal over a broad frequency range (0.4 Hz–1.0 MHz) to an electrochemical cell, EIS allows for the selective probing of overlapping dynamics of several electrochemical and physicochemical phenomena.[8] The frequency domain operation of EIS enables the deconvolution of complex electrochemical behavior into discrete processes characterized by distinct time constants, such as ionic and electronic transport occurring in the high-frequency (kHz–MHz) to mid-frequency (Hz–kHz), as well as ionic mass transport governed by diffusion occurring in the low frequency range (<10 Hz).[8] This frequency-resolved analysis facilitates a more nuanced and comprehensive understanding of the electrochemical system under investigation, in comparison to the time-domain techniques such as cyclic voltammetry and chronoamperometry, rendering the individual contributions of slower processes particularly difficult, if not impractical, to resolve. With the EIS technique, low-frequency (<0.1 Hz) measurements are constrained by time requirements, as data acquisition at such low frequencies can extend several hours per data point, and therefore are not included in the measurement range.[7]

In a Nyquist plot, the Warburg element appears as a linear trajectory inclined at 45° to the real axis in the low-frequency domain (typically <10 Hz), indicative of semi-infinite linear diffusion.[11] Therefore, Warburg impedance provides mechanistic insight into diffusion-controlled mass transport phenomena arising due to the finite rate of ionic diffusion through a solid-phase medium. The frequency-dependent behavior of the Warburg element is governed by a ($\omega^{-1/2}$) relationship with angular frequency ω, arising from the temporal dispersion of concentration gradients during AC perturbation. Quantitatively, the Warburg coefficient (σ) can be obtained from the slope of linear fits to Warburg plots, constructed by correlating the real component of impedance (Z_{re}) with $\omega^{-1/2}$, using the following equation: [9,10]

$$Z_{re} = R_T + \sigma\omega^{-1/2} \qquad \text{(Equation 5.5)}$$

where, R_T is the total resistance. The characteristic region of the Warburg impedance is the low-frequency domain, and therefore Z_{re} associated with low frequency (<1.4 Hz) was considered for creating the Warburg plots. Determination of σ enables the calculation of the diffusion coefficient (D) of charge carriers, linking impedance spectroscopy to fundamental mass-transfer kinetics through the following relation: [9,10]

$$D = \frac{R^2T^2}{2n^4F^4C^2A^2\sigma^2} \qquad \text{(Equation 5.6)}$$

where R is the gas constant (8.314 J K^{-1} mol^{-1}), T is the operational temperature of the electrochemical cell (298 K), n is the number of electrons transferred from electrolyte to the electrode ($n = 1$), F is Faraday's constant (96458 C mol^{-1}), C is the concentration of the charge carriers in the electrolyte solution (1 M), A is the surface area of the electrode (2.54 cm^2), and σ is the Warburg coefficient (Ω $s^{-1/2}$), respectively.

5.6.3. Synthesis and molecular characterization

5.6.3.1. Building block synthesis

1,3,6,8-Tetrakis(4,4,5,5-tetramethyl-1,3,2-dioxaborolan-2-yl)pyrene

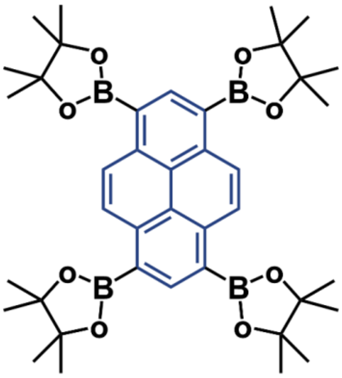

1,3,6,8-Tetrakis(4,4,5,5-tetramethyl-1,3,2-dioxaborolan-2-yl)pyrene was synthesized according to previously reported procedures with some modifications.[12] Under Ar atmosphere, 1,3,6,8-tetrabromopyrene (1500 mg, 2.90 mmol, 1.0 eq.), bis(pinacolato)diboron (4400 mg, 17.33 mmol, 6.0 eq.), Pd(dppf)Cl_2 (189 mg, 0.23 mmol, 0.08 eq.), and KOAc (1992 mg, 20.3 mmol 7.0 eq.) were dissolved in anhydrous DMSO (50 mL) and stirred at 90 °C for 48 h. After cooling to RT, the product was extracted with DCM (600 mL) and washed with H_2O multiple times to remove most DMSO. The organic phase was washed with brine, dried over $MgSO_4$ and further dried under reduced pressure to afford a brownish powder (1884 mg, 2.67 mmol, yield 92%).

^{1}H NMR (400 MHz, $CDCl_3$) δ (TMS, ppm): 9.16 (s, H), 8.99 (s, 2H), 1.50 (s, 48H).

^{13}C NMR (101 MHz, $CDCl_3$) δ (TMS, ppm): 141.47, 138.13, 129.57, 124.13, 83.97, 25.24.

HRMS-EI: calculated (m/z): 706.42, measured (m/z): 706.4194.

7-Bromo-4-(5,5-dimethyl-1,3-dioxan-2-yl)benzo[*c*][1,2,5]thiadiazole

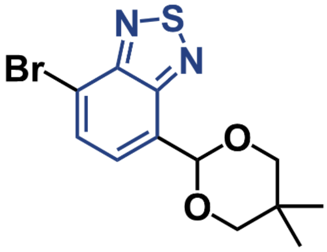

7-Bromo-4-(5,5-dimethyl-1,3-dioxan-2-yl)benzo[*c*][1,2,5]thiadiazole was synthesized according to previously reported procedures with some modifications.[13] 7-Bromo-2,1,3-benzothiadizole-4-carboxaldehyde (2000 mg, 8.23 mmol, 1 eq.), 2,2-dimethylpropane-1,3-diol (1286 mg, 12.35 mmol, 1.5 eq.), and *p*-toluenesulfonic acid monohydrate (156 mg, 0.82 mmol, 0.1 eq.) were dissolved in anhydrous toluene and refluxed at 115 °C for 4 h under N_2 atmosphere. A saturated aqueous solution of $NaHCO_3$ was added (100 mL) and the organic phase was extracted with DCM, washed with brine twice and dried over $MgSO_4$. The excess solvents were removed under reduced pressure. Further, the product was precipitated out with MeOH, and the solid was filtered and washed with MeOH to afford a yellow powder (2276 mg, 6.91 mmol, yield 84%).

^{1}H NMR (400 MHz, $CDCl_3$) δ (TMS, ppm): 7.88 (d, J = 7.6 Hz, 1H), 7.78 (d, J = 7.6 Hz, 1H), 6.11 (s, 1H), 3.85 – 3.78 (m, 4H), 1.34 (s, 3H), 0.84 (s, 3H).

^{13}C NMR (101 MHz, $CDCl_3$) δ (TMS, ppm): 153.54, 152.50, 132.00, 130.55, 127.47, 114.97, 97.90, 78.04, 30.58, 23.15, 21.96.

HRMS-EI: calculated (m/z): 327.99, measured (m/z): 327.9852.

1,3,6,8-Tetrakis(7-(5,5-dimethyl-1,3-dioxan-2-yl)benzo[*c*][1,2,5]thiadiazol-4-yl)pyrene

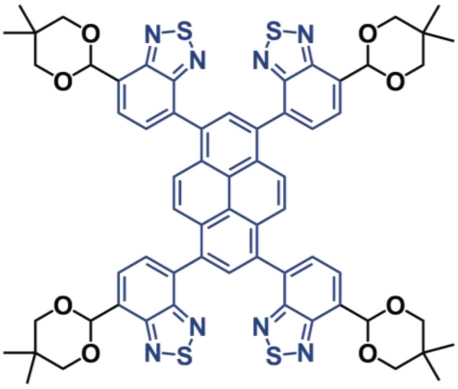

Under Ar atmosphere, 1,3,6,8-tetrakis(4,4,5,5-tetramethyl-1,3,2-dioxaborolan-2-yl)pyrene (859 mg, 1.21 mmol, 1.0 eq.), 7-bromo-4-(5,5-dimethyl-1,3-dioxan-2-yl)benzo[*c*][1,2,5]thiadiazole (1000 mg, 3.04 mmol, 2.5 eq.), $Pd(PPh_3)_4$ (168 mg, 0.15 mmol, 0.12 eq.), and K_2CO_3 (1672 mg, 12.10 mmol, 10 eq.) were dissolved in 1,4-dioxane (40 mL) and H_2O (10 mL) and refluxed at 110 °C for 72 h. After cooling to RT, the product was precipitated with H_2O, filtrated, and washed with H_2O and MeOH. The resulting powder was recrystallized from MeOH, yielding a bright orange powder (984 mg, 0.82 mmol, yield 68%).

^{1}H NMR (400 MHz, $CDCl_3$) δ (TMS, ppm): 8.24 (s, 2H), 8.12 (m, 4H), 7.94 (m, 4H), 7.86 (m, 4H), 6.30 (s, 4H), 3.92 – 3.86 (m, 16H), 1.41 (s, 12H), 0.88 (s, 12H).

^{13}C NMR (101 MHz, $CDCl_3$) δ (TMS, ppm):): 155.07, 153.06, 134.67, 132.80, 131.20, 131.14, 130.44, 129.78, 126.84, 125.98, 125.93, 98.34, 78.16, 30.66, 23.24, 22.04.

MALDI-MS: calculated (m/z): 1194.33, measured (m/z): 1195.68.

7,7',7'',7'''-(Pyrene-1,3,6,8-tetrayl)tetrakis(benzo[*c*][1,2,5]thiadiazole-4-carbaldehyde)

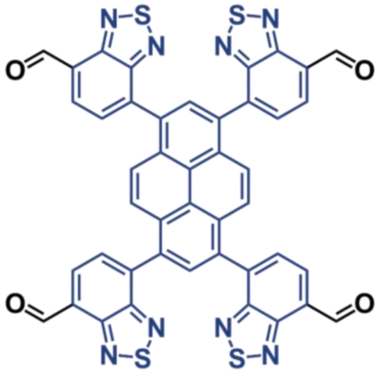

Under N_2 atmosphere, 1,3,6,8-tetrakis(7-(5,5-dimethyl-1,3-dioxan-2-yl)benzo[*c*][1,2,5]thiadiazol-4-yl)pyrene (800 mg, 0.67 mmol, 1.0 eq.) was dissolved in $CHCl_3$ (80 mL). To the solution, trifluoracetic acid (18 mL) was added dropwise, followed by dropwise addition of H_2O (1.2 mL). After stirring at RT for 12 h, the mixture was added into a saturated aqueous solution of $NaHCO_3$. The mixture was filtrated and the precipitate was washed with excess amounts of H_2O, MeOH, $CHCl_3$ and acetone to afford a dark purple powder (365 mg, 0.43 mmol, yield 64%).

^{13}C CP-MAS NMR (125 MHz) δ (ppm): 187.00, 152.53, 138.33, 135.22, 127.52, 122.79.

HRMS-EI: calculated (m/z): 850.03, measured (m/z): 850.0345.

5.6.3.2. Building block characterization

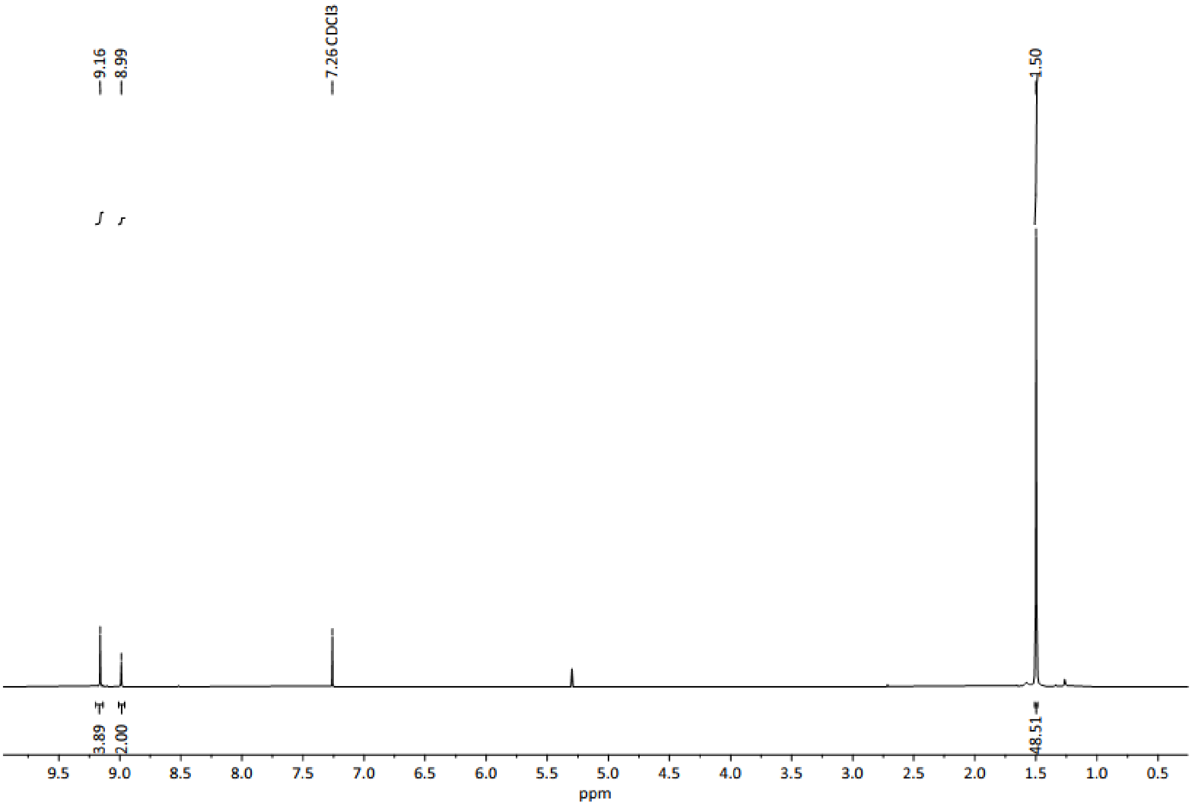

Figure 5.4 Liquid ^{1}H NMR spectrum of 1,3,6,8-tetrakis(4,4,5,5-tetramethyl-1,3,2-dioxaborolan-2-yl)pyrene.

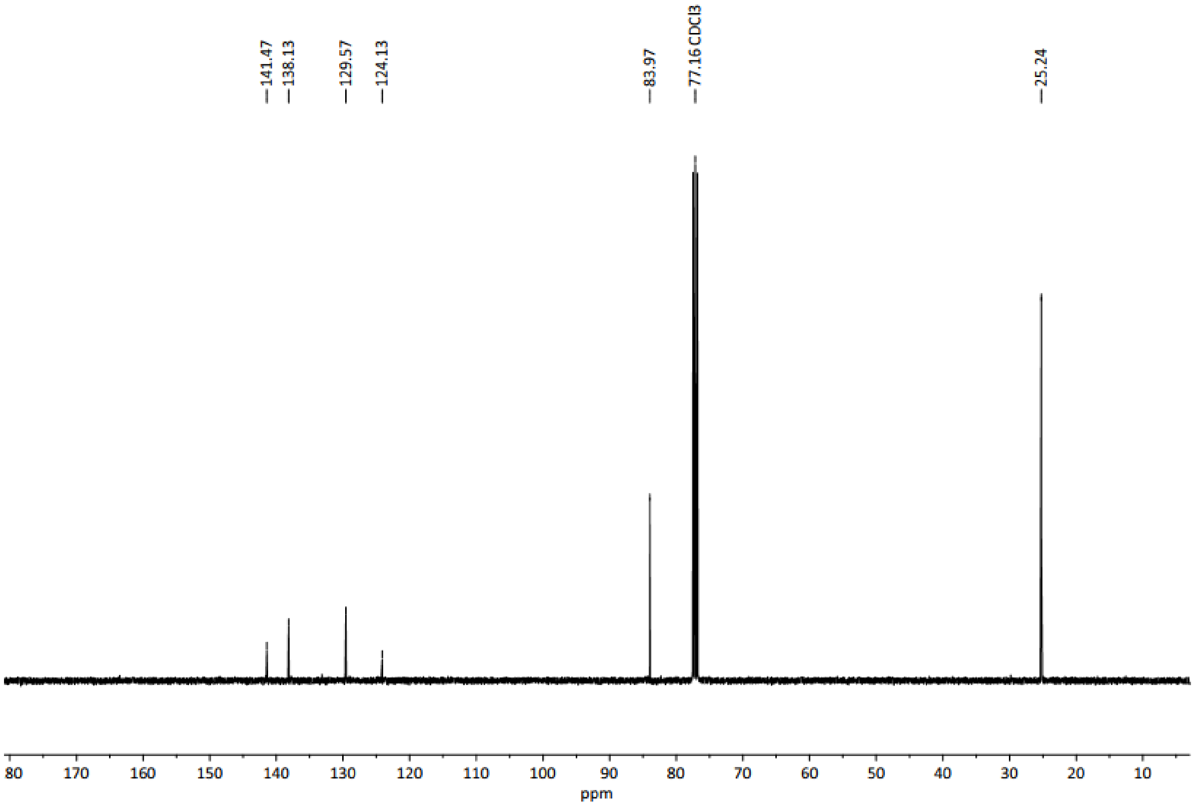

Figure 5.5 Liquid ^{13}C NMR spectrum of 1,3,6,8-tetrakis(4,4,5,5-tetramethyl-1,3,2-dioxaborolan-2-yl)pyrene.

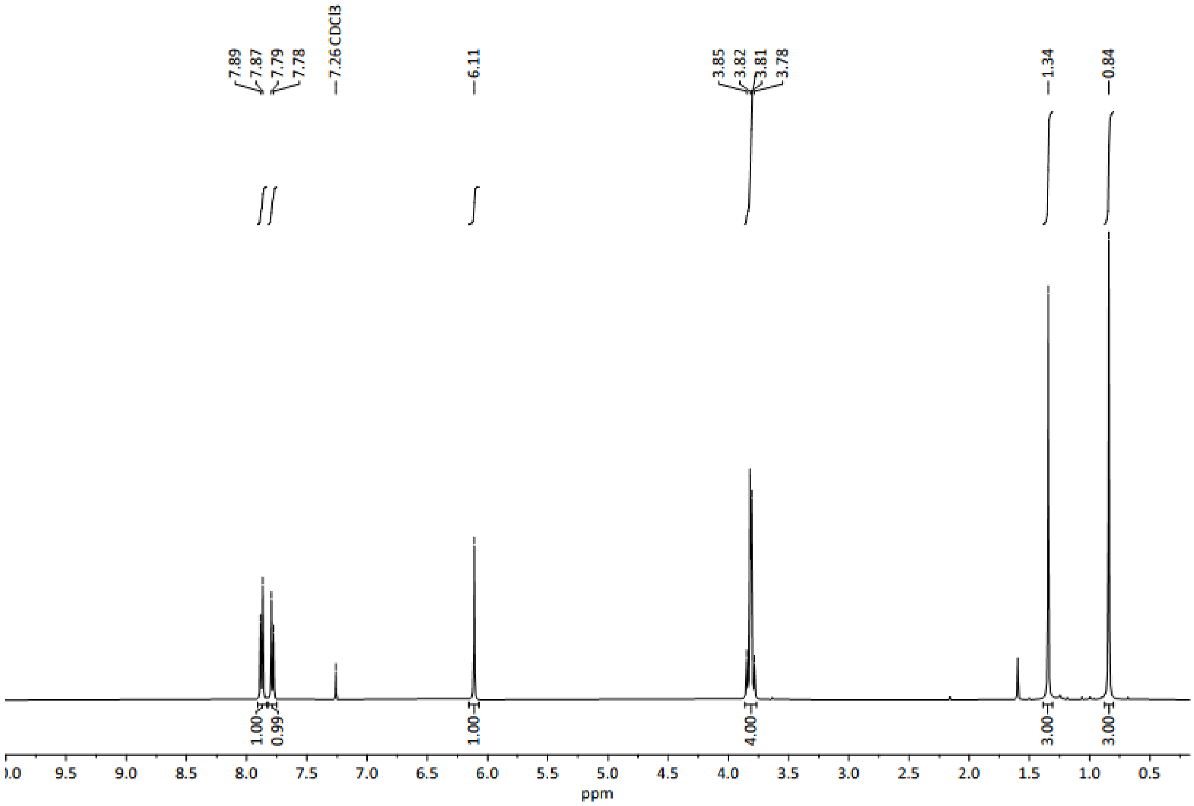

Figure 5.6 Liquid ^{1}H NMR spectrum of 7-bromo-4-(5,5-dimethyl-1,3-dioxan-2-yl)benzo[*c*][1,2,5]thiadiazole.

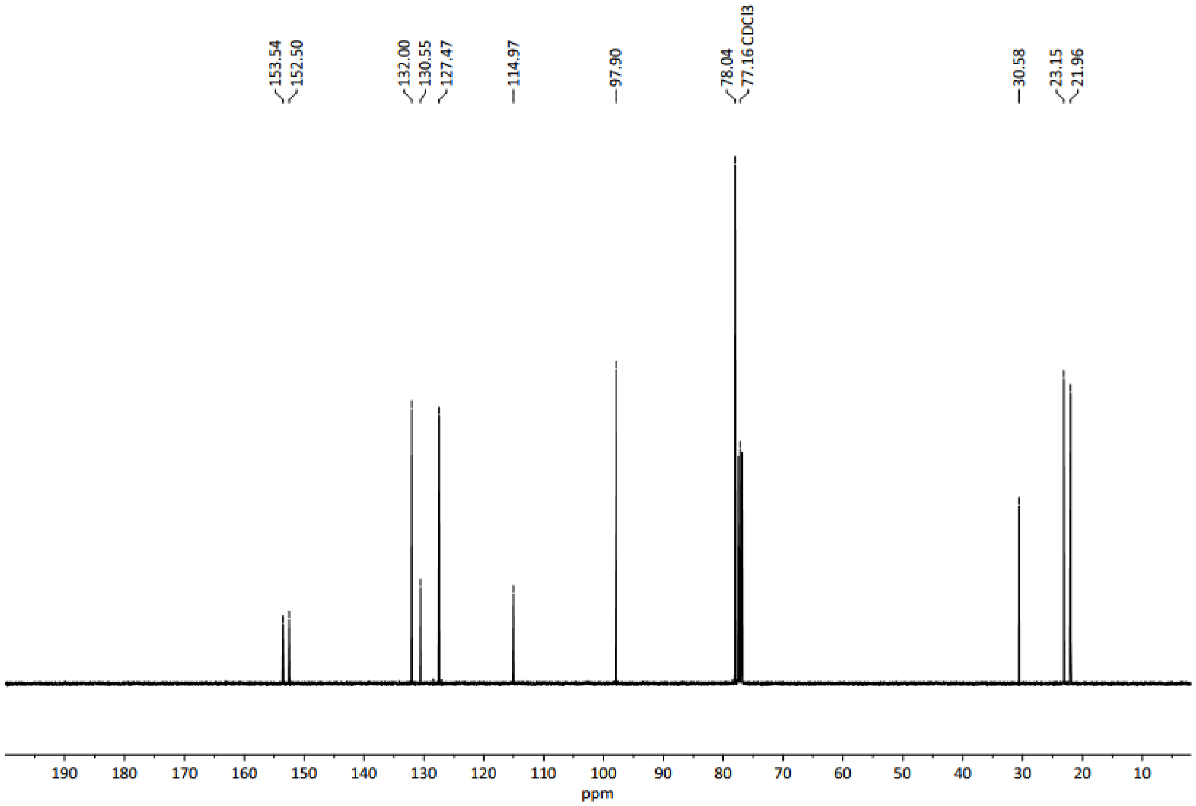

Figure 5.7 Liquid ^{13}C NMR spectrum of 7-bromo-4-(5,5-dimethyl-1,3-dioxan-2-yl)benzo[*c*][1,2,5]thiadiazole.

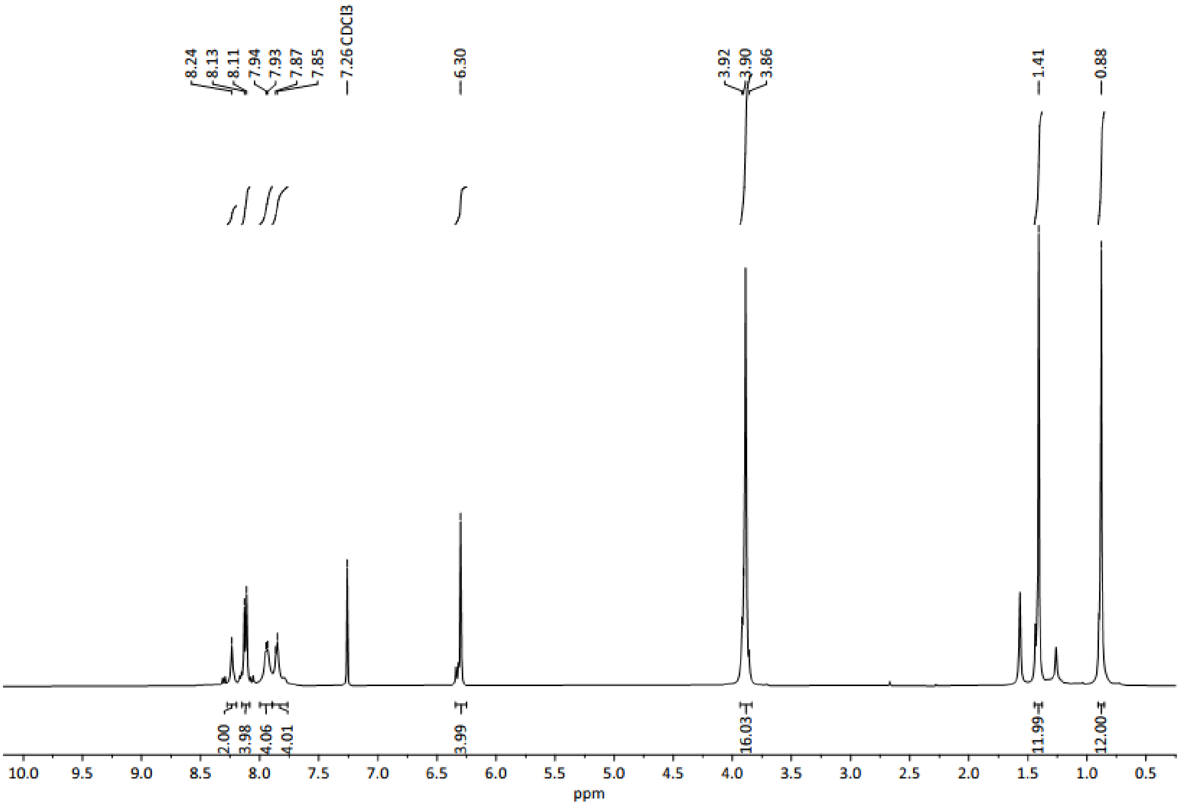

Figure 5.8 Liquid ^{1}H NMR spectrum of 1,3,6,8-tetrakis(7-(5,5-dimethyl-1,3-dioxan-2-yl)benzo[*c*][1,2,5]thiadiazol-4-yl)pyrene.

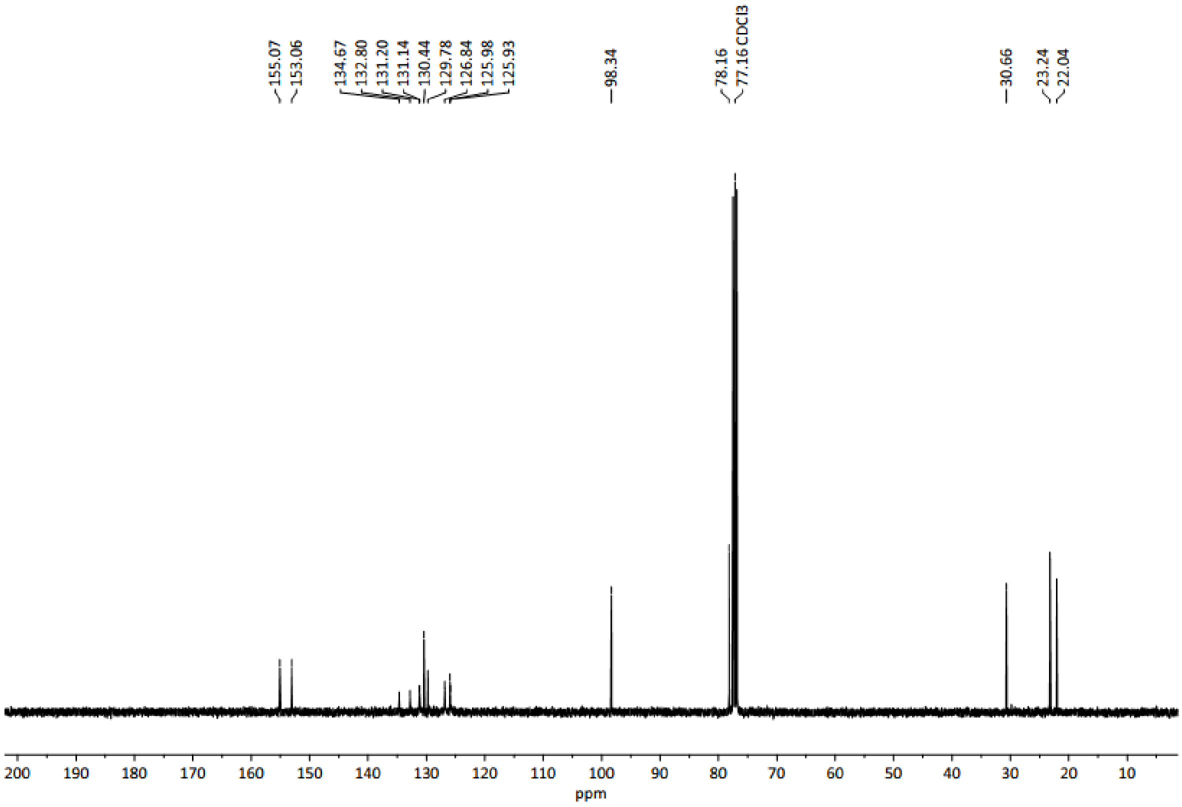

Figure 5.9 Liquid ^{13}C NMR spectrum of 1,3,6,8-tetrakis(7-(5,5-dimethyl-1,3-dioxan-2-yl)benzo[c][1,2,5]thiadiazol-4-yl)pyrene.

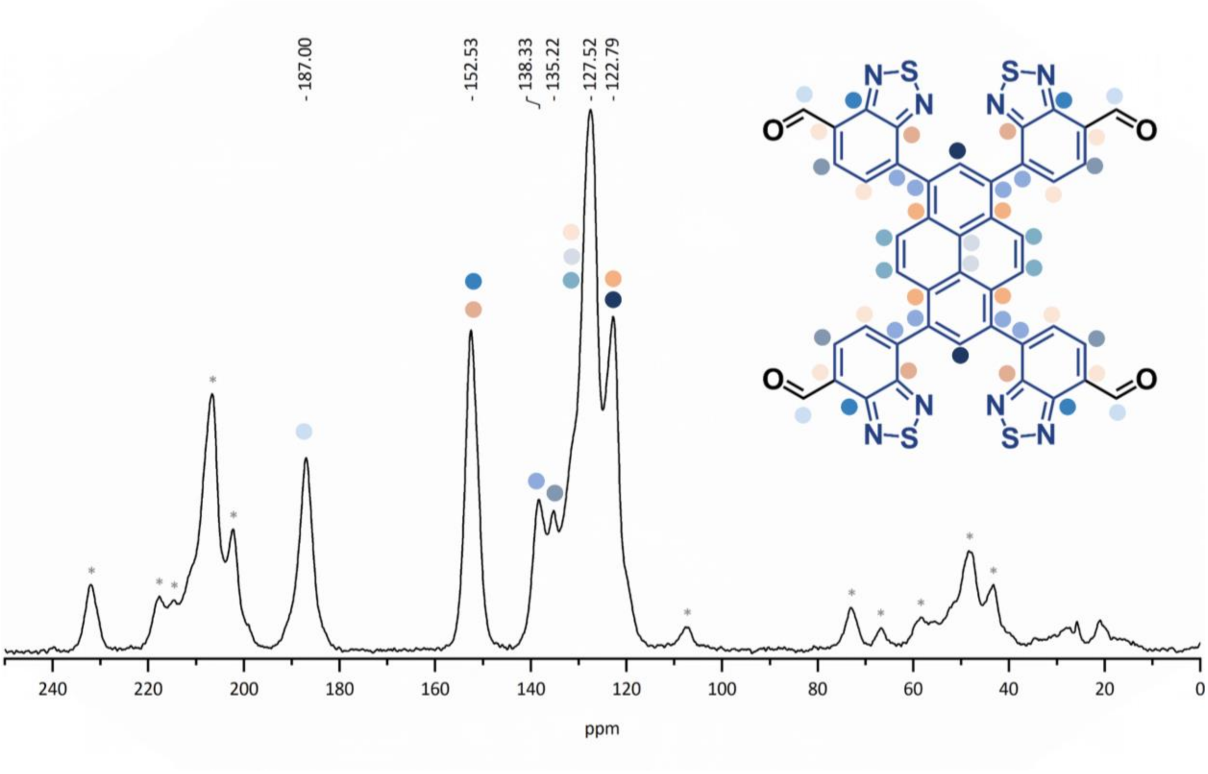

Figure 5.10 Solid-state ^{13}C CP-MAS NMR spectra of 7,7',7'',7'''-(pyrene-1,3,6,8-tetrayl)tetrakis-(benzo[*c*][1,2,5]thiadiazole-4-carbaldehyde). The peak at 187 ppm is assigned to the aldehyde functionality, indicating successful formation. The absence of signals around 100 and 80 ppm confirms the deprotection and consequent removal of the acetal groups. Weak signals below 40 ppm are likely attributable to residual solvents. The signals marked with asterisks correspond to spinning sideband artefacts.

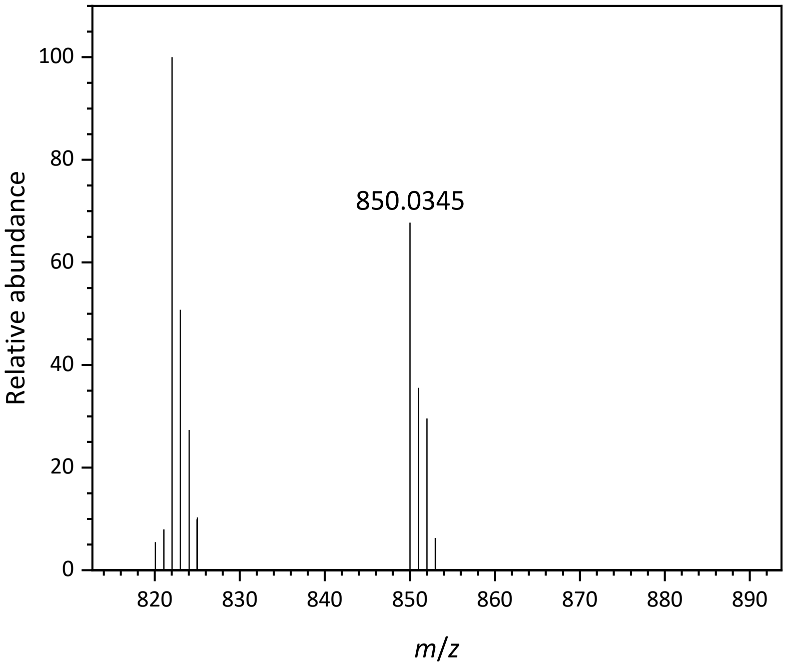

Figure 5.11 HRMS-EI spectrum of 7,7',7'',7'''-(pyrene-1,3,6,8-tetrayl)tetrakis-(benzo[c][1,2,5]thiadiazole-4-carbaldehyde) with its molecular peak and fragmentation.

5.6.3.3. COF synthesis

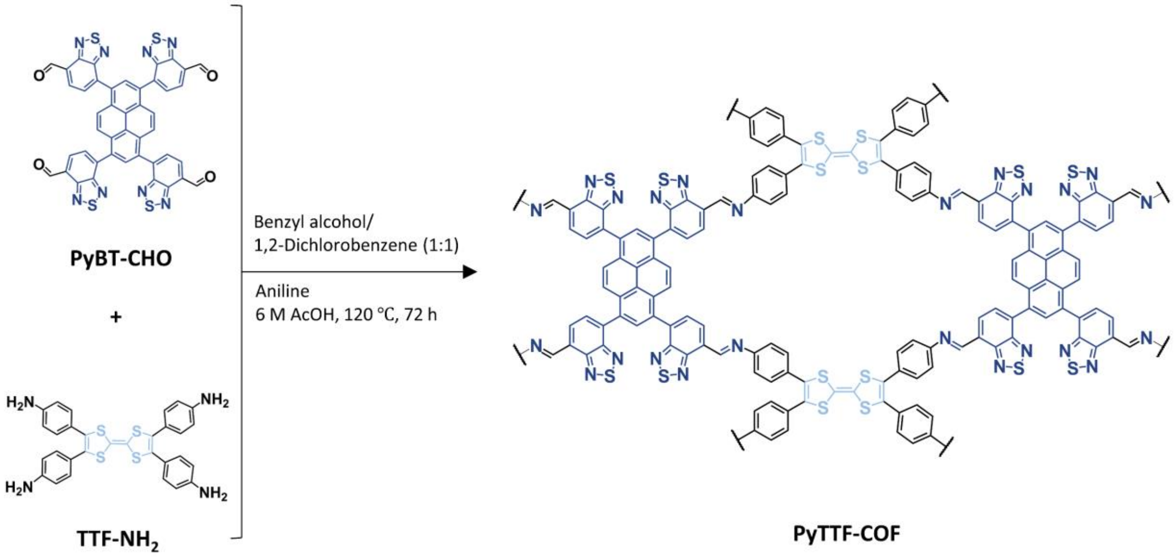

Scheme 5.1 Synthesis of PyTTF-COF.

Optimized conditions: 4,4',4'',4'''-([2,2'-Bi(1,3-dithiolylidene)]-4,4',5,5'-tetrayl)tetraaniline (TTF-NH_2, 8.53 mg, 0.015 mmol, 1.0 equiv. BLD Pharmatech GmbH), 7,7',7'',7'''-(pyrene-1,3,6,8-tetrayl)tetrakis-(benzo[*c*][1,2,5]thiadiazole-4-carbaldehyde) (PyBT-CHO, 12.75 mg, 0.015 mmol, 1.0 equiv.), aniline (2µL, 0.021 mmol, ~1.5 equiv.), and 0.1 mL of 6 M aqueous acetic acid were added to a Pyrex tube containing a mixture of benzyl alcohol (0.5 mL) and 1,2-dichlorobenzene (0.5 mL) inside an argon filled glovebox. The reaction tube was then heated to 120 °C for 3 days. The resulting COF powder was thoroughly washed with tetrahydrofuran (THF) and subsequently dried *in vacuo* for 6 h yielding dark brown-black COF powder.

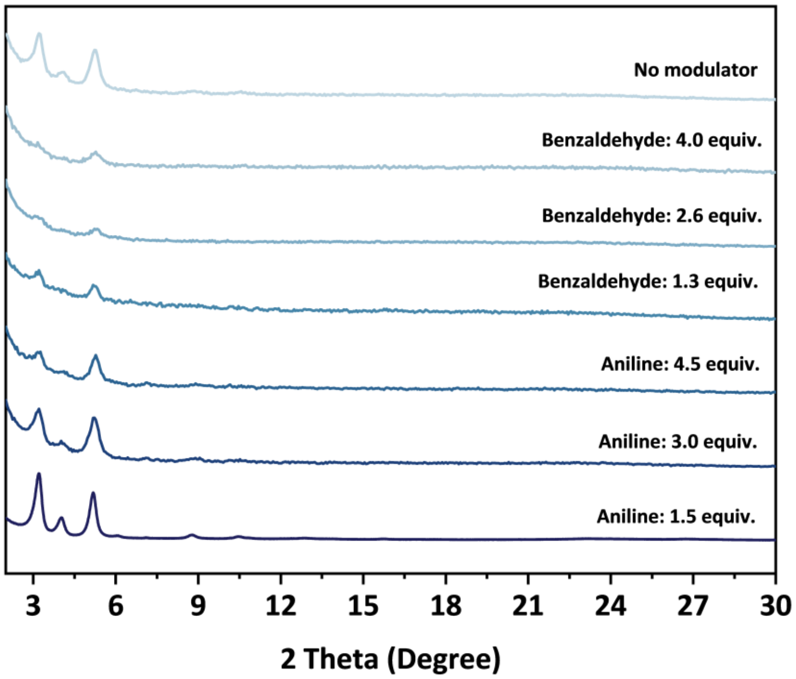

Figure 5.12. COF synthesis screening. Comparative experimental powder X-ray diffractograms for synthesized PyTTF-COF samples by utilizing two different modulators, aniline and benzaldehyde, at varying equivalent ratios. Addition of 1.5 equiv. ratio of aniline as modulating agent yielded the most crystalline COF sample.

5.6.3.4. COF characterization

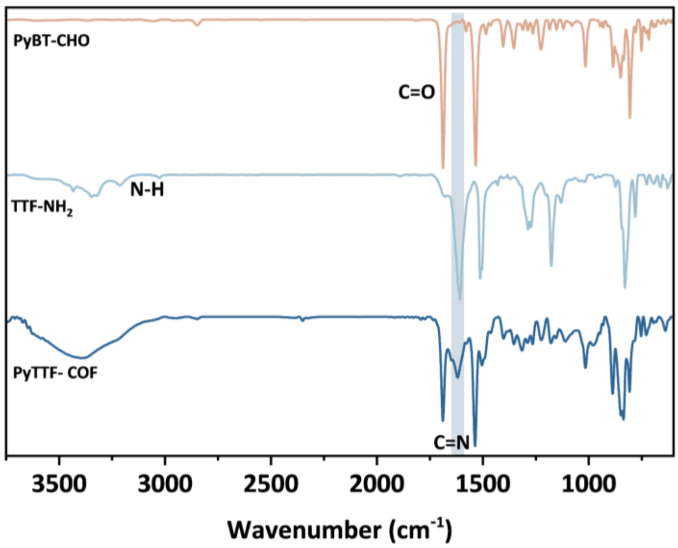

Figure 5.13 Fourier transform infrared (FT-IR) spectroscopy analysis of building blocks PyBT-CHO and TTF-NH_2, and resulting PyTTF-COF. The emergence of a characteristic band for the C=N bond vibration for the PyTTF-COF is marked in blue.

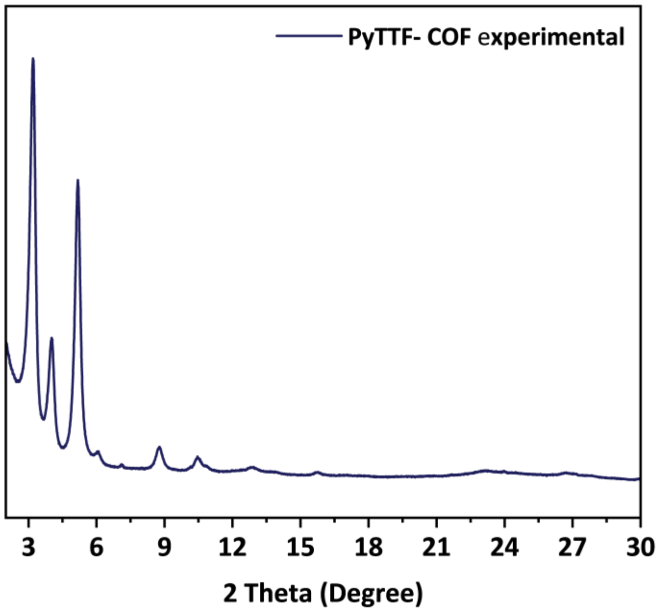

Figure 5.14 Experimental powder X-ray diffractogram of synthesized PyTTF-COF.

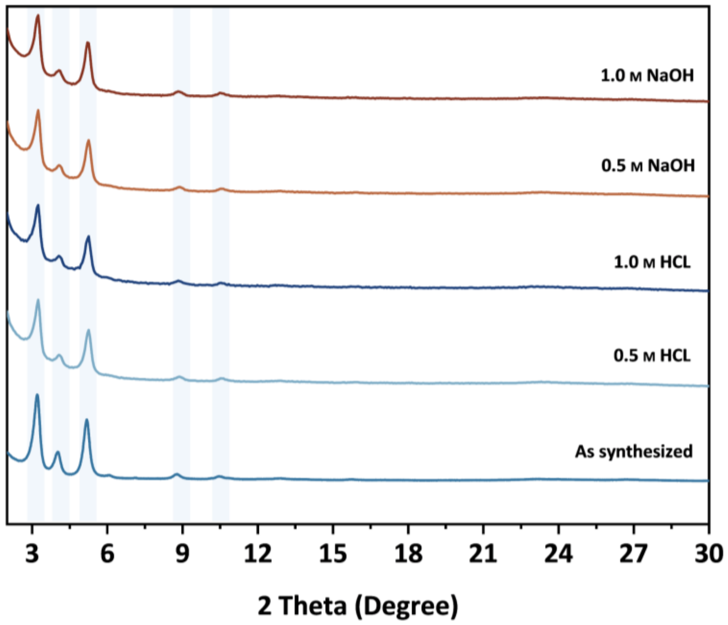

Figure 5.15. The PXRD patterns of PyTTF-COF after 12 hours of exposure to various acidic and basic media are shown, contrasted against the as-synthesized material. Relative to the pristine framework, PyTTF-COF displays only subtle structural perturbations under both acidic and basic conditions.

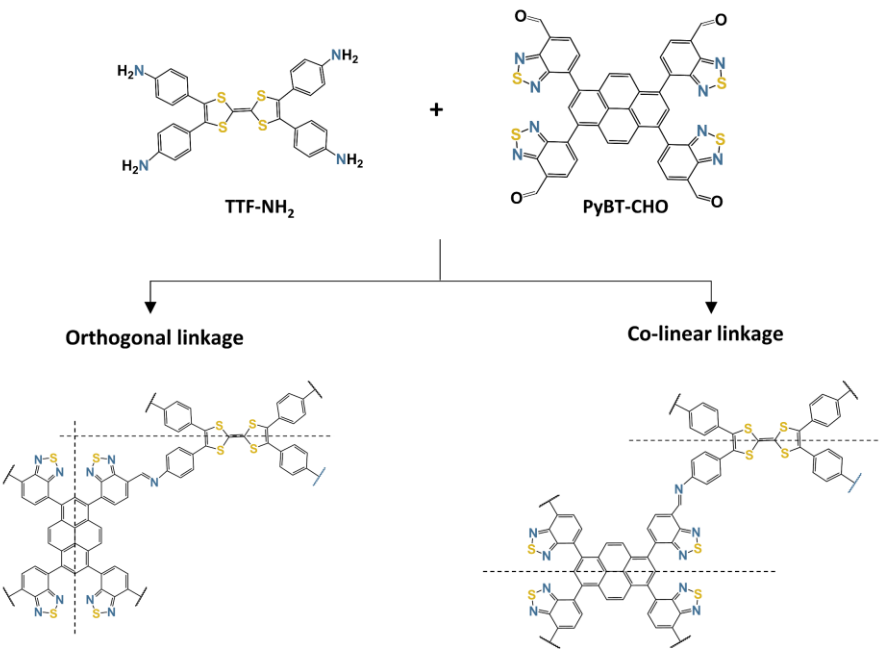

Figure 5.16 Pictorial representation of orthogonal linkage and co-linear linkage.

Table 5.1 Description of the simulated structure models explored for PyTTF-COF.

Structure	**Description**
Orthogonal linkage-1	AA-eclipsed, orthogonal connection of subunits featuring BT units preferentially oriented toward the smaller pore channels
Orthogonal linkage-2	AA-eclipsed, orthogonal connection of subunits featuring BT units preferentially oriented toward the larger pore channels
Co-linear linkage-1	AA-eclipsed, co-linear connection of subunits featuring BT units preferentially oriented toward the smaller pore channels
Co-linear linkage-2	AA-eclipsed, co-linear connection of subunits featuring BT units preferentially oriented toward the larger pore channels
Linear-PyBT	AA-eclipsed, orthogonal connection of subunits featuring BT units preferentially oriented toward the smaller pore channels, PyBT-CHO monomer being partially reacted leading to incomplete (linear) linkage
AB stacking	AB-stacking, orthogonal connection of subunits featuring BT units preferentially oriented toward the smaller pore channels
1-BT flip	AA-eclipsed, orthogonal connection of subunits featuring 3 BT units oriented toward the smaller pore, while 1 BT unit is oriented toward the larger pore per unit cell
BT propeller	AA-eclipsed, orthogonal connection of subunits featuring 2 BT units oriented toward the smaller pore and 2 BT units oriented toward the larger pore in a propeller-like fashion per unit cell
Random BT supercell	AA-eclipsed, orthogonal connection of subunits featuring random orientation of BT units in one supercell

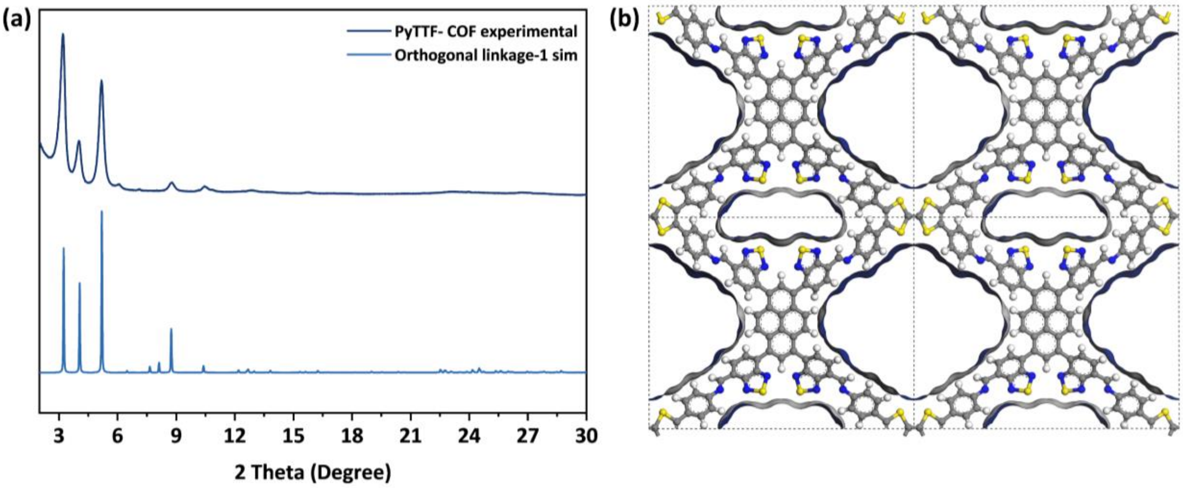

Figure 5.17 (a) Experimental powder X-ray diffractogram for synthesized PyTTF-COF, and simulated diffraction pattern for orthogonal linkage-1 structure model. (b) Respective simulated structure of the orthogonal linkage-1 structure model.

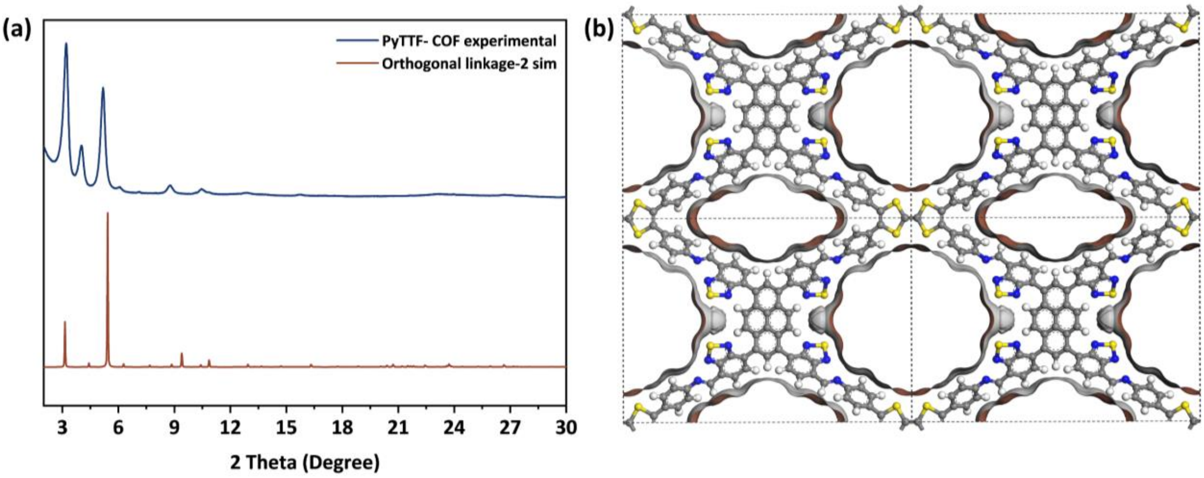

Figure 5.18 (a) Experimental powder X-ray diffractogram for synthesized PyTTF-COF, and simulated diffraction pattern for orthogonal linkage-2 structure model. (b) Respective simulated structure of the orthogonal linkage-2 structure model.

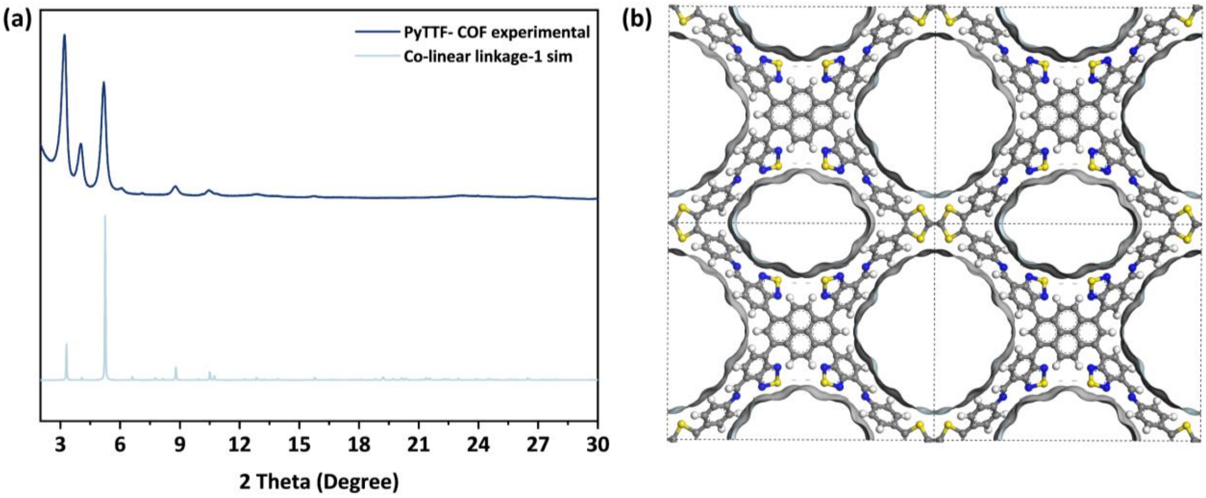

Figure 5.19 (a) Experimental powder X-ray diffractogram for synthesized PyTTF-COF, and simulated diffraction pattern for co-linear linkage-1 structure model. (b) Respective simulated structure of the co-linear linkage-1 structure model.

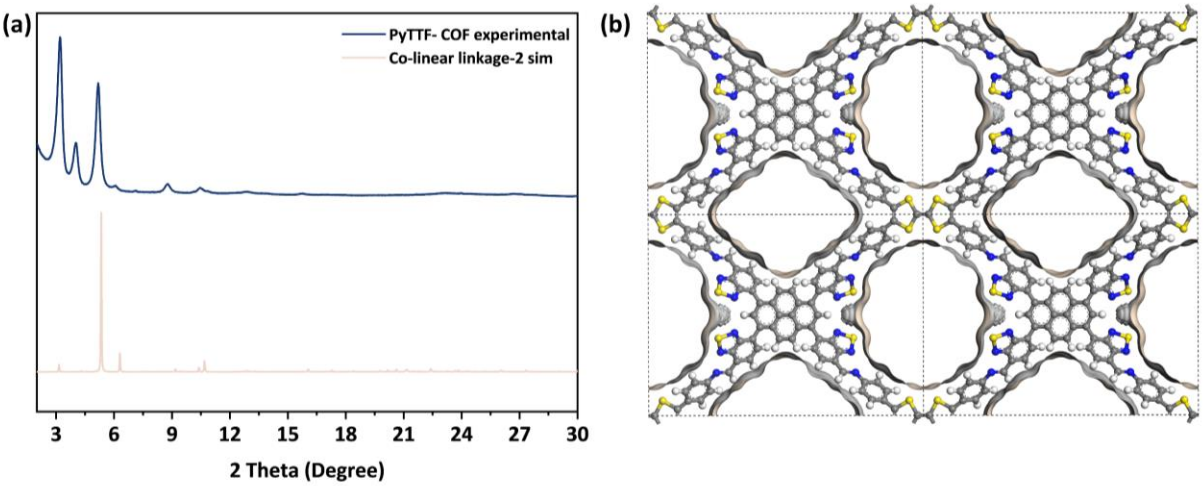

Figure 5.20 (a) Experimental powder X-ray diffractogram for synthesized PyTTF-COF, and simulated diffraction pattern for co-linear linkage-2 structure model. (b) Respective simulated structure of the co-linear linkage-2 structure model.

Table 5.2 Lattice parameters of simulated structural models of PyTTF-COF involving the building blocks connected through orthogonal and co-linear linkage.

Simulated structures	**Space group**	***a***	***b***	***c***	***α***	***β***	***γ***
Orthogonal linkage-1	*P2*	28.36 Å	21.77 Å	4.01 Å	90.00°	105.98°	90.00°
Orthogonal linkage-2	*P2/m*	29.81 Å	19.97 Å	4.53 Å	90.00°	70.74°	90.00°
Co-linear linkage-1	*P2/m*	28.66 Å	21.67 Å	4.82 Å	90.00°	68.81°	90.00°
Co-linear linkage-2	*P2/m*	30.04 Å	20.51 Å	4.61 Å	90.00°	68.95°	90.00°

These structures were modeled based on an AA-eclipsed stacking configuration.

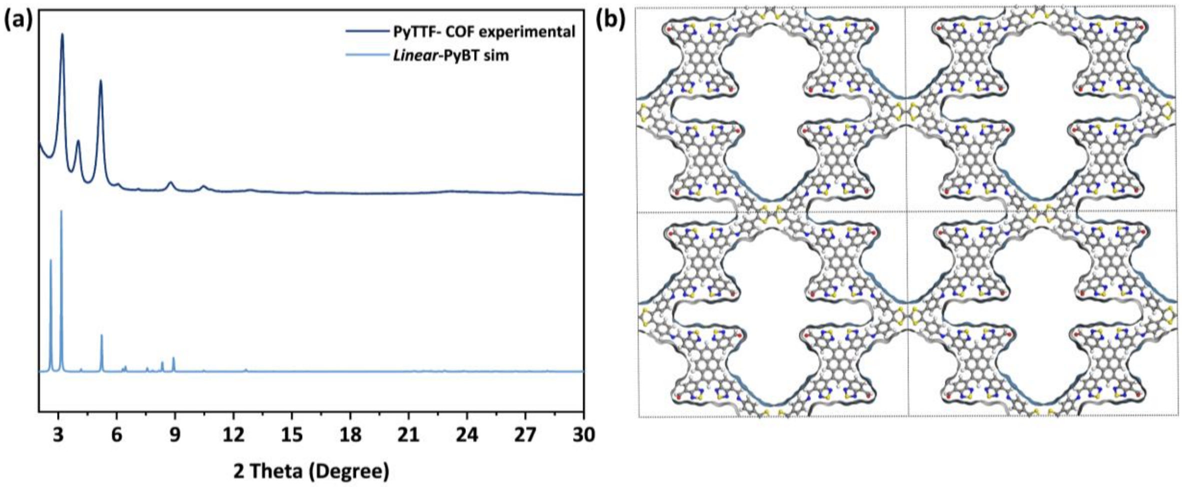

Figure 5.21 (a) Experimental powder X-ray diffractogram for synthesized PyTTF-COF, and simulated diffraction pattern for *linear*-PyBT structure model. (b) Respective simulated structure of the *linear*-PyBT structure model.

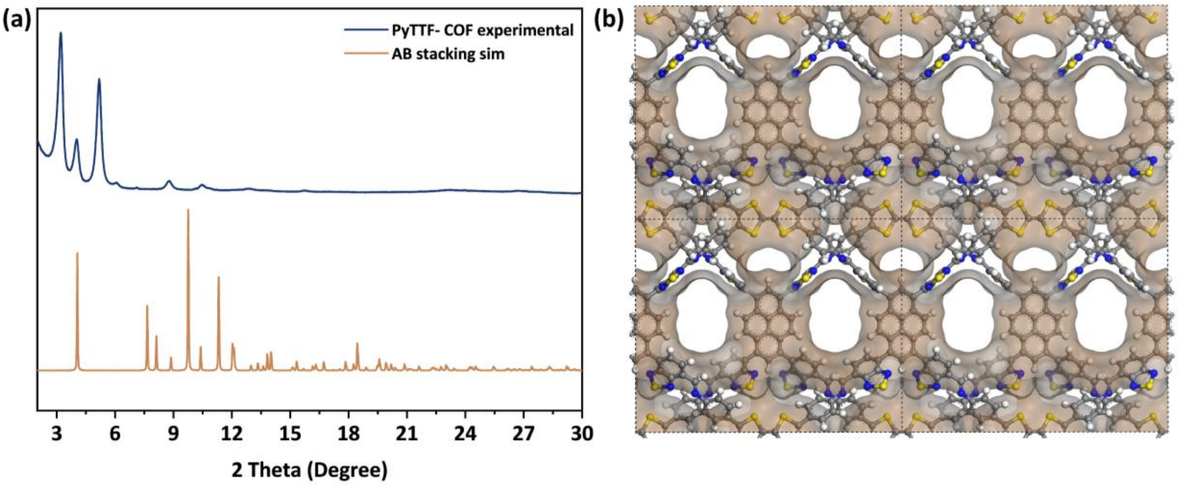

Figure 5.22 (a) Experimental powder X-ray diffractogram for synthesized PyTTF-COF, and simulated diffraction pattern for AB stacking structure model. (b) Respective simulated structure of the AB stacking structure model.

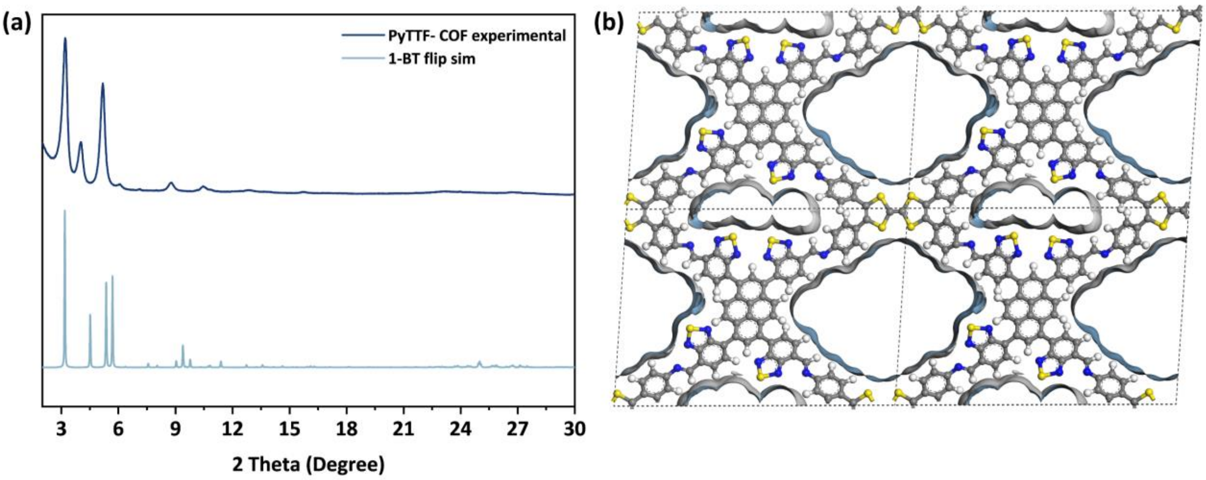

Figure 5.23 (a) Experimental powder X-ray diffractogram for synthesized PyTTF-COF, and simulated diffraction pattern for 1-BT flip structure model. (b) Respective simulated structure of the 1-BT flip structure model.

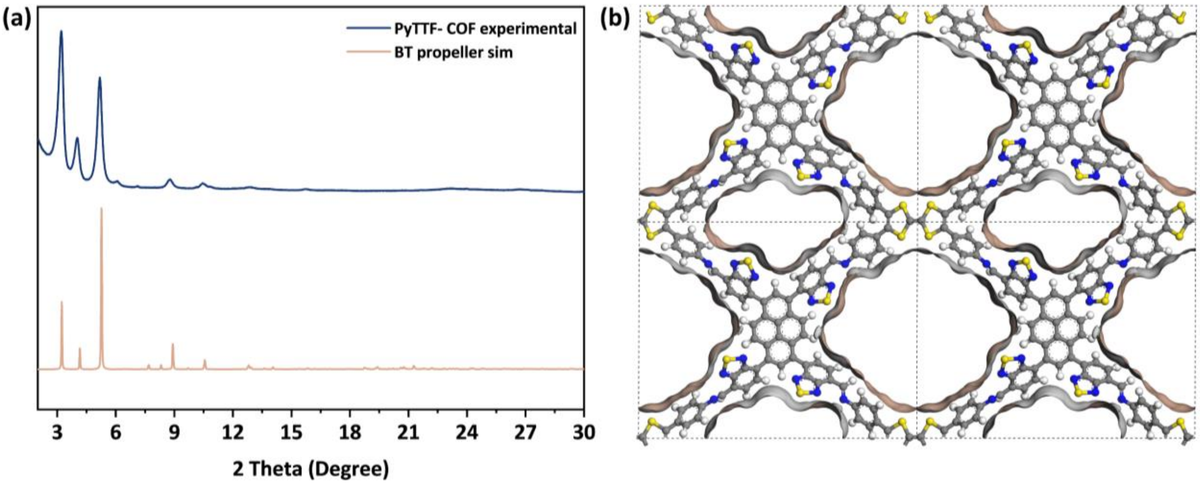

Figure 5.24 (a) Experimental powder X-ray diffractogram for synthesized PyTTF-COF, and simulated diffraction pattern for BT propeller structure model. (b) Respective simulated structure of the BT propeller structure model.

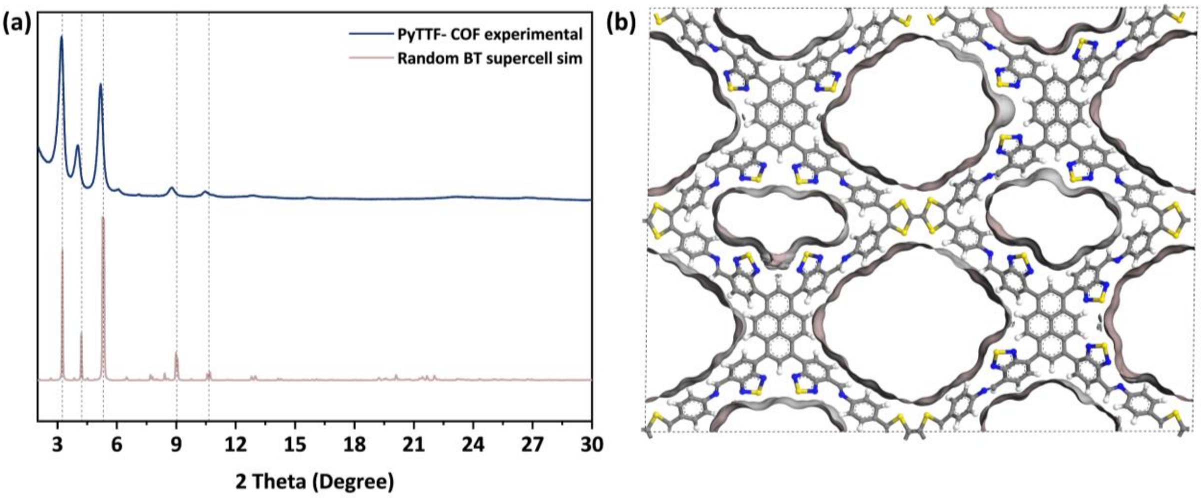

Figure 5.25 (a) Experimental powder X-ray diffractogram for synthesized PyTTF-COF, and simulated diffraction pattern for random BT super cell structure model. (b) Respective simulated structure of the BT super cell structure model.

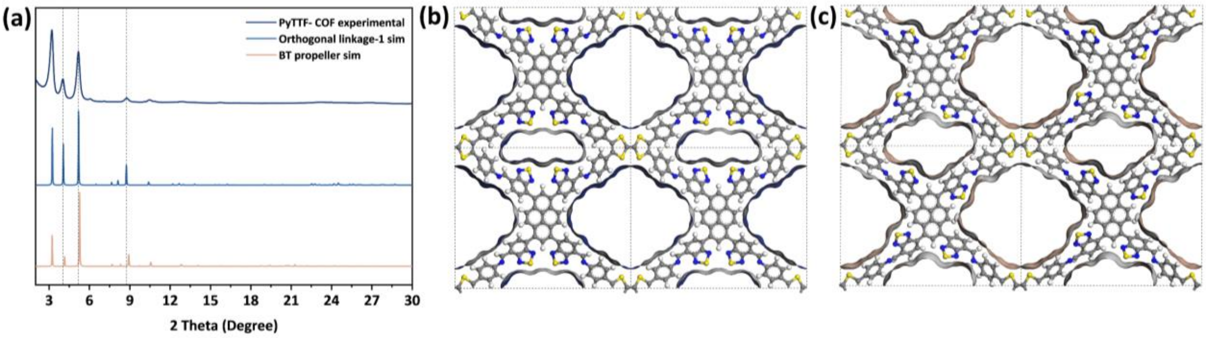

Figure 5.26 (a) Experimental powder X-ray diffractogram for synthesized PyTTF-COF and simulated diffraction pattern for orthogonal linkage-1 and BT propeller structure models. Respective simulated structure of (b) the orthogonal linkage-1 and (c) the BT propeller structure models.

Table 5.3 Lattice parameters of simulated structural models of PyTTF-COF involving the building blocks connected through orthogonal linkage.

Simulated structures	Space group	*a*	*b*	*c*	*α*	*β*	*γ*
Linear-PyBT	*P2*	57.20 Å	42.39 Å	4.26 Å	90.00°	78.13°	90.00°
AB stacking	*P1*	28.36 Å	21.77 Å	10.00 Å	90.00°	105.9°	90.00°
1-BT flip	*P1*	29.47 Å	20.16 Å	3.98 Å	103.6°	70.78°	91.09°
BT propeller	*P1*	28.55 Å	21.29 Å	4.78 Å	93.67°	73.26°	90.82°
Random BT supercell	*P1*	57.74 Å	42.07 Å	4.69 Å	92.54°	70.40°	90.14°

Orthogonal connectivity was employed to assemble these simulated structures.

Atomic coordinates (*P2*) for optimized structure (Orthogonal linkage-1) of PyTTF- COF.

Atom	*a/x*	*b/y*	*c/z*
C1	0.54549	0.57324	0.61415
C2	0.58955	0.53767	0.72468
C3	0.58912	0.47179	0.67431
C4	0.54526	0.436	0.58708
C5	0.4545	0.6417	0.38874
C6	0.45468	0.36748	0.41391
C7	0.59174	0.32786	0.67656
C8	0.59366	0.27245	0.48254
C9	0.63674	0.23753	0.55845

C10	0.68137	0.25806	0.82001
C11	0.67954	0.3105	1.03105
C12	0.63483	0.34299	0.96989
N13	0.63208	0.18506	0.35566
S14	0.57045	0.17622	0.04785
N15	0.55497	0.24895	0.21248
C16	0.6753	0.76273	0.82524
C17	0.67156	0.70333	0.65335
C18	0.62923	0.66514	0.57887
C19	0.59145	0.68217	0.70156
C20	0.59642	0.7421	0.87677
C21	0.63672	0.78142	0.9304
N22	0.63475	0.83864	1.079
S23	0.57926	0.8463	1.16313
N24	0.56292	0.76694	0.99636
C25	0.71624	0.80739	0.86691
N26	0.748	0.79604	0.71928
C27	0.78677	0.83878	0.71971
C28	0.7295	0.2279	0.86902
N29	0.73193	0.18543	0.64472
C30	0.77397	0.15062	0.63947
C31	0.82198	0.8162	0.59191
C32	0.85859	0.85749	0.56701
C33	0.86097	0.92253	0.67412
C34	0.8283	0.94211	0.83028
C35	0.78976	0.90283	0.83394
C36	0.82306	0.16897	0.82998
C37	0.86214	0.13166	0.80967
C38	0.85285	0.07474	0.6084
C39	0.80324	0.05947	0.40593
C40	0.7646	0.09694	0.42275
C41	0.89539	1.03372	0.60974
C42	0.89817	0.96809	0.6282
S43	0.94752	1.07724	0.57524
C44	0.97888	1.0049	0.53219
S45	0.95122	0.93034	0.58364
H46	0.62533	0.55988	0.84683
H47	0.62421	0.4501	0.70974
H48	0.71259	0.32564	1.24675
H49	0.63403	0.38059	1.15124

H50	0.69991	0.68879	0.55588
H51	0.62511	0.62368	0.41006
H52	0.71776	0.85091	1.01443
H53	0.76212	0.2418	1.09067
H54	0.81969	0.76707	0.49925
H55	0.88357	0.83891	0.4492
H56	0.83308	0.98839	0.94973
H57	0.76357	0.92278	0.93482
H58	0.83132	0.21153	0.99294
H59	0.89991	0.14626	0.95847
H60	0.79315	0.01668	0.25087
H61	0.7266	0.08383	0.27027
C62	0.5	0.47015	0.5
C63	0.5	0.53903	0.5
C64	0.5	0.67373	0.5
C65	0.5	0.3351	0.5
H66	0.5	0.28296	0.5
H67	0.5	0.72555	0.5

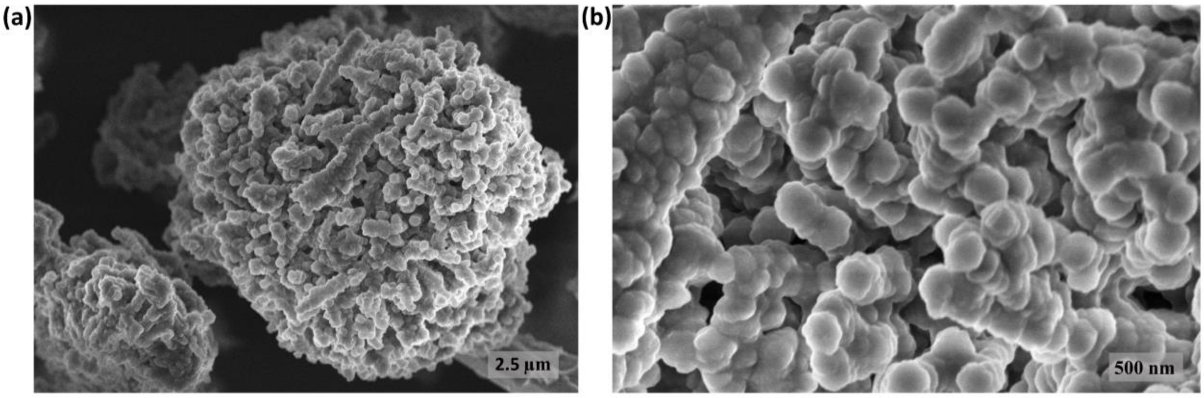

Figure 5.27 Scanning electron microscopy (SEM) images of PyTTF-COF bulk powder.

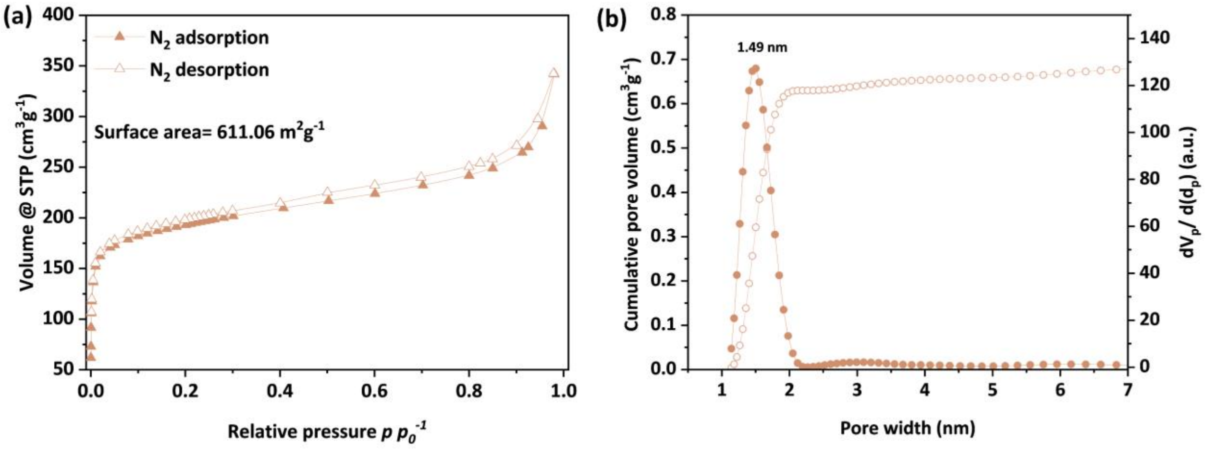

Figure 5.28 (a) Nitrogen (N_2) gas sorption isotherms, (b) pore size distribution and cumulative pore volume profile of PyTTF-COF.

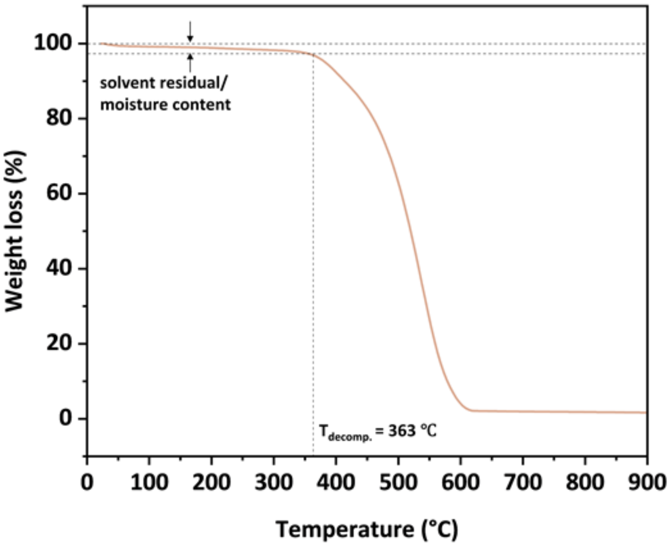

Figure 5.29 Thermogravimetric analysis (TGA) of PyTTF-COF obtained by heating the sample from room temperature to 900 °C under a synthetic air flow at a heating rate of 10 °C min^{-1}.

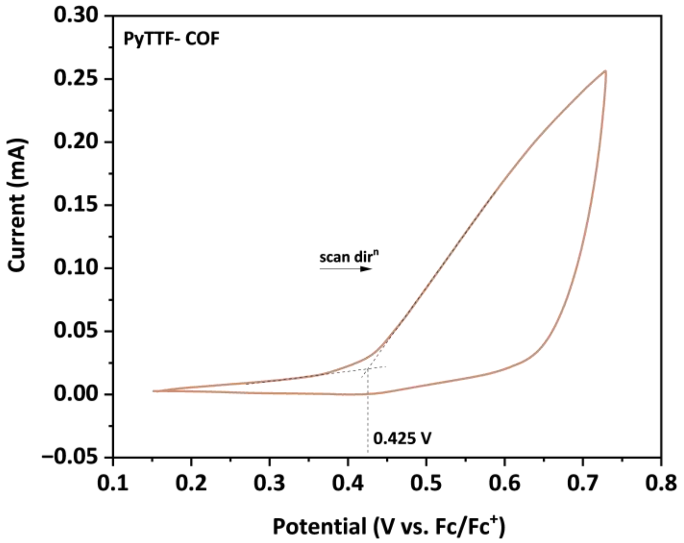

Figure 5.30 CV of PyTTF-COF calibrated against Fc/Fc$^+$ redox couple using 0.1 M tetrabutylammonium hexafluorophosphate (NBu_4PF_6) in an anhydrous acetonitrile solution serving as electrolyte.

5.6.4. Electrochemical characterization

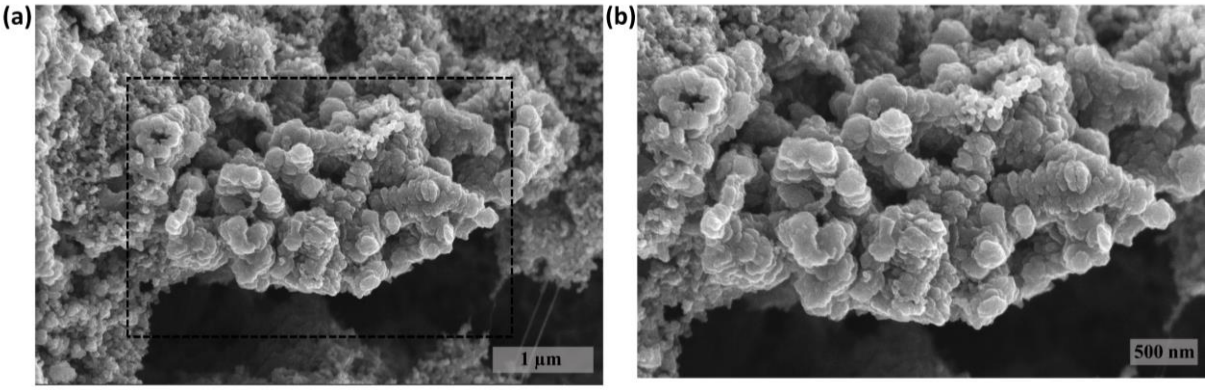

Figure 5.31 Scanning electron microscopy (SEM) images of pristine PyTTF electrode comprising PyTTF (60 wt.%), Ketjenblack (20 wt.%), and PVDF (20 wt.%) coated on a Cu-foil.

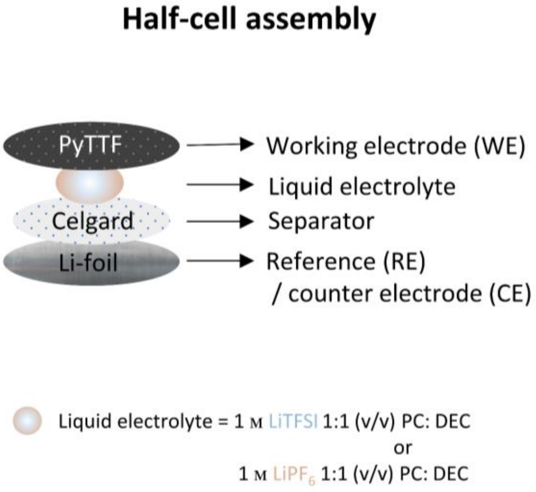

Figure 5.32 Schematic representation of half-cell assembly using PyTTF-COF as WE, 1 M LiTFSI in propylene carbonate (PC): diethyl carbonate (DEC) or 1 M $LiPF_6$ in propylene carbonate (PC): diethyl carbonate (DEC) (1:1 v/v) as the liquid electrolyte, celgard as separator to avoid short-circuits, and Li-foil (thickness: 0.75 mm) as RE and CE.

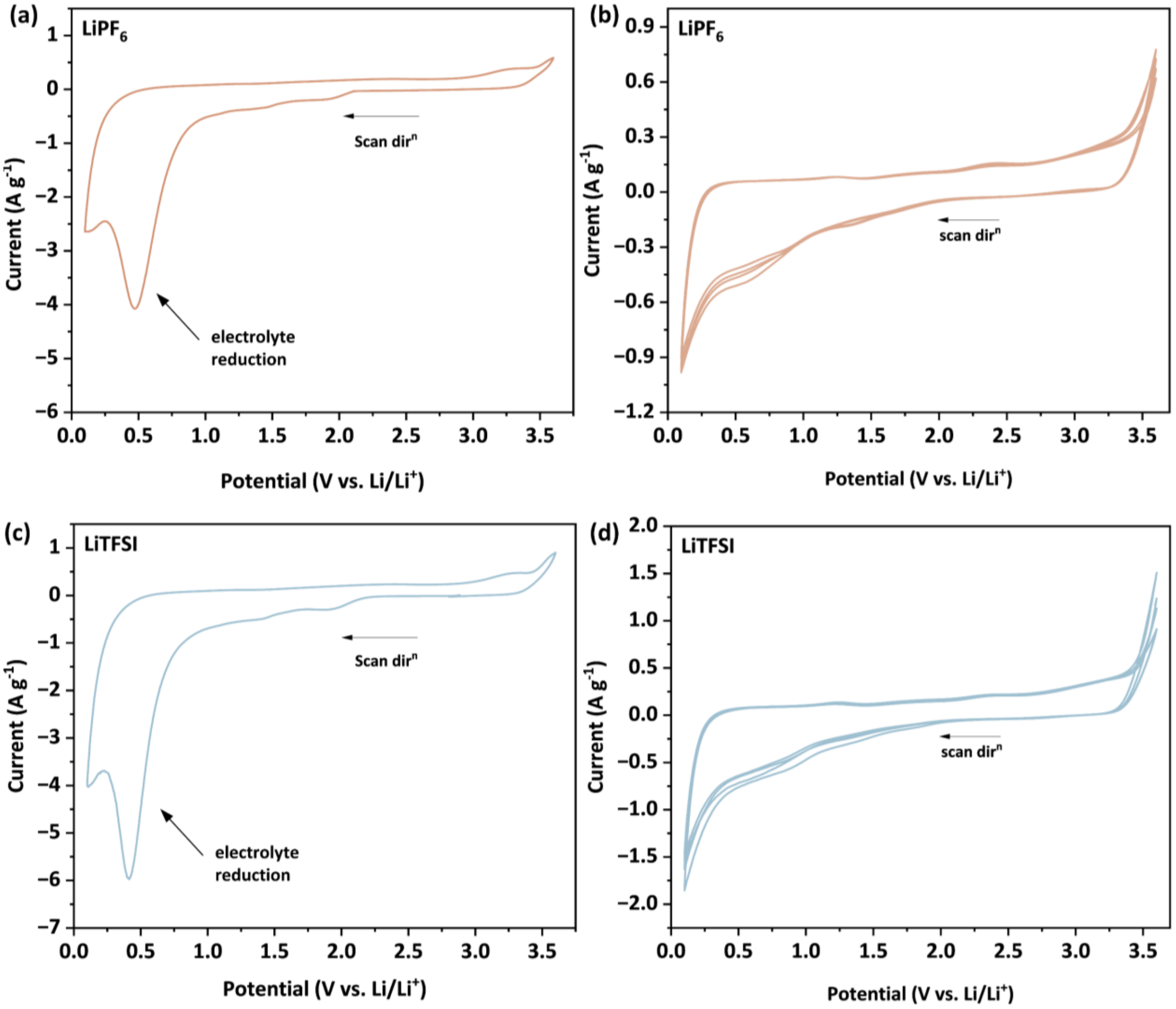

Figure 5.33 Cyclic voltammogram for (a,c) 1st and (b,d) consecutive 2nd–5th cycles at $\nu = 1.0$ mV s^{-1} for electrochemical half cells using PyTTF as WE, Li-foil as CE and RE, and (a,b) 1 ᴍ $LiPF_6$ in PC:DEC 1:1 (v/v), and (c,d) 1 ᴍ LiTFSI in PC:DEC 1:1 (v/v) as liquid electrolytes, respectively.

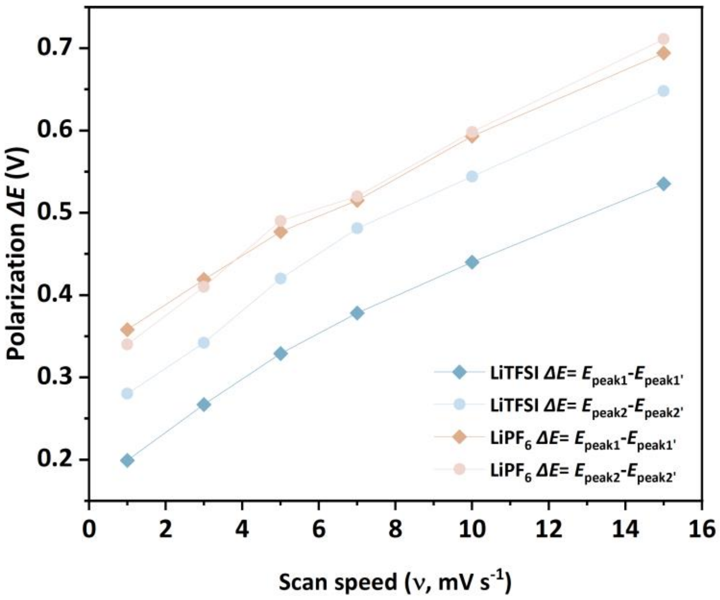

Figure 5.34. Separation (potential polarization, Δ*E*) between the anodic peaks: Peak 1 (E_{peak1}) and Peak 2 (E_{peak2}), and cathodic peaks: Peak 1' ($E_{peak1'}$) and Peak 2' ($E_{peak2'}$) in the CV curves for the half-cells utilizing PyTTF-COF as WE, Li-foil as CE and RE, and 1 M LiPF$_6$ in PC:DEC 1:1 (v/v), and 1 M LiTFSI in PC:DEC 1:1 (v/v) as liquid electrolytes, respectively, as a function of scanning speed (ν).

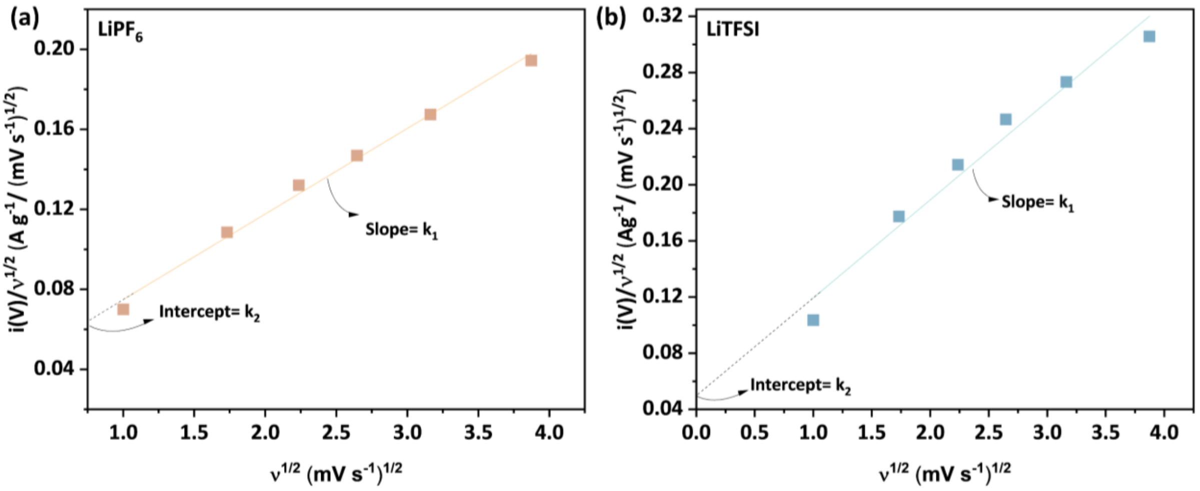

Figure 5.35 Determination of the values of k_1 and k_2 as the slope and intercept between $i(V)/\nu^{1/2}$ vs. $\nu^{1/2}$ where V = 1 V vs. Li/Li$^+$ during anodic sweep at scanning speeds ν = 1.0–15.0 mV s^{-1} for half-cells utilizing PyTTF-COF as WE, Li-foil as CE and RE, and (a) 1 M LiPF$_6$ in PC:DEC 1:1 (v/v), and (b) 1 M LiTFSI in PC:DEC 1:1 (v/v) as liquid electrolytes, respectively.

5.6.5. Electrochemical impedance spectroscopy (EIS) and Warburg element

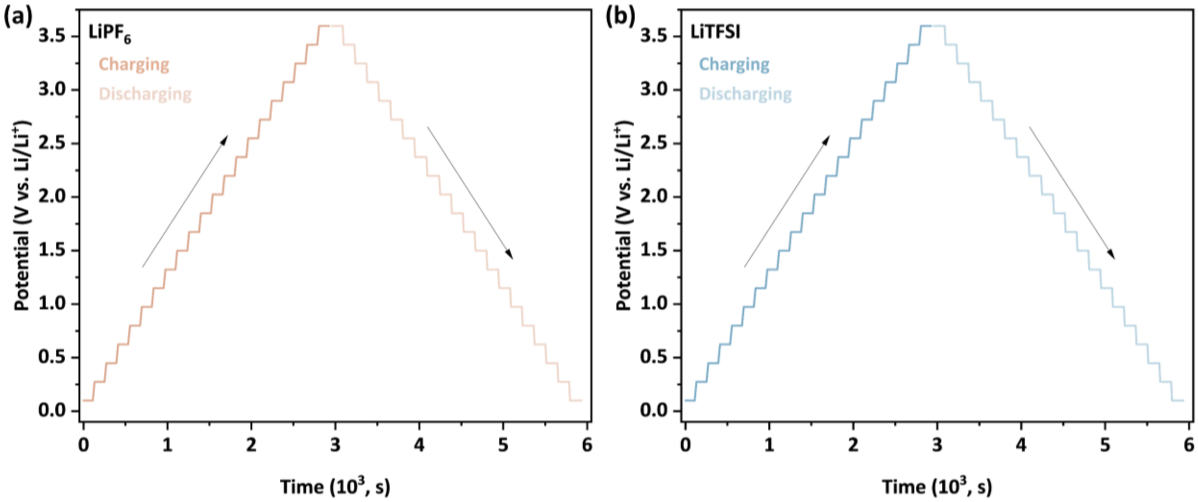

Figure 5.36 Potential-dependent electrochemical impedance spectroscopy (EIS) measurement at different operating potentials between 0.1−3.6 V. Applied potential (V) versus time (s) plot with no. of steps n = 42 in negative (discharging) and positive (charging) sweep directions for electrochemical half cells using PyTTF as WE, Li-foil as CE and RE, and (a) 1 M LiPF$_6$ in PC:DEC 1:1 (v/v), and (b) 1 M LiTFSI in PC:DEC 1:1 (v/v) as liquid electrolytes, respectively.

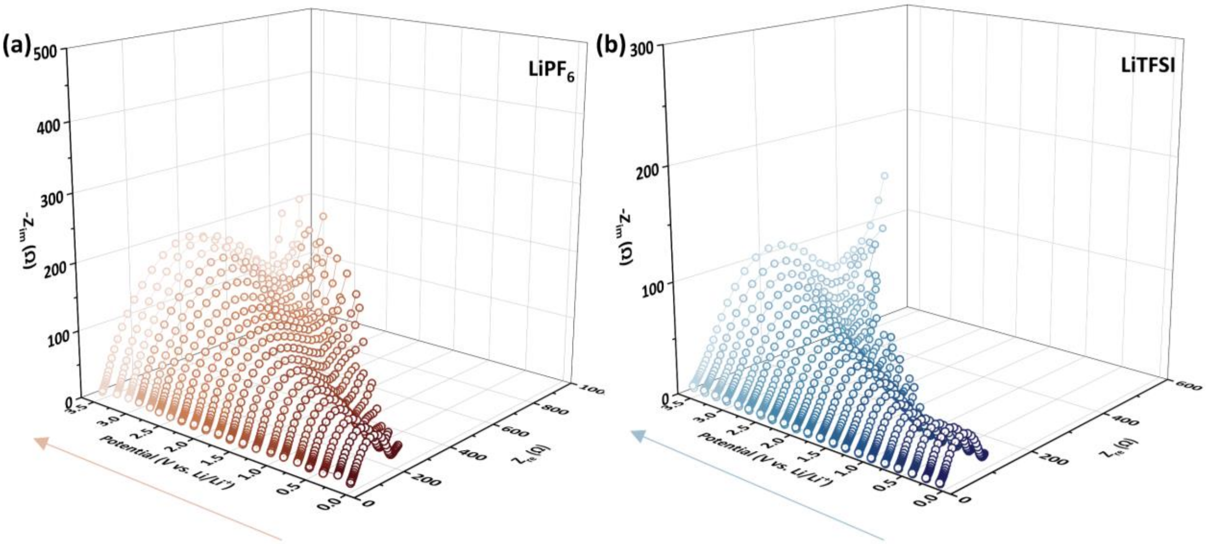

Figure 5.37 Potential-dependent electrochemical impedance spectroscopy (EIS) measurement at different operating potentials between 0.1−3.6 V recorded during positive sweep step, representing Nyquist plots for the electrochemical half cells using PyTTF as WE, Li-foil as CE and RE, and (a) 1 M LiPF$_6$ in PC:DEC 1:1 (v/v), and (b) 1 M LiTFSI in PC:DEC 1:1 (v/v) as liquid electrolytes, respectively.

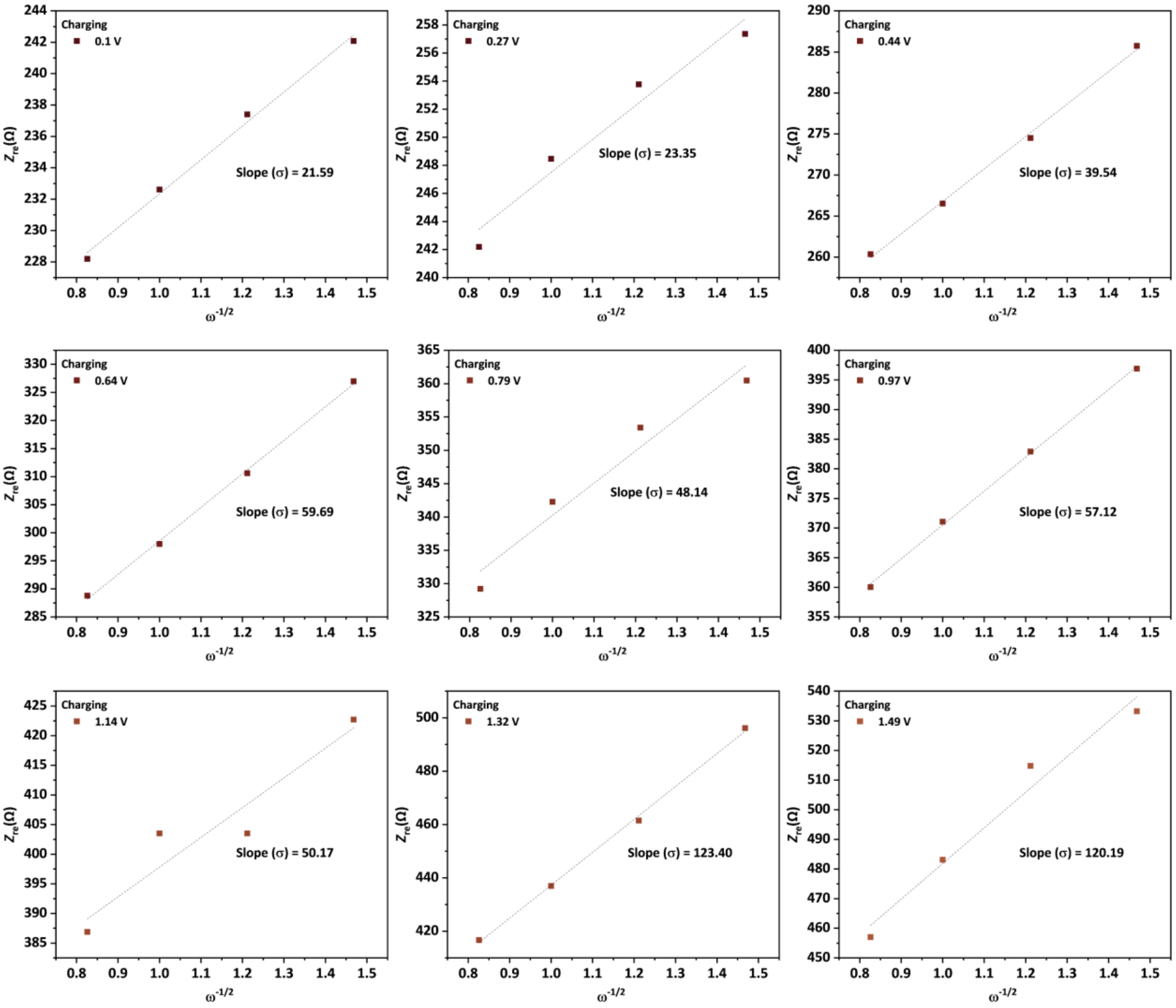

Figure 5.38 Warburg plots for the electrochemical half cells using PyTTF as WE, Li-foil as CE and RE, and 1 м $LiPF_6$ in PC:DEC 1:1 (v/v) during positive sweep in a potential range between 0.1–1.49 V.

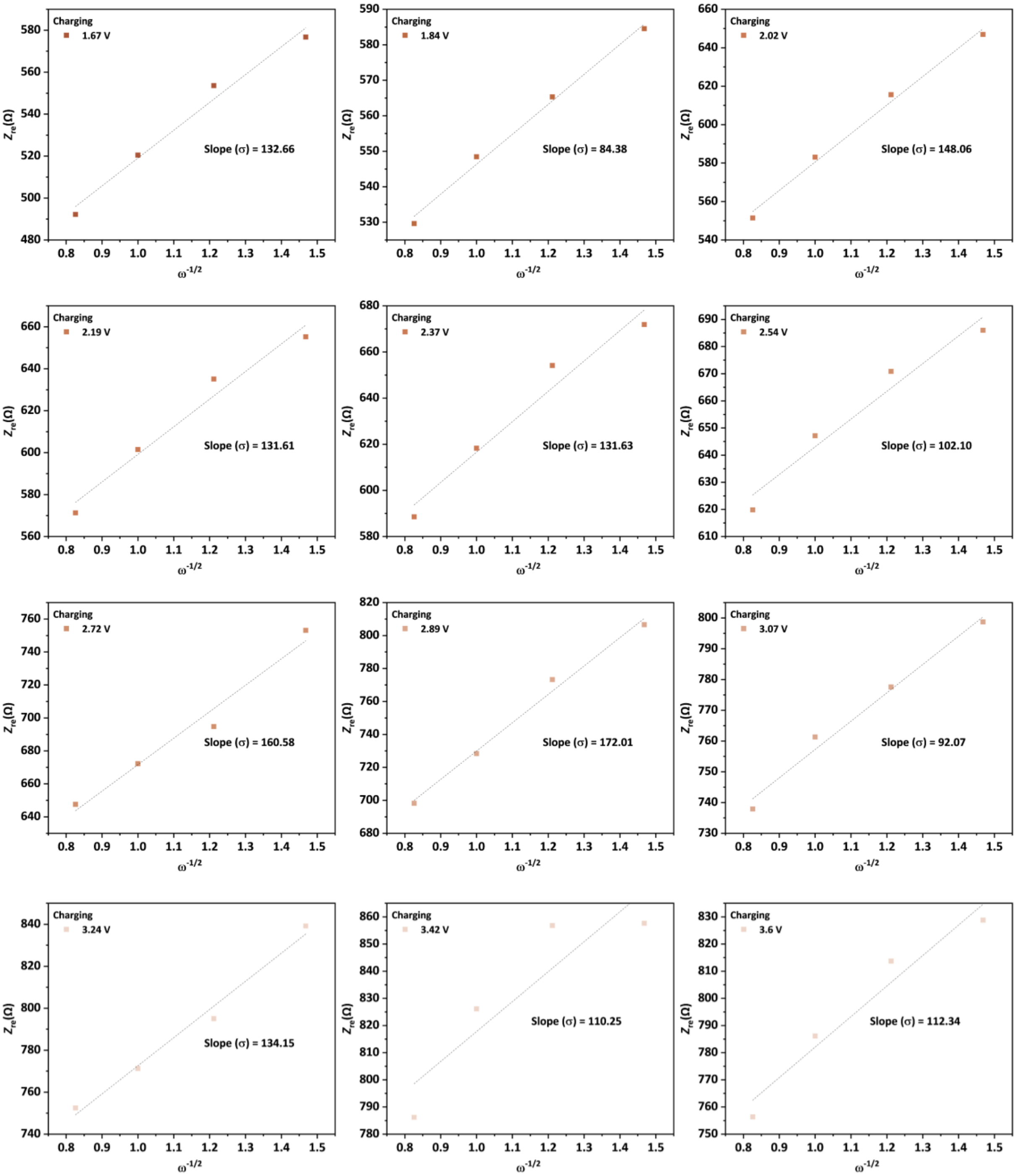

Figure 5.39 Warburg plots for the electrochemical half cells using PyTTF as WE, Li-foil as CE and RE, and 1 м $LiPF_6$ in PC:DEC 1:1 (v/v) during positive sweep in a potential range between 1.67–3.6 V.

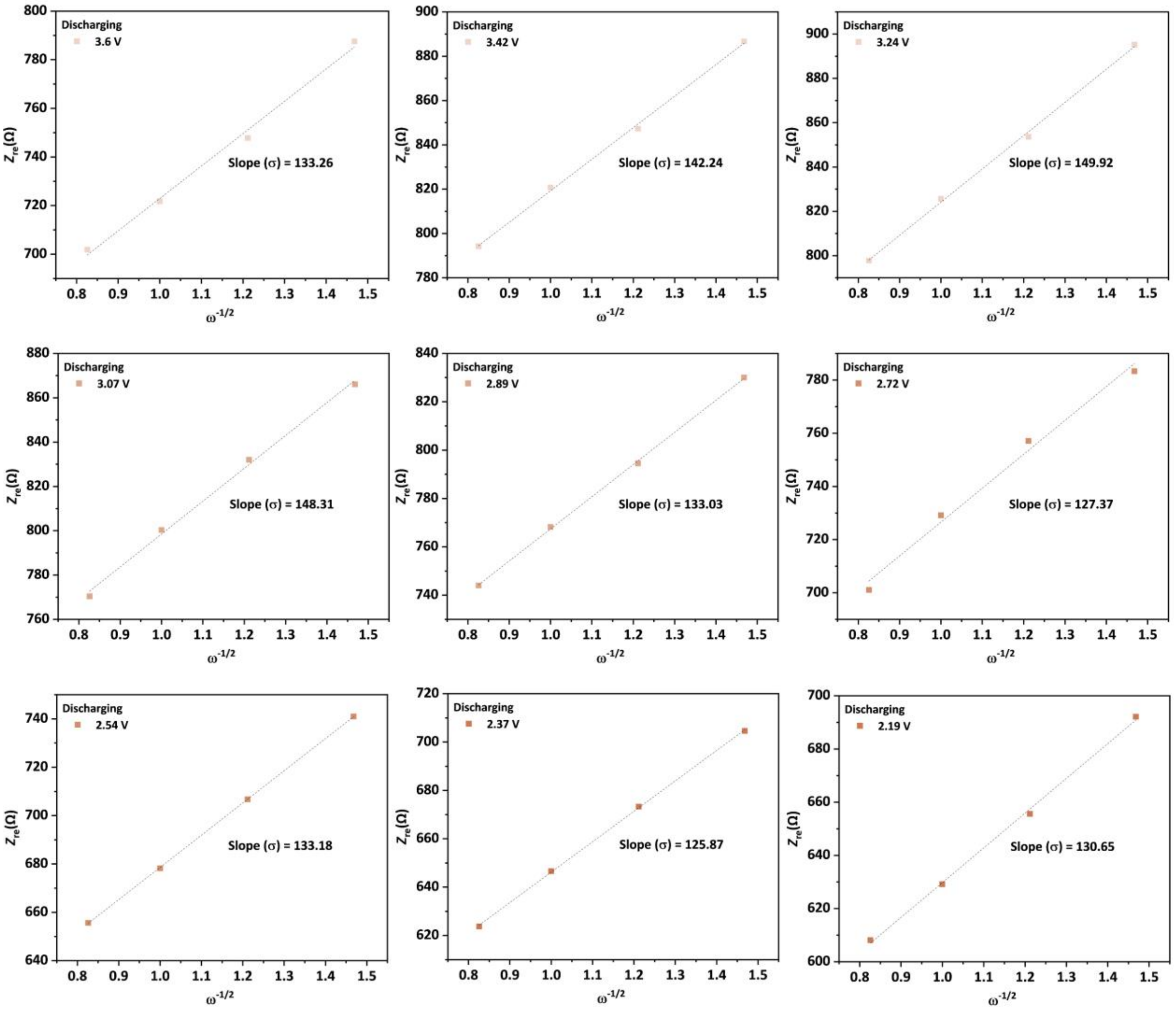

Figure 5.40 Warburg plots for the electrochemical half cells using PyTTF as WE, Li-foil as CE and RE, and 1 м $LiPF_6$ in PC:DEC 1:1 (v/v) during negative sweep in a potential range between 3.6 – 2.19 V.

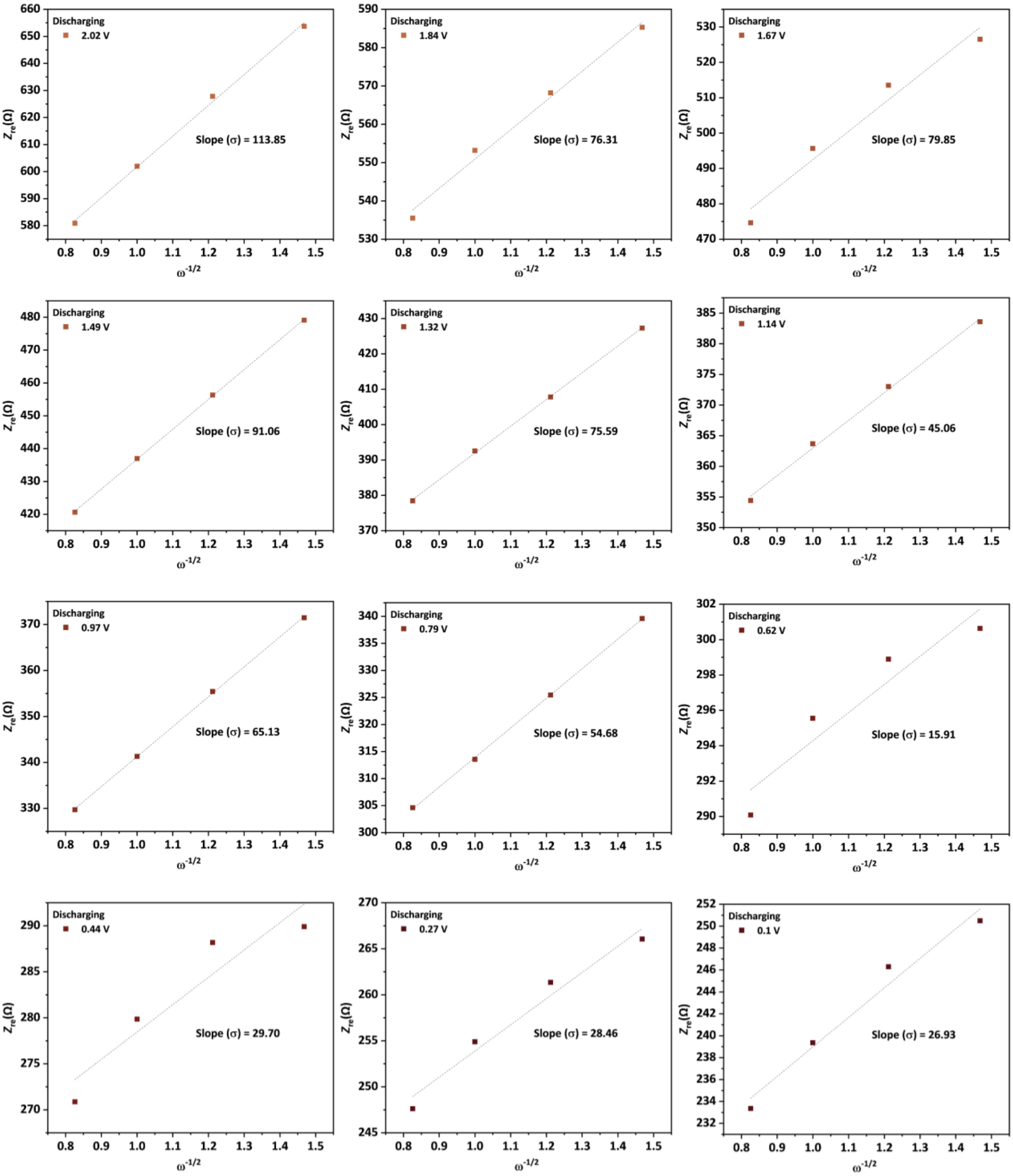

Figure 5.41 Warburg plots for the electrochemical half cells using PyTTF as WE, Li-foil as CE and RE, and 1 M $LiPF_6$ in PC:DEC 1:1 (v/v) during negative sweep in a potential range between 2.02–0.1 V.

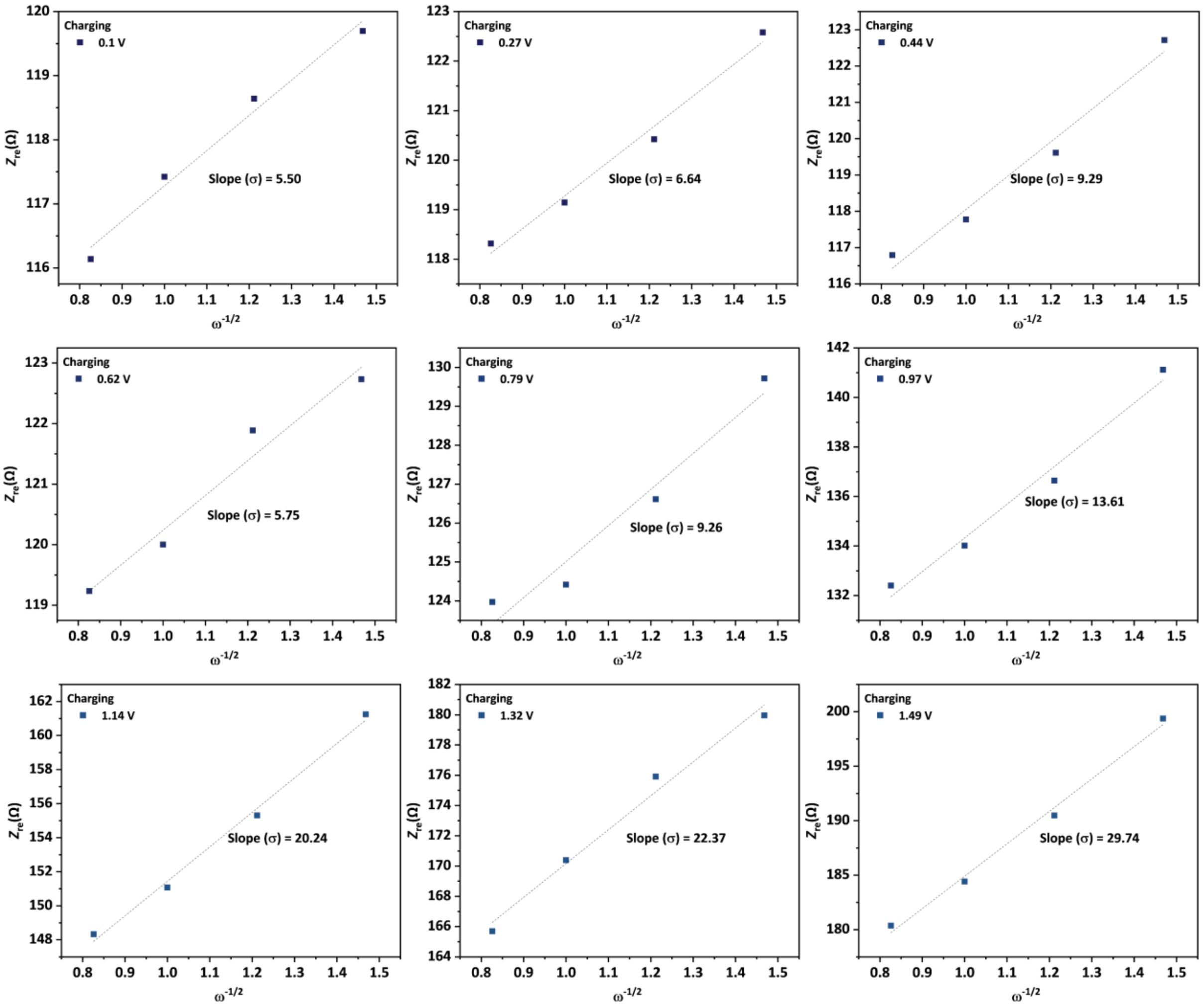

Figure 5.42 Warburg plots for the electrochemical half cells using PyTTF as WE, Li-foil as CE and RE, and 1 м LiTFSI in PC:DEC 1:1 (v/v) during positive sweep in a potential range between 0.1–1.49 V.

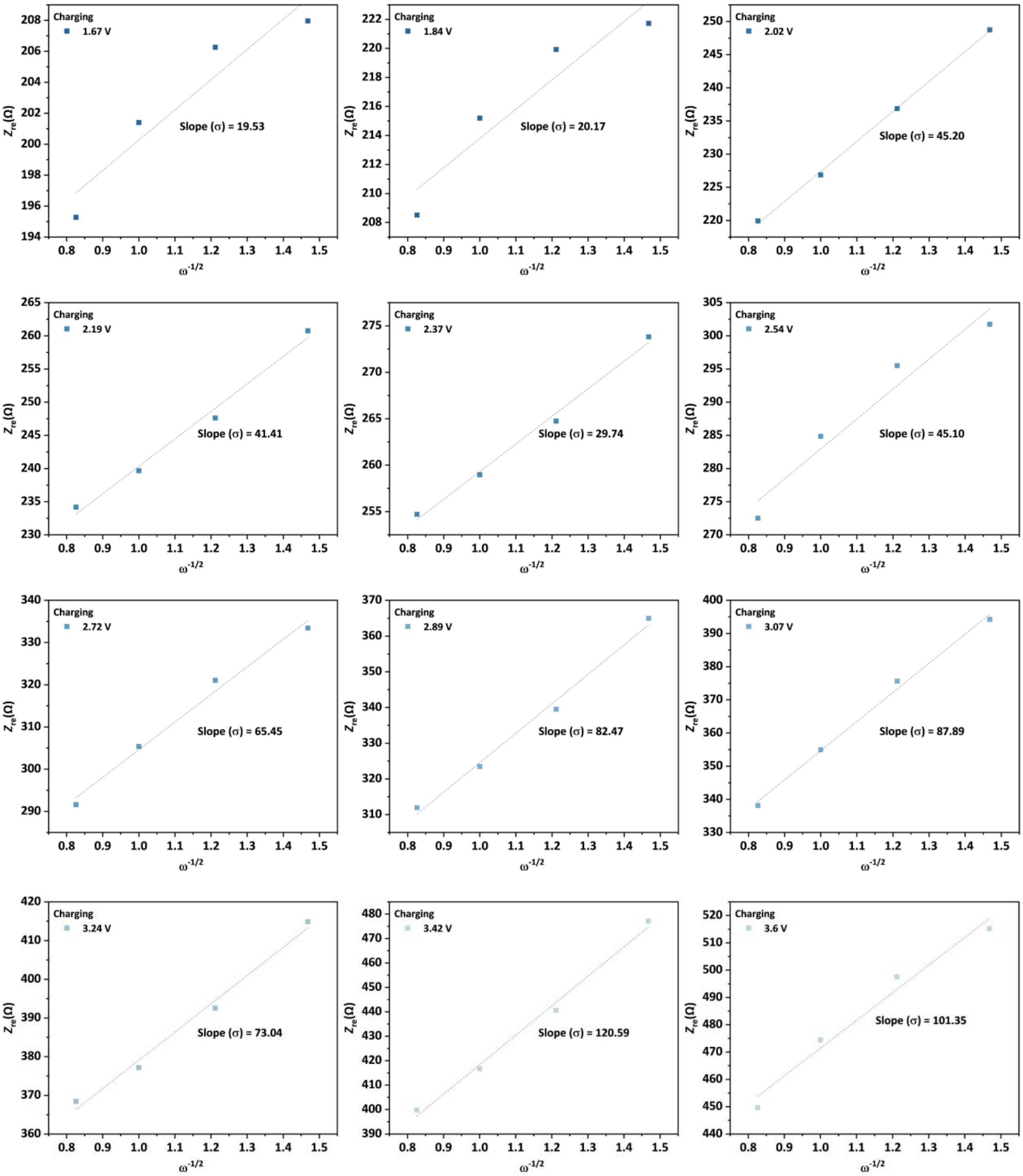

Figure 5.43 Warburg plots for the electrochemical half cells using PyTTF as WE, Li-foil as CE and RE, and 1 M LiTFSI in PC:DEC 1:1 (v/v) during positive sweep in a potential range between 1.67–3.6 V.

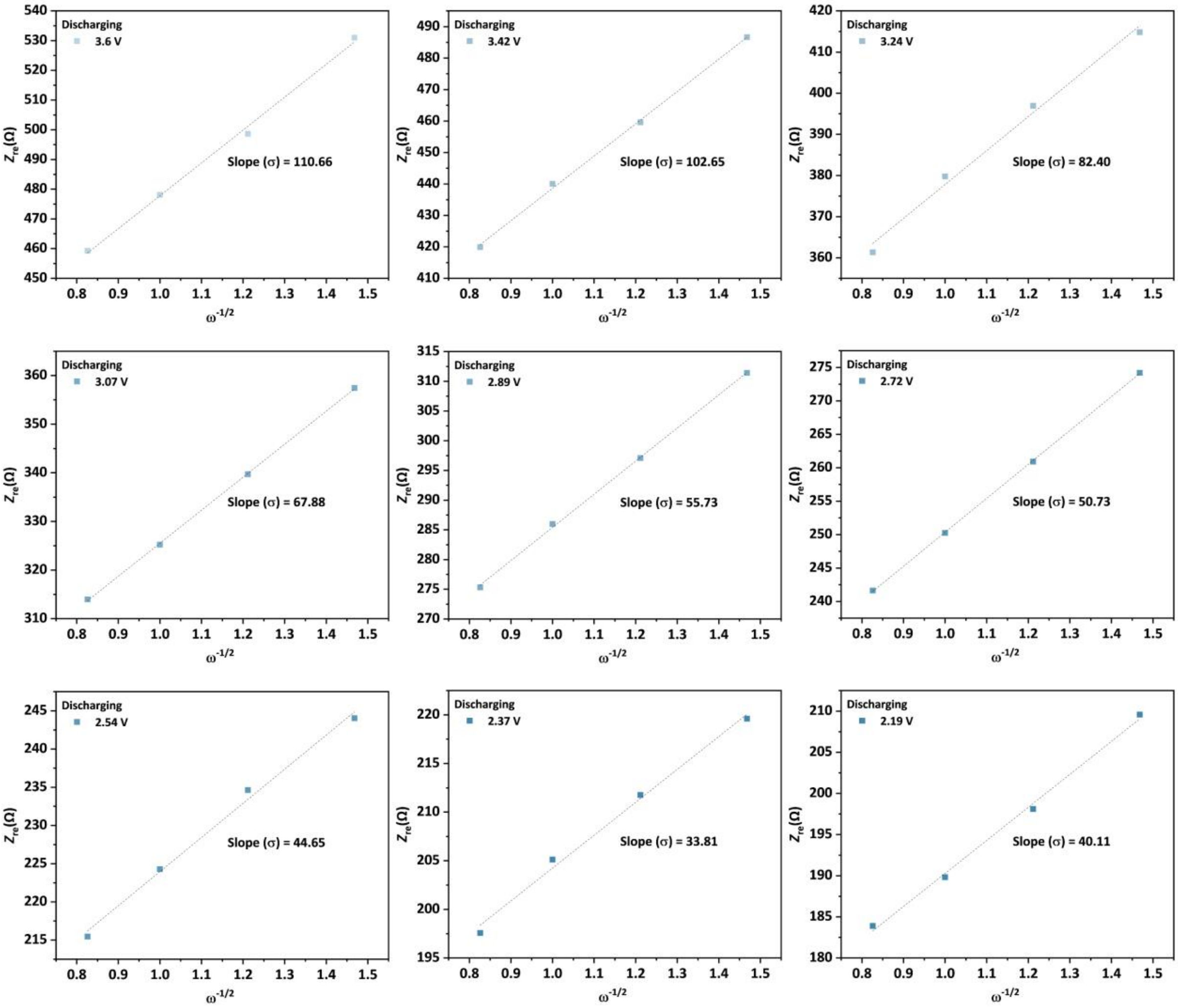

Figure 5.44 Warburg plots for the electrochemical half cells using PyTTF as WE, Li-foil as CE and RE, and 1 M LiTFSI in PC:DEC 1:1 (v/v) during negative sweep in a potential range between 3.6–2.19 V.

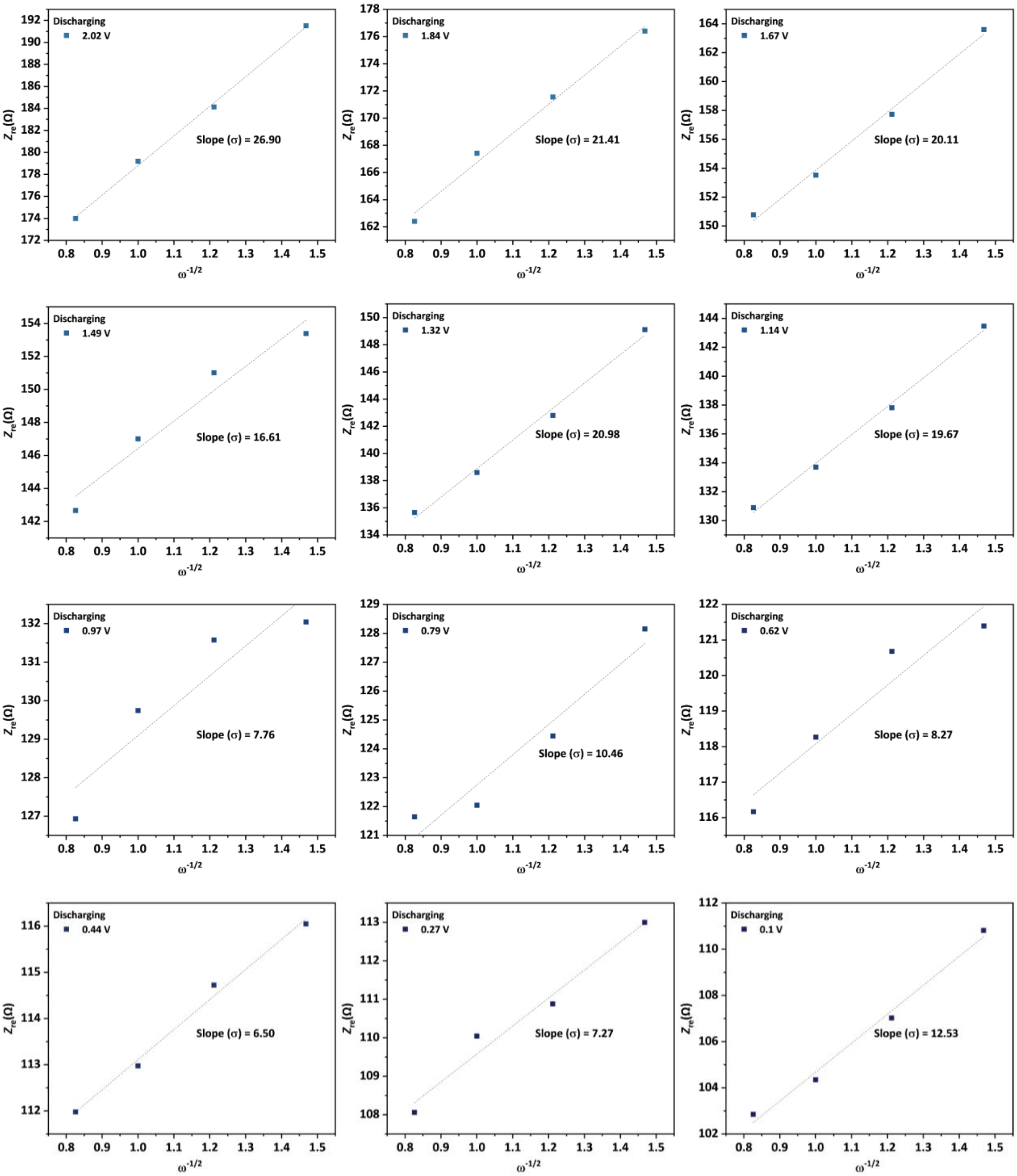

Figure 5.45 Warburg plots for the electrochemical half cells using PyTTF as WE, Li-foil as CE and RE, and 1 M LiTFSI in PC:DEC 1:1 (v/v) during negative sweep in a potential range between 2.02–0.1 V.

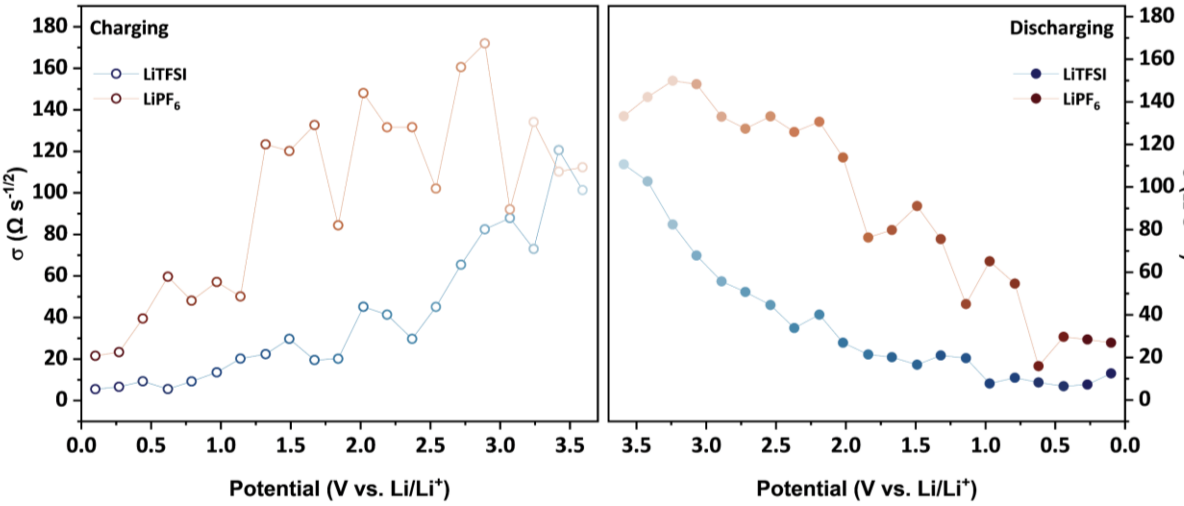

Figure 5.46 Comparative Warburg coefficients corresponding to the positive (left) and negative (right) sweep directions at different operating potentials between 0.1−3.6 V for the electrochemical half cells using PyTTF as WE, Li-foil as CE and RE, and 1 M $LiPF_6$ in PC:DEC 1:1 (v/v), and 1 M LiTFSI in PC:DEC 1:1 (v/v) as liquid electrolytes, respectively.

Table 5.4 Diffusion coefficient calculation corresponding to the EIS measurements during the negative and positive sweep directions at different operating potentials between 0.1−3.6 V for the electrochemical half cells using PyTTF as WE, Li-foil as CE and RE, and 1 м $LiPF_6$ in PC:DEC 1:1 (v/v) as electrolyte.

Positive Sweep			**Negative Sweep**		
Potential (V)	**Slope (σ, Ω $s^{-1/2}$)**	**Diffusion coefficient ($cm^2\ s^{-1}$)**	**Potential (V)**	**Slope (σ, Ω $s^{-1/2}$)**	**Diffusion coefficient ($cm^2\ s^{-1}$)**
0.1	21.59	1.17×10^{-11}	0.1	26.93	7.57×10^{-12}
0.27	23.35	1.01×10^{-11}	0.27	28.46	6.78×10^{-12}
0.44	39.54	3.51×10^{-12}	0.44	29.7	6.22×10^{-12}
0.62	59.69	1.54×10^{-12}	0.62	15.91	2.17×10^{-11}
0.79	48.14	2.37×10^{-12}	0.79	54.68	1.83×10^{-12}
0.97	57.12	1.68×10^{-12}	0.97	65.13	1.29×10^{-12}
1.14	50.17	2.18×10^{-12}	1.14	45.06	2.70×10^{-12}
1.32	123.4	3.60×10^{-13}	1.32	75.59	9.61×10^{-13}
1.49	120.19	3.80×10^{-13}	1.49	91.06	6.62×10^{-13}
1.67	132.66	3.12×10^{-13}	1.67	79.85	8.61×10^{-13}
1.84	84.38	7.71×10^{-13}	1.84	76.31	9.43×10^{-13}
2.02	148.06	2.50×10^{-13}	2.02	113.85	4.23×10^{-13}
2.19	131.61	3.17×10^{-13}	2.19	130.65	3.21×10^{-13}
2.37	131.63	3.17×10^{-13}	2.37	125.87	3.46×10^{-13}
2.54	102.1	5.27×10^{-13}	2.54	133.189	3.09×10^{-13}
2.72	160.58	2.13×10^{-13}	2.72	127.37	3.38×10^{-13}
2.89	172	1.85×10^{-13}	2.89	133.03	3.10×10^{-13}
3.07	92.07	6.48×10^{-13}	3.07	148.31	2.49×10^{-13}
3.24	134.15	3.05×10^{-13}	3.24	149.92	2.44×10^{-13}
3.42	110.25	4.52×10^{-13}	3.42	142.24	2.71×10^{-13}
3.59	112.34	4.35×10^{-13}	3.59	133.26	3.09×10^{-13}

$\boldsymbol{R} =$ 8.314 J K^{-1} mol^{-1}, $\boldsymbol{T}$ =298.15 K, $\boldsymbol{n} = 1$, $\boldsymbol{F}$= 96458 C mol^{-1}, $\boldsymbol{C}$ =1.0 м, $\boldsymbol{A}$ = 0.000254 m^2
$R^2T^2/2n^4F^4C^2A^2 = 5.49474 \times 10^{-13}$

Table 5.5 Diffusion coefficient calculation corresponding to the EIS measurement during the negative and positive sweep directions at different operating potentials between 0.1−3.6 V for the electrochemical half cells using PyTTF as WE, Li-foil as CE and RE, and 1 M LiTFSI in PC:DEC 1:1 (v/v) as electrolyte.

Positive Sweep			**Negative Sweep**		
Potential (V)	**Slope (σ, Ω $s^{-1/2}$)**	**Diffusion coefficient ($cm^2\ s^{-1}$)**	**Potential (V)**	**Slope (σ, Ω $s^{-1/2}$)**	**Diffusion coefficient ($cm^2\ s^{-1}$)**
0.1	5.5	1.82×10^{-10}	0.1	12.53	3.49×10^{-11}
0.27	6.64	1.25×10^{-10}	0.27	7.27	1.03×10^{-10}
0.44	9.29	6.37×10^{-11}	0.44	6.5	1.30×10^{-10}
0.62	5.57	1.77×10^{-10}	0.62	8.27	8.03×10^{-11}
0.79	9.26	6.41×10^{-11}	0.79	10.46	5.02×10^{-11}
0.97	13.61	2.97×10^{-11}	0.97	7.76	9.12×10^{-11}
1.14	20.24	1.34×10^{-11}	1.14	19.67	1.42×10^{-11}
1.32	22.37	1.10×10^{-11}	1.32	20.98	1.24×10^{-11}
1.49	29.74	6.21×10^{-12}	1.49	16.61	1.99×10^{-11}
1.67	19.53	1.44×10^{-11}	1.67	20.11	1.35×10^{-11}
1.84	20.17	1.35×10^{-11}	1.84	21.41	1.19×10^{-11}
2.02	45.2	2.69×10^{-12}	2.02	26.9	7.59×10^{-12}
2.19	41.41	3.02×10^{-12}	2.19	40.11	3.41×10^{-12}
2.37	29.74	6.21×10^{-12}	2.37	33.81	4.80×10^{-12}
2.54	45.1	2.70×10^{-12}	2.54	44.65	2.75×10^{-12}
2.72	65.45	1.28×10^{-12}	2.72	50.73	2.13×10^{-12}
2.89	82.47	8.08×10^{-13}	2.89	55.74	1.76×10^{-12}
3.07	87.89	7.11×10^{-13}	3.07	67.88	1.19×10^{-12}
3.24	73.04	1.03×10^{-12}	3.24	82.4	8.09×10^{-13}
3.42	120.59	3.78×10^{-13}	3.42	102.65	5.21×10^{-13}
3.59	101.35	5.35×10^{-13}	3.59	110.66	4.48×10^{-13}

$\boldsymbol{R} =$ 8.314 J K^{-1} mol^{-1}, $\boldsymbol{T}$ =298.15 K, $\boldsymbol{n} = 1$, $\boldsymbol{F}$= 96458 C mol^{-1}, $\boldsymbol{C}$ =1.0 M, $\boldsymbol{A}$ = 0.000254 m^2
$R^2T^2/2n^4F^4C^2A^2$= 5.49474×10^{-13}

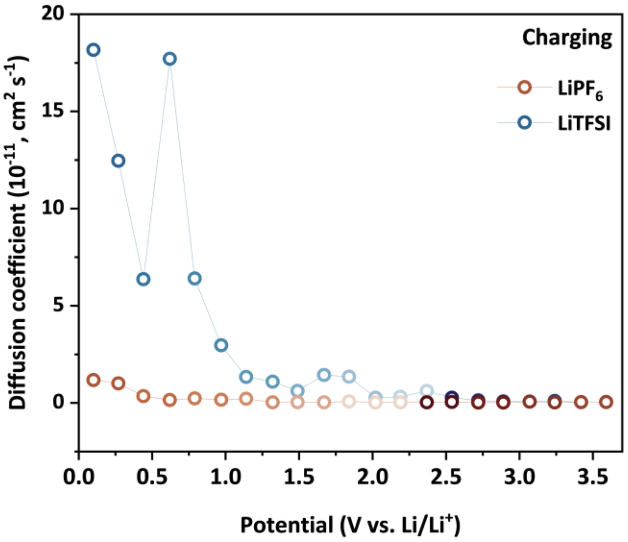

Figure 5.47 The comparative calculated diffusion coefficient (*D*) corresponding to the EIS measurements during positive sweep directions at different operating potentials between 0.1−3.6 V for the electrochemical half cells using PyTTF as WE, Li-foil as CE and RE, and 1 м $LiPF_6$ in PC:DEC 1:1 (v/v) and 1 м LiTFSI in PC:DEC 1:1 (v/v) as electrolytes, respectively.

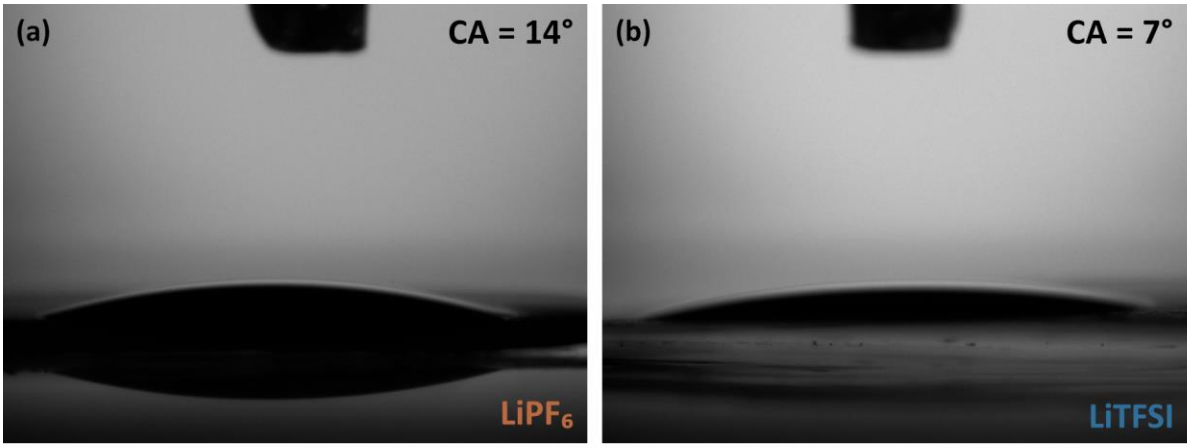

Figure 5.48. Contact angles were measured at the solid/air interface of PyTTF-electrode with 1 м $LiPF_6$ in PC:DEC 1:1 (v/v), and 1 м LiTFSI in PC:DEC 1:1 (v/v), respectively. Both electrolytes exhibited good wettability on the electrode surface, with contact angles <90°.

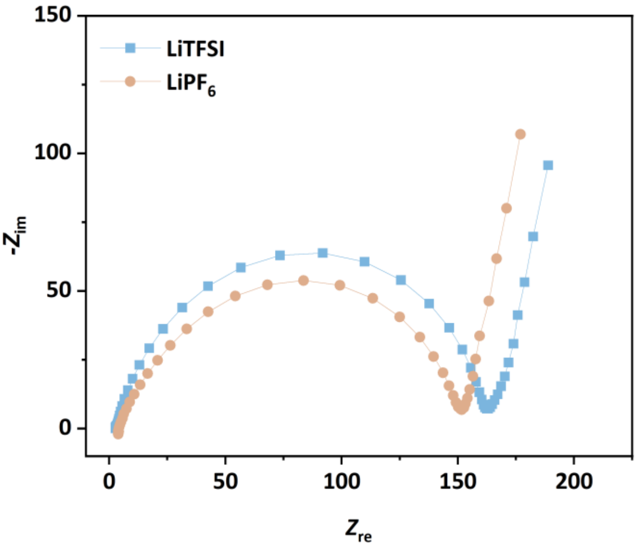

Figure 5.49. Electrochemical impedance spectroscopy (EIS) measurements before cycling for the electrochemical half cells using PyTTF as WE, Li-foil as CE and RE, and 1 ᴍ $LiPF_6$ in PC:DEC 1:1 (v/v), and 1 ᴍ LiTFSI in PC:DEC 1:1 (v/v) as liquid electrolytes, respectively. The measured solution resistance (R_{sol}) was 3.9 Ω for the $LiPF_6$-based electrolyte and 2.9 Ω for the LiTFSI-based electrolyte.

5.6.6. Battery performance

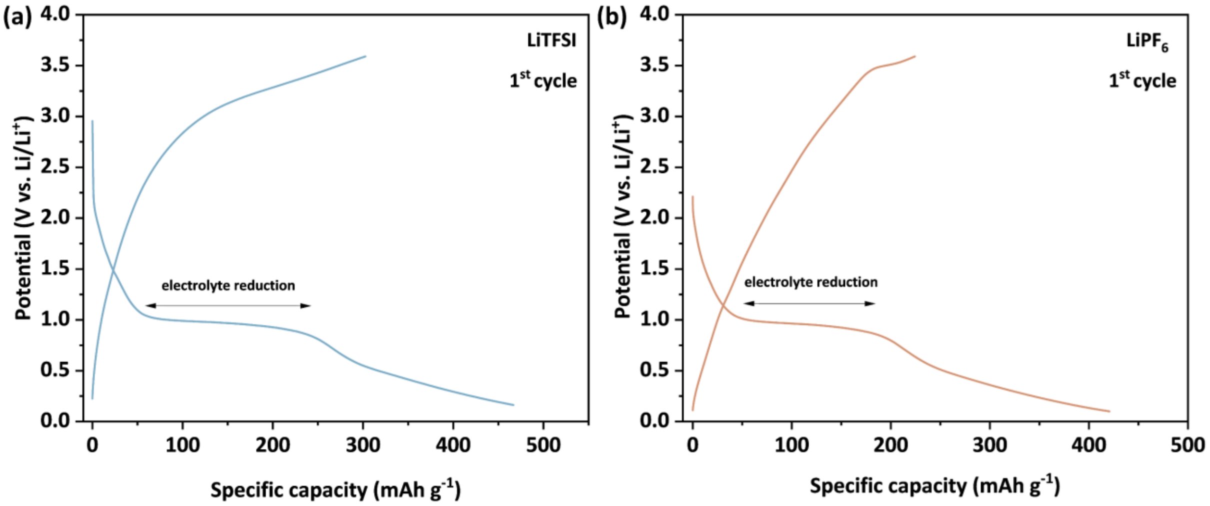

Figure 5.50 First galvanostatic charge–discharge cycles at a current density of 0.3 A g^{-1} within the potential range of 0.1 - 3.6 V for electrochemical half cells using PyTTF as WE, Li-foil as CE and RE, and (a) 1 ᴍ $LiPF_6$ in PC:DEC 1:1 (v/v), and (b) 1 ᴍ LiTFSI in PC:DEC 1:1 (v/v) as liquid electrolytes, respectively.

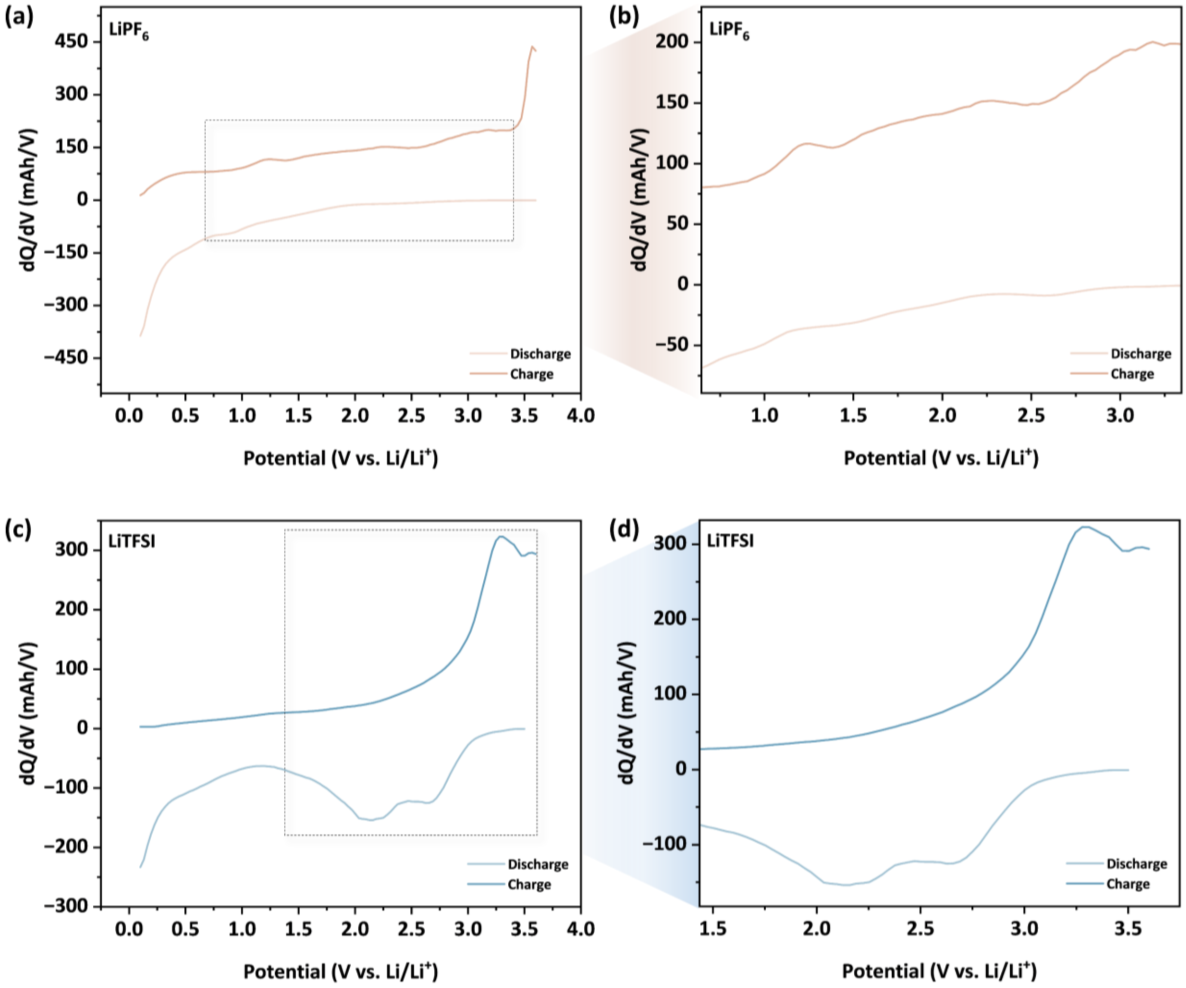

Figure 5.51 dQ/dV curves during charging and discharging cycles at 0.3 A g^{-1} within the potential range of 0.1–3.6 V and most prominent features zoom-in for PyTTF as WE, Li-foil as CE and RE, and (a,b) 1 ᴍ LiPF$_6$ in PC:DEC 1:1 (v/v), and (c,d) 1 ᴍ LiTFSI in PC:DEC 1:1 (v/v) as liquid electrolytes, respectively.

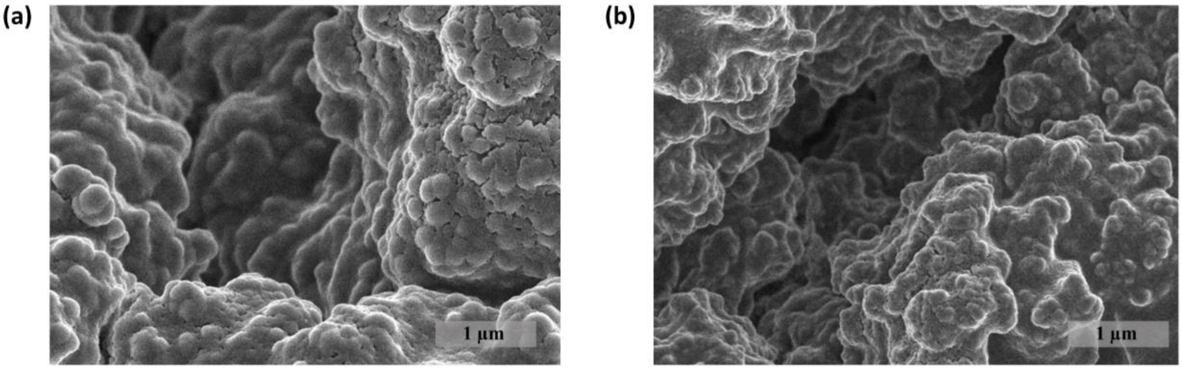

Figure 5.52. Scanning electron microscopy (SEM) images of PyTTF electrode after galvanostatic charge−discharge cycles for (a) $LiPF_6$ and (b) LiTFSI systems, respectively.

Table 5.6 A comprehensive electrochemical performance comparison between previously reported bipolar electrodes and the current study, evaluating key parameters including the nature of redox-active moieties within the linker and the linkages, the identity and quantity of charge carriers, the content of conductive carbon integrated within the electrode matrix, the electrochemical stability window, and the specific capacity delivered.

Bipolar electrode	**Redox-active group in linker**		**Redox-active linkage**	**Charge carrier**	**Number of charge carriers stored**	**Conductive additive**	**Potential window (V)**	**Specific capacity (mAh g^{-1})**	**Ref.**
	***n*-type**	***p*-type**							
PTB-DHZ-COF40	-	triphenylamine	hydrazone	4Li$^+$, 6PF$_6^-$	8	20% CNT	1.2–4.2	114.2 at 1 A g^{-1}	[14]
TPPDA-CuPor-COF	porphyrin	triphenylamine	imine	2Li$^+$, 2PF$_6^-$	4	40% Super P	1.5–4.2	142 at 0.06 A g^{-1}	[15]
TAPP-Pz-COF-40%CNT	porphyrin	porphyrin, phenazine	imine	4Li$^+$, 4PF$_6^-$	8	40% CNT, 20% KB	1.2–4.4	314 at 0.2 A g^{-1}	[16,17]
NTPI-COF	naphthalene-diimide	triphenylamine	-	2Li$^+$, 2PF$_6^-$	4	30% Super P	1.5–4.25	165 at 0.03 A g^{-1}	[17]
2D-NT-COF30	imide	triazine	-	2AlCl$_2^+$, 1AlCl$_4^-$	3	30% CNT	0.5–2.1	132 at 0.1 A g^{-1}	[18]
TP-TA-COF	-	triphenylamine	imine	4Li$^+$, 2PF$_6^-$	6	30% KB	1.2–4.3	207 at 0.2 A g^{-1}	[19]
COF$_{\text{TPDA-PMDA}}$@50%CNT	Polyimide	triphenylamine	-	4Li$^+$, 2TFSI$^-$	6	50% CNT	1.2–4.3	233 at 0.5 A g^{-1}	[20]
NTPI-COF	polyimide	triphenylamine	-	6Na$^+$, 6Cl$^-$	12	20% AB	-0.9–0.3	109 at 1 A g^{-1}	[21]
TPAD-COF	quinone,	secondary amine	imine	Na$^+$, PF$_6^-$		30% AB	1.5–4.1	186 at 0.05 A g^{-1}	[22]
WTTF-COF	-	triphenylamine, dithiolylidene	imine	8Li$^+$, 4PF$_6^-$	12	20% KB	0.1–3.6	200 at 0.5 A g^{-1}	[9]
IISERP-COF22	diamino diphenyl squaramide, triformyl phloroglucinol	-	-	4Zn^{2+}, *I$_3^-$	*	15% Super P	0.2–1.6	690 at 0.0015 A g^{-1}	[23]
TT-TPDA-COF	-	triphenylamine, thienothiophene	imine	4Li$^+$, 6PF$_6^-$	10	20% KB	1.2-4.3	309 at 0.2 A g^{-1}	[24]
PyTTF-COF	pyrene–benzothiadiazole	dithiolylidene	imine	14Li$^+$, 2PF$_6^-$	16	20% KB	0.1–3.6	184 at 0.3 A g^{-1}	This work
PyTTF-COF	pyrene–benzothiadiazole	dithiolylidene	imine	14Li$^+$, 2TFSI$^-$	16	20% KB	0.1–3.6	286 at 0.3 A g^{-1}	This work

* = unspecified, KB = Ketjenblack, AB = acetylene black, CNT = carbon nanotubes

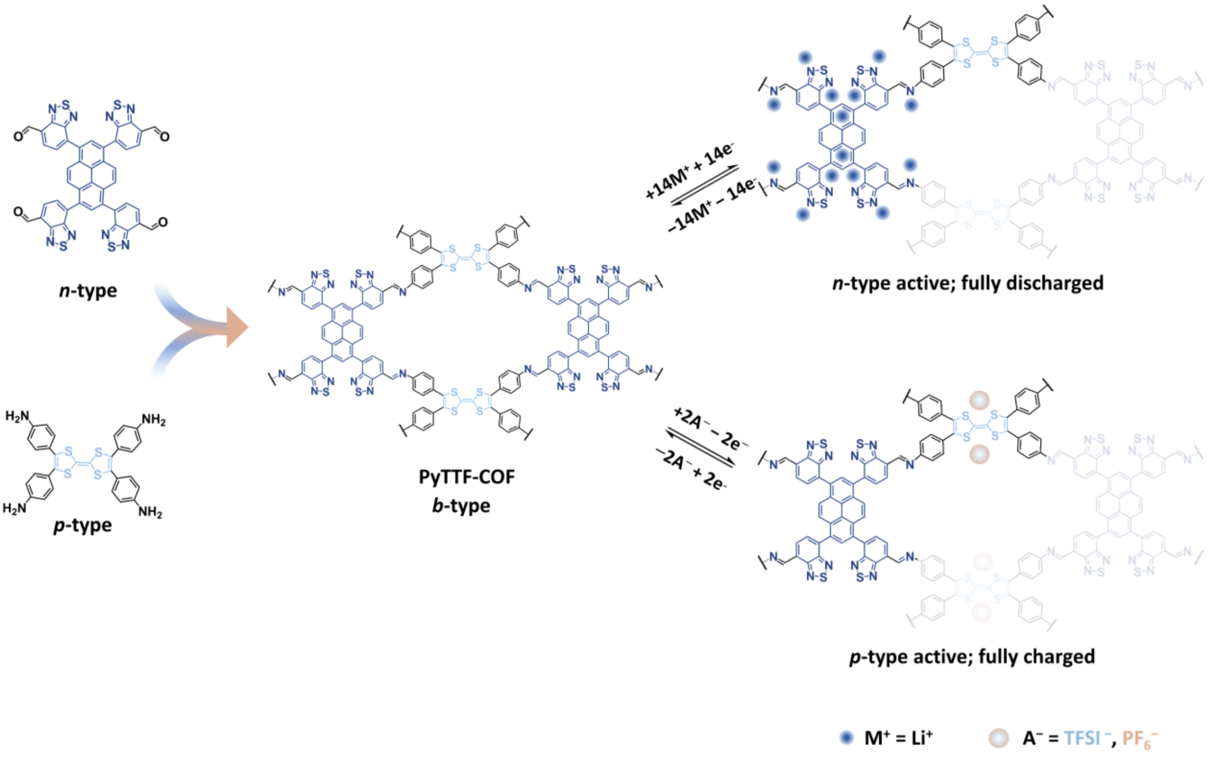

Figure 5.53 Proposed redox-mechanism for PyTTF-COF based on the individual redox features of the *n*-type PyBT-node, the *p*-type TTF-node, and the *n*-type imine linkage.

Calculation of theoretical capacity:

Theoretical capacity (mAh g^{-1}) =

$$\frac{n \times F \times 1000}{3600 \times M}$$

(Equation 5.7)

where, $n = 16$ is the number of electrons involved in the redox reaction per formula unit of the active material of molar mass M = 1347 g mol^{-1}, F = 96 458 C mol^{-1} is Faraday's constant, and 1000/3600 is the factor to get the unit mAh g^{-1}.

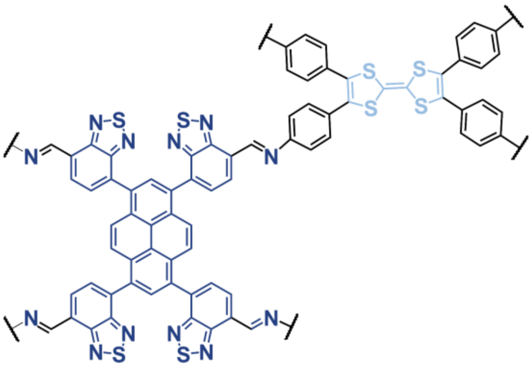

Based on the above mentioned proposed redox-mechanism, the theoretical capacity of PyTTF electrode is 318 mAh g^{-1}.

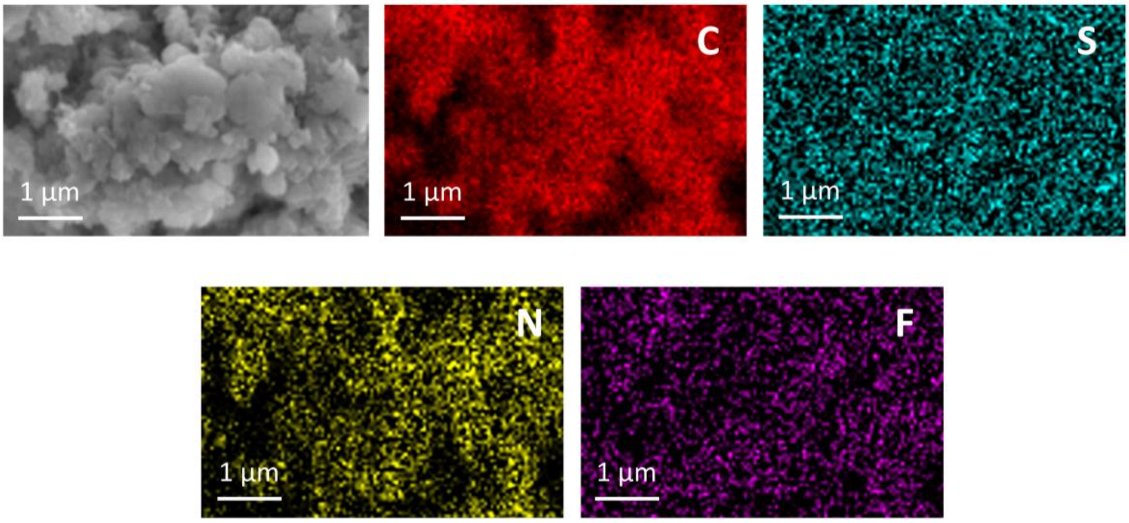

Figure 5.54 Pre-cycling analysis. SEM images PyTTF electrode (PyTTF-COF: Ketjenblack: PVDF = 60:20:20) before cycling and the corresponding energy dispersive X-ray analysis (EDX) mapping of the elements carbon (C), sulfur (S), nitrogen (N), and fluorine (F).

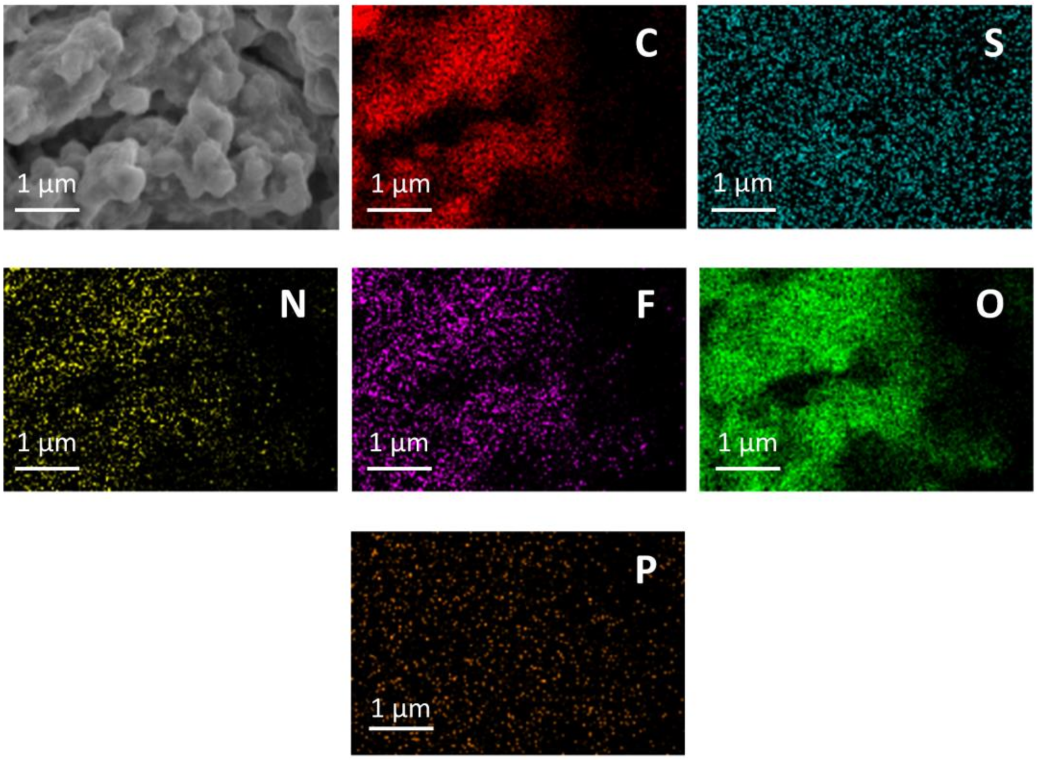

Figure 5.55 Post-mortem analysis: Ex-situ SEM image of PyTTF electrode (PyTTF-COF: Ketjenblack: PVDF = 60:20:20) discharged to 0.1 V in a half-cell configuration utilizing 1 M $LiPF_6$ in PC:DEC 1:1 (v/v) and the corresponding energy dispersive X-ray analysis (EDX) mapping of the elements carbon (C), sulfur (S), nitrogen (N), fluorine (F), oxygen (O), and phosphorus (P).

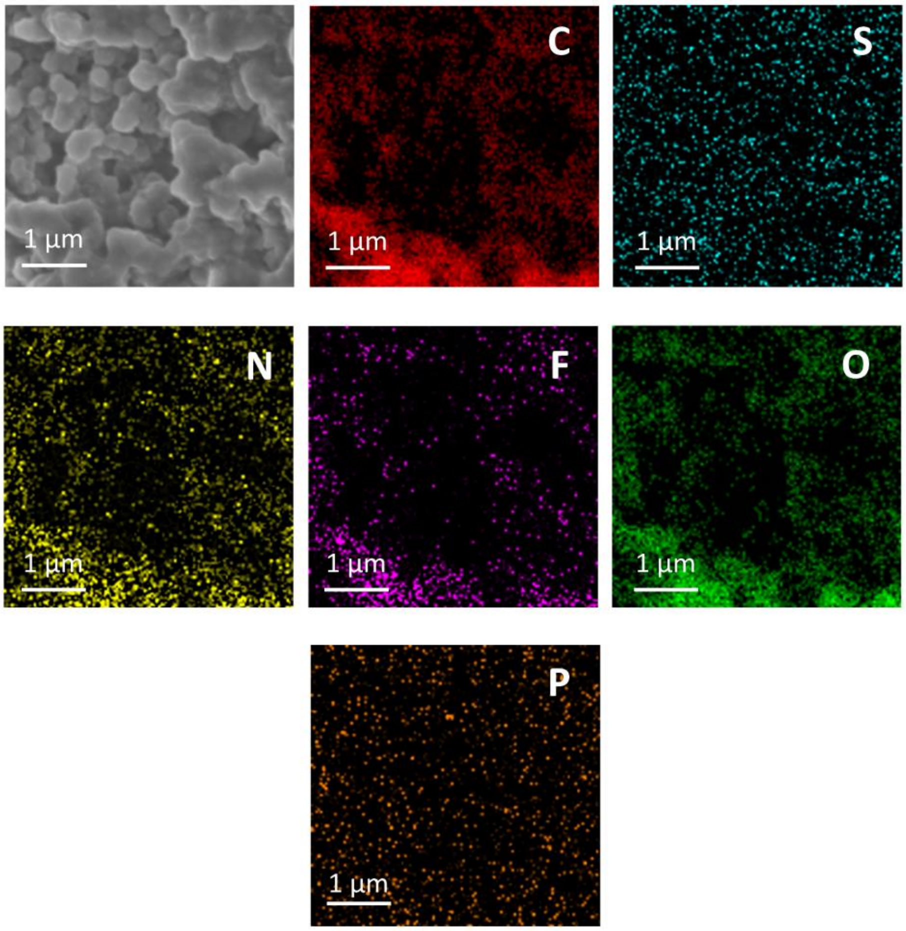

Figure 5.56 Post-mortem analysis: Ex-situ SEM image of PyTTF electrode (PyTTF-COF: Ketjenblack: PVDF = 60:20:20) charged to 3.6 V in a half-cell configuration utilizing 1 м $LiPF_6$ in PC:DEC 1:1 (v/v) and the corresponding energy dispersive X-ray analysis (EDX) mapping of the elements carbon (C), sulfur (S), nitrogen (N), fluorine (F), oxygen (O), and phosphorus (P).

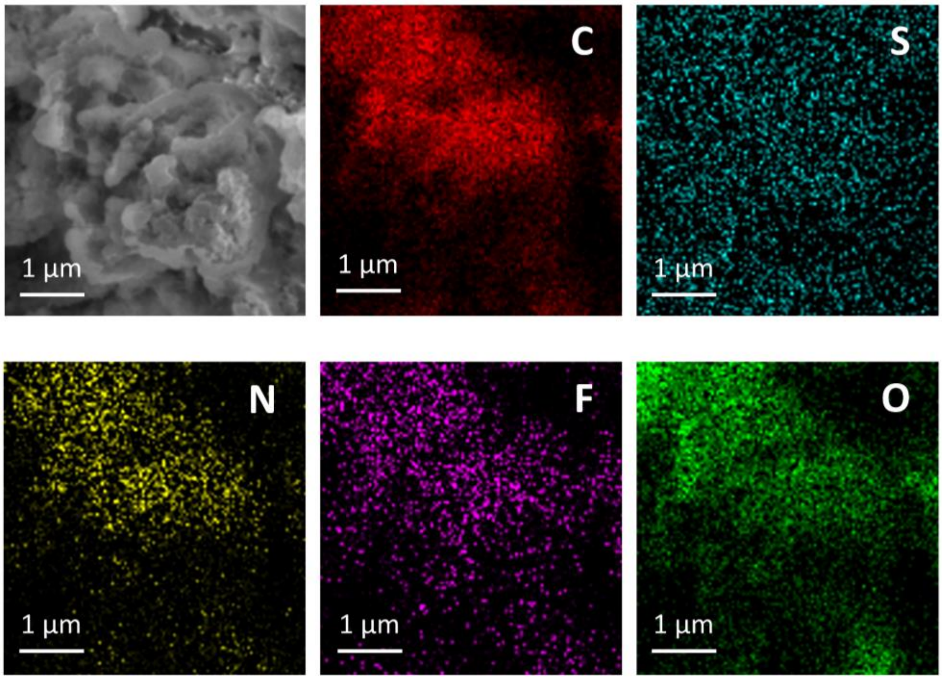

Figure 5.57 Post-mortem analysis: Ex-situ SEM image of PyTTF electrode (PyTTF-COF: Ketjenblack: PVDF = 60:20:20) discharged to 0.1 V in a half-cell configuration utilizing 1 M LiTFSI in PC:DEC 1:1 (v/v) and the corresponding energy dispersive X-ray analysis (EDX) mapping of elements carbon (C), sulfur (S), nitrogen (N), fluorine (F), and oxygen (O).

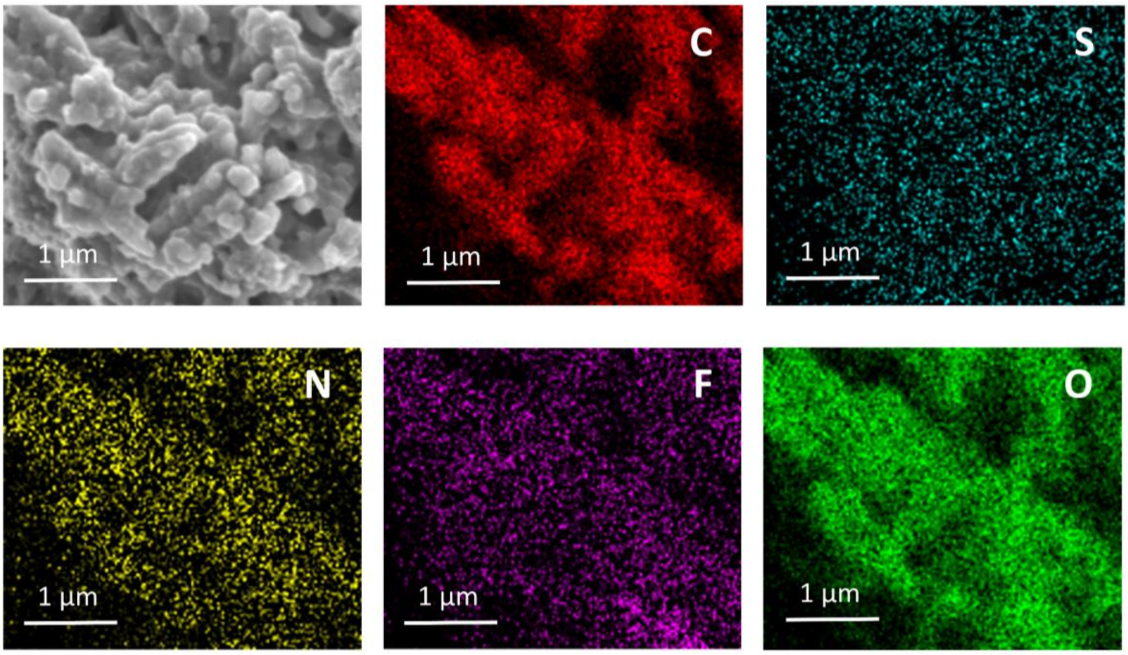

Figure 5.58 Post-mortem analysis: Ex-situ SEM image of PyTTF electrode (PyTTF-COF: Ketjenblack: PVDF = 60:20:20) charged to 3.6 V in a half-cell configuration utilizing 1 M LiTFSI in PC:DEC 1:1 (v/v) and the corresponding energy dispersive X-ray analysis (EDX) mapping of elements carbon (C), sulfur (S), nitrogen (N), fluorine (F), and oxygen (O).

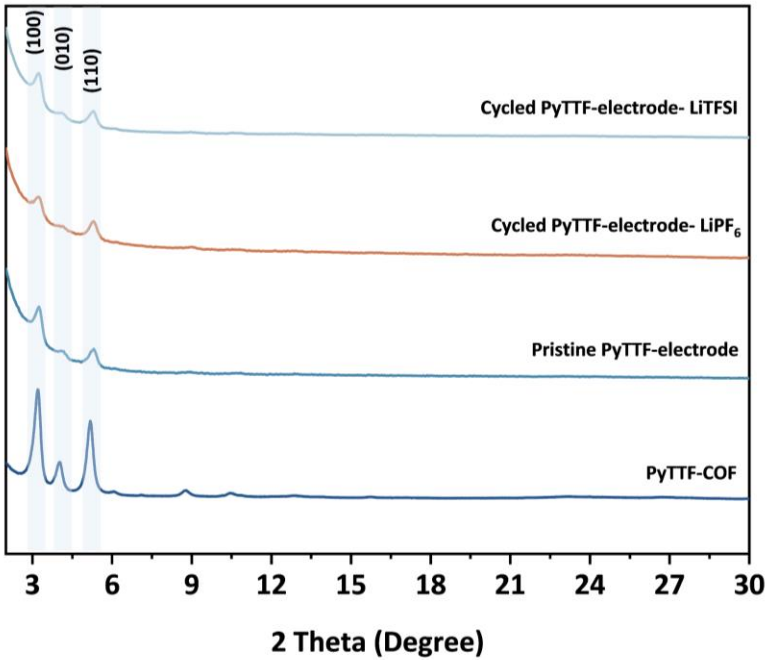

Figure 5.59. Ex-situ PXRD analysis of PyTTF-electrode (PyTTF-COF: Ketjen Black: PVDF = 60:20:20 wt.%) before and after 2 galvanostatic charge-discharge cycles at a current density of 0.3 A g^{-1} with most prominent peaks indexed to the corresponding (*hkl*) planes.

Table 5.7 Atom percentage of PyTTF pristine electrode before cycling, and PyTTF electrode after cycling utilizing 1 M $LiPF_6$ in PC:DEC 1:1 (v/v) and 1 M LiTFSI in PC:DEC 1:1 (v/v), obtained from EDX measurements, focusing on nitrogen (N), fluorine (F), sulfur (S), and phosphorus (P) content.

Elements	**Pristine**	**$LiPF_6$**		**LiTFSI**	
		0.1 V	**3.6 V**	**0.1 V**	**3.6 V**
N	39.11	13.59	13.39	25.70	31.53
F	5.66	15.13	16.15	10.15	17.74
S	55.23	67.38	62.50	64.16	50.73
P	/	3.90	7.96	/	/

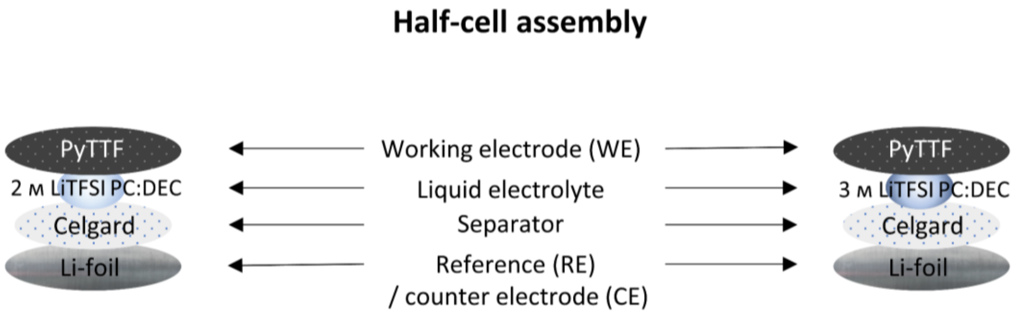

Figure 5.60 Schematic representation of half-cell assembly using PyTTF-COF as WE, 2 м LiTFSI in propylene carbonate (PC): diethyl carbonate (DEC) or 3 м LiTFSI in propylene carbonate (PC): diethyl carbonate (DEC) (1:1 v/v) as the liquid electrolyte, celgard as separator to avoid short-circuits, and Li-foil (thickness: 0.75 mm) as RE and CE.

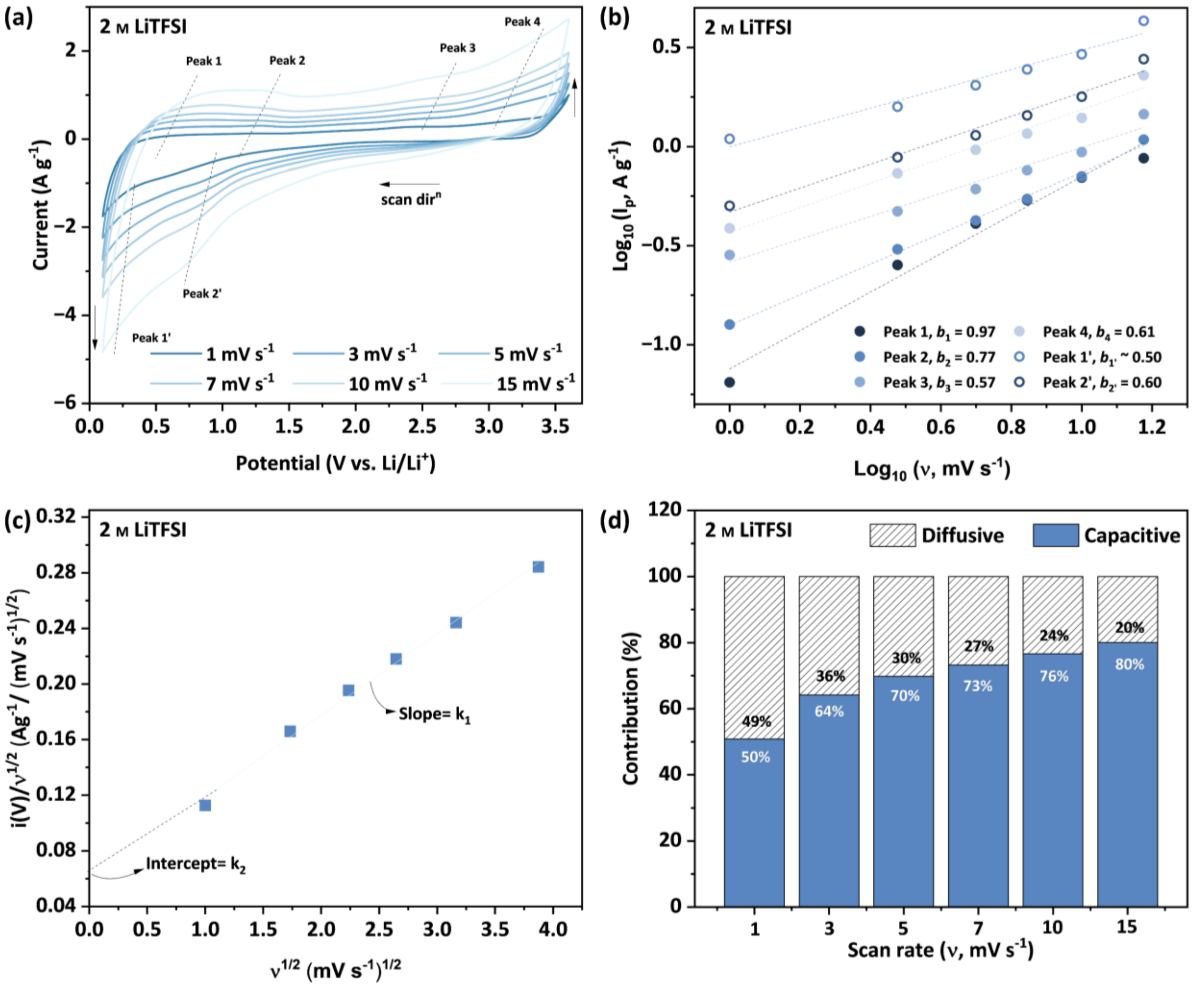

Figure 5.61 (a) Cyclic voltammogram of electrochemical Li-ion half-cells employing PyTTF-COF as WE, Li-foil as CE and RE, and 2 м LiTFSI in PC:DEC (1:1 v/v) as the liquid electrolyte, respectively, recorded at ν ranging from 1.0–15.0 mV s^{-1}, within the potential window 0.1–3.6 V vs. Li/Li$^+$. (b) The associated b-values obtained as the slope of log$_{10}$ (i_p) vs. log$_{10}$ (ν) with i_p corresponding to the most prominent redox peaks. (c) Determination of the values of k_1 and k_2 as the slope and intercept between $i(V)/\nu^{1/2}$ vs. $\nu^{1/2}$, where V = 1 V vs. Li/Li$^+$ during anodic sweep, and (d) the deconvolution of total charge-storage into diffusion-controlled and capacitive components as a function of applied ν.

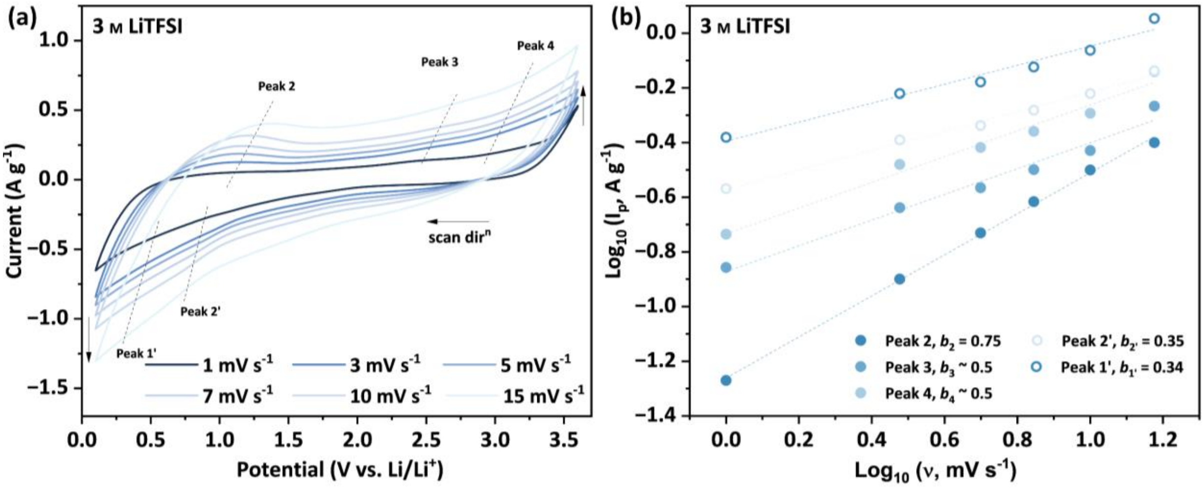

Figure 5.62 (a) Cyclic voltammogram of electrochemical Li-ion half-cells employing PyTTF-COF as WE, Li-foil as CE and RE, and 3 M LiTFSI in PC:DEC (1:1 v/v) as the liquid electrolyte, respectively, recorded at v ranging from 1.0–15.0 mV s^{-1}, within the potential window 0.1–3.6 V vs. Li/Li^{+}. (b) The associated b-values obtained as the slope of $\log_{10}(i_p)$ vs. $\log_{10}(v)$ with i_p corresponding to the most prominent redox peaks. Due to b-values ≤ 0.5, the deconvolution of total charge-storage into diffusion-controlled and capacitive components was not performed here.

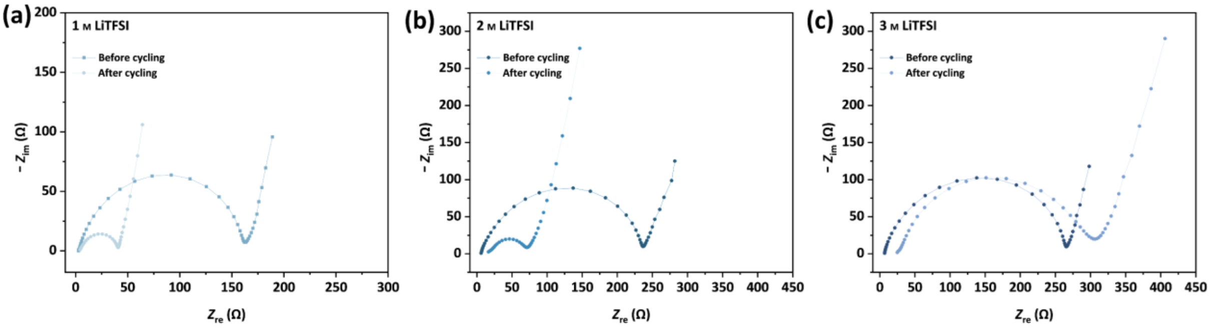

Figure 5.63 Nyquist plots for the electrochemical Li-ion half-cells employing PyTTF-COF as WE, Li-foil as CE and RE, and (a) 1 M LiTFSI, (b) 2 M LiTFSI, and (c) 3 M LiTFSI in PC:DEC (1:1 v/v), respectively, as the liquid electrolyte before and after CV cycles.

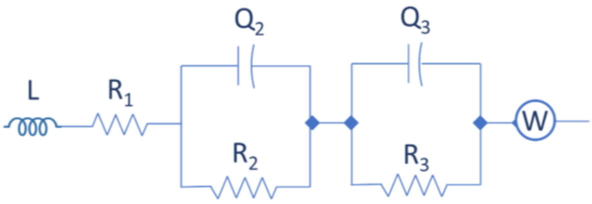

Figure 5.64 The equivalent electric circuit (ECC) utilized to fit the data obtained by the EIS measurements of the electrochemical Li-ion half-cells employing PyTTF-COF as WE, Li-foil as CE and RE, and 1 M LiTFSI, 2 M LiTFSI, and 3 M LiTFSI in PC:DEC (1:1 v/v), respectively, as the liquid electrolyte before and after CV cycles. L = inductor, R = resistance, Q = constant phase element, and W = Warburg element.

Table 5.8 Electrochemical impedance spectroscopy (EIS) analysis for the electrochemical Li-ion half-cells employing PyTTF-COF as WE, Li-foil as CE and RE, and 1−3 M LiTFSI PC:DEC (1:1 v/v), as the liquid electrolyte before and after CV cycles. Units are presented in the table notes.

	Potential	R_1	R_2	Q_2	n_2	f_2	R_3	Q_3	n_3	f_3	χ 2
1 M	Before	2.39	0.85	4.15E-07	1	4.48E+05	160.9	7.48E-06	8.49E-01	4.38E+02	5.26E-05
	After	3.46	4.47	1.07E-03	0.52174	4.49E+03	33.28	2.38E-05	0.86441	6.17E+02	1.51E-05
2 M	Before	5.82	35.9	1.65E-05	0.78775	1.98E+03	194.8	5.01E-06	0.88902	3.87E+02	7.77E-05
	After	13.8	9.10	7.27E-05	0.60976	2.60E+04	47.82	2.32E-05	0.84356	5.07E+02	1.95E-05
3 M	Before	6.62	58.6	1.04E-05	0.83502	1.12E+03	200.2	4.97E-06	0.91495	3.04E+02	2.81E-05
	After	24.02	4.76	1.15E-06	0.85208	2.39E+05	265.1	2.84E-06	0.83554	8.71E+02	2.51E-05

R_1= internal resistance (Ω), R_2= resistance (Ω) due to SEI (R_{SEI}), and R_3= resistance (Ω) due to charge-transfer (R_{ct}). Q_2= constant phase element ($\Omega^{-1}s^n$) associated with R_2, n_2 is the exponent associated with Q_2, f_2 is the frequency (Hz) associated with R_2, Q_2, and n_2. Q_3= constant phase element ($\Omega^{-1}s^n$) associated with R_3, n_3 is the exponent associated with Q_3, f_3 is the frequency (Hz) associated with R_3,Q_3, and n_3. Frequency was calculated using the following formula: f= $1/2\pi(RQ)^{1/n}$ (Hz). χ^2 represents the deviation of the observed data from expected values; a small value ($\chi^2 \leq 10^{-4}$) means a good fit, a large value ($\chi^2 \geq 10^{-4}$) means a poor fit.

5.6.7. References

[1] C. Choi, D. S. Ashby, D. M. Butts, R. H. DeBlock, Q. Wei, J. Lau, B. Dunn, *Nat Rev Mater* **2020**, *5*, 5.

[2] S. Fleischmann, J. B. Mitchell, R. Wang, C. Zhan, D.-E. Jiang, V. Presser, V. Augustyn, *Chemical reviews* **2020**, *120*, 6738.

[3] J. Wang, J. Polleux, J. Lim, B. Dunn, *J. Phys. Chem. C* **2007**, *111*, 14925.

[4] H. Lindström, S. Södergren, A. Solbrand, H. Rensmo, J. Hjelm, A. Hagfeldt, S.-E. Lindquist, *J. Phys. Chem. B* **1997**, *101*, 7717.

[5] J. E. B. Randles, *Trans. Faraday Soc.* **1948**, *44*, 327.

[6] A. Ševčík, *Collect. Czech. Chem. Commun.* **1948**, *13*, 349.

[7] Alexandros Ch. Lazanas, Mamas I. Prodromidis **2023**, *2*, 162.

[8] W. Choi, H.-C. Shin, J. M. Kim, J.-Y. Choi, W.-S. Yoon, *J. Electrochem. Sci. Technol* **2020**, *11*, 1.

[9] A. Singh, P. Bhauriyal, L. Quincke, D. Blätte, R. Guntermann, J. L. M. Rupp, T. Heine, T. Bein, *Advanced Energy Materials* **2025**.

[10] R. Nandan, N. Takamori, K. Higashimine, R. Badam, N. Matsumi, *ACS Appl. Energy Mater.* **2024**, *7*, 2088.

[11] S. Wang, J. Zhang, O. Gharbi, V. Vivier, M. Gao, M. E. Orazem, *Nat Rev Methods Primers* **2021**, *1*, 1.

[12] S. Bhunia, S. K. Das, R. Jana, S. C. Peter, S. Bhattacharya, M. Addicoat, A. Bhaumik, A. Pradhan, *ACS applied materials & interfaces* **2017**, *9*, 23843.

[13] D. Bessinger, L. Ascherl, F. Auras, T. Bein, *Journal of the American Chemical Society* **2017**, *139*, 12035.

[14] W. Li, Q. Huang, H. Shi, W. Gong, L. Zeng, H. Wang, Y. Kuai, Z. Chen, H. Fu, Y. Dong, C. Zhang, *Adv Funct Materials* **2024**, *34*, 2310668.

[15] L. Gong, X. Yang, Y. Gao, G. Yang, Z. Yu, X. Fu, Y. Wang, D. Qi, Y. Bian, K. Wang, J. Jiang, *J. Mater. Chem. A* **2022**, *10*, 16595.

[16] Q. Xu, Z. Liu, Y. Jin, X. Yang, T. Sun, T. Zheng, N. Li, Y. Wang, T. Li, K. Wang, J. Jiang, *Energy Environ. Sci.* **2024**, *17*, 5451.

[17] S. Gu, J. Chen, R. Hao, X. Chen, Z. Wang, I. Hussain, G. Liu, K. Liu, Q. Gan, Z. Li, H. Guo, Y. Li, H. Huang, K. Liao, K. Zhang, Z. Lu, *Chemical Engineering Journal* **2023**, *454*, 139877.

[18] Y. Liu, Y. Lu, A. Hossain Khan, G. Wang, Y. Wang, A. Morag, Z. Wang, G. Chen, S. Huang, N. Chandrasekhar, D. Sabaghi, D. Li, P. Zhang, D. Ma, E. Brunner, M. Yu, X. Feng, *Angewandte Chemie (International ed. in English)* **2023**, *62*, e202306091.

[19] M. Wu, Y. Zhao, R. Zhao, J. Zhu, J. Liu, Y. Zhang, C. Li, Y. Ma, H. Zhang, Y. Chen, *Adv Funct Materials* **2022**, *32*, 2107703.

[20] L. Yao, C. Ma, L. Sun, D. Zhang, Y. Chen, E. Jin, X. Song, Z. Liang, K.-X. Wang, *Journal of the American Chemical Society* **2022**, *144*, 23534.

[21] D. Geng, H. Zhang, Z. Fu, Z. Liu, Y. An, J. Yang, D. Sha, L. Pan, C. Yan, Z. Sun, *Advanced science (Weinheim, Baden-Wurttemberg, Germany)* **2024**, *11*, e2407073.

[22] L. Cheng, X. Yan, J. Yu, X. Zhang, H.-G. Wang, F. Cui, Y. Wang, *Advanced materials (Deerfield Beach, Fla.)* **2025**, *37*, e2411625.

[23] R. Kushwaha, C. Jain, P. Shekhar, D. Rase, R. Illathvalappil, D. Mekan, A. Camellus, C. P. Vinod, R. Vaidhyanathan, *Advanced Energy Materials* **2023**, *13*, 2301049.

[24] Q. Xu, K. Fu, Z. Liu, T. Sun, L. Xu, X. Ding, L. Gong, Q. Yu, J. Jiang, *Adv Funct Materials* **2025**, *1*, 2506111.

6

Summary and Perspective

To summarize, this thesis has been devoted to the design and the fabrication of COF-based battery components, accompanied by comprehensive investigations, through both experimental characterization and computational modeling, into how the individual COF molecular framework controls charge and ion transport, redox kinetics as well as storage mechanisms, and ultimately the rate capability of the electrochemical cells. The results elucidate the intrinsic correlation between structural topology and functional performance, offering deeper insights into structure–performance interplay, essential for advancing COF-based energy storage technologies.

The *first* research project of this thesis focuses on developing two COF-based quasi-solid-state electrolytes (QSSEs), undertaking a comprehensive exploration of their structural features, physicochemical properties, ion transport behavior, and diffusion mechanisms. Initially, two crystalline β-ketoenamine COFs, COF-TpPaSO$_3$Na and COF-TpPa(SO$_3$Na)$_2$, containing varying concentrations of sulfonate groups were synthesized. The sodiated COFs exhibit serrated stacking arrangements, with Na-ions interacting with the oxygen atoms of the sulfonate (O$_{\text{sulfonate}}$) and keto (O$_{\text{keto}}$) groups decorating the walls of the COFs. Further, QSSEs were subsequently prepared by incorporating *N*-methyl-*N*-propylpyrrolidinium bis(fluorosulfonyl)imide (Pyr$_{13}$FSI) ionic-liquid to the sodiated COFs at varying mass fractions. The molecular distribution models of Na$^+$, [FSI]$^-$, and [Pyr$_{13}$]$^+$ in the COFs revealed a preferable placement of [FSI]$^-$ near the pore wall, close to Na$^+$ ions and sulfonate groups, while [Pyr$_{13}$]$^+$ were predicted to be confined towards the center of the COF pore due to experienced electrostatic repulsion. The pristine COF TpPa(SO$_3$Na)$_2$ exhibited a higher ionic conductivity of 2.5×10^{-4} S cm^{-1}

than COF $TpPaSO_3Na$ with 2.0×10^{-4} S cm^{-1} at 50 °C, owing to the higher concentration of charged species available in the electrolyte sample. On the other hand, the composite ionogels containing COF $TpPaSO_3Na$ demonstrated higher ionic conductivity ranging between $2.1 - 5.6 \times 10^{-3}$ S cm^{-1} in comparison to the ionogels with COF $TpPa(SO_3Na)_2$, which displayed conductivity values ranging from $1.7 - 4.1 \times 10^{-3}$ S cm^{-1} at the equivalent ratios. The composite electrolyte $TpPaSO_3Na$@ $Pyr_{13}FSI$ exhibited a higher transport number of t_{Na^+} = 0.79, whereas $TpPa(SO_3Na)_2$@$Pyr_{13}FSI$ displayed a lower t_{Na^+} of 0.67, pointing to distinct diffusion mechanisms governed by the concentration of SO_3^- groups present in the COF skeletons. Ab initio molecular dynamics (AIMD) simulations elucidated that Na^+ transport in $Pyr_{13}FSI$ proceeds via a dual mechanism: a hopping process mediated by Na–$O_{sulfonate}$ interactions, and a vehicle-type mechanism involving solvated Na^+ species. Notably, solvated Na^+ ions exhibited faster diffusion in $TpPaSO_3Na$@$Pyr_{13}FSI$ ($D_{Na^+} \approx 13.00 \times 10^{-7}$ cm^2 s^{-1}) compared to more de-solvated ions in $TpPa(SO_3Na)_2$@$Pyr_{13}FSI$ ($D_{Na^+} \approx 7.06 \times 10^{-7}$ cm^2 s^{-1}), which primarily rely on a hopping mechanism. By strategically engineering the COF scaffold, charge-carrier diffusion within corresponding composite electrolytes can be precisely tuned, unlocking new pathways for the rational design of high-performance COF-based QSSEs.

The *second* research project focuses on the development of a novel bipolar 2D COF electrode, and investigation of its structural and electrochemical properties, and ultimately the adaptation of the bipolar COF electrode in varying battery configurations. A highly crystalline bipolar WTTF-COF was produced by combining two high-rate electroactive *p*-type building blocks, *N*,*N*,*N′*,*N′*-tetrakis(4-aminophenyl)-1,4-phenylenediamine (W) and 4,4′,4″,4‴-([2,2'-bi(1,3-dithiolylidene)]-4,4′,5,5′-tetrayl)tetrabenzaldehyde (TTF), through *n*-type imine (–C=N) linkages. Owing to the two strong electron donating units, and π-π interactions between inclined 2D COF layers, WTTF-COF exhibits an optical band gap of ~1.85 eV. The density functional theory (DFT) derived band structure revealed a relatively flat dispersion of valence band (VB) and conduction band (CB) in the *x*-*y* direction (planar), and a notable axial band dispersion and therefore high electronic mobility in the *z*-direction. The corresponding charge density distribution indicated the CB localization over the *n*-type imine linkage, while the VB involved the *p*-type units TTF and W. In Li-ion half-cells, the WTTF electrode demonstrated the highest stable potential window of 3.5 V, and one of the highest reversible specific capacities of 271 mAh g^{-1} at a current density of 0.1 A g^{-1} (~0.3C rate), recorded for a COF-based bipolar-type system without the inclusion of carbon nanotubes (CNTs). Additionally, the WTTF electrode exhibited stable cycling at an elevated current density of 1.0 A g^{-1} (~3C rate) with ~99 ± 1% coulombic efficiency maintained to at least 350 cycles, along with a surface-redox and pseudocapacitive intercalation charge storage mechanism, enabled by the presence of rapid kinetics of the redox-active moieties and the tunnel-like nanostructure. The conjunction of molecular electrostatic potential (MESP) analysis and DFT calculations revealed, per unit cell, a total of 12 e^- dual-ion storage, with 4 PF_6^- binding to the W and TTF units, forming $[WTTF][PF_6]_4$ in a charged (oxidized) state, while 4 Li^+ bind to the imine linkages and an additional 4 intercalate between the COF sheets, forming $[WTTF][Li]_8$ in the final discharged (reduced) state. The hybrid redox character of the WTTF electrode engenders anisotropic ion-transport behavior, with Li^+ ions preferentially diffusing within the 2D planes, and PF_6^- ions migrating along the axial COF channels, as predicted by the nudged elastic band (NEB) method. Experimentally, the effective diffusion coefficients (D) were determined to span 1.81×10^{-10} to 9.87×10^{-13} $cm^2\ s^{-1}$ across the operational potential window of 0.1–3.6 V vs. Li/Li^+, signifying efficient and tunable ionic transport within the framework. Finally, symmetric all-organic dual-ion full cells constructed with WTTF-COF electrodes demonstrated the intrinsic bipolar versatility of the WTTF electrode, operating effectively as both negative and positive electrodes. The electrochemical cells exhibited enhanced pseudocapacitive/capacitive charge-storage behavior, maintaining excellent reversibility and stability even at scan rates as high as 200 mV s^{-1}. The successful implementation of WTTF as a bipolar-type electrode in a fully symmetric configuration underscores the strong potential of COF-based materials for all-organic symmetric lithium-ion batteries, offering a promising route towards efficient and sustainable energy storage technologies.

The *third* research project builds upon and unifies the insights obtained from the preceding two studies, highlighting the intricate interdependence between the architectural design of COFs and the electrolyte environment, and thereby collectively governing the performance of both the COF electrodes and the resulting electrochemical cell. This project was designed to develop a comprehensive perspective that bridges the disciplines of emerging COF chemistry and more established Li-based energy storage, by approaching a cooperative and integrative framework, wherein the optimization of COF topology, electronic properties, and electrolyte composition occurs in tandem in an electrochemical cell, rather than in isolation. To this end, a novel highly crystalline 2D bipolar-type PyTTF-COF was constructed by connecting a new *n*-type 7,7',7'',7'''-(pyrene-1,3,6,8-tetrayl)tetrakis(benzo[*c*][1,2,5]thiadiazole-4-carbaldehyde) (PyBT) building unit and a *p*-type 4,4',4'',4'''-([2,2'-bi(1,3-dithiolylidene)]-4,4',5,5'-tetrayl)tetraaniline ($TTF-NH_2$) monomer via *n*-type imine linkages. The PyTTF bipolar COF was designed to exhibit a 16 e^- dual-ion redox chemistry per unit cell, with *n*-type centers, when reduced, capable of accommodating 14 Li^+, while *p*-type TTF unit, when oxidized, could store 2 counter anions (A^-). The extended π-conjugation in the donor–acceptor (D–A) architecture of PyTTF-COF resulted in a reduced optical band gap of ~1.84 eV, in comparison to the individual PyBT (2.20 eV) and $TTF-NH_2$ (2.40 eV) molecular building blocks. The electrochemical response of the PyTTF-COF electrode was first explored within a Li-ion half-cell configuration to unravel the role of anion identity in dictating charge-storage behavior. Two analogous liquid electrolytes, 1 M $LiPF_6$ and 1 M LiTFSI in a 1:1 (v/v) propylene carbonate (PC) and diethylene carbonate (DEC) mixture, were employed to probe the ionic interactions and their impact on dual-ion redox dynamics. Across both systems, the bipolar-type PyTTF electrode exhibited a broad and stable potential window spanning 0.1–3.6 V vs. Li/Li^+, alongside competitive rate capability. Notably, the LiTFSI-based system demonstrated markedly enhanced pseudocapacitive charge-storage kinetics and ion-diffusion characteristics relative to $LiPF_6$, yielding specific capacities of 286 mAh g^{-1} (LiTFSI) and 184 mAh g^{-1} ($LiPF_6$) at an applied current density of 0.3 A g^{-1} (~1C rate), revealing the anion as an active determinant of electrochemical performance. Further investigations, involving a systematic variation of LiTFSI concentration from 1–3 м, revealed a strong correlation between electrolyte composition, ion-storage dynamics, solution resistance (R_{sol}) and interfacial charge-transfer resistance (R_{ct}). Increasing salt concentration was observed to elevate the R_{ct} and R_{sol}, thereby impeding ion-transport kinetics and moderating overall charge-storage performance. Taken together, this study illuminates the dual importance of charge-carrier identity and concentration as governing parameters for optimizing bipolar COF electrodes.

Extending these concepts further, one can envision the realization of a fully COF-based all-organic battery, wherein both the electrodes and the electrolyte are constructed from covalent organic frameworks. In such a configuration, bipolar COF electrodes would function as both the cathodic and anodic components, leveraging their intrinsic ability to store cations and anions within a single redox-active architecture, as demonstrated in the second project. These could be seamlessly interfaced with a solid or quasi-solid-state COF electrolyte exhibiting high ionic conductivity and well-defined transport channels tailored for dual-ion mobility. Through rational molecular design and electrolyte engineering, it could be possible to modulate pore environments and functional groups to simultaneously enhance the conductivity of both ionic species, thereby achieving efficient charge balance and fast kinetics. Such a monolithic COF-based energy storage system could represent a transformative step toward lightweight, sustainable, safe, and entirely organic batteries, wherein structural precision and chemical modularity converge to define electrochemical performance at the molecular scale.

7

Publications and Conferences

Scientific Publications

- *Covalent Organic Framework Bipolar Pseudocapacitive Electrodes in an All-Organic Symmetric Lithium-Ion Battery.*

  Published as: **Apeksha Singh**, Preeti Bhauriyal, Lucie Quincke, Dominic Blätte, Roman Guntermann, Jennifer L.M. Rupp, Thomas Heine and Thomas Bein*, *Adv. Energy Mater.* **2025**, *15*, e01494

- *Tuning Redox Behavior of Pyrene–benzothiadiazole/TTF–Based Covalent Organic Framework Electrodes in Dual-Ion Batteries.*

  Apeksha Singh, Dominic Blätte, Roman Guntermann, Lucie Quincke, Jennifer L. M. Rupp, and Thomas Bein*

  Manuscript accepted in Angewandte Chemie

- *Unveiling the Sodium-Ion Diffusion Mechanism in Covalent Organic Framework−Based Quasi-Solid-State Electrolytes.*

  Apeksha Singh,‡ Preeti Bhauriyal,‡ Roman Guntermann, Thomas Heine, Thomas Bein*

  Manuscript in preparation

- *Redox-Active Microporous Covalent Organic Frameworks for Additive-Free Supercapacitors.*

  Published as: Roman Guntermann, Julian M. Rotter, **Apeksha Singh**, Dana D. Medina, Thomas Bein*, *Small Sci*. **2025**, *5*, 2400585

- *Tunable Isometric Donor-Acceptor Wurster-Type Covalent Organic Framework Photocathodes.*

  Published as: Roman Guntermann,‡ David Helminger,‡ Laura Frey, Peter M. Zehetmaier, Christian Wangnick, **Apeksha Singh**, Tianhao Xue, Dana D. Medina,* and Thomas Bein*, *Angew. Chem. Int. Ed.* **2024**, *63*, e202407166

- *Trioxoazatriangulene-Based Covalent Organic Frameworks as Electrodes for Lithium-Ion Batteries.*

  Fanni Fekecs, **Apeksha Singh**, Dominic Blätte, Thomas Bein, Manuel Souto*

  Manuscript in preparation

‡ These authors have contributed equally to the work.

*Corresponding author.

Conference Participation

- 36. Deutsche Zeolith Tagung (DZT) 2025, Erlangen, Germany – *Redox-active Covalent Organic Framework as Bipolar-type Electrode for Fast-charging Lithium-ion Batteries*. – ***Poster***
- Porous Materials in Energy Science 2024, Herrsching, Germany – *Covalent Organic Framework as Bipolar Electrode for Fast-charging Lithium-ion Batteries*. – ***Poster***
- 35. Deutsche Zeolith Tagung (DZT) 2024, Jena, Germany – *Redox-active Covalent Organic Framework as Bipolar-type Electrode for Fast-charging Lithium-ion Batteries*. – ***Poster***
- 5th European Conference on Metal Organic Frameworks and Porous Polymers (EuroMOF) 2023, Granada, Spain – *Designing Covalent Organic Framework-based Electrolyte for Fast Charging Sodium-ion Batteries. –* ***Oral***
- e-conversion Conference 2023, Tutzing, Germany – *Redox-active covalent organic framework as bipolar-type electrode for fast-charging lithium-ion batteries*. – ***Poster***
- e-conversion Graduate Program – winter retreat 2023, Bayrischzell, Germany – *Covalent Organic Framework-based Ionogel Electrolytes* for *Sodium-ion Batteries. –* ***Oral***
- 34. Deutsche Zeolith Tagung (34. DZT) 2023, Vienna, Austria – *Covalent Organic Framework and Ionic-liquid Composite Electrolyte for Directional Ion Transport in Sodium-ion Batteries. –* ***Oral***
- 8th International Conference on Metal-Organic Frameworks and Open Framework Compounds (MOF 2022) 2022, Dresden, Germany – *Covalent Organic Framework and Ionic-liquid Composite Electrolyte for Directional Ion Transport in Sodium-ion Batteries. –* ***Poster***
- 33. Deutsche Zeolith Tagung (33. DZT) 2022, Frankfurt, Germany – ***Networking***